The Modelling of Granular Flow Using the Particle-in-Cell Method

by

Corné J Coetzee

Dissertation approved for the degree of Doctor of Philosophy in Mechanical Engineering at Stellenbosch University

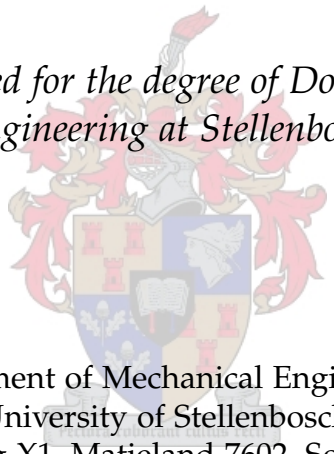

Department of Mechanical Engineering,
University of Stellenbosch,
Private Bag X1, Matieland 7602, South Africa.

Promoters:

Prof A.H. Basson	Prof P.A. Vermeer
Mechanical Engineering	Institut für Geotechnic
University of Stellenbosch	Universität Stuttgart

April 2004

Copyright ©2004 University of Stellenbosch
All rights reserved.

Declaration

I, the undersigned, hereby declare that the work contained in this dissertation is my own original work and that I have not previously in its entirety or in part submitted it at any university for a degree.

Signature: .....
CJ Coetzee

Date: .....

Abstract

The Modelling of Granular Flow Using the Particle-in-Cell Method

CJ Coetzee

Granular flow occurs in a broad spectrum of industrial applications that range from separation and mixing in the pharmaceutical industry, to grinding and crushing, blasting, stockpile construction, flow in and from hoppers, silos, bins, and conveyer belts, agriculture, mining and earthmoving.

Two totally different approaches of modelling granular flow are the Discrete Element Method (DEM) and continuum methods such as Finite Element Methods (FEM). Continuum methods can be divided into nonpolar or classic continuum methods and polar continuum methods. Large displacements are usually present during granular flow which, without remeshing, cannot be solved with standard finite element methods due to severe mesh distortion. The Particle-in-Cell (PIC) method, which is a so-called meshless method, eliminates this problem since all the state variables are traced by material points moving through a fixed mesh.

The main goal of this research was to model the flow of noncohesive granular material in front of flat bulldozer blades and into excavator buckets using a continuum method. A PIC code was developed to model these processes under plane strain conditions. A contact model was used to model Coulomb friction between the material and the bucket/blade. Analytical solutions, published numerical and experimental results were used to validate the contact model and to demonstrate the code's ability to model large displacements and deformations.

The ability of both DEM and PIC to predict the forces acting on the blade and bucket and the material flow patterns were demonstrated. Shear bands that develop during the flow of material were investigated. As part of the PIC analyses, a comparison between classic continuum and polar continuum (Cosserat) results were made. This includes mesh size and orientation dependency, flow patterns and the forces acting on the blade and the bucket.

It is concluded that the interaction of buckets and blades with granular materials can successfully be modelled with PIC. In the cases conducted here, the nonpolar continuum was more accurate than the polar continuum, but the polar continuum results were less dependent on the mesh size. The next step would be to apply this technology to solve industrial problems.

Keywords: Granular flow; Particle-in-Cell method; Discrete Element Method; Bucket filling; Silo discharging

Uittreksel

The Modelling of Granular Flow Using the Particle-in-Cell Method

CJ Coetzee

Partikelvloei kom voor in 'n verskeidenheid industriële toepassings vanaf skeiding en mengprosesse in die farmaseutiese industrie tot vergruising, die vloei in vulbakke en silos, vervoerbande, landboubewerkings, mynwese en grondverskuiwing.

Twee verskillende metodes om partikelvloei te modelleer kan onderskei word, naamlik Diskrete Element Metodes (DEM) en kontinuum metodes soos Eindige Element Metodes. Kontinuum metodes kan verdeel word in nie-polêre of klassieke kontinuum metodes en polêre kontinuum metodes. Groot verplasings is gewoontlik teenwoordig tydens partikelvloei wat dit moeilik maak om dit met behulp van Eindige Element Metodes op te los weens groot vervorming van die elemente. Die "Particle-in-Cell" (PIC) metode is 'n sogenaamde roosterlose metode wat hierdie probleem elimineer aangesien al die toestandsveranderlikes gekoppel is aan materiaalpunte wat deur die vaste rooster beweeg.

Die hoofdoel van die navorsing was om die partikelvloei van kohesielose materiale soos veroorsaak deur 'n plat lem en 'n masjiengraaf laaibak te modelleer deur van 'n kontinuum metode gebruik te maak. 'n PIC kode is ontwikkel om dié prosesse onder die aanname van vlakspanning the modelleer. 'n Kontakmodel is gebruik om Coulomb wrywing tussen die materiaal en die bak/lem te modelleer. Analitiese oplossings en gepubliseerde numeriese en eksperimentele resultate is gebruik om die kontakmodel en die vermoë van die kode om groot verplasings en vervormings te modelleer, te valideer.

Die mate waarin DEM en PIC die kragte wat op die lem en bak uitgeoefen word en die vloeipatrone, kan voorspel, word gedemonstreer. Glipvlakke wat gedurende die vloei van materiaal ontstaan is ondersoek. As deel van die PIC analises, is die nie-polêre en polêre (Cosserat) kontinua met mekaar vergelyk. Dit sluit in roostergrootte en oriëntasie onafhanklikheid, vloeipatrone en die kragte wat op die lem en bak inwerk.

Die gevolgtreking word gemaak dat die interaksie van bakke en lemme met 'n korrelrige materiaal suksesvol met behulp van PIC gemodelleer kan word. In die gevalle hier getoets, was die nie-polêre kontinuum meer akkuraat as die polêre kontinuum, maar die nie-polêre kontinuum resultate minder afhanklik van die roostergrootte. Die volgende stap sou wees om hierdie tegnologie in die industrie toe te pas.

Contents

List of Figures

List of Tables

Nomenclature

Symbol

A	area
a_i	initial position vector (Lagrangian formulation), direction cosines
a_1, a_2, a_3	Cosserat elasto-plasticity factors
b	base coordinate system
b_1, b_2, b_3	Cosserat elasto-plasticity factor
C	curve, speed of elastic wave propagation
C_i	vector resulting from a cross product operation
C_{ij}	damping matrix
c_i	body couple vector per unit mass
c^{cv}	geometric coefficients
D	Eulerian linear cubical dilation, damping ratio
D_{ij}	stiffness matrix containing the elastic moduli
$\tilde{D}$	Lagrangian linear cubical dilation
dS	differential surface element
dt	differential time increment
d_{50}	mean grain diameter
dV	differential volume element
E	Young's modulus
E_{ij}	Eulerian nonlinear strain tensor, transformation matrix
e_{ij}	Eulerian linear strain tensor
F_i	body force
f	general function, yield function
f_i	body force per unit mass, nodal force
$\tilde{f}_i$	body force per unit volume
G	shear modulus
G^c	Cosserat shear modulus
G_i	general function
g	potential (flow) function
h	height, depth, element size
h_i	angular momentum vector
h_i^c	spin angular momentum vector (Cosserat continuum)
I	integrand
i	counter, index

J	determinant of the Jacobian tensor
J_{ij}	Jacobian matrix
J_2	second invariant of deviatoric stress tensor
J_2'	second invariant of deviatoric strain tensor
j	counter, index
K	bulk modulus
K_o	coefficient of earth pressure at rest
k_{ij}	stiffness matrix
k_ϕ	Drucker-Prager material constant
L_{ij}	Lagrangian nonlinear strain tensor
l	length, depth, Cosserat characteristic length
l_{ij}	Lagrangian linear strain tensor
M	mass
M_i	moment vector
M_{ij}	mass matrix
m_i	surface couple moment
m_p	material point (particle) mass
N	normal component of the stress vector
N_i	vector containing shape functions
N_{dof}	total number of degrees-of-freedom
N_{ep}	total number of particles within element
N_p	total number of particles in the system
N_ϕ	Mohr-Coulomb constitutive model friction parameter
N_ψ	Mohr-Coulomb constitutive model dilatancy parameter
n_i	unit normal vector, direction cosines
n	general number
O	origin
p	generalised normal stress component
p_i	linear momentum
q	generalised tangential stress component
q_ϕ	Drucker-Prager friction property
q_ψ	Drucker-Prager dilatancy property
r_i	position vector, element equivalent load vector
S	surface, shear component of the stress vector
s	coordinate system
s_{ij}	deviatoric stress tensor
t	time
t_i	tangential unit vector at contact node
u_i	displacement vector
V	volume
v_i	velocity vector

W	weighing factor
w_i	Eulerian linear rotation vector, test function (weak form)
w_i^c	Cosserat rotational degree-of-freedom
w_{ij}	Eulerian linear rotation tensor
$\tilde{w}_{ij}$	Lagrangian linear rotation tensor
X_i^p	material point initial position vector
x	coordinate direction
x_i^p	material point position vector
x_i	general position vector
y	coordinate direction
z	coordinate direction

Greek

α	angle, non-viscous damping ratio
$\alpha_1, \alpha_2, \alpha_3$	elastic variables
β	angle, elastic variables, drag angle (draglines)
γ	hardening factor
Δ	increment
Δt	time step (increment size)
δ	Dirac delta function
ϵ	lumping factor
ε_i	vector containing strain components
ε_i^c	vector containing Cosserat strain components
ε_p	generalised volumetric strain component
ε_q	generalised shear strain component
ζ_i	vorticity vector
η	element local coordinate direction
θ	general angle
κ_{ij}	Cosserat curvature tensor
λ	plastic multiplier
λ_{ij}	Cosserat tensorial deformation measure
μ	contact friction coefficient
μ_i	couple-stress vector
μ_{ij}	couple-stress tensor
μ_{ij}^s	specific couple-stress tensor
ν	Poisson's ratio
ξ	element local coordinate direction
ρ	material density
ρ_c	density at element centre
ρ_0	initial material density
$\tilde{\rho}_0$	initial discrete density

σ	magnitude of the stress vector, normal stress on a surface
σ_c	normal stress at centre of Mohr circle
σ^t	tensile limit
σ_i	Cauchy traction vector (stress vector)
σ_i^c	vector containing Cosserat stress components
σ_{ij}	Cauchy stress tensor
σ_{ij}^s	specific stress tensor
$\sigma_1, \sigma_2, \sigma_3$	principal stresses
τ	shear stress on surface
τ_i	surface traction
ϕ	scalar variable
ϕ_i	surface traction vector, test function (weak form)
ψ_{ij}	rate of strain tensor
Ω	eigenvector size
Ω_i	Cosserat relative rotation vector, rotation vector
ω_{ij}	vorticity tensor

Operators

D_c	discrete divergence operator
G_c	discrete gradient operator
δ_{ij}	Kronecker delta
ε_{ij}	permutation symbol
∇_{ij}	del operator

Chapter 1

An Introduction: Modelling of Granular Flow

1.1 Introduction

Those involved in modelling tend to become more interested in the process than its purpose: The stimulation of simulation is greater than the pleasurement of measurement - but it makes you blind (Wood, 2000).

Granular flow occurs in a broad spectrum of industrial applications. These range from separation and mixing in the pharmaceutical industry, to grinding and crushing, blasting, stockpile construction, generic flows in and from hoppers, silos, bins, conveyer belts and many more. The worldwide annual production of grains and aggregates of various kinds is gigantic, reaching approximately ten billion metric tons. The processing of granular material consumes roughly 10% of all the energy produced on this planet and on the scale of priorities of human activity it ranks second, immediately behind the supplying of water (Rhodes, 1998). As such, any advance in understanding the physics of granular material is bound to have a major economic impact. Not much has been optimised, despite the fact that methods of transport, storage and mixing figure in all stages of the industrial processing of granules.

Granular materials such as sand and clay are complex materials that exhibit both solid and fluid properties. There are three reasons for this. The first is that geomechanic materials, such as soil, are three-phase mixtures of solid, liquid and gas. The second is that granular materials are not a continuous body in the microscopic scale, but consist of many discrete particles that have complex interactions. The third is that natural soil is not homogeneous. It is necessary to construct relevant theories for granular materials to analyse their behaviour. There are two common approaches to formulating the behaviour of granular materials: A microscopic approach considering a completely discrete structure and a macroscopic approach based on continuum mechanics. However, a complete theory for granular materials has not yet been proposed. In addition, it is worth noting that these two types of approaches are complementary and have their respective roles in the modelling of granular material behaviour.

This chapter summarises the results of a literature study on the different theories of modelling granular material. The thesis goals and outline are also presented.

1.2 Theories for Modelling Granular Materials

The advantages and disadvantages of the Discrete Element Method (DEM) and continuum modelling of granular material are discussed. The differences between the classic (nonpolar) continuum and polar continuums are also presented.

1.2.1 Discrete Element Methods

The discrete element methods are based on the simulation of the motion of granular material as separate particles. It involves following the trajectories, spins and orientations of all the particles and predicting their interactions with other particles and with their environment.

DEM was introduced by Cundall in 1971 for the analysis of rock mechanics problems and then applied to soils by Cundall & Strack (1979). Calculations performed during a DEM simulation alternate between the application of Newton's second law to the particles and a force-displacement law at the contacts. The motion of each particle is calculated by applying Newton's second law to each particle, while the force-displacement law is used to update the contact forces arising from the relative motion at each contact.

DEM has the advantage that it can easily be used for the simulation of granular flow subjected to large deformations and free boundaries. Segregation and mixing which are experienced when vibration is introduced can also be modelled (Cleary *et al.*, 1998). The main problem with the discrete element methods is how to specify the micro-properties (particle contact properties) so that the flow on macro-level of thousands of particles behaves in the same way as real granular flow. Laboratory experiments (e.g. shear tests, biaxial tests and oedometer tests) are necessary to determine these properties before any useful modelling and predictions can be made.

DEM research is focused on the representation of the particle shape, contact detection between particles and between particles and the environment, contact force models, experimental calibration, validation and industrial application.

The choice of particle shape representation in DEM is critical to the accuracy of the simulation of real particle behaviour, the method used for contact detection and the method of computation of contact forces (Favier *et al.*, 1999). The earliest discrete models were two-dimensional and employed either circular (Cundall and Strack, 1979) or polygonal elements (Walton, 1982). Later work extended shape representation to three dimensions, using spheres, ellipses and ellipsoids. Contact detection and computation time are very important and the time spent by a code in dealing with contact detection ($\pm$80%), far exceeds that involved with solving the equations of Newtonian physics (Williams and O'Connor, 1995). The more

complex the particle shape, the more difficult and time consuming contact detection and the calculation of contact forces become. Although contact detection and computation time are very important, the critical objective in DEM is accurate simulation of the behaviour of an assembly of real particles. The influence of particle shape on the predicted behaviour is less well documented than the relationship between shape and the efficiency of contact detection.

One of the main fields of research is to develop and verify different contact constitutive models. It is mainly these different constitutive or contact models that distinguish between different DEM models. Different contact and damping models have been proposed. Cundall & Strack (1979) represented the contact force with a linear spring and used a viscous damper (dashpot) to dissipate energy. The viscous damping was later replaced by hysteretic damping. Walton & Braun (1986) made use of a partially-latching-spring mechanism in the contact normal direction. Mindlin (1949) and Mindlin & Deresiewicz (1953) based their formulation on the Hertz contact model, which is derived from the principle of elasticity of two spheres in contact. This results in a non-linear formulation of the contact force. The size of a system (number of particles) and the complexity of the contact laws that can be modelled, strongly depend on the computer power available.

Cleary (2000, 1998*a*, 1997) and Cleary & Sawley (1999) are some of the researchers that have successfully modelled industrial granular flows with large displacements using DEM. They have modelled ore segregation on conveyer belts, the functioning of ball mills and dragline bucket filling. Coetzee (2000) modelled the two-dimensional flow of granular material in front of a blade (bulldozer) and the flow of granular material into a dragline-type bucket. Nouguier *et al.* (2000) and Bohatier & Nouguier (1999, 2000) investigated dynamic soil-tool interaction forces. Bohatier & Nouguier (2000) investigated the interaction between a two-dimensional granular assembly and a flat blade using DEM. The results were compared to a simple analytical model. Nouguier *et al.* (2000) performed similar simulations but in three dimensions. Bohatier & Nouguier (1999) compared DEM results with continuum results and conclude that the continuum approach seems well adapted to the case of cohesive soils like clay, whereas the discrete approach is probably a better approach for modelling sand or gravel.

1.2.2 Continuum Theory

Many problems in engineering mechanics are concerned with the behaviour of matter in motion or in equilibrium under the action of externally applied forces in various environments. A material body may be envisioned as a collection of a large number of *deformable particles* (subcontinua or

microcontinua) that contribute to the macroscopic behaviour of the body (Eringen, 1999). For engineering purposes, it is usually possible to study the behaviour of a material body by assuming the matter to be totally continuous. This simplifying assumption means that the *particle* structure of matter is disregarded, and the matter is pictured without gaps or empty spaces. Such study of the behaviour of matter can be accomplished by applying the classical laws of mechanics and thermodynamics that relate the properties of matter at a point. A material that can be treated this way is called a *continuum*, or *continuous medium*, and the theory describing the behaviour of such a material is called *continuum mechanics* or the *theory of a continuous medium* (Frederick and Chang, 1972).

The interest of developing continuous models for discrete structures is that discrete type analyses are very computer time intensive and, at least for periodic structures, one might argue that a homogenised continuum model would allow for a much more elegant and efficient solution. A continuum approach can be used to incorporate constitutive models such as visco-plasticity and strain-softening and -hardening. Shear bands can be observed which is difficult to capture with a DEM model (Coetzee, 2000).

The formulation of the classical continuum is found in most textbooks on elasticity and continuum mechanics (Frederick and Chang, 1972; Boresi and Chong, 2000; Malvern, 1969; Timoshenko and Goodier, 1970). In this theory every point in the continuum has three translational degrees-of-freedom. This formulation is good enough when material such as steel or other metals are modelled.

In granular materials the discreteness of the system is often important and rotational degrees of freedom are active, which might require enhanced theoretical approaches like microcontinua (Herrmann, 1999). The concept of microcontinuum naturally brings a length scale into the continuum theory. The response of the continuum body is influenced heavily with the ratio of the characteristic length λ (associated with external stimuli) to the internal characteristic length l (Eringen, 1999). When $\frac{\lambda}{l} \gg 1$, the classical continuum theory gives reliable predictions since a large number of particles act collaboratively. However, when $\frac{\lambda}{l} \simeq 1$, the response of the microcontinua (particles) becomes important. There are many other natural substances which also clearly point to the necessity for microcontiua (Eringen, 1999). Suspensions, blood flow, liquid crystals, porous media, polymers, solids with microcracks, slurries and composites are a few examples which require consideration of the motion of their microconstituents, e.g., blood cells, suspended particles, fibres, grains, crystals, etc.

In polar continuum theories, the material points are considered to possess orientations. Eringen (1999) classified the different polar theories as follows: A material point carrying three deformable directors (*micromorphic continuum*) introduces nine extra degrees of freedom over the classical theory. When the directors are constrained, then we have *microstretch con-*

tinuum, and the extra degrees of freedom are reduced to four: three microrotations and one microstretch. In *micropolar (polar) continuum*, a point is endowed with three rigid directors only. A material point is then equipped with three degrees of freedom for rigid rotations only, in addition to the classical translational degrees of freedom. Eringen (1999) describes these three continuums (called $3M$ continua) in detail.

It appears that there is a considerable scatter in opinions concerning the appropriate formulation of a micropolar continuum theory. Some authors advocate a constrained (dependent) formulation taking into account the continuum rotations in order to incorporate higher displacement gradient effects (Steinmann, 2000). On the other hand, some authors prefer to formulate a polar continuum theory in terms of an unconstrained (independent) rotation field.

Steinmann (2000) highlights the variational interrelation between these two prominent formulations of polar continua: the gradient type continuum with constrained rotations and the Cosserat continuum with unconstrained rotations. Because of the additional rotational degrees-of-freedom, nonpolar constitutive laws cannot be used with polar continua. The nonpolar constitutive laws must be adapted to include the rotational degrees-of-freedom which leads to new laws such as polar elasticity and polar plasticity. The rotations are induced by couple stresses within the continuum. The presence of couple stresses result in a stress tensor, which is no longer symmetric as in the case of a nonpolar continuum. In the case of a Cosserat continuum where the rotations are unconstrained, the rotations are called Cosserat rotations and the couple stresses are called Cosserat couple stresses.

The Cosserat continuum is the most transparent and straightforward extension of nonpolar continuum models (de Borst, 1991). The Cosserat continuum was proposed as early as in 1909 by E. and F. Cosserat. Probably because of its relative complexity, it received little attention. Nevertheless, renewed interest arose after a dormant period of some 50 years, primarily due to the works of Mindlin (1964) and Toupin (1962). These researchers were attracted by the theoretical challenges and beauties of nonconventional continuum theories. Large-scale numerical computations were, obviously, not possible in those years. These contributions have considerably broadened the original concept of the Cosserat brothers and the terminology *polar elasticity* has become the vogue to describe these extended or generalised elasticity theories. Yet, interest died in the late 1960's, probably because of the inherent complexity of the theory, which results in a governing set of differential equations that is analytically insoluble except for the most simplest cases. Other arguments against the use of polar elasticity were put forward by Koiter who unfortunately based his conclusions on a rather special type of polar elastic solid, which may have blurred a proper assessment (de Borst, 1993).

There are two reasons why the applicability and usefulness of the Cosserat continuum should now be viewed differently than a few decades ago. First, there is the development of numerical methods, which makes that the degree of complexity that is inherent in polar solids is only marginally greater than in conventional continuum models. Secondly, renewed interest for polar continua arose recently within the context of inelastic localisation computations where boundary layer effects prevail. It is well-known that the nonpolar modelling of materials exhibiting softening, leads to mesh dependence of the post peak response when the deformation pattern is limited to a highly localised zone (Steinmann, 2000).

The Cosserat approach was *rediscovered* mainly by researchers (Muhlhaus and Vardoulakis, 1987) looking for a remedy for this deficiency of numerical computations within the nonpolar continuum theory since it turned out that rotations are an essential ingredient in failure zones where shear failure mechanisms play a dominant role. Oda (1993) observed the presence of rotations and couple stresses in shear zones during experimental shear tests.

The Cosserat continuum possesses some significant advantages compared to the discrete element method (Dai *et al.*, 1996). For example, it is flexible and economical when used with numerical methods. Cosserat elements (with rotational degrees-of-freedom and the conventional translational degrees-of-freedom) can be implemented into conventional finite elements without the necessity of interface elements as used in hybrid codes, which combine finite elements and discrete elements. Typical computer times required for problem solutions are about 50% higher than the computer times of nonpolar continuum analyses, whereas in the case of the discrete method the time increase may be 10-100 times. Because the Cosserat continuum deals with the discontinuum as a continuum, most of the concepts and methodology of conventional continuum mechanics can be used in a straightforward fashion.

Tejchman & Wu (1996) numerically investigated the localisation of shear bands in dry sand during biaxial compression tests with a finite element method using a hypoplastic constitutive law. The hypoplastic constitutive law was established within the frame of a classical (nonpolar) continuum. The calculations were carried out with an initial imperfection in the form of a weak element in the mesh. The numerical results showed that a hypoplastic model could be useful for investigating the shear zones inside granular bodies. The calculated thickness of the shear zone and the calculated inclination of the shear zone inside the sand specimen were found, however, to be dependent on the spatial discretisation. The calculated thickness was equal to the dimensions of the finite elements, and the calculated inclination of the shear zone corresponded to the orientation of the mesh lines. Loss of ellipticity of field equations describing the body motion when using nonpolar softening constitutive laws, related to the absence of a characte-

ristic length, is the reason for the mesh size and mesh alignment dependence. The shortcoming of nonpolar laws for investigating localisation in granular materials can be overcome with the aid of a Cosserat continuum, which enables a characteristic length to be included into the constitutive relation. In this case, numerical results converged to a finite size of the shear zone upon mesh refinement (Tejchman and Bauer, 1996). The numerical results show that the polar hypoplastic model implemented in a finite element code can be useful for investigating the shear zones inside granular materials. The calculated results of biaxial compression tests are in good agreement with the experimental data. The difference between the nonpolar continuum and Cosserat continuum formulations is significant in the shear zone, wherein the Cosserat rotations and the couple stresses are noticeable. The stress tensor is nonsymmetric here. Outside the shear zone, the Cosserat effects (Cosserat rotations and couple stresses) are negligible (Tejchman and Bauer, 1996).

Muhlhaus & Vardoulakis (1987) and Muhlhuas & Hornby (1997) assumed that slow granular flow could be described within the framework of an incremental Cosserat plasticity theory (plasticity theory adapted for the Cosserat continuum). They predicted shear band thickness of the order of 10-20 average grain diameters, a result that is in good agreement with the range of shear band thicknesses observed in experiments. Cerrolaza *et al.* (1999) developed Cosserat non-linear finite element analysis software for blocky structures. Cramer *et al.* (1999) also used a Cosserat finite element method to solve elasto-plastic problems with associated and non-associated flow rules. In non-associated plasticity, localisation phenomena are encountered which may lead to an ill-posed problem when the nonpolar continuum theory is used. Their results demonstrated the superior behaviour of the Cosserat continuum in contrast to the classical continuum, which leads to strain concentrations in shear bands of finite width. Other researchers (de Borst, 1993; Iordache and Willam, 1998) have also shown that the Cosserat continuum gives better results when strain-softening, strain-hardening, localisation and shear banding are present.

The Cosserat continuum has also been used to model practical problems and industrial granular flow. Adhikary *et al.* (1999) modelled large deformations in stratified media and Tejchman & Gudehus (1993) and Tejchman (1996) modelled silo filling. Comparison between the numerical calculations and the experimental results shows rather satisfactory agreement. The Cosserat effect was also observed to be significant in the shear zones, which are created along the silo walls. In a shear zone, Cosserat rotations and couple stresses are noticeable. Outside a shear zone, Cossserat effects are negligible. Thus, the Cosserat rotation is a suitable indicator of shear zones (Tejchman, 1996). The calculated thickness of the shear zones was also realistic.

Fatemi & van Keulen (2002) presented a three-dimensional finite ele-

ment model based on the Cosserat continuum theory for stress analysis in bone structures. The internal length scale is incorporated to account for the microstructural effects on the macroscopic behaviour of bone. It is observed that stress and strain distributions predictions based on Cosserat theory significantly differ from classical theory, especially in areas with high gradient of deformations.

1.3 Numerical Methods

The use of the Finite Element Method (FEM) to specifically model problems related to soil mechanics and granular flow is discussed. The disadvantages of FEM and the need for meshless methods are presented.

1.3.1 The Finite Element Method

Well-known numerical methods that are available to solve the partial differential equations of the continuum formulation are FEM and the finite difference method. Over the last 25 years, the finite element method has developed into the industry standard for solving a wide variety of solid mechanics problems. The problem of computational mechanics however grows more challenging. For example, in the simulation of manufacturing processes such as extrusion and molding, it is necessary to deal with extremely large deformations of the mesh while in computations of castings the propagation of interfaces between solids and liquids is crucial. In simulations of failure processes, we need to model the propagation of cracks with arbitrary and complex paths.

These problems are not well suited to conventional computational methods such as FEM or finite difference methods. The underlying structure of these methods, which originates from their reliance on a mesh, is not well suited to the treatment of discontinuities, which do not coincide with the original mesh lines. In fracture problems, for instance, element edges provide natural lines along which cracks can grow. This is advantageous if the crack path is known a priori, but in most complex fracture phenomenon the crack path is unknown. Thus, the most viable strategy for dealing with moving discontinuities in methods based on meshes is to remesh in each step of the evolution so that mesh lines remain coincident with the discontinuities throughout the evolution of the problem. This can, of course, introduce numerous difficulties such as the need to project between meshes in successive stages of the problem, not to mention the burden associated with a large number of remeshings (Belytschko *et al.*, 1996).

FEM is also not sufficiently robust in the case of large strains, because it leads to excessive distortions of the element mesh. As a remedy, remeshing techniques may be used but all the state variables have to be mapped from

the distorted mesh to a newly-defined one. Such a kind of mapping introduces additional computational errors and makes them ineffective (Wieckowski, 2002).

FEM has successfully been applied in the geo-environment to solve problems where the strains remain relatively small. Goh (1993) modelled a cantilever retaining wall under static conditions. Chi & Kushwaha (1991) investigated the three-dimensional forces on a soil tillage tool at the point of soil failure. Their results were in agreement with experimental results. The authors mentioned above, used the classical continuum formulation. Other authors have used FEM based on the Cosserat formulation. Cramer *et al.* (1999) used a finite element method that employs mesh refinement strategies based on both the classical continuum and the Cosserat continuum. They modelled a strip footing on cohesive soil and slope stability of cohesionless soil. They obtained good results and showed that the Cosserat continuum has superior behaviour in contrast to the standard continuum in those applications. Tejchman (1996) implemented the Cosserat continuum into a finite element method to investigate the filling of a silo. The numerical simulation of the filling process in the silo models was performed in such a way that the entire weight of the silo fill was incrementally fed into the silo, i.e. element layer by element layer. The calculated stresses were found to be in accordance with the experimental data. Tejchman & Bauer (1996) investigated shear band formation in dry sand during biaxial compression and used a Cosserat finite element method. Adhikary *et al.* (1999), Iordache & Willam (1998) and de Borst (1991) have also based their finite element methods on the Cosserat continuum, but did not apply it to geomechanics problems. In all of the above examples, the displacements and deformations were small enough to be modelled with a standard finite element method.

Some authors have used FEM and applied remeshing successfully. Bohatier & Nouguier (1999) modelled soil cutting using software developed for metal forming or cutting which incorporates an efficient automatic remeshing procedure. They, however, excluded gravity because the software did not take it into account. They compared their results to that of similar DEM simulations and obtained good qualitative agreement of the displacements and velocity fields. Remeshing can however be problematic where history-dependent material properties are present (Sulsky *et al.*, 1995).

The objective of meshless methods is to eliminate at least part of the mesh structure by constructing the approximation entirely in terms of nodes (Belytschko *et al.*, 1996). However in many meshless methods, recourse must be taken to meshes in at least parts of the method. Thus, it becomes possible to solve large classes of problems (e.g. large deformations, cracks and discontinuities) that are very awkward with mesh-based methods.

1.3.2 Meshless Methods

Although meshless methods originated about twenty years ago, little research effort has been devoted to them until recently. The starting point, which seems to have the longest continuous history, is the smooth particle hydrodynamics (SPH) method presented by Lucy (1977), who used it for modelling astrophysical phenomena without boundaries such as exploding stars and dust clouds. Compared to other methods in these times, the rate of publications was very modest for many years and is mainly reflected in the papers of Monaghan and co-workers (Monaghan, 1982, 1988). In these papers, the method was explained as a kernel estimate to provide a more rational basis. However, except for some estimates on the accuracy of the kernel estimate, which is not directly relevant to the accuracy of the method in the solution of partial differential equations, there was little in the way of estimation of the accuracy of the method.

Recently there has been substantial improvement in these methods. Swegle *et al.* (1995) have shown the origin of the so-called tensile instability through a dispersion analysis of the linearised equations and proposed a viscosity term to stabilise it. Johnson & Beissel (1996) have proposed a method for improving the strain calculation. Liu *et al.* (1995) have proposed a correction function for kernels in both the discrete and continuous case.

A parallel path to constructing meshless approximations, which commenced much later, is the use of moving least square approximations. Nayroles *et al.* (1992) were evidently the first to use moving least square approximations in a Galerkin method called the diffuse element method. Belytschko *et al.* (1994) refined and modified the method and called their method, element-free Galerkin. This class of methods is consistent and, in the forms proposed, quite stable, although substantially more expensive than SPH.

Other methods such as SPH, FLIP (Fluid-Implicit Particle, Brackbill & Ruppel (1988)) and Particle-in-Cell (PIC, Sulsky *et al.* (1995)) are called particle methods. Particle methods can be characterised as methods where the solution variables are attributed to Lagrangian point masses instead of computational cells (Benson, 1992). The particle methods were originally used for fluids but can be applied to solids.

1.3.3 The Particle-in-Cell Method

Sulsky *et al.* (1995) developed a particle-in-cell method (called Material-Point-Method, MPM) applicable to solid mechanics that can be used to model impact, penetration and large deformations. Their formulation is an extension of the FLIP particle-in-cell method. The particle-in-cell method represents a material by Lagrangian mass points, called particles, moving through a computational grid (finite element or finite difference). The clas-

sical PIC method (Harlow, 1964) is partially Lagrangian in that only a mass and position is attributed to each particle. This procedure is highly successful in tracking contact discontinuities and modelling highly distorted flow. However, to reduce the amount of numerical dissipation, the MPM method has been developed in which each particle is attributed all the properties of the material, including momentum and energy and is sometimes referred to as a "full-particle" method.

In the PIC method, a single-valued velocity field is used which precludes the interpenetration of two bodies or any two media with different path-independent constitutive relations. This no-slip condition between different bodies is contained in the basic algorithm at no additional cost. Bardenhagen *et al.* (2000) developed a contact model that still forbids interpenetration of different bodies, but allows separation and sliding and rolling with friction.

Wieckowski and co-workers presented several papers on PIC modelling of silo filling and discharging (Wieckowski, 2002, 2001, 2000; Wieckowski *et al.*, 1999; Wieckowski, 1998). They used a classic continuum approach under plane strain and axisymmetric conditions. Drucker-Prager elastio-plastic and hypoplastic constitutive models were employed with Coulomb friction between the material and the silo walls. The results of flow rates were compared to empirical results with good agreement. Muhlhaus *et al.* (2000) used the Particle-in-Cell method based on the Cosserat formulation to model silo flow (discharging). A Drucker-Prager elastio-plastic constitutive model was used, but no comparisons with empirical or experimental results were made.

The research group of Schreyer have used the PIC method with good results for a wide range of large deformation problems (such as metal cutting, impacts and penetrations). According to them, the PIC method has the advantage of simplicity over other meshless methods and materials governed by history dependent constitutive models can successfully be modelled (Sulsky *et al.*, 1994; Burgess *et al.*, 1992). Mechanical contact and impact arise in a large number of situations. The problem is difficult because possible contact must be sensed, normals to surfaces constructed and interaction forces assigned to prevent interpenetration. Problems of this type usually involve large deformations and inelastic response. Sulsky & Schreyer (1993) demonstrated that the PIC method can be used to model such impact and contacts without the need for a special contact algorithm, in fact, because the displacement field is forced to be single valued, the PIC method handles impact and contact as a natural consequence of the algorithm. Sulsky & Shreyer (1996) developed an axisymmetric form of the PIC method. Results from the Taylor problem of cylinders impacting a rigid wall were presented and the results compared well with experimental data and existing numerical solutions. In Bardenhagen *et al.* (2000), the PIC method is used for modelling shear deformation of an assembly of

granules. A special contact algorithm is used to model the Coulomb friction between the individual granules. In Sulsky *et al.* (1995) and Sulsky & Schreyer (1993), they have modelled the impact of an elastic steel disk on an elastic-perfectly plastic (von Mises) aluminium target at high velocity. Both plane strain and axisymmetric approaches were used and the results were in good agreement with experimental measurements. Schreyer *et al.* (2002) modelled delamination, a type of failure that can occur in layered composites. The PIC method was used to avoid remeshing and remapping of history variables. The solutions showed no sensitivity of delamination propagation with mesh orientation. Shen *et al.* (2000) studied the deformation characteristics of ductile polycrystalline materials at elevated temperatures by considering a square segment of material subjected to different stress modes. The PIC method was used to model the polycrystalline microstructure numerically.

A common feature of meshless methods such as the element-free Galerkin method, is their computational cost and routine use for a wide range of applications appears not to be feasible (Schreyer *et al.*, 2002). SPH is much less complex, but unfortunately this method is subject to instabilities under tensile states of stress and must be applied carefully (Swegle *et al.*, 1995; Schreyer *et al.*, 2002). In comparison with these meshless methods, PIC appears to be considerably less complex. With the use of an explicit time integration scheme, the computational cost increase of PIC is about 20% over that associated with the use of low-order finite elements, compared to current forms of the explicit element-free Galerkin approach where the cost exceeds that of low-order elements by a factor of 4-10 (Schreyer *et al.*, 2002). The PIC method is based on standard FEM, which is used to solve the equations of motion, conservation of mass and temperature evolution. Advantages include the whole body of theory from FEM, the fact that most of the code can be standard, and the robustness of the method.

1.4 Thesis Goals and Outline

1.4.1 Goals

Earthmoving equipment is not only used for mining, it also plays an important role in the agricultural and earthmoving industries. The equipment is highly diverse in shape and function, but most of the soil cutting machines can be categorised into one of three principal classes: blades, rippers and buckets or shovels. Tools that resemble blades include bulldozer front blades, road graders, hauling scrapers, snowplows and other straight-edged blades. These instruments cut and push soil or other granular material at a depth that is generally less than their width. Ripper type tools are narrower compared to their working depth and are often attached to bulldozers and graders when it is necessary to cut and loosen hard soil.

Figure 1.1: A typical walking dragline

Buckets are blades equipped with sides that form a space in which soil or other materials can be cut and lifted up. The basic shape of earthmoving tools has not changed a great deal since antiquity, although most are operated today by mechanical power sources and their construction benefits from modern metallurgical engineering.

Draglines are used to remove blasted overburden from open cast mines. Its removal exposes the coal deposits beneath for mining. A dragline, as depicted in figure 1.1, is a crane-like structure with a huge bucket of up to 100 m^3 in volume. Draglines are an expensive and essential part of mine operations and play an important role in the competitiveness of South African mines. In the coal mining industry it is generally accepted that a 1% improvement in the efficiency of a dragline will result in an R 1 million increase in annual production per dragline (Esterhuyse, 1997).

The main goal of this dissertation is to model the flow of loose (cohesionless) granular material in front of flat bulldozer blades and into dragline type buckets using a continuum method. During these processes, the material experiences large deformations, free surface flow and the formation of shear bands. All of these must be accurately modelled so that predictions of soil flow patterns and resultant forces and moments on the blade and bucket are possible.

To reach this goal, a PIC code was developed to model these processes under plane strain conditions. The code called PICCUS (***P**article-**i**n-**C**ell **C**ode **U**niversity of **S**tellenbosch*) is based on both the Cosserat and classic continuum formulations. Published numerical and experimental results were used to validate the code. Blade and bucket results were compared to experimental measurements and observations as well as DEM simulations

(Coetzee, 2000).

1.4.2 Novelty

The only known researchers who used the PIC method based on the Cosserat continuum are Muhlhaus *et al.* (2000). They modelled silo and trapdoor flow , i.e. natural gravitational flow. Bohatier & Nouguier (1999) investigated forced flow (blade cutting) but based on the classic continuum formulation for history independent material and FEM with remeshing and in the absence of gravity.

The application of the Particle-in-Cell method based on the Cosserat continuum formulation with history-dependent constitutive equations on *forced* granular flow is unique. Neither Muhlhaus *et al.* (2000) nor Bohatier & Nouguier (1999) compared their results with experiments. Tejchman (1996) performed numerical simulations of silo filling with a hypoplastic Cosserat continuum and compared his results to that of an experiment. The silo was, however, filled layer-by-layer and standard FEM could be used under the assumed quasi-static conditions.

The numerical simulation of bucket filling has only been performed by Cleary (1998*b*) and Coetzee (2000). Both authors used discrete element methods. The modelling of bucket filling with a continuum method has not yet been done.

1.4.3 Outline

Chapter 2 gives a brief overlook of the Particle-in-Cell method based on the classic nonpolar continuum formulation. Chapter 3 gives an overview of the different boundary conditions and initial conditions that were used.

In Chapter 4, analytical and published numerical data are used to evaluate and validate the code. Particle-in-Cell simulations performed by other authors are repeated to validate the correct implementation of the code. This includes the impact of an elastic steel disk on a perfectly plastic aluminium target and the discharge of a silo. The analytical solution of a rigid disk on an inclined plane is used to validate the contact model. Different values of friction coefficient and angles of inclination are used to model either a stick-rolling contact or a slip-rolling contact. The impact of two elastic bodies is modelled to demonstrate the conservation of momentum and energy. The analytical solution of a simple oedometer test is used to validate the implementation of a Mohr-Coulomb constitutive model. In an oedometer experiment, two of the principle stress components are equal, and during plastic flow, the stress point evolves along a shear-shear edge of the Mohr-Coulomb criterion representation in the principal stress space.

The method of characteristics is used to determine the forces acting on a flat blade and the shape of the material shear band. The results for different

blade depths and mesh sizes are compared. The analysis of a strip loading on an elastic mass is compared to an analytical model. The distribution of the major and minor principal stresses below the footing is compared to the analytical solution.

In Chapter 5 published experimental results are used to evaluate and validate the code. Not all of the problems being analysed involve large displacements. The simulation of slope stability and anchor pull-out tests for instance, can be performed with standard FEM codes. It does, however, indicate that these types of applications, typical to civil and geotechnical engineering, can be modelled using PIC. It also shows that using PIC, no special contact elements are needed, between the anchor and the soil for instance, which is the case when FEM is used.

The polar continuum method is only used in blade, bucket and silo modelling. In Chapter 6 the flow of loose granular material in front of a flat bulldozer blade, into an excavator type bucket and the discharge of a silo is modelled. Blade and bucket results are compared to published experimental data and published DEM results. Silo experiments and DEM simulations were performed as part of this dissertation and the results compared to polar and nonpolar continuum results.

Chapter 7 concludes with some recommendations and possible further work. Appendix A describes the notations used: index notation and Hassenpflug notation. Appendix B gives an overview of classic continuum mechanics and Appendix C describes the Cosserat continuum theory. Appendix D describes rigid body kinematics used in the Cosserat continuum theory. Appendix E gives the essential finite element theory on which PIC is based. Only four noded isoparametric elements are treated. In Appendix F, a detailed description of the Particle-in-Cell method based on the Cosserat continuum is given. Appendix G describes the PIC contact model. This model is based on Coulomb friction theory. Appendix H and Appendix I describe the nonpolar and polar constitutive models respectively. The constitutive models and their implementation are described.

Chapter 2

Governing Equations

2.1 Introduction

In this chapter, a brief description of the Particle-in-cell (PIC) method based on the classic continuum formulation is given. In the first part of this chapter, index notation is used to denote vectors and matrices. In the latter part, Hassenpflug notation is used (Hassenpflug, 1993) to avoid confusion between node numbers and indices. Numerical subscripts indicate node numbers and x, y and z indicate coordinate directions. A description of the notations is given in Appendix A. Plane strain conditions are assumed. A more complete description based on the Cosserat continuum is given in Appendix F.

2.2 Space Discretisation

First, the initial configuration of the body is divided into a number of subregions. This is done as depicted in figure 2.1. In the centre of each subregion a material point or particle is placed. This material point represents the subspace, and is given a mass m_p. The mass is calculated by assuming that the whole mass of the subregion is concentrated at the material point. The mass of a material point is constant and does not change with time or position. The density $\rho(x_i)$ represented by this collection of discrete mass points is approximated using the Dirac delta function,

$$\rho(x_i) = \sum_{p=1}^{N_p} m_p \delta\left(x_i - x_i^p\right) \tag{2.2.1}$$

where x_i is an arbitrary position vector, x_i^p is the position vector at material point p, N_p is the total number of material points and the Dirac delta function is defined as follows:

$$\delta(x-a) = \begin{cases} 0 & x \neq a \\ \infty & x = a \end{cases} \quad \text{and} \quad \int_{-\infty}^{+\infty} \delta(x-a)\, dx = 1 \tag{2.2.2}$$

For clarity, the equations of motion are derived for a single element only. The whole system would be analysed by assembling the matrices and vectors as in standard FEM routines. The mass of each material point is fixed which ensures mass conservation. The well known linear momentum

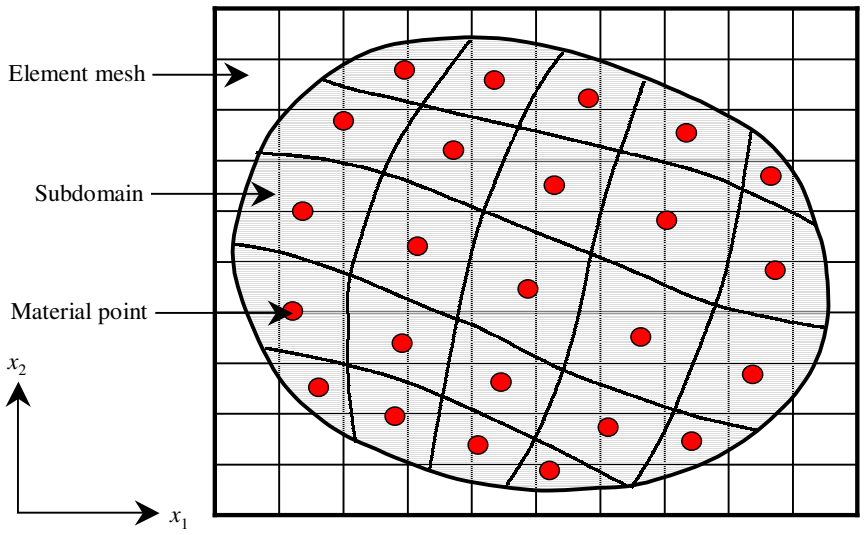

Figure 2.1: The element mesh and material points within the subdomains

equation of a continuum is given by (Appendix B),

$$\rho \frac{dv_i}{dt} = \rho f_i + \sigma_{ij,j} \tag{2.2.3}$$

with v_i the velocity vector, f_i a vector containing the body forces and σ_{ij} is the Cauchy stress tensor. As in FEM, the equation of virtual work is used as the starting point. The equation of virtual work is obtained by multiplying equation 2.2.3 by a test (weighted) function w_i followed by integration over the space V which satisfies the boundary conditions:

$$\int_V \rho \frac{dv_i}{dt} w_i \, dV = \int_V \rho f_i w_i \, dV + \int_V \sigma_{ij,j} w_i \, dV \tag{2.2.4}$$

The specific stress is defined as the stress tensor divided by the material density:

$$\sigma^s_{ij} = \frac{\sigma_{ij}}{\rho} \quad \rightarrow \quad \sigma_{ij} = \rho \sigma^s_{ij} \tag{2.2.5}$$

Substituting this definition of the specific stress into equation 2.2.4, and applying integration by parts, give

$$\int_V \rho \frac{dv_i}{dt} w_i \, dV = \int_V \rho f_i w_i \, dV - \int_V \rho \sigma^s_{ij} w_{i,j} \, dV + \int_S \tau_i w_i \, dS \tag{2.2.6}$$

where τ_i is the surface traction acting on surface S with a unit normal vector n_j. Substitution of the discrete density representation, equation 2.2.1, into equation 2.2.6 and making use of the definition of the Dirac delta function

yields an discrete expression where the integration is performed as a sum of material point properties:

$$\boxed{\sum_{p=1}^{N_p} m_p \frac{dv_i^p}{dt} w_i^p = \sum_{p=1}^{N_p} m_p f_i^p w_i - \sum_{p=1}^{N_p} m_p \, \sigma_{ij}^{sp} w_{i,j}^p + \int_S \tau_i w_i \, dS} \tag{2.2.7}$$

The superscript p indicates a variable evaluated at the material point. For example, the specific stress $\sigma_{ij}^{sp} \equiv \sigma_{ij}^s \left(x_i^p\right)$.

2.3 Element Formulation

The element mesh used is similar to that of FEM. Four noded quadrilateral elements are used. Under the assumption of two-dimensional conditions, the acceleration field $\dot{v}_i \equiv \frac{dv_i}{dt}$, for example, can be written in terms of nodal- and shape function-values

$$\dot{\overline{\boldsymbol{v}}}\left(\overline{\boldsymbol{x}}, t\right) \equiv \begin{bmatrix} \dot{v}_x \\ \dot{v}_y \end{bmatrix} = \underline{\overline{\boldsymbol{N}}} \, \dot{\overline{\boldsymbol{v}}}_n \tag{2.3.1}$$

where $\underline{\overline{\boldsymbol{N}}}$ is a matrix containing the shape functions. This matrix, for a single element, can be written as follows:

$$\underline{\overline{\boldsymbol{N}}} \equiv \begin{bmatrix} N_1 & 0 & N_2 & 0 & N_3 & 0 & N_4 & 0 \\ 0 & N_1 & 0 & N_2 & 0 & N_3 & 0 & N_4 \end{bmatrix} \tag{2.3.2}$$

where the subscripts indicate the element node number. The element nodal acceleration vector $\dot{\overline{\boldsymbol{v}}}_n$ contains the nodal values of the acceleration field,

$$\dot{\overline{\boldsymbol{v}}}_n \equiv \begin{bmatrix} \dot{v}_{x1} & \dot{v}_{y1} & \dot{v}_{x2} & \dot{v}_{y2} & \dot{v}_{x3} & \dot{v}_{y3} & \dot{v}_{x4} & \dot{v}_{y4} \end{bmatrix}^{\mathrm{T}} \tag{2.3.3}$$

where the first subscript indicates the coordinate direction and the number indicates the element node number. The same can be applied to the vector field w_i to obtain a vector $\overline{\boldsymbol{w}}$. Define the following vectors for plane strain conditions,

$$\overline{\boldsymbol{\sigma}}^s \equiv \begin{bmatrix} \sigma_{xx}^s \\ \sigma_{yy}^s \\ \sigma_{xy}^s \end{bmatrix}, \qquad \overline{\boldsymbol{f}} \equiv \begin{bmatrix} f_x \\ f_y \end{bmatrix}, \qquad \overline{\boldsymbol{\tau}} \equiv \begin{bmatrix} \tau_x \\ \tau_y \end{bmatrix} \tag{2.3.4}$$

with $\sigma_{xy}^s = \sigma_{yx}^s$. Using these definitions, equation 2.2.7 can be written as follows:

$$\overline{\boldsymbol{w}}^{\mathrm{T}} \sum_{p=1}^{N_p} m_p \left(\underline{\overline{\boldsymbol{N}}}^p\right)^{\mathrm{T}} \underline{\overline{\boldsymbol{N}}}^p \dot{\overline{\boldsymbol{v}}}_n =$$
$$\overline{\boldsymbol{w}}^{\mathrm{T}} \sum_{p=1}^{N_p} m_p \left(\underline{\overline{\boldsymbol{N}}}^p\right)^{\mathrm{T}} \overline{\boldsymbol{f}}^p - \overline{\boldsymbol{w}}^{\mathrm{T}} \sum_{p=1}^{N_p} m_p \left(\underline{\overline{\boldsymbol{B}}}^p\right)^{\mathrm{T}} \overline{\boldsymbol{\sigma}}^{sp} + \overline{\boldsymbol{w}}^{\mathrm{T}} \int_S \left(\underline{\overline{\boldsymbol{N}}}^p\right)^{\mathrm{T}} \overline{\boldsymbol{\tau}} \, \mathrm{d}S \quad (2.3.5)$$

where the superscript p indicates values evaluated at the material points, e.g., $\underline{\overline{\boldsymbol{N}}}^p \equiv \underline{\overline{\boldsymbol{N}}}(\overline{\boldsymbol{x}}^p)$. The arbitrary test vector $\overline{\boldsymbol{w}}$ appears in all the above terms and can thus be dropped. The final discretised system of equations follows as

$$\boxed{\underline{\overline{\boldsymbol{M}}} \, \dot{\overline{\boldsymbol{v}}}_n = \overline{\boldsymbol{F}}^{\,\mathrm{int}} + \overline{\boldsymbol{F}}^{\,\mathrm{ext}}} \quad (2.3.6)$$

where the mass matrix $\underline{\overline{\boldsymbol{M}}}$ is given by

$$M_{ij} \equiv \underline{\overline{\boldsymbol{M}}} = \sum_{p=1}^{N_p} m_p \left(\underline{\overline{\boldsymbol{N}}}^p\right)^{\mathrm{T}} \underline{\overline{\boldsymbol{N}}}^p \quad (2.3.7)$$

the internal force vector is given by

$$F_i^{\,\mathrm{int}} \equiv \overline{\boldsymbol{F}}^{\,\mathrm{int}} = -\sum_{p=1}^{N_p} m_p \left(\underline{\overline{\boldsymbol{B}}}^p\right)^{\mathrm{T}} \overline{\boldsymbol{\sigma}}^{sp} \quad (2.3.8)$$

and the external force vector is given by

$$F_i^{\,\mathrm{ext}} \equiv \overline{\boldsymbol{F}}^{\,\mathrm{ext}} = \sum_{p=1}^{N_p} m_p \left(\underline{\overline{\boldsymbol{N}}}^p\right)^{\mathrm{T}} \overline{\boldsymbol{f}}^p + \int_S \left(\underline{\overline{\boldsymbol{N}}}^p\right)^{\mathrm{T}} \overline{\boldsymbol{\tau}} \, \mathrm{d}S \quad (2.3.9)$$

The matrix $\underline{\overline{\boldsymbol{B}}}^p$ contains shape function gradients, and for a single element it can be written as

$$\underline{\overline{\boldsymbol{B}}}^p = \begin{bmatrix} N_{1,x} & 0 & N_{2,x} & 0 & N_{3,x} & 0 & N_{4,x} & 0 \\ 0 & N_{1,y} & 0 & N_{2,y} & 0 & N_{3,y} & 0 & N_{4,y} \\ N_{1,y} & N_{1,x} & N_{2,y} & N_{2,x} & N_{3,y} & N_{3,x} & N_{4,y} & N_{4,x} \end{bmatrix}^p \quad (2.3.10)$$

where the subscripts $(,i)$ are interpreted as the derivatives with respect to the i global coordinate direction, e.g., $N_{1,x} = \frac{\partial N_1}{\partial x}$. In practice, to simplify computations, a lumped mass matrix is used instead of the consistent mass matrix given by equation 2.3.7. The lumped mass matrix is a diagonal matrix with each entry being the corresponding row sum of the consistent mass matrix. Matrix inversions become trivial if a lumped matrix is used, at the cost of introducing a small amount of numerical dissipation (Burgess

et al., 1992; Brackbill *et al.*, 1988). The consistent mass matrix can also be singular for certain arrangements of the particles. There appears to be only a few arrangements of particles that yield a singular consistent mass matrix, but nearby arrangements might result in an ill-conditioned matrix. On the other hand, the lumped matrix is diagonal and well conditioned.

2.4 Time Integration

Let the time step size be Δt. The solution to the system of equations 2.3.6 is found at discrete instants in time $t, t+1, \ldots, t+n$. The calculation during each time increment consists of three phases: an initialisation phase, a Langrangian phase and a convective phase.

2.4.1 Initialisation phase

Assume that the position and velocity vector, stress tensor, strain tensor and history dependent variables of each material point are known at time t. With the position of each particle known, its shape function values can be computed and hence the mass matrix, $\underline{\overline{\boldsymbol{M}}}^t$, given by equation 2.3.7. Mapping of the particle velocities to the nodes is required for the initial data for the solution to equation 2.3.6. The following equation is solved to obtain the nodal velocity $\overline{\boldsymbol{v}}_n^t$ at time t:

$$\underline{\overline{\boldsymbol{M}}}^t \, \overline{\boldsymbol{v}}_n^t = \sum_{p=1}^{N_p} m_p \left(\underline{\overline{\boldsymbol{N}}}^{p,t} \right)^{\mathrm{T}} \begin{bmatrix} v_x^{p,t} \\ v_y^{p,t} \end{bmatrix} \tag{2.4.1}$$

where $[v_1^{p,t} \; v_2^{p,t}]^{\mathrm{T}}$ is the material point velocity vector at time t, containing the velocity components in the x- and y-directions respectively. This equation expresses equivalence of momentum calculated for the material points and for the nodes (Wieckowski *et al.*, 1999).

2.4.2 Lagrangian phase

With the shape functions and stresses of each particle known, the internal- and external-force vectors can be calculated using equations 2.3.8 and 2.3.9 respectively. With these two vectors and the mass matrix known, equations 2.3.6 is solved for the nodal acceleration at time t:

$$\dot{\overline{\boldsymbol{v}}}_n^t = \left(\underline{\overline{\boldsymbol{M}}}^t \right)^{-1} \left(\overline{\boldsymbol{F}}^{\,\mathrm{int},t} + \overline{\boldsymbol{F}}^{\,\mathrm{ext},t} \right) \tag{2.4.2}$$

The "new" nodal velocity, $\overline{\boldsymbol{v}}_n^{t+1}$, at time $t+1$ is obtained by using an explicit time integrator:

$$\overline{\boldsymbol{v}}_n^{t+1} = \overline{\boldsymbol{v}}_n^t + \Delta t \, \dot{\overline{\boldsymbol{v}}}_n^t \tag{2.4.3}$$

Using the new nodal velocity, the increment in strains can be calculated at the particles. Define the vector of strain increment as follows:

$$\Delta\overline{\boldsymbol{\varepsilon}}^{p} \equiv \begin{bmatrix} \varepsilon^{p}_{xx} \\ \varepsilon^{p}_{yy} \\ \varepsilon^{p}_{xy} \end{bmatrix} \tag{2.4.4}$$

This vector can be calculated using matrix $\overline{\underline{\boldsymbol{B}}}^{p,t}$,

$$\Delta\overline{\boldsymbol{\varepsilon}}^{p,t+1} = \Delta t\, \overline{\underline{\boldsymbol{B}}}^{p,t} \overline{\boldsymbol{v}}_{n}^{t+1} \tag{2.4.5}$$

During the Lagrangian phase the shape function values at the particle positions do not change. Thus, the shape functions and the matrix $\overline{\underline{\boldsymbol{B}}}^{p}$ can be evaluated at time t. With the increment in strain known, the stress state at each particle can be calculated based on the chosen constitutive model:

$$\Delta\overline{\boldsymbol{\varepsilon}}^{p,t+1} \quad \xrightarrow{\textit{constitutive model}} \quad \overline{\boldsymbol{\sigma}}^{p,t+1} \tag{2.4.6}$$

History dependent variables, such as strain-hardening parameters, may also be updated at this stage. During the Lagrangian phase the nodes are assumed to move at the computed nodal velocity $\overline{\boldsymbol{v}}_{n}^{t+1}$. Thus, points in the interior of the element move in proportion to the motion of the nodes, as given by the representation using the nodal shape functions. Since shape functions are used to map the nodal velocity continuously to the interior of the element, the positions of the material points are updated by moving them in a single-valued, continuous velocity field. Similarly, the velocity of a material point is updated by mapping the nodal accelerations to the material point position. The updated material point position vector follows as

$$\boxed{\overline{\boldsymbol{x}}^{p,t+1} = \overline{\boldsymbol{x}}^{p,t} + \Delta t\, \overline{\underline{\boldsymbol{N}}}^{p,t}\, \overline{\boldsymbol{v}}_{n}^{t+1}} \tag{2.4.7}$$

Similarly, the updated velocity vector is given by

$$\boxed{\overline{\boldsymbol{v}}^{p,t+1} = \overline{\boldsymbol{v}}^{p,t} + \Delta t\, \overline{\underline{\boldsymbol{N}}}^{p,t}\, \dot{\overline{\boldsymbol{v}}}_{n}^{t}} \tag{2.4.8}$$

Because the velocity field is single-valued, interpenetration of material is precluded. This feature of the algorithm allows simulations of impact and penetration without the need for a special contact algorithm.

2.4.3 Convective phase

At this point in the computational cycle, the material points are completely updated and carry the complete solution, i.e., all the state variables needed to start a new calculation step are carried by the material points. During the convective phase, the material points are held fixed and the element

mesh can be redefined. The mesh can be chosen in any convenient manner, for example adaptive meshes can be used to resolve sharp gradients and interfaces. The simplest and most convenient choice is, however, to keep the existing mesh. Since the material points do not move during the convective phase, material point properties have the same value at the end of the convective phase as they had at the end of the Lagrangian phase. This completes the computational cycle. A new cycle is begun using the information carried by the material points to initialise nodal values on the element mesh.

2.5 Stability

In the previous sections, a simple explicit time integrator is used of which the time step should satisfy the stability condition, i.e., the critical time step should be the smallest ratio of the element size to the wave speed through the material. For small displacements, the spatial discretisation in PIC is equivalent to that of FEM using Gauss points at the same locations as those of the material points in each element. Therefore, the convergence behaviour of the integrator used is similar to that employed to integrate the corresponding equations in FEM. However, according to Chen *et al.* (2002), no consistent theoretical results have been obtained for the convergence behaviour of time integrators when larger deformations occur and a reasonable time step is usually found through numerical experiments.

2.6 The Polar Continuum

In the previous sections a description of the PIC method was given based on the classic continuum. In Appendix F, a more detailed description is given of PIC, based on the Cosserat continuum. In this section the Cosserat continuum is briefly discussed. A detailed description of the Cosserat continuum theory is given in Appendix C.

The kinematics of Cosserat continua are characterised by rotational degrees of freedom w_i^c, which are independent of the translation described by the displacement field u_i. Thus, the field of continuum macro-rotations no longer coincides with that of micro-rotations at each material point. The micro-rotation w_i^c differs from the classical macro-rotation w_i since three rotational degrees-of-freedom are introduced in addition to the conventional three translational degrees-of-freedom. Under two-dimensional conditions each material point has two translational degrees-of-freedom and one rotational degree-of-freedom w_3^c.

For the formulation of constitutive relationships, deformation measures which are invariant with respect to rigid body motions are needed. In the

Cosserat theory two deformation measures are defined. Relative rotation,

$$\Omega_i = w_i - w_i^c \tag{2.6.1}$$

and the curvature,

$$\kappa_{ij} = w_{i,j}^c \tag{2.6.2}$$

which is a measure of the relative rotation between neighbouring material points. The symmetric linear strain tensor of the classic continuum is combined with the relative rotation to form a single tensorial deformation measure,

$$\lambda_{ij} = u_{i,j} + \varepsilon_{ijk} w_k^c \tag{2.6.3}$$

where ε_{ijk} is the permutation symbol.

In a Cosserat continuum the couple per unit area (couple-stresses μ_{ij}), acting across a surface within a material volume or on its boundary, is taken into account in addition to the usual force per unit area (stresses σ_{ij}). The couple-stresses are conjugate to the micro-curvatures κ_{ij}.

The presence of the couple-stresses does not affect the linear momentum principle, hence the equations of motion of the nonpolar continuum still applies,

$$\rho \frac{\mathrm{d}v_i}{\mathrm{d}t} = \rho f_i + \sigma_{ij,j} \tag{2.6.4}$$

where v_i is the velocity field. The moment of momentum equation of the nonpolar continuum, however, should be reconsidered. This equation is extended in two ways. Firstly, the body moment c_i per unit mass and the couple stresses μ_{ij} are introduced in addition to the moments of the body force per unit mass f_i and the moments of the stresses σ_{ij}. Secondly, it is supposed that each material point has *spin angular momentum* h_i^c per unit mass ($\mathrm{m}^2 \cdot \mathrm{s}^{-1}$). In the two-dimensional case the angular momentum can be written as $h_3^c = J_{33}\, \dot{w}_3^c$ where J_{33} is the material points moment of inertia in the direction perpendicular to the working plane. The angular momentum balance becomes:

$$\varepsilon_{ijk}\sigma_{kj} + \mu_{ij,j} + \rho c_i = \rho \frac{\mathrm{d}h_i^c}{\mathrm{d}t} \tag{2.6.5}$$

This results in a stress tensor that is nonsymmetric, e.g. in general $\sigma_{12} \neq \sigma_{21}$.

2.7 Constitutive Models

During the Lagrangian phase of the PIC calculation cycle, increments in strain are calculated and related to increments in stress using a constitutive model (equation 2.4.6). For a detailed description of the nonpolar and

polar constitutive models and their implementation, see Appendix H and Appendix I respectively.

Nonpolar elastic, Drucker-Prager and Mohr-Coulomb models were used. The Drucker-Prager (FLAC, 1998) model is expressed in terms of two generalised stress components: the tangential stress q and mean normal stress p defined as

$$\begin{aligned} q &= \sqrt{J_2} \\ p &= \tfrac{1}{3}\left(\sigma_{11} + \sigma_{22} + \sigma_{33}\right) \end{aligned} \tag{2.7.1}$$

where J_2 is the second invariant of the stress deviator tensor. The failure criteria is described in the pq-plane, with the shear yield function given by

$$f^s = q + q_\phi p - k_\phi \tag{2.7.2}$$

and the tension yield function (tension cutoff) by

$$f^t = p - \sigma^t \tag{2.7.3}$$

where q_ϕ and k_ϕ are constant material properties and σ^t is the material tensile strength. The constant q_ϕ is related to the material friction angle. The shear potential function g^s corresponds in general to a non-associated flow rule and has the form

$$g^s = q + q_\psi p \tag{2.7.4}$$

where q_ψ is a material constant related to the material dilatancy angle. With q_ψ equal to q_ϕ, the flow rule is termed associated, otherwise it is called non-associated. The flow rule for tensile failure is associated and given by

$$g^t = p \tag{2.7.5}$$

With the current stress state known, the new stress state is calculated using a single-step return algorithm. The algorithm assumes that the total strain increment is elastic which is then used to calculate an increment in stress. This stress increment is then added to the current stress state to obtain the trial stress state. The trial stress state is then checked against the failure criteria (shear and tension). If either of the failure criteria is violated, a one step return algorithm is used to bring the trial stress state back to the yield surface using the two potential functions respectively.

The Mohr-Coulomb model (FLAC, 1998) with tension cutoff has a non-associated shear flow rule and an associated tensile flow rule. The shear and tension yield functions are given by

$$\begin{aligned} f^s &= \sigma_1 - \sigma_3 N_\phi + 2c\sqrt{N_\phi} \\ f^t &= \sigma^t - \sigma_3 \end{aligned} \tag{2.7.6}$$

where σ_1 and σ_3 are principal stresses with $\sigma_1 \leq \sigma_3$, σ^t is the material tensile strength, c the cohesion and

$$N_\phi = \frac{1 + sin\phi}{1 - sin\phi} \tag{2.7.7}$$

with ϕ the material friction angle. The shear and tension potential functions are given by

$$\begin{aligned} g^s &= \sigma_1 - \sigma_3 N_\psi \\ g^t &= -\sigma_3 \end{aligned} \tag{2.7.8}$$

where

$$N_\psi = \frac{1 + sin\psi}{1 - sin\psi} \tag{2.7.9}$$

and ψ is the material dilatancy angle. The same single-step return algorithm used in the Drucker-Prager model, is used in the Mohr-Coulomb model.

In the principal stress space, the Drucker-Prager shear criterion is represented by a cone with its axis along the line $\sigma_1 = \sigma_2 = \sigma_3$. The Mohr-Coulomb shear criterion is represented by an irregular hexagonal pyramid. The parameters q_ϕ and k_ϕ can be adjusted so that the Drucker- Prager cone will either pass through the outer or the inner edges of the Mohr-Coulomb pyramid (FLAC, 1998). For outer adjustment,

$$\begin{aligned} q_\phi &= \frac{6}{\sqrt{3}\,(3 - sin\phi)}\, sin\phi \\ k_\phi &= \frac{6}{\sqrt{3}\,(3 - sin\phi)}\, c\, cos\phi \end{aligned} \tag{2.7.10}$$

and for inner adjustment,

$$\begin{aligned} q_\phi &= \frac{6}{\sqrt{3}\,(3 + sin\phi)}\, sin\phi \\ k_\phi &= \frac{6}{\sqrt{3}\,(3 + sin\phi)}\, c\, cos\phi \end{aligned} \tag{2.7.11}$$

A polar elastic and Drucker-Prager model were used. In formulating Cosserat elasticity and elasto-plasticity, it is useful to make use of generalised curvatures, e.g. $\kappa_{31} l$, where l is a material parameter with the dimension of length. It is this parameter which effectively sets the internal length scale in the continuum, and therefore has the role of a "characteristic length". Assuming plane strain conditions, the strain and stress

components can be assembled in two vectors, de Borst (1991) and de Borst (1993):

$$\overline{\boldsymbol{\varepsilon}}^c = [\lambda_{11}\ \lambda_{22}\ \lambda_{33}\ \lambda_{12}\ \lambda_{21}\ \kappa_{31}l\ \kappa_{32}l]^{\mathrm{T}} \tag{2.7.12}$$

$$\overline{\boldsymbol{\sigma}}^c = \left[\sigma_{11}\ \sigma_{22}\ \sigma_{33}\ \sigma_{12}\ \sigma_{21}\ \frac{\mu_{31}}{l}\ \frac{\mu_{32}}{l}\right]^{\mathrm{T}} \tag{2.7.13}$$

Note that by multiplying the curvatures by the length parameter l, all components of the strain vector have the same dimension. The couple-stresses are divided by the characteristic length to obtain a stress vector in which all the entries have the same dimension.

Assuming that the elastic strain vector is linearly related to the stress vector, the following equation can be written

$$\overline{\boldsymbol{\sigma}}^c = \underline{\overline{\boldsymbol{D}}}^e \overline{\boldsymbol{\varepsilon}}^{ce} \tag{2.7.14}$$

where $\underline{\overline{\boldsymbol{D}}}^e$ is the stiffness matrix containing the elastic moduli:

$$\underline{\overline{\boldsymbol{D}}}^e = \begin{bmatrix} 2Gc_1 & 2Gc_2 & 2Gc_2 & 0 & 0 & 0 & 0 \\ 2Gc_2 & 2Gc_1 & 2Gc_2 & 0 & 0 & 0 & 0 \\ 2Gc_2 & 2Gc_2 & 2Gc_1 & 0 & 0 & 0 & 0 \\ 0 & 0 & 0 & (G+G^c) & (G-G^c) & 0 & 0 \\ 0 & 0 & 0 & (G-G^c) & (G+G^c) & 0 & 0 \\ 0 & 0 & 0 & 0 & 0 & 2G & 0 \\ 0 & 0 & 0 & 0 & 0 & 0 & 2G \end{bmatrix} \tag{2.7.15}$$

with $c_1 = \frac{1-\nu}{1-2\nu}$ and $c_2 = \frac{\nu}{1-2\nu}$, G is the shear modulus and v Poisson's ratio. G^c is an additional material constant, completing the four material constants that are needed to describe the elastic behaviour of an isotropic Cosserat continuum under planar deformations. The coefficient 2 has been introduced in terms D^e_{66} and D^e_{77} in order to arrive at a convenient form of the elasto-plastic constitutive equations. The total (bending) stiffness that sets the relation between the micro-curvatures and the couple stresses is basically determined by the value of the internal length scale l.

The Cosserat Drucker-Prager model used was proposed by Muhlhaus (1987). The yield function f is given by

$$f = q + \alpha(\gamma)p - c \tag{2.7.16}$$

and the potential function g by

$$g = q + \beta(\gamma)p \tag{2.7.17}$$

where

$$q = \sqrt{J_2} \tag{2.7.18}$$

and

$$p = \frac{1}{2}\left(\sigma_{11} + \sigma_{22} + \sigma_{33}\right) \tag{2.7.19}$$

The second invariant of the deviatoric stress tensor J_2 is given by:

$$J_2 = a_1 s_{ij} s_{ij} + a_2 s_{ij} s_{ji} + \frac{a_3 \mu_{ij} \mu_{ij}}{l^2} \tag{2.7.20}$$

where s_{ij} is the deviatoric stress tensor, α is a friction factor, β a dilatancy factor, c is cohesion, γ the hardening parameter and a_1, a_2 and a_3 are material parameters. Muhlhaus (1987) derived, on a macroscopic level and by taking into account slip and rotation in a random assembly of circular rods with a fixed diameter, the following set of parameters: $a_1 = \frac{3}{8}$, $a_2 = \frac{1}{8}$ and $a_3 = 1$. This set is referred to as the *standard set*. From micromechanical considerations it was also shown by Muhlhaus & Vardoulakis (1987) that:

$$G^c = \frac{G}{2\left(a_1 - a_2\right)} \tag{2.7.21}$$

The new stress state is calculated using an iterative trial stress method. An elastic predictor and a plastic corrector with radial return mapping is used and convergence is achieved within two to three iterations (Tejchman, 1997).

A rigid body model was also implemented and used for the modelling of strip footings, anchors, blades and buckets.

Chapter 3

Boundary and Initial Conditions

3.1 Introduction

Correctly specified boundary and initial conditions are needed to obtain specific solutions of the partial differential equations that describe the mechanics of granular flow. This chapter gives an overview of the different boundary and initial conditions used.

3.2 Boundary Conditions

In general, boundary conditions can be either fixed boundaries, applied traction or absorbing boundaries. In fixed boundaries, displacement and rotation can be fixed in one or more of the coordinate directions.

Modelling sometimes involves media which, at the scale of the analysis, are better represented as unbounded. An unbounded medium can be modelled as a bounded medium if the correct artificial numerical boundaries are enforced. In static analyses, fixed boundary conditions can be placed at some distance from the region of interest. In dynamic simulations, however, such boundaries lead to the reflection of outward propagating waves back into the model. The use of a large enough model would minimise the problem, since material damping will absorb most of the energy in the waves reflected from the boundaries. The alternative is to use absorbing boundaries of which the viscous boundary developed by Lysmer & Kuhlemeyer (1969) and Kunar *et al.* (1977) is an example.

In PICCUS nodes can be fixed in one or more of the coordinate directions or a constant traction (pressure) can be applied. In all the models where the reflection of waves from the boundaries could have an influence on the results, the models were made large enough for the reflecting waves to have no significant effect. No absorbing boundaries were used.

In the basic PIC algorithm no slip contact between different bodies is achieved without additional cost. This is the result of the bodies moving in a single-valued velocity field. A contact model developed by Bardenhagen *et al.* (2000) was used to apply Coulomb friction at the boundary nodes of contacting entities. This model allows no interpenetration of the entities in the contact normal direction, but do allow frictional slip in the tangential direction. A detailed description of the contact model and its implementation is given in Appendix G.

Strip footings, anchors, blades and buckets were modelled as rigid bodies. The contact model was used to model the contact between these rigid

bodies and the granular material by specifying the friction coefficient μ. The Cosserat rotation at the contacting interface could either be free or fixed ($w_3^c = 0$).

The roughness of a wall can quantitatively be characterised by the average distance r_w from the peak to the valley of asperities (Tejchman, 1997). It is, however, the ratio between the wall roughness and the mean grain diameter, $\frac{r_w}{d_{50}}$, that determines the interface behaviour between the wall and the grains. According to Tejchman (1997) no rotation should be allowed at relatively smooth interfaces. Tejchman (1997) reports that shear tests on sand showed that in the case of rough surfaces, particles experience both sliding and rotation. In the case of smooth surfaces the sand mass simply slided along the surface with very little rotation. The rotation along a smooth surface was about 200 times smaller than for rough walls. A smooth interface is defined when $\frac{r_w}{d_{50}} < 0.1$.

3.3 Initial Conditions and Damping

In many situations the precise initial stress field is not known. In some simple cases it can be calculated analytically, but for most practical problems, this is not possible. It is, however important to specify realistic initial conditions, since it can have an influence on the results and the stability of the computation.

In PICCUS, the initial velocity and/or stresses at a material point can be specified. When the initial velocity is specified, only a uniform velocity field can be used, i.e., the velocity of all material points will be the same. Different methods of specifying the initial stresses are provided in PICCUS.

3.3.1 Uniform Stress Field

Using this method, a uniform stress field is created by specifying the individual stress components $\sigma_{11}, \sigma_{12} = \sigma_{21}, \sigma_{22}$ and σ_{33} for a nonpolar continuum and $\sigma_{11}, \sigma_{12}, \sigma_{21}, \sigma_{22}, \sigma_{33}, \mu_{31}$ and μ_{31} for a Cosserat continuum. Care should be taken since the initial conditions may cause the material not to be in equilibrium and it may also violate the yield criterion.

A uniform initial stress field is a realistic approach for deep underground excavations. In such a case, the gravitational variation of stress from top to bottom of the excavation may be neglected because the variation is small in comparison with the magnitude of stress acting on the volume of material to be modelled.

3.3.2 Stress Field with a Gradient

Near the ground's surface, the variation in stress with depth cannot be ignored. In a uniform layer of soil with a horizontal free surface, the ver-

tical stresses (σ_{22}) are usually equal to $-\rho g h$, where g is the magnitude of the gravitational acceleration in the vertical direction (x_2) and usually taken as $g = 9.81\,\mathrm{m{\cdot}s^{-2}}$. Note that this results in a negative value in σ_{22}, i.e. a compressive stress. The mass density of the material is denoted by ρ and h is the depth below the free surface. However, the horizontal stresses (σ_{11} and σ_{33}) are more difficult to estimate. It is common to represent the ratio of horizontal to vertical effective stress by the "in rest" coefficient, Ting *et al.* (1994):

$$K_o = \frac{\sigma_h}{\sigma_v} \Rightarrow \sigma_h = K_o\,\sigma_v \tag{3.3.1}$$

Under the assumption that gravity is suddenly applied to an elastic mass of material, initially stress free, in which lateral movement is prevented, it can be shown that

$$K_o = \frac{\nu}{1-\nu} \tag{3.3.2}$$

where ν is Poisson's ratio. For natural soil this condition hardly ever applies in practice (FLAC, 1998) due to repeated tectonic movements, material failure, overburden removal and locked-in stresses due to faulting and localisation. Of course, if enough knowledge of the history of the particular volume of material is available, it is possible to simulate the whole process numerically, to arrive at the initial conditions. This approach is seldom feasible. Several theoretical and empirical relationships for K_o have been postulated for natural soil. Probably the simplest and most widely known is the approximation to the theoretical formula by Jaky (1944):

$$K_o = 1 - sin(\phi) \tag{3.3.3}$$

where ϕ is the material friction angle. This method of estimating the initial stresses, of course, is only applicable when the free surface is horizontal and without steps.

3.3.3 Layer-by-Layer Method

Figure 3.1 shows the configuration of a blade or wall typically used to model retaining walls or earthmoving equipment respectively. The bottom and side boundaries can be either fixed in one or more of the coordinate directions. A layer-by-layer method is used to generate initial stresses. One layer of material is created, starting at the bottom, with initial stresses given by

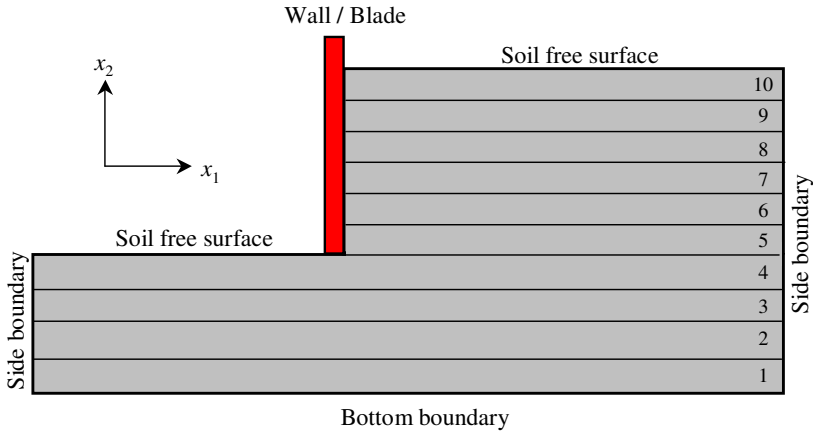

Figure 3.1: Layer-by-layer method of generating initial stresses

$$\begin{aligned} \sigma_{22} &= -\rho g h \\ \sigma_{11} &= K_o \sigma_{22} \\ \sigma_{33} &= K_o \sigma_{22} \\ \sigma_{12} &= \sigma_{21} = 0 \\ \mu_{31} &= \mu_{32} = 0 \quad \text{only for Cosserat continuum} \end{aligned} \tag{3.3.4}$$

where $K_o = 1 - sin(\phi)$ and h the height measured from the free surface of the current layer to the material point. With gravity activated, heavy damping is applied until static equilibrium is reached, equilibrium being defined when the maximum value in particle velocity is smaller or equal to 1×10^{-8} m·s^{-1}. After an equilibrium state has been reached, the next layer is added. This procedure is followed until the bottom edge of the wall/blade is reached. The wall/blade is then created and material added to the right of the wall/blade, layer-by-layer. The wall/blade may be smooth or have a specified friction.

In order to obtain the static equilibrium state, the equations of motion must be damped. The objective is to achieve the steady state in a numerically stable way with minimal computational effort. A form of damping called local non-viscous damping was implemented in which the damping force on a node is proportional to the magnitude of the unbalanced force at the node (FLAC, 1998). The direction of the damping force is such that energy is always dissipated. The damping force is simply added to the equation of motion, equation 2.3.6, and is given by

$$\overline{F}_i^{\text{damp}} = -\alpha \left| \overline{F}_i^{\text{int}} + \overline{F}_i^{\text{ext}} \right| \; sign(\overline{v}_n) \tag{3.3.5}$$

where $\overline{v}_n$ is the nodal velocity vector and α the damping factor. For a detailed description of the damping implementation see Appendix G.

Chapter 4

Numerical and Analytical Validation

4.1 Introduction

In order to use PICCUS for practical applications, it should be thoroughly evaluated and validated. In this chapter, published numerical data as well as analytical results are used to validate the code. Some of the simulations are exactly the same as performed by other authors using PIC, thus those only validate the implementation of the code.

4.2 Simulation of a High Velocity Impact

This simulation consists of an AISI 52-100 chromium steel disk impacting an elastic-perfectly plastic target of 6061-T6 aluminium under plane strain conditions. The material properties are summarised in table 4.1. The aluminium target has dimensions of 60 mm wide and 40 mm high. The steel disk has a diameter of 9.53 mm and an initial velocity of $1160\,\mathrm{m{\cdot}s^{-1}}$. The steel disk is assumed to be linear elastic and the aluminium target to be elastic-perfect plastic and obeying a von Mises yield criterion. The yield stress σ_y is the yield stress for the material in simple tension.

The computational domain is 60×60 mm in size and consists of 50×50 elements, i.e the size of one element is 1.2×1.2 mm. There are, initially, 4 particles per element. No contact model is used, so the contact interface between the disk and the target is a non-slip contact. All the boundaries are fixed.

Figure 4.1 shows the penetration after 24 µs, computed by Sulsky & Schreyer (1993). Figure 4.2 shows the penetration at the same time, using PICCUS.
There are differences in the position of individual particles, but this might be as a result of the original positions of the particles within the elements,

Table 4.1: Material properties used in impact simulation

Description	Symbol	Steel	Aluminium
Young's modulus	E	200 GPa	78.2 GPa
Density	ρ	$7850\,\mathrm{kg{\cdot}m^{-3}}$	$2700\,\mathrm{kg{\cdot}m^{-3}}$
Poisson's ratio	ν	0.3	0.3
Yield stress	σ_y	-	300 MPa

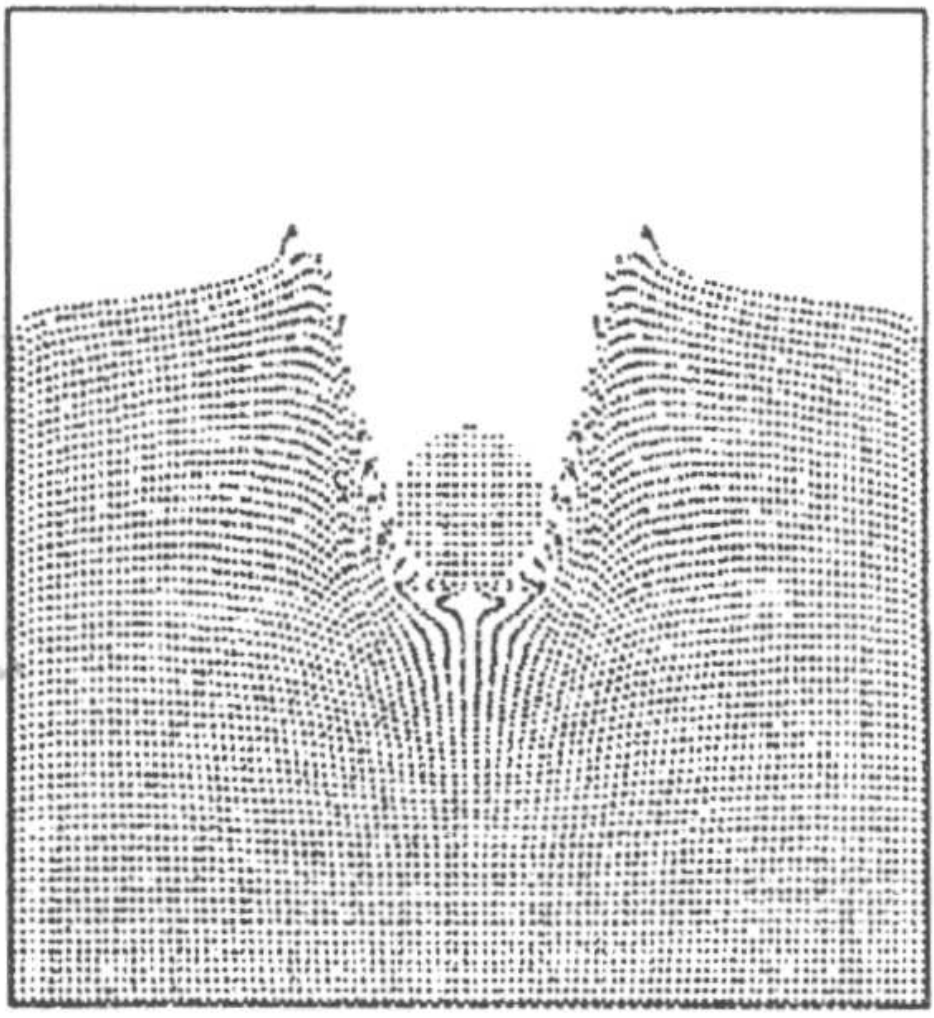

Figure 4.1: Penetrated configuration at $t = 24\,\mu s$, (Sulsky and Schreyer, 1993)

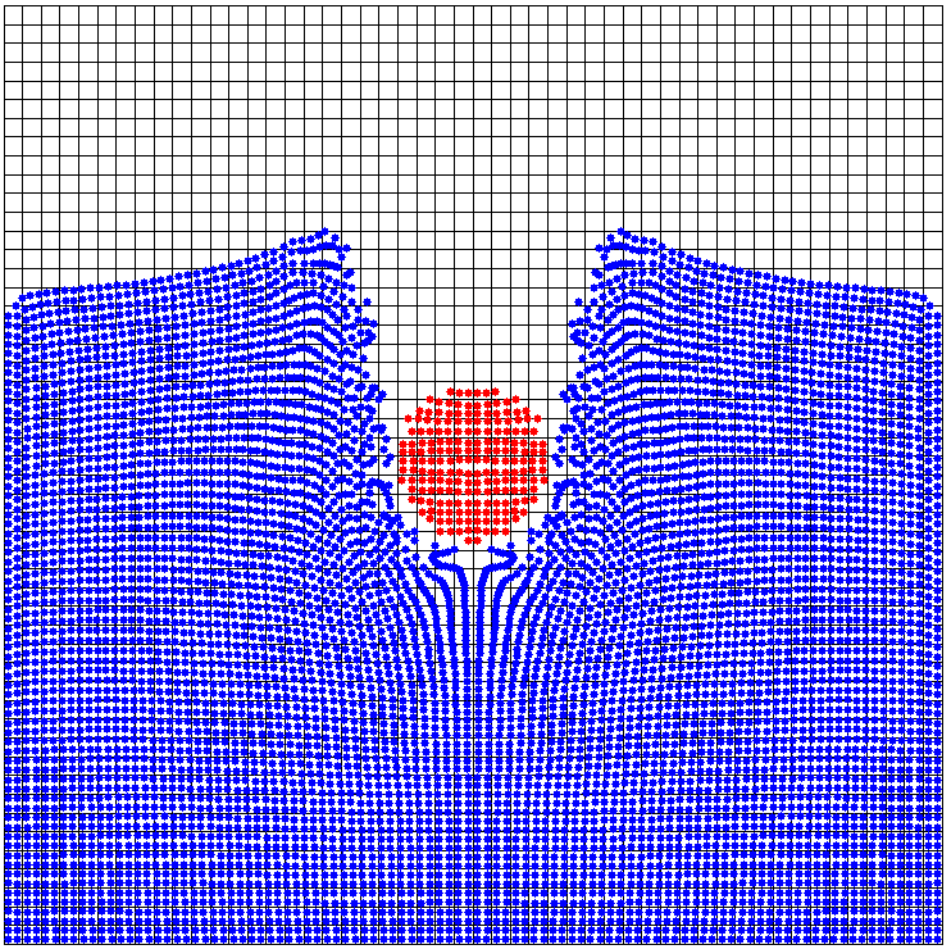

Figure 4.2: Penetrated configuration at $t = 24\,\mu s$, (PICCUS)

which were not given by Sulsky & Schreyer (1993). Figure 4.3 shows the penetration depth as a function of time. Here it can be seen that the penetration predicted by PICCUS is in close agreement with the published data from Sulsky & Schreyer (1993).

The final depth of penetration is 19 mm. Silling (1992) made use of an Eulerian code, CTH, and obtained a final penetration depth of 20 mm. Trucano & Grady (1985) performed experiments and measured a final penetration depth of 21 mm. Sulsky & Schreyer (1993) showed that the results from plane strain (19 mm) and plane stress (25 mm) conditions bracket the experimental result, while Sulsky *et al.* (1995) made use of two-dimensional axisymmetric cylindrical coordinates and obtained a final depth of 18 mm. The experimental data shows that the sphere is more or less undeformed after penetration (Trucano and Grady, 1985).

Figures 4.4 to 4.10 show the configuration at different times during the

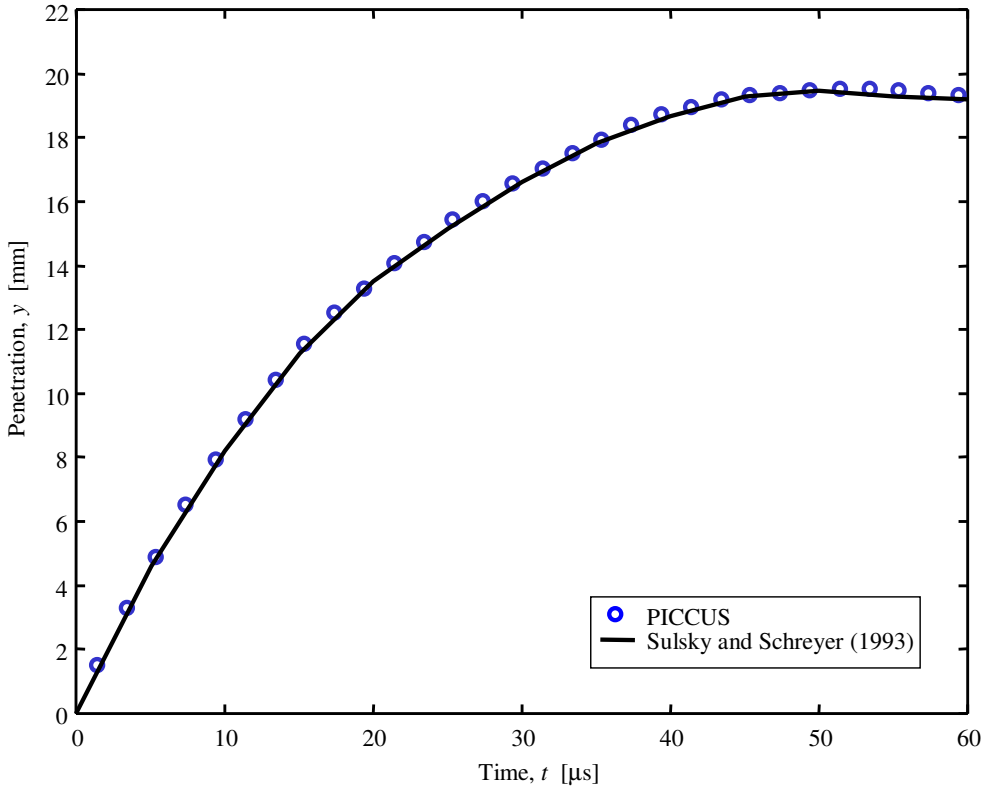

Figure 4.3: Depth of penetration as a function of time

simulation. The von Mises stress contours are also shown. The von Mises stress reaches a maximum of 300 MPa, the yield stress in simple tension. The stresses are high at the boundaries due to the applied fixed constraints.

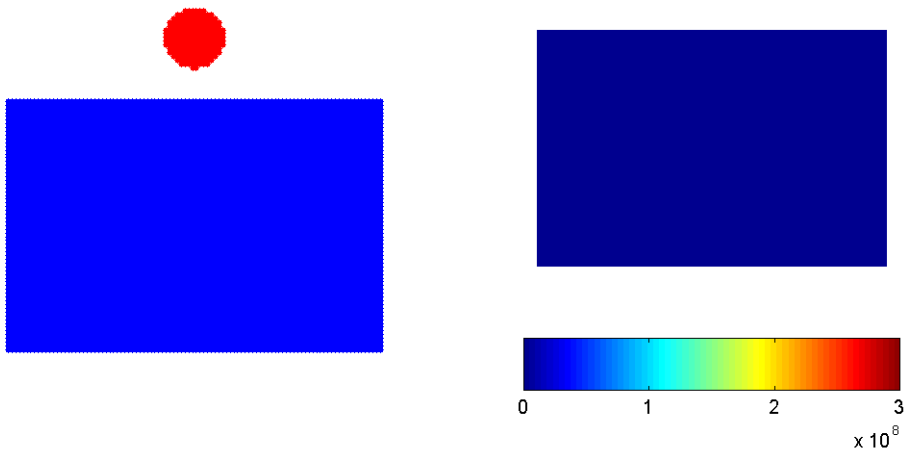

Figure 4.4: Penetration at $t = 0\,\mu s$, particles configuration and von Mises stress

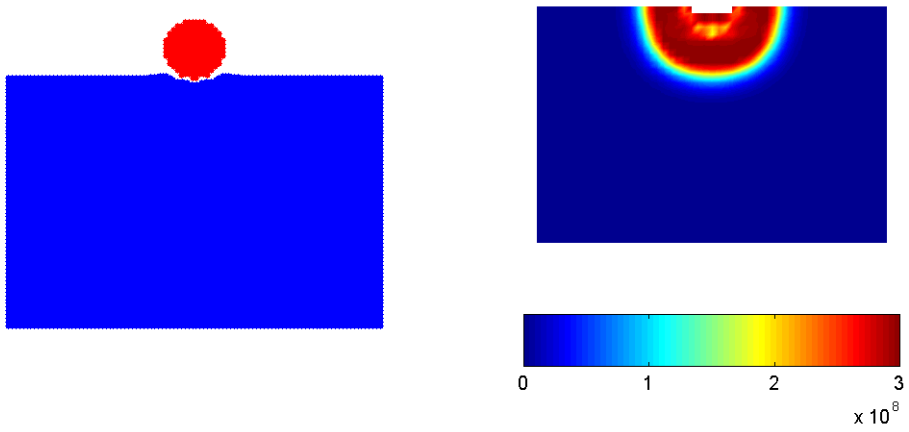

Figure 4.5: Penetration at $t = 3.2\,\mu s$, particles configuration and von Mises stress

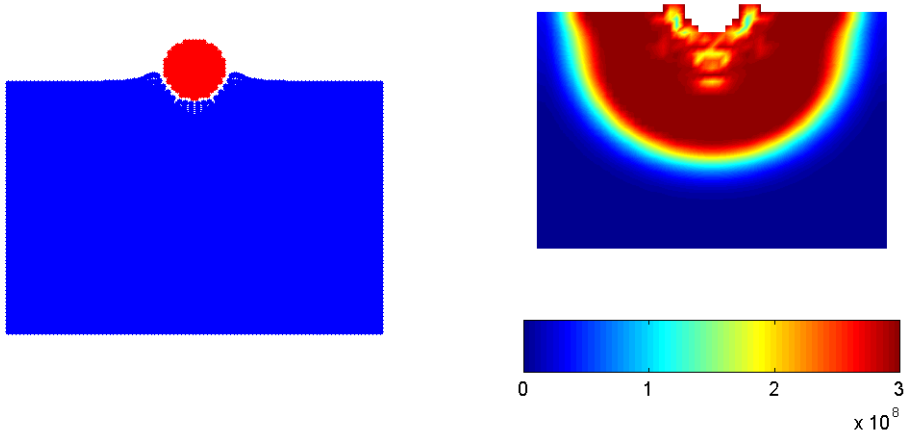

Figure 4.6: Penetration at $t = 6.4\,\mu s$, particles configuration and von Mises stress

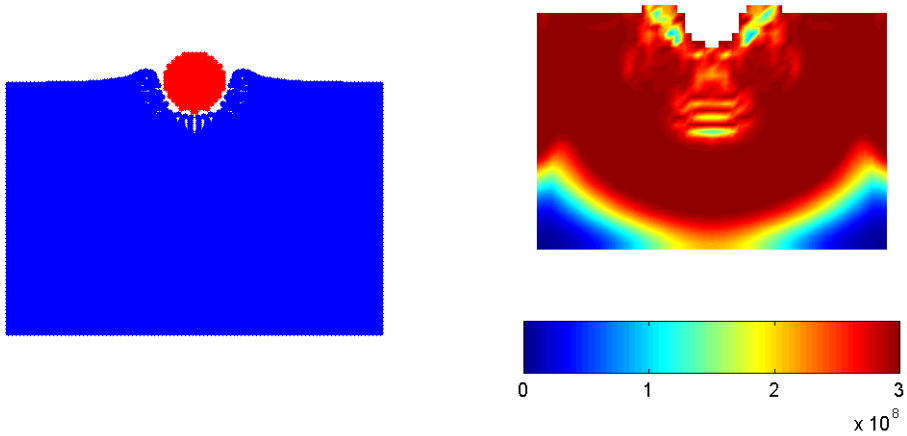

Figure 4.7: Penetration at $t = 9.6\,\mu s$, particles configuration and von Mises stress

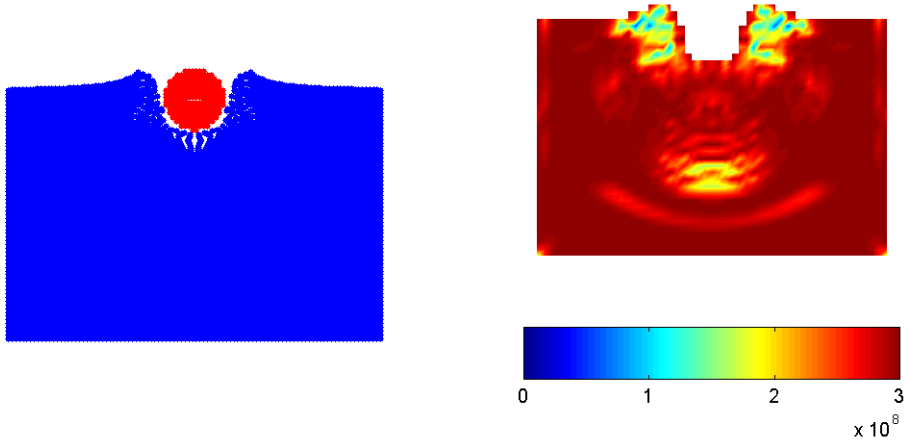

Figure 4.8: Penetration at $t = 12.8\,\mu s$, particles configuration and von Mises stress

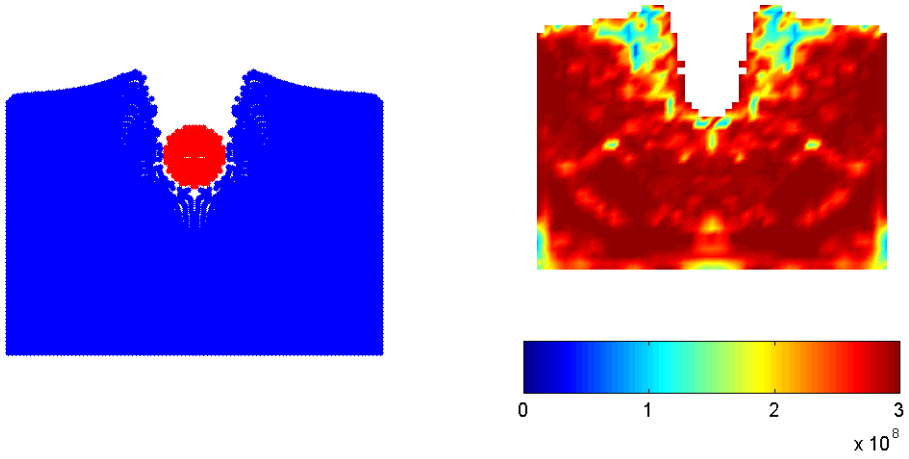

Figure 4.9: Penetration at $t = 32\,\mu s$, particles configuration and von Mises stress

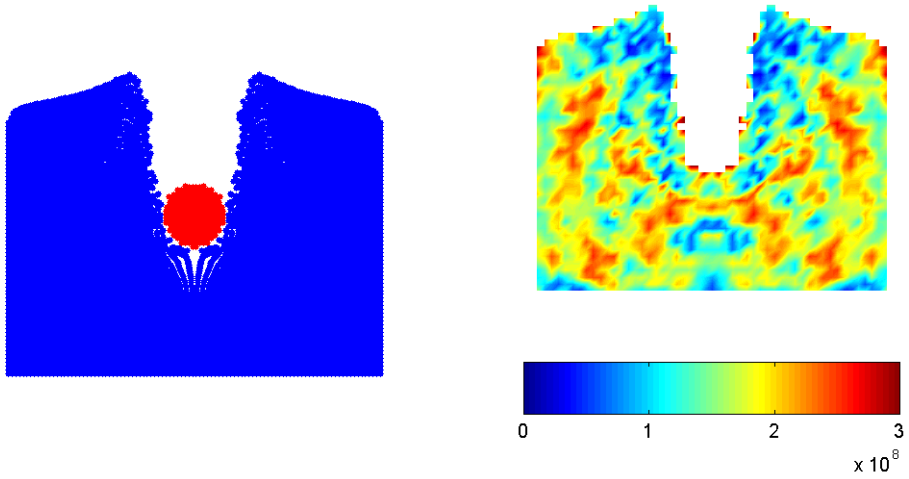

Figure 4.10: Penetration at $t = 80\,\mu s$, particles configuration and von Mises stress

4.3 Inclined Plane Simulation

Without the use of a special contact model, all contacts are automatically handled as non-slip contacts in the PIC method. This is a direct result of the single-valued velocity field used to update the particle positions. In order to model slip, a special contact algorithm must be employed. The model used in PICCUS assumes a Coulomb friction model. This allows frictional slip in the tangential contact direction and no interpenetration in the contact normal direction. This model is described by Bardenhagen *et al.* (2000) and the PICCUS implementation is given in Appendix G.

The simple case of an cylinder rolling down an inclined plane is used to demonstrate the ability of PICCUS to model Coulomb frictional contacts, figure 4.11a. The plane is inclined at an angle of θ to the horizontal, while gravity acts vertically down. Figure 4.11b shows the geometry for the simulation where the plane is aligned with the computational boundary, where friction is applied, and gravity makes an angle θ to the vertical. If the disk is rigid, its centre-of-mass velocity is tangent to the surface of the inclined plane, figure 4.11a, and tangent to the horizontal boundary, figure 4.11b.

A rigid disk on an inclined plane will either roll and stick at the contact point or roll and slip at the contact point. Whether the disk sticks or slips depends on the coefficient of friction and the inclination angle. It can be shown that if $tan\theta > 3\mu$ the disk will roll and slip (μ is the coefficient of friction), otherwise the disk will roll without slipping. For a rigid disk, starting from rest, the x_1-component of the centre position as a function of

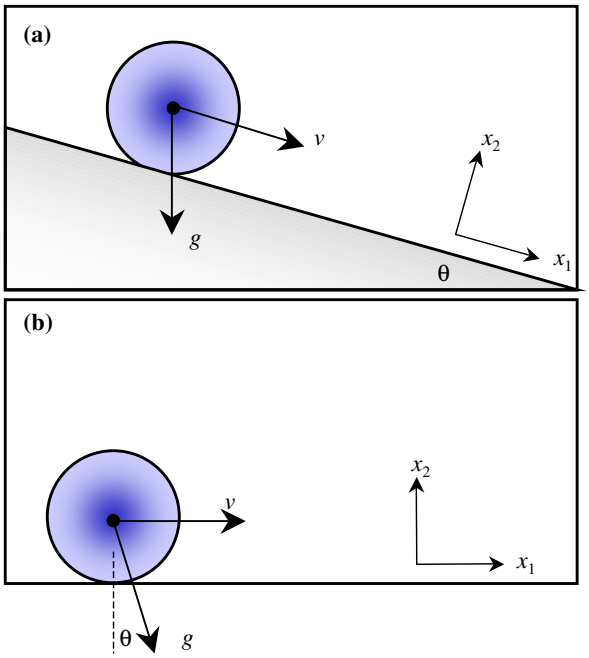

Figure 4.11: (a) Cylinder on an inclined plane, (b) Geometry for simulation of cylinder on inclined plane

time is given by equation 4.3.1.

$$x_1(t) = \begin{cases} x_o + \frac{1}{2}|\overline{g}|t^2(sin\theta - \mu cos\theta), & tan\theta > 3\mu \text{ (slip)} \\ x_o + \frac{1}{3}|\overline{g}|t^2 sin\theta, & tan\theta \leqslant 3\mu \text{ (stick)} \end{cases} \tag{4.3.1}$$

where x_o is the initial centre position.

Simulations were performed with a linear elastic disk with a radius of 0.5 m and gravitational acceleration of magnitude 9.81 m·s^{-2}. The computational domain had a size of 1.625 × 1.250 m with 26 × 20 square elements, i.e. 16 elements across the disk diameter. There are initially 4 particles per element. The disk has a shear modulus G = 2.5 MPa, a bulk modulus $K = 10$ MPa and a density of $\rho = 3000$ kg·m^{-3}. The stresses at the particles are initialised with a value given by the solution to the plane strain static problem, $\sigma_{11} = \sigma_{22} = -\rho g h$, $\sigma_{33} = \nu(\sigma_{11} + \sigma_{22})$, where g is the magnitude of the gravitational acceleration and h is the position of the material point measured from the top free surface of the disk (Timoshenko and Goodier, 1970). Figure 4.12 shows the disk after 0.3 seconds with $\theta = 60°$ and $\mu = 0.9$, i.e. a roll and stick contact occurs. The velocity vector of each material point is shown, scaled to one-tenth.

Figure 4.13 shows the centre displacement (x_1-component) as a function of time for $\theta = 60°$ and $\mu = 0.3$ (slip), $\theta = 30°$ and $\mu = 0.1$ (slip) and $\theta = 60°$

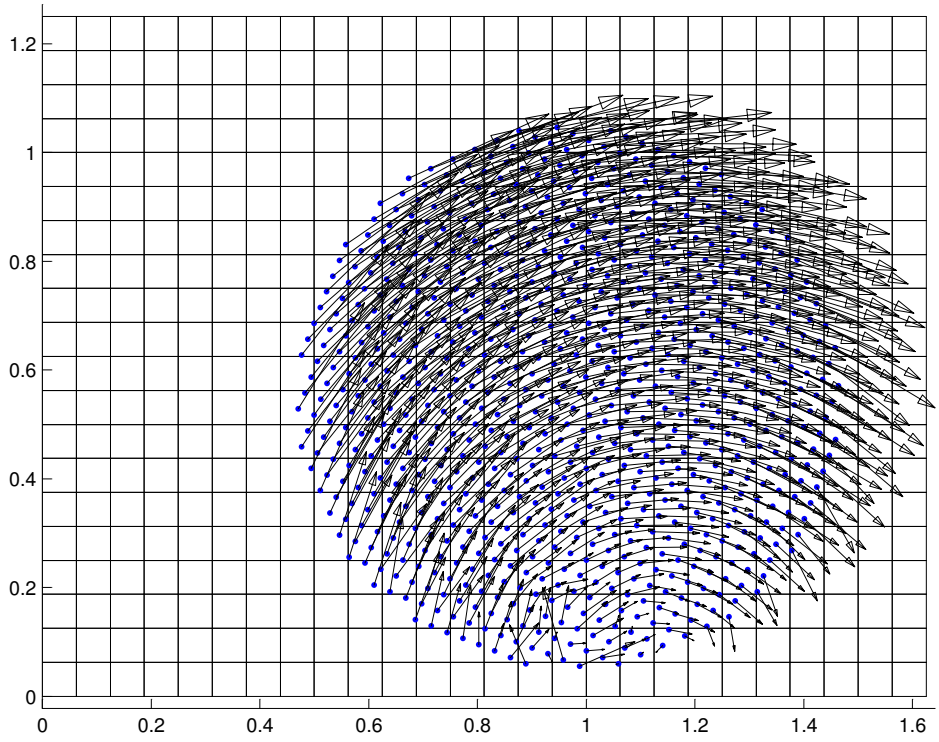

Figure 4.12: Disk at time $t = 0.3\,\text{s}$, $\theta = 60°$, $\mu = 0.9$. Velocity vectors $\frac{\vec{V}}{10}$

Table 4.2: The effect of mesh refinement on inclined plane simulation

Mesh size	# Particles	Initial DOF	Running time	Error at $t = 0.3\,\text{s}$
26×20	812	510	415 s	14.60 %
52×40	3228	1788	2128 s	6.40 %
104×80	12892	6780	23 400 s	0.56 %
Computing times with $dt = 1 \times 10^{-5}$ s, $\theta = 60°$, $\mu = 0.9$				

and $\mu = 0.9$ (stick). The errors in centre position calculated at $t = 0.3\,\text{s}$ are 0.05%, 0.50% and 0.56% respectively. Mesh sizes of 26×20, 52×40 and 104×80 were used to investigate mesh dependency. With a finer mesh the results are more accurate, as expected, and it also shows convergence. The number of particles, running times and accuracy are summarised in table 4.2. The simulations were run on an AMD 1.33GHz with 512 MB RAM.

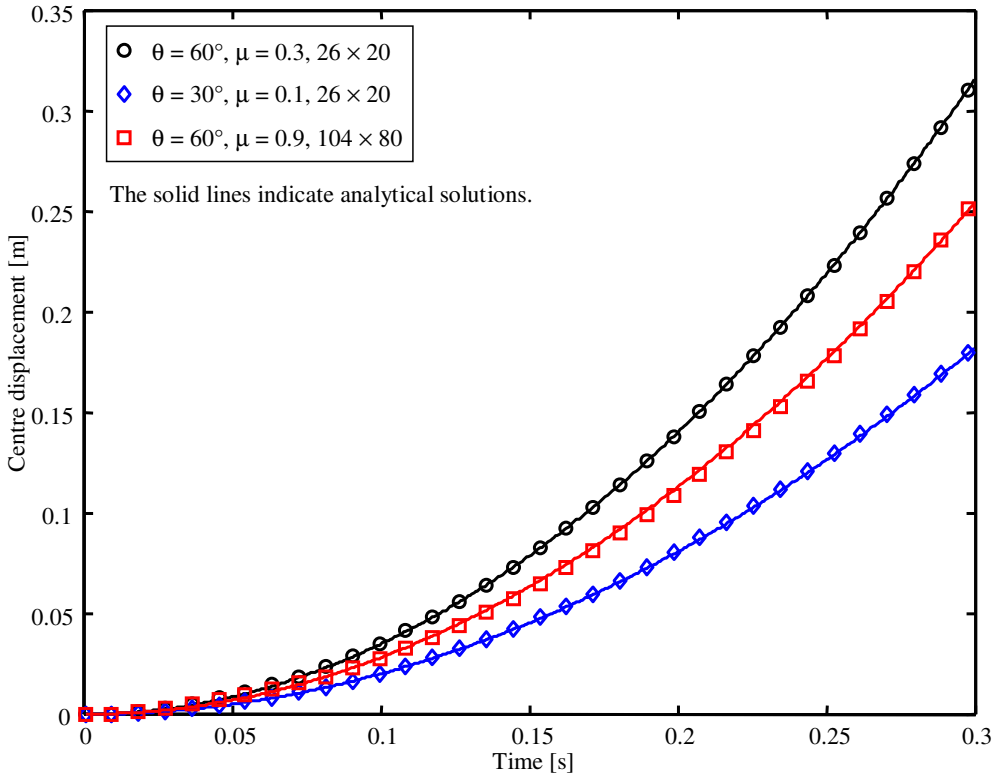

Figure 4.13: Inclined plane simulation: Centre position for different incline angles, friction coefficients and mesh sizes

4.4 Impact of Two Elastic Bodies

The simple impact of two elastic disks were analysed to evaluate the conservation of momentum and energy. Figure 4.14 shows the two disks at time $t = 0$. The domain size is 1.0×1.0 m with 25 elements in each direction. With initially 4 particles per element, each disk has 316 particles. Each disk has a diameter of 0.4 m. Simulations are performed in the absence of gravity. The material density is $\rho = 1000\,\mathrm{kg{\cdot}m^{-3}}$, Young's modulus $E = 1000\,\mathrm{Pa}$ and Poisson's ratio $\nu = 0.3$. Figure 4.15 to figure 4.17 show the disks at the point of contact, minimum kinetic energy and the point where contact is broken respectively. The contact between two bodies A and B is defined at the contacting nodes and not the material points and therefore it seems as if there is a gap between the two bodies in contact. Nodal contact occurs when a node is common to two elements, say 1 and 2, and element 1 contains at least one material point belonging to say entity A, and element 2 contains at least one material point belonging to entity B.

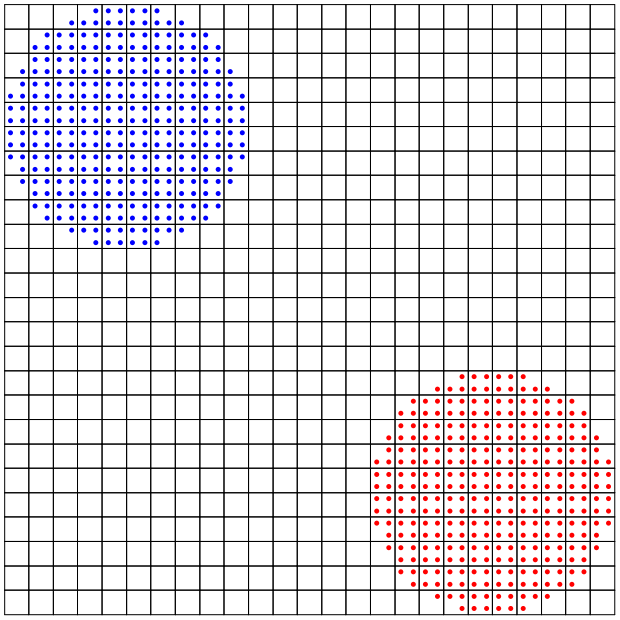

Figure 4.14: Initial positions of the disks at time $t = 0.00\,\mathrm{s}$

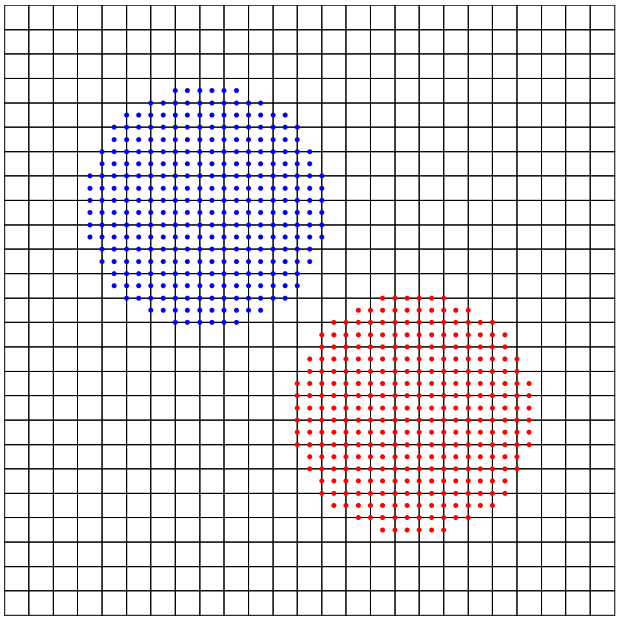

Figure 4.15: Positions of the disks at the point of contact, $t = 1.30\,\mathrm{s}$

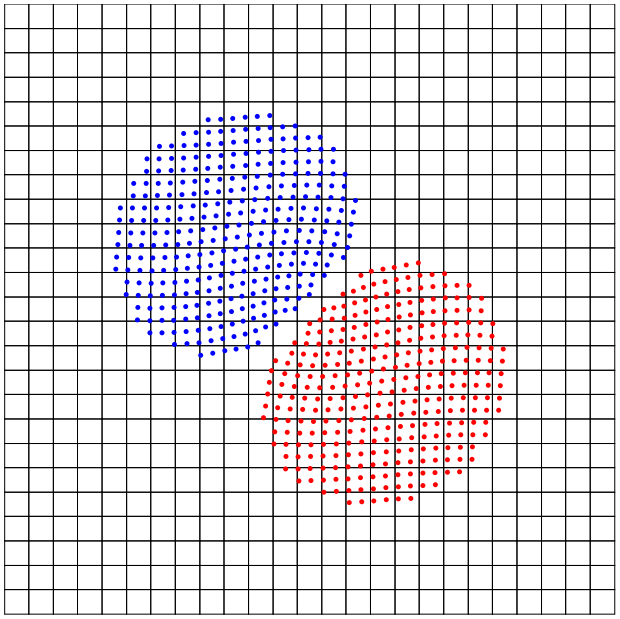

Figure 4.16: Positions of the disks at the point of minimum kinetic energy, $t = 1.96\,\mathrm{s}$

The disks start in the upper left and lower right hand corners with initial velocity components of $(0.1, -0.1)$ and $(-0.1, 0.1)$ $\mathrm{m{\cdot}s^{-1}}$ respectively. Figure 4.18 shows the x_1- and negative x_2- components of the momentum for the disk starting in the upper left hand corner. A time step of $\Delta t = 1 \times 10^{-5}$ s was used. There is no error in the numerical solution associated with a uniform translation of the disk through the grid. This can be seen by the fact that there is no change in momentum over the first 1.30 s, i.e. up to the point of contact. The disks rebound and translate in the opposite direction after the impact has occurred and the momentum switches sign. The negative of the x_2-component of momentum is indistinguishable from the x_1-component both before and after impact, which is expected as the displacement of the disk makes an angle of 45° with respect to the axis. The x_1-momentum at time $t = 4.00\,\mathrm{s}$ is slightly less than at time $t = 0.00\,\mathrm{s}$, but with the error being only 0.235% it is acceptable.

Figure 4.19 shows the energy plots. All of the initial energy is kinetic energy. The kinetic energy decreases during impact and is then mostly recovered after separation. The strain energy reaches its maximum value at the point of maximum deformation during impact and then decreases to a value associated with free vibration of the disk. After impact, the strain energy is small, but not zero. The fact that a zero value is not achieved can be attributed to the activation of several modes which do not exhibit zeros at the same time (Sulsky *et al.*, 1994).

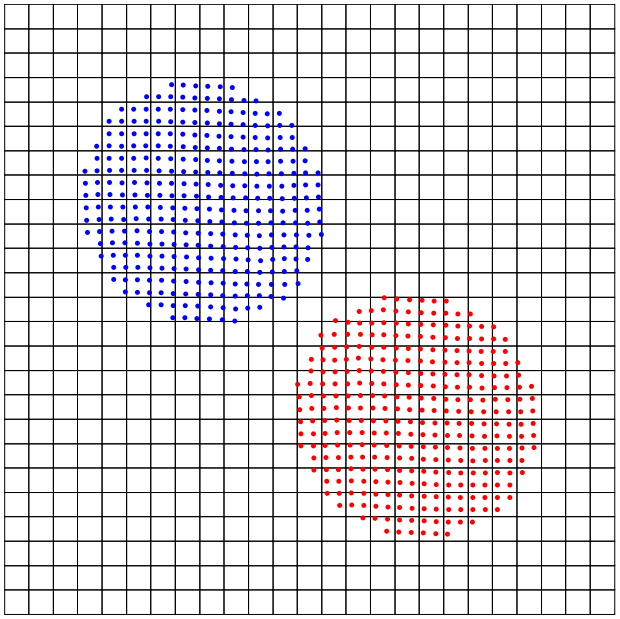

Figure 4.17: Positions of the disks at the point where contact is broken, $t = 2.68\,\mathrm{s}$

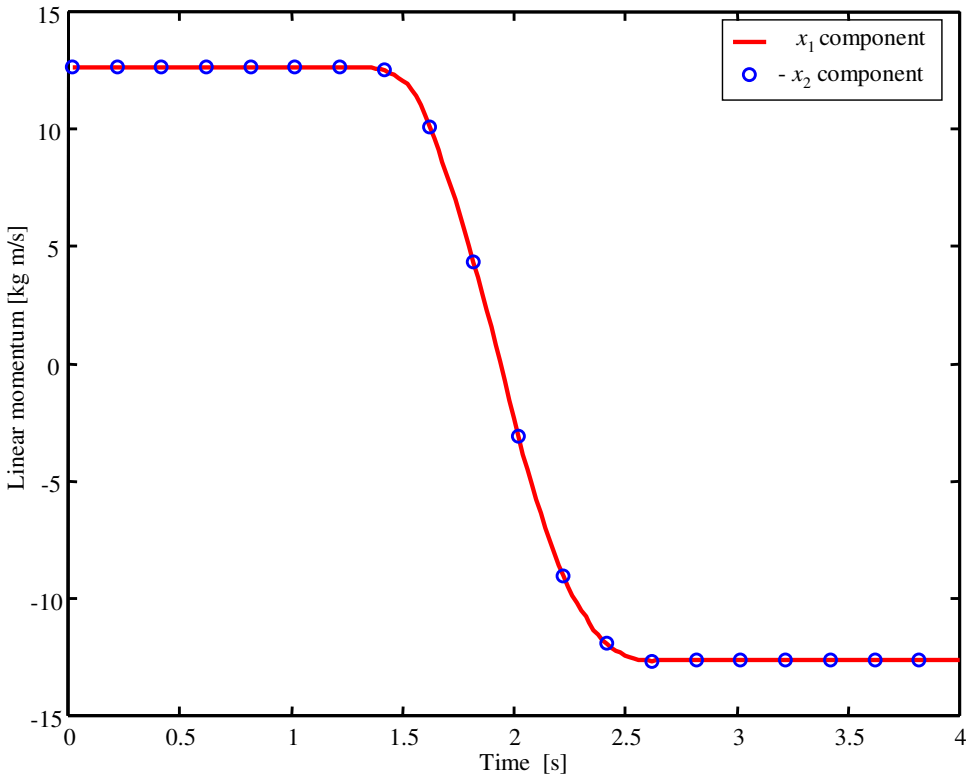

Figure 4.18: Momentum as a function of time for the disk starting in the upper left hand corner, $\Delta t = 1 \times 10^{-5}\,\mathrm{s}$

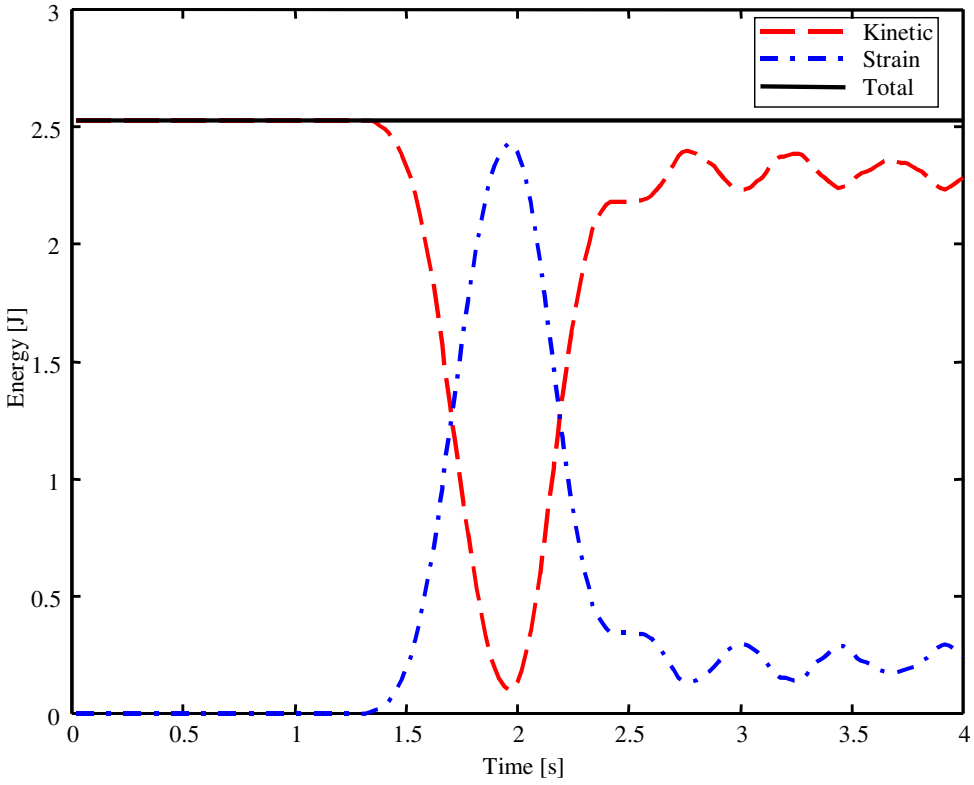

Figure 4.19: Energy as a function of time, $\Delta t = 1 \times 10^{-5}$ s. No slip contact

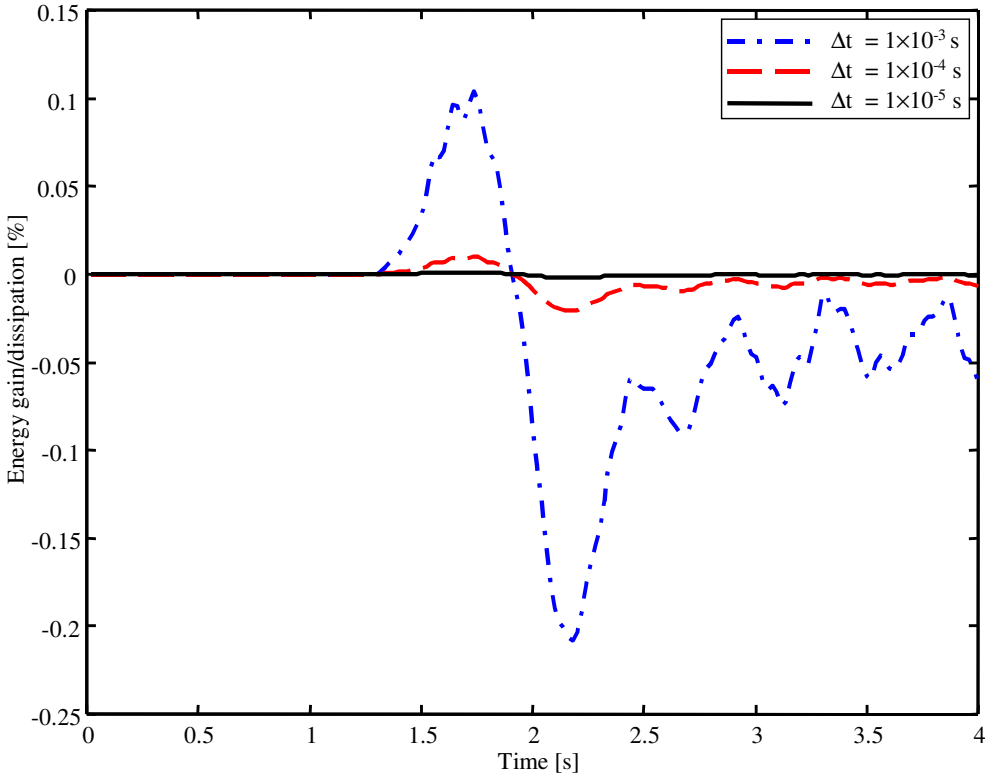

Figure 4.20: Gain/Dissipation in total energy as a percentage of the total energy at $t = 0$. Gain being positive and dissipation negative. No slip contact

Table 4.3: Energy gain/dissipation using different time steps

Time step	Max gain	Max dissipation
1×10^{-3} s	0.104 %	0.208 %
1×10^{-4} s	0.010 %	0.021 %
1×10^{-5} s	0.001 %	0.002 %

Figure 4.20 shows the dissipation and/or gain in total energy as a percentage of the energy at time $t = 0$ for different time steps. For the time up to contact, there is no dissipation or gain in energy. During and after contact, however, there are some dissipation and gain. As expected, with a decrease in the size of the time step, there is a decrease in error. Table 4.3 summarises the results.

In the above simulations no contact model was used, i.e. no slip conditions were assumed. If the contact model is used, Coulomb friction between the two disks can be modelled. A friction coefficient of $\mu = 0.1$ was assumed. It took 36 s to complete a simulation assuming no slip, and applying the contact model, the simulation took 42 s. When the contact model is used, boundary nodes must be found each time step and the unit normal vector calculated at contacting nodes before a contact correction can be applied. Thus the 16.7% increase in computation time.

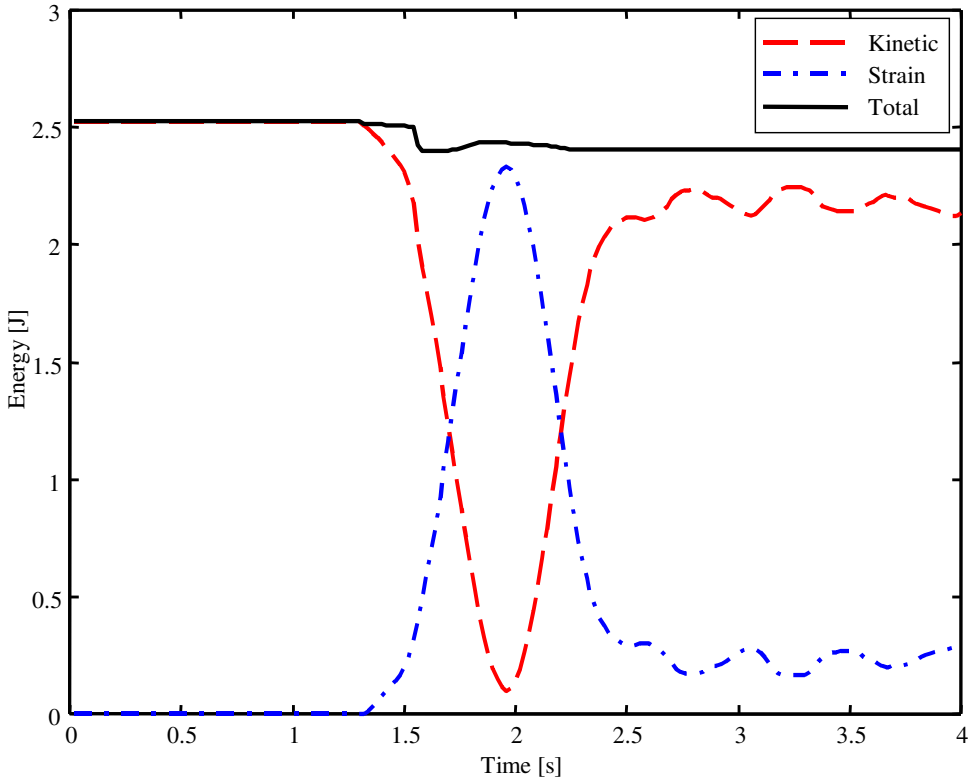

Figure 4.21: Energy as a function of time, $\Delta t = 1 \times 10^{-5}$ s, $\mu = 0.1$

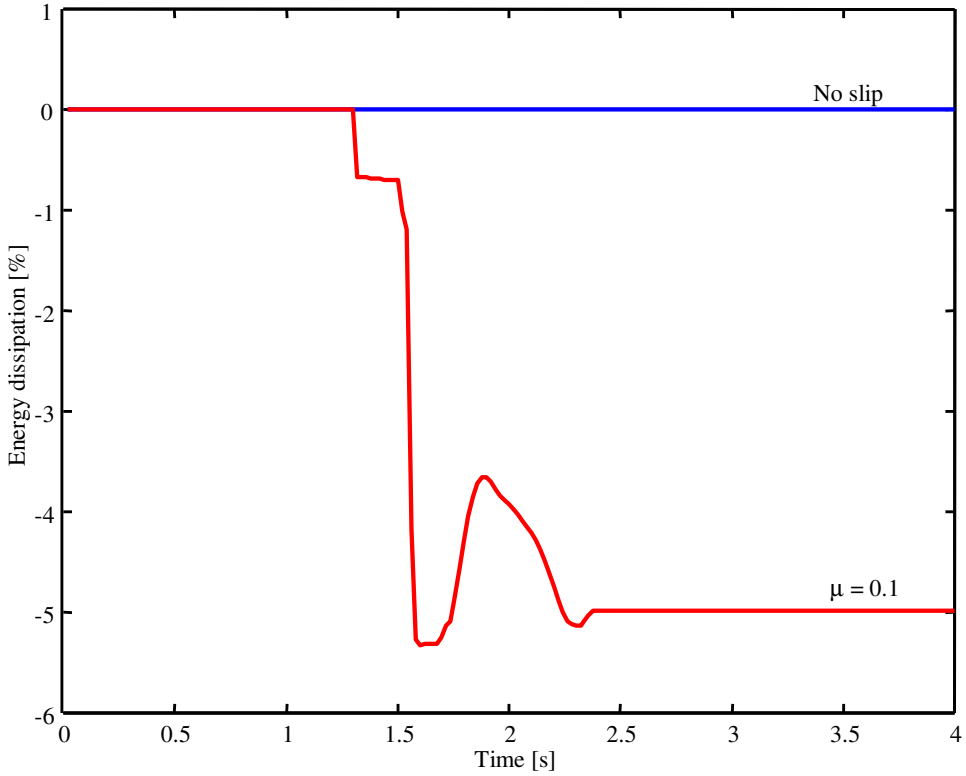

Figure 4.22: Gain/Dissipation in total energy as a percentage of the total energy at $t = 0$. Gain being positive and dissipation negative, $\Delta t = 1 \times 10^{-5}$ s

Figure 4.21 shows the total energy as a function of time when the Coulomb friction model is used. It can be seen that during impact there is a loss in total energy, but after impact, there is no additional dissipation. Figure 4.22 shows the dissipation as a percentage of the total energy at $t = 0$. On the scale used in this figure, there is no discernable dissipation when a no slip contact is assumed.

4.5 Oedometer Test

This example (FLAC, 1998) is used to evaluate the ability of the code to determine stresses in a Mohr-Coulomb material subjected to an oedometer test. In the principal stress space the Mohr-Coulomb shear criterion is represented by an irregular hexagonal pyramid (Appendix H). In an oedometer experiment, two of the principal stress components are equal, and during plastic flow, the stress point evolves along an edge of the pyramid. The purpose of this simulation is to indicate that the Mohr-Coulomb model as implemented in PICCUS, can handle such a situation. Results are compared to analytical solutions.

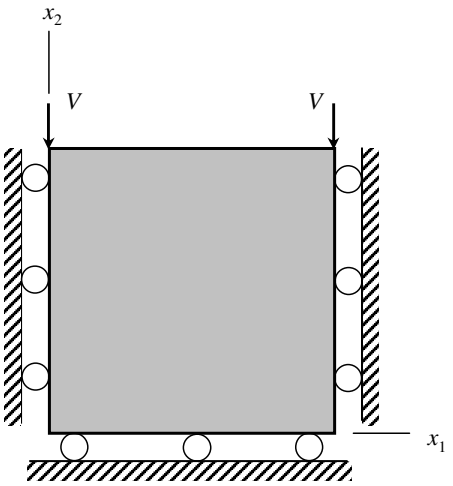

Figure 4.23: Boundary conditions for oedometer test (FLAC, 1998)

Table 4.4: Material properties used in oedometer test

Description	Symbol	Value
Bulk modulus	K	200 MPa
Shear modulus	G	200 MPa
Cohesion	c	1 MPa
Friction angle	ϕ	10°
Dilatancy angle	ψ	10° and 0°
Tensile limit	σ^t	5.67 MPa

The boundary conditions for the plane strain oedometer test are shown in figure 4.23. This corresponds to the uniform strain rates

$$\begin{aligned} \Delta\varepsilon_{11} &= 0 \\ \Delta\varepsilon_{22} &= \frac{V\Delta t}{L} \\ \Delta\varepsilon_{33} &= 0 \\ \Delta\varepsilon_{12} &= \Delta\varepsilon_{21} = 0 \end{aligned} \tag{4.5.1}$$

Since the shear stresses are all zero, the normal stresses are principal stresses. A constant velocity V is applied to the sample ($V < 0$) with a height L.

The application of Hook's law and the Mohr-Coulomb yield criterion leads to a closed-form solution to this problem (Appendix H). This analytical solution is compared to a numeric experiment using one element with 9 particles (3x3), figure 4.24. A rigid body plunger is used to induce the constant velocity at the upper boundary. The plunger also has 9 particles in a single element and the contact between the plunger and the Mohr-

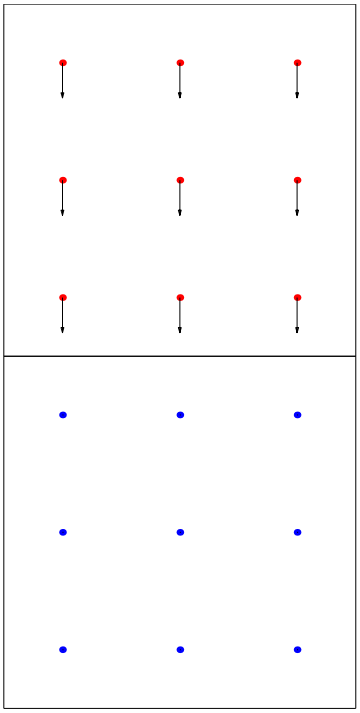

Figure 4.24: Oedometer test: Simulation setup with 9 particles per element. Plunger material point velocity vectors $\frac{\vec{v}}{100}$

Coulomb material is frictionless, i.e. perfectly smooth. The other boundary conditions are the same as in figure 4.23. The material properties used are shown in table 4.4.

A time step of 1×10^{-6} s, and a velocity of $10\,\mathrm{m{\cdot}s^{-1}}$ were applied. Two runs were carried out, one with $\psi = 10^\circ$ and the other with $\psi = 0^\circ$. The stress and strain in the x_2-direction is monitored. To make a comparison between the numeric and analytic results, the stress-strain curve is used. The results are shown in figure 4.25 and the numerical predictions correspond well with the analytical predictions. This shows that the model implemented can handle the case where the stress path follows an edge on the yield surface, automatically. The technique is only applicable to small-strain increments, as at each time step only one flow rule and corresponding stress correction is involved in case of plastic flow. As the stress point follows the edge, it receives stress corrections alternating between two criteria. In this process, two yield criteria are fulfilled to an accuracy which depends on the magnitude of the strain increment.

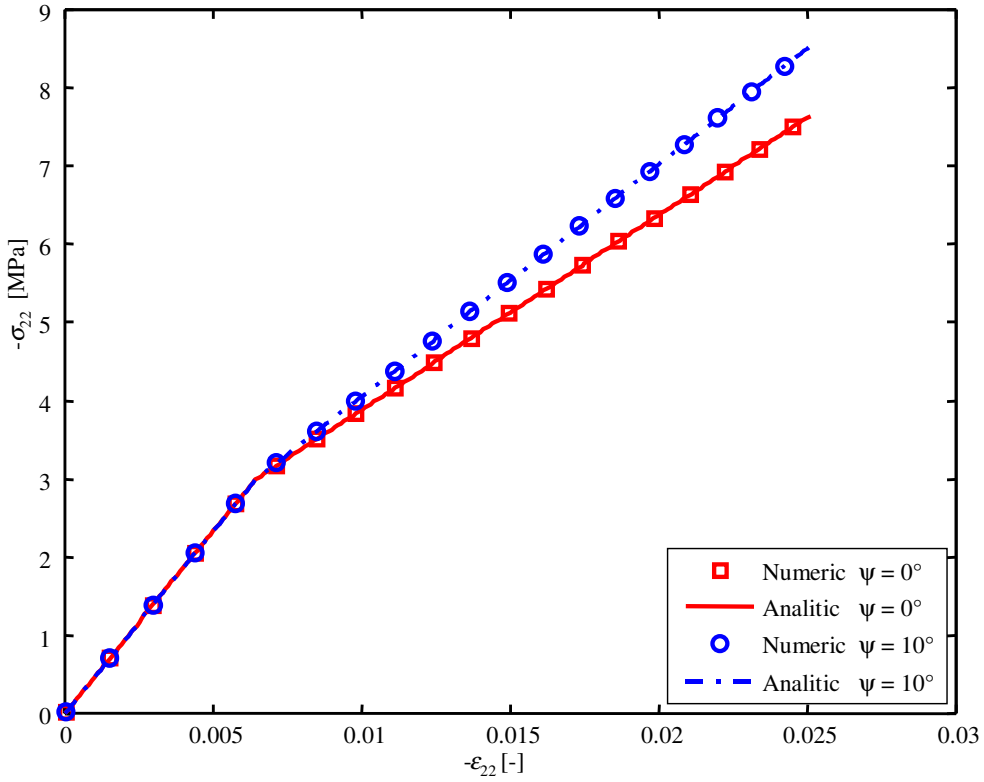

Figure 4.25: Oedometer test: Comparison between numerical and analytical predictions

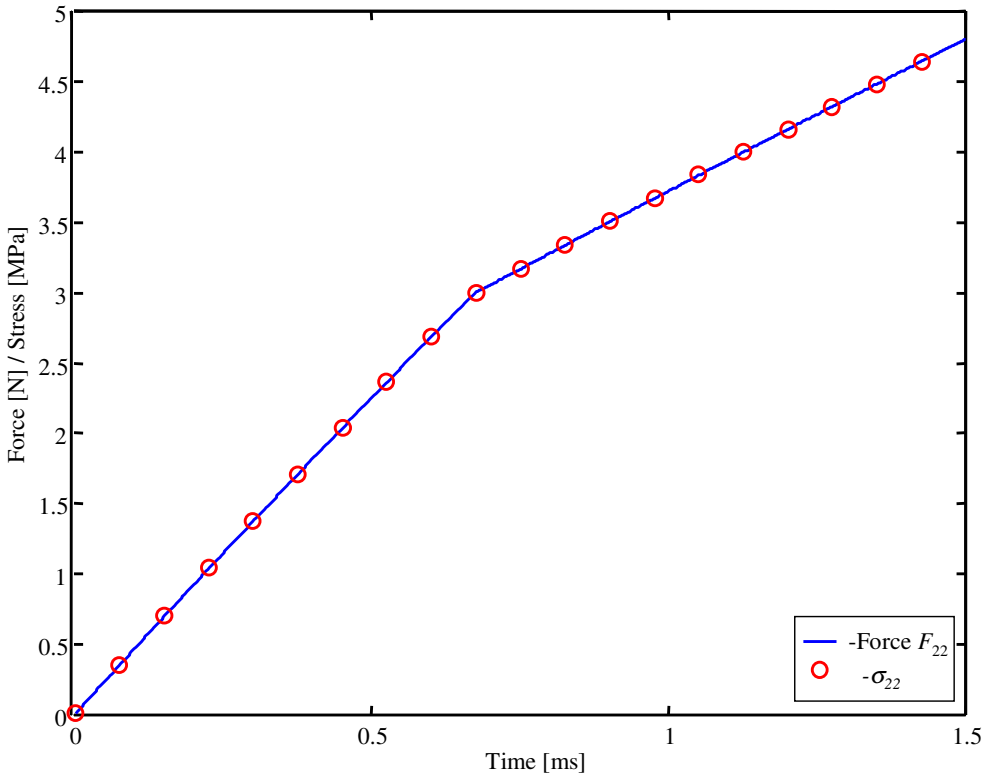

Figure 4.26: Oedometer test: Rigid body (plunger) force and normal stress (absolute values)

Using the nodal forces, the total force on the rigid body (plunger) can be calculated from the simulation. With the stress σ_{22} known, the force exerted by the plunger can be calculated analytically. With the width of the oedometer being 1 m and plane strain conditions, the contact area between the plunger and the material is 1 m^2, i.e. the force on the plunger should be equal to the normal stress σ_{22}. Figure 4.26 shows the comparison. It can be seen that the prediction of the plunger force is accurate.

4.6 Silo Discharging

The problem of flow of a granular material during silo discharging is considered. The flow patterns and flow rate are of importance. The entire discharge process is analysed which is difficult to model with FEM because the flow of material is highly distorted. When the updated Lagrangian formulation of the finite element method is used, the original mesh becomes distorted so significantly that mesh re-mapping is needed to restore proper element shapes (Wieckowski, 1998). Using an Eulerian formulation of the finite element method, the granular material can be treated as a

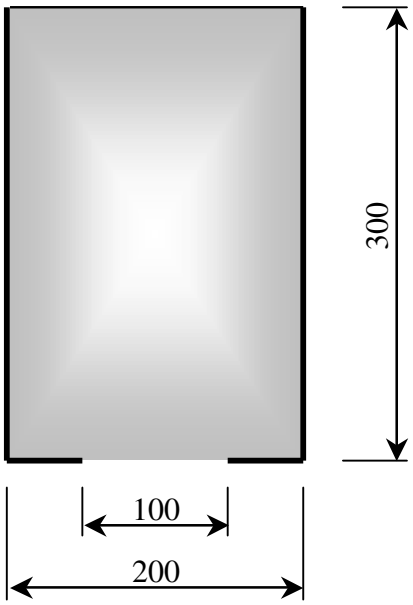

Figure 4.27: Silo shape. Dimensions in mm

Table 4.5: Drucker-Prager material data for silo discharging

Description	Symbol	Value
Young's modulus	E	1 MPa
Poisson's ratio	ν	0.3
Density	ρ	1500 kg·m^{-3}
Friction variable	q_ϕ	0.862
Tensile limit	σ^t	0 Pa
Friction variable	k_ϕ	0
Dilatancy variable	q_ψ	0
Material-wall friction	μ_{wall}	0.364 (20°)

non-classical fluid. The analysis is most useful in the case of continuously refilling the silo. The discrete element method can also be used, but this solution seems to be useful only when the ratio between the silo outlet diameter and the material grain diameter is not large.

The silo shape is depicted in figure 4.27. A Drucker-Prager material model was used with the material data summarised in table 4.5. The friction coefficient between the wall and the material is given by μ_{wall}, while the other parameters are defined in Chapter 2.7.

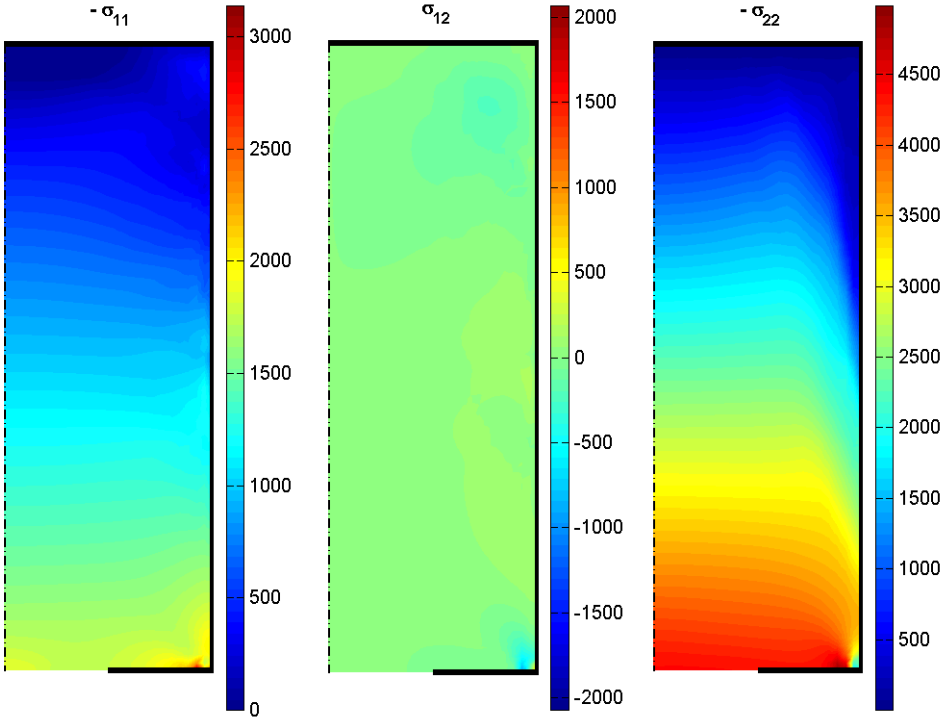

Figure 4.28: Material stresses at equilibrium

Because of symmetry, only half of the domain pictured in figure 4.27 was analysed. The half-silo was divided into square elements, 25×75, i.e., 4×4 mm. Initially, four particles per element were introduced. This resulted in a total of 1875 elements and 7500 particles. The particles were all created with zero initial stresses. Gravity was then applied with the silo opening closed. Applying a damping constant, $\alpha = 0.8$, an equilibrium (static) state could be obtained. The system was assumed static when the maximum value of velocity of all the particles satisfied $|v_i^{max}| \leq 1 \times 10^{-6}$ m·s^{-1}. Figure 4.28 shows the different stress components in the material at equilibrium.

After a static state was obtained, the silo was opened and material allowed to flow out the silo. Figure 4.29 shows the results obtained by Wieckowski (1998). In this analysis, 2194 triangular elements (of which the sides were no longer than 6.25 mm) were used and four particles per element, i.e, 8776 particles. Calculations had been performed with a time increment $\Delta t = 5 \times 10^{-5}$ s. Figure 4.30 shows the results obtained using PICCUS, the time increment also being $\Delta t = 5 \times 10^{-5}$ s.

Quantitatively, there is very good agreement in the flow patterns. The friction models employed are not exactly the same and the discretisation also differs (triangular vs square elements), which would account for the slight differences.

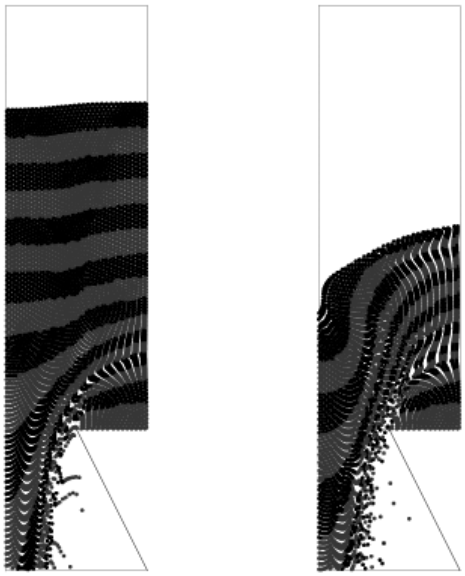

Figure 4.29: Deformations at time 0.2 and 0.4 seconds, Wieckowski (1998)

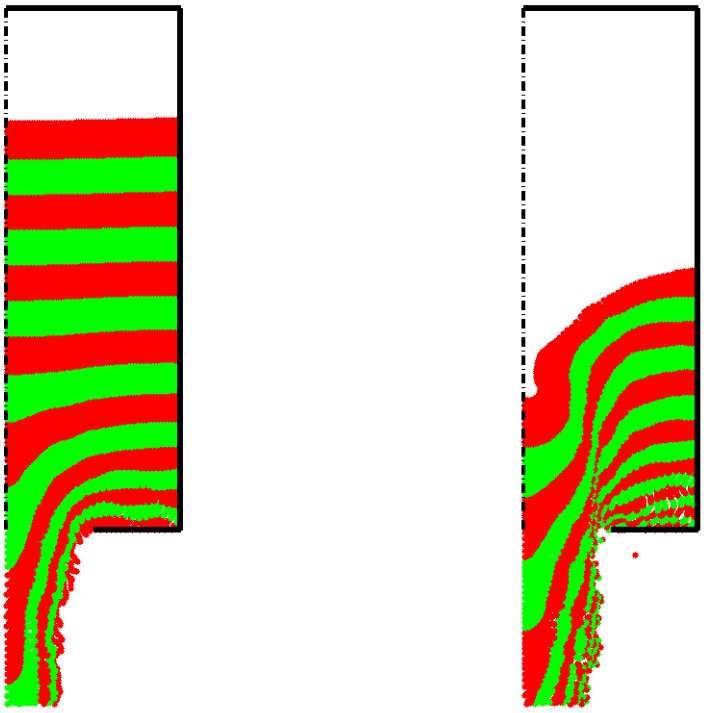

Figure 4.30: Deformations at time 0.2 and 0.4 seconds, PICCUS

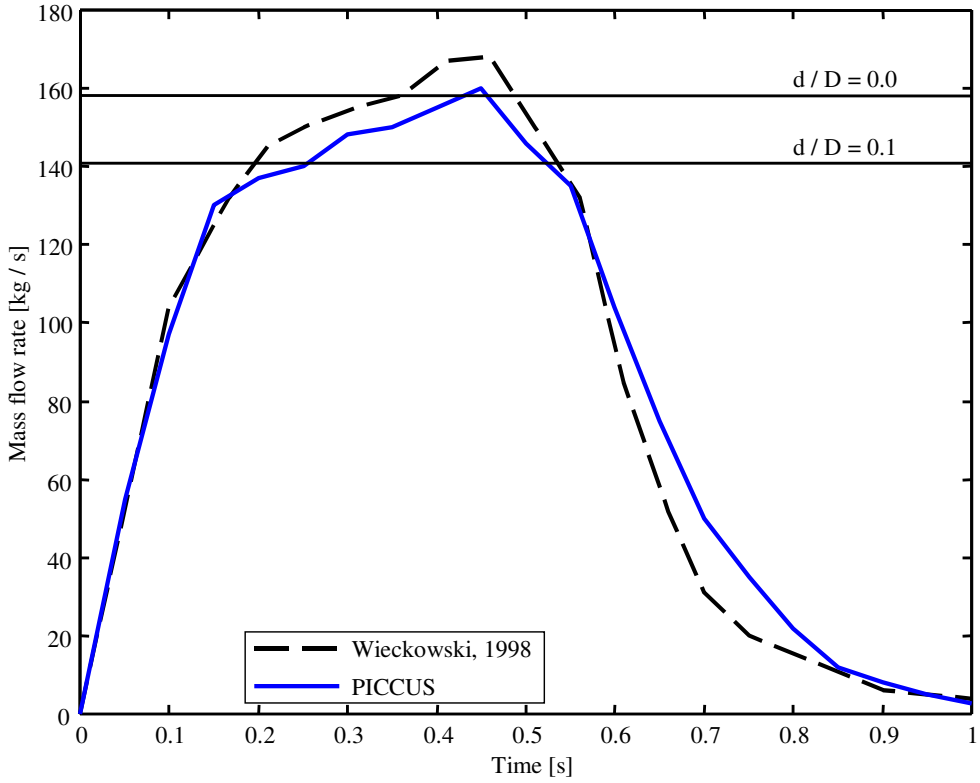

Figure 4.31: Silo flow rate

Wieckowski (1998) compared the flow rate with results obtained from the empirical formula established by Beverloo *et al.* (1961)

$$W = 45\rho\sqrt{2g}\left[D\left(1 - 0.7\frac{d}{D}\right)\right]^{1.5} \tag{4.6.1}$$

where $\rho = 1500\,\mathrm{kg{\cdot}m^{-3}}$, $g = 9.81\,\mathrm{m{\cdot}s^{-2}}$, $D = 0.1\,\mathrm{m}$ is the width of the outlet, and d is the diameter of the material grains measured in metres. The flow rate W is then given in $\mathrm{kg{\cdot}min^{-1}}$. The results are summarised in figure 4.31. The result obtained by Wieckowski (1998) is shown as well as those predicted by PICCUS. The two horizontal lines are the empirical predictions using ratios $\frac{d}{D} = 0.0$ and $\frac{d}{D} = 0.1$ respectively. A fairly good agreement between the numerical and empirical results is observed for the time interval when the flow rate is nearly stabilised.

Wieckowski (1998) did not compare his results to experiments. The aim of this analyses is only to validate the implementation of the code. Silo discharging is studied in more detail in Chapter 6, where the results are compared to experiments and DEM simulations.

4.7 Blade Simulations

All soil cutting, moving and tillage instruments transfer soil from its original position. Thus the mechanical failure of the soil is involved in the sense that the mass of soil being moved does not retain its original geometric shape. The design of effective and efficient implements begins with the analysis of the soil failure in order to predict the forces and energy required by the implements.

The simplest form of soil cutting or tillage is that of a flat blade moving through the soil. Different theories to predict the forces acting on a blade were proposed. The methods of Coulomb (Hansen, 1961) and Perumpral (Perumpral *et al.*, 1980, 1983) assume that the material in front of the blade fails and moves as a rigid body. The sum of all forces acting on this rigid body can be used to solve for the forces acting on the blade.

A totally different method is based on the theory of plasticity (Sokolovski, 1954). This theory is based on the assumption that a state of failure exists at any point within a certain area (zone ruptures) or on a certain curve (line ruptures). By means of this assumption and using the equations of equilibrium, it is possible to solve soil pressure problems. The material is assumed to be macroscopically homogeneous and in a critical state. The definition for critical state is when the material or part thereof is stressed to the limit of the Mohr-Coulomb yield criterion at the point just before slip occurs. The analysis is conducted for static equilibrium and no dynamic effects are taken into account. Deformation effects such as dilation are not accounted for. A set of differential equations, derived from the Mohr-Coulomb yield criterion and the equations of equilibrium, is numerically solved using the method of characteristics and appropriate boundary conditions and material properties. Figure 4.32 shows the result from such a calculation where the blade makes an angle θ with the vertical. The different characteristic curves (ξ_i, η_i), a direct result from the solution, are shown. The outer curve ξ_9 is called the rupture line or shear band. All the material points within the region of the characteristic curves are in a critical state. With the stresses at each node known, the forces acting on the blade can be estimated.

In order to compare Sokolovski's method to results from PICCUS, simulations were performed with a vertical blade $(\theta = 0)$ at different depths, h. Figure 4.33 shows the initial particle configuration close to the blade for $h = 0.27$ m. There were initially four particles per element and the total domain size is 1.0×0.5 m, with 100×50 square elements, resulting in 15840 particles. The bottom boundary was fixed in the x_2-direction and free in the x_1-direction, while the left- and right-hand boundaries were fixed in the x_1-direction and free in the x_2-direction. A Mohr-Coulomb elastic-perfectly-plastic material was used, with the properties summarised in table 4.6

Particles were all created with zero stresses. With only gravitational

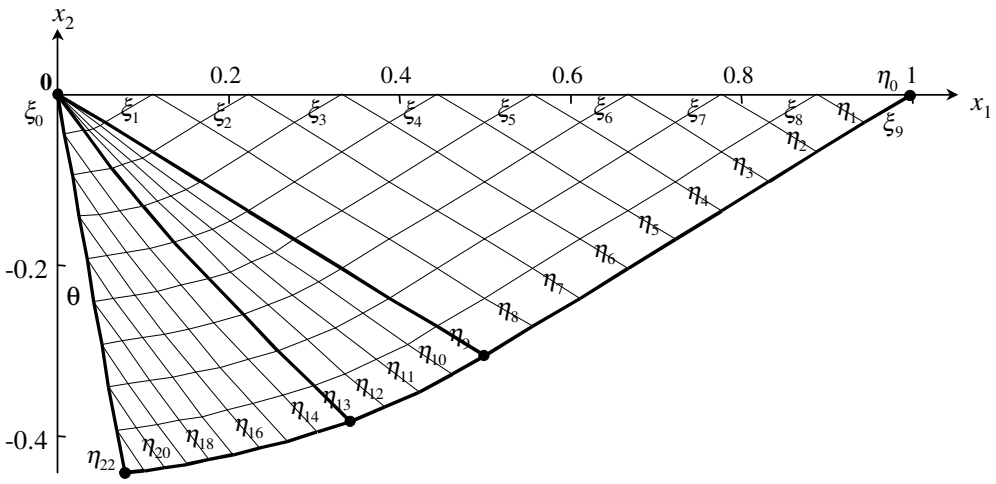

Figure 4.32: Blade forces - sample calculation

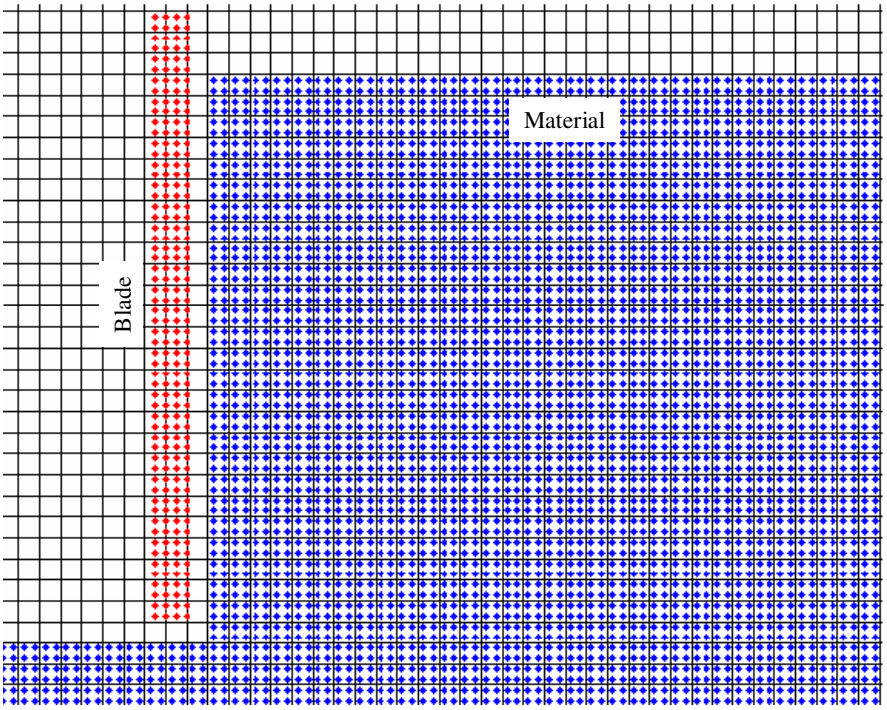

Figure 4.33: Initial particle configuration close to the blade, $h = 0.27\,\mathrm{m}$

Table 4.6: Material properties used in blade simulation

Name	Symbol	Value
Young's modulus	E	1 GPa
Density	ρ	1500 kg·m^{-3}
Poisson's ratio	ν	0.3
Friction angle	ϕ	35°
Dilatancy angle	ψ	0°
Cohesion	c	0 Pa
Tensile limit	σ^t	0 Pa

Table 4.7: Blade simulation parameters

Name	Symbol	Value
Integration time step	Δt	1×10^{-5} s
Damping	α	0
Gravity	g_i	$(0.00, -9.81)$ m·s^{-2}
Blade-material friction	μ	0.2
Blade velocity	v	0.005 m·s^{-1}

forces acting on the material, and using a damping constant of $\alpha = 0.8$, the material was then allowed to reach static equilibrium. Equilibrium was defined when the maximum value in particle velocity satisfied $|v_i^{max}| \leq 1 \times 10^{-8}$m·s^{-1}.
The stresses at static equilibrium are shown in figure 4.34. Using the simulation parameters summarised in table 4.7, the blade was given a constant velocity in the x_1-direction. This resulted in the material in front of the blade being pushed forward until it yielded. Figure 4.35 shows the x_1- and x_2-forces exerted by the blade on the material during a typical simulation. The negative x_2-force indicates that the material tended to push the blade upwards, out of the material.

The blade forces start from almost zero and then increase in value as the material is being accelerated. After 1.5 s the forces seem to reach a steady value and only small oscillations are present. The average force between 2.0 and 7.0 s was compared to the forces predicted by Sokolvski's method. Figure 4.36 shows the results from using different blade depths. From this it can be seen that there is good agreement between the two different methods. PICCUS's predictions of the x_1-force are roughly between 64 and

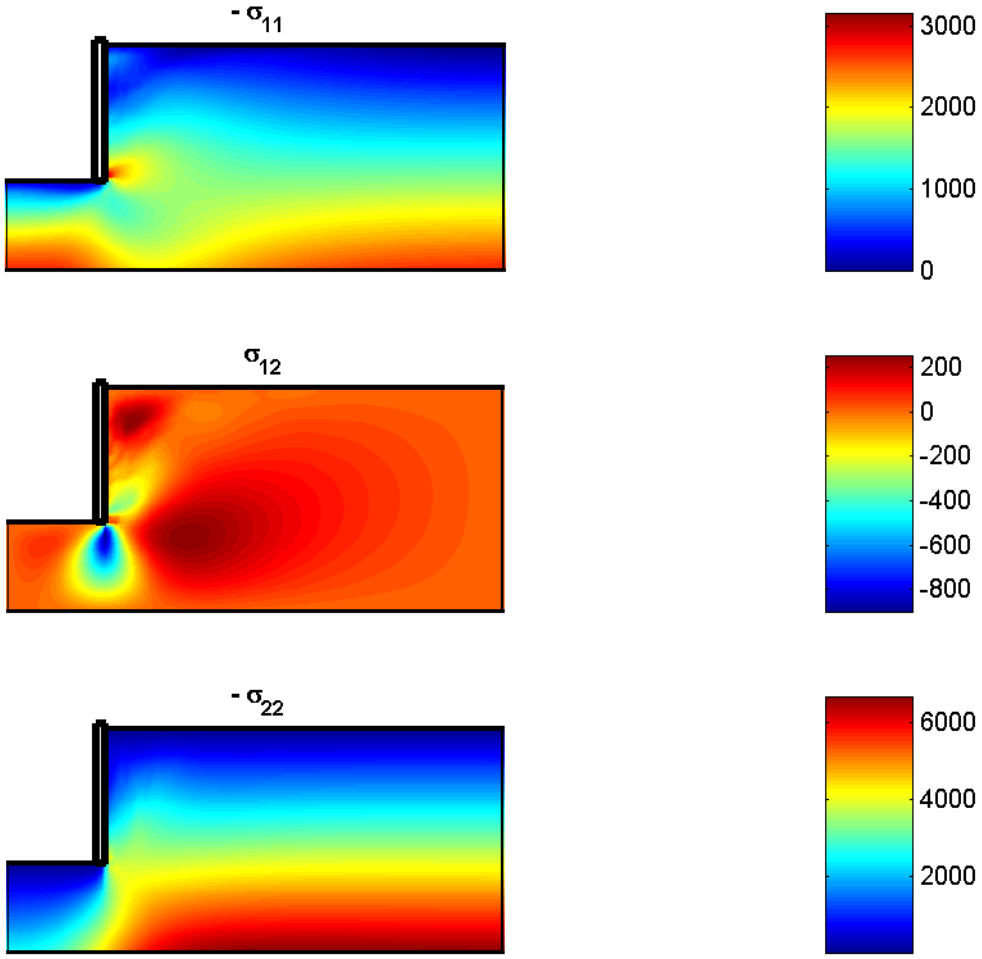

Figure 4.34: Blade simulation: initial stresses, $h = 0.27\,\mathrm{m}$

103 N too high, while there is excellent agreement on the x_2-force. The percentage difference, defined as

$$\Delta F_{\%} = \frac{F^{\text{PICCUS}} - F^{\text{Sokolovski}}}{F^{\text{Sokolovski}}}\,100\% \tag{4.7.1}$$

is shown in figure 4.37. From this it can be seen that as the blade depth increases, the difference decreases.

The material failure can be investigated by looking at the velocity of the particles. The Coulomb and Perumpral methods assume that the material within the yield region moves as a rigid body with a definite shear band separating it from the virgin material. Figure 4.38 shows the velocity vector of every tenth particle and the shear band calculated by Sokolovski's method. It is clear that the material points above the shear band have a much higher velocity then the material points below the line.

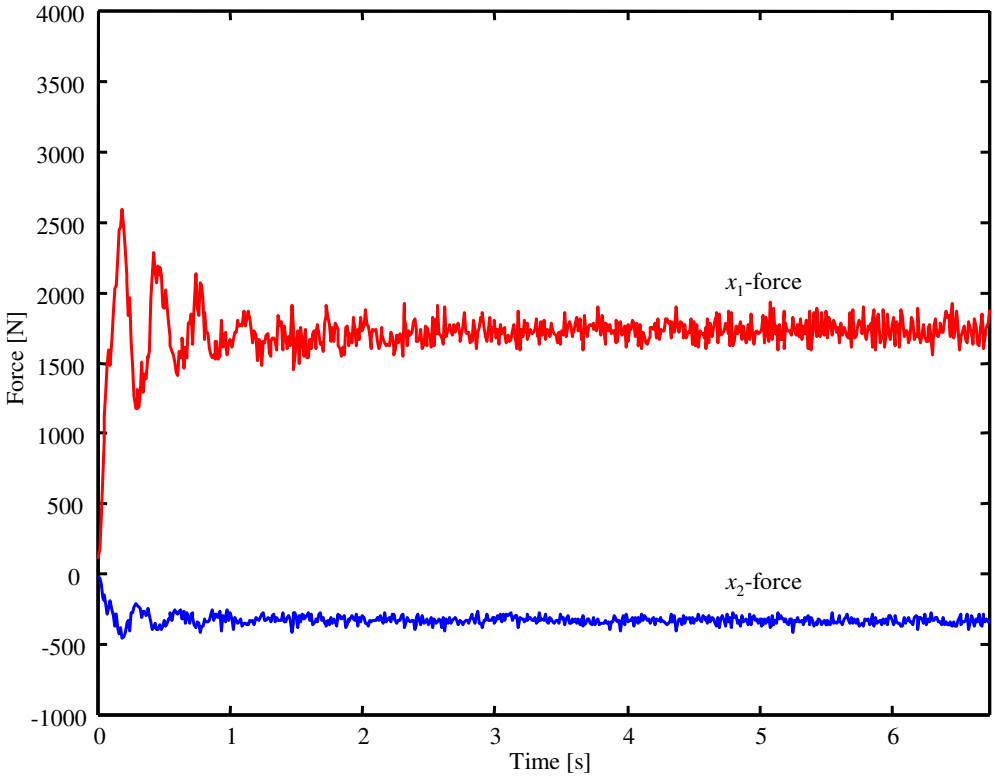

Figure 4.35: Blade simulation: typical blade forces, $h = 0.21\,\text{m}$

The material failure can also be investigated by looking at which material points are stressed up to the Mohr-Coulomb yield surface $f^s = 0$. Figure 4.39 and figure 4.40 show the material as well as the Sokolovski predicted shear bands for $h = 0.27\,\text{m}$ and $0.15\,\text{m}$ respectively. The material is coloured according to the stress at each point. The lighter regions indicate material points with the stresses on the yield surface, i.e., material yielding at that time, and the darker regions indicate material with stresses such that $f^s > 0$, i.e., in an elastic state of stress. These figures also indicate good agreement between the Sokolovski predictions and those obtained using PICCUS. The material in the shear band and above it yields, while the material below the shear band stays in the elastic range. No cohesion was used which means that the apex of the yield surface is at $\sigma_1 = \sigma_2 = \sigma_3 = 0$. The material at the free surface has stress components close to zero and therefore it shows yielding even away from the region affected by the blade.

Different mesh sizes were used to investigate the effect of mesh refinement on the blade forces. A blade depth $h = 0.21\,\text{m}$ was used. Figure 4.41 shows that the forces acting on the blade converge with mesh refinement. The effect of mesh refinement on the shear bands are shown in Chapter 6, where polar and nonpolar results are compared to experiments,

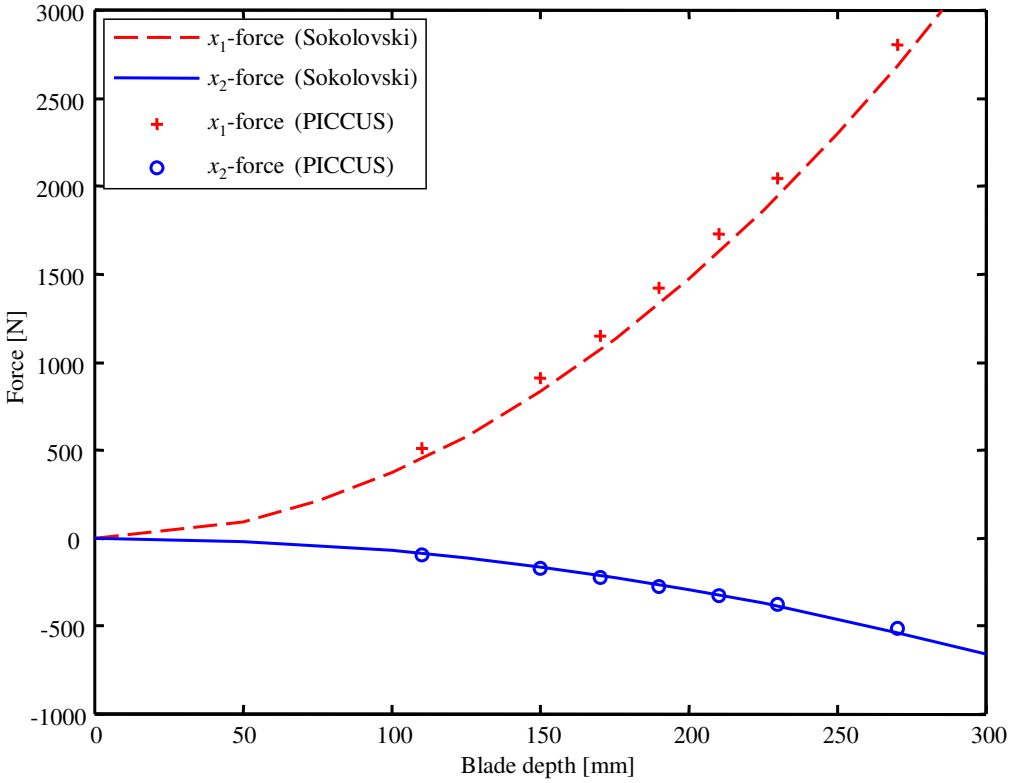

Figure 4.36: Blade simulation: Comparison of blade forces

Sokolovski's method and DEM results.

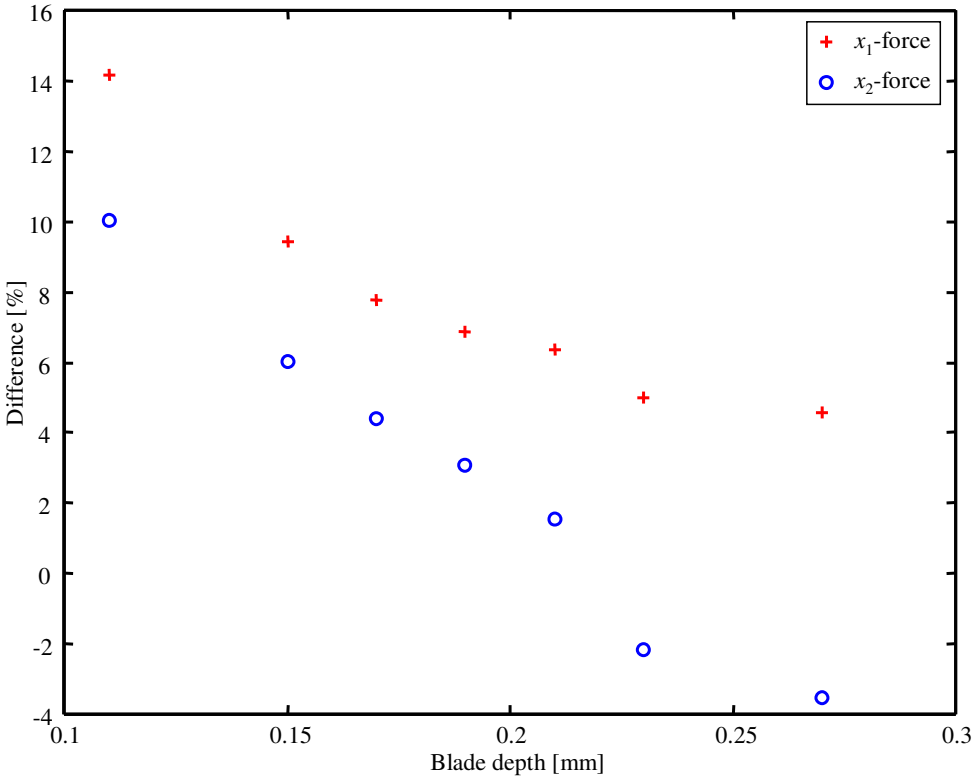

Figure 4.37: Blade simulation: Percentage difference in the prediction of the blade forces

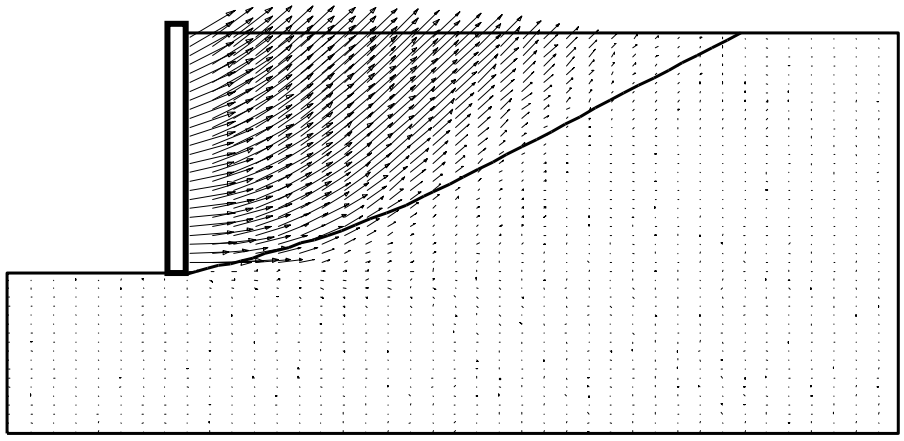

Figure 4.38: Blade simulation: Particle velocity vectors, scaled 15 times, $h = 0.27\,\mathrm{m}$

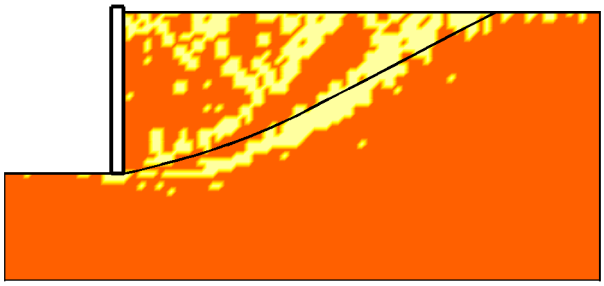

Figure 4.39: Blade simulation: Material stress, lighter regions - material yielding, darker regions - material in an elastic state, $h = 0.27\,\mathrm{m}$

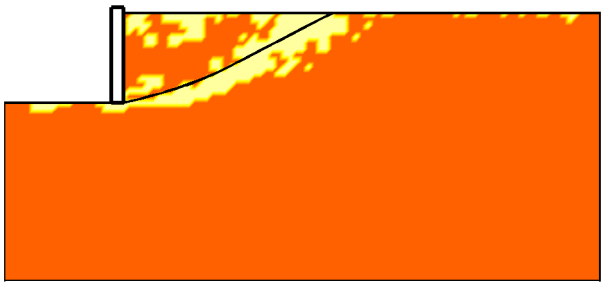

Figure 4.40: Blade simulation: Material stress, lighter regions - material yielding, darker regions - material in an elastic state, $h = 0.15\,\mathrm{m}$

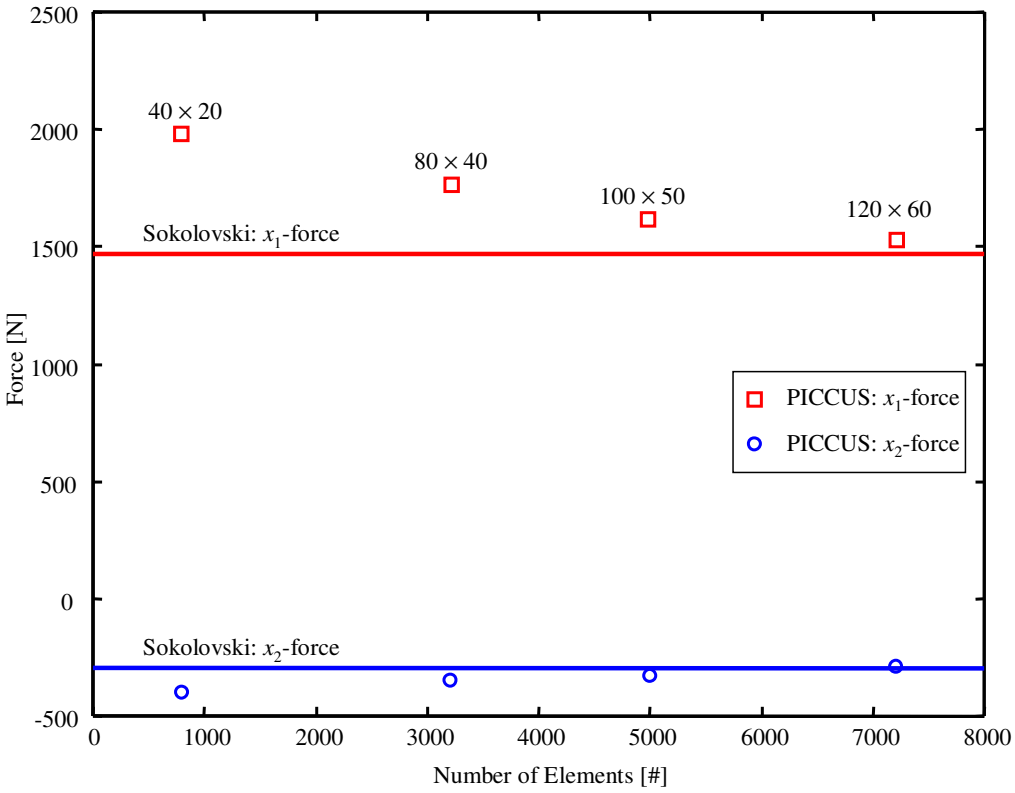

Figure 4.41: The effect of the mesh size on the blade forces, $h = 0.21\,\mathrm{m}$

4.8 Elastic Strip Footing

This analysis concerns a strip loading on an elastic mass. Figure 4.42 shows the geometry of the problem being analysed and the PICCUS discritisation. Only one symmetric half of the problem is analysed with the boundary conditions as shown in the figure. A square mesh of 80×80 elements is utilised with a smooth interface between the rigid footing and the material. The elastic material properties are summarised in table 4.8.

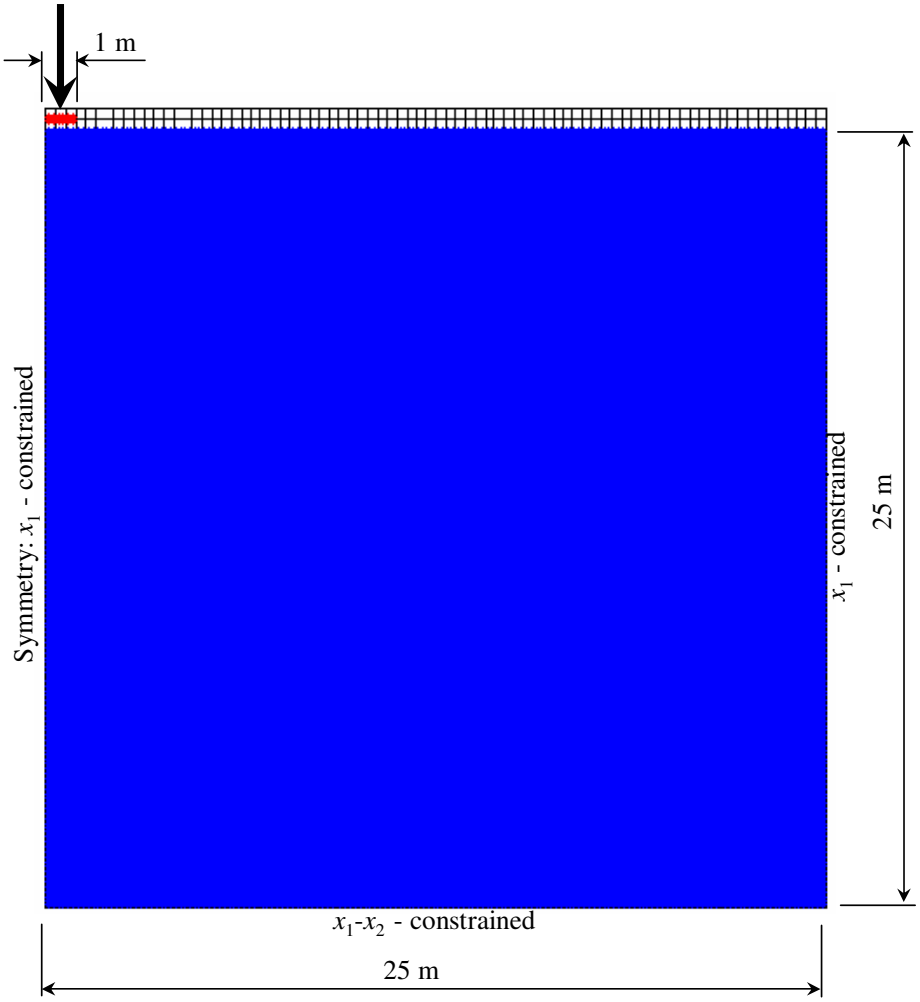

Figure 4.42: PICCUS model for strip loading on an elastic mass

The footing was given a downward velocity of $V = 0.01\,\mathrm{mm{\cdot}s^{-1}}$ until the pressure reached a 100 kPa. The footing was then kept still and a damping factor of $\alpha = 0.8$ was applied until a equilibrium state was reached.

Table 4.8: Material properties used in elastic footing simulation

Name	Symbol	Value
Young's modulus	E	20 GPa
Density	ρ	1000 kg·m^{-3}
Poisson's ratio	ν	0.2

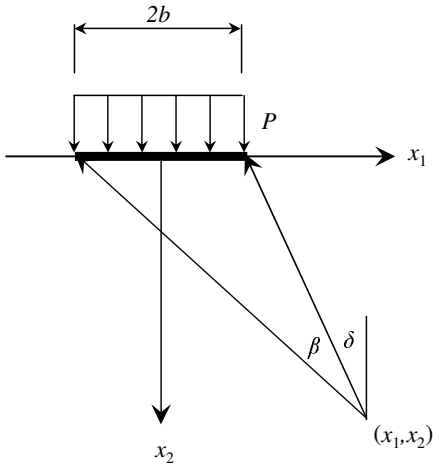

Figure 4.43: Definition of parameters used in the elastic solution to the footing problem

A closed-form solution for this problem, using the notation given in figure 4.43, is given by Poulos & Davis (1974). The stresses at the coordinates $(x_1 x_2)$ under the surface are given by

$$\begin{aligned} \sigma_{11} &= \frac{P}{\pi}\left[\beta - sin\beta\ cos(\beta + 2\delta)\right] \\ \sigma_{22} &= \frac{P}{\pi}\left[\beta + sin\beta\ cos(\beta + 2\delta)\right] \\ \tau_{12} &= \frac{P}{\pi} sin\beta\ sin(\beta + 2\delta) \end{aligned} \tag{4.8.1}$$

and the principal stresses are

$$\begin{aligned} \sigma_1 &= \frac{P}{\pi}\left(\beta + sin\beta\right) \\ \sigma_2 &= \frac{P}{\pi}\left(\beta - sin\beta\right) \\ \tau_{max} &= \frac{P}{\pi} sin\beta \end{aligned} \tag{4.8.2}$$

Figure 4.44 shows the principal stresses along $x_1 = 0$ under the strip foo-

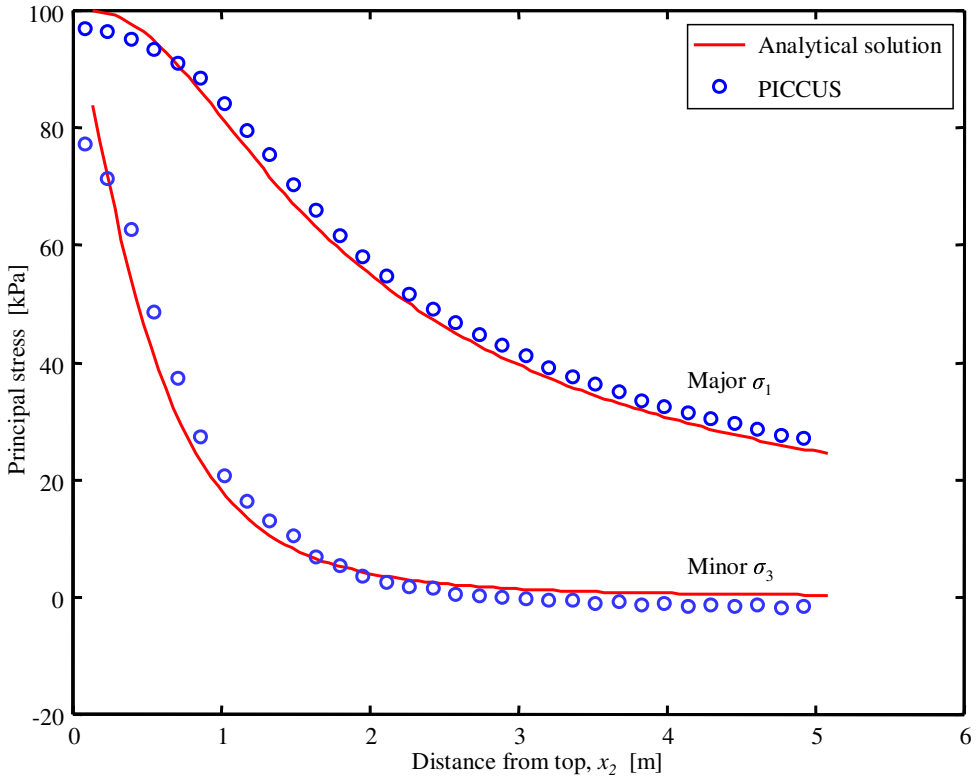

Figure 4.44: Comparison of stresses σ_1 and σ_3 along $x_1 = 0$ under the strip footing

ting. The PICCUS results are within 6% of the analytical results. This comparison shows that the stresses within the material can be accurately predicted. The analyses of a more realistic problem is considered in Chapter 5 where a strip footing on a elasto-plastic clay is modelled and the results compared to field experiments.

Chapter 5

Experimental Validation

5.1 Introduction

In the previous chapter analytical solutions and published numerical results were used to validate PICCUS. In this chapter published experimental data is used for validation.

5.2 Anchor Plates in Sand

Anchors form an important component of many civil engineering projects. Anchors are typically used to support other structures such as towers, bridges and roofs. Rowe & Davis (1982*a*,*b*), review the methods used to model and analyse anchor behaviour.

The prediction of anchor plate behaviour is usually restricted to the limiting conditions of elastic displacement or ultimate capacity. The elastic analysis only yields a load-displacement response within the elastic range. Many approaches have been given to estimate the ultimate capacity or collapse load. These methods involve the use of limit equilibrium concepts, the method of characteristics and empirical corrections.

In general, anchor behaviour is influenced by the material properties, the initial stress state, the boundary conditions and the anchor roughness (Rowe and Davis, 1982*b*). As validation, the passive resistance of rectangular anchors embedded in sand is modelled. The results are compared to experimental results, under the assumption of plane strain. Vertically pulled anchors and anchors pulled upwards at an angle of 45° are investigated.

5.2.1 Vertically Pulled Anchors

Rowe & Davis (1982*a*) investigated the behaviour of vertically and horizontally pulled anchors in sand. Model tests were performed using a dry, medium grained quartz Sydney sand. The tests were performed in a steel box 450 mm × 606 mm × 692 mm high, figure 5.1. The anchor was a 51 mm wide and 8 mm thick mild steel plate with length to breadth ratios of $\frac{L}{B} = 1, 2, 3, 4, 5, 8.75$. All of the experimental load-displacement curves are not published, and only the results with a ratio of $\frac{L}{B} = 8.75$ were used for comparisons. The load was applied to the centre of the anchor via a 8 mm diameter rod at a constant velocity of $0.025\,\mathrm{mm{\cdot}s^{-1}}$.

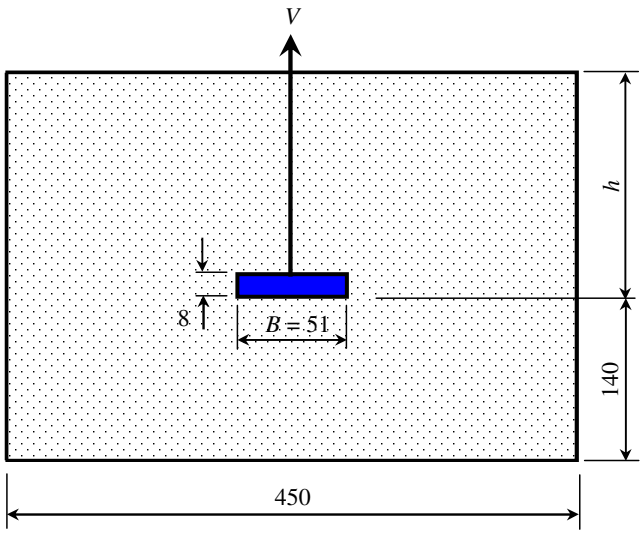

Figure 5.1: Geometry for vertically pulled anchor. Dimensions are in mm.

The anchor plate was put on top of a 140 mm layer of sand in the bottom of the box. Additional sand was than added until the anchor was buried to the required depth. The sand was sprinkled from a height of 25 mm above the surface. The unit weight of the sand γ was determined by weighing the sand in the box and measuring the total volume occupied. Triaxial tests were performed to determine the friction and dilatancy angles. No attempt was made to measure the K_0 value of the sand in the box, but empirical correlations were used to make an estimate. Poisson's ratio was also estimated. The stiffness of the material is not given at all, and simulations were performed with different stiffness values.

Figure 5.2 shows the simulation model. A symmetry plane is used to model only half of the problem depicted in figure 5.1. The other boundary conditions are shown in the figure. Initial stresses were specified using $K_0 = 0.47$. Damping ($\alpha = 0.8$) was used to reach an equilibrium state, after which the damping was removed and the anchor, modelled as a rigid body, moved at constant velocity in the vertical x_2-direction. The material properties and simulation parameters are summarised in table 5.1 and table 5.2 respectively.

Two embedded ratios were used for comparison: $\frac{h}{B} = 3$ and $\frac{h}{B} = 5$. The domain was divided into 44×58 and 44×78 square elements respectively, to model the different ratios. Figure 5.3 shows the load-displacement curves for $\frac{h}{B} = 3$, stiffness values of $E = 700\,\mathrm{kN{\cdot}m^{-2}}$ and $E = 1000\,\mathrm{kN{\cdot}m^{-2}}$ and a rough and smooth sand-anchor interface. The higher stiffness value of $E = 1000\,\mathrm{kN{\cdot}m^{-2}}$ clearly follows the experimental result more closely in the initial elastic region. The difference between a rough and smooth interface has no effect on the ultimate capacity, which is within 5% of the

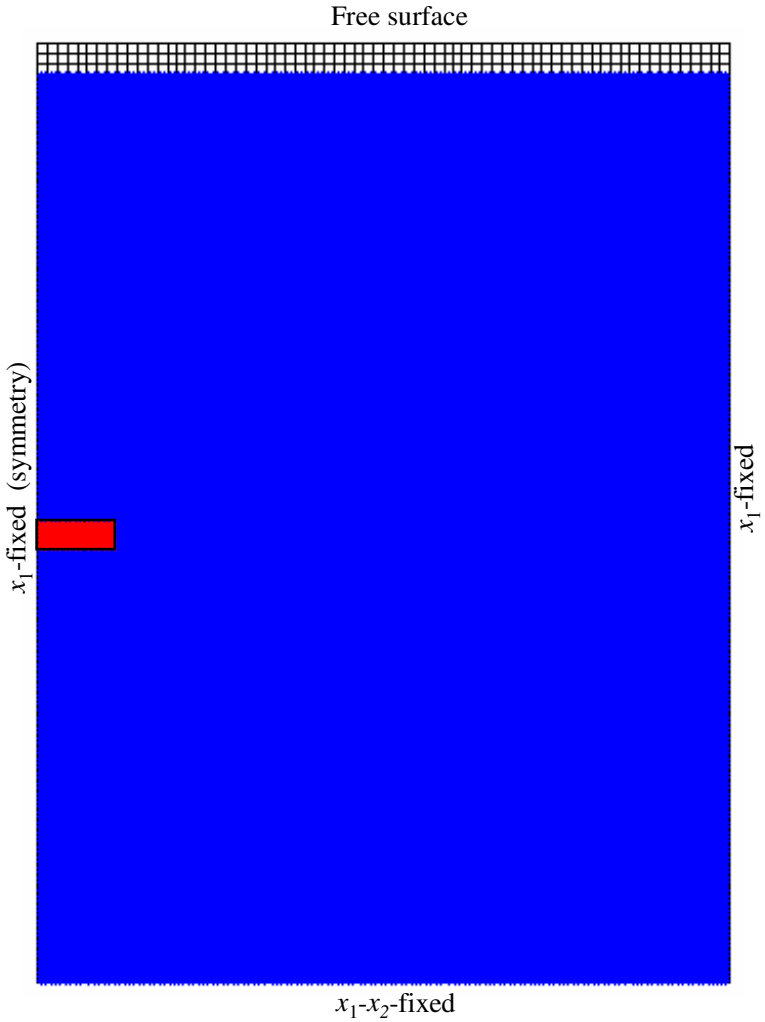

Figure 5.2: Simulation model for vertically pulled anchor.

Table 5.1: Mohr-Coulomb material data vertical anchor pull-out test

Description	Symbol	Value
Young's modulus	E	700 MPa / 1000 MPa
Poisson's ratio	ν	0.2
Unit weight	γ	$14.9\,\mathrm{kN{\cdot}m^{-3}}$
Friction angle	ϕ	32°
Tensile limit	σ^t	0 Pa
Dilatancy angle	ψ	4°
Cohesion	c	0 Pa
Material-wall friction	μ_{wall}	Smooth/Rough
Coefficient of earth pressure	K_0	$1 - sin(\phi) = 0.47$

Table 5.2: Vertically pulled anchor simulation parameters

Name	Symbol	Value
Integration time step	Δt	1×10^{-5} s
Damping	α	0
Gravity	g_i	$(0.00, -9.81)\ \mathrm{m{\cdot}s^{-2}}$
Anchor velocity	v	$0.025\,\mathrm{mm{\cdot}s^{-1}}$
Number of material points	N_p	10608 - 14303
Initial number of degrees-of-freedom	DOF	5095

measured value. It is also observed by Rowe & Davis (1982*a*) that for vertically pulled anchors, the anchor roughness has little effect on the ultimate capacity.
Figure 5.4 shows the experimental and numerical results for $\frac{h}{B} = 5$. The anchor is assumed to be smooth and the stiffness taken as $E = 1000\,\mathrm{kN{\cdot}m^{-2}}$. The simulation accurately predicts the load-displacement behaviour in the elastic region and over predicts the ultimate capacity by roughly 3%.

All of the above simulations were performed using a Mohr-Coulomb constitutive model with the parameters given in table 5.1. Figure 5.5 shows the results using a Drucker-Prager model. The same friction and dilatancy angles were used, and the Drucker-Prager parameters were chosen such that the yield surface fits within the Mohr-Coulomb yield surface (inner adjustment, equation H.6.2). Using the Drucker-Prager model, there is a slightly more gradual transition from the elastic state to the plastic state.

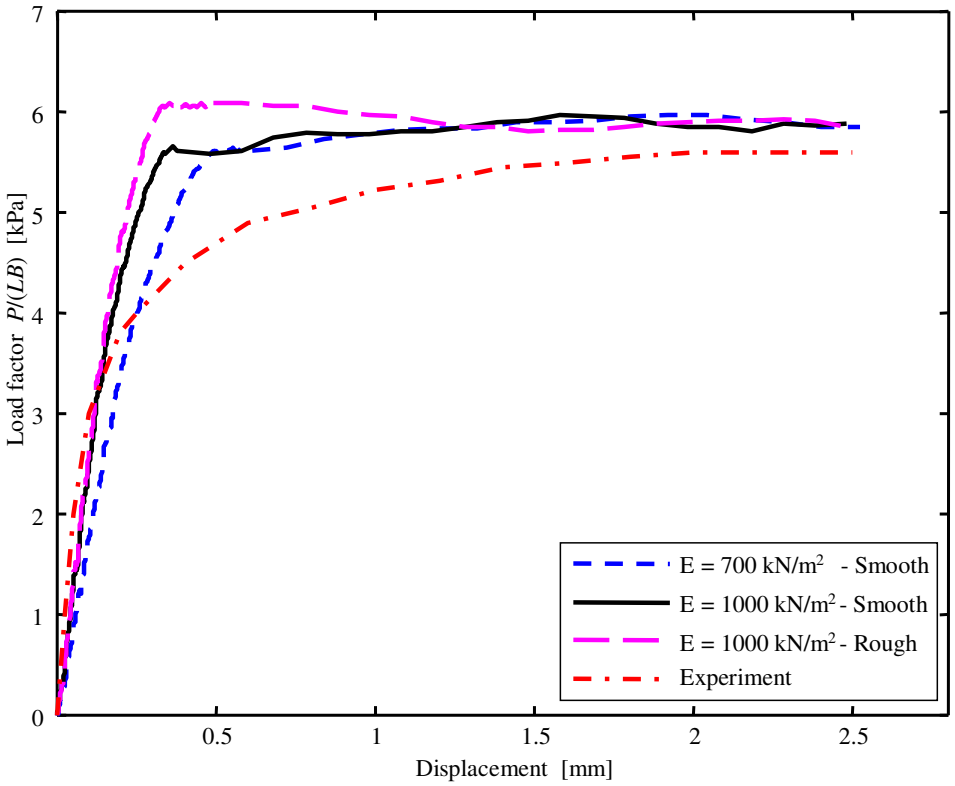

Figure 5.3: Load-displacement curve for vertically pulled anchor, $\frac{h}{B} = 3$.

The ultimate capacity, however, is the same. The experiments were all three-dimensional, while the simulations were two-dimensional. The effect of the edges of the anchor might be the reason for the differences in measured and calculated loads.

5.2.2 Anchor Pulled at 45°

Murray & Geddes (1989) experimentally investigated the behaviour of anchors pulled at angles of 0° to 90° with the vertical. In this analysis, comparisons are made only to the case where the anchor was pulled at 45°. The results are also compared to that of upper and lower bound analysis where the limit theorems of soil plasticity have been used. The upper and lower bound theorems enable the theoretical failure load of an idealised material to be bracketed. These theorems are based on the Mohr-Coulomb constitutive model. Figure 5.6 shows the problem geometry. The anchor width $B = 51\,\text{mm}$ is the same as in the previous section, but the thickness $t = 6.35\,\text{mm}$ differs. The anchor width to length ratio used for comparisons is $\frac{L}{B} = 10$, although experiments were also performed for ratios $\frac{L}{B} = 1, 2$ and 5.

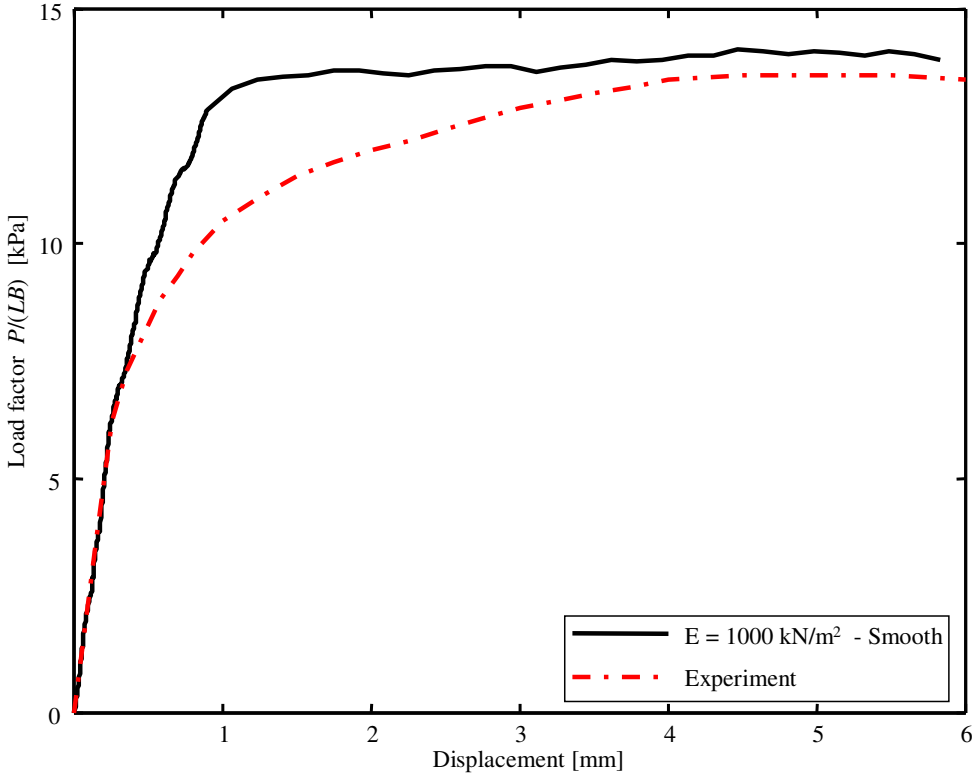

Figure 5.4: Load-displacement curve for vertically pulled anchor, $\frac{h}{B} = 5$.

A medium grained sand, known as Portishead Fines, was compacted in layers by vibration with the anchor fixed in position in the test container. The sand in the container was weighed to calculate the average unit weight γ. Direct shear box tests on the sand yielded the friction angle ϕ and cohesion c. A modified shear box was used to determine the interface friction μ_{wall}. No attempt has been made to determine the material stiffness E, Poisson's ratio ν, the dilatancy angle ψ or the coefficient at rest K_0. It has, however been shown in the previous section that the stiffness has little effect on the limit load. Poisson's ratio is taken to be $\nu = 0.2$ and Murray & Geddes (1989) estimated the dilatancy angle to be within the range $\psi = 5^\circ - 12^\circ$. Table 5.3 summarises the material properties. Figure 5.7 shows the PICCUS model and table 5.4 summarises the simulation parameters. The domain was divided into 80×32, 80×45 and 80×59 square elements for the different embedded ratios $\frac{h}{B} = 2, 4$ and 6.

Murray & Geddes (1989) do not provide the load-displacement curves obtained from their experiments, but only give the ultimate loads for different embedded depths. The definition given by Rowe & Davis (1982*a*,*b*) is used to determine the ultimate capacity, given a load-displacement curve. The k_n failure load is defined as the load which produces n times the dis-

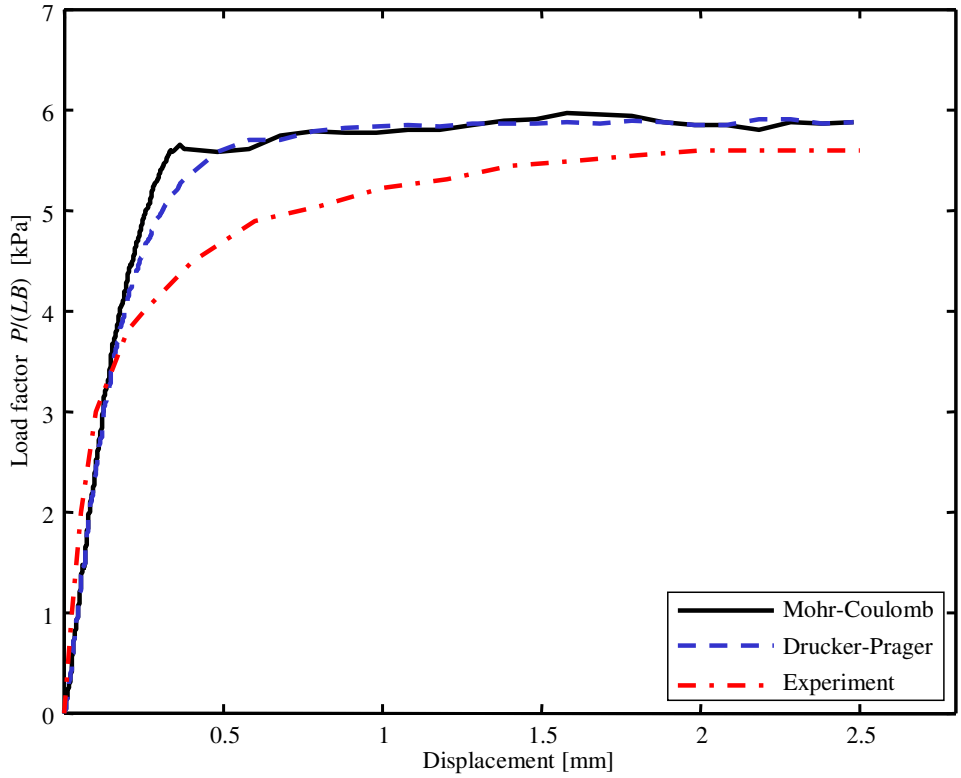

Figure 5.5: Comparison between Mohr-Coulomb and Drucker-Prager models on vertically pulled anchor, $\frac{h}{B} = 3$, smooth interface, $E = 1000\,\mathrm{kN{\cdot}m^{-2}}$

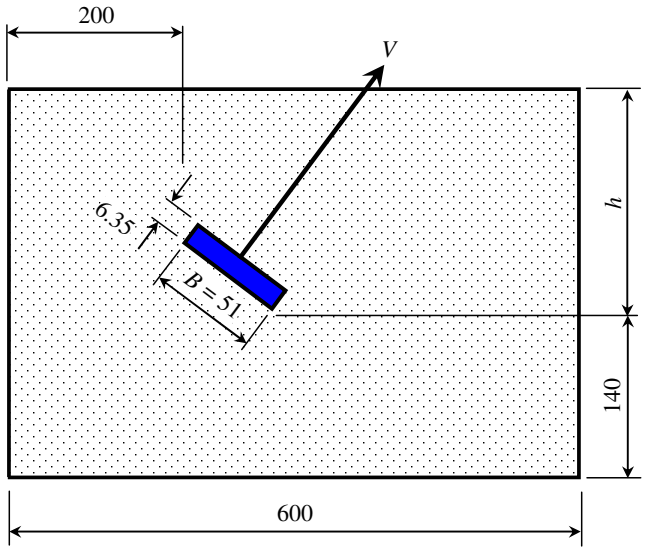

Figure 5.6: Geometry for anchor pulled at 45°. Dimensions are in mm.

Table 5.3: Mohr-Coulomb material data for 45° anchor pull-out

Description	Symbol	Value
Young's modulus	E	1500 MPa
Poisson's ratio	ν	0.2
Unit weight	γ	16.8 kN·m^{-3}
Friction angle	ϕ	44°
Tensile limit	σ^t	0 Pa
Dilatancy angle	ψ	12°
Cohesion	c	0 Pa
Anchor-sand friction	μ_{wall}	11°, (0.19)
Coefficient of earth pressure	K_0	$1 - sin(\phi) = 0.31$

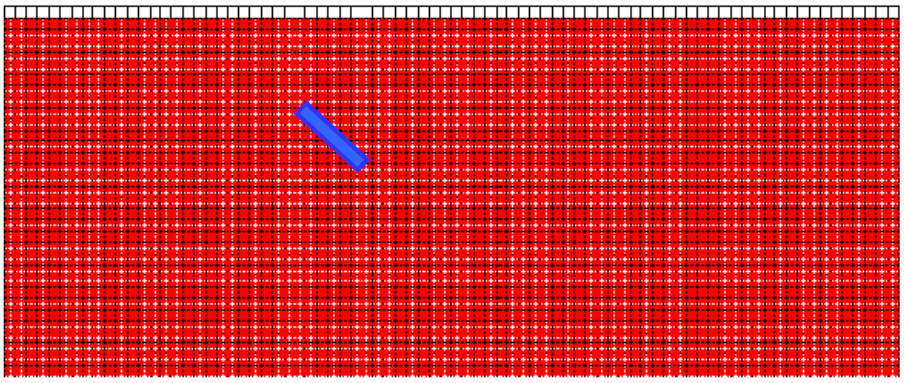

Figure 5.7: Computed Geometry for anchor pulled at 45°.

Table 5.4: Anchor pulled at 45° simulation parameters

Name	Symbol	Value
Integration time step	Δt	1×10^{-5} s
Damping	α	0
Gravity	g_i	$(0.00, -9.81)$ m·s^{-2}
Anchor velocity	v	0.012 mm·s^{-1}
Number of material points	N_p	10221 - 19021
Initial number of degrees-of-freedom	DOF	5120 - 9602

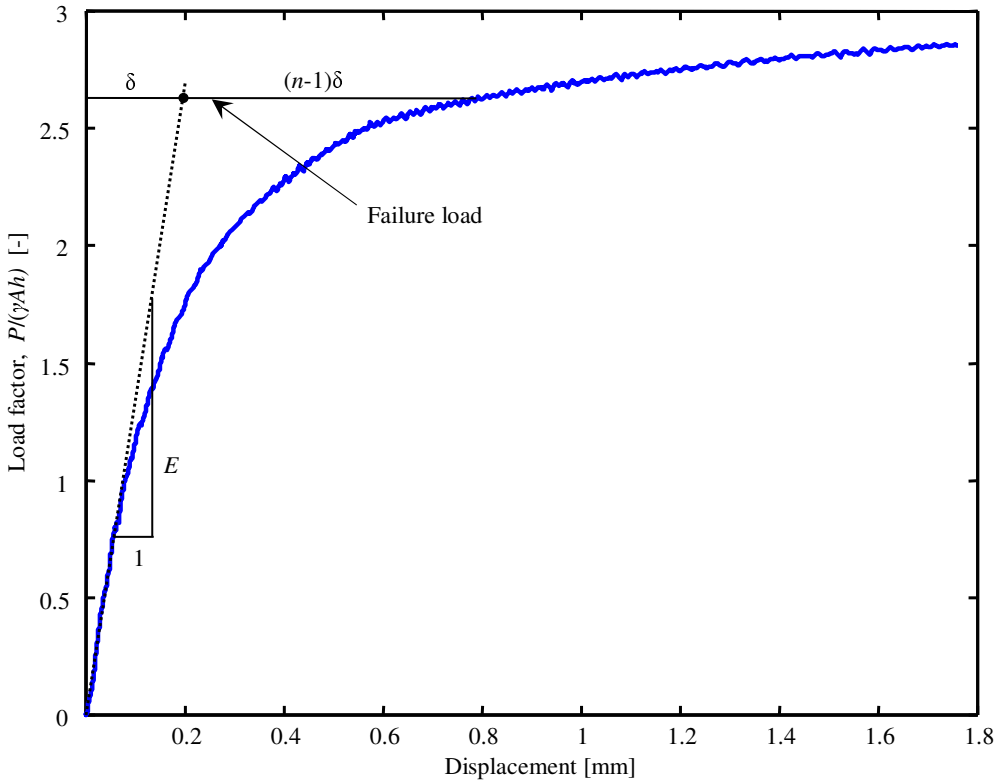

Figure 5.8: Load-displacement curve for anchor pulled at 45°, $\frac{h}{B} = 2$.

placement that would have occurred had the soil remained elastic. This definition is not dependent on scale or stiffness modulus, but the value of n remains arbitrary. Rowe & Davis (1982*a*,*b*) suggest a value $n = 4$, i.e., k_4 failure load. Figure 5.8 plots the dimensionless load factor $P/\gamma Ah$ against the anchor displacement. P is the load on the anchor measured in N, γ the unit weight, $A = BL$ is the frontal area of the anchor and h the embedded depth. The calculation of the k_n failure load is also shown by the figure.
The ultimate failure loads at different depth ratios are plotted in figure 5.9. The simulations under predict the measured ultimate capacity for all three depth ratios. The maximum difference is 9.3%. The upper-bound limit is also shown. The biggest unknown in this problem is the initial stress state. The value of K_0 has been taken to be $1 - sin(\phi)$ according to Jaky (1944). The way of preparing the sand bed, however, will have an influence on this value. Rowe & Davis (1982*a*) have shown, that for a particular case, an increase in K_0 from 0.5 to 1.0, caused a 6% increase in the ultimate capacity.

The results show that PICCUS can model anchor pull-out tests which is difficult to model with FEM. Special FEM contact elements would be needed to model the interface between the soil and the anchor. The contact elements should be able to model break-away of the soil behind the an-

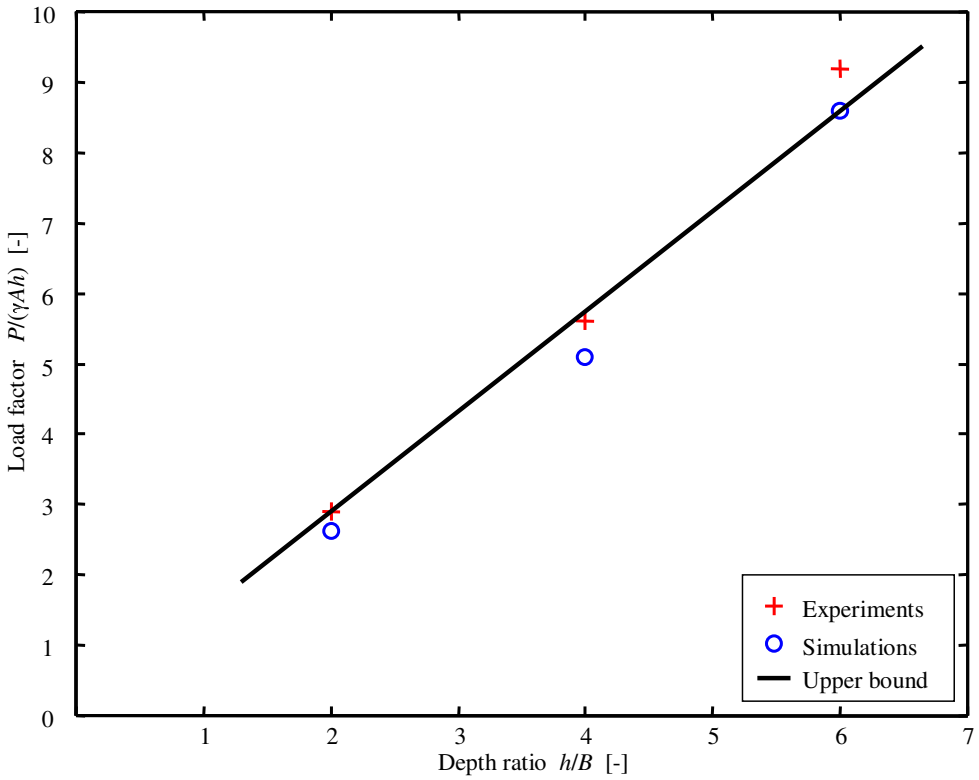

Figure 5.9: The ultimate capacity at different depth ratios for the anchor pulled at 45°.

chor. The PICCUS contact model automatically allows break-away since contact correction is only applied at nodes where the two bodies approach each other in the contact normal direction. The bodies are allowed to freely move away from one another.

5.3 Strip Footings

In this section two strip footing problems are analysed: the one being a slope stability problem (vertical cut) and the other a bearing capacity problem. Rilling (1994) performed well documented large-scale field tests under plane strain conditions. PICCUS results are compared to the experimental results, as well as to the results from PLAXIS. PLAXIS (PLAXIS, 2 June 2003) is a quasi-static finite element code based on implicit integration of the differential constitutive law. The PLAXIS simulations were performed by the Institute of Geotechnical Engineering at the University of Stuttgart.

5.3.1 Test Setup

The frame depicted in figure 5.10 was used to perform tests under plane strain conditions. In order to ensure plane strain on a middle section, the strip footing was divided into three parts; the outer parts were one metre long and the middle part 0.4 metre. Measurements were only done on the middle section. The sections were placed close together, but without contact. The loading was controlled by hydraulic presses and in such a way that all three sections had the same vertical displacements. With measurements made only on the middle section, plane strain conditions (measurements) can be assumed.

Figure 5.11 shows typically measured load-settlement curves. This graph clearly indicates the different stress levels present in the two different problems being analysed. During the slope stability test, test A, the loading pressure is in the order of 150 kPa, while during the bearing capacity test, tests B1 and B2, it is in the order of 800 kPa $-$ 1000 kPa. The difference between the two B-tests, B1 and B2, is due to different locations and soil heterogeneity.

Although both tests involve plane strain strip footings on the same type of soil, they are completely different. The footing near the vertical cut involves a collapse mechanism as considered in slope stability analyses and the other one yields a Prandl-type failure. This is also reflected in the magnitudes of the collapse loads, being very low for the slope-type failure and high for the usual bearing capacity problem. Considering these different stress levels and different collapse mechanisms, these field model tests are outstanding for validating numerical collapse load calculations. Numerical collapse load analyses are not directly needed for simple situations such as a footing on a homogeneous half space, as this bearing capacity problem has been solved analytically, but it is essential for more complex problems, e.g. for a footing near a slope as also considered in this study.

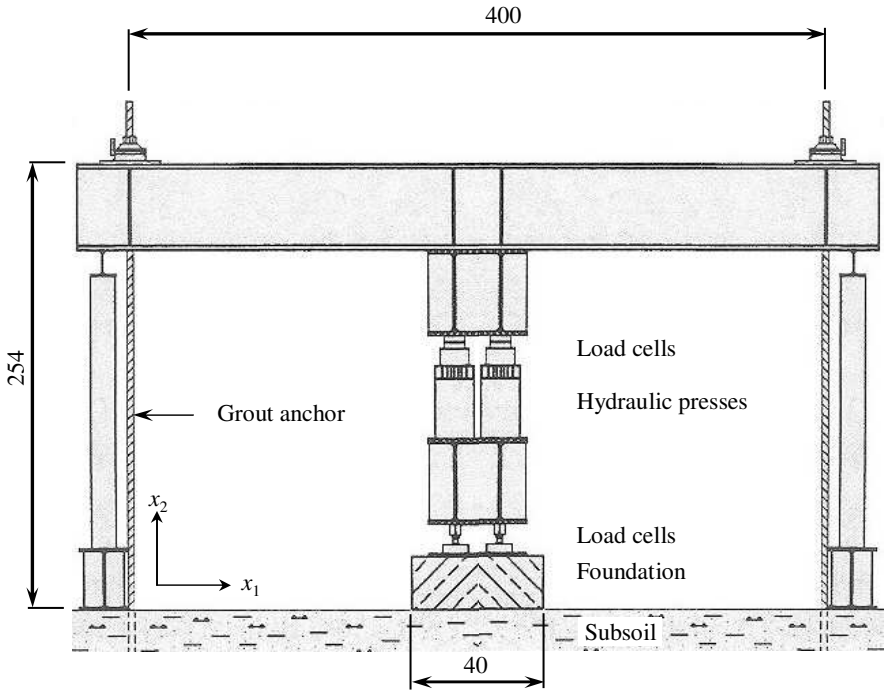

Figure 5.10: Test setup, Rilling (1994). Dimensions in cm

5.3.2 Soil Parameters

The tests were performed on a clayey silt near the city of Heilbronn in southern Germany. The soil consists of about 70% quartz, 15% feldspar and 15% lime, but field heterogeneity caused considerable variations about these mean values. The soil has a field porosity of about $n = 35\%$ with $n_{water} \simeq 30\%$ and $n_{air} \simeq 5\%$. This gives a unit soil weight of $\gamma = 20.5\,\mathrm{kN/m^3}$. The Heilbronn clay is a stiff clay with a plasticity index of $I_p = 20\%$. Finally it should be noted that we consider a so-called man-made soil that was deposited in layers of 35 cm and then compacted to a thickness of 25 cm.

Triaxial tests were carried out on soil samples taken from the artificially compacted test site. Figure 5.12 shows the results from 16 different test sets. Confining pressures of 50, 100 and 200 kPa were used. The friction angle and cohesion were obtained by fitting the straight line shown in the figure to the data points using linear regression. They were found to be $c = 26\,\mathrm{kPa}$ and $\phi = 27°$. No consistent data on the soil stiffness is given by Rilling (1994), therefore the stiffness used in the numerical modelling was obtained by curve-fitting: Load-displacement curves for different stiffness values were compared to the measured curve, and a stiffness of $E = 25\,\mathrm{MN{\cdot}m^{-2}}$ was chosen for use in an elastic perfectly plastic Mohr-Coulomb model. The soil parameters are summarised in table 5.5.

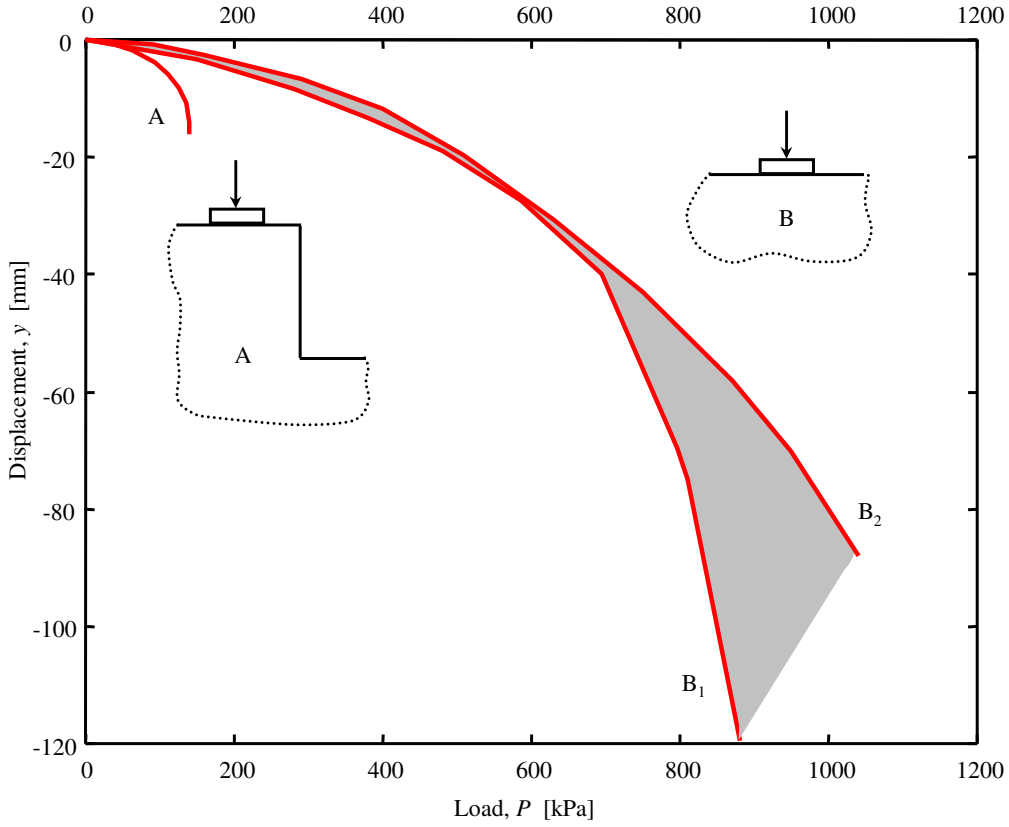

Figure 5.11: Load-displacement curves from field tests.

Table 5.5: Mohr-Coulomb material data footing problems, Heilbronn silt

Description	Symbol	Value
Young's modulus	E	25 MPa
Poisson's ratio	ν	1/3
Unit weight	γ	20.5 kN·m^{-3}
Friction angle	ϕ	27°
Tensile limit	σ^t	0 Pa
Dilatancy angle	ψ	0°
Cohesion	c	26 kPa
Coefficient of earth pressure	K_0	$1 - sin(\phi) = 0.55$

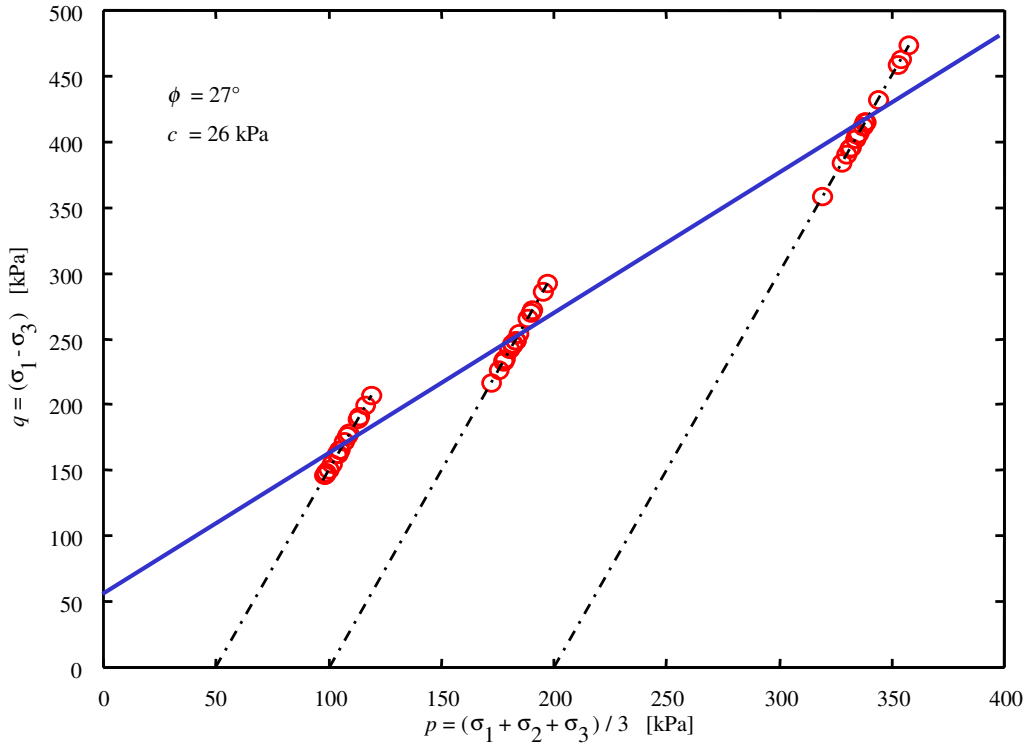

Figure 5.12: Triaxial results for Heilbronn silt

5.3.3 Bearing Capacity

Figure 5.13 shows the geometry used to model the bearing capacity problem. In the case of PICCUS, the material points are also shown. In PLAXIS a total of 1050 6-noded elements were used with 2171 nodes. In PICCUS a regular grid of $45 \times 30 = 1350$ square 4-noded elements was used with a total of 1426 nodes. Despite the comparable number of nodes the PICCUS-grid is finer than the PLAXIS mesh, as the PICCUS-analysis was carried out for half a symmetric footing. The side boundaries were assumed smooth, i.e., only constrained in the horizontal direction. The bottom boundary was constrained in both the horizontal and vertical directions. A $K_o = 1 - sin\phi$ initial stress state was assumed.

Table 5.6 shows the parameters used to perform the bearing capacity simulations. Figure 5.14 shows the load-displacement curves obtained from field measurements, PICCUS and PLAXIS. There is a good correspondence between the PICCUS and PLAXIS results, predicting failure loads of 692 and 668 kPa respectively. The numerical methods accurately predict the measured initial stiffness and correspond well to the field data up to the stage where the predicted failure loads are reached. The failure load, however, is underestimated by approximately 25%. This difference might be due to

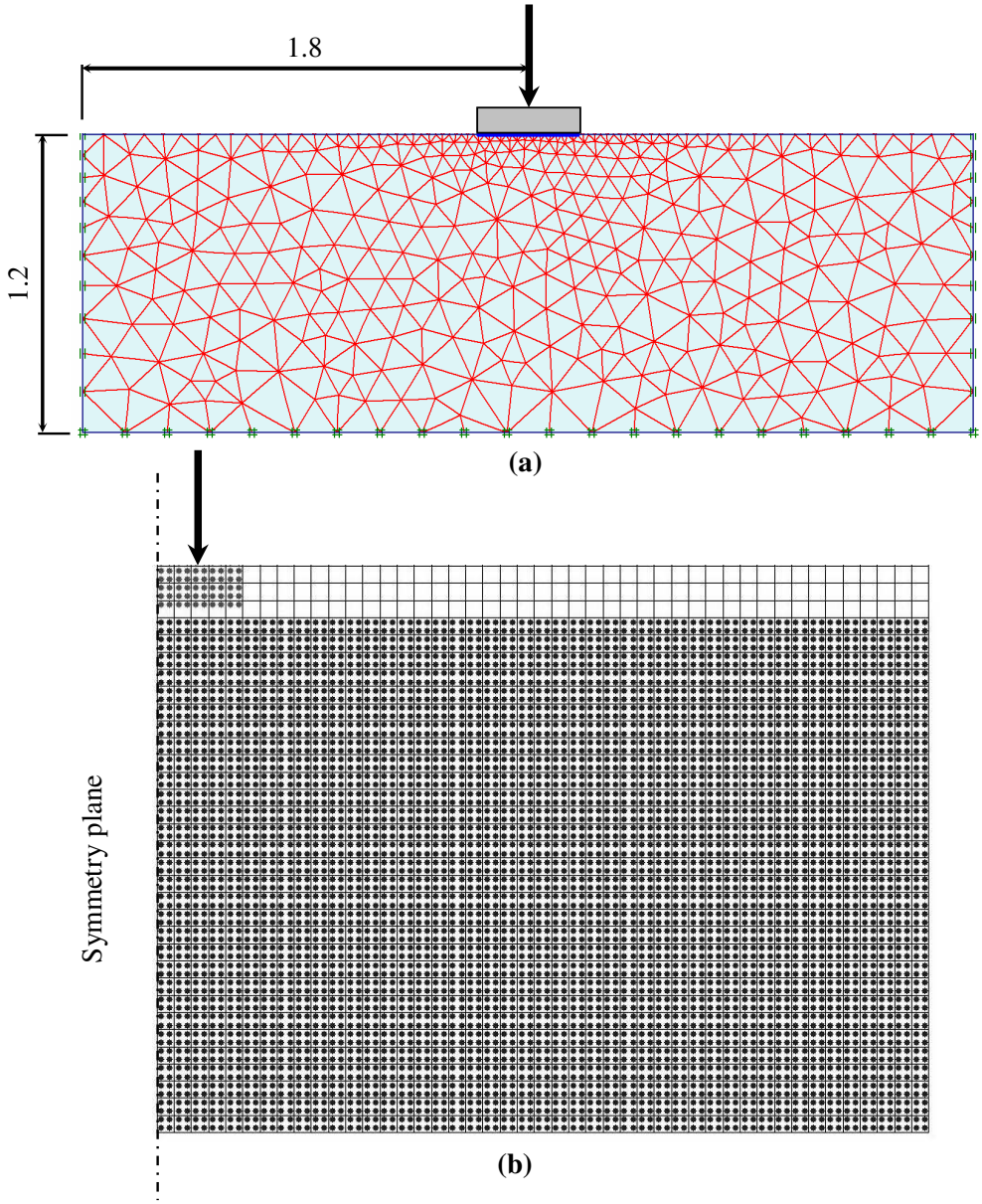

Figure 5.13: Discretisation of the bearing capacity problem: (a) PLAXIS and (b) PICCUS (not to the same scale). Dimensions in m

Table 5.6: Bearing capacity and slope stability simulation parameters

Name	Symbol	Value
Integration time step	Δt	1×10^{-5} s
Damping	α	0
Gravity	g_i	$(0.00, -9.81)$ m·s^{-2}
Footing velocity	v	0.5 mm·s^{-1}

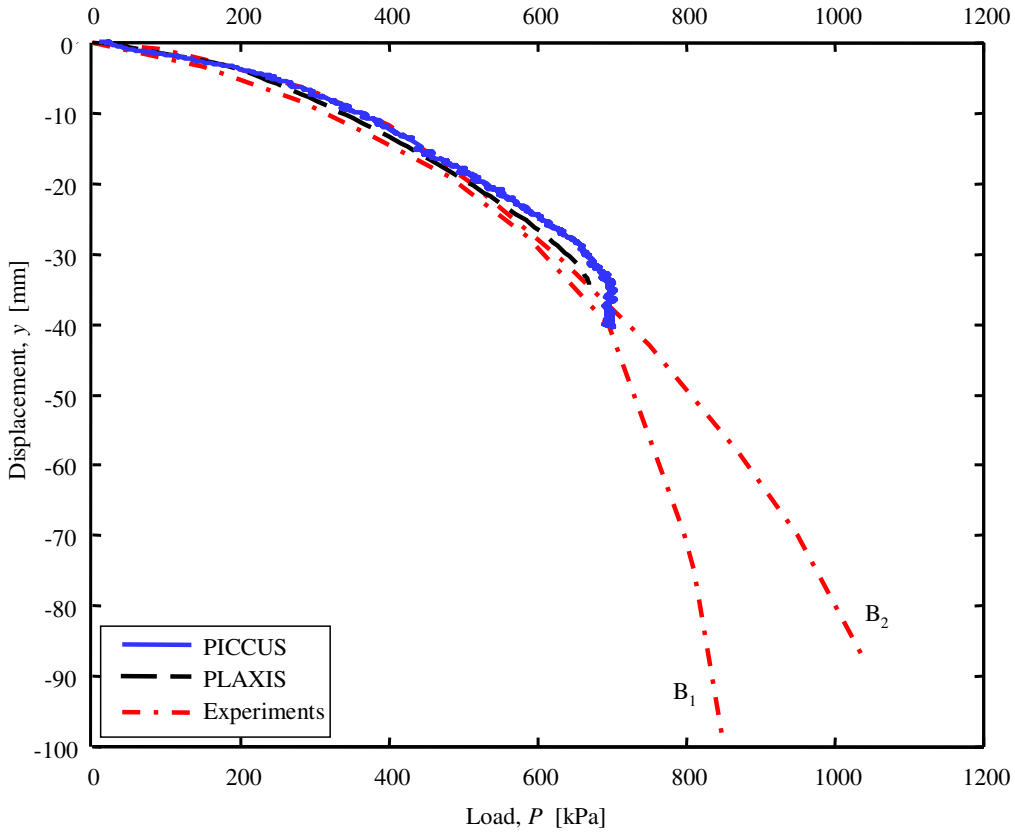

Figure 5.14: Load-displacement curves for bearing capacity

several factors which are discussed at the end of the next section.

5.3.4 Slope Stability

Figure 5.15 shows the meshes that were used to model the slope stability problem. In PLAXIS a total of 774 6-noded elements were used with 1664 nodes. In the PICCUS analysis a regular grid of $50 \times 35 = 1750$ square 4-node elements was used with a total of 1836 nodes. The left side boundary

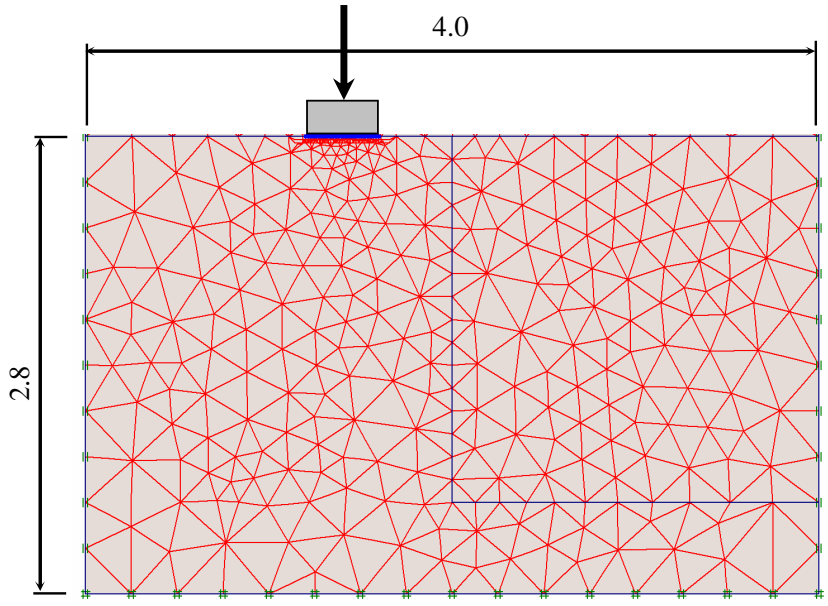

(a)

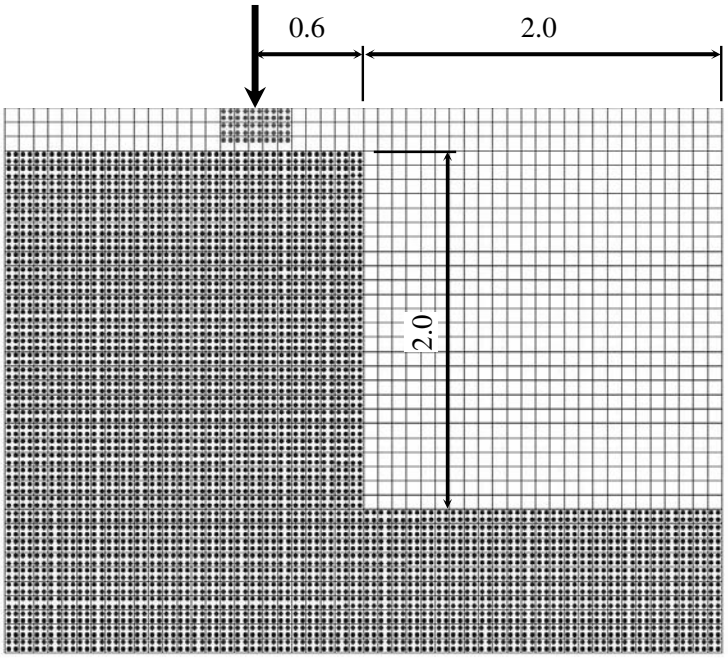

(b)

Figure 5.15: Discretisation of the slope stability problem: (a) PLAXIS and (b) PICCUS. Dimensions in m

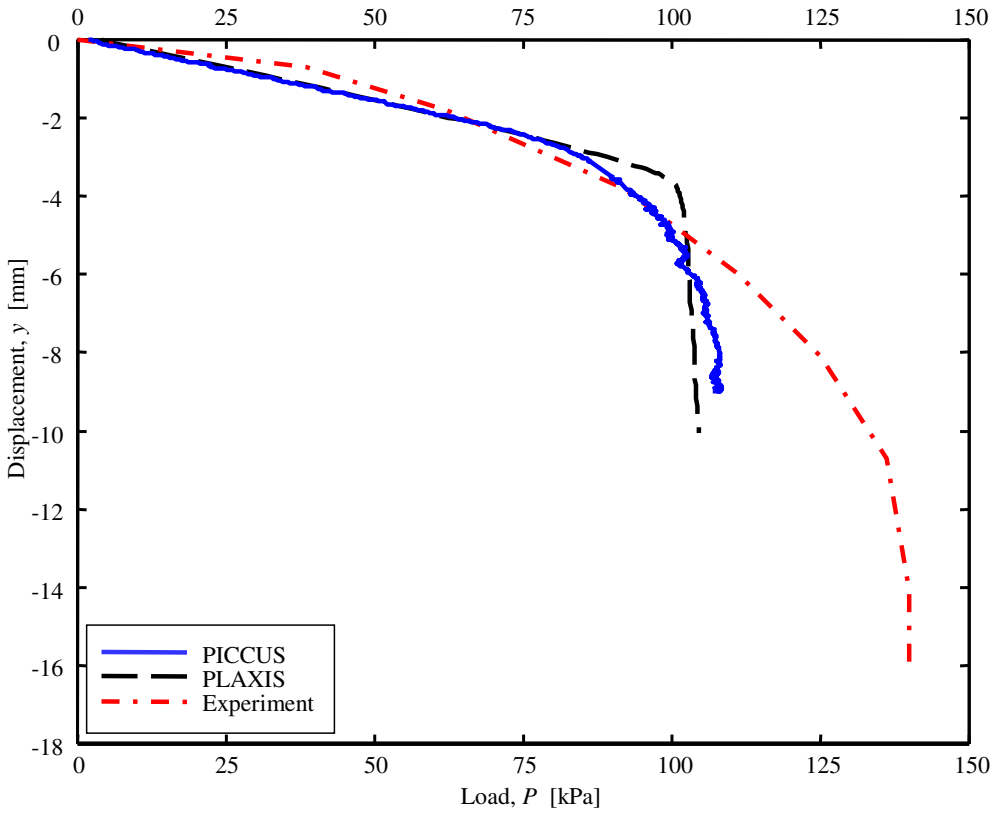

Figure 5.16: Load-displacement curves for slope stability

was assumed smooth, i.e., only constrained in the horizontal direction. The bottom boundary was constrained in both the horizontal and vertical directions. The initial stress state was generated by first creating material over the whole domain, using $K_0 = 1 - sin\phi$. The vertical cut was than generated by removing the material layer by layer. After each removal, the material was allowed to deform and to reach static equilibrium. The simulation parameters are summarised in table 5.6. Figure 5.16 shows the load-displacement curves for this problem. The PICCUS and PLAXIS results are in good agreement, but underestimate the failure load by roughly 30%.

5.3.5 Conclusions

The results lead to the conclusions that PICCUS produces results that coincide with the results from a conventional nonlinear elasto-plastic finite element method. Another observation is that the failure load is significantly underestimated by both numerical analyses. In order to understand this one might consider the analytical solution of Soil Mechanics text books for

the bearing capacity, which reads

$$P_{max} = c\ N_c + \gamma\ b\ N_b \tag{5.3.1}$$

where b is the footing width and

$$\begin{aligned} N_c &= \frac{N_d - 1}{tan\phi} \\ N_b &= (N_d - 1)tan\phi \\ N_d &= \frac{1 + sin\phi}{1 - sin\phi} e^{\pi tan\phi} \end{aligned} \tag{5.3.2}$$

Using the triaxial friction angle, $\phi_{tr} = 27^\circ$, the ultimate capacity is calculated $P_{max} = 674\,\text{kPa}$. The value of 674 kPa corresponds well to the numerical results, but not to the measured values. In order to match the latter values, one would have to use a plane strain friction angle of $\phi_{ps} = 30^\circ$ which would yield $P_{max} = 946\,\text{kPa}$. The friction angle $\phi_{tr} = 27^\circ$ has been determined from triaxial experiments and used here in plane strain modelling. The ratio between the triaxial- and plane strain friction angle is $\frac{\phi_{ps}}{\phi_{tr}} = 1.1$. For cohesive soils, this ratio of 1.1 is also suggested by Kulhawy & Mayne (1990), whilst Wroth (1984) suggested the very similar ratio of $\frac{9}{8} = 1.125$. Indeed, triaxial compression tests give relatively low friction angles and the use of such values in computations is conservative. For geotechnical design, it may be right to choose conservative values, but this would not result in accurate predictions when numerical analyses are used to predict reality.

Chapter 6

Blade, Bucket and Silo Modelling

6.1 Introduction

In this chapter, the flow of granular material (corn and sand) in front of flat blades, into buckets and silo discharging are investigated. The blade and bucket modelling follows on that of Coetzee (2000) who performed two-dimensional DEM simulations and compared the results to experiments with corn. In this study, PICCUS results of blades and buckets are compared to both the DEM and experimental results of Coetzee (2000). PICCUS and DEM results of silo discharging are compared to experiments with corn and sand which were done as part of this study. Polar and nonpolar continua are used. The blade and the bucket are modelled as rigid bodies, while the corn and sand are modelled with Drucker-Prager and Mohr-Coulomb theories.

6.2 Blade and Bucket Modelling

6.2.1 Two-dimensional Test Rig

Figure 6.1 shows the main components of the test rig. Two glass panels, 2200×820 mm are mounted on the base structure. The distance between these two panels is about 200 mm and is slightly adjustable to ensure that the tool profile is lined up between the two panels. The one panel (viewing side) consists of two glass sheets, one 10 mm and one 6 mm thick. The 10 mm glass is to resist the high lateral pressures created by the material being pushed forward by the blade/bucket. The 6 mm glass sheet can easily be replaced if it gets scratched. The other panel (non-viewing side) consists of a 3 mm steel sheet and a 6 mm glass sheet. The steel mainly resists the lateral pressure while the function of the glass is to have the friction on both sides the same.

The profile is attached to the trolley via a four-bar linkage mechanism. The trolley is mounted on two sets of linear ball bearings. A stepper motor connected to a ball screw moves the trolley forwards and backwards. Figure 6.2 shows the use of the arm-mechanism. When ground-engagement tools such as dragline buckets are used, the bucket must have freedom of motion in both the vertical and lateral directions for three-dimensional simulations and at least freedom of motion in the vertical direction for two-dimensional simulations. The arm-mechanism allows freedom of motion in the vertical direction. Arm 1 is always fixed to the trolley, figure 6.2a,

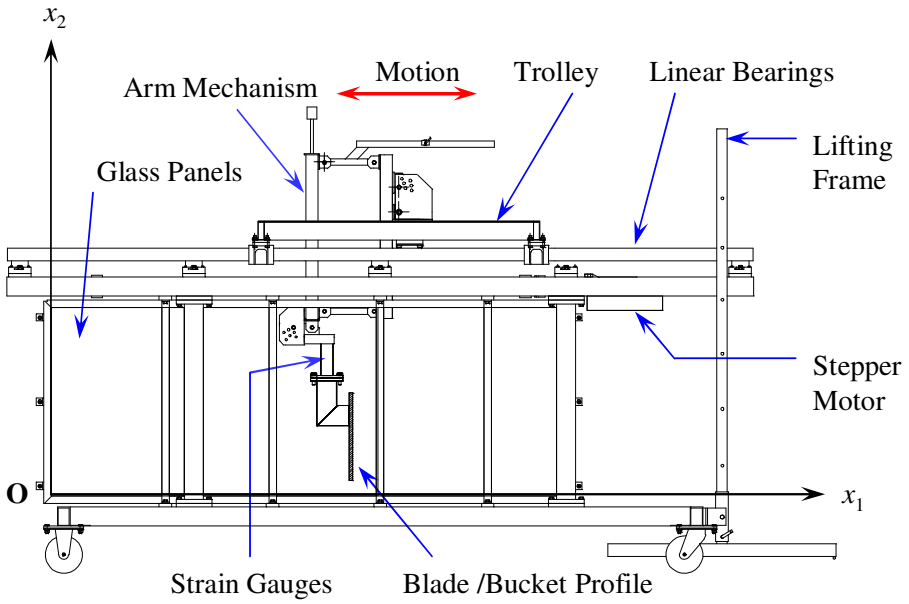

Figure 6.1: Two-dimensional test rig, Coetzee (2000)

while arm 2 can move freely in the vertical direction, figure 6.2c. Counter weights can be added at the positions indicated, figure 6.2a. This allows the weight of the bucket to be changed and the weight of the arms and linkages to be cancelled. For simulation of other ground-engagement tools such as bulldozer blades and cutting tools, arm 2 can be locked.

The whole test rig can be inclined with the use of the lifting frame. This can be used to simulate the drag angle of draglines or any other tool working on an incline. The test rig can be inclined in steps of 5° up to a maximum of $\beta = 30°$. When the test rig makes an angle β with the horizontal, the two vertical arms are also at an angle β to the vertical. This means that the freedom of motion is no longer in the vertical direction. To overcome this problem arm 1 can be rotated relative to the trolley as in figure 6.2b. This ensures that arm 2 stays in a vertical position. Further, the angle of the profile relative to vertical arm 2, i.e. the attack angle, can be changed since it is a parameter that influences the profile performance. The profiles are fitted with two teflon wipers, one on each side, to prevent particles from moving between the profile and the glass. Three sets of strain gauges are used to measure the x_1-force, x_2-force and moment acting on the profile. The x_1- and x_2-directions are indicated in figure 6.1.

The blade in the experiments had a height of 350 mm and the bucket dimensions are shown in figure 6.3. The moment centre O_m is the point at which the moment acting on the bucket is measured.

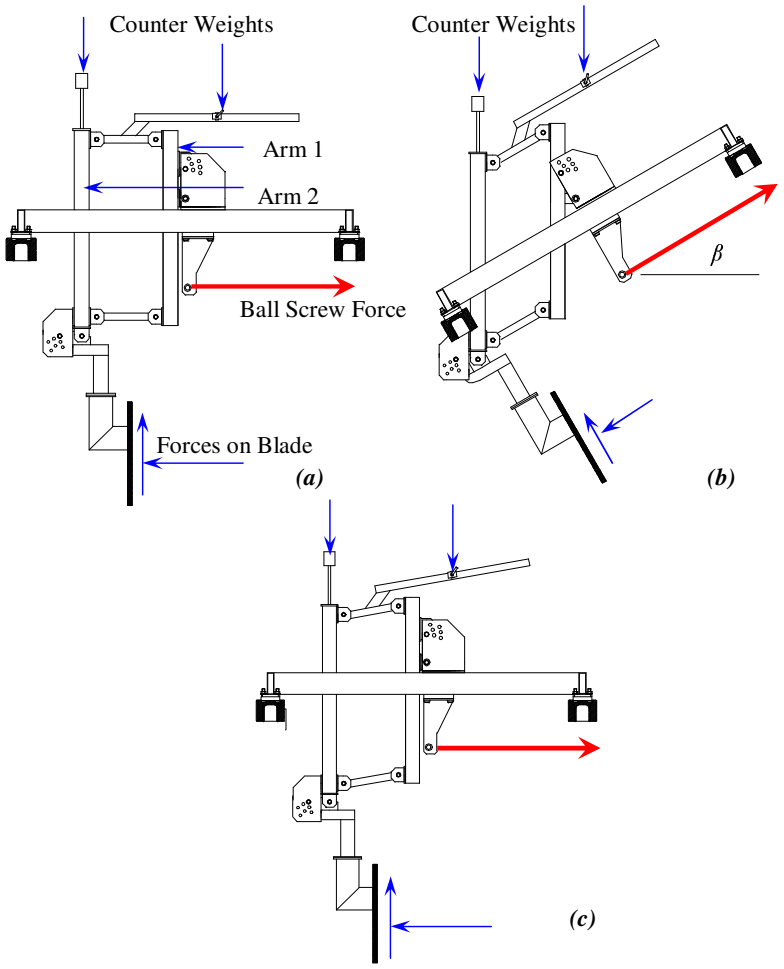

Figure 6.2: 2-D Test rig arm mechanism, Coetzee (2000)

6.2.2 Material

Rowlands (1991) observed that seed grains are suitable for experimental testing and closely resemble natural granular flow into dragline buckets. The grains have a relatively low friction coefficient with glass, which makes it a perfect experimental material. The seed grains were also found suitable for DEM simulations because the stiffness of the grains is less than the stiffness of, say, gravel. The smaller stiffness results in a larger time step, Coetzee (2000). For a close-packed assembly the stable time step is roughly inversely proportional to the particle stiffness. Coetzee (2000) made use of corn and wheat grains. These two materials have very similar properties and in this study, only the results from using corn will be used (figure 6.4).

Oedometer and shear box tests were performed to determine the corn properties. The oedometer tests yielded an oedometer stiffness E_{oed}. The

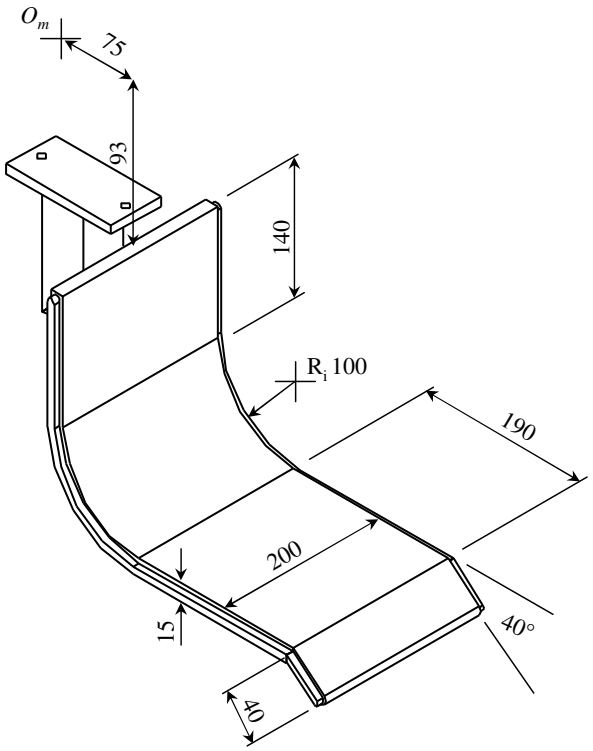

Figure 6.3: Bucket dimensions in mm

Figure 6.4: Corn grains, Coetzee (2000)

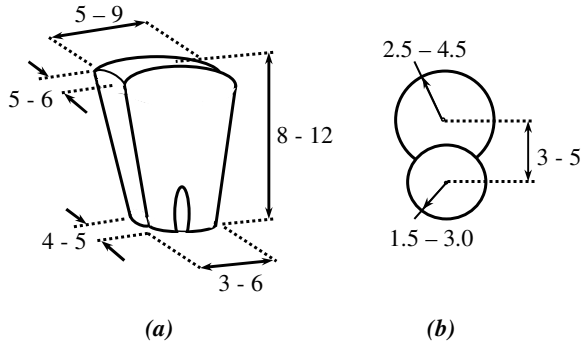

Figure 6.5: Corn grains (a) measured [mm] (b) DEM grain, Coetzee (2000)

material stiffness or Young's modulus E is related to the oedometer stiffness by the following relation (Coetzee, 2000)

$$E = E_{oed}\frac{(1+\nu)(1-2\nu)}{1-\nu} \tag{6.2.1}$$

where ν is Poisson's ratio. From the shear tests, the friction angle ϕ and cohesion c were determined. By replacing half of the shear box with a glass or steel sheet, the friction between corn and glass and corn and steel could be determined. Poisson's ratio and the dilatancy angle were not measured.

6.2.3 DEM Simulations

Coetzee (2000) performed DEM simulations using the commercial code PFC^{2D} (Itasca, 1999). Figure 6.5 shows the range of the measured dimensions of the grains and the DEM particles used to model a single grain. A single particle consists of two circular particles rigidly joined to form a so-called clump. The particle density, inter-particle friction coefficient and stiffness were determined through a series of numerical experiments. The particles density was changed until the bulk density of an assembly of particles was the same as the measured value. To determine the inter-particle friction and stiffness, the oedometer and shear box experiments were repeated numerically. The oedometer tests showed that the inter-particle friction had little to no effect on the oedometer stiffness E_{oed}. Using different inter-particle stiffness', the tests were repeated until the measured E_{oed} was obtained. The results showed that E_{oed} increases linearly with an increase in inter-particle stiffness. The friction angle calculated from the shear box results was influenced by both the inter-particle stiffness and friction. But, with the stiffness known from the oedometer tests, only the friction coefficients were changed until the measured friction angle was obtained.

Table 6.1 summarises the corn macro properties, and the micro properties used in the DEM simulations. The macro properties were found to be

Table 6.1: Corn material properties, Coetzee (2000)

Macro Properties	Symbol	Experiment	DEM simulation
Young's modulus	E	2.76 MPa	1.84 MPa
Poisson's ratio	ν	0.2	-
Density	ρ	778 kg·m^{-3}	778 kg·m^{-3}
Friction angle	ϕ	26°	24°
Dilatancy angle	ψ	2°	-
Cohesion	c	0 Pa	0 Pa
Tension cutoff	σ^t	0 Pa	-
Friction with glass	ϕ_g	12°	-
Friction with steel	ϕ_s	14°	14°
Micro Properties	Symbol	Experiment	DEM simulation
Particle stiffness	$k_n = k_s$	-	420 kN·m^{-1}
Particle density	ρ_p	-	855 kg·m^{-3}
Particle friction	μ	-	0.1

within the range measured by Reimbert & Reimbert (1976). Poisson's ratio has been estimated $\nu = 0.2$ and the calculation of the dilatancy angle ψ will be explained later.

6.2.4 Effect of Tool Velocity

Coetzee (2000) investigated the effect of blade velocity on the blade draft force. The velocity could be varied continuously from 0 to 100 mm·s^{-1}. Velocity changes within this range had no significant influence on the draft force. This is in accordance with results from Albert *et al.* (1998) and Grisso *et al.* (1996), but Bohatier & Nouguier (2000), Siemens *et al.* (1965), Bagster & Bridgwater (1967) and Luth & Wismer (1971) showed that the draft force does depend on the velocity. Bohatier & Nouguier (2000), Siemens *et al.* (1965) and Luth & Wismer (1971) observed a quadratic relation and Bagster & Bridgwater (1967) a linear relation at high velocities and independence at low velocities. To summarise from the literature study, it seems that the tool forces are only significantly influenced at relatively high velocities (> 1 km·h^{-1}). The shape of the tool and soil properties also were showed to have an influence. It is well known that the shear strength of soil is dependent on the shear rate, especially in soil with a high cohesion factor

such as clay. For non-cohesive materials, the velocity has less of an effect on the tool forces.

6.2.5 Vertical Blade Modelling

The blade was given a constant velocity of $10\,\mathrm{mm{\cdot}s^{-1}}$ during all experiments and simulations. The material was created layer-by-layer in the simulations, with the blade in position, and given an initial stress state assuming $K_0 = 1 - sin\phi$. Using a damping coefficient of $\alpha = 0.8$, the material was allowed to reach an equilibrium state under the influence of gravity alone. The two side boundaries were constraint in the x_1-direction (horizontal) and in the polar case the horizontal and rotational directions. The bottom boundary was fixed, i.e., constraint in both the horizontal and vertical directions and in the polar case the horizontal, vertical and rotational directions. No Cosserat rotation was allowed at the blade-material interface which is true for a relatively smooth surface (Tejchman, 1997). Figure 6.6 shows typical stresses at equilibrium. This is the same for the polar and nonpolar case, since in the polar case, all the couple stresses are zero.

Figure 6.7 and figure 6.8 show the flow of material in front of the blade using the nonpolar continuum. With only the dilatancy angle unknown, the simulation is repeated for three different values $\psi = 2^\circ, 10^\circ$ and $\psi = \phi = 26^\circ$. The blade depth is $h = 200\,\mathrm{mm}$. There is good qualitative agreement between the DEM and PICCUS flow patterns, as shown by the coloured layers of material.

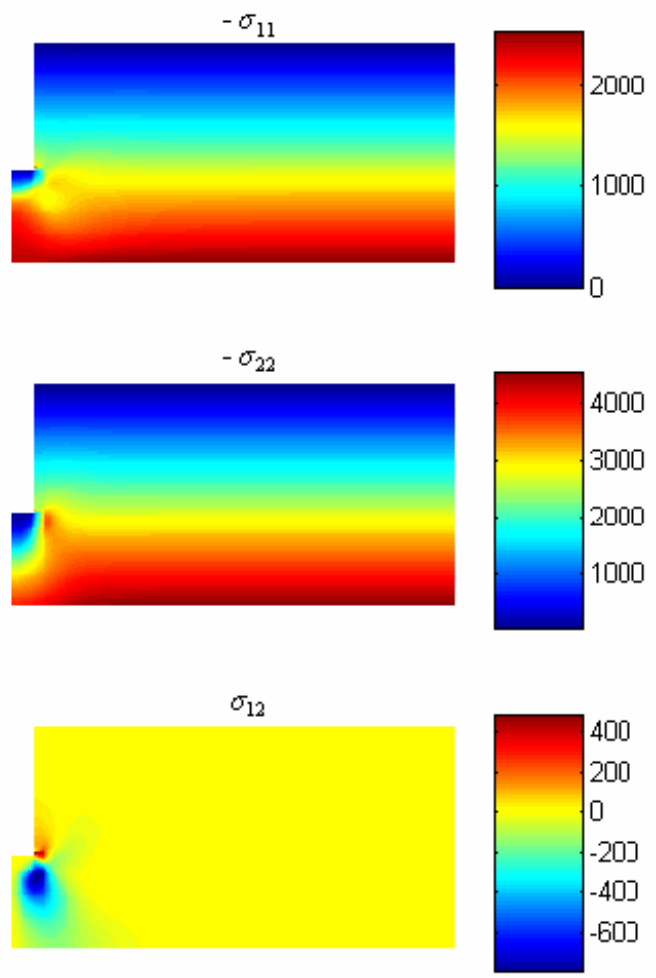

Figure 6.6: Stresses at equilibrium

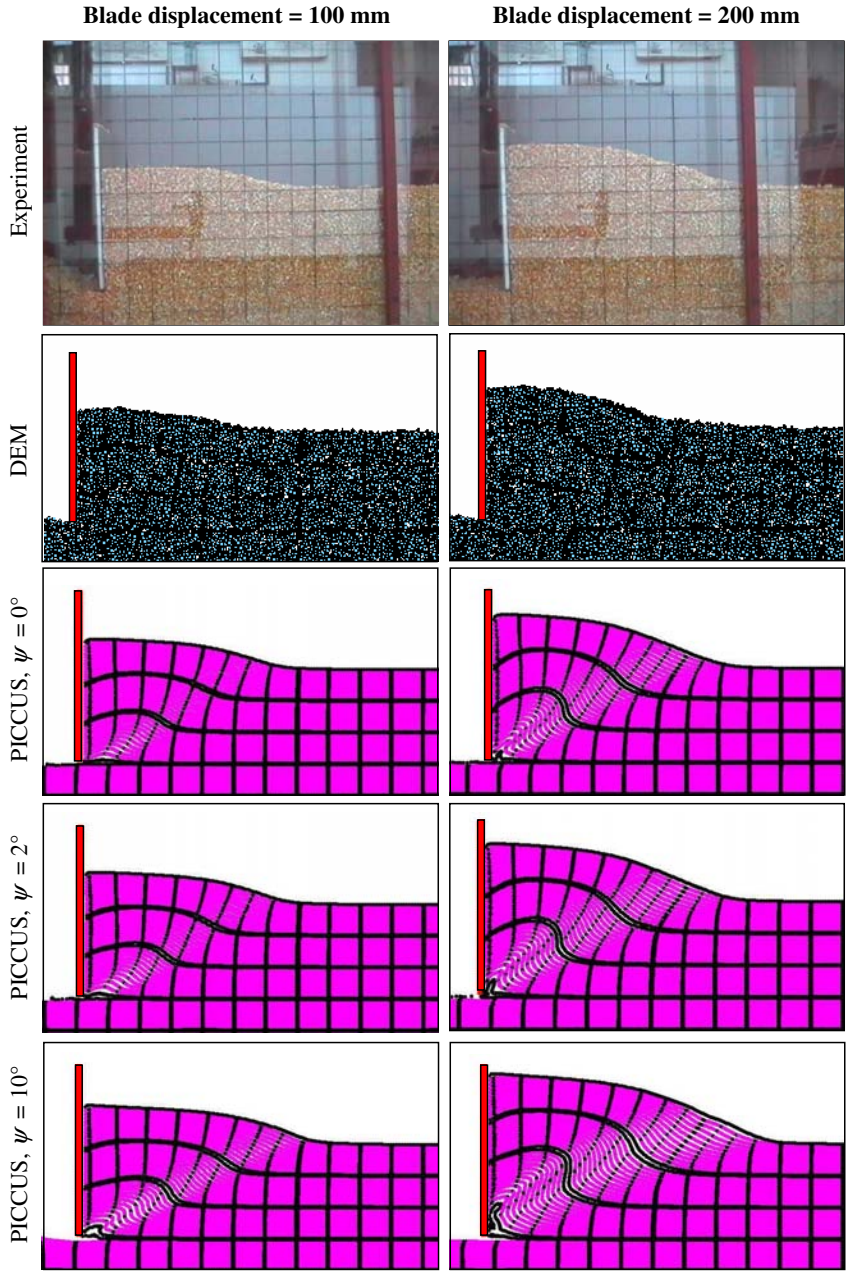

Figure 6.7: Comparison between experimental, DEM and nonpolar results of corn flowing in front of the blade, displacement = 100 mm and 200 mm

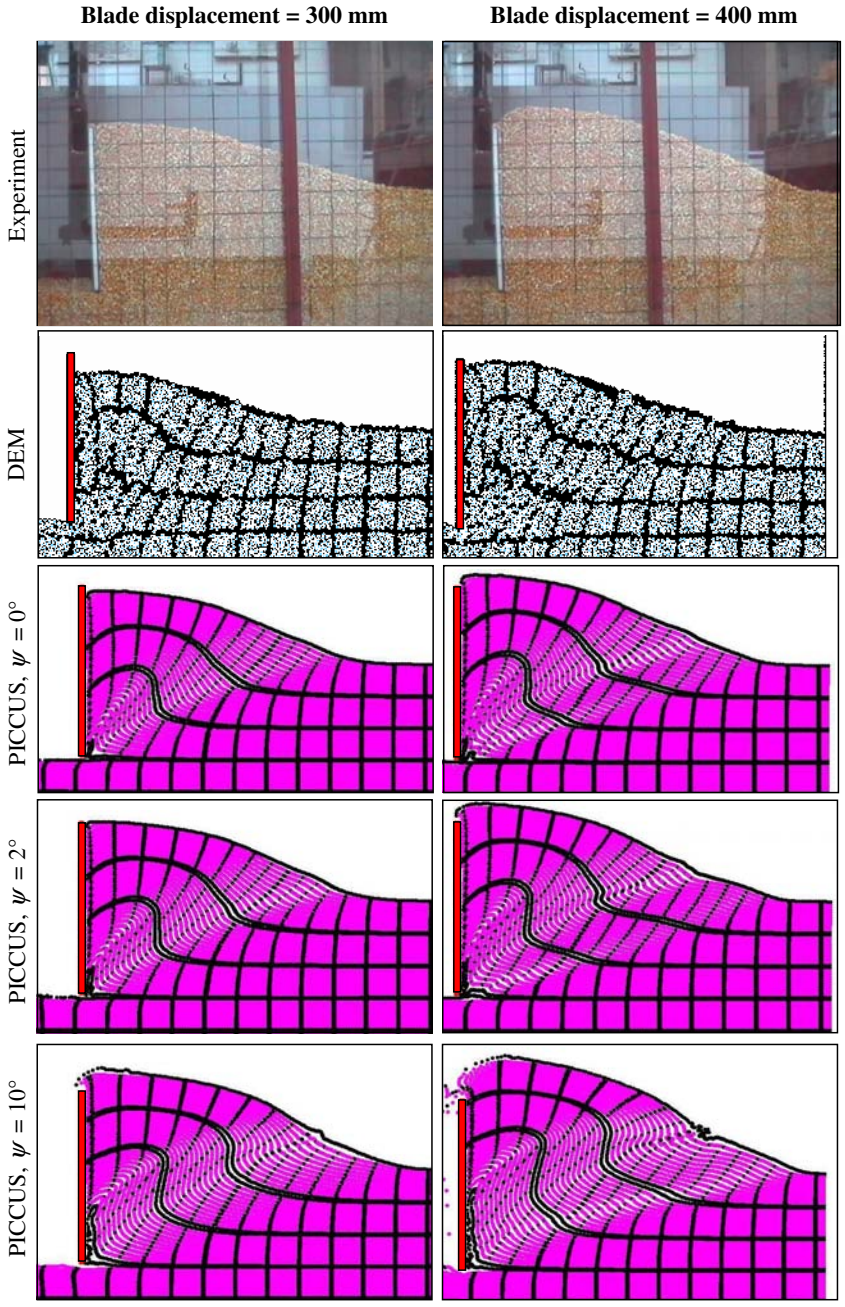

Figure 6.8: Comparison between experimental, DEM and nonpolar results of corn flowing in front of the blade, displacement = 300 mm and 400 mm

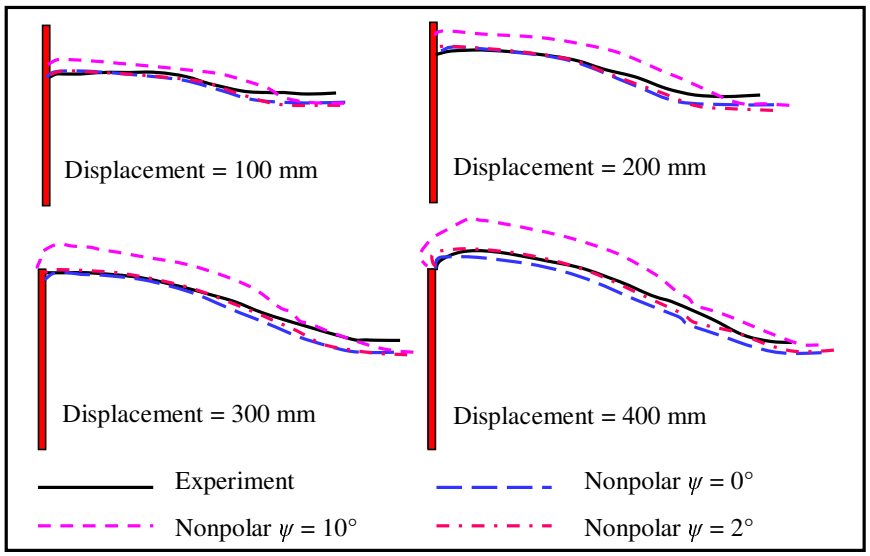

Figure 6.9: Comparison of the free surfaces using different dilatancy angles

Curves were fitted to the free surfaces to make a quantitative comparison of the flow of material (figure 6.9). The free surfaces exhibit the effect of the dilatancy angle: with an increase in dilatancy angle, there is an increase in material volumetric expansion. The free surface is the most accurately predicted using a dilatancy angle $\psi = 2^\circ$. The value $\psi = 2^\circ$ is assumed for all other simulations.

The simulation was repeated with a Cosserat continuum. The material properties used are summarised in table 6.2. The standard set of coefficients a_1, a_2 and a_3 was used. The moment of inertia J_{33} was assumed to be that for a cylinder with a diameter equal to the characteristic length l which has been taken to be the same order of magnitude as the size of the corn grains. The friction- and dilatancy parameters are calculated as proposed by Tejchman (1997). For a detailed description of the Cosserat constitutive model see Appendix I.5. A comparison of the polar and nonpolar continuum flow patterns is given in figure 6.10. At a displacement of 100 mm there is good agreement, but as the blade moves further, the polar continuum seems to show less dilation than the nonpolar continuum. The curves fitted to the free surfaces are shown in figure 6.11. From these curves it can be seen that the nonpolar continuum predicts the free surface the most accurately. The DEM predicted free surface is in close agreement with the polar continuum predicted free surface up to a displacement of 200 mm, but both fail to predict the experimental free surface accurately.

The forces that should be applied to the blade to move it at constant velocity are shown in figure 6.12 for different values of ψ. The force in the vertical x_2-direction is negative, which indicates that the material tends to

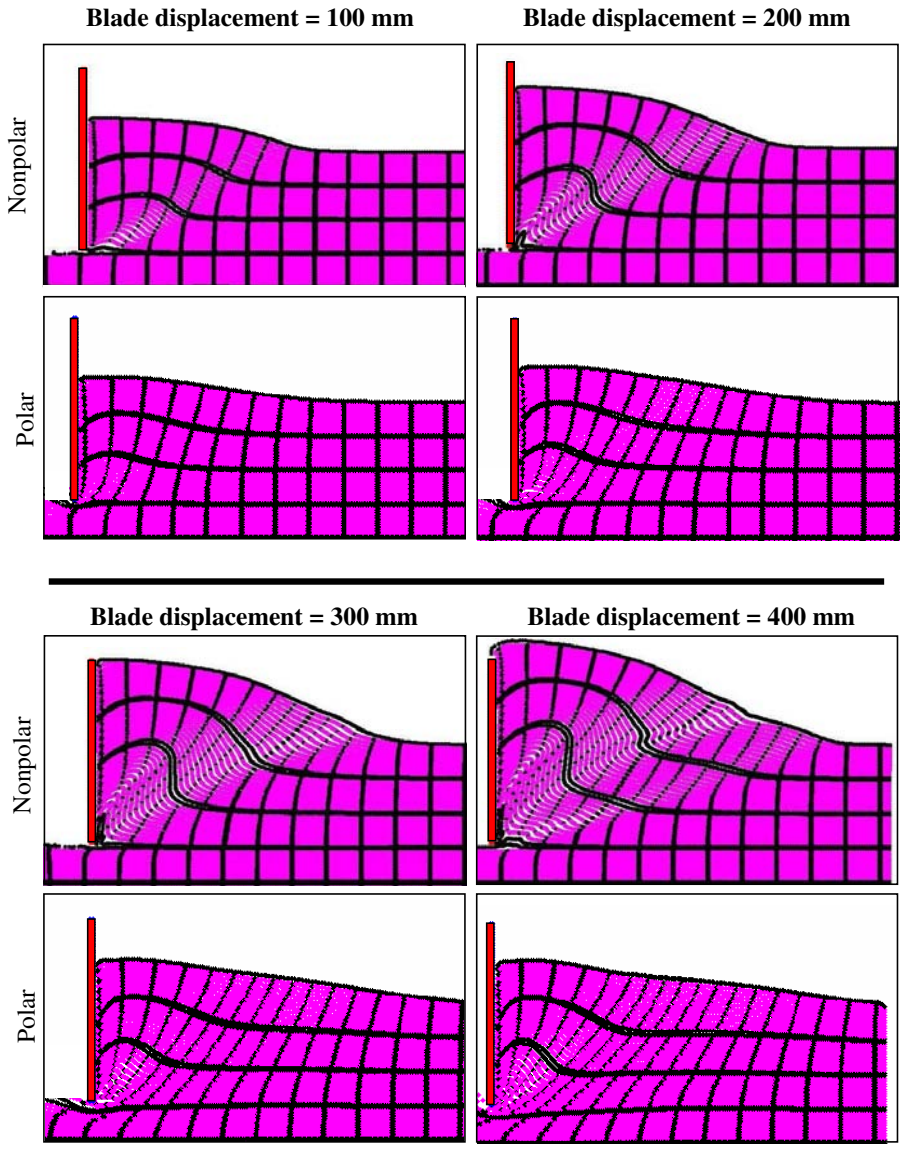

Figure 6.10: Comparison between polar and nonpolar results of corn flowing in front of the blade, $\psi = 2^\circ$

Table 6.2: Corn material properties - Cosserat continuum

Young's modulus	E	2.76 MPa
Poisson's ratio	ν	0.2
Density	ρ	778 kg·m^{-3}
Friction angle	ϕ	26°
Friction parameter	$\alpha = \sin\phi$	0.44
Dilatancy angle	ψ	2°
Dilatancy parameter	$\beta = \sin\psi$	0.035
Cohesion	c	0 Pa
Tension cutoff	σ^t	0 Pa
Friction with steel	ϕ_s	14°
Constitutive coefficients	$a_1; a_2; a_3$	0.375;0.125;1
Cosserat shear modulus	$G^c = 2G$	2.3 MPa
Characteristic length	l	10 mm
Moment of inertia	$J_{33} = 0.5(0.5\,l)^2$	12.5×10^{-6}m^2

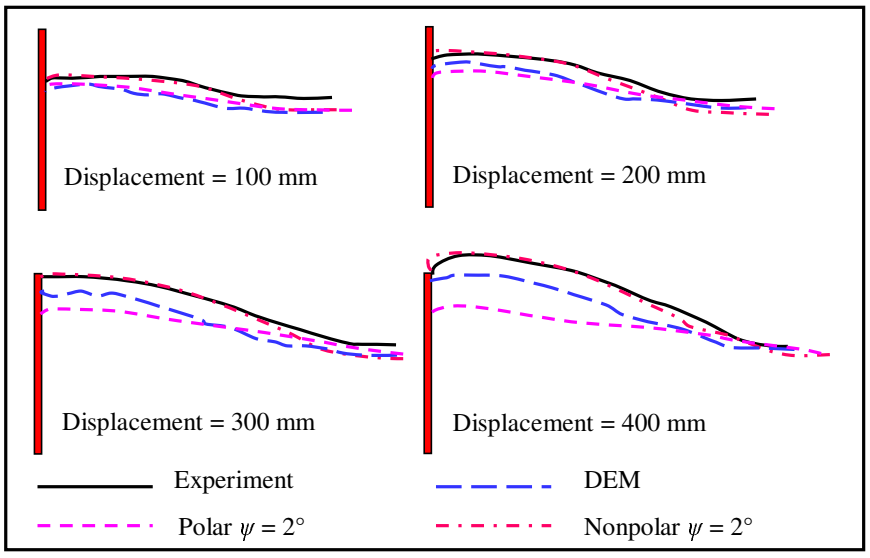

Figure 6.11: Comparison of the experimental, polar ($\psi = 2°$), nonpolar ($\psi = 2°$) and DEM free surfaces

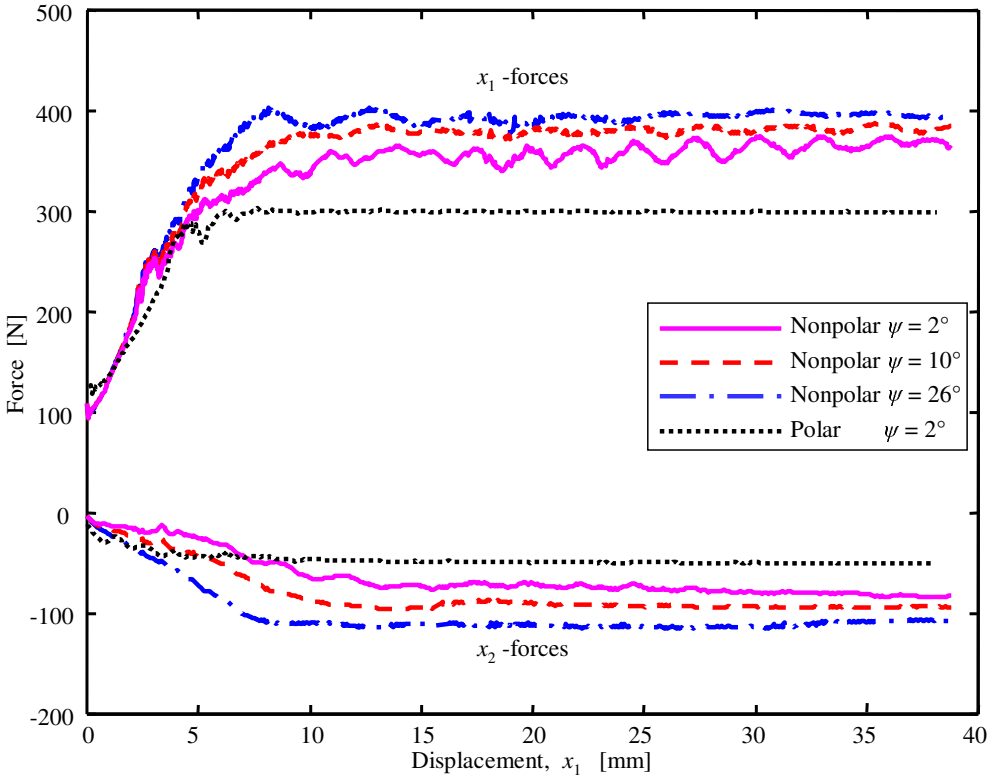

Figure 6.12: The effect of the dilatancy angle ψ on the blade forces, $h = 350\,\text{mm}$

push the blade upwards, hence a negative force should be applied to the blade to prevent vertical movement. Over the first part of the displacement the responses, using a nonpolar continuum, are the same because the material is in a total elastic state. In the plastic regions, however, there is an increase in blade forces with an increase in dilatancy angle. This phenomenon has also been observed for cone penetration tests (Vermeer and De Borst, 1984). The polar result, with $\psi = 2°$ is also shown. The polar continuum, however, predicts forces 13% lower than the nonpolar continuum with $\psi = 2°$. The polar continuum also shows an initial elastic stiffness that slightly differs from that of the nonpolar continuum. According to Tejchman (1997), the constitutive constants, a_1, a_2, a_3 and the Cosserat shear modulus G^c have an influence on the material stiffness.

Using the dilatancy angle $\psi = 2°$ and a nonpolar continuum, the effect of blade depth h on the blade forces is shown in figure 6.13, using depths $h = 150\,\text{mm}, 250\,\text{mm}$ and $350\,\text{mm}$. As expected, the forces increase with an increase in blade depth. In order to compare the PICCUS results to that from DEM, experiments and Sokolovski's method of characteristics (Sokolovski, 1954), the average draft forces are calculated. The draft force is defined as the force needed to push or pull a blade through the material, in the di-

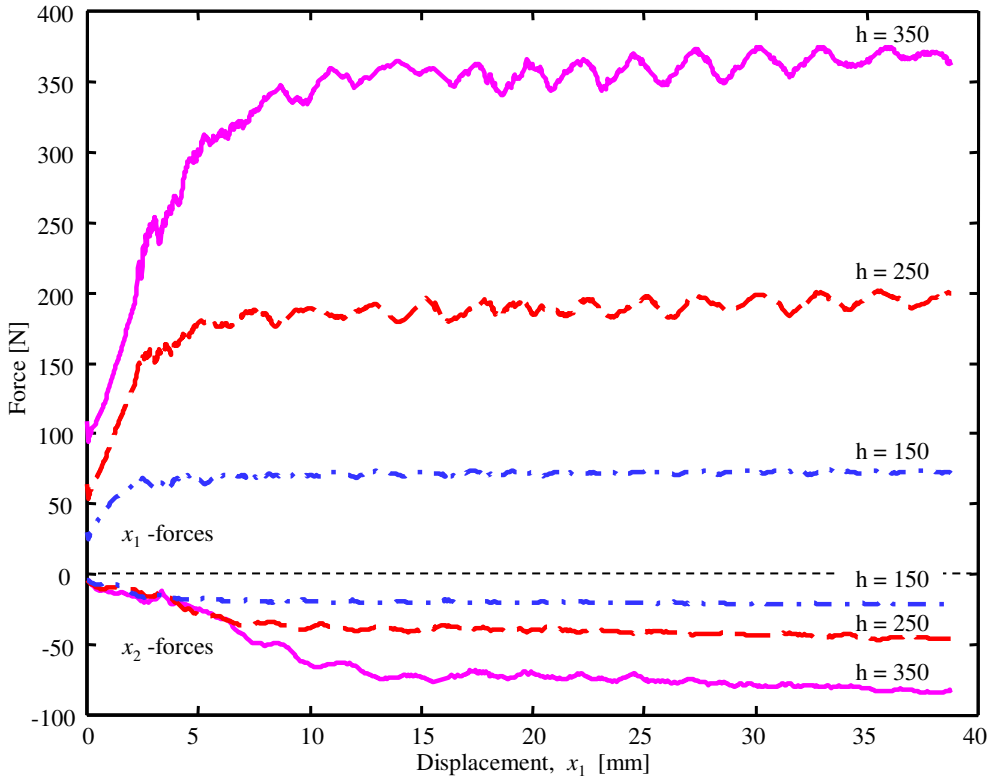

Figure 6.13: The effect blade depth h on the blade forces using a nonpolar continuum and $\psi = 2°$

rection of the motion and is important in industrial applications such as ploughs, tillers and bulldozers. In this case the draft force is simply the force in the x_1-direction. The average draft forces were calculated from figure 6.13, using the data between 15 mm and 35 mm in displacement. A similar procedure was applied to the experimental results, DEM results, and polar results. All the results are shown in figure 6.14 and show the same general trend that the draft force is exponentially dependent on the blade depth. The nonpolar results are in close agreement with the results from Sokolovski's method, overestimating it by 12%, 6% and 5% for the depths $h = 150\,\text{mm}, 250\,\text{mm}$ and $350\,\text{mm}$ respectively. The nonpolar results underestimate the experimental results by 25%, 11% and 9% for the depths $h = 150\,\text{mm}, 250\,\text{mm}$ and $350\,\text{mm}$ respectively. There might be different reasons for the fact that the simulations predict lower draft forces than were measured. Although the friction coefficient between the corn and glass is low, there are still friction forces which will result in measured values that are higher than it would have been under purely plane strain two dimensional conditions. The polar result predicts draft forces 30%, 21% and 20% lower than the measured values for the three different depths respectively

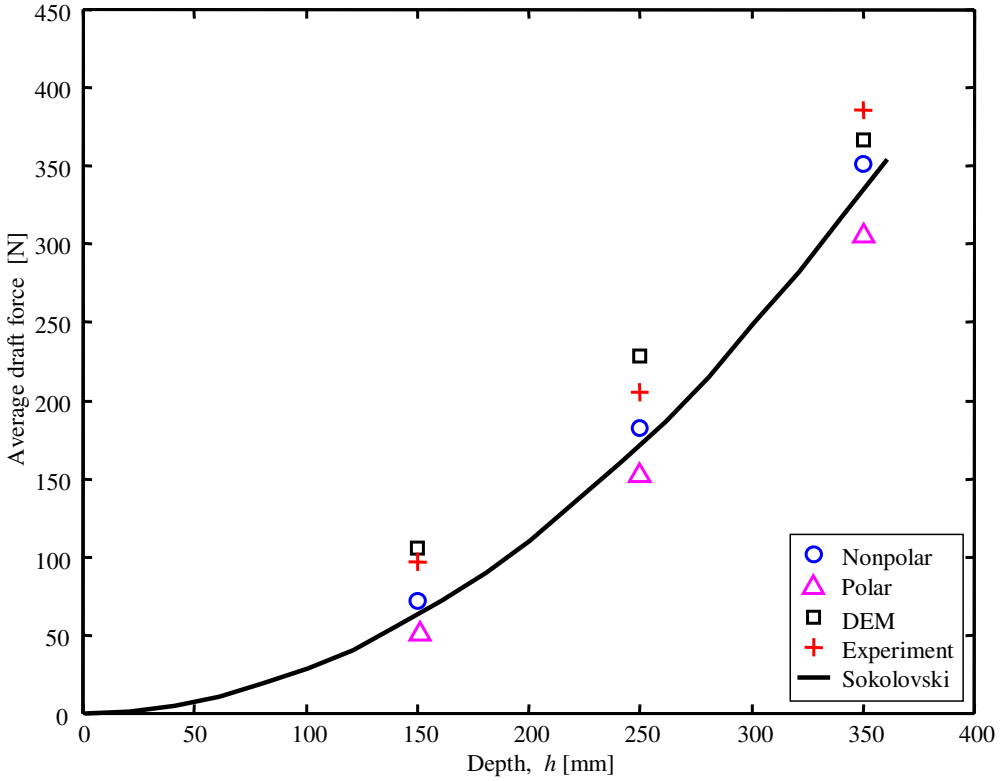

Figure 6.14: Comparison between average draft fores: PICCUS, DEM, experiments and Sokolovski's method

and 28%, 14% and %10 lower than the nonpolar results. Tejchman (1997) reports a 30% difference in polar and nonpolar continuum results in modelling a strip footing. The percentage difference in polar and nonpolar results compared to experiments seems to decrease with an increase in blade depth, i.e. an increase in stress. The same phenomenon can be seen by comparing the polar results to the nonpolar results. The DEM result (Coetzee, 2000), compared to the measured values, predicts a higher draft force with $h = 150$ mm and $h = 250$ mm and a lower draft force with $h = 350$ mm

When the blade pushes the material forward, a shear band develops, reaching from the bottom tip of the blade to the free surface. The ability of PICCUS and DEM to predict these shear bands was investigated. Using DEM, it can be very difficult to predict the shear bands, but there is definitely evidence that such lines exist. Coetzee (2000) made use of the particle displacement ratio (PDR) to find shear bands. PDR is defined as the ratio of the magnitude of the particle displacement vector to the magnitude of the blade displacement vector. The top of figure 6.15 shows the results using PDR = 0.15, i.e., all the darker particles have been displaced a distance of at least 0.15 times the displacement of the blade. The experimentally ob-

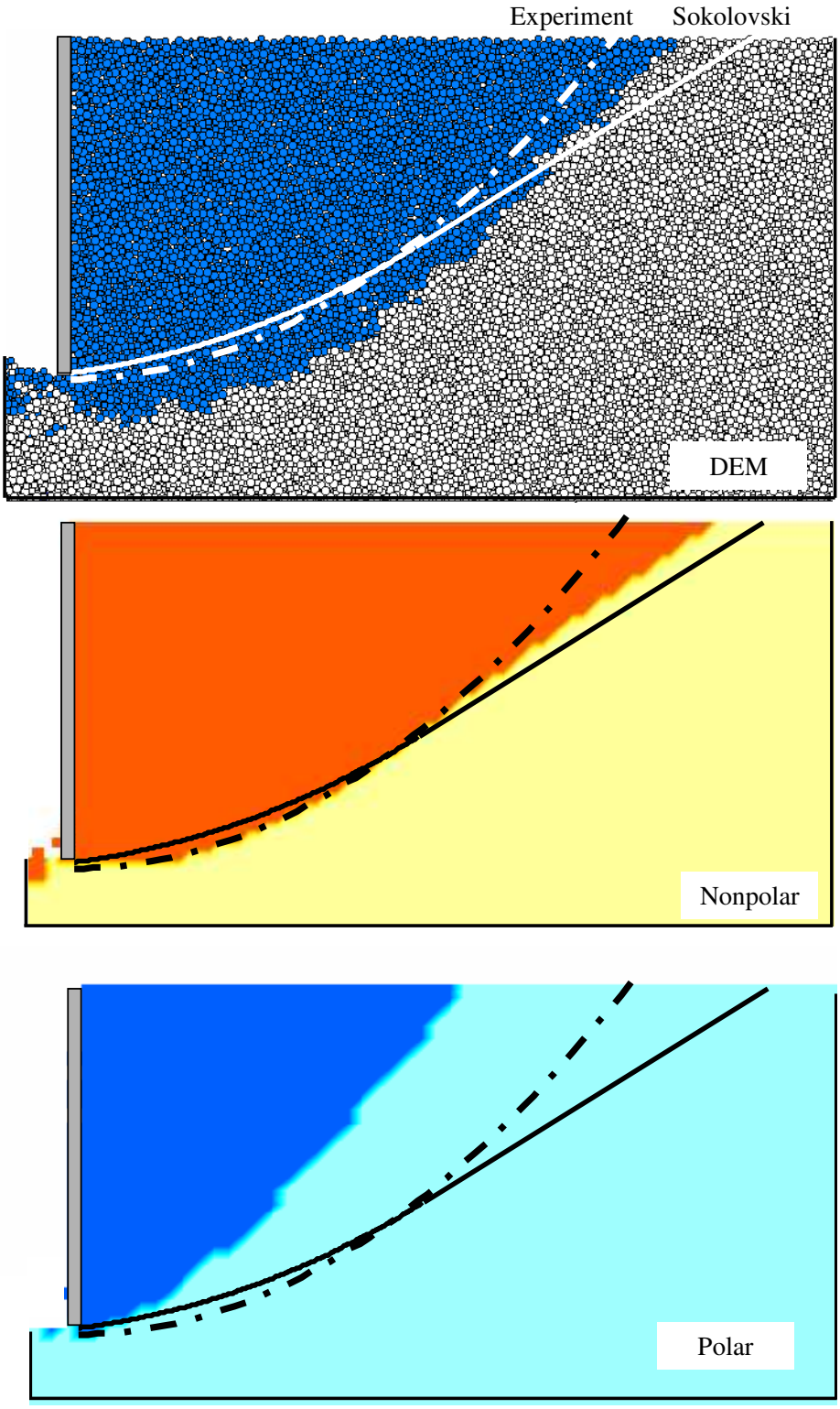

Figure 6.15: Predicted shear bands using a particle displacement ratio PDR = 0.15, $x_1 = 15\,\text{mm}$

served shear band and the line predicted by Sokolovski's method are also shown. The line shown on the figure indicates the centre of the observed shear band. With PDR = 0.15, the predicted shear band falls between the observed line and the Sokolovski line at the free surface. Closer to the bottom edge of the blade, however, the shear band is outside of that predicted by Sokolovski's method. This is because the particles have a finite size whereas in Sokolovski's method, the shear band is assumed to start at the bottom edge of the blade.

The lower two images in figure 6.15 show similar results from the nonpolar and polar continuums respectively. All the material points within the darker region have PDR $\geq$ 0.15. The nonpolar continuum predicted shear band meets the free surface at almost exactly the same place as the DEM predicted shear band. Closer to the blade tip, however, the shear band more closely follows that of the observed and Sokolovski lines. Contrary to the DEM modelling, using a continuum, there are no particles with a finite size, which causes the DEM shear band to be outside the Sokolovski line. The polar continuum predicts a shear band at almost 45° and it is less curved than the observed and nonpolar shear band.

The predicted shear band can be manipulated by changing the PDR value to obtain a better fit. A more precise method of predicting the shear band is possible with a continuum method, but not with DEM. Using the nonpolar continuum, figure 6.16 shows all the regions which have a stress state on the yield surface as lighter (yellow) patches and those which have stress states below the yield surface (elastic state) as darker (red) patches. Two mesh sizes were used, 120×70 and 80×50. Yields points are concentrated around the observed and Sokolovski shear bands. The coarser mesh shows more yield points and a broader shear region. Figure 6.17 shows the nonpolar shear strain intensity. The shear strain shows a definite band, bounding the observed and Sokolovski shear bands. Again the coarser mesh predicts a slightly broader shear band than the fine mesh, but the general shape remains the same.

It is well-known that the Cosserat rotation is an indication of shear bands (Tejchman, 1997). Figure 6.18 shows the rotation for two different mesh sizes with the rotation at the blade interface unconstrained (free). Again, the shear regions differ from the nonpolar and experimental results, but do agree with the polar displacement field as depicted in figure 6.15. There is little difference in the results from the two different mesh sizes. Figure 6.19 shows the nonpolar shear strain and the polar rotation using a 80×50 mesh rotated through 35° anticlockwise. Comparing the nonpolar result to that of figure 6.17, shows that the direction of the shear band is only slightly influenced by the mesh orientation. Comparing the polar result to that of figure 6.18, shows that the shear band is not influenced by the mesh orientation.

The observed slip line had a width of about 7 - 8 particle diameters, i.e.,

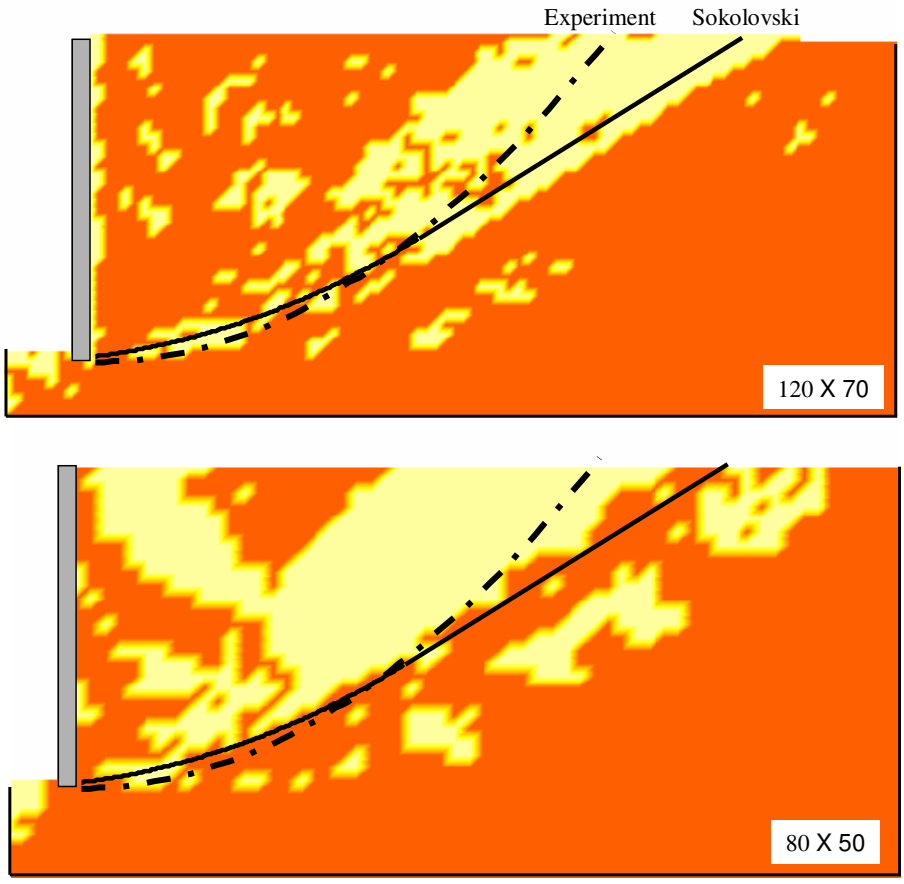

Figure 6.16: Nonpolar yield points: mesh sizes 120×70 and 80×50, $x_1 = 15\,\text{mm}$

70 mm - 80 mm (Coetzee, 2000). The simulations, polar and nonpolar, predict shear bands 60 mm - 80 mm wide. Tejchman (1997) states that if the size of the elements is smaller than five times the mean grain diameter d_{50}, i.e. 50 mm, the polar results are independent on the mesh size. The 120×70 and 80×50 had element sizes 10 mm $\times$ 10 mm and 15 mm $\times$ 14 mm respectively. These sizes are well below five times the mean grain diameter.

Figure 6.20 shows the material translational velocity fields in front of the blade. Comparing this figure to figure 6.15, it can be seen that the displacement field and velocity field, resulting from the polar- and nonpolar continuum, is in close agreement. Although the DEM displacement field is similar to the nonpolar displacement field, there is big difference in the velocity fields. The displacement fields have been calculated after a 10 mm blade displacement, i.e., it can be viewed as an average velocity field. The velocity fields, however, are just a snapshot at a specific moment in time. This indicates that using DEM, the particles move in a step-like fashion (stick-slip) and it should be averaged over a period of time to get the

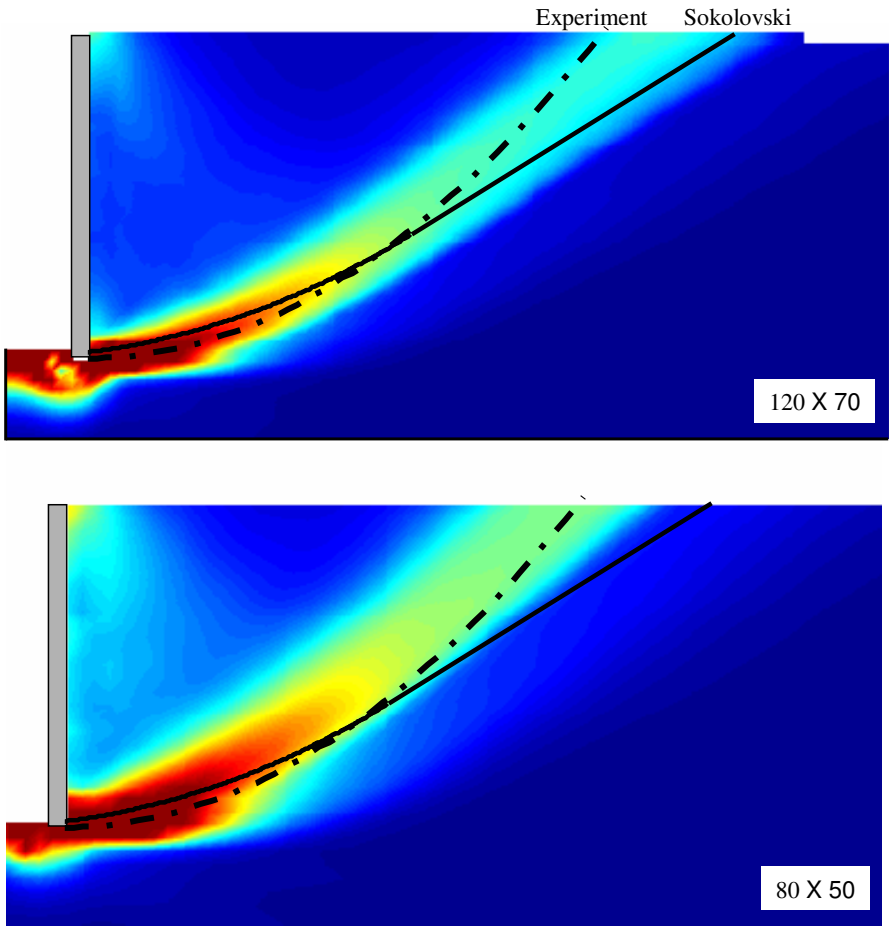

Figure 6.17: Nonpolar shear strains for mesh sizes 120×70 and 80×50, $x_1 = 15\,\text{mm}$

total effect. The polar continuum velocity field compares well to the DEM velocity field, but not to the nonpolar velocity field.

The standard set of Cosserat coefficients a_1, a_2 and a_3 has been used. Muhlhaus & Vardoulakis (1987) derived the values of these coefficients by taking into account slip and rotation in a random assembly of circular rods. Tejchman (1997) investigated the effect of the Cosserat material parameters on biaxial simulations and concludes that the standard set of parameters turned out to be useful and sufficient in numerical calculations involving localisation. The influence of a_3 on the results was rather insignificant and, in general, the larger the difference between a_1 and a_2, the larger the non-symmetry of the stress tensor. Tejchman (1997) also showed that when the following set is used, $a_1 = 0.25, a_2 = 0.25, a_3 = 0.5$, the response is slightly less stiff compared to the standard set. It was found that by changing the value of G^c from $G^c = 2G$ to $G^c = 0.5G$ the draft force on the blade decre-

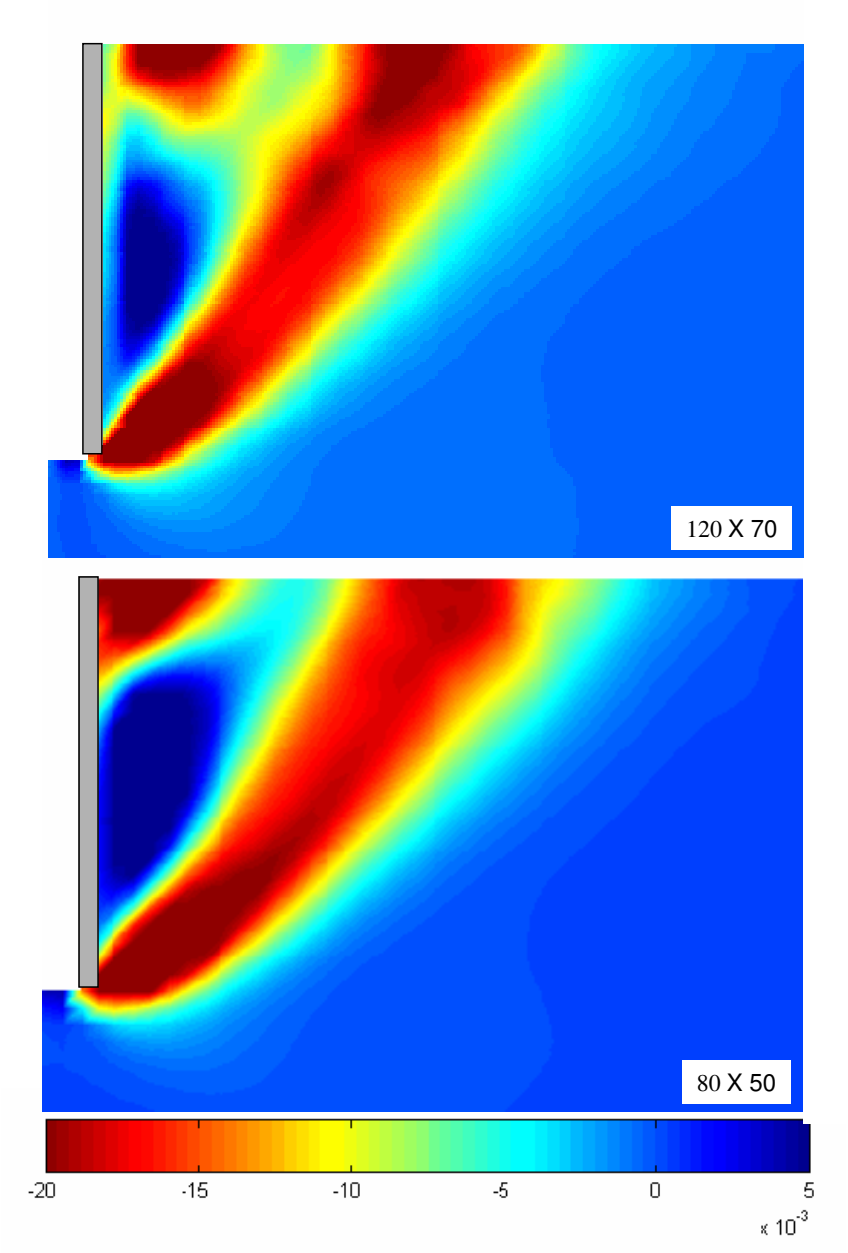

Figure 6.18: Polar rotations [rad] for mesh sizes 120×70 and 80×50, $x_1 = 15\,\text{mm}$

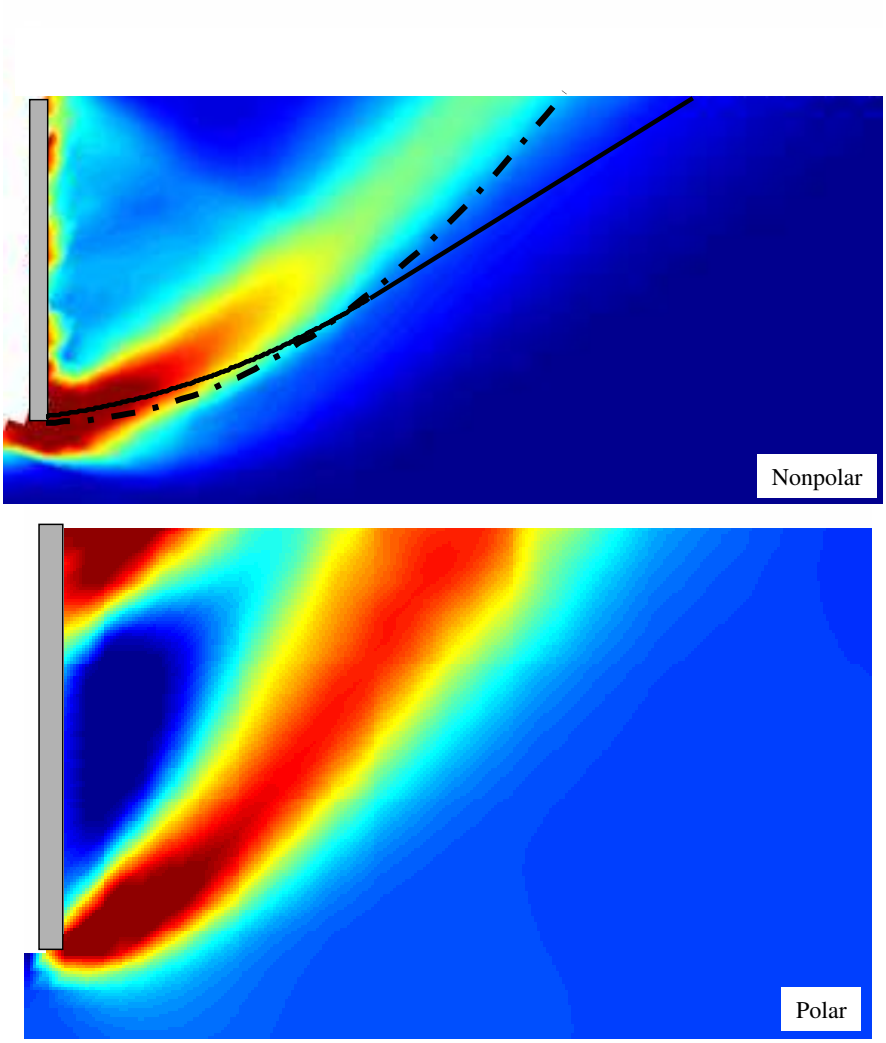

Figure 6.19: Nonpolar shear strain and polar rotation using a 80×50 mesh rotated through 35° , $x_1 = 15\,\text{mm}$

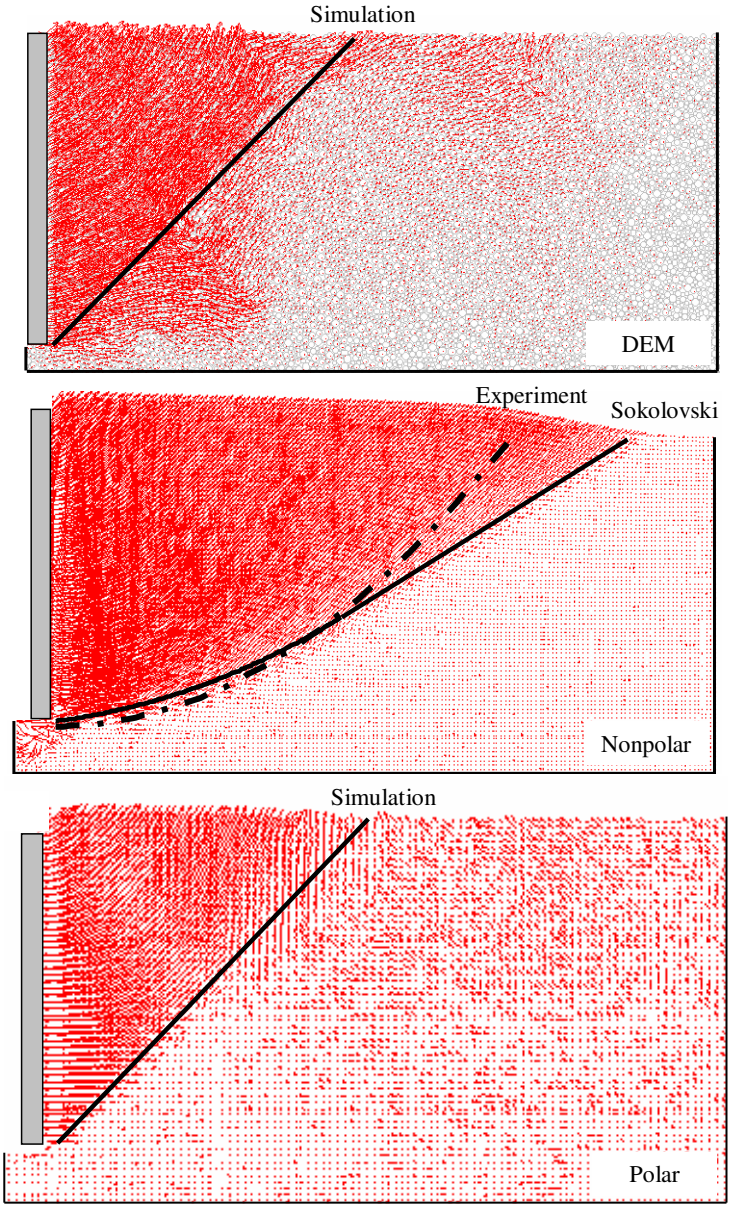

Figure 6.20: The velocity fields in front of the blade, $x_1 = 15\,\text{mm}$

ased by 1.3%. Changing the internal length from $l = 10\,\text{mm}$ to $l = 2\,\text{mm}$, the draft force decreased by only 1.9%. These results show that the model is not sensitive to changes in the values of G^c and l.

Figure 6.21 shows the normal and shear stress at the blade as predicted by the nonpolar continuum and Sokolovski's method. The continuum results were obtained from the nodal forces acting on the blade. The irregularity in the stress close to the bottom edge of the blade is due to the

unit normal vector at the bottom node which is not horizontal and possible stress concentrations. The nonpolar results are in good agreement with the Sokolovski predictions. Figure 6.22 shows the polar continuum results for two boundary conditions: no rotation at the blade $w^c = 0$ and free rotation at the blade. The polar results predict normal and shear stresses lower than that of the nonpolar continuum and Sokolovski's method. Having no rotation or free rotation at the blade has little effect on the normal stress, but the shear stress with free rotation, is almost half the stress when no rotation is allowed. This means that the rotation has an influence on the friction between the material and the blade. This has also been observed by Tejchman (1997).

Figure 6.23 shows the DEM contact force chains between particles and between the particle and the blade. The thickness of the force chains is directly proportional to the magnitude of the contact force. In this particular case there were 50 contacts between particles and the blade. Taking the average contacting force of two neighbouring contacts and dividing it by the distance between the contacting points along the blade, the stress at the blade could be estimated. Due to the particles moving in a step-like fashion, a time average was used to calculate the stress at the blade. The average was calculated between a blade displacement of 18 mm and 22 mm and the result is shown in figure 6.24. The normal and shear stress are lower than the stresses predicted by Sokolovski's method.

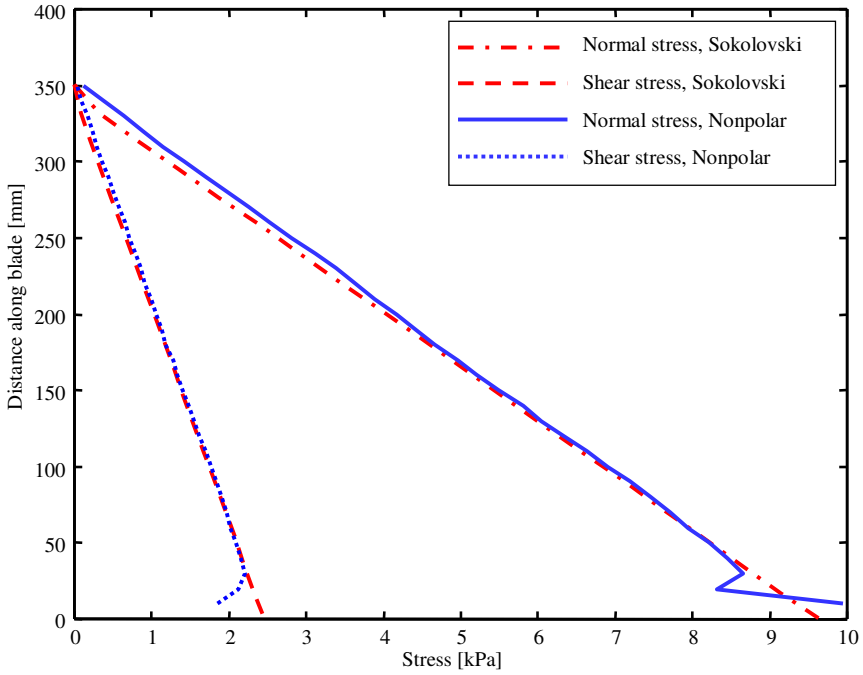

Figure 6.21: Normal and shear stress at the blade for $h = 350\,\text{mm}$: Nonpolar continuum and Sokolovski's method, $x_1 = 20\,\text{mm}$

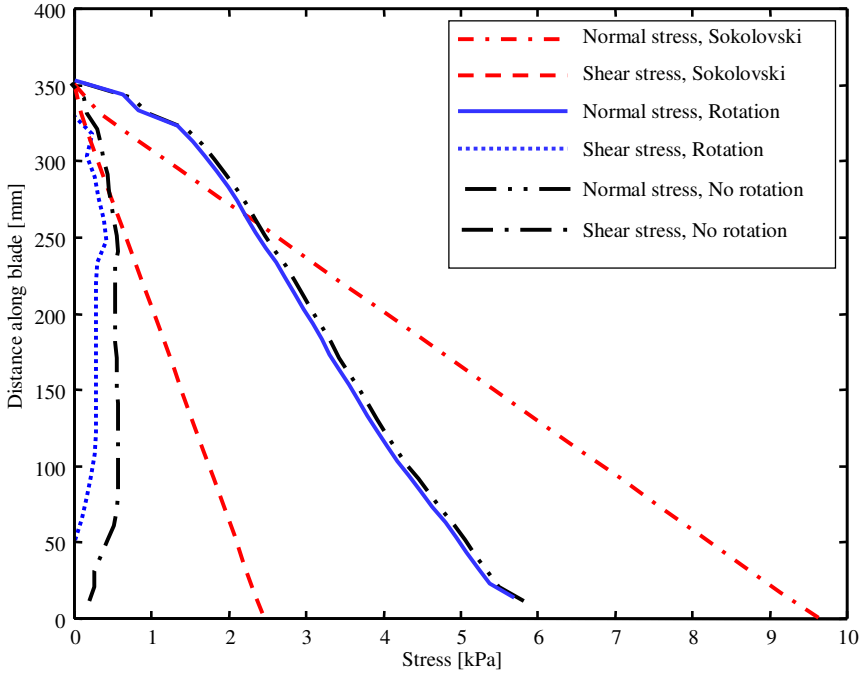

Figure 6.22: Normal and shear stress at the blade for $h = 350\,\text{mm}$: Polar continuum, with and without rotation at the blade, and Sokolovski's method, $x_1 = 20\,\text{mm}$

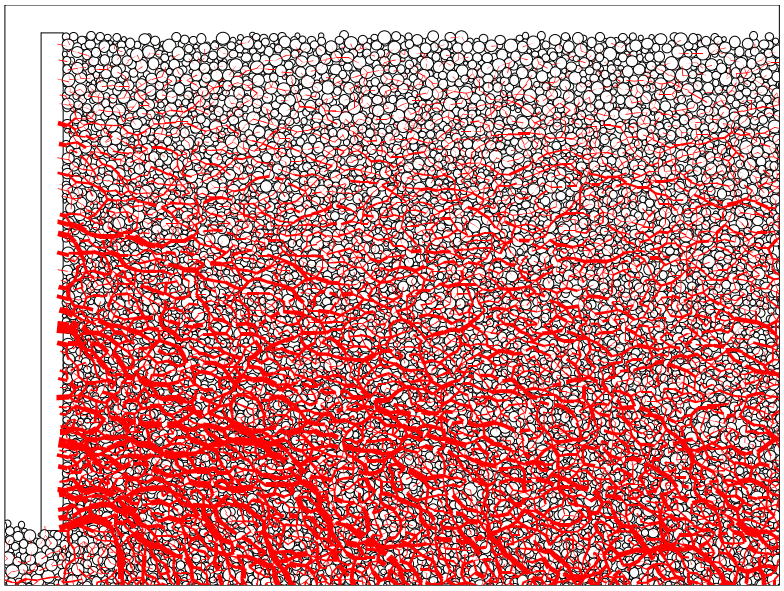

Figure 6.23: Force chains at the blade for $h = 350\,\text{mm}$, $x_1 = 20\,\text{mm}$

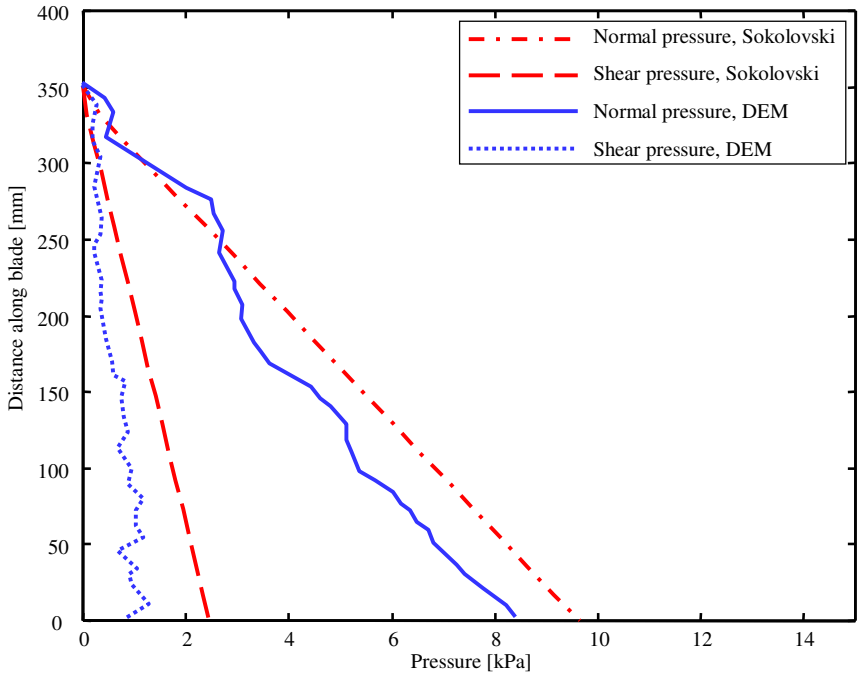

Figure 6.24: Normal and shear pressures at the blade for $h = 350\,\text{mm}$: DEM and Sokolovski's method

6.2.6 Bucket Modelling

Coetzee (2000) investigated the ability of DEM to simulate the filling of a scaled model bucket with corn grains. The bucket used in experiments was a dragline type of bucket with freedom of motion in the vertical direction. The vertical motion of the bucket was determined by the bucket weight and the effect of the material flowing into the bucket. The bucket was given a constant velocity of $10\,\text{mm}\cdot\text{s}^{-1}$ in the x_1-direction and the drag force and vertical displacement recorded. The vertical velocity was found to be constant and used as input to the DEM models and in this evaluation of PICCUS. The $2.0\,\text{m} \times 0.7\,\text{m}$ domain was divided into 200×100 elements, each of size $10\,\text{mm} \times 7\,\text{mm}$. The bottom boundary was fixed in the horizontal, vertical and rotational (polar) directions and the two side boundaries in the horizontal and rotational (polar) directions. The boundaries were too far away from the bucket to have a significant effect on the results. No polar rotation was allowed at the bucket-material interface. The material stresses were initialised using a coefficient of earth pressure $K_o = 1 - sin\phi$. The bucket was created with its bottom surface against the material free surface with the tooth already engaged into the material.

Figure 6.25 shows the measured, nonpolar continuum, polar continuum and DEM draft force on the bucket. The nonpolar draft force corresponds well to the measured force up to a displacement of 600 mm, but thereafter it under predicts the force and at 800 mm the error is 12%. The DEM predicted force is more-or-less 20 N lower than the measured force up to a displacement of 600 mm. The polar continuum predicts a draft force lower than the measured force and the nonpolar predicted force.

Figure 6.26 to figure 6.29 show the experimental, DEM, nonpolar continuum and polar continuum filling process at increments of 100 mm in bucket displacement. Figure 6.30 shows the curves fitted to the material free surface during the filling process. During the initial stages of filling, there is an upheave of material right above the tooth. Up to a displacement of 200 mm the nonpolar continuum predicts the free surface and the upheave the most accurately while the polar continuum predicts less upheave of material during these initial stages of filling. Between the displacements of 300 mm and 600 mm, the polar continuum predicts the free surface more accurately than the nonpolar continuum. Compared to the experimental free surface, the DEM model predicts less upheave of material during the entire filling process.

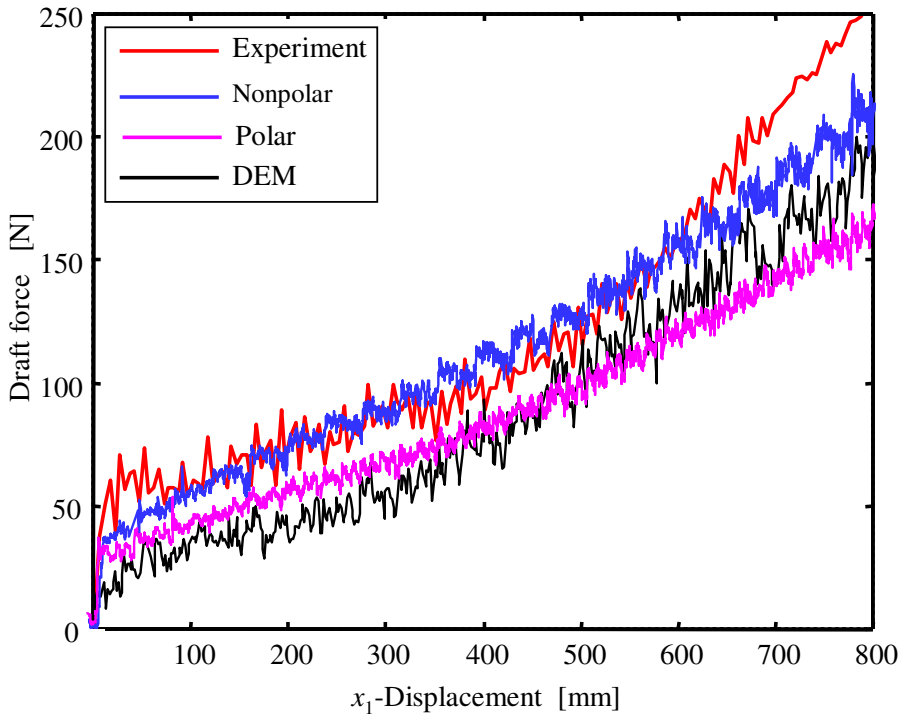

Figure 6.25: Bucket draft force as measured and predicted by the nonpolar continuum, polar continuum and DEM

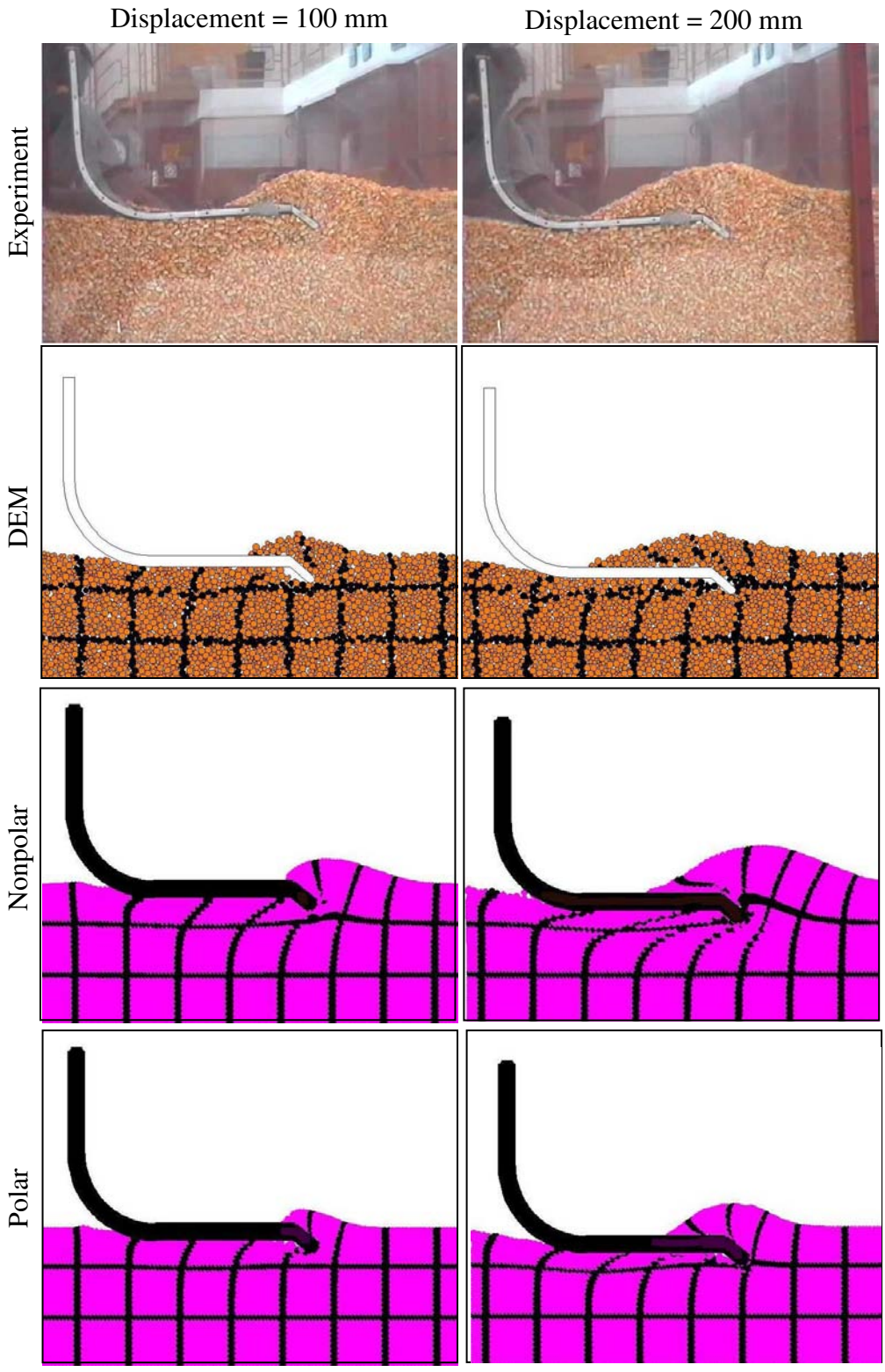

Figure 6.26: The flow of corn into the bucket: displacement = 100 mm - 200 mm

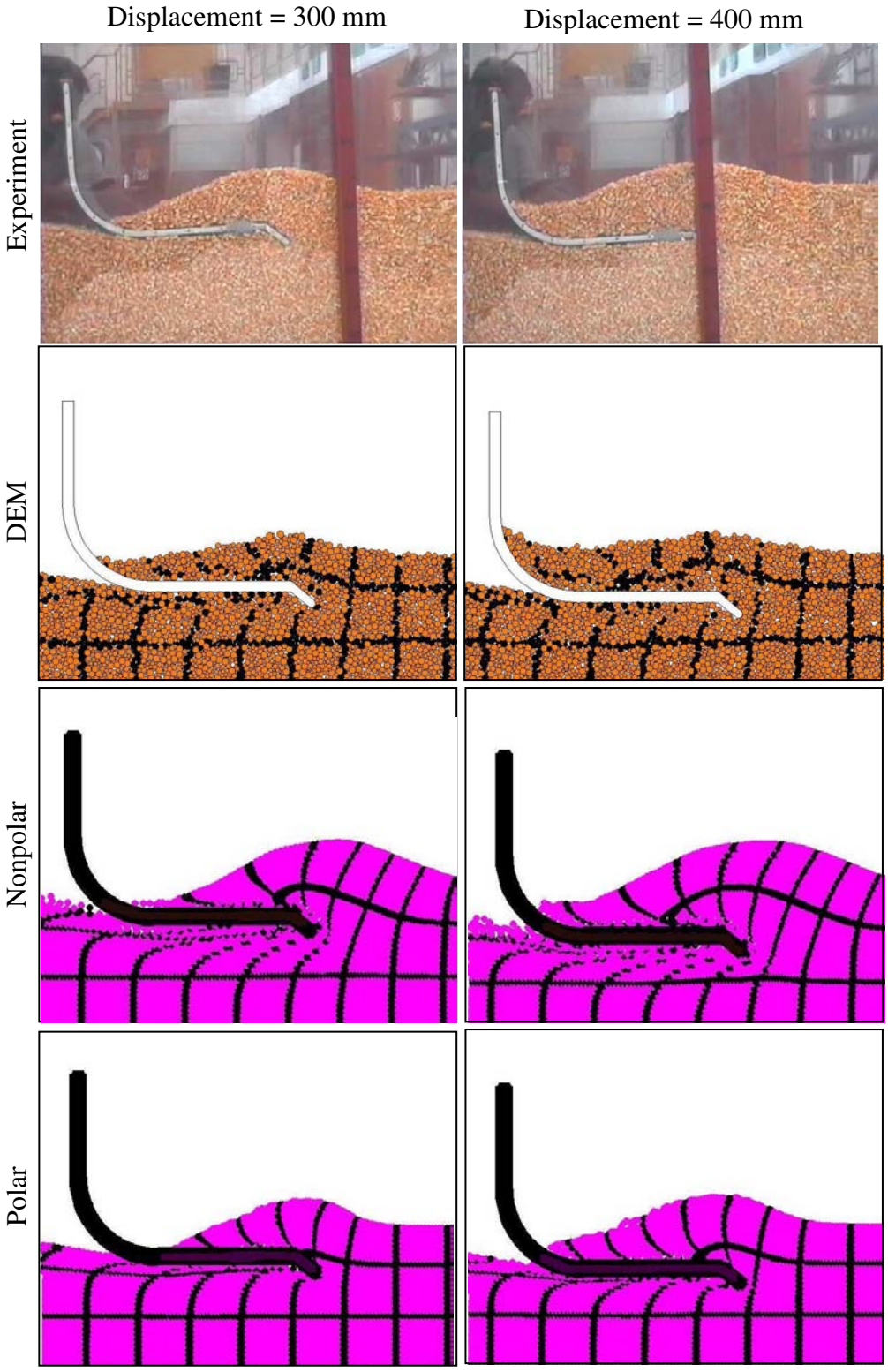

Figure 6.27: The flow of corn into the bucket: displacement = 300 mm - 400 mm

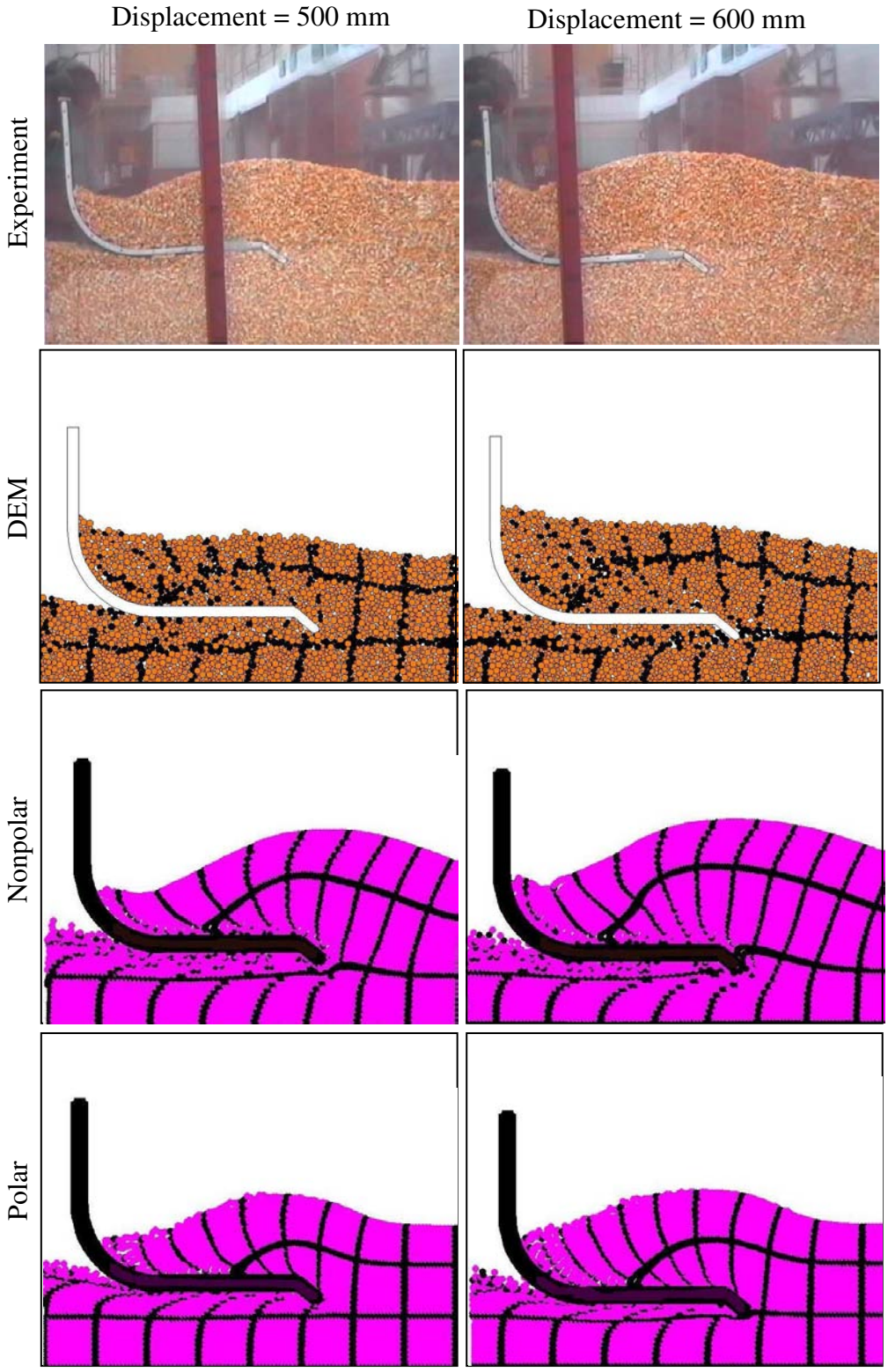

Figure 6.28: The flow of corn into the bucket: displacement = 500 mm - 600 mm

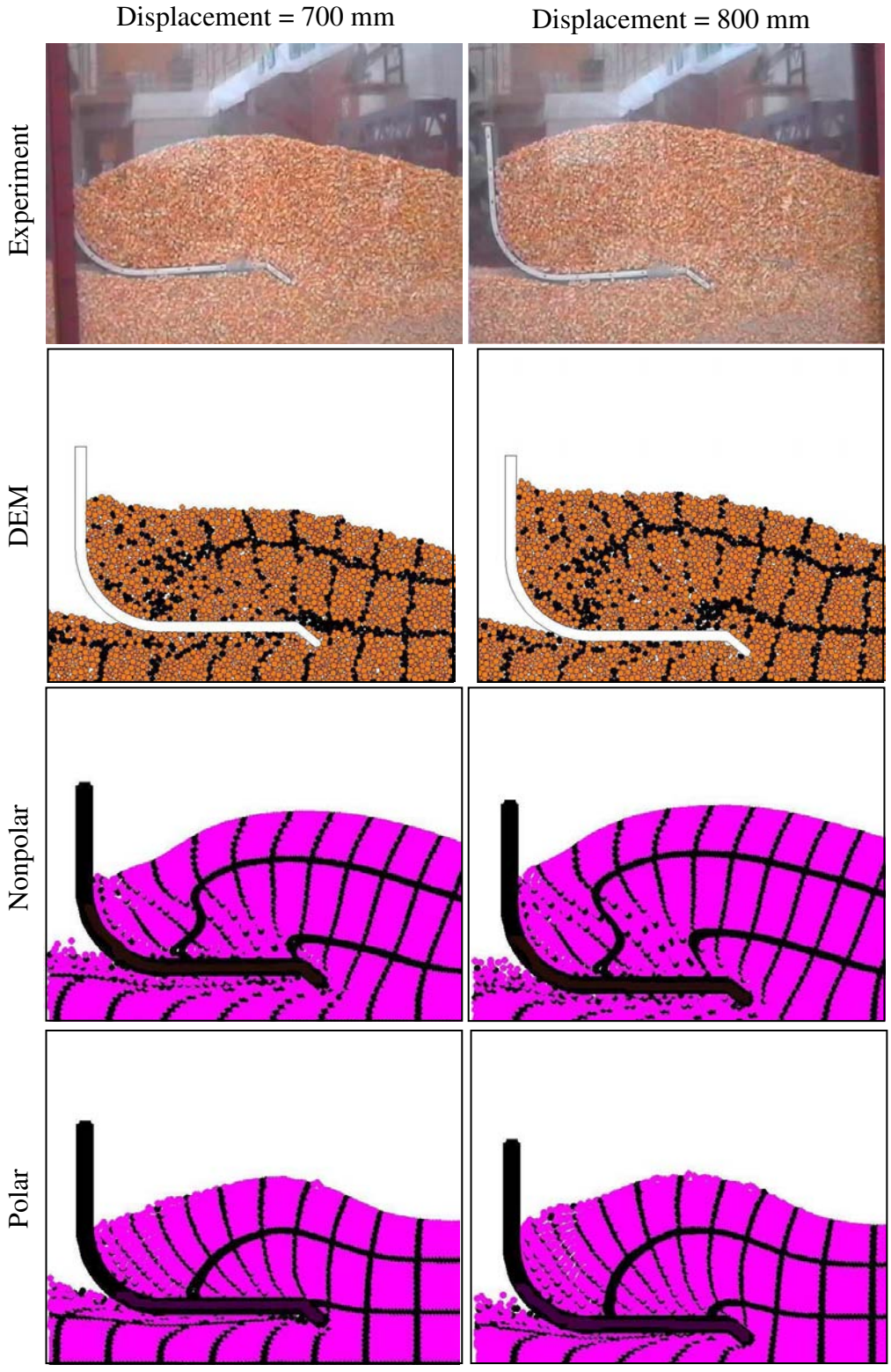

Figure 6.29: The flow of corn into the bucket: displacement = 700 mm - 800 mm

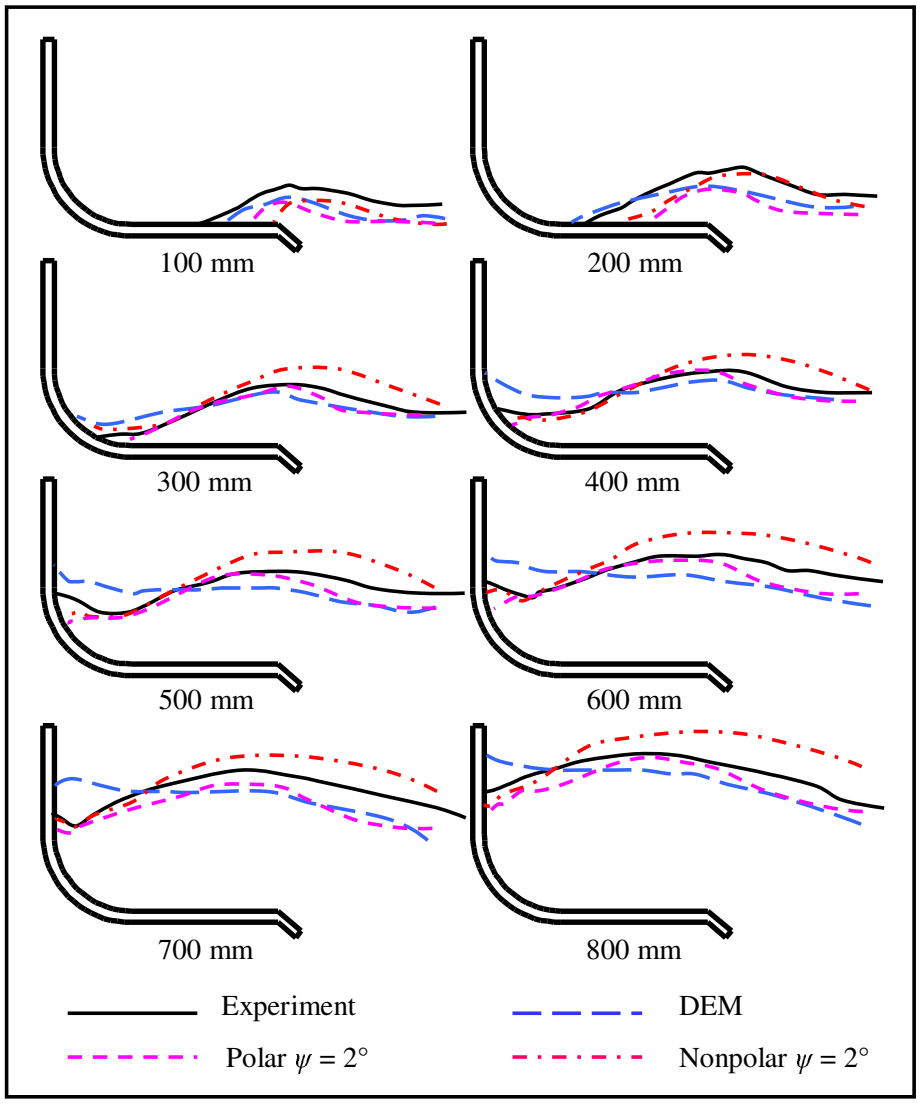

Figure 6.30: Comparison of the free surface of the material flowing into the bucket

Rowlands (1991) made use of mixtures of millet, peas and corn in his test rig which is similar to the rig used by Coetzee (2000). The observation of the filling behaviour led to the development of a theory that describes the flow characteristics and patterns of material entering the bucket. Rowlands (1991) named this concept the *Shear Zone Theory*. He observed that definite planes of shear formed between distinct moving material regimes. These shear planes changed orientation and location depending on initial setup and during the filling process itself.

The experiments by Coetzee (2000) with corn confirmed this theory. The generalised theory is shown in figure 6.31. The movements of the material relative to the bucket are indicated by the arrows. The *Virgin Material* remains largely undisturbed until the final third of the drag during which "bulldozing" occurs. The *Initial Laminar Layer* flows into the bucket during the first third of the drag. After entering to a certain distance, this layer fails at the bucket lip and subsequently becomes stationary with respect to the bucket for the remainder of the drag. With the laminar layer becoming stationary, a new zone, the *Active Flow Zone*, develops. In this zone, the material displacement is predominantly in the vertical direction. The *Active Dig Zone* is located above the teeth and bucket lip. This area develops as material starts to enter the bucket and increases in size after failure of the *Initial Laminar Layer*. In this zone, the *Virgin Material* fails and either flows into the bucket as part of the laminar layer during the first part of filling or moves into the *Active Flow Zone* during the latter part of filling. The *Dead Load* that has resulted from "live" material in the *Active Flow Zone* ramps up and over the *Initial Laminar Layer*. Some of the material in the *Initial Laminar Layer* fails and starts to form part of the *Dead Load*.

During the experiments two shear bands could be observed. The one extended from the tip of the tooth up to the free surface. This is known as the *Cutting Shear Band*. The second line is the one between the *Initial Laminar Layer* and the *Dead Load*, called the *Dead Load Shear Band*. The *Dead Load Shear Band* stretches from the tooth up to the free surface with an angle close to the material internal friction angle (measured relative to the bottom part of the bucket). This is indicated by the dotted line in figure 6.31.

To investigate the ability of DEM to predict the shear zone theory, Coetzee (2000) made use of the particle displacement ratio PDR. The bucket was moved through the material and "paused" after each 100 mm. The displacement vector of each particle was then set to be zero after which the bucket was given a further displacement of 10 mm - 15 mm. The particles were then coloured according to their PDR values which is defined as the ratio of the magnitude of the particle displacement vector to the bucket displacement vector. The same procedure has been used with the PICCUS results and are shown in figure 6.32 to figure 6.34 for displacements of 100 mm, 500 mm and 800 mm. All three methods (DEM, polar and nonpolar PICCUS) are capable of predicting the different flow zones, although the orientation

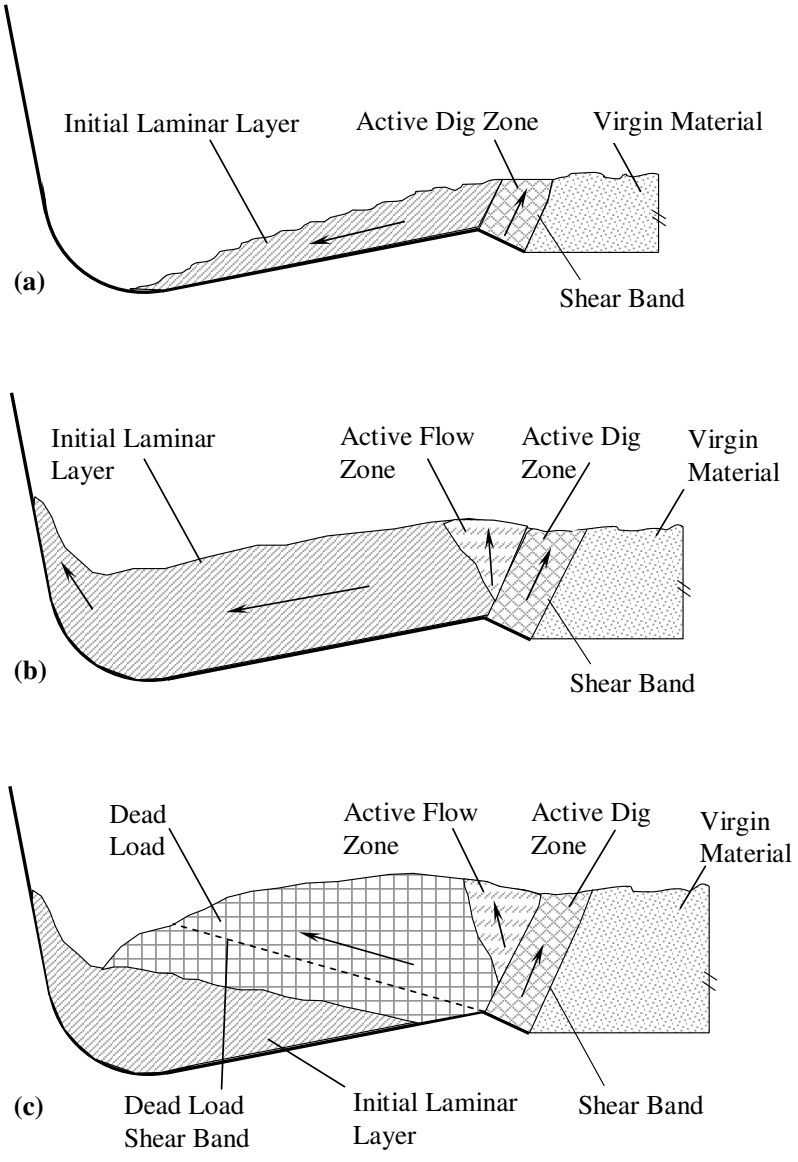

Figure 6.31: The Shear Zone Theory developed by Rowlands (1991)

of the shear bands between the zones differ slightly.

The prevention of excessive wear on buckets plays a very important role in bucket design. Special replaceable wear packages are designed and added to buckets. In order to minimise and predict bucket wear, the contact forces or pressures at the bucket-material interface should be known. From a DEM model all the particle-bucket contacts are known. The contact position, normal and tangential forces and the particle velocity are available at each contact and can be used to predict bucket wear. Thirty to forty years ago Finnie (1960, 1972) developed a simple model for predicting wear. The model essentially uses the kinetic energy of the incoming particle and knowledge about the impact angle to predict wear rates. Cleary (1998*b*) modelled bucket filling with DEM and made use of the Finnie model to predict the wear. Realistic wear patterns were obtained, but no experimental data was available for comparisons of the flow patterns, drag forces, wear patterns and wear rates.

Figure 6.35 and figure 6.36 show the normal and shear stress on the inside of the bucket. For the DEM models the contact normal and shear forces were used to calculate the stress, while for the PICCUS models the nodal forces were used. The maximum stresses occur on the tooth. The DEM predicted stresses are in general lower than the nonpolar predicted pressures and the polar predicted pressures lower than both the nonpolar and DEM predicted stress.

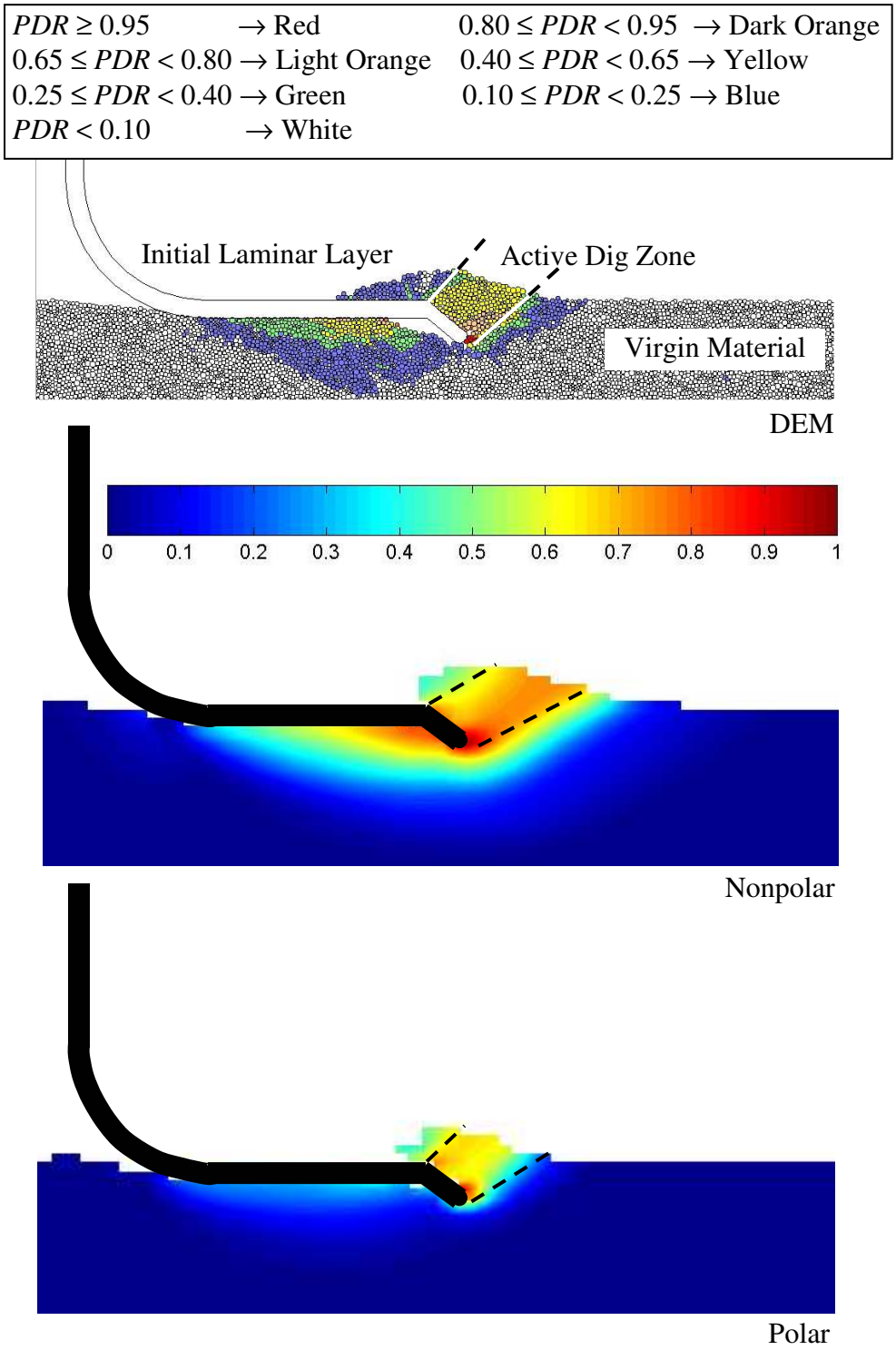

Figure 6.32: The Shear Zone Theory at a displacement of 100 mm

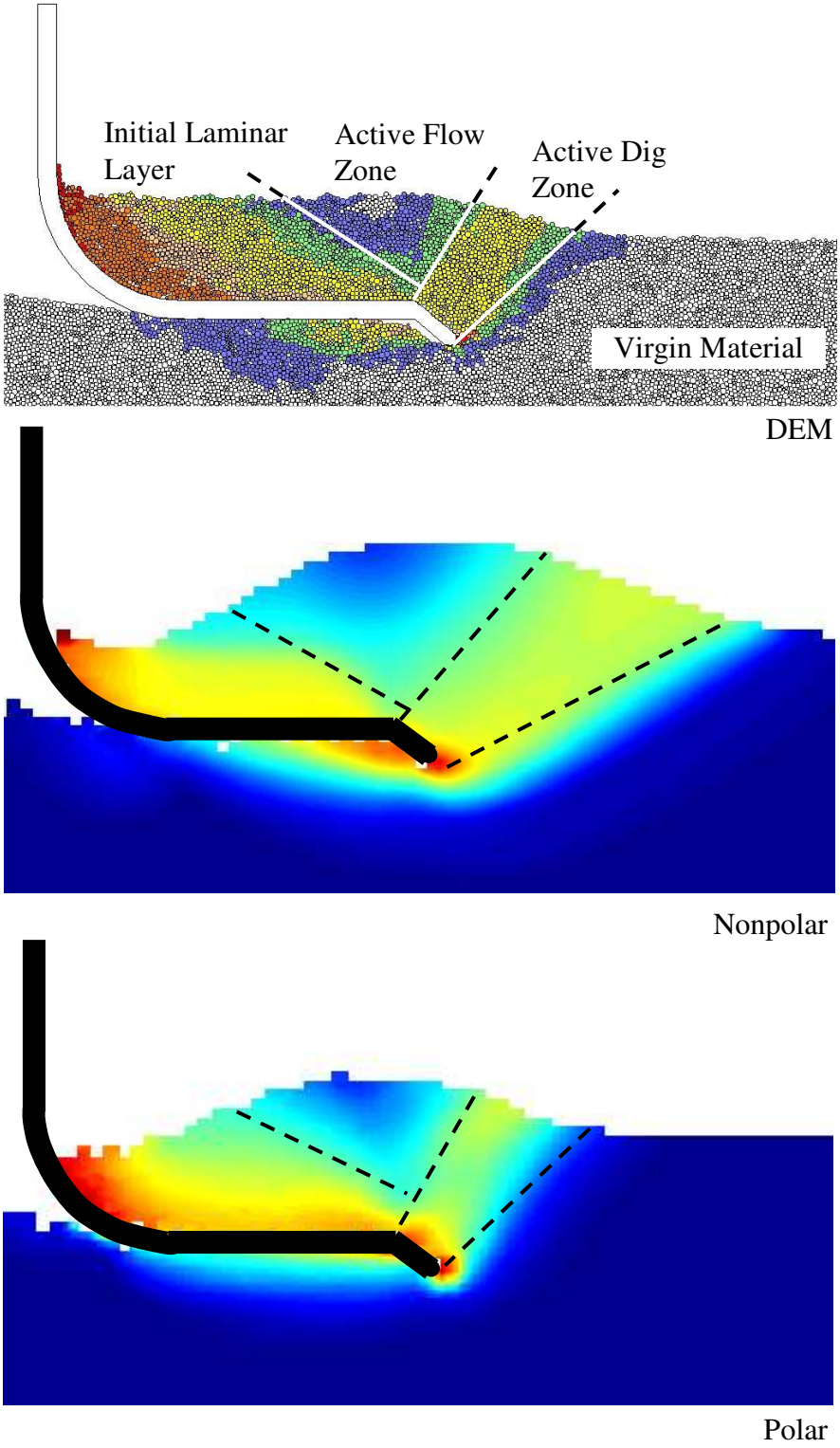

Figure 6.33: The Shear Zone Theory at a displacement of 500 mm

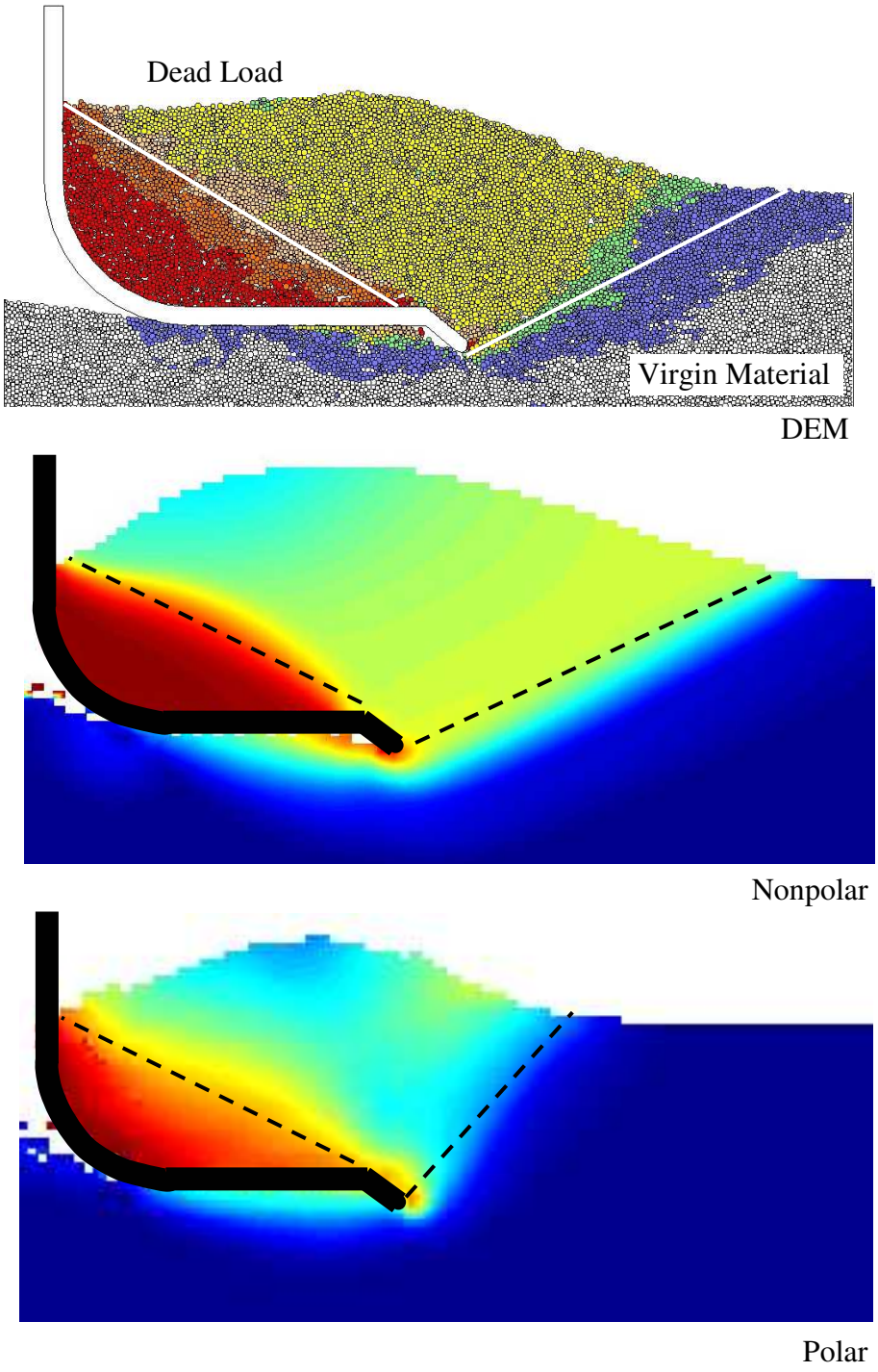

Figure 6.34: The Shear Zone Theory at a displacement of 800 mm

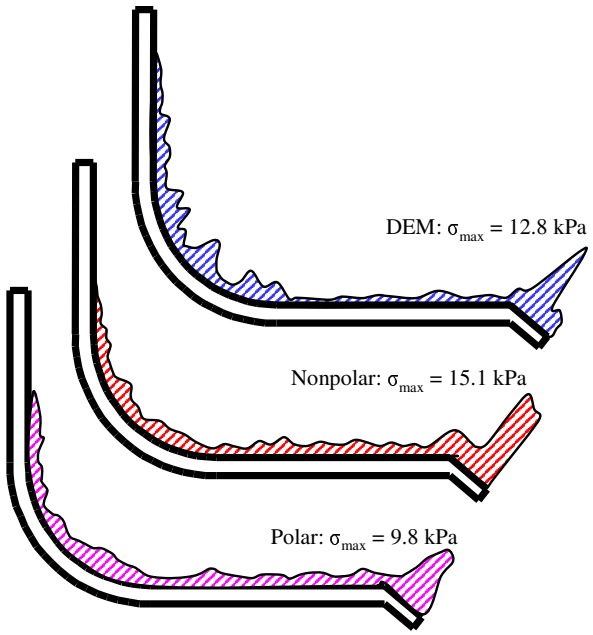

Figure 6.35: The normal stress on the inside of the bucket at a displacement of 800 mm

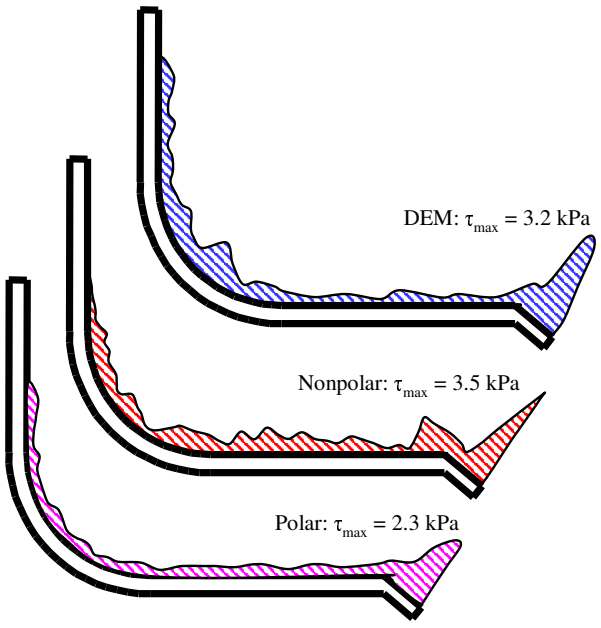

Figure 6.36: The shear stress on the inside of the bucket at a displacement of 800 mm

6.3 Silo Modelling

Roughly one-half of the products and about three-quarters of the raw materials of the chemical industry are in the form of granular material that are usually stored in silos or bunkers (Yang and Hsiau, 2001). Although the silo is widely used, definite theories for the flow of material in silos are not available (Yang and Hsiau, 2001).

Yang & Hsiau (2001) investigated silo discharge using experiments and DEM simulations. They, however, used a "perfect" material: a single column of equally sized glass beads. It is relatively easy to determine the particle micro parameters such as particle-particle friction and contact stiffness for such a material. The modelling of irregular shaped particles, such as sand or seed grains, is not addressed. They, however, obtained good results by comparing flow rates and flow patterns. Masson & Martinez (2000) used equally sized acrylic cylinders in experiments and compared the results to DEM simulations. Friction and contact stiffness proved to play a major role in the flow and the stress field during filling and discharging.

Rectangular planform silos have not been studied as often as circular silos, and relatively little detailed information exists on pressure patterns which develop on their walls (Brown *et al.*, 2000). Rectangular silos have advantages over circular silos when available space is limited and simplicity in construction is important. Brown *et al.* (2000) investigated the pressure on a model rectangular silo using a series of strain gauges and wall pressure sensors. Loading of the silo was achieved by filling a small hopper suspended above the silo. The hopper was then discharged into the silo through its base. Brown *et al.* (2000) state that it is known that filling a silo in such a matter can display anisotropy, but focused on repeatability rather than uniformity. After filling, the wall pressures also displayed asymmetry, which could only be attributed to the filling process.

Martinez *et al.* (2002) investigated silo discharge using FEM with remeshing. The authors conclude that the remeshing introduces additional costs and meshless methods can avoid this inconvenience. Karlsson *et al.* (1998) used FEM based on the Eulerian frame of reference. The major disadvantage of this approach is that all boundaries are fixed. The upper free surface in a silo requires refilling to be fixed, and as a result it is not possible to simulate the complete discharging process. However, the redistribution of stresses when the flow develops is very fast, and the upper surface does not move much during this time. Thus, the Eulerian approach could be used to simulate only the initial stress transients.

As part of this research, a model silo was build to investigate the flow of material out of a plane strain flat bottomed silo. The focus is mainly on flow patterns and flow rate. The flow pattern in a silo is of great importance when handling material that degenerates with time. Then it is important to achieve the first-in-first-out storage principle (Karlsson *et al.*, 1998). The

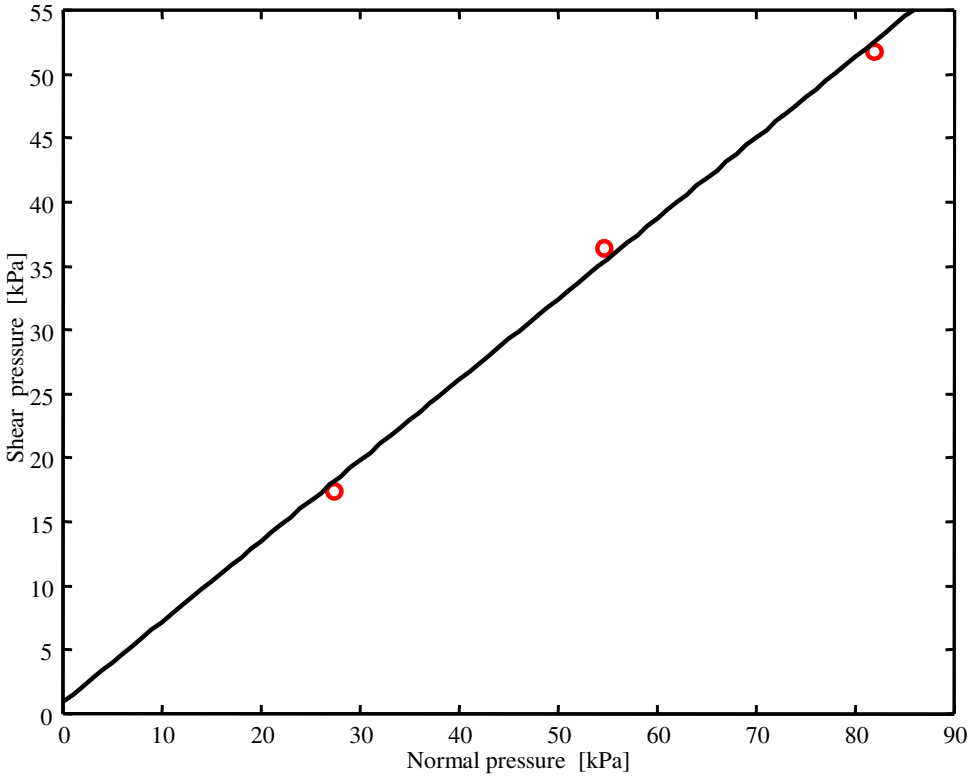

Figure 6.37: The sand shear test results

model silo used for the experiments had dimensions of 310 mm wide, a maximum fill height of 600 mm and a depth of 730 mm. All the sides were constructed of glass and the opening width could be varied. The door could be opened without affecting the initial flow and the depth to width ratio was high enough for the flow to be two-dimensional.

Two types of material were used: corn and sand. The corn was from the same batch as used by Coetzee (2000), so the macro properties were known for continuum modelling and the micro properties for DEM modelling. A dry graded silica sand was used with the following main constituents: $SiO_2 = 98\%$ and $Fe_2O_3 = 0.18\%$. A shear test (figure 6.37) and an oedometer test were used to determine the sand friction angle and elastic modulus respectively. The bottom half of the shear box was replaced by a glass panel to measure the friction between the sand and glass. Table 6.3 summarises the measured sand properties and the different values used in the material models. The Drucker-Prager constitutive model was used for modelling both the corn and the sand. The same commercial package (PFC^{2D}) used by Coetzee (2000) was used for the DEM simulations.

The sand grains had an average size of more or less 1 mm and from there the internal length $l = 1$ mm. Again the moment of inertia has been

Table 6.3: Sand material properties

Young's modulus	E	21.5 MPa
Poisson's ratio	ν	0.2
Density	ρ	1286 kg·m^{-3}
Friction angle	ϕ	32°
Cosserat friction parameter	$\alpha = \sin\phi$	0.53
Drucker-Prager friction parameter	q_ϕ	0.52
Dilatancy angle	ψ	2°, 5°
Cosserat dilatancy parameter	$\beta = \sin\psi$	0.035, 0.174
Drucker-Prager dilatancy parameter	β	0.040, 0.098
Cohesion	c	0.9 kPa
Tension cutoff	σ^t	0 Pa
Friction with glass	ϕ_s	18°
Constitutive coefficients	$a_1; a_2; a_3$	0.375;0.125;1
Cosserat shear modulus	$G^c = 2G$	17.9 MPa
Characteristic length	l	1 mm
Moment of inertia	$J_{33} = 0.5(0.5\,l)^2$	12.5×10^{-8}m^2

calculated by assuming a cylinder with a diameter equal to the internal length. The Drucker-Prager dilatancy and friction parameters were calculated using equation H.6.2. It is difficult to measure the bulk density in a flowing granular material and the assumption of constant density is made for the sake of simplicity and numerical efficiency. The silo was filled in the same way used by Brown *et al.* (2000). A hopper was suspended above the silo and its door (200 mm × 200 mm) opened until the silo was filled. The top surface was then carefully levelled. In the DEM model, the same procedure was used and in the PICCUS models the material was created layer-by-layer and allowed to reach an equilibrium state after each layer was added. Coloured grains were used to create layers within the material which are used to compare flow patterns. In the PICCUS models a symmetry plane was used and friction applied at the walls. No polar rotations were allowed at the walls which is the case for relatively smooth walls (Tejchman, 1997). The 40 × 50 rectangular mesh had elements of size 3.875 mm × 10 mm. Time steps of $\Delta t = 5 \times 10^{-5}$s and $\Delta t = 2 \times 10^{-5}$s were used for the modelling of corn and sand respectively. In the DEM models no

symmetry plane was used and as a result the flow patterns are not perfectly symmetric.

Figure 6.38 and figure 6.39 show the flow of corn out of the silo with the opening $w = 45\,\text{mm}$ and the initial fill height $h = 500\,\text{mm}$. The experimental, polar, nonpolar and DEM results are shown at increments of one second, up to eight seconds. Looking at the DEM results, there is good agreement with the experimental results with regard to flow patterns although the DEM discharge rate is higher. Qualitatively, the nonpolar flow patterns and flow rate compare well to the experiment. The polar continuum shows a higher flow rate and there is a definite difference in the flow patterns compared to the nonpolar continuum. To make a quantitative comparison of the flow patterns is difficult. The flow rate can, however, be compared quantitatively. The mass of the material within the silo was measured by hanging the silo from a load cell. The question however arises whether the measured mass of the material during discharge is a true representation of the flow rate. Close to the silo opening the free falling material will not contribute to the measured value although the material is still within the silo. The acceleration and deceleration of the material as it flows in the silo will also create dynamic effects. The flow rate is defined as the rate at which material flows through the silo opening measured in $\text{kg}\cdot\text{s}^{-1}$. The results of the DEM simulations were used to clarify this point. Figure 6.40 shows the two methods of calculating the mass of material within the silo. The first method is to simply add up the mass of all the particles above the silo opening at each time step. The second method is to add the resultant vertical force of all the walls at each time step. The second approach is similar to the experiments. From the figure it can be seen that the resultant vertical force on the silo walls show high fluctuations due to the collisions between the particles and the walls. The result from the first method is a very good fit to the result from the second method and it can be concluded that the measured values are a good representation of the material mass in the silo.

Figure 6.41 shows the corn mass within the silo as a function of time for two openings: $w = 45\,\text{mm}$ and $w = 80\,\text{mm}$. For both openings, DEM predicts a higher flow rate than the measured rates. With $w = 45\,\text{mm}$, the nonpolar continuum predicts a higher flow rate and with $w = 80\,\text{mm}$ a lower flow rate. The polar continuum predicts a higher flow rate for both openings and the results are in close agreement with the DEM results. Figure 6.42 shows the sand mass within the silo as a function of time with $w = 45\,\text{mm}$ and the initial fill height $h = 550\,\text{mm}$. Since the dilatancy angle could not be measured, two values $\psi = 2^\circ$ and 5° were used. As expected, with an increase in dilatancy angle there is a decrease in mass flow from the silo. The results with $\psi = 2^\circ$ are closer to the measured values and as in the case with corn, the polar continuum predicts a higher flow rate than the nonpolar continuum. The dilatancy angle for loose sand is only a few degrees according to (Vermeer and De Borst, 1984).

Figure 6.38: Corn flowing from a silo with $w = 45\,\text{mm}$

Figure 6.39: Corn flowing from a silo with $w = 45\,\text{mm}$ continues

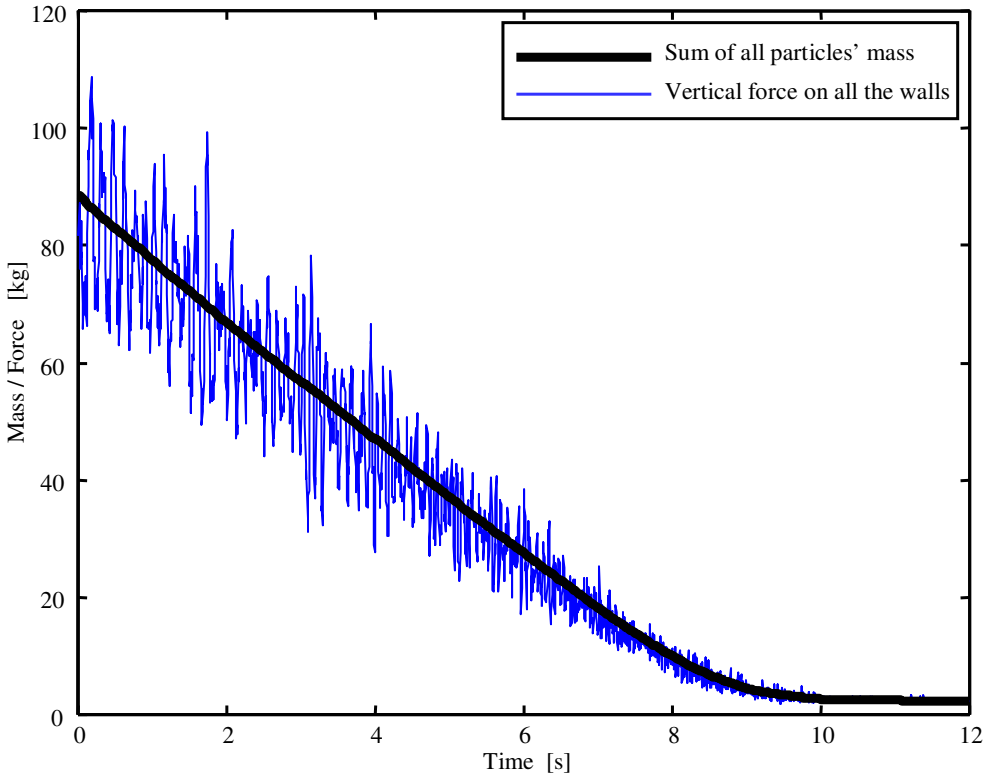

Figure 6.40: The two methods of calculating the mass flow out of the silo with DEM, $w = 45\,\text{mm}$

DEM simulations of sand were not performed since it would be impractical to model each individual particle. The computing power needed to model such a large number of particles was not available. If, however, it could be computed, a series of DEM numerical experiments first needs to be performed to determine the particle micro properties suitable for modelling the sand.

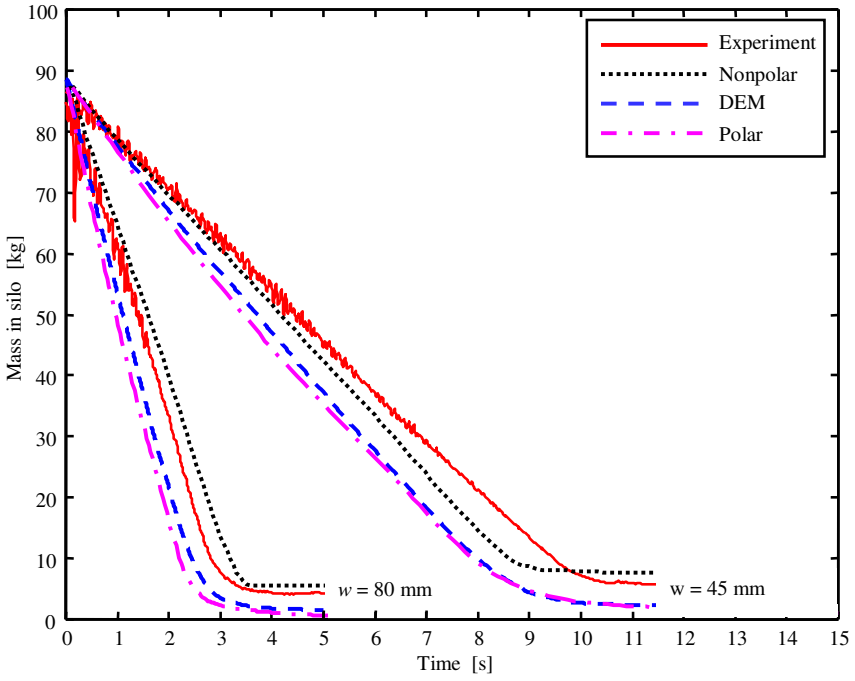

Figure 6.41: The flow rate of corn out of the silo

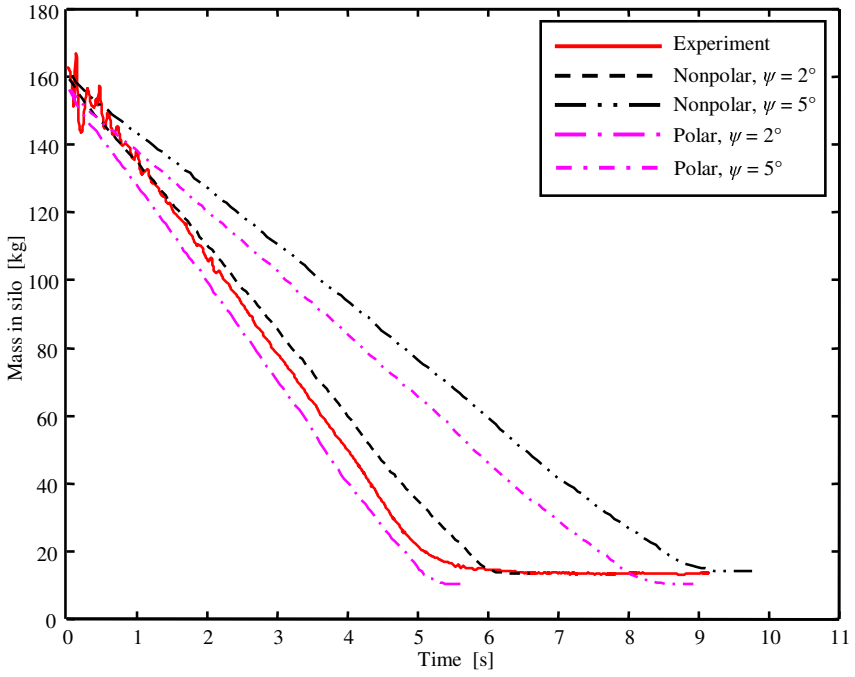

Figure 6.42: The flow rate of sand out of the silo with $w = 45\,\text{mm}$

6.4 Computing Times

DEM, nonpolar continuum and polar continuum simulations were used to model corn flowing from the silo. The run time to model the first 10 s of silo discharge is shown in table 6.4 for each simulation. The simulations were all run on a Pentium IV 2.4 GHz with 512 MB RAM. The DEM model had 5348 circular particles making up 2674 clumps. Four PICCUS models were used: a polar continuum with a symmetry plane and the full geometry, a nonpolar continuum with a symmetry plane and the full geometry. The full geometry (310 mm $\times$ 500 mm) was divided into $80 \times 50 = 4000$ elements and the geometry with the symmetry plane (155 mm $\times$ 500 mm) was divided into 40×50 elements. A time step of $\Delta t = 5 \times 10^{-5}$ was used in all the simulations including DEM. In table 6.5, a comparison of the run times is made. When a symmetry plane is used, the nonpolar and polar continuum methods are both quicker than the DEM simulation by 39% and 9.3% respectively. When the full geometry is modelled, the number of degrees-of-freedom is more or less doubled and the simulations slower by 134% and 266.5% compared to the DEM simulation respectively. The polar continuum is slower than the nonpolar continuum by more or less 50% which is expected because of the three degrees-of-freedom compared to the two degrees-of-freedom per node of the nonpolar continuum. In the DEM models, the physical size of the corn grains was used to model the particles. This lead to run times which are comparable to PICCUS run times. To model materials with relatively small particles such as sand, it would require a large number of particles, and more computing power if physical particle sizes are used. On the other hand, the continuum method with the same mesh size should still yield good results.

Table 6.4: Run time to model 10 s of silo discharge

Model	Run time	Number of particles	Initial DOF
DEM	2.92 h	5348	–
Nonpolar symmetry	1.78 h	8000	4011
Nonpolar full	6.83 h	16000	8022
Polar symmetry	2.65 h	8000	6102
Polar full	10.70 h	16000	11983

Table 6.5: Comparison of the run times of the different methods used

	DEM	Nonpolar symmetry	Nonpolar full	Polar symmetry	Polar full
DEM	–				
Nonpolar sym.	-39.0%	–			
Nonpolar full	134.0%	283.7%	–		
Polar sym.	-9.3%	48.9	-61.2%	–	
Polar full	266.5%	501.1%	56.7%	303.8%	–

Chapter 7

Concluding Remarks and Recommendations

A Particle-in-Cell code (PICCUS) was developed to model polar (Cosserat) and nonpolar (classic) continua subjected to large deformations and displacements under plane strain conditions. The no-slip contact which is a natural consequence of the PIC method has been relaxed by the implementation of a contact algorithm. The algorithm is based on the Coulomb friction theory and is applied at the boundary nodes of two bodies in contact. Three nonpolar continuum constitutive models have been implemented: elastic, Drucker-Prager and Mohr-Coulomb models. The Ducker-Prager model reduces to the von Mises model and the Mohr-Coulomb model to the Tresca model if the material friction angle is set to zero. Two polar continuum constitutive models have been implemented: elastic and a Drucker-Prager type of model. A rigid body model has also been implemented for the modelling of anchors, strip footings, blades and buckets. No strain softening or hardening has been used although it has been implemented as part of the nonpolar Mohr-Coulomb model and the polar Drucker-Prager model.

Various simulations were performed to validate the implementation of the nonpolar continuum. The simulation of an elastic steel disk impacting on an elasto-plastic aluminium target was compared to published data of a similar simulation and experimental data. A comparison of the penetration depth as a function of time showed good agreement and the final depth compared well to experimental values. This demonstrates the ability of PIC to model large displacements, deformations and the no-slip contact between two different bodies.

The simulation of an elastic disk rolling down an elastic inclined surface was used to validate the contact model. The centre position of the disk, as a function of time, was compared to analytical results. Different friction coefficients, incline angles and mesh sizes were used. The results show that an accuracy of 0.5% can be achieved, although the analytical model assumes a rigid disk and surface.

The impact of two elastic bodies was modelled to show the conservation of momentum and energy. The results show that the linear momentum and the total energy are generally conserved although small gains/dissipations could be observed with an increase in time step size.

The modelling of an oedometer test was used to validate the implementation of the Mohr-Coulomb constitutive model and the ability to model plastic flow where the stress point evolves along a shear-shear edge of the

Mohr-Coulomb criterion in the principal stress space.

The method of characteristics was proposed by Sokolovski to model the passive case of a static retaining wall. This theory can also be used to model the initial stages of a flat blade pushing against a "wall" of material. From this theory, the normal and shear forces acting on the blade as well as the shear band can be determined. Simulations were performed with a blade at different depths h, and the forces and shear bands were compared to results from Sokolovski's method. The results showed that the yield points are a good indicator of the shear band and that the forces acting on the blade converge with mesh refinement.

The different problems analysed, indicate that PIC can be used to model applications where the displacements are relatively small (strip footings and anchor pull-out tests) and where large deformations occur (silo discharging). No special contact elements are needed to model frictional contacts (blade and bucket modelling).

The analysis of a strip footing on an elastic mass was investigated. Assuming an elastic mass, an analytical solution to this problem is available and the stresses in the material could be compared to the analytical solution. The results indicated that the stresses in the material can be accurately predicted. A more realistic analysis of two strip footing problems was also done. In this case, an elasto-plastic material was used to model clay. A bearing capacity and a strip footing close to a vertical cut were analysed. Published data from field tests under plane strain conditions was used for comparisons. Triaxial tests on the clay were previously performed and the published data could be used to determine the clay material properties. The FEM code PLAXIS was also used for comparisons with good results.

Anchors form an important component of civil engineering projects. They are typically used to support structures such as towers, bridges and roofs. An anchor pulled in the vertical direction and one pulled at 45° were modelled. Published experimental data from anchor pull-out tests were used for comparisons. The results show that the limit load on the anchors could be accurately predicted to within 5% of the measured values.

Draglines excavators are used to remove blasted overburden from open cast mines to expose the coal deposits beneath for mining. Draglines are an expensive and essential part of mine operations. DEM simulations of bucket filling have been done in the past, but not bucket filling with a continuum method. The results obtained here shows that bucket filling can be modelled with both a nonpolar and a polar continuum. The nonpolar continuum predicted draft forces more accurately, but the polar continuum modelled the flow patterns of material into the bucket more accurately. It was demonstrated that the normal and shear stresses on the bucket can be predicted. The highest pressures, as expected, acted on the tooth. It should be possible to use these pressures to predict the bucket wear.

The modelling of a flat blade was used to investigate the forces acting

on the blade and the thickness and orientation of shear bands in the material. DEM simulations could accurately predict the shape of the shear bands. The nonpolar continuum could accurately predict the shape and position of the shear bands. Yield points were found to be concentrated in the shear regions. The shear strain also proved to be a good indicator of shear bands. It is known that in a granular material, rotation of the grains occurs in the shear regions. The Cosserat rotations could be used to visualise the shear bands. The position of these shear bands, however, was not accurate compared to experimental observations. Both the polar and nonpolar continuum predicted the thickness of the shear bands as 6 - 8 particle diameters. The polar continuum showed to be less dependent on the mesh size than the nonpolar continuum. It has been reported that the orientation of the shear bands is dependent on the orientation of a FEM mesh. The PIC simulations, however, showed that the mesh orientation had little effect on the results. The effect of the Cosserat parameters a_1, a_2 and a_3 on the blade and bucket forces and the flow patterns needs further investigation. The problem, however, is to easily obtain these parameters for a given granular material. One way would be to get a sample of the material and perform biaxial or triaxial compression tests. These tests should than be numerically repeated and the parameters changed until good results are achieved in terms of shear planes and the force-displacement response.

The normal and shear stress distributions on the blade and bucket can be predicted. These stresses can be used to predict the tool wear if a relation between the stress and the wear rates can be found.

Published data on PIC modelling of silo discharging was used to validate the implementation of the code to model large deformations. The flow patterns and the material flow rate were compared with good results. A model silo was built to compare the results from PICCUS simulations with experiments. The silo had vertical walls and a flat bottom with glass panels and the width to depth ratio such that the flow was two-dimensional (plane strain). DEM, polar and nonpolar continuum simulations were performed and the flow patterns and flow rates compared. Sand and corn were used. The polar and nonpolar continuum showed different flow patterns. The nonpolar continuum predicted lower and higher flow rates (depending on the silo opening) compared to the measured flow rate. The polar continuum and DEM, predicted flow rates lower than the measured rate. The polar continuum and DEM flow rates compared well. It was also shown that the dilatancy angle has an influence on the flow rate. There is a 33% decrease in sand flow rate with an increase in dilatancy angle from $\psi = 2^\circ$ to $\psi = 5^\circ$.

The computing time to model silo discharge with DEM, a nonpolar continuum and a polar continuum was compared. First a symmetry plane was used in the continuum methods, i.e., only half the silo was modelled while the full geometry was modelled in DEM. The nonpolar continuum

simulations ran 39.0% quicker and the polar continuum simulation 9.3% quicker than the DEM simulation. The full geometry was then also modelled with the continuum methods. The number of degrees-of-freedom doubled and it was found that the nonpolar continuum simulation was 2.3 times slower than the DEM simulation and the polar continuum simulation 3.7 times. The polar continuum is in general 50% slower than the nonpolar continuum. It should, however, be noted that a relatively small number of particles was used in the DEM model. If a material such as sand would be modelled, a large number of particles is required and computing times would be orders higher. DEM also has the disadvantage that numerical experiments have to be conducted to determine all the micro properties of the material. This is not needed for continuum methods as the material properties follows directly from experiments.

Granular flow can only be modelled as a continuum as long as the material behaves like a continuum. If the material consists of a few big rocks, the behaviour would be more discrete than continuous and better modelled by DEM. There is no clearly defined boundary and more research is needed to determine when a material can be modelled as a continuum or not.

Good results were obtained without the use of strain softening or strain hardening. Further research is needed to determine the effect of strain softening and strain hardening on applications such as bucket filling. Loss of ellipticity of the governing equations when nonpolar softening is used, leads to mesh size and mesh alignment dependence. Thus, when strain softening is used, a polar continuum should be used to overcome this problem.

No problems are expected in extending the code to model three dimensional and axisymmetric problems. The three-dimensional Cosserat continuum has already been used by other researchers to model bone structures. The general feeling is that if a two-dimensional continuum method is extended to three dimensions, the penalty paid in computing times would be less then when a two-dimensional DEM code is extended to three dimensions. This, however, needs to be investigated.

Except for the modelling of the strip footing on clay, mainly cohesionless materials were analysed. A further extension of this research would be to include material cohesion and adhesion between the blade/bucket and soil.

It can be concluded that a continuum method can be used to accurately model the filling of an excavator/dragline bucket. This technology can now be applied to industrial applications: Buckets can be optimised in terms of fill rates (time needed to fill a bucket), energy consumption and wear.

Appendix A

Notation and Basic Principles

A.1 Introduction

Matrix tensor (vector) notation and index notation are described. Matrix tensor notation proposed by Hassenpflug (1993) is used. All vectors are in 3-dimensional Euclidean space ($\mathbb{R}^3$). The description of the notation used is important for understanding and following the mathematical derivations and formulations in the following appendices.

A.2 Index Notation

Index notation is frequently used to formulate the basic principles and expressions in continuum mechanics (Frederick and Chang, 1972).

A.2.1 Index Notation of a Vector

Introduce the well-known unit vectors $\overrightarrow{e_1}$, $\overrightarrow{e_2}$ and $\overrightarrow{e_3}$ referred to the rectangular Cartesian axes shown in Figure A.1.

Using the classical vector notation, any vector such as $\overrightarrow{A}$ situated at any

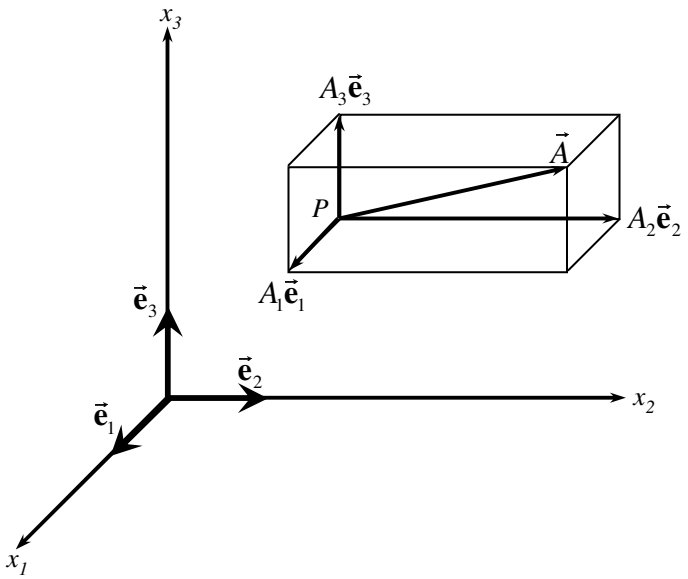

Figure A.1: Representation of vector $\overrightarrow{A}$

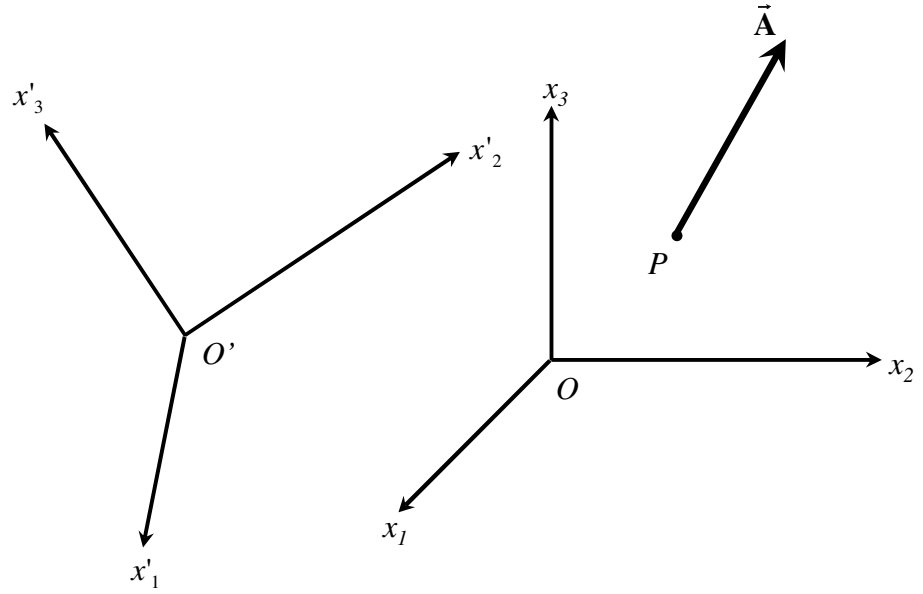

Figure A.2: Representation of a vector in two sets of right-handed Cartesian axes with different orientation

arbitrary point P in space can be written as

$$\overrightarrow{A} = A_1 \overrightarrow{e_1} + A_2 \overrightarrow{e_2} + A_3 \overrightarrow{e_3} \tag{A.2.1}$$

where (A_1, A_2, A_3) are the rectangular projections of the vector $\overrightarrow{A}$ in the (x_1, x_2, x_3)-directions, respectively. The Cartesian components (A_1, A_2, A_3) may be represented by the symbol A_i where i = 1,2,3. The subscript i is understood to take on the values (1,2,3) in that order. Therefore, the symbol A_i represents the set of three Cartesian components (A_1, A_2, A_3) in the same order. In index notation, A_i is the symbol used to designate the vector $\overrightarrow{A}$ in ordinary three-dimensional space. It should be noted that when referred to another coordinate system, the components of a vector will change, but the vector will remain invariant. It has the same magnitude and direction in space regardless of the coordinate system to which it is referred.

A.2.2 Transformation Law of a Vector

From the discussion in the previous section, it is obvious that the vector $\overrightarrow{A}$ can be expressed in the index notation referred to any arbitrary set of right-handed Cartesian axes. In figure A.2, the vector $\overrightarrow{A}$ is drawn from an arbitrary point P in space and will be referred to a set of unprimed right-handed Cartesian axes with origin at O, and to a set of primed right-handed Cartesian axes with origin at O'. Both sets of axes may be translated without rotation to the common origin at P without loss of generality in the

following discussion. Projecting $\overrightarrow{A}$ onto the unprimed axes gives the Cartesian components A_i, and onto the primed axes A_i'. It is now desirable to understand how the primed components A_i' are related to the unprimed components A_i, and vice versa.

Introduce the direction cosines between the two sets of axes as follows:
(a_{11}, a_{12}, a_{13}) = direction cosines of the x_1'-axis with respect to the (x_1, x_2, x_3)-axes
(a_{21}, a_{22}, a_{23}) = direction cosines of the x_2'-axis with respect to the (x_1, x_2, x_3)-axes
(a_{31},a_{32}, a_{33}) = direction cosines of the x_3'-axis with respect to the (x_1, x_2, x_3)-axes

It is now easy to relate the two sets of Cartesian components. Recall from analytical geometry and vector analysis that the projection of the vector $\overrightarrow{A}$ onto the x_1'-axis is equal to the sum of the projections of the A_i components on the same axis

$$A_1' = a_{11}A_1 + a_{12}A_2 + a_{13}A_3$$

similarly for the other components

$$A_2' = a_{21}A_1 + a_{22}A_2 + a_{23}A_3 \tag{A.2.2}$$

$$A_3' = a_{31}A_1 + a_{32}A_2 + a_{33}A_3$$

Interchanging the role of the primed and unprimed axes, it follows

$$A_1 = a_{11}A_1' + a_{21}A_2' + a_{31}A_3'$$

$$A_2 = a_{12}A_1' + a_{22}A_2' + a_{32}A_3' \tag{A.2.3}$$

$$A_3 = a_{13}A_1' + a_{23}A_2' + a_{33}A_3'$$

Equations A.2.2 and A.2.3 are the transformation laws for the Cartesian components of a vector. Any set of three Cartesian components satisfying these transformation laws is called a vector in ordinary three-dimensional space.

A.2.3 Rules of the Index Notation and Transformation Laws

Having introduced numerical subscripts to denote various axes and components of vectors, it is important now to introduce a "shorthand" notation for writing the terms and equations in which they appear. These rules, which are valid for tensors of all orders, are the *range convention* and *summation convention*.

Range Convention

Whenever a small Latin letter subscript occurs unrepeated in a term, it is understood to take on the values of 1,2,3 (unless stated otherwise), the number of dimensions of the physical space. It is possible to define the order of a tensor as the number of range indices appearing with the base letter. As examples,

$$\begin{aligned} A &= \text{tensor of zero order (scalar)} \\ A_i &= \text{tensor of the first order (vector)} \\ A_{ij} &= \text{tensor of second order (matrix)} \\ A_{ijk} &= \text{tensor of the third order} \end{aligned}$$

and so on. In three-dimensional space, a tensor of order N has 3^N components.

Summation Convention

The second important rule is the summation convention. Whenever a small Latin letter subscript occurs repeated in a term, it is understood to represent a summation over the range of 1,2,3 (unless stated otherwise). Capital Latin letter suffixes will be used to indicate a particular numerical value. They do not imply range or summation.

Utilising the range rule, the transformation law for a vector equation A.2.2 can be written as

$$A'_i = a_{i1}A_1 + a_{i2}A_2 + a_{i3}A_3 \tag{A.2.4}$$

Note that i occurs in every term. It is a general rule that all equations are homogeneous in all range indices, for otherwise the equations become meaningless. Observe that "1" occurs twice in the first term, "2" twice in the second term, and "3" twice in the third. This is a convenient spot to introduce the use of the summation index. Any small Latin letter other than i can be used, for using i would give a term with the same index appearing three times, which has no meaning. Thus, in its most compact form, equation A.2.4 would be

$$A'_i = a_{ij}A_j \tag{A.2.5}$$

In similar manner, the inverse laws, equation A.2.3, might be written as

$$A_r = a_{sr}A'_s \tag{A.2.6}$$

To illustrate some common manipulations in index notation, derive the orthogonal conditions that the "transformation matrix" a_{ij} must satisfy. First, introduce the *Kronecker delta*, δ_{ij}, defined as follows

$$\delta_{ij} = \begin{cases} 1 & \text{if } i = j, \\ 0 & \text{if } i \neq j \end{cases} \tag{A.2.7}$$

Then A_i can be written in terms of the Kronecker delta as

$$A_i = \delta_{ij} A_j \tag{A.2.8}$$

Now, transforming the left-hand side of equation A.2.8 by using equation A.2.6, it follows that

$$a_{si} A'_s = \delta_{ij} A_j \tag{A.2.9}$$

and transforming A'_s by using equation A.2.5, the preceding equation becomes

$$\begin{aligned} a_{si} a_{sj} A_j &= \delta_{ij} A_j \\ \therefore \left(a_{si} a_{sj} - \delta_{ij} \right) A_j &= 0 \end{aligned} \tag{A.2.10}$$

Since A_j are the components of an arbitrary vector, and the terms in the brackets are independent of A_j, it follows that

$$a_{si} a_{sj} = \delta_{ij} \tag{A.2.11}$$

In a similar manner, it can be shown that

$$a_{is} a_{js} = \delta_{ij} \tag{A.2.12}$$

Equations A.2.11 and A.2.12 are the well-known orthonormal conditions that the direction cosines between two sets of Cartesian axes must satisfy. It is now appropriate to set down the transformation law for a Cartesian tensor of order N. First of all, note that a tensor of order zero (scalar) is invariant under coordinate transformation, or

$$A = A' \tag{A.2.13}$$

and that a tensor of order 1 (vector) transforms as follows

$$A'_r = a_{ri} A_i \tag{A.2.14}$$

A Cartesian tensor of order N transforms according to the law

$$A_{rst\ldots} = a_{ri} a_{sj} a_{tk\ldots} A_{ijk\ldots} \tag{A.2.15}$$

Therefore, the transformation law of a tensor of order 2 is

$$A'_{rs} = a_{ri} a_{sj} A_{ij} \tag{A.2.16}$$

A.2.4 Addition and Subtraction of Vectors and Cartesian Tensors

The addition and subtraction of two Cartesian tensors of the same order is defined in index notation as follows

$$A_{ij\ldots} \pm B_{ij\ldots} = C_{ij\ldots} \tag{A.2.17}$$

where $A_{ij\ldots}$ and $B_{ij\ldots}$ are two Cartesian tensors of the same order and $C_{ij\ldots}$ is a Cartesian tensor that results from the addition or subtraction and is of the same order as $A_{ij\ldots}$and $B_{ij\ldots}$.

Equation A.2.17 implies that the addition or subtraction is to be carried out for each pair of corresponding elements of the Cartesian tensors $A_{ij\ldots}$ and $B_{ij\ldots}$.

A.2.5 Scalar or Dot Product

The scalar product of two vectors $\overrightarrow{A}$ and $\overrightarrow{B}$ denoted by $\overrightarrow{A} \bullet \overrightarrow{B}$ is a scalar defined as

$$\overrightarrow{A} \bullet \overrightarrow{B} = AB\cos\theta \tag{A.2.18}$$

where θ is the angle between the two vectors $\overrightarrow{A}$ and $\overrightarrow{B}$. From elementary vector analysis, it is well known that the scalar product of two vectors $\overrightarrow{A}$ and $\overrightarrow{B}$ can be expressed as the sum of the products of the corresponding Cartesian components of the vectors. Thus

$$\overrightarrow{A} \bullet \overrightarrow{B} = A_1B_1 + A_2B_2 + A_3B_3 \tag{A.2.19}$$

Using the index notation, equation A.2.19 becomes

$$\overrightarrow{A} \bullet \overrightarrow{B} = A_iB_i \tag{A.2.20}$$

A.2.6 Vector or Cross Product

The vector product of the two vectors $\overrightarrow{A}$ and $\overrightarrow{B}$, denoted by $\overrightarrow{A} \times \overrightarrow{B}$ is a vector $\overrightarrow{C}$, which is normal to both $\overrightarrow{A}$ and $\overrightarrow{B}$ such that $\overrightarrow{A}$, $\overrightarrow{B}$ and $\overrightarrow{C}$ form a right-handed system. The magnitude of $\overrightarrow{C}$ is given by

$$C = AB\sin\theta \tag{A.2.21}$$

where θ is the smaller of the two angles between the vectors $\overrightarrow{A}$ and $\overrightarrow{B}$. Form elementary vector analysis, it is also known that the vector product

$\overrightarrow{C}$ of two vectors $\overrightarrow{A}$ and $\overrightarrow{B}$ can be represented by three Cartesian components, which are in turn related to the Cartesian components of $\overrightarrow{A}$ and $\overrightarrow{B}$. These relations are

$$\begin{aligned} C_1 &= A_2B_3 - A_3B_2 \\ C_2 &= A_3B_1 - A_1B_3 \\ C_3 &= A_1B_2 - A_2B_1 \end{aligned} \tag{A.2.22}$$

In order to express equation A.2.22 in index notation, it is necessary to introduce a *permutation symbol* ε_{ijk}. The components of the permutation symbol are defined to have the following constant values

$$\varepsilon_{ijk} = \begin{cases} 0 & \text{if the values of } i,j,k \text{ do not form a permutation of 1,2,3,} \\ +1 & \text{if the values of } i,j,k \text{ form an even permutation of 1,2,3,} \\ -1 & \text{if the values of } i,j,k \text{ form an odd permutation of 1,2,3,} \end{cases} \tag{A.2.23}$$

With the permutation symbol, equation A.2.22 can be represented by the following indicial equation

$$C_i = \varepsilon_{ijk}A_jB_k \tag{A.2.24}$$

A.2.7 Multiplication of Cartesian Tensors

The scalar and vector products of two vectors are but two very special cases of multiplication of Cartesian tensors. In general, all multiplications of Cartesian tensors can be classified into two types. These are defined below.

Outer Product

An outer product of two Cartesian tensors is a Cartesian tensor obtained by placing the two original tensors side by side, with no summation indices involving the suffixes from both tensors. An example of this is the outer product of two second-ordered tensors A_{ij} and B_{ij}. The result is a Cartesian tensor of the fourth order $A_{ij}B_{rs}$.

Inner Product

First, define *contraction* as the process of identifying any two indices of a tensor. An inner product of any two tensors is an outer product followed by a contraction involving indices from both tensors. As an example, the inner products of the tensors A_i and B_{ij} are

$$A_iB_{ij} \text{ and } A_iB_{ji} \tag{A.2.25}$$

A.3 Matrix Tensor Notation

Matrix tensor notation can effectively be used to formulate kinematic and dynamic principles of rigid body motion.

A.3.1 Vector

A column vector is indicated by an overbar.

$$\overline{v} = \begin{bmatrix} v_1 \\ v_2 \\ v_3 \end{bmatrix} \tag{A.3.1}$$

A row vector is indicated by an underbar.

$$\underline{v} = \begin{bmatrix} v_1 & v_2 & v_3 \end{bmatrix} \tag{A.3.2}$$

The transpose changes the row column character of a vector and therefore the transpose vector has a transposed vector bar symbol.

$$\overline{v}^T = \underline{v} \tag{A.3.3}$$

$$\underline{v}^T = \overline{v} \tag{A.3.4}$$

A.3.2 Matrix

Matrices are indicated by an underbar as well as an overbar.

$$\overline{\underline{M}} = \begin{bmatrix} m_{11} & m_{12} & m_{13} \\ m_{21} & m_{22} & m_{23} \\ m_{31} & m_{32} & m_{33} \end{bmatrix} \tag{A.3.5}$$

A.3.3 Multiplication Rules

Vector bars cancel diagonally across the multiplication sign and the remaining vector bar symbols on both sides of the equation must be equal after calculation.

$$\overline{\underline{A}} \cdot \overline{v} = \overline{r} \tag{A.3.6}$$

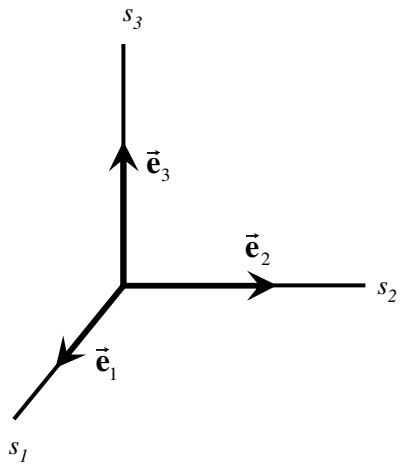

Figure A.3: Coordinate axis and base vectors

A.3.4 Scalar Product

The scalar or dot product of two vectors is a scalar.

$$\begin{aligned} \overline{a} \bullet \overline{c} &= \underline{a}\, \overline{c} \\ &= |\overline{a}||\overline{c}| \cos\theta \\ &= a_1 c_1 + a_2 c_2 + a_3 c_3 \end{aligned} \tag{A.3.7}$$

It can be seen that the scalar product of two column vectors may be obtained by multiplying the one vector with the transpose of the other vector.

A.3.5 Norm

The norm of a vector is the magnitude or length of the vector.

$$|\overline{v}| = v = \sqrt{\overline{v} \bullet \overline{v}} = \sqrt{v_1^2 + v_2^2 + v_3^2} \tag{A.3.8}$$

A.3.6 Physical Vectors

Physical vectors are indicated by an arrow above the vector name, $\overrightarrow{v}$. Figure A.3 shows three orthogonal coordinates axes s_1, s_2, s_3 and three unit vectors $\overrightarrow{e_1}$, $\overrightarrow{e_2}$ and $\overrightarrow{e_3}$. Any physical vector in 3D Euclidean space can be described as

$$\overrightarrow{v} = \overrightarrow{e_1} v_1 + \overrightarrow{e_2} v_2 + \overrightarrow{e_3} v_3 \tag{A.3.9}$$

The unit vectors have the physical dimensions of direction only and a numerical size of one. These vectors form a base of $(\mathbb{R}^3)$.

A.3.7 Base

The base vectors have a very important physical meaning and are defined as a single quantity. The row vector of the orthogonal base vectors is defined as

$$\overrightarrow{\underline{E}} = \begin{bmatrix} \overrightarrow{e_1} & \overrightarrow{e_2} & \overrightarrow{e_3} \end{bmatrix} \tag{A.3.10}$$

With this relation, one can write equation A.3.9 as

$$\overrightarrow{v} = \overrightarrow{\underline{E}}\ \overline{v} \tag{A.3.11}$$

We distinguish a base of a coordinate system by adding the name to the underbar of the base. We define the base of coordinate system s as $\overrightarrow{\underline{E}}_s = \begin{bmatrix} \overrightarrow{e_{s1}} & \overrightarrow{e_{s2}} & \overrightarrow{e_{s3}} \end{bmatrix}$.

The components of a vector measured in a base are subscripted similarly to the direction vectors. The base name is added to the vector bar.

$$\overline{v}^s = \begin{bmatrix} v_{s1} \\ v_{s2} \\ v_{s3} \end{bmatrix} \tag{A.3.12}$$

Using this relation, one can describe a physical vector in base $\overrightarrow{\underline{E}}_s$ with the equation:

$$\begin{aligned} \overrightarrow{v} &= \overrightarrow{e_{s1}} v_{s1} + \overrightarrow{e_{s2}} v_{s2} + \overrightarrow{e_{s3}} v_{s3} \\ &= \begin{bmatrix} \overrightarrow{e_{s1}} & \overrightarrow{e_{s2}} & \overrightarrow{e_{s3}} \end{bmatrix} \begin{bmatrix} v_{s1} \\ v_{s2} \\ v_{s3} \end{bmatrix} \\ &= \overrightarrow{\underline{E}}_s\ \overline{v}^s \end{aligned} \tag{A.3.13}$$

The base is an orthogonal matrix because its columns $\overrightarrow{e_1}$, $\overrightarrow{e_2}$ and $\overrightarrow{e_3}$ form an orthogonal set. The inverse of the base is equal to its transpose.

$$\left[\overrightarrow{\underline{E}}\right]^{-1} = \left[\overrightarrow{\underline{E}}\right]^T = \overrightarrow{\underline{E}} \tag{A.3.14}$$

With this relation the following outer product can be written

$$\left[\overrightarrow{\underline{E}}\right]^{-1}\ \overrightarrow{\underline{E}} = \overrightarrow{\underline{E}}\ \overrightarrow{\underline{E}} = \overline{\underline{E}} = \overline{\underline{I}} \tag{A.3.15}$$

with $\overline{\underline{I}}$ the (3×3) identity matrix.

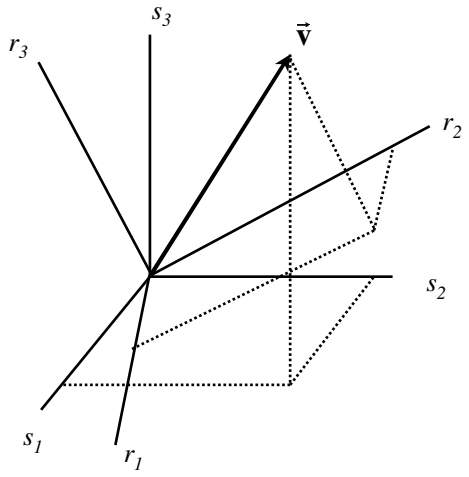

Figure A.4: Representation of a vector in two sets of right-handed Cartesian axes with different orientation

A.3.8 Transformations

From the discussion of bases, it is obvious that a physical vector $\overrightarrow{v}$ can be expressed with respect to any set of Cartesian coordinate systems. Consider two Cartesian coordinate systems s and r as shown in figure A.4.

The base of coordinate systems is defined by

$$\underline{\overrightarrow{E}}_s = \begin{bmatrix} \overrightarrow{e}_{s1} & \overrightarrow{e}_{s2} & \overrightarrow{e}_{s3} \end{bmatrix} \tag{A.3.16}$$

$$\underline{\overrightarrow{E}}_r = \begin{bmatrix} \overrightarrow{e}_{r1} & \overrightarrow{e}_{r2} & \overrightarrow{e}_{r3} \end{bmatrix} \tag{A.3.17}$$

The direction vectors of base r can be described in base s by applying equation A.3.13 and equation A.3.14 to each of the base vectors of base r.

$$\begin{aligned} \begin{bmatrix} \overline{e}^s_{r1} & \overline{e}^s_{r2} & \overline{e}^s_{r3} \end{bmatrix} &= \left[\underline{\overrightarrow{E}}^s \overrightarrow{e}_{r1} \quad \underline{\overrightarrow{E}}^s \overrightarrow{e}_{r2} \quad \underline{\overrightarrow{E}}^s \overrightarrow{e}_{r3} \right] \\ &= \underline{\overrightarrow{E}}^s \begin{bmatrix} \overrightarrow{e}_{r1} & \overrightarrow{e}_{r2} & \overrightarrow{e}_{r3} \end{bmatrix} \\ &= \underline{\overrightarrow{E}}^s \underline{\overrightarrow{E}}_r \\ &= \underline{\overline{E}}^s_r \end{aligned} \tag{A.3.18}$$

The quantity $\underline{\overline{E}}^s_r$ is called the transformation matrix between the two sets of coordinate axis s and r and it is defined as:

$$\underline{\overline{E}}^s_r = \begin{bmatrix} \overline{e}^s_{r1} & \overline{e}^s_{r2} & \overline{e}^s_{r3} \end{bmatrix} \tag{A.3.19}$$

This is also an orthogonal matrix and the following relations can be stated:

$$\begin{aligned} \overline{\underline{E}}_r^s &= \left[\overline{\underline{E}}_s^r\right]^T \\ &= \left[\overline{\underline{E}}_s^r\right]^{-1} \end{aligned} \tag{A.3.20}$$

The physical vector $\overrightarrow{v}$ can be described with respect to both bases as:

$$\begin{aligned} \overrightarrow{v} &= \overrightarrow{\underline{E}}_s \overline{v}^s = \overrightarrow{\underline{E}}_r \overline{v}^r \\ \overline{v}^s &= \left[\overrightarrow{\underline{E}}_s\right]^T \overrightarrow{\underline{E}}_r \overline{v}^r = \overline{\underline{E}}_r^s \overline{v}^r \text{ or} \\ \overline{v}^r &= \left[\overrightarrow{\underline{E}}_r\right]^T \overrightarrow{\underline{E}}_s \overline{v}^s = \overline{\underline{E}}_s^r \overline{v}^s \end{aligned} \tag{A.3.21}$$

The transformation matrix is also called the direction cosine matrix.

A.3.9 Vector or Cross Product

The cross product of two vectors is a vector perpendicular to both these two vectors. The computational rule for the cross product is usually given in the form:

$$\begin{aligned} \overrightarrow{a} \times \overrightarrow{c} &= \begin{vmatrix} \overrightarrow{e_1} & \overrightarrow{e_2} & \overrightarrow{e_3} \\ a_1 & a_2 & a_3 \\ c_1 & c_2 & c_3 \end{vmatrix} \\ &= (a_2c_3 - a_3c_2)\ \overrightarrow{e_1} + (a_3c_1 - a_1c_3)\ \overrightarrow{e_2} + (a_1c_2 - a_2c_1)\ \overrightarrow{e_3} \end{aligned} \tag{A.3.22}$$

or in orthogonal base notation

$$\overrightarrow{a} \times \overrightarrow{c} = \begin{vmatrix} \overline{e}_1 & \overline{e}_2 & \overline{e}_3 \\ a_1 & a_2 & a_3 \\ c_1 & c_2 & c_3 \end{vmatrix} = \begin{bmatrix} \overline{e}_1 & \overline{e}_2 & \overline{e}_3 \end{bmatrix} \begin{bmatrix} a_2c_3 - a_3c_2 \\ a_3c_1 - a_1c_3 \\ a_1c_2 - a_2c_1 \end{bmatrix} \tag{A.3.23}$$

One can write this equation in matrix form as

$$\overline{a} \times \overline{c} = \underline{\tilde{\overline{a}}}\ \overline{c} \tag{A.3.24}$$

where $\underline{\tilde{\overline{a}}}$ is the skew symmetric tensor of the components of the column vector $\overline{a}$. It is also called the cross product tensor and is defined as:

$$\underline{\tilde{\overline{a}}} = \begin{bmatrix} 0 & -a_3 & a_2 \\ a_3 & 0 & -a_1 \\ -a_2 & a_1 & 0 \end{bmatrix} \tag{A.3.25}$$

This tensor has the property that its transpose is equal to the negative of the tensor.

$$\underline{\tilde{\overline{a}}}^T = -\underline{\tilde{\overline{a}}} \tag{A.3.26}$$

A.3.10 Rotating Base

Let $\overrightarrow{\underline{E}}_r$ be a rotating base. The time derivative of a rotating base is given by

$$\begin{aligned} \frac{\mathrm{d}}{\mathrm{d}t}\overrightarrow{\underline{E}}_r = \dot{\overrightarrow{\underline{E}}}_r &= \overrightarrow{\omega} \times \overrightarrow{\underline{E}}_r \\ &= \tilde{\overrightarrow{\omega}}\ \overrightarrow{\underline{E}}_r \end{aligned} \tag{A.3.27}$$

where $\tilde{\overrightarrow{\omega}}$ is defined as the cross product tensor of the angular velocity vector $\overrightarrow{\omega}$. One can also write

$$\dot{\underline{E}}_r^s = \tilde{\underline{\omega}}_s^s\, \underline{E}_r^s \tag{A.3.28}$$

in the fixed base $\overrightarrow{\underline{E}}_s$.

A.4 Combined Notation

In continuum mechanics, index notation is usually used since higher order tensors can easily be represented. The kinematic and dynamic relations of rigid body motion, on the other hand, are usually expressed in matrix tensor notation. In this text, the notation used is clearly stated. It is, however, sometimes convenient to use a combination of matrix tensor notation and index notation. The use of the indices in cases like this is clearly stated where necessary.

A.5 General Principles

Some general principles are derived and given in this section. Either tensor or index notation is used in the derivation of the equations, but the important results are stated, where possible, in both notations.

A.5.1 Gradient of a Scalar Function

It is known from elementary vector analysis that the gradient of a scalar function of position, $\phi(x_1,x_2,x_3)$, in a region R can be expressed as follows

$$\mathrm{grad}\phi = \overrightarrow{\nabla}\phi = \overrightarrow{e}_1\frac{\partial\phi}{\partial x_1} + \overrightarrow{e}_2\frac{\partial\phi}{\partial x_2} + \overrightarrow{e}_3\frac{\partial\phi}{\partial x_3} \tag{A.5.1}$$

where $\phi = \phi(x_1, x_2, x_3)$ is a scalar function of position which is single-valued and continuous with continuous derivatives in the region R, and where

$$\overrightarrow{\nabla} = \overrightarrow{e}_1\frac{\partial}{\partial x_1} + \overrightarrow{e}_2\frac{\partial}{\partial x_2} + \overrightarrow{e}_3\frac{\partial}{\partial x_3} \tag{A.5.2}$$

is called the *del operator*. The gradient of the function ϕ can be expressed in index notation as

$$\frac{\partial \phi}{\partial x_i} = \phi_{,i} \tag{A.5.3}$$

where the subscript $(,i)$ denotes partial differentiation with respect to x_i.

A.5.2 Divergence of a Vector Function

In classical vector notation, the divergence of a vector function of position in a region R is a scalar function of position given as follows

$$\operatorname{div} \overrightarrow{A} = \overrightarrow{\nabla} \bullet \overrightarrow{A} = \frac{\partial A_1}{\partial x_1} + \frac{\partial A_2}{\partial x_2} + \frac{\partial A_3}{\partial x_3} \tag{A.5.4}$$

where $\overrightarrow{A} = \overrightarrow{A}(x_1, x_2, x_3)$ is a vector function of position that is single-valued and continuous with continuous derivatives in a region R. In index notation, the divergence of a vector function of position $\overrightarrow{A}$ is simply

$$\operatorname{div} \overrightarrow{A} = A_{i,i} \tag{A.5.5}$$

A.5.3 Curl of a Vector Function

From elementary vector mechanics, we know that the curl of a vector function of position is a vector function of position, defined as follows

$$\begin{aligned} \operatorname{curl} \overrightarrow{A} &= \overrightarrow{\nabla} \times \overrightarrow{A} \\ &= \overrightarrow{e_1}\,(A_{3,2} - A_{2,3}) + \overrightarrow{e_2}\,(A_{1,3} - A_{3,1}) + \overrightarrow{e_3}\,(A_{2,1} - A_{1,2}) \end{aligned} \tag{A.5.6}$$

Since the curl of a vector can be considered formally as the cross product of the del operator and the vector, the components of the curl of the vector $\overrightarrow{A}$ can be expressed in terms of the permutation symbol as

$$\operatorname{curl} \overrightarrow{A} = \varepsilon_{ijk} A_{k,j} \tag{A.5.7}$$

A.5.4 Gauss' Theorem

In classical vector notation, Gauss' theorem may be expressed as

$$\int_S \overrightarrow{A} \bullet \overrightarrow{n}\, \mathrm{d}S = \int_R \overrightarrow{\nabla} \bullet \overrightarrow{A}\, \mathrm{d}V \tag{A.5.8}$$

where $\overrightarrow{A}(x_1, x_2, x_3)$ is a vector field that is single-valued and continuous with continuous derivatives in a region R, S is the surface enclosing R, $\overrightarrow{n}$ is

the unit vector to a small differential element of area dS on the surface S. In index notation, Gauss' theorem reads

$$\int_S A_i n_i \, \mathrm{d}S = \int_R A_{i,i} \, \mathrm{d}V \tag{A.5.9}$$

A.5.5 Lagrangian and Eulerian Descriptions of Deformation or Flow

When a medium deforms or flows, the small volumetric elements change position as they move along space curves. Their positions as functions of time can be specified in two ways. These are the Lagrangian and Eulerian descriptions presented below.

Lagrangian Description

Introduce a set of right-handed Cartesian axes, x_i, fixed in space. At time $t = 0$, let the position of a small volumetric element in the continuum be a_i, and at any other time t, let its coordinates be x_i. Obviously, the position of each element can be specified as a function of its initial coordinates a_i and time t

$$x_i = x_i\,(a_1, a_2, a_3, t) \tag{A.5.10}$$

This type of description of motion, where each particle (small volumetric element) is tracked in terms of its initial position and time, is called the *Lagrangian description*. Each initial position vector a_i defines a different particle, and a_i is sometimes called the *name*, or *label, of the particle*. By definition, the displacement vector u_i of each particle is the difference of the position vectors at time t and time $t = 0$ (figure A.5).

$$u_i = x_i - a_i \tag{A.5.11}$$

In the Lagrangian description, the displacement vector u_i is specified as a function of a_i and t, which are treated as four independent variables

$$u_i = u_i\,(a_1, a_2, a_3, t) \tag{A.5.12}$$

An example of such a description of flow is

$$\begin{aligned} x_1 &= a_1 t^2 + 2a_2 t + a_1 \\ x_2 &= 2a_1 t^2 + a_2 t + a_2 \\ x_3 &= \tfrac{1}{2} a_3 t + a_3 \end{aligned} \tag{A.5.13}$$

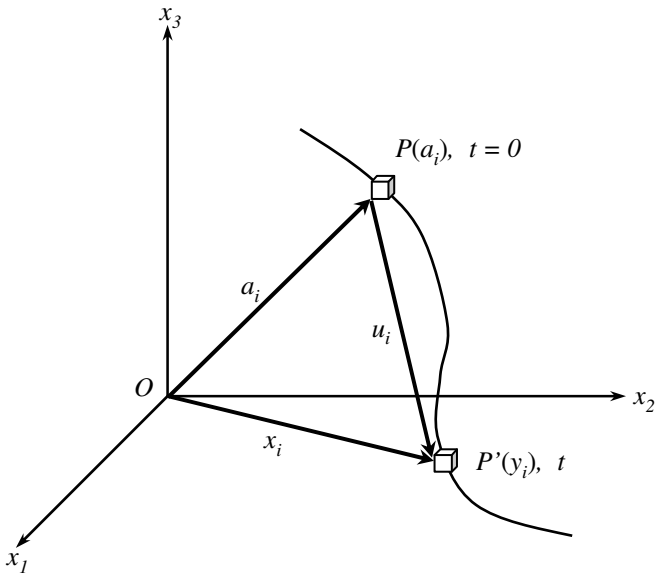

Figure A.5: Representation of a vector in two sets of right-handed Cartesian axes with different orientations

The corresponding displacements u_i are given by substituting these equations for the position vector x_i in equation A.5.11

$$\begin{aligned} u_1 &= x_1 - a_1 = a_1 t^2 + 2a_2 t \\ u_2 &= x_2 - a_2 = 2a_1 t^2 + a_2 t \\ u_3 &= x_3 - a_3 = \tfrac{1}{2} a_3 t \end{aligned} \tag{A.5.14}$$

Eulerian Description

Instead of expressing the movement of a continuous medium in terms of the initial position and time, it is also possible to express it in terms of the instantaneous position vector x_i and time t. For instance, the same displacement vector u_i can alternatively be expressed in terms of x_i and t

$$u_i = u_i\left(x_1, x_2, x_3, t\right) \tag{A.5.15}$$

This is possible, because the relationship between x_i and a_i, as described in equation A.5.10, can always be converted to express a_i in terms of x_i and t

$$a_i = a_i\left(x_1, x_2, x_3, t\right) \tag{A.5.16}$$

Whenever the motion of a continuum is expressed in terms of the instantaneous position vector and time, the motion is said to be described by the *Eulerian method*.

Conversion

The usual practice in classical linear elasticity is to refer all field functions to the initial geometry of the continuum. In all cases, the undeformed dimensions of a structure are known, whereas the deformed dimensions must be found. If the derivatives of the displacements are assumed small, the Eulerian description can be converted to the Lagrangian description. As an example, convert the following Eulerian derivative

$$\frac{\partial F\left(x_i, t\right)}{\partial x_i} \tag{A.5.17}$$

to the Lagrangian description. Note that

$$\begin{aligned} \frac{\partial F(x_i, t)}{\partial x_j} &= \frac{\partial F(a_i, t)}{\partial a_k} \frac{\partial a_k}{\partial x_j} \\ &= \frac{\partial F(a_i, t)}{\partial a_k} \frac{\partial \left(x_k - u_k(a_i, t)\right)}{\partial x_j} \\ &= \frac{\partial F(a_i, t)}{\partial a_k} \left(\delta_{kj} - \frac{\partial u_k(a_i, t)}{\partial x_j}\right) \end{aligned} \tag{A.5.18}$$

Now, invoking the assumption that the derivative of the displacement is small, equation A.5.18 becomes

$$\frac{\partial F\left(x_i, t\right)}{\partial x_j} = \frac{\partial F\left(a_i, t\right)}{\partial a_k}\, \delta_{kj} = \frac{\partial F\left(a_i, t\right)}{\partial a_j} \tag{A.5.19}$$

In other words, to convert an Eulerian partial derivative, we need only to express the Eulerain function in terms of the Lagrangian coordinates, and then consider the partial differentiation to be with respect to the Lagrangian coordinates. As far as the comoving derivative are concerned, we know that

$$\frac{\mathrm{d}F\left(x_i, t\right)}{\mathrm{d}t} = \frac{\mathrm{d}F\left(a_i, t\right)}{\mathrm{d}t} = \frac{\partial F\left(a_i, t\right)}{\partial t} \tag{A.5.20}$$

The only assumption required for the preceding conversions is that the displacement gradients be small. If the displacement vector u_i is also relatively small, the functional forms of F in both the Eulerain and Lagrangian description become equivalent.

A.5.6 The Comoving Derivative

As a particle of a continuum moves, many of the properties characterising the element also undergo changes. Use the symbol $\phi_{ij\ldots}$ (which may be a scalar, a vector, or a Cartesian tensor of any order) to denote one of the properties characterising the particle. As the particle moves in space with time,

the function $\phi_{ij...}$also changes with time. The rate at which $\phi_{ij...}$changes with time while fixing attention to the same particle is called the *comoving* (or *substantial*, or *material*, or *convective*, or *particle*) derivative of $\phi_{ij...}$and will be denoted in this text by the symbol $\frac{\mathrm{d}\phi_{ij...}}{\mathrm{d}t}$ unless noted otherwise. Physically, this derivative can also be interpreted as the rate at which $\phi_{ij...}$changes, as seen by an observer attached to the particle. In the Lagrangian description, $\phi_{ij...}$ is expressed as a function of the "label" of the particle a_i and the time t

$$\phi_{ij...} = \phi_{ij...}\left(a_1, a_2, a_3, t\right) \tag{A.5.21}$$

Since the initial coordinates a_i for an individual particle remain constant, the comoving derivative of $\phi_{ij...}$ using the Lagrangian method is obtained by treating the coordinates a_i as constants. Therefore

$$\begin{aligned} \frac{\mathrm{d}\phi_{ij...}(a_1, a_2, a_3, t)}{\mathrm{d}t} &= \frac{\partial\phi_{ij...}(a_1, a_2, a_3, t)}{\partial t} + \frac{\partial\phi_{ij...}(a_1, a_2, a_3, t)}{\partial a_m}\,\frac{\mathrm{d}a_m}{\mathrm{d}t} \\ &= \frac{\partial\phi_{ij...}(a_1, a_2, a_3, t)}{\partial t} \end{aligned} \tag{A.5.22}$$

since $\frac{\mathrm{d}a_m}{\mathrm{d}t} = 0$. When using the Eulerian description, the function $\phi_{ij...}$ is expressed in terms of the instantaneous position vector x_i and the time t. As the particle moves, x_i varies with time. Therefore, the comoving derivative of $\phi_{ij...}$ using the Eulerian description is

$$\begin{aligned} \frac{\mathrm{d}\phi_{ij...}(x_1, x_2, x_3, t)}{\mathrm{d}t} &= \frac{\partial\phi_{ij...}(x_1, x_2, x_3, t)}{\partial t} + \frac{\partial\phi_{ij...}(x_1, x_2, x_3, t)}{\partial x_m}\,\frac{\mathrm{d}x_m}{\mathrm{d}t} \\ &= \frac{\partial\phi_{ij...}(x_1, x_2, x_3, t)}{\partial t} + \frac{\partial\phi_{ij...}(x_1, x_2, x_3, t)}{\partial x_m}\,v_m \end{aligned} \tag{A.5.23}$$

where v_m is the absolute velocity.

A.5.7 The Reynolds Transport Theorem

Consider a certain Eulerian property $F_{ij...}(x_i, t)$ per unit mass in space, such as the specific energy per unit mass and momentum per unit mass. The integral of $\hat{F}_{ij...}(t)$,

$$\hat{F}_{ij...}(t) = \int_R \rho F_{ij...}\left(x_i, t\right)\,\mathrm{d}V \tag{A.5.24}$$

over a portion of the continuum occupying a region of space R in which $F_{ij...}(x_i, t)$ is defined, is a measure of the total entity of $F_{ij...}$contained in the portion of the continuum at a given time t. Notice that the region of integration can be considered as either the region of space R or the region of

the continuum, which at time t occupies the region of space R. When considering the time rate of change of such an integral, however, care must be exercised as to whether the region of integration is the fixed region of space R or the portion of the continuum occupying R.

If we are interested in the explicit time rate of change of the total amount of $F_{ij\ldots}$ inside the fixed region R, then compute the time rate of change of $\hat{F}_{ij\ldots}(t)$ for the fixed region, or

$$\int_R \frac{\partial}{\partial t}\left(\rho F_{ij\ldots}\right)\, \mathrm{d}V \tag{A.5.25}$$

When we are interested in the time rate of change of the total amount of $F_{ij\ldots}$ contained in the portion of the continuum that occupies the region of space R at time t, then the region of integration must be visualised as variable, changing with the motion of the medium. Such a time rate is defined as the *comoving derivative* of $\hat{F}_{ij\ldots}(t)$ and is usually denoted by

$$\frac{\mathrm{d}}{\mathrm{d}t}\int_R \rho F_{ij\ldots}\, \mathrm{d}V \tag{A.5.26}$$

Such a derivative is convenient for assigning physical meanings, but is not convenient for mathematical manipulations because the differentiation is to be applied to an integral whose region of integration moves with the medium in time. Therefore seek relations that will enable us to express such a comoving derivative of an integral in terms of integrals where the region of integration may be visualised as a fixed region in space.

By the definition of the comoving derivative of $\hat{F}_{ij\ldots}(t)$, we recognise that it is the same as the integral of the comoving derivatives of $\rho F_{ij\ldots}\mathrm{d}V$ associated with the individual volumetric elements contained in region R. But the mass $\rho \mathrm{d}V$ contained in a volumetric element $\mathrm{d}V$ that moves with the medium is a constant. Therefore

$$\frac{\mathrm{d}}{\mathrm{d}t}\left(\rho F_{ij\ldots}\mathrm{d}V\right) = \rho\frac{\mathrm{d}F_{ij\ldots}}{\mathrm{d}t}\, \mathrm{d}V \tag{A.5.27}$$

and

$$\frac{\mathrm{d}}{\mathrm{d}t}\int_R \rho F_{ij\ldots}\, \mathrm{d}V = \int_R \rho\frac{\mathrm{d}F_{ij\ldots}}{\mathrm{d}t}\, \mathrm{d}V \tag{A.5.28}$$

Writing out the comoving derivative for $\frac{\mathrm{d}F_{ij\ldots}}{\mathrm{d}t}$, we obtain

$$\begin{aligned}\frac{\mathrm{d}}{\mathrm{d}t}\int_R \rho F_{ij\ldots}\, \mathrm{d}V &= \int_R \rho\frac{\mathrm{d}F_{ij\ldots}}{\mathrm{d}t}\, \mathrm{d}V \\ &= \int_R \rho\frac{\partial F_{ij\ldots}}{\partial t}\, \mathrm{d}V + \int_R \rho v_r F_{ij\ldots,r}\, \mathrm{d}V\end{aligned} \tag{A.5.29}$$

where v_r is the absolute velocity vector. Since the integrals

$$\int_R \rho \frac{\partial F_{ij\ldots}}{\partial t}\, \mathrm{d}V \text{ and } \int_R \rho v_r F_{ij\ldots,r}\, \mathrm{d}V$$

are expressed explicitly in terms of the Eulerian variables, we no longer need to be concerned with the rate of change of the integrals with time. The region of integration can now be visualised as the region of space R, which the continuum occupies at time t, without ambiguity. The usual theorems of Cartesian tensor calculus can now be applied to these integrals. Equation A.5.29 can be written as

$$\begin{aligned}\frac{\mathrm{d}}{\mathrm{d}t}\int_R \rho F_{ij\ldots}\, \mathrm{d}V &= \int_R \rho \frac{\mathrm{d}F_{ij\ldots}}{\mathrm{d}t}\, \mathrm{d}V \\ &= \int_R \frac{\partial}{\partial t}\left(\rho F_{ij\ldots}\right)\, \mathrm{d}V + \int_R \left(\rho v_r F_{ij\ldots,r} - F_{ij\ldots}\frac{\partial \rho}{\partial t}\right) \mathrm{d}V\end{aligned} \tag{A.5.30}$$

where the integral

$$\int_R \frac{\partial}{\partial t}\left(\rho F i j \ldots\right)\, \mathrm{d}V$$

is the explicit time rate of increase of the total entity $F_{ij\ldots}$ in the fixed region R, as mentioned before. Using the Eulerian continuity equation derived in Appendix B, equation B.4.3,

$$\frac{\partial \rho}{\partial t} = -\left(\rho v_r\right)_{,r} \tag{A.5.31}$$

in the last term of equation A.5.30, we obtain

$$\begin{aligned}\frac{\mathrm{d}}{\mathrm{d}t}\int_R \rho F_{ij\ldots}\, \mathrm{d}V &= \int_R \rho \frac{\mathrm{d}F_{ij\ldots}}{\mathrm{d}t}\, \mathrm{d}V \\ &= \int_R \frac{\partial}{\partial t}\left(\rho F_{ij\ldots}\right)\, \mathrm{d}V + \int_R \left(\rho v_r F_{ij\ldots}\right)_{,r}\, \mathrm{d}V\end{aligned} \tag{A.5.32}$$

Equation A.5.32 is called the *Reynolds transport theorem*. The last two integrals are amenable to the basic theorems of Cartesian tensor calculus. As an example, apply Gauss' theorem to the last integral in equation A.5.32. We obtain

$$\begin{aligned}\frac{\mathrm{d}}{\mathrm{d}t}\int_R \rho F_{ij\ldots}\, \mathrm{d}V &= \int_R \rho \frac{\mathrm{d}F_{ij\ldots}}{\mathrm{d}t}\, \mathrm{d}V \\ &= \int_R \frac{\partial}{\partial t}\left(\rho F_{ij\ldots}\right)\, \mathrm{d}V + \int_S \rho\, v_r\, n_r\, F_{ij\ldots}\, \mathrm{d}S\end{aligned} \tag{A.5.33}$$

where S is the surface enclosing the region R and n_r is the unit outward normal of the differential surface element $\mathrm{d}S$ on S.

Appendix B

Nonpolar Continuum Mechanics

B.1 Introduction

The principles and fundamental laws of a classic or nonpolar continuum are presented. In a nonpolar continuum no assigned traction couples or body couples and couple stresses are present, but only external surface traction forces and body forces.

Many problems in engineering mechanics are concerned with the behaviour of matter in motion or in equilibrium under the action of externally applied forces in various environments. For engineering purposes, it is often possible to study such behaviour of matter by assuming the matter to be totally continuous. A material that can be treated this way is called a continuum, or continuous medium, and the theory describing the behaviour of such a material is called continuum mechanics, or theory of a continuous medium. Both the Eulerian and Lagrangian descriptions are used. The rest of this appendix closely follows the description given by Frederick & Chang (1972).

B.2 Cauchy Stress Tensor

Forces acting on a body of a continuum medium may be divided into two groups: those that act across a surface (internal or external), owing to direct contact with another body, and those that act at a distance and not as a result of direct contact.

Body forces are forces that act on all particles in a body as a result of some external body or effect not due to direct contact. An example of this is the gravitational force exerted on a body and which is due to another body. This type of force will be defined as a force intensity at a point in the continuum on a per unit mass or per unit volume basis. Let ΔF_i be the body force acting on the mass ΔM inside a volume ΔV. Then the definitions of a body force at a point are

$$f_i = \lim_{\Delta M \to 0} \frac{\Delta F_i}{\Delta M} = \frac{\mathrm{d}F_i}{\mathrm{d}M} = \frac{\mathrm{d}F_i}{\rho \mathrm{d}V} \quad \text{(force per unit mass)} \tag{B.2.1}$$

$$\tilde{f}_i = \lim_{\Delta V \to 0} \frac{\Delta F_i}{\Delta V} = \frac{\mathrm{d}F_i}{\mathrm{d}V} \quad \text{(force per unit volume)} \tag{B.2.2}$$

with

$$\rho f_i = \tilde{f}_i \tag{B.2.3}$$

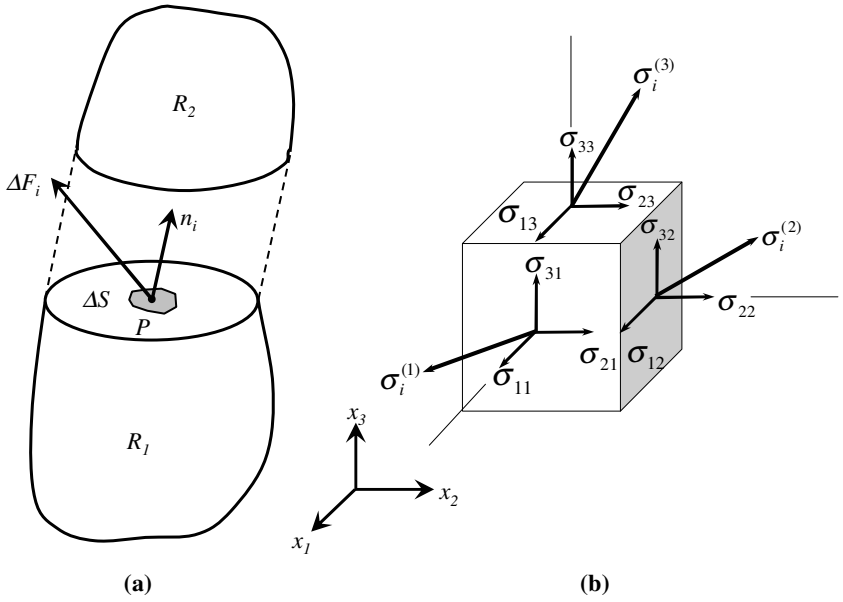

Figure B.1: Traction vector

Surface forces are contact forces that act across some surface of the body, which may be internal or external. In continuum studies, this type of force is usually introduced as a force per unit area at a point in the medium. consider a planar surface area ΔS (figure B.1a), oriented by the unit normal vector n_i and containing the point P. Let ΔF_i be the total force that the material on the $+n_i$ side exerts on the material on the $-n_i$ side across the surface.
The stress vector σ_i at the point P corresponding to the direction n_i is defined as

$$\sigma_i = \lim_{\Delta S \to 0} \frac{\Delta F_i}{\Delta S} = \frac{\mathrm{d}F_i}{\mathrm{d}S} \tag{B.2.4}$$

Note that the stress vector (sometimes referred to as the *traction vector*, *Cauchy traction vector*, or *true traction vector*) is a function of position, time, the orientation of the surface element as specified by the direction of n_i, and the sense of n_i. Cauchy's stress theorem states that there exists a unique second-order tensor field σ_{ij} so that

$$\sigma_i = \sigma_{ij} n_j \tag{B.2.5}$$

where σ_{ij} denotes the spatial tensor field called the *Cauchy* (or *true*) *stress tensor*. To prove equation B.2.5, again consider a point P in a continuum. Take the unit normal vector n_i of the surface containing point P to be in the direction of the positive x_2-direction. This orients the surface element

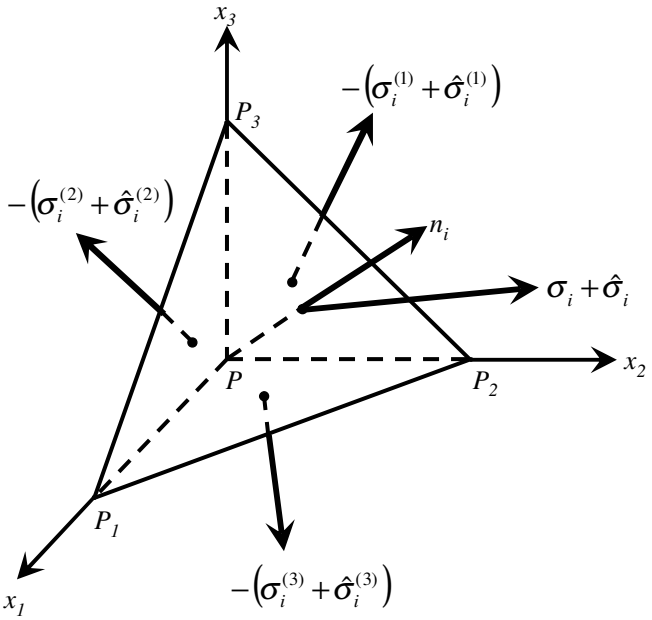

Figure B.2: Small tetrahedron at point P

normal to the x_2-axis (the shaded surface in figure B.1b). The stress vector $\sigma_i^{(2)}$ on this element is, in general, in some arbitrary direction, but may be resolved into normal and shearing components. The shearing component lying in dS then may be resolved into two components along the x_1- and x_3-directions. The net result is that the stress vector has been resolved into components $\sigma_i^{(2)}$along the x_i axes as shown in figure B.1b. Similarly, we can visualise two other stress vectors $\sigma_i^{(1)}$ and $\sigma_i^{(3)}$acting on surface elements whose normals are in the positive x_1- and x_3-directions. The three stress vectors have a total of nine components, which are called the *components of stress* or the *stress tensor* at point P. Three of these, σ_{11}, σ_{22} and σ_{33} are *normal stresses* and the remaining six, σ_{21}, σ_{31}, σ_{12}, σ_{32}, σ_{13} and σ_{23} are *shearing stresses*.

Consider a small but finite tetrahedron at point P, bounded by three coordinate planes and a sloping face normal to n_i, as shown in figure B.2. Introduce local Cartesian axes with the origin at P and the following nomenclature:

$\sigma_i =$ stress vector at P acting across a small surface element whose normal is n_i
$\sigma_{ij} =$ components of stress (stress tensor) at point P
$f_i =$ body force per unit mass at point P
$h =$ depth of the tetrahedron measured from the sloping face that is normal to the unit vector n_i
$\rho =$ density at point P

It is clear that average quantities must be introduced, since the tetrahedron is finite. Define the following average quantities.

$\sigma_i + \hat{\sigma}_i =$ average stress vector across the sloping surface $P_1P_2P_3$ on the tetrahedron

$-\left(\sigma_i^{(1)} + \hat{\sigma}_i^{(1)}\right) =$ average stress vector across the surface PP_2P_3 on the tetrahedron. The negative sign appears because $\left(\sigma_i^{(1)} + \hat{\sigma}_i^{(1)}\right)$ would denote the average traction on a surface whose outward normal pointed in the positive x_1-direction.

$-\left(\sigma_i^{(2)} + \hat{\sigma}_i^{(2)}\right) =$ average stress vector across the surface PP_3P_1 on the tetrahedron

$-\left(\sigma_i^{(3)} + \hat{\sigma}_i^{(3)}\right) =$ average stress vector across the surface PP_1P_2 on the tetrahedron

$f_i + \hat{f}_i =$ average body force per unit mass acting on the tetrahedron

$\rho + \hat{\rho} =$ average density of the tetrahedron

The area of the sloping surface $P_1P_2P_3$ is A and

$$\lim_{h \to 0} \left(\hat{\sigma}_i, \hat{\sigma}_{ij}, \hat{f}_i, \hat{\rho}\right) = 0 \tag{B.2.6}$$

As the altitude h approaches zero, so that the volume and the four surface areas simultaneously approach zero, while the position of P does not change. It follows that the average values will approach the local values at the point P, and the result will be an expression for the stress vector σ_i

at point P in terms of the other three special surface stress vectors at P. Applying the translational equations of motion yields

$$(\rho+\hat{\rho})\left(f_i+\hat{f}_i\right)\left(\tfrac{1}{3}Ah\right)-\left(\sigma_i^{(1)}+\hat{\sigma}_i^{(1)}\right)(n_1A)-\left(\sigma_i^{(2)}+\hat{\sigma}_i^{(2)}\right)(n_2A)-\left(\sigma_i^{(3)}+\hat{\sigma}_i^{(3)}\right)(n_3A)+(\sigma_i+\hat{\sigma}_i)\,A=(\rho+\hat{\rho})\left(\tfrac{1}{3}Ah\right)\frac{\mathrm{d}v_i}{\mathrm{d}t} \quad \text{(B.2.7)}$$

where v_i is the velocity vector at some interior point. Now let h approach zero and noting that the conditions of equation B.2.6 apply, the preceding equation becomes

$$\begin{aligned}\sigma_i &= \sigma_i^{(1)}n_1+\sigma_i^{(2)}n_2+\sigma_i^{(3)}n_3\\ \therefore\ \sigma_i &= \sigma_{ij}n_j\end{aligned} \quad \text{(B.2.8)}$$

This equation relates the stress vector σ_i at P corresponding to the direction n_i to the stress components σ_{ij} at P. The normal component, N, of the stress vector σ_i acting on the surface oriented by the unit normal vector n_i is given by the dot product of the vectors n_i and σ_i.

$$N=\sigma_i n_i \quad \text{(B.2.9)}$$

and from equation B.2.8 it follows that

$$N=\sigma_{ij}n_jn_i \quad \text{(B.2.10)}$$

and the magnitude of the shearing component S

$$S=\sqrt{\sigma_i\sigma_i-N^2} \quad \text{(B.2.11)}$$

B.3 Principal Stresses and Principal Axes

At a given point P in the continuum, the stress vector acting on an area whose normal is n_i is given by equation B.2.8. We now seek a direction n_i (if any) for which the stress vector will be normal to the area. That is,

$$\sigma_i=\sigma n_i \quad \text{(B.3.1)}$$

where σ is the magnitude of the stress vector. Such a direction is called a principal direction, and the corresponding stress magnitude σ is called a principal stress. Hence, given the stress tensor σ_{ij} at P, the condition for determining the principle stresses and their corresponding directions is

$$\sigma_i=\sigma_{ij}n_j=\sigma n_i=\sigma\delta_{ij}n_j \quad \text{(B.3.2)}$$

or

$$\left(\sigma_{ij} - \sigma\delta_{ij}\right) n_j = 0 \tag{B.3.3}$$

These three linear algebraic equations together with

$$n_i n_i = 1 \tag{B.3.4}$$

are four equations for the four unknowns σ and n_i. Equation B.3.3 has the trivial solution $n_1 = n_2 = n_3 = 0$, which cannot be valid, since they must satisfy the condition equation B.3.4. For equation B.3.3 to possess nontrivial solutions, the determinant of the coefficients of n_i in the set of three equations must vanish.

$$|\sigma_{ij} - \sigma\delta_{ij}| = 0 \tag{B.3.5}$$

or

$$-\sigma^3 + \Theta\sigma^2 - \Phi\sigma + \Psi \tag{B.3.6}$$

where $\Theta = \sigma_{ii}$ (sum of diagonals of stress vector)

$$\begin{aligned} \Phi &= \sigma_{22}\sigma_{33} - \sigma_{23}^2 + \sigma_{33}\sigma_{11} - \sigma_{31}^2 + \sigma_{11}\sigma_{22} - \sigma_{12}^2 \\ \Psi &= |\sigma_{ij}| \ \text{(determinant of the stress vector)} \end{aligned} \tag{B.3.7}$$

Equation B.3.6 is a cubic equation in σ, which will yield three principal stresses σ_1, σ_2 and σ_3.

B.4 Conservation of Mass

One of the most important physical laws governing the motion of a continuous medium is the principle of conservation of mass. An equation derived from the law of conservation of mass is called a *continuity equation.* Every continuum body possesses mass, denoted by m. It is a fundamental physical property commonly defined to be a measure of the amount of material contained in the body.

B.4.1 Eulerian Description

In order to perform a macroscopic study we assume that mass is continuously distributed over an arbitrary region R with boundary surface S at time t. We define a system as a quantity of mass or a particular collection of matter in space. In non-relativistic physics mass cannot be produced or destroyed. The mass m of a body is a conserved quantity. Consider a surface S enclosing a fixed region R, through which a continuum flows, as shown in figure B.3.

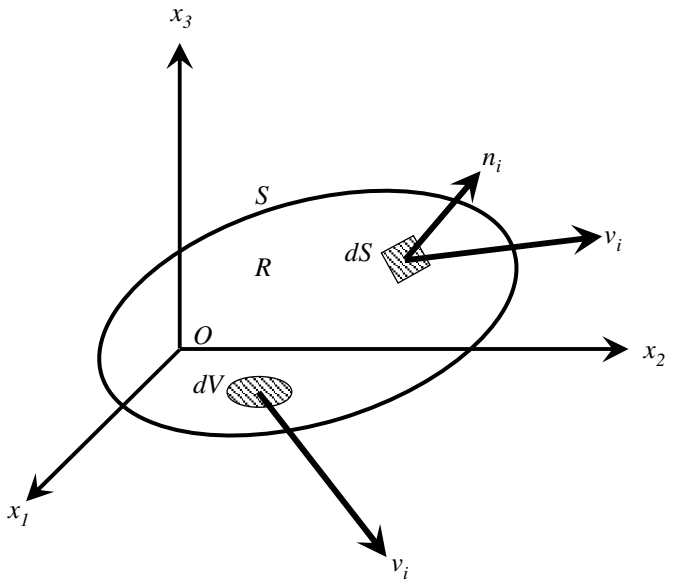

Figure B.3: A fixed region in space through which the continuum flows

Let the outer unit normal vector to a differential surface element dS be $n_i(x_1, x_2, x_3)$, let the velocity vector of a particle inside the region R be $v_i(x_1, x_2, x_3)$ and let the density of the same particle be $\rho(x_1, x_2, x_3)$. It is obvious from the concept of conservation of mass that the rate of increase of mass in the region R is exactly equal to the amount of mass flowing into the region per unit of time.
With R and dV fixed, it follows that

$$\int_R \frac{\partial \rho}{\partial t}\, \mathrm{d}V$$

is the rate of increase of mass inside R. Identifying $v_i n_i$ as the normal component of spatial velocity ($v_i = \frac{\mathrm{d}x_i}{\mathrm{d}t}$) to the surface element dS, it follows that

$$-\int_S \rho v_i n_i \, \mathrm{d}S$$

is the rate of mass flowing into the region per unit of time. Therefore we set

$$\begin{aligned} \int_R \frac{\partial \rho}{\partial t}\, \mathrm{d}V &= -\int_S \rho v_i n_i \, \mathrm{d}S \\ \therefore \int_R \frac{\partial \rho}{\partial t}\, \mathrm{d}V + \int_S \rho v_i n_i \, \mathrm{d}S &= 0 \end{aligned} \tag{B.4.1}$$

where the integrations are taken over a fixed region R and surface S, and not following the particle. Equation B.4.1 is called the Eulerian integral con-

tinuity equation. Applying Gauss' theorem to convert the surface integral to a volume integral, equation B.4.1 becomes

$$\int_R \left[\frac{\partial \rho}{\partial t} + (\rho v_i)_{,i} \right] \mathrm{d}V = 0 \tag{B.4.2}$$

However, this equation should be satisfied for any arbitrary but fixed region of space. This means that the integrand of the left-hand side of equation B.4.2 should be identically equal to zero, or

$$\begin{aligned} \frac{\partial \rho}{\partial t} + (\rho v_i)_{,i} &= 0 \\ \therefore \frac{\partial \rho}{\partial t} + v_i \rho_{,i} + \rho v_{i,i} &= 0 \end{aligned} \tag{B.4.3}$$

Recognising the first two terms as the comoving derivatives of ρ,

$$\frac{\mathrm{d}\rho}{\mathrm{d}t} + \rho v_{i,i} = 0 \tag{B.4.4}$$

Equations B.4.3 and B.4.4 are the three forms of the Eulerian differential continuity equation. Whenever the density of each particle of the medium remains constant (incompressible flow), then

$$\frac{\mathrm{d}\rho}{\mathrm{d}t} = 0 \tag{B.4.5}$$

For this case, the continuity equation has the following form

$$v_{i,i} = 0 \tag{B.4.6}$$

and if the motion of the medium is steady, then the continuity equation becomes

$$\frac{\partial \rho}{\partial t} = 0 \Leftrightarrow (\rho v_i)_{,i} = 0 \tag{B.4.7}$$

B.4.2 Lagrangian Description

In the Lagrangian description, the density ρ is a function of the initial position vector a_i and time t, $\rho = \rho(a_1, a_2, a_3, t)$. Consider a region R^0 occupied by the continuum at time $t = 0$ with an initial density distribution of $\rho(a_1, a_2, a_3, 0)$. This region of the continuum will move to some new position and form a new region R^t at time t (which may or may not overlap the original region) with a new density distribution of $\rho(a_1, a_2, a_3, t)$.

Consider the continuum in the initial region R^0 at $t = 0$ to be bounded by lines parallel to the x_i-axes, figure B.4. After deformation, these lines will describe curves in the region R^t at time t. These curves along which only one of the values of a_i vary, may be considered as a set of curvilinear

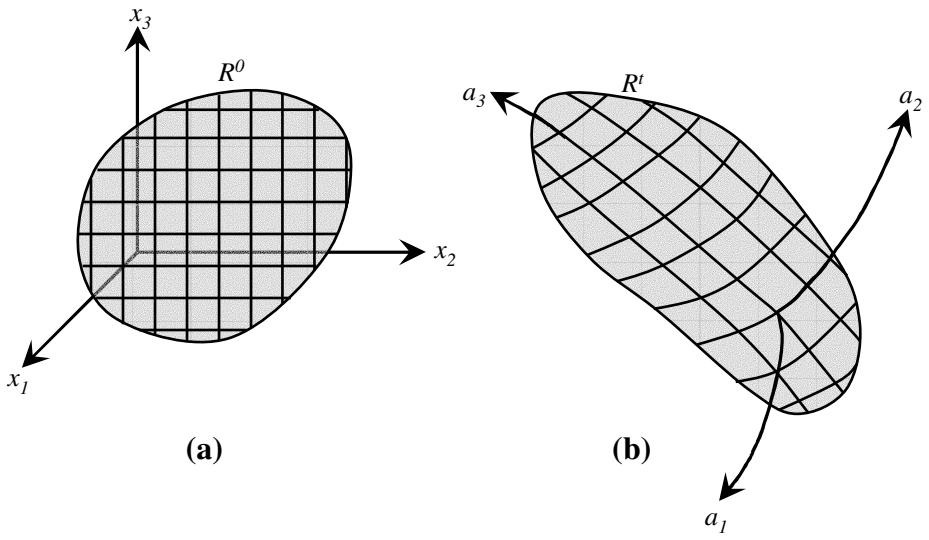

Figure B.4: The curves of a_i = constants in the (a) undeformed and (b) deformed configurations of a continuous medium

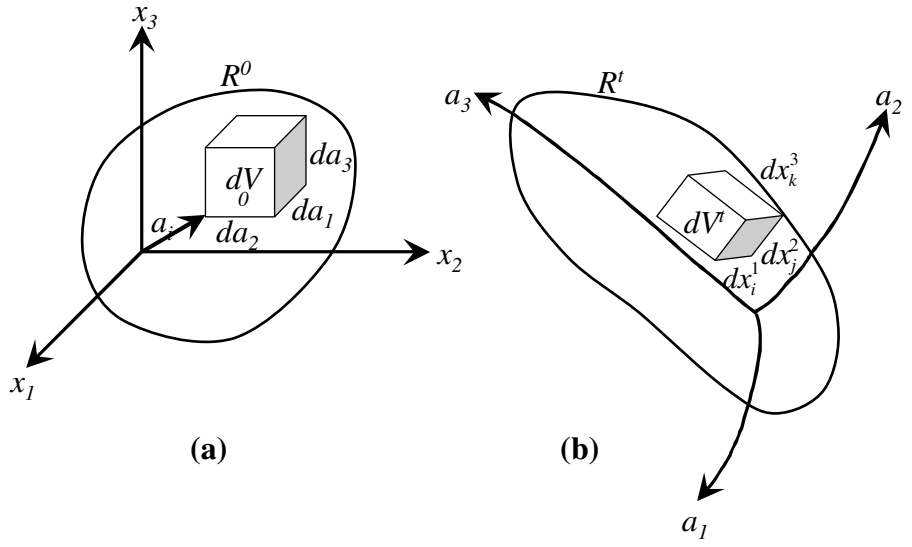

Figure B.5: The (a) undeformed and (b) deformed volumetric elements

coordinates in the deformed body. Each infinitesimal rectangular parallelepiped of

$$\mathrm{d}V^0 = \mathrm{d}a_1\mathrm{d}a_2\mathrm{d}a_3 \tag{B.4.8}$$

will be deformed into a small nonrectangular parallelepiped of volume $\mathrm{d}V^t$ in the deformed body at time t, figure B.5. The sides $\mathrm{d}x_i^1, \mathrm{d}x_j^2, \mathrm{d}x_k^3$ of the parallelepiped $\mathrm{d}V^t$ corresponds to the differential line segments along

the curvilinear coordinates in the deformed body, owing to the differential changes

$$\mathrm{d}x_i^1 = \frac{\partial x_i}{\partial a_1}\mathrm{d}a_1, \qquad \mathrm{d}x_j^2 = \frac{\partial x_j}{\partial a_2}\mathrm{d}a_2, \qquad \mathrm{d}x_k^3 = \frac{\partial x_k}{\partial a_3}\mathrm{d}a_3 \tag{B.4.9}$$

The volume of the parallelepiped $\mathrm{d}V^t$ can be shown to be

$$\begin{aligned} \mathrm{d}V^t &= \varepsilon_{ijk}\frac{\partial x_i}{\partial a_1}\mathrm{d}a_1\frac{\partial x_j}{\partial a_2}\mathrm{d}a_2\frac{\partial x_k}{\partial a_3}\mathrm{d}a_3 \\ &= J\mathrm{d}a_1\mathrm{d}a_2\mathrm{d}a_3 \end{aligned} \tag{B.4.10}$$

where

$$\begin{aligned} J &= \frac{\partial(x_1, x_2, x_3)}{\partial(a_1, a_2, a_3)} = \varepsilon_{ijk}\frac{\partial x_i}{\partial a_1}\frac{\partial x_j}{\partial a_2}\frac{\partial x_k}{\partial a_3} \\ &= \begin{vmatrix} \frac{\partial x_1}{\partial a_1} & \frac{\partial x_2}{\partial a_1} & \frac{\partial x_3}{\partial a_1} \\ \frac{\partial x_1}{\partial a_2} & \frac{\partial x_2}{\partial a_2} & \frac{\partial x_3}{\partial a_2} \\ \frac{\partial x_1}{\partial a_3} & \frac{\partial x_2}{\partial a_3} & \frac{\partial x_3}{\partial a_3} \end{vmatrix} \end{aligned} \tag{B.4.11}$$

is called the *Jacobian* of transformation of x_i with respect to a_i. Since the mass contained in R^0 should be identically the same as that in R^t, the following integral continuity equation using Lagrangian description must be valid

$$\int_{R^t} \rho\left(a_1, a_2, a_3, t\right)\ \mathrm{d}V^t = \int_{R^0} \rho\left(a_1, a_2, a_3, 0\right)\ \mathrm{d}V^0 \tag{B.4.12}$$

or

$$\int_{R^0} \rho\left(a_1, a_2, a_3, t\right)\ J\,\mathrm{d}V^0 = \int_{R^0} \rho\left(a_1, a_2, a_3, 0\right)\ \mathrm{d}V^0 \tag{B.4.13}$$

But this equation should hold true for any region R^0. Therefore

$$\rho\left(a_1, a_2, a_3, t\right) J = \rho\left(a_1, a_2, a_3, 0\right) \tag{B.4.14}$$

Equation B.4.12 implies that the quantity $\rho\left(a_1, a_2, a_3, t\right) J$ is independent of time for a given particle, or a_i. Therefore the comoving derivative of ρJ must vanish

$$\frac{\mathrm{d}}{\mathrm{d}t}\left[\rho\left(a_1, a_2, a_3, t\right) J\right] = 0 \tag{B.4.15}$$

This is a differential continuity equation from the Lagrangian viewpoint.

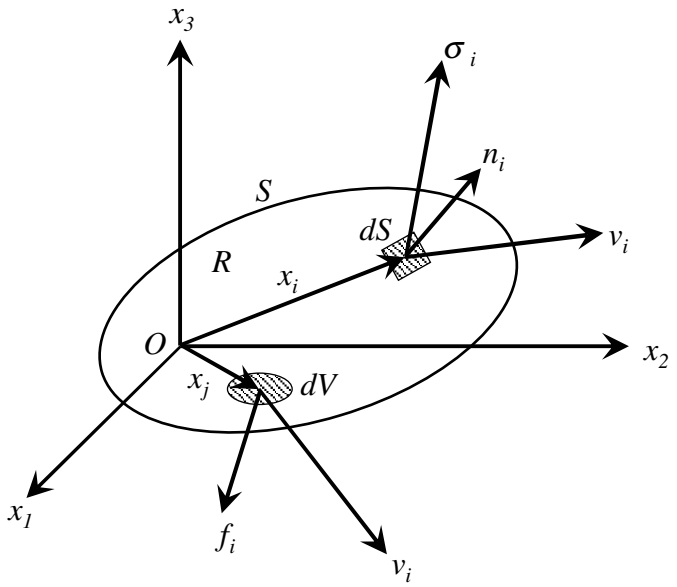

Figure B.6: Free body diagram of an arbitrary region in space in which a continuum moves

B.5 Momentum Balance Principles

The momentum principle for a collection of particles states that the time rate of change of the total momentum of a given set of particles equals the vector sum of all the external forces acting on the particles of the set, provided Newton's Third Law of action and reaction governs the internal forces. The continuum form of this principle is a basic postulate of continuum mechanics.

B.5.1 Eulerian Description

Consider a given mass of the medium, instantaneously occupying a region R bounded by surface S (as in figure B.6) and acted upon by a stress vector σ_i and body force f_i. If $\sigma_i(x_i, t)$ is acting on a surface element $\mathrm{d}S$ on S, $\rho(x_i)$ is the density of the volumetric element $\mathrm{d}V$ in region R, and $f_i(x_i, t)$ is the body force per unit mass of the same volumetric element; then Cauchy's first law of motion becomes

$$\int_S \sigma_i \, \mathrm{d}S + \int_R \rho f_i \, \mathrm{d}V = \int_R \rho \frac{\mathrm{d}v_i}{\mathrm{d}t} \, \mathrm{d}V \tag{B.5.1}$$

where $v_i(x_i, t)$ is the velocity vector at a point in the continuum. Using the Reynolds transport theorem (Appendix A), equation B.5.1 becomes

$$\int_S \sigma_i \, \mathrm{d}S + \int_R \rho f_i \, \mathrm{d}V = \int_R \frac{\partial (\rho v_i)}{\partial t} \, \mathrm{d}V + \int_S \rho v_i v_j n_j \, \mathrm{d}S \tag{B.5.2}$$

where $n_i(x_i)$ is the unit normal vector to the surface element $\mathrm{d}S$ on S. Expressing σ_i in terms of the stress tensor σ_{ij}, we can rewrite equation B.5.2 as

$$\int_S \sigma_{ij} n_j \,\mathrm{d}S + \int_R \rho f_i \,\mathrm{d}V = \int_R \frac{\partial\left(\rho v_i\right)}{\partial t} \,\mathrm{d}V + \int_S \rho v_i v_j n_j \,\mathrm{d}S \tag{B.5.3}$$

This is called the momentum integral equation governing the motion of the continuum through the control volume. Transforming the surface integrals in equation B.5.3 to a volume integral using Gauss' theorem yields

$$\int_R \left[\sigma_{ij,j} + \rho f_i - \frac{\partial\left(\rho v_i\right)}{\partial t} - \left(\rho v_i v_j\right)_{,j}\right] \mathrm{d}V = 0 \tag{B.5.4}$$

This equation should hold true for any arbitrary region of the continuum in motion, which means that the integrand on the left side should be identically equal to zero, or

$$\frac{\partial\left(\rho v_i\right)}{\partial t} + \left(\rho v_i v_j\right)_{,j} = \rho f_i + \sigma_{ij,j} \tag{B.5.5}$$

This is one form of the equation of motion. An alternative form can be obtained by first rewriting equation B.5.5 as follows

$$\begin{aligned} \left[v_i \frac{\partial \rho}{\partial t} + \rho \frac{\partial v_i}{\partial t}\right] + \left[v_i \left(\rho v_j\right)_{,j} + \rho v_j v_{i,j}\right] &= \rho f_i + \sigma_{ij,j} \\ \therefore v_i \frac{\partial \rho}{\partial t} + v_i \left(\rho v_j\right)_{,j} + \rho \frac{\partial v_i}{\partial t} + \rho v_j v_{i,j} &= \rho f_i + \sigma_{ij,j} \end{aligned} \tag{B.5.6}$$

Multiplying the continuity equation, equation B.4.3 by v_i yields

$$v_i \frac{\partial \rho}{\partial t} + v_i \left(\rho v_i\right)_{,i} = 0 \tag{B.5.7}$$

Equation B.5.7 corresponds to the first two terms in equation B.5.6, which on substitution yields

$$\rho \frac{\partial v_i}{\partial t} + \rho v_j v_{i,j} = \rho f_i + \sigma_{ij,j} \tag{B.5.8}$$

Further note that the comoving derivative of the velocity vector v_i is

$$\frac{\mathrm{d}v_i}{\mathrm{d}t} = \frac{\partial v_i}{\partial t} + \frac{\partial v_i}{\partial x_j}\frac{\mathrm{d}x_j}{\mathrm{d}t} = \frac{\partial v_i}{\partial t} + v_j v_{i,j} \tag{B.5.9}$$

Thus, the left side of equation B.5.8 is just the product of ρ and the comoving derivative of the velocity vector v_i. The equation of motion becomes

$$\rho \frac{\mathrm{d}v_i}{\mathrm{d}t} = \rho f_i + \sigma_{ij,j} \tag{B.5.10}$$

In the special case of static equilibrium of the medium the acceleration $\frac{\mathrm{d}v_i}{\mathrm{d}t}$ is zero and equation B.5.10 reduces to the partial differential equation of equilibrium

$$\rho f_i + \sigma_{ij,j} = 0 \tag{B.5.11}$$

Next the moment of momentum principle is considered. In a collection of particles whose interactions are equal, opposite, and co-linear forces, the time rate of change of the total moment of momentum for the given collection of particles is equal to the vector sum of the moments of the external forces acting on the system. In the absence of distributed couples, we postulate the same principle for a continuum.

Recall from elementary mechanics that the moment of any force F_i about the origin O is the vector product of the position vector x_i and the force F_i, or $\varepsilon_{ijk} x_j F_k$, where ε_{ijk} is the permutation symbol. Applying the moment equation to the free body diagram of figure B.6 gives rise to the following equation

$$\int_S \varepsilon_{ijk} x_j \sigma_k \,\mathrm{d}S + \int_R \varepsilon_{ijk} x_j f_k \rho \,\mathrm{d}V = \frac{\mathrm{d}}{\mathrm{d}t} \int_R \rho \varepsilon_{ijk} x_j v_k \,\mathrm{d}V \tag{B.5.12}$$

Substituting $\sigma_k = \sigma_{kr} n_r$ from equation B.2.8 yields

$$\int_S \varepsilon_{ijk} x_j \sigma_{kr} n_r \,\mathrm{d}S + \int_R \varepsilon_{ijk} x_j f_k \rho \,\mathrm{d}V = \frac{\mathrm{d}}{\mathrm{d}t} \int_R \varepsilon_{ijk} x_j \rho v_k \,\mathrm{d}V \tag{B.5.13}$$

The surface integral in equation B.5.13 can be reduced to a volume integral by using Gauss' theorem

$$\begin{aligned}
\int_S \varepsilon_{ijk} x_j \sigma_{kr} n_r \,\mathrm{d}S &= \int_R \left(\varepsilon_{ijk} x_j \sigma_{kr}\right)_{,r} \,\mathrm{d}V \\
&= \int_R \varepsilon_{ijk} \left(x_{j,r} \sigma_{kr} + x_j \sigma_{kr,r}\right) \,\mathrm{d}V \\
&= \int_R \varepsilon_{ijk} \left(\delta_{jr} \sigma_{kr} + x_j \sigma_{kr,r}\right) \,\mathrm{d}V \\
&= \int_R \varepsilon_{ijk} \left(\sigma_{kj} + x_j \sigma_{kr,r}\right) \,\mathrm{d}V
\end{aligned} \tag{B.5.14}$$

Hence, equation B.5.13 becomes

$$\begin{aligned}
\int_R \varepsilon_{ijk} \left(\sigma_{kj} + x_j \sigma_{kr,r}\right) \,\mathrm{d}V + \int_R \varepsilon_{ijk} x_j f_k \rho \,\mathrm{d}V &= \frac{\mathrm{d}}{\mathrm{d}t} \int_R \varepsilon_{ijk} x_j \rho v_k \,\mathrm{d}V \\
&= \int_R \varepsilon_{ijk} \rho \left(v_j v_k + x_j \frac{\mathrm{d}v_k}{\mathrm{d}t}\right) \,\mathrm{d}V
\end{aligned} \tag{B.5.15}$$

therofore

$$\int_R \varepsilon_{ijk} \left[\sigma_{kj} - \rho v_j v_k + x_j \left(\sigma_{kr,r} + \rho f_k - \rho \frac{\mathrm{d}v_k}{\mathrm{d}t} \right) \right] \mathrm{d}V = 0 \tag{B.5.16}$$

Noting that $\varepsilon_{ijk} v_j v_k = 0$, since $v_j v_k$ is symmetric in the indices jk while ε_{ijk} is antisymmetric and that

$$\sigma_{kr,r} + \rho f_k - \rho \frac{\mathrm{d}v_k}{\mathrm{d}t} = 0$$

is the equation of motion (equation B.5.10). Thus, equation B.5.16 reduces to

$$\int_R \varepsilon_{ijk} \sigma_{kj} \, \mathrm{d}V = 0 \tag{B.5.17}$$

Again this equation should hold true for any arbitrary region R of the continuum, which results in

$$\varepsilon_{ijk} \sigma_{kj} = 0 \tag{B.5.18}$$

This is the equation of angular momentum for a classic continuum. In expanded form equation B.5.18 becomes

$$\begin{aligned} &\text{for } i = 1 \quad \sigma_{32} - \sigma_{23} = 0 \\ &\text{for } i = 2 \quad \sigma_{13} - \sigma_{31} = 0 \\ &\text{for } i = 3 \quad \sigma_{21} - \sigma_{12} = 0 \end{aligned} \tag{B.5.19}$$

This establishes the symmetry of the stress tensor in general without any assumption of equilibrium or of uniformity of the stress distribution.

B.5.2 Lagrangian Description

The Eulerian form of the linear momentum equation is given by equation B.5.10.

$$\rho \frac{\mathrm{d}v_i}{\mathrm{d}t} = \rho f_i + \sigma_{ij,j}$$

where $\rho = \rho(x_i, t)$, $f_i = f_i(x_i, t)$, $\sigma_i = \sigma_i(x_i, t)$, $v_i(x_i, t) = \frac{\mathrm{d}x_i}{\mathrm{d}t}$. Using the rules to convert from the Eulerian to the Lagrangian description (Appendix A), we have

$$\frac{\mathrm{d}v_i(x_i, t)}{\mathrm{d}t} = \frac{\partial v_i(a_i, t)}{\mathrm{d}t} = \frac{\partial^2 u_i(a_i, t)}{\partial t^2} \tag{B.5.20}$$

$$\frac{\partial \sigma_{ij}(x_i, t)}{\partial x_i} = \frac{\partial \sigma_{ij}(a_i, t)}{\partial a_i} \tag{B.5.21}$$

We can also express the Eulerian functions ρ and f_i in terms of the Lagrangian coordinates, i.e.

$$\begin{aligned} \rho\left(x_i, t\right) &= \rho\left(a_i, t\right) \\ f_i\left(x_i, t\right) &= f_i\left(a_i, t\right) \end{aligned} \tag{B.5.22}$$

Therefore, the equation of linear momentum can be written as

$$\rho \frac{\partial^2 u_i}{\partial t^2} = \rho f_i + \sigma_{ij,j} \tag{B.5.23}$$

where all functions are expressed in terms of the Lagrangian coordinates a_i and time t, and the subscript "$,i$" means $\frac{\partial}{\partial a_i}$. The equation of angular momentum, equation B.5.18, is formulated in the Eulerian description. Using the same rules, this equation in the Lagrangian description becomes

$$\varepsilon_{ijk}\sigma_{kj} = 0 \tag{B.5.24}$$

where $\sigma_{kj} = \sigma_{kj}(a_i, t)$.

B.6 Strain Tensor

As the continuum moves from one configuration to another, the matter in the neighbourhood of each point is translated and rotated as a rigid body, and strained. Strain of an elemental volume is that part of the relative motion between neighbouring particles that is not due to rigid body motion.

B.6.1 General or Finite Strain

This is the strain that occurs in the medium when no restrictions are placed on the magnitude of the displacements or derivatives of the displacement with respect to position. The latter are called *displacement gradients*.

Eulerian Nonlinear Strain Tensor

Let P and Q be two neighbouring points in the medium before deformation, at time = 0. After a given motion, at time = t, these two points move to new positions p and q (figure B.7).

Using the Eulerian description, the vectors to the points can be written as follows

$$\begin{aligned} &P : a_i \\ &Q : a_i + da_i \\ &p : x_i = a_i + u_i\left(x_i, t\right) \\ &q : x_i + dx_i = a_i + da_i + u_i\left(x_i + dx_i, t\right) \end{aligned} \tag{B.6.1}$$

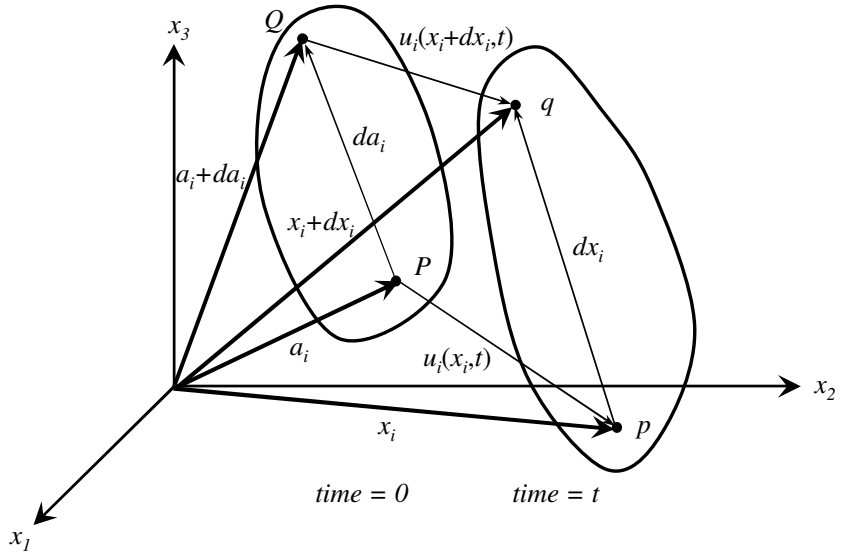

Figure B.7: Relative displacements between two neighbouring points in a continuum

where $u_i(x_i, t)$ and $u_i(x_i + dx_i, t)$ are the displacement vectors of P and Q respectively. The relative displacement vector between $P$and Q after a given deformation at a given time t is therefore the difference of the displacement vectors u_i^Q and u_i^P of the two points.

$$\mathrm{d}u_i = u_i^Q - u_i^P = u_i(x_i + dx_i, t) - u_i(x_i, t) \tag{B.6.2}$$

Assuming that the conditions that guarantee the existence of a derivative are met, the differential $\mathrm{d}u_i$ can be written as

$$\mathrm{d}u_i = \left(\frac{\partial u_i}{\partial x_j}\right)_p \mathrm{d}x_j \tag{B.6.3}$$

where the partial derivatives are evaluated at point p and at time t. As the medium moves as a result of the displacements, the volumetric element in the neighbourhood of P will translate and rotate as a rigid body and be strained. To distinguish between the local rigid body motion and straining, compute the difference of the square of the differential lengths between p, q and P, Q. This is done because mathematically it is more convenient to discuss than the difference of the same lengths. The squares of the lengths are

$$\begin{aligned} |PQ|^2 = (\mathrm{d}a)^2 &= \mathrm{d}a_i \mathrm{d}a_i \\ |pq|^2 = (\mathrm{d}x)^2 &= \mathrm{d}x_i \mathrm{d}x_i \end{aligned} \tag{B.6.4}$$

Therefore

$$(\mathrm{d}x)^2 - (\mathrm{d}a)^2 = \mathrm{d}x_i \mathrm{d}x_i - \mathrm{d}a_i \mathrm{d}a_i \tag{B.6.5}$$

At a given time t, the differential vector $\mathrm{d}a_i$ due to the difference of the position vectors at P and Q can be expressed as follows

$$\mathrm{d}a_i = \left(\frac{\partial a_i}{\partial x_j}\right)_p \mathrm{d}x_j \tag{B.6.6}$$

where the partial derivative is again evaluated at point p and at time t. Equation B.6.5 becomes

$$\begin{aligned}(\mathrm{d}x)^2 - (\mathrm{d}a)^2 &= \mathrm{d}x_i \mathrm{d}x_i - \mathrm{d}a_i \mathrm{d}a_i \\ &= \mathrm{d}x_i \mathrm{d}x_i - \frac{\partial a_r}{\partial x_i}\mathrm{d}x_i \frac{\partial a_r}{\partial x_j}\mathrm{d}x_j \\ &= \mathrm{d}x_i \left(\delta_{ij}\mathrm{d}x_j\right) - \frac{\partial a_r}{\partial x_i}\mathrm{d}x_i \frac{\partial a_r}{\partial x_j}\mathrm{d}x_j \\ &= \left[\delta_{ij} - \frac{\partial a_r}{\partial x_i}\frac{\partial a_r}{\partial x_j}\right]\mathrm{d}x_i \mathrm{d}x_j\end{aligned} \tag{B.6.7}$$

From the third equation in equation B.6.1 it follows that

$$x_i = a_i + u_i\left(x_i, t\right) \Leftrightarrow a_i = x_i - u_i\left(x_i, t\right) \tag{B.6.8}$$

Substituting this expression into the last of equation B.6.7 yields

$$\begin{aligned}(\mathrm{d}x)^2 - (\mathrm{d}a)^2 &= \left[\delta_{ij} - \frac{\partial a_r}{\partial x_i}\frac{\partial a_r}{\partial x_j}\right]\mathrm{d}x_i \mathrm{d}x_j \\ &= \left[\delta_{ij} - \frac{\partial}{\partial x_i}\left(x_r - u_r\right)\frac{\partial}{\partial x_j}\left(x_r - u_r\right)\right]\mathrm{d}x_i \mathrm{d}x_j \\ &= \left[\delta_{ij} - \left(\delta_{ri} - \frac{\partial u_r}{\partial x_i}\right)\left(\delta_{rj}x_r - \frac{\partial u_r}{\partial x_j}\right)\right]\mathrm{d}x_i \mathrm{d}x_j \\ &= \left[\delta_{ij} - \delta_{ij} + \delta_{ri}\frac{\partial u_r}{\partial x_j} + \delta_{rj}\frac{\partial u_r}{\partial x_i} - \frac{\partial u_r}{\partial x_i}\frac{\partial u_r}{\partial x_j}\right]\mathrm{d}x_i \mathrm{d}x_j \\ &= \left[\frac{\partial u_i}{\partial x_j} + \frac{\partial u_j}{\partial x_i} - \frac{\partial u_r}{\partial x_i}\frac{\partial u_r}{\partial x_j}\right]\mathrm{d}x_i \mathrm{d}x_j\end{aligned} \tag{B.6.9}$$

This equation can now be written as

$$(\mathrm{d}x)^2 - (\mathrm{d}a)^2 = 2E_{ij}\mathrm{d}x_i \mathrm{d}x_j \tag{B.6.10}$$

where

$$E_{ij} = \frac{1}{2}\left[\frac{\partial u_i}{\partial x_j} + \frac{\partial u_j}{\partial x_i} - \frac{\partial u_r}{\partial x_i}\frac{\partial u_r}{\partial x_j}\right] \tag{B.6.11}$$

is defined as the *Eulerian nonlinear strain tensor*. It is clear that the strain tensor as given by equation B.6.11 is symmetrical.

Lagrangian Nonlinear Strain Tensor

Following the same procedure used in the preceding discussion, but using a_i as the independent coordinates instead of x_i, we obtain the displacement vector

$$u_i = u_i\left(a_i, t\right) \tag{B.6.12}$$

and the differential $\mathrm{d}u_i$ becomes

$$\mathrm{d}u_i = \left(\frac{\partial u_i}{\partial a_j}\right)_P \mathrm{d}a_j \tag{B.6.13}$$

The *Lagrangian nonlinear strain tensor* then becomes

$$L_{ij} = \frac{1}{2}\left[\frac{\partial u_i}{\partial a_j} + \frac{\partial u_j}{\partial a_i} + \frac{\partial u_r}{\partial a_i}\frac{\partial u_r}{\partial a_j}\right] \tag{B.6.14}$$

B.6.2 Infinitesimal Strain

Infinitesimal strain tensors are characterised by small displacement gradients, i.e. $\frac{\partial u_i}{\partial x_j} << 1$ in the Eulerian description and $\frac{\partial u_i}{\partial a_j} << 1$ in the Lagrangian description.

Eulerian Linear Strain Tensor

Assuming the derivatives of the displacements to be small, the term involving the product of these derivatives in equation B.6.9 can be neglected in comparison with the other two terms, so that

$$(\mathrm{d}x)^2 - (\mathrm{d}a)^2 = \left[\frac{\partial u_i}{\partial x_j} + \frac{\partial u_j}{\partial x_i}\right]\mathrm{d}x_i\mathrm{d}x_j \tag{B.6.15}$$

We now define the *Eulerian linear strain tensor*

$$e_{ij} = \frac{1}{2}\left[\frac{\partial u_i}{\partial x_j} + \frac{\partial u_j}{\partial x_i}\right] \tag{B.6.16}$$

so that equation B.6.15 can be written as

$$(\mathrm{d}x)^2 - (\mathrm{d}a)^2 = 2e_{ij}\mathrm{d}x_i\mathrm{d}x_j \tag{B.6.17}$$

It should be emphasised that in the derivation given above, the assumption that the displacements are infinitesimal has not been used. The linear strain tensor e_{ij} is also symmetric and follows the usual law of transformation

for a second order Cartesian tensor. Let us now derive an expression for the change of length per unit of final length (length after deformation) for the line element *pq* (figure B.7). Introducing the symbol e as the change in length per unit of final length, this becomes

$$e = \frac{\mathrm{d}x - \mathrm{d}a}{\mathrm{d}x} \tag{B.6.18}$$

Factoring the left side of equation B.6.17 as follows

$$(\mathrm{d}x + \mathrm{d}a)\,(\mathrm{d}x - \mathrm{d}a) = 2e_{ij}\mathrm{d}x_i\mathrm{d}x_j \tag{B.6.19}$$

and using the assumption of small changes of length $(\mathrm{d}x + \mathrm{d}a) \approx 2\mathrm{d}x$, equation B.6.19 becomes

$$\begin{aligned} 2\mathrm{d}x\,(\mathrm{d}x - \mathrm{d}a) &= 2e_{ij}\mathrm{d}x_i\mathrm{d}x_j \\ \therefore \frac{(\mathrm{d}x - \mathrm{d}a)}{\mathrm{d}x} &= e_{ij}\frac{\mathrm{d}x_i}{\mathrm{d}x}\frac{\mathrm{d}x_j}{\mathrm{d}x} \end{aligned} \tag{B.6.20}$$

Substitution in equation B.6.18 yields

$$e = e_{ij}n_in_j \tag{B.6.21}$$

where

$$n_i = \frac{\mathrm{d}x_i}{\mathrm{d}x} \tag{B.6.22}$$

are the direction cosines of the line element *pq*.

Lagrangian Linear Strain Tensor

Following the same procedure as in the preceding section, the terms involving the product of displacement gradients can be ignored so that the equivalent of equation B.6.15 can be written as

$$(\mathrm{d}x)^2 - (\mathrm{d}a)^2 = \left[\frac{\partial u_i}{\partial a_j} + \frac{\partial u_j}{\partial a_i}\right]\mathrm{d}a_i\mathrm{d}a_j \tag{B.6.23}$$

We now define the *Lagrangian linear strain tensor*

$$l_{ij} = \frac{1}{2}\left(\frac{\partial u_i}{\partial a_j} + \frac{\partial u_j}{\partial a_i}\right) \tag{B.6.24}$$

so that equation B.6.23 becomes

$$(\mathrm{d}x)^2 - (\mathrm{d}a)^2 = 2l_{ij}\mathrm{d}a_i\mathrm{d}a_j \tag{B.6.25}$$

The tensor l_{ij} is also symmetric and follows the usual law of transformation for a second order Cartesian tensor. The change of length per unit initial length for the line PQ can be shown to be

$$l = \frac{dx - da}{da} = l_{ij}\frac{da_i}{da}\frac{da_j}{da} = l_{ij}n_i n_j \tag{B.6.26}$$

B.6.3 The Linear Rotation Tensor and Rotation Vector

Our studies of the roles of the rotation tensor and vector will be restricted to the case of the infinitesimal displacement gradients only.

Eulerian Description

Earlier it was established that the relative displacement of two neighbouring points, P and Q, using the Eulerian description, is (equation B.6.3)

$$\mathrm{d}u_i = \left(\frac{\partial u_i}{\partial x_j}\right)_p \mathrm{d}x_j \tag{B.6.27}$$

where it is understood that the partial derivatives are to be evaluated at p and at time t. Equation B.6.27 can be written as the sum of a symmetric part and a antisymmetric part

$$\mathrm{d}u_i = \left[\frac{1}{2}\left(\frac{\partial u_i}{\partial x_j} + \frac{\partial u_j}{\partial x_i}\right) + \frac{1}{2}\left(\frac{\partial u_i}{\partial x_j} - \frac{\partial u_j}{\partial x_i}\right)\right]\mathrm{d}x_j \tag{B.6.28}$$

Define the *Eulerian linear rotation tensor*

$$w_{ij} = \frac{1}{2}\left(\frac{\partial u_i}{\partial x_j} - \frac{\partial u_j}{\partial x_i}\right) \tag{B.6.29}$$

and equation B.6.27 can be written as

$$\mathrm{d}u_i = \left[e_{ij} + w_{ij}\right]\ \mathrm{d}x_j \tag{B.6.30}$$

If a given set of displacements constitute rigid body motion, then the $e_{ij} = 0$ everywhere. The converse is also true. Hence, the necessary and sufficient condition of the continuum to have no straining in the vicinity of a point p is that $e_{ij} = 0$. Study the relative displacement of q with respect to p for this case. Equation B.6.30 then becomes

$$\mathrm{d}u_i = w_{ij}\mathrm{d}x_j \tag{B.6.31}$$

This should represent the displacement of q relative to p due to an infinitesimal rigid body rotation of the vector dx_i only. The tensor w_{ij} is antisymmetric, i.e.

$$\begin{aligned} w_{11} &= w_{22} = w_{33} = 0 \\ w_{23} &= -w_{32} \\ w_{13} &= -w_{31} \\ w_{12} &= -w_{21} \end{aligned} \tag{B.6.32}$$

This means that the entire rotation tensor can be defined by three independent components. The following notation is introduced for these three components

$$\begin{aligned} w_1 = w_{32} &= -w_{23} \\ w_2 = w_{13} &= -w_{31} \\ w_3 = w_{21} &= -w_{12} \end{aligned} \tag{B.6.33}$$

The three components of w_i forms a vector called the *Eulerian linear rotation vector*. Equations B.6.32 and B.6.33 imply that the rotation vector w_i is expressible in terms of the rotation tensor

$$2w_i = \varepsilon_{ijk} w_{kj} \tag{B.6.34}$$

or inversely

$$w_{ji} = \varepsilon_{ijk} w_k \tag{B.6.35}$$

Furthermore, upon substitution of the linear rotation tensor, equation B.6.29, into equation B.6.34, the three components of the rotation vector can be shown to be identical to the components of one-half the curl of the displacement vector

$$w_i = \tfrac{1}{2} \varepsilon_{ijk} u_{k,j} \tag{B.6.36}$$

Lagrangian Description

Thus far, only the Eulerian description has been used. It is obvious that the same discussion may be applied to the relative displacement using the Lagrangian description referring everything to the undeformed length PQ and the coordinates a_i. Here, $\mathrm{d}u_i$ becomes

$$\mathrm{d}u_i = \left[l_{ij} + \tilde{w}_{ij} \right] \mathrm{d}a_j \tag{B.6.37}$$

where

$$l_{ij} = \frac{1}{2} \left(\frac{\partial u_i}{\partial a_j} + \frac{\partial u_j}{\partial a_i} \right) \tag{B.6.38}$$

is the linear Lagrangian strain tensor defined earlier and

$$\tilde{w}_{ij} = \frac{1}{2}\left(\frac{\partial u_i}{\partial a_j} - \frac{\partial u_j}{\partial a_i}\right) \tag{B.6.39}$$

is called the *Lagrangian linear rotation tensor*. The corresponding rotation vector is

$$2\tilde{w}_i = \varepsilon_{ijk}\tilde{w}_{kj} \tag{B.6.40}$$

or inversely

$$\tilde{w}_{ji} = \varepsilon_{ijk}\tilde{w}_k \tag{B.6.41}$$

Furthermore, these components can also be written as the components of one-half the curl of the displacement vector

$$\tilde{w}_i = \tfrac{1}{2}\varepsilon_{ijk}u_{k,j} \tag{B.6.42}$$

where

$$\begin{aligned} \tilde{w}_{11} &= \tilde{w}_{22} = \tilde{w}_{33} = 0 \\ \tilde{w}_{23} &= -\tilde{w}_{32} \\ \tilde{w}_{13} &= -\tilde{w}_{31} \\ \tilde{w}_{12} &= -\tilde{w}_{21} \end{aligned} \tag{B.6.43}$$

and

$$\begin{aligned} \tilde{w}_1 = \tilde{w}_{32} &= -\tilde{w}_{23} \\ \tilde{w}_2 = \tilde{w}_{13} &= -\tilde{w}_{31} \\ \tilde{w}_3 = \tilde{w}_{21} &= -\tilde{w}_{12} \end{aligned} \tag{B.6.44}$$

Except that the coordinates x_i are replaced by a_i, all properties and meanings assigned to the Eulerian rotation tensor and vector hold for the Lagrangian rotation tensor and vector. Finally, under the assumption of infinitesimal displacement gradients, it follows that

$$\begin{aligned} \tilde{w}_{ij} &\approx w_{ij} \\ l_{ij} &\approx e_{ij} \end{aligned} \tag{B.6.45}$$

Hence, the Eulerian description should yield approximately the same result as the Lagrangian description.

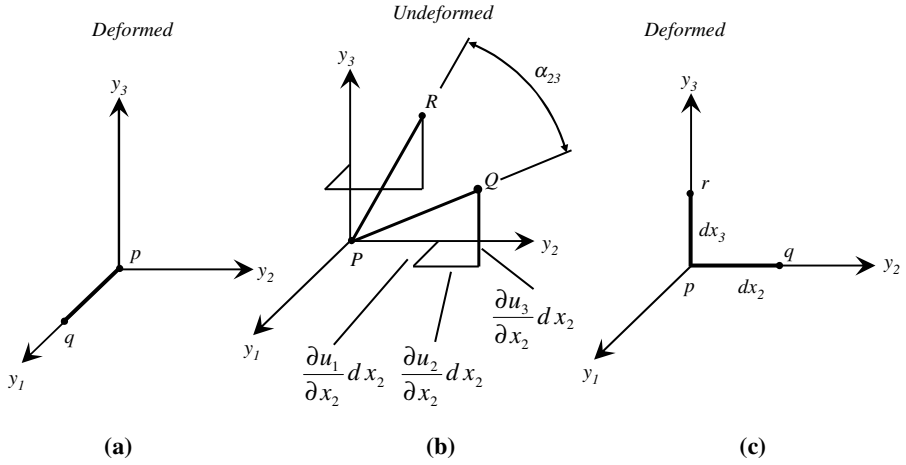

Figure B.8: (a) Line segment pq in the y_1 direction (b) Undeformed and (c) deformed states of two line segments finally orientated in the y_2- and y_3-directions

B.6.4 Geometrical Meanings of the Linear Strain Tensors

Eulerian Description

The Eulerian linear strain tensor is given by equation B.6.16.

$$e_{ij} = \frac{1}{2}\left[\frac{\partial u_i}{\partial x_j} + \frac{\partial u_j}{\partial x_i}\right] \tag{B.6.46}$$

Also the change of length per unit of final length of a line element is (equation B.6.21).

$$e = e_{ij} n_i n_j \tag{B.6.47}$$

and the relative displacement of q with respect to p (equation B.6.27)

$$\mathrm{d}u_i = \left(\frac{\partial u_i}{\partial x_j}\right)_P \mathrm{d}x_j \tag{B.6.48}$$

These three equations will now be used to give a geometrical or physical meaning to the components of strain. Let us first obtain a physical meaning of the diagonal components e_{11}, e_{22} and e_{33}. To begin, take the differential line segment pq in the x_1-direction, or along the y_1-(local) axis, as shown in Fig. B.8a. The direction cosines for this element are

$$n_i = (1, 0, 0) \tag{B.6.49}$$

Substituting these into equation B.6.47 yields

$$e = e_{11} \tag{B.6.50}$$

Therefore, e_{11} is the change of length per unit of original length of a differential line segment in the y_1-direction. Similarly, it can be shown that e_{22} and e_{33} are changes of length per unit length of the differential line segments drawn from p along the y_2- and y_3-directions respectively. Next, lets investigate the e_{23} off-diagonal element of the linear strain tensor as an example of all the off-diagonal elements.

Figures B.8b and B.8c show two sets of local Cartesian coordinates. The vector y_i has its origin at P in the undeformed body and the second y_i has its origin at p, the point to which the particle at P moves after deformation. Both sets are parallel to the global x_i-axes. A line segment pq after deformation along the y_2-axis has components of (0, $\mathrm{d}x_2$, 0), and the relative displacement of q with respect to Q after deformation has the components

$$\mathrm{d}u_i = \frac{\partial u_i}{\partial x_j}\mathrm{d}x_j \Rightarrow \left(\frac{\partial u_1}{\partial x_2}\mathrm{d}x_2, \frac{\partial u_2}{\partial x_2}\mathrm{d}x_2, \frac{\partial u_3}{\partial x_2}\mathrm{d}x_2\right) \tag{B.6.51}$$

The size of this vector is approximately

$$|\mathrm{d}u_i| = \sqrt{\left(\frac{\partial u_1}{\partial x_2}\mathrm{d}x_2\right)^2 + \left(\frac{\partial u_2}{\partial x_2}\mathrm{d}x_2\right)^2 + \left(\frac{\partial u_3}{\partial x_2}\mathrm{d}x_2\right)^2} \approx \mathrm{d}x_2 \tag{B.6.52}$$

Therefore, to the lowest order, the components of a unit vector in the direction of the undeformed line segment PQ are approximately as follows

$$\left(\frac{\partial u_1}{\partial x_2}, 1, \frac{\partial u_3}{\partial x_2}\right) \tag{B.6.53}$$

In the same way, if we consider a differential line segment pr after deformation in the y_3-direction, it will have components in the deformed state of (0,0,$\mathrm{d}x_3$). The unit vector along the line element PR in the undeformed state has the components

$$\left(\frac{\partial u_1}{\partial x_3}, \frac{\partial u_2}{\partial x_3}, 1\right) \tag{B.6.54}$$

Hence, to the lowest order, the cosine of the angle α_{23} between the two undeformed line segments PQ and PR is given by taking the dot product of the two unit vectors specified by equation B.6.53 and B.6.54. Thus,

$$\begin{aligned} \cos\alpha_{23} &= \frac{\partial u_1}{\partial x_2}\frac{\partial u_1}{\partial x_3} + \frac{\partial u_2}{\partial x_3} + \frac{\partial u_3}{\partial x_2} \\ &\approx \frac{\partial u_2}{\partial x_3} + \frac{\partial u_3}{\partial x_2} = 2e_{23} \end{aligned} \tag{B.6.55}$$

Let the increase from the angle α_{23} in the undeformed state to the right angle in the deformed state between the two differential line segments be β_{23}. Then

$$\beta_{23} = \tfrac{\pi}{2} - \alpha_{23} \tag{B.6.56}$$

But in the infinetesimal theory, β_{23} is very small, so that

$$\beta_{23} \approx \sin\beta_{23} = \cos\alpha_{23} \tag{B.6.57}$$

Therefore, the difference in angle between the two line segments is

$$\begin{aligned} &\beta_{23} = 2e_{23} = 2e_{32} \text{ and also} \\ &\beta_{13} = 2e_{13} = 2e_{31} \\ &\beta_{13} = 2e_{13} = 2e_{31} \end{aligned} \tag{B.6.58}$$

The three strain tensor components e_{23}, e_{31}, and e_{12}, are thus equal to one-half the change of angle between two line segments that lie along the y_i-directions in the deformed medium.

Lagrangian Description

The same procedures can be used to demonstrate the geometrical meanings of the components of the Lagrangian linear strain tensor. The diagonal components of the strain tensor l_{11}, l_{22} and l_{33} can be shown to be the change of length per unit *original* length of a differential line segment *originally* in the y_1, y_2 and y_3-directions respectively. The two line segments PQ and PR are assumed to be orthogonal and in the direction of the local y_2 and y_3-directions as depicted in figure B.9a.

Figure B.9b shows the two line segments in the deformed state. Using the relative displacements depicted in figure B.9 and following the same procedures as in the previous section, it follows that

$$\begin{aligned} \beta_{23} = 2l_{23} &= 2l_{32} \\ \beta_{13} = 2l_{13} &= 2l_{31} \\ \beta_{12} = 2l_{12} &= 2l_{21} \end{aligned} \tag{B.6.59}$$

The three tensor strain components l_{23}, l_{31} and l_{12} are thus equal to one-half the change of angle between two line segments *originally* 90° apart along the directions indicated by the numerical subscripts. These are one-half the familiar "shearing strains" as defined in a course in strength of materials.

B.7 Principal Strains and Principal Axes

In this section the principal axis theory for the linear strain tensor is given. Consider a general movement of the continuum in the vicinity of a point

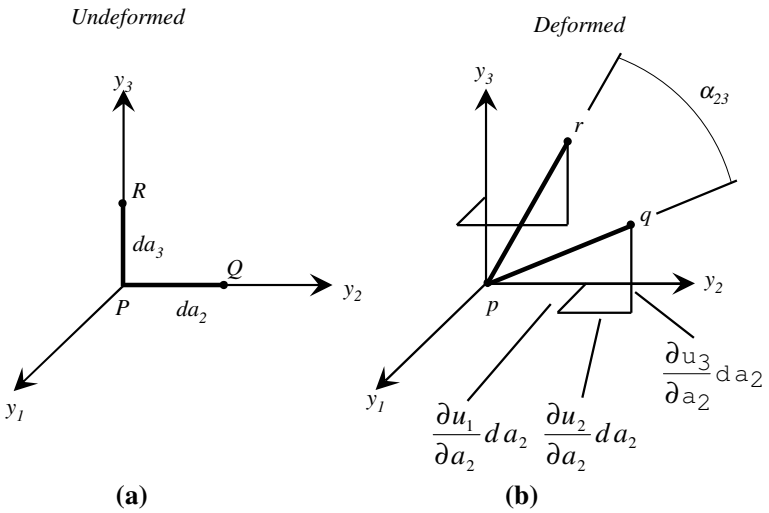

Figure B.9: (a) Undeformed and (b) deformed state of two line segments

P, which consists of straining and rigid body rotation and translation. The effects of rigid body rotation and straining can be studied separately and then superimposed. In this section we shall consider the effects of pure strain only. Due to straining only, the displacement vector of a neighbouring point Q relative to P is

$$\mathrm{d}u_i = l_{ij}\mathrm{d}a_j \tag{B.7.1}$$

or the relative displacement of Q with respect to P per unit of original length is a vector whose components are

$$l_i = \frac{\mathrm{d}u_i}{\mathrm{d}a} = l_{ij}n_j \tag{B.7.2}$$

where $\mathrm{d}a$ is the differential length PQ and $n_i\mathrm{d}a_i/\mathrm{d}a$ is the unit vector in the direction of PQ. In general the relative displacement vector per unit length is not in the original direction of the line segment PQ, nor is it in the deformed direction of the line segment pq. Following the same procedure that was used in defining principal directions for the stress tensor, define a *principal direction for the strain tensor* as an orientation of the line segment PQ for which the line element retains the property of perpendicularity to the surface of the particles originally in its perpendicular plane. Considering the effects of strain only, this means that the relative displacement vector l_i per unit of length has the same direction as the original line element PQ. This should not be confused with the idea of an invariant direction, for when the effects of rotation are added, the principal line elements will be rotated from their original orientations. The magnitude of such a relative displacement per unit length (now a normal strain) is called a *principal strain*, and

the corresponding axis is called a *principal axis* of strain. By definition, for such a direction, the following equation must be satisfied

$$l_i = ln_i = l\delta_{ij}n_j \tag{B.7.3}$$

where l is the principal strain. Substituting for l_i from equation B.7.2, equation B.7.3 becomes

$$\left(l_{ij} - l\delta_{ij}\right) n_j = 0 \tag{B.7.4}$$

Furthermore, the components of the unit vector always satisfy $n_i n_i = 1$. The nontrivial solution for n_i in equation B.7.4 require that the determinant of the coefficients of the n_i be equal to zero

$$\left|l_{ij} - l\delta_{ij}\right| = 0 \tag{B.7.5}$$

In general, equation B.7.5 will yield three values of l. These three principal strains will be denoted by l_1, l_2 and l_3. In the Eulerian description, the principal directions are defined as those for which the displacement vector per unit length of deformed line due to pure strain

$$e_i = e_{ij}n_j \tag{B.7.6}$$

is in the direction of the deformed segment. Stated in a different way, a principal direction is one for which the deformed line element retains the property of perpendicularity to the surface of particles originally in its perpendicular plane. The direction cosines are $\bar{n}_i$. The magnitude of e_i for a principal direction is a principal strain. Equations for determining this are

$$\begin{aligned} \left(e_{ij} - \delta_{ij}e\right) n_j &= 0 \\ n_i n_i &= 1 \end{aligned} \tag{B.7.7}$$

where e is a principal strain. The principal values e_1, e_2 and e_3 are given by the following determinant

$$\left|e_{ij} - e\delta_{ij}\right| = 0 \tag{B.7.8}$$

B.8 The Linear Cubical Dilatation

The cubical dilatation D, in the Eulerian description, is defined as the increase of volume per unit of final volume in the neighbourhood of a point p in the continuum. Infinitesimal theory applies.

Consider a differential rectangular parallelepiped in the deformed medium with one corner at p. Let its three edges of lengths $\mathrm{d}x_1$, $\mathrm{d}x_2$ and $\mathrm{d}x_3$

coincide with the principal directions of strain. From the definition of D, the cubical dilatation of this parallelepiped is given by

$$\begin{aligned} D &= \frac{V_{\text{deformed}} - V_{\text{undeformed}}}{V_{\text{deformed}}} \\ &= \frac{\mathrm{d}x_1\mathrm{d}x_2\mathrm{d}x_3 - \mathrm{d}x_1\,[1+e(1)]\,\mathrm{d}x_2\,[1+e(2)]\,\mathrm{d}x_3\,[1+e(3)]}{\mathrm{d}x_1\mathrm{d}x_2\mathrm{d}x_3} \end{aligned} \tag{B.8.1}$$

Neglecting terms involving product of e_1, e_2, e_3 because of the infinitesimal assumption, D becomes

$$D = e_1 + e_2 + e_3 = e_{ii} \tag{B.8.2}$$

where e_{ii} is the first invariant of the Eulerian strain tensor. Therefore the first strain invariant e_{ii} in any coordinate system is the cubical dilatation D. In the Lagrangian description, the cubical dilatation $\tilde{D}$ is defined as the increase of volume per unit of original volume in the neighbourhood of a point P in the continuum. Letting the three edges of the rectangular parallelepiped be $\mathrm{d}a_1$, $\mathrm{d}a_2$ and $\mathrm{d}a_3$ and following the same procedure it follows that

$$\tilde{D} = l_1 + l_2 + l_3 = l_{ii} \tag{B.8.3}$$

B.9 Compatibility Equations for Linear Strain Components

B.9.1 Eulerian Description

The symmetric Eulerian linear strain tensor given by equation B.6.16

$$e_{ij} = \frac{1}{2}\left[\frac{\partial u_i}{\partial x_j} + \frac{\partial u_j}{\partial x_i}\right]$$

is equivalent to six equations with the six independent components e_{ij} on the one side and the three displacements u_i on the other. If the strains are determined first, we have six equations for the determining the three unknown displacements u_i. In general, a set of displacements for any elasticity problem will not exist unless the strains e_{ij} satisfy certain conditions. The equations that the strains components must satisfy in order that the displacements be single-valued and continuous are called *compatibility equations*. They are both necessary and sufficient conditions.

We shall derive these equations and establish their necessity and sufficiency. Consider two points in a continuum whose coordinates are $x_i(1)$

and $x_i(2)$, using the Eulerian description. We wish to compute the displacements $u_i(1)$, relative to $u_i(2)$, along some curve C joining the two points. If the displacement vector u_i is single-valued and continuous, then

$$u_i(2) = u_i(1) + \int_C \mathrm{d}u_i \tag{B.9.1}$$

where C is any continuous curve joining $x_i(1)$ and $x_i(2)$. But from equation B.6.30

$$\mathrm{d}u_i = \left[e_{ij} + w_{ij}\right] \mathrm{d}x_j$$

Therefore

$$u_i(2) = u_i(1) + \int_C e_{ij}\mathrm{d}x_j + \int_C w_{ij}\mathrm{d}x_j \tag{B.9.2}$$

For convenience in integrating, substitute $\mathrm{d}\left[x_j - x_j(2)\right]$ for $\mathrm{d}x_j$ in the second integral. This is an identity, for x_j is any point on C, and $x_j(2)$ is constant for the second end point. Hence,

$$u_i(2) = u_i(1) + \int_C e_{ij}\mathrm{d}x_j + \int_C w_{ij}\mathrm{d}\left[x_j - x_j(2)\right] \tag{B.9.3}$$

Using the technique of integration by parts on the second integral, it can be expressed as

$$\begin{aligned}\int_C w_{ij}\mathrm{d}\left[x_j - x_j(2)\right] &= \left[w_{ij}\left[x_j - x_j(2)\right]\right]_{(1)}^{(2)} - \int_C \left[x_j - x_j(2)\right] w_{ij,k}\,\mathrm{d}x_k \\ &= -w_{ij}(1)\left[x_j(1) - x_j(2)\right] - \int_C \left[x_j - x_j(2)\right] w_{ij,k}\,\mathrm{d}x_k\end{aligned} \tag{B.9.4}$$

But

$$\begin{aligned}w_{ij,k} &= \tfrac{1}{2}\left(u_{i,j} - u_{j,i}\right)_{,k} = \tfrac{1}{2}\left(u_{i,jk} - u_{j,ik}\right) \\ &= \tfrac{1}{2}\left(u_{i,jk} + u_{k,ij}\right) - \tfrac{1}{2}\left(u_{j,ik} + u_{k,ij}\right) \\ &= e_{ik,j} - e_{jk,i}\end{aligned} \tag{B.9.5}$$

Hence the integral of equation B.9.4 can be written as

$$\int_C w_{ij}\mathrm{d}\left[x_j - x_j(2)\right] = -w_{ij}(1)\left[x_j(1) - x_j(2)\right] + \int_C \left[x_j - x_j(2)\right]\left(e_{jk,i} - e_{ik,j}\right)\mathrm{d}x_k \tag{B.9.6}$$

Thus, substituting equation B.9.6 into equation B.9.3, it becomes

$$u_i(2) = u_i(1) + \int_C e_{ik}\mathrm{d}x_k - w_{ij}(1)\left[x_j(1) - x_j(2)\right] + \int_C \left[x_j - x_j(2)\right]\left(e_{jk,i} - e_{ik,j}\right)\mathrm{d}x_k \tag{B.9.7}$$

or

$$u_i(2) = u_i(1) - w_{ij}(1)\left[x_j(1) - x_j(2)\right] + \int_C F_{ik}\mathrm{d}x_k \tag{B.9.8}$$

where

$$F_{ik} = e_{ik} + \left[x_j - x_j(2)\right]\left(e_{jk,i} - e_{ik,j}\right) \tag{B.9.9}$$

Since the displacement vector is single-valued and continuous, the integral $\int_C F_{ik}\mathrm{d}x_k$ must be independent of the path of integration. In other words, the integral should yield the same result for any continuous curve C joining $x_i(1)$ and $x_i(2)$. Hence there must exist three functions $G_i(x)$ that are single-valued and have continuous derivatives such that

$$F_{ik}\mathrm{d}x_k = \mathrm{d}G_i = G_{i,k}\mathrm{d}x_k \tag{B.9.10}$$

This means that

$$F_{ik} = G_{i,k} \tag{B.9.11}$$

But the functions G_i have continuous derivatives through the second-ordered ones, so the necessary and sufficient conditions that the u_i can be calculated are

$$G_{i,kl} = G_{i,lk} \tag{B.9.12}$$

and therefore

$$F_{ik,l} = F_{il,k} \tag{B.9.13}$$

Writing equation B.9.13 in terms of the strain components, we obtain

$$\begin{aligned} e_{ik,l} + \left[x_j - x_j(2)\right]\left(e_{jk,il} - e_{ik,jl}\right) + \left(e_{jk,i} - e_{ik,j}\right)\delta_{jl} \\ = e_{il,k} + \left[x_j - x_j(2)\right]\left(e_{jl,ik} - e_{il,jk}\right) + \left(e_{jl,i} - e_{il,j}\right)\delta_{jk} \end{aligned} \tag{B.9.14}$$

in this equation all terms containing derivatives of strain alone or with the Kronecker delta as a coefficient cancel, leaving the following

$$\left[x_j - x_j(2)\right]\left(e_{jk,il} + e_{il,jk} - e_{ik,jl} - e_{jl,ik}\right) = 0 \tag{B.9.15}$$

Equation B.9.15 holds for any arbitrary point x_i. Consequently, the coefficient of $\left[x_j - x_j(2)\right]$ must vanish. Thus, a necessary and sufficient condition for the displacement vector u_i to be single-valued and continuous is

$$e_{ik,jl} + e_{jl,ik} = e_{jk,il} + e_{il,jk} \tag{B.9.16}$$

or by interchanging the indices j and k

$$e_{ij,kl} + e_{kl,ij} = e_{jk,il} + e_{il,jk} \tag{B.9.17}$$

where the symmetry property of the strain tensor has been used in the first term on the right-hand side and the order of the differentiation has been changed in the last. For the final form, the indices i and j on the right-hand side of equation B.9.17 are switched, and the same properties are used again on the left side. Thus

$$e_{ij,kl} + e_{kl,ij} = e_{ik,jl} + e_{jl,ik} \tag{B.9.18}$$

Equation B.9.18 represents a set of $3^4 = 81$ equations. They are called the *compatibility equations* for the linear strain components in the Eulerian description. Of these 81 equations only 6 are independent. The numerical choices for the indices for the independent equations are the following

$$\begin{array}{rcccccc} i: & 1 & 3 & 2 & 1 & 2 & 3 \\ j: & 1 & 3 & 2 & 1 & 2 & 3 \\ k: & 2 & 1 & 3 & 2 & 3 & 1 \\ l: & 2 & 1 & 3 & 3 & 1 & 2 \end{array} \tag{B.9.19}$$

B.9.2 Lagrangian Description

Using the Lagrangian linear strain tensor l_{ij}, the same discussion will hold true for the Lagrangian description, provided that $\frac{\partial u_i(a_i,t)}{\partial a_j} << 1$. With this restriction, the compatibility equations are

$$l_{ij,kl} + l_{kl,ij} = l_{ik,jl} + l_{jl,ik} \tag{B.9.20}$$

B.10 The Rate of Strain Tensor and the Vorticity Tensor

The stress required to deform a medium may be some function of the magnitudes of the strains and the rate at which the deformation takes place. The exact functional relationship varies from material to material. In a purely elastic solid, rates of straining are not important, whereas the stresses in a fluid depend mainly upon the rates of strain. In this section, we shall be interested primarily in the rate at which deformation takes place.

Introduce the Eulerian velocity field $v_i(x_i,t)$ of each particle of the continuum as a function of its instantaneous position and time. Consider a given instance in time t. At this instant, the velocity of a particle p in the deformed medium is v_i, figure B.10. Consider the variation of velocity due to position only, the velocity of a neighbouring particle q, where the vector

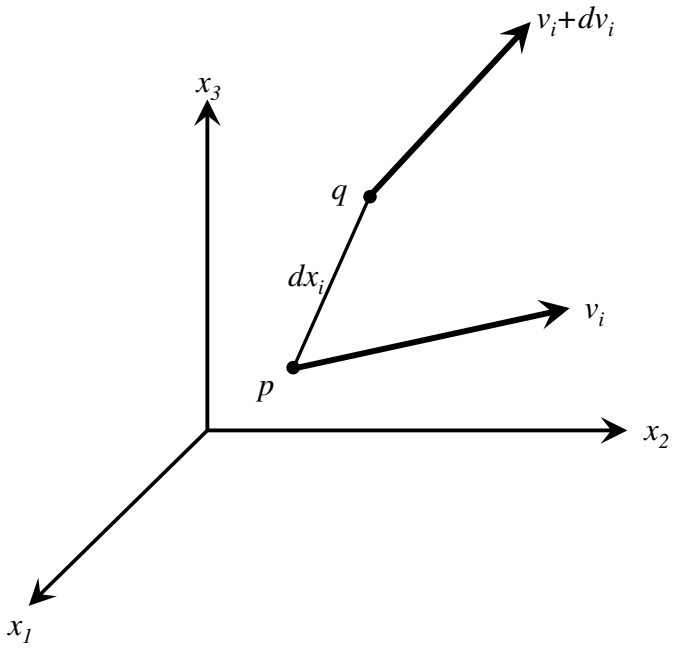

Figure B.10: Velocity components for neighbouring particles p and q

from p to q is $\mathrm{d}x_i$, will be $v_i + \mathrm{d}v_i$. Or, using $\mathrm{d}v_i = \frac{\partial v_i}{\partial x_j}\mathrm{d}x_j = v_{i,j}\mathrm{d}x_j$, we may write

$$v_i\left(x_i + \mathrm{d}x_i, t\right) = v_i\left(x_i, t\right) + v_{i,j}\mathrm{d}x_j$$

where $v_{i,j}$ is called the *velocity gradient tensor*. It is a measure of the relative velocity between two neighbouring particles in the deformed medium. The velocity gradient tensor can be expressed as the sum of a symmetric and a skew-symmetric part.

$$v_{ij} = \tfrac{1}{2}\left(v_{i,j} + v_{j,i}\right) + \tfrac{1}{2}\left(v_{i,j} - v_{j,i}\right) \tag{B.10.1}$$

or

$$v_{ij} = \psi_{ij} + \omega_{ij} \tag{B.10.2}$$

where

$$\psi_{ij} = \tfrac{1}{2}\left(v_{i,j} + v_{j,i}\right) \tag{B.10.3}$$

is defined as the *rate of strain tensor* (*rate of deformation tensor, strain rate tensor* or *velocity strain tensor*).

$$\omega_{ij} = \tfrac{1}{2}\left(v_{i,j} - v_{j,i}\right) \tag{B.10.4}$$

is called the *vorticity tensor*. The velocity of q relative to p, or $\mathrm{d}v_i$, can be written as

$$\mathrm{d}v_i = v_i\left(x_i + \mathrm{d}x_i, t\right) - v_i\left(x_i, t\right) = \left(\psi_{ij} + \omega_{ij}\right)\mathrm{d}x_j \tag{B.10.5}$$

Let us now relate the rate of strain tensor ψ_{ij} to the Eulerian linear strain tensor e_{ij} and the vorticity tensor ω_{ij} to the rotation tensor w_{ij}. The linear strain tensor follows from equation B.6.16

$$e_{ij} = \frac{1}{2}\left[u_{i,j} + u_{j,i}\right]$$

Now take the comoving derivative of both sides

$$\frac{\mathrm{d}e_{ij}}{\mathrm{d}t} = \frac{1}{2}\left(\frac{\mathrm{d}}{\mathrm{d}t}u_{i,j} + \frac{\mathrm{d}}{\mathrm{d}t}u_{j,i}\right) \tag{B.10.6}$$

But $\frac{\mathrm{d}u_i}{\mathrm{d}t} = v_i$ are the Eulerian velocity components. Upon interchanging the order of differentiation on the right side of equation B.10.6 gives

$$\frac{\mathrm{d}e_{ij}}{\mathrm{d}t} = \frac{1}{2}\left[\left(\frac{\mathrm{d}u_i}{\mathrm{d}t}\right)_{,j} + \left(\frac{\mathrm{d}u_j}{\mathrm{d}t}\right)_{,i}\right] = \tfrac{1}{2}\left(v_{i,j} + v_{j,i}\right) = \psi_{ij} \tag{B.10.7}$$

In the same way it can be shown that

$$\frac{\mathrm{d}w_{ij}}{\mathrm{d}t} = \omega_{ij} \tag{B.10.8}$$

Thus, ψ_{ij} and ω_{ij} are simply comoving derivatives of e_{ij} and w_{ij} respectively. Physically, $\psi_{ij}$is a measure of the rate of straining, and ω_{ij} is the time rate of rigid body rotation for the medium in the neighbourhood of p.

B.11 The Rate of Rotation Vector and the Vorticity Vector

From the definition of the vorticity tensor, equation B.10.4

$$\omega_{ij} = \tfrac{1}{2}\left(v_{i,j} - v_{j,i}\right)$$

which is a symmetric tensor, i.e.

$$\begin{aligned}
\omega_{11} &= \omega_{22} = \omega_{33} = 0 \\
\omega_{23} &= -\omega_{32} \\
\omega_{31} &= -\omega_{13} \\
\omega_{12} &= -\omega_{21}
\end{aligned} \tag{B.11.1}$$

Since there are only three independent components, this means that the components of the vorticity tensor can be related to the components of a vector as follows

$$\begin{aligned} \omega_1 = -\omega_{23} &= \omega_{32} \\ \omega_2 = -\omega_{31} &= \omega_{13} \\ \omega_3 = -\omega_{12} &= \omega_{21} \end{aligned} \tag{B.11.2}$$

The vector ω_i is called the *rate of rotation vector*. The rate of rotation vector and the vorticity vector are related to the vorticity tensor as follows

$$\begin{aligned} 2\omega_i = \zeta_i &= \varepsilon_{ijk}\omega_{kj} \\ \omega_{ji} = \varepsilon_{ijk}\omega_k &= \tfrac{1}{2}\varepsilon_{ijk}\zeta_k \end{aligned} \tag{B.11.3}$$

where ζ_i is called the *vorticity vector*, defined as twice the rate of rotation vector. The rate of rotation vector and the vorticity vector can also be related to the curl of the velocity field

$$2\omega_i = \zeta_i = \varepsilon_{ijk}v_{k,j} \tag{B.11.4}$$

Appendix C

Polar Continuum Mechanics

C.1 Introduction

In Appendix B we have assumed the nonpolar case with no distributed couples (moments) on the boundary surface and internal surfaces and no body couples. External couple distributions could result from the action of an external magnetic field on magnetised particles of the material or the action of an electric field on polarised matter. Even without assigned external couples, couple-stress can arise from interactions between adjacent parts of the material other than central-force interactions.

We have considered only the force per unit area transmitted across a surface at a point and not a possible couple. When a continuous distribution of force acts across a finite area ΔS, the resultant of the distributions, in general, is a force and a couple. If the result is divided by ΔS and the limit taken as ΔS tends to zero, it is found that the couple per unit area produced at the point by the continuous distribution of force is zero. This does not, of course, preclude the possibility that there might also be a continuous distribution of couple, whose limit (per unit area) would be different from zero, i.e. a couple-stress.

C.2 The Cosserat Equations

In a theory of deformation of continua by E. Cosserat and F. Cosserat in 1909, the couple per unit area (*couple-stresses*), acting across a surface within a material volume or on its boundary, is taken into account in addition to the usual force per unit area.

C.2.1 The Couple-Stress Tensor and Couple-Stress Vector

As in Appendix B.2, consider a planar surface area ΔS oriented by the unit normal vector n_i and containing the point P. This planar surface separates a portion of a material volume R_1 from the remainder R_2. Let ΔF_i be the total force that the material on the $+n_i$ side exerts on the material on the $-n_i$ side across the surface (figure C.1). In addition to the force, a total moment ΔM_i is also exerted on the material. The moment vector ΔM_i is taken as positive in the direction of advance of a right handed thread.

The stress vector at point P is defined by equation B.2.4. The couple-

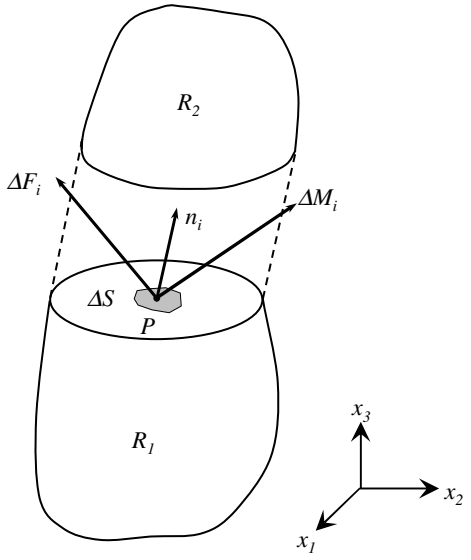

Figure C.1: Resultant force and couple acting on area ΔS

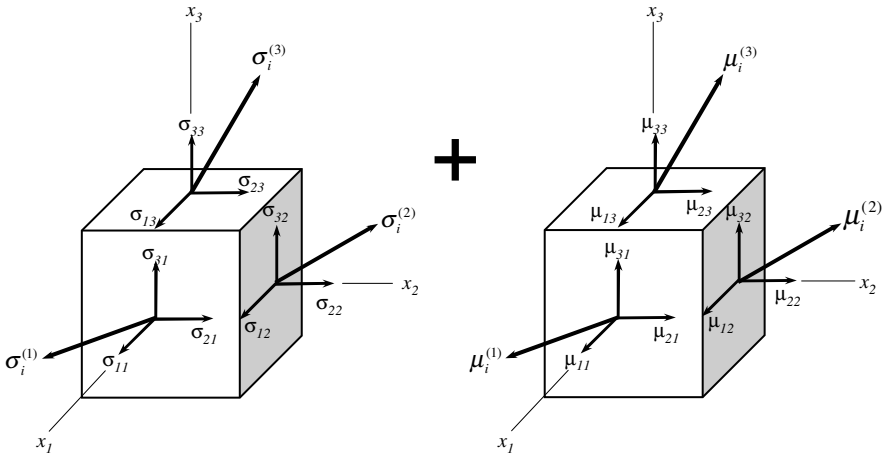

Figure C.2: (a) Stress vectors and stress tensor components (b) Couple-stress vectors and couple-stress components

stress vector (also at point P) is defined similarly

$$\mu_i = \lim_{\Delta S \to 0} \frac{\Delta M_i}{\Delta S} \tag{C.2.1}$$

The Cauchy stress theorem relating the stress tensor σ_{ij} and the stress vector σ_i was shown to be

$$\sigma_i = \sigma_{ij} n_j \tag{C.2.2}$$

An similar expression can be written that relates the couple-stress tensor μ_{ij} and the couple-stress vector μ_i.

$$\mu_i = \mu_{ij} n_j \tag{C.2.3}$$

To prove equation C.2.3, consider a point P in a continuum. Figure C.2a shows the stress vectors and stress tensor components as shown in Appendix B and figure C.2b shows the couple-stress vectors and couple-stress tensor components. These two sets of stresses act simultaneously at point P, but are shown separately to avoid confusion. Take the unit vector n_i of the surface containing point P to be in the direction of the x_2-axis (the shaded surface in figure C.2b).

The couple-stress vector μ_i on this element is, in general, in some arbitrary direction, but may be resolved into three orthogonal components. The components of the couple-stress vector $\mu_i^{(2)}$ are μ_{12}, μ_{22} and μ_{32}, where the first subscript indicates the direction of the couple stress component and the second subscript indicates the direction of the normal vector to the surface. Similarly we can visualise two other couple-stress vectors $\mu_i^{(1)}$ and $\mu_i^{(3)}$ acting on surface elements whose normals are in the positive x_1- and x_3-directions respectively. They have couple-stress components of μ_{11}, μ_{21}, μ_{31} and μ_{13}, μ_{23}, μ_{33} respectively. Consider a Cauchy tetrahedron at point P, bounded by three coordinate planes and a sloping face normal to n_i as shown in figure C.3. The local Cartesian coordinate system has its origin at P.

Figure C.3a shows the stress vectors acting on the four sides of the tetrahedron and figure C.3b shows the couple-stress vectors acting on the same tetrahedron. Again these two sets of traction vectors act simultaneously on the tetrahedron, but are shown separately to avoid confusion. The presence of the couples does not affect the consideration of linear momentum, and the relation between the stress vector and the stress tensor still holds

$$\sigma_i = \sigma_{ij} n_j \tag{C.2.4}$$

We now apply the moment of momentum principle to the mass inside the tetrahedron. Couple-stresses and -forces acting on the tetrahedron are

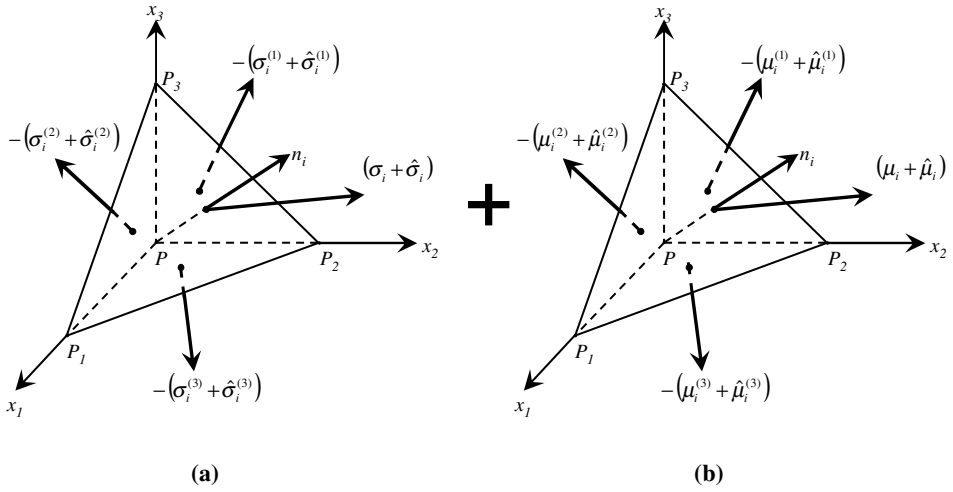

Figure C.3: Small tetrahedron at point P with (a) stress vectors and (b) with couple-stress vectors

μ_i = couple-stress vector at P acting across a small surface element whose normal is n_i

μ_{ij} = couple-stress tensor at point P

c_i = body-couple vector per unit mass

h = depth of tetrahedron measured from the sloping face

ρ = density at point P

It is clear that average quantities must be introduced, since the tetrahedron is finite. Define the following average quantities:

$\mu_i + \hat{\mu}_i$ = average couple-stress vector

$-\left(\mu_i^{(1)} + \hat{\mu}_i^{(1)}\right)$ = average couple-stress vector across surface PP_2P_3 on the tetrahedron. The negative sign appears because $\left(\mu_i^{(1)} + \hat{\mu}_i^{(1)}\right)$ would denote the average couple-stress vector on a surface whose outward normal pointed in the positive x_1-direction. Couples are defined as positive if the couple vector (axis vector according to the right-hand-rule) points in the positive axis direction.

$-\left(\mu_i^{(2)} + \hat{\mu}_i^{(2)}\right)$ = average couple-stress vector across surface PP_1P_3 on the tetrahedron.

$-\left(\mu_i^{(3)} + \hat{\mu}_i^{(3)}\right)$ = average couple-stress vector across surface PP_1P_2 on the tetrahedron.

$c_i + \hat{c}_i$ = average body couple per unit mass

$\rho + \hat{\rho}$ = average density of the tetrahedron

The area of the sloping surface $P_1P_2P_3$ is A and

$$\lim_{h\to 0}\left(\hat{\mu}_i, \hat{\mu}_{ij}, \hat{c}_i, \hat{\rho}\right) = 0 \tag{C.2.5}$$

As the altitude h will be allowed to approach zero so that the volume of the four surface areas simultaneously approach zero, while the position of P does not change. It follows that the average values will approach the local values at the point P, and the result will be an expression for the couple-stress vector μ_i at point P in terms of the other three special surface couple-stress vectors at P.

Suppose that the particles of the continuum may posses *spin angular momentum* h_i^c (per unit mass, i.e. $\mathrm{kg{\cdot}m^2{\cdot}s^{-1}{\cdot}kg^{-1}} = \mathrm{m^2{\cdot}s^{-1}}$). The expression for the total moment of momentum is derived in Appendix D, and the expression for h_i^c is given in vector notation as $\overrightarrow{\boldsymbol{h}}^c$. The Eulerian moment of momentum equation of the classical non-polar continuum, equation B.5.12

$$\int_S \varepsilon_{ijk} x_j \sigma_k \,\mathrm{d}S + \int_R \varepsilon_{ijk} x_j f_k \rho \,\mathrm{d}V = \frac{\mathrm{d}}{\mathrm{d}t}\int_R \varepsilon_{ijk} x_j \rho v_k \,\mathrm{d}V \tag{C.2.6}$$

is extended in two ways. Firstly, the volume body moment c_i per unit mass and the surface moment per unit area μ_i are introduced in addition to the moments of the body force per unit mass f_i and the surface force per unit area σ_i. Secondly, include the *spin angular momentum* h_i^c as described above. The angular momentum balance with reference to point P in figure C.3 becomes

$$\int_S \left(\varepsilon_{ijk} x_j \sigma_k + \mu_i\right)\, \mathrm{d}S + \int_R \rho \left(\varepsilon_{ijk} x_j f_k + c_i\right)\, \mathrm{d}V = \frac{\mathrm{d}}{\mathrm{d}t} \int_R \rho \left(\varepsilon_{ijk} x_j v_k + h_i^c\right)\, \mathrm{d}V \quad \text{(C.2.7)}$$

With x_j measured from the vertex of the tetrahedron, it is apparent that for non-vanishing μ_i, c_i and h_i^c and for finite σ_k, f_k and v_i the contributions of the terms containing the cross products are of an order higher than the other terms as the altitude h of the tetrahedron tends to zero. We accordingly omit them now and apply the mean-value theorem of integral calculus to the integrals over the faces and the volume of the tetrahedron. We thus obtain

$$-\left(\mu_i^{(1)} + \hat{\mu}_i^{(1)}\right)(n_1 A) - \left(\mu_i^{(2)} + \hat{\mu}_i^{(2)}\right)(n_2 A) - \left(\mu_i^{(3)} + \hat{\mu}_i^{(3)}\right)(n_3 A) + \left(\mu_i + \hat{\mu}_i\right) A + \left(\rho + \hat{\rho}\right)\left(c_i + \hat{c}_i\right)\left(\tfrac{1}{3} A h\right) = \left(\rho + \hat{\rho}\right) \frac{\mathrm{d}h_i^c}{\mathrm{d}t} \left(\tfrac{1}{3} A h\right) \quad \text{(C.2.8)}$$

where $PP_2P_3 = n_1 A$ and according to equation A.5.28

$$\frac{\mathrm{d}}{\mathrm{d}t} \int_R \rho h_i^c \, \mathrm{d}V = \int_R \rho \frac{\mathrm{d}h_i^c}{\mathrm{d}t} \, \mathrm{d}V \quad \text{(C.2.9)}$$

Now let h approach zero and noting that the conditions in equation C.2.5 hold, equation C.2.8 becomes

$$\begin{aligned} \mu_i &= \mu_i^{(1)} n_1 + \mu_i^{(2)} n_2 + \mu_i^{(3)} n_3 \\ \therefore \mu_i &= \mu_{ij} n_j \end{aligned} \quad \text{(C.2.10)}$$

where the couple-stress vector μ_i on an arbitrary plane is expressed in terms of the couple-stress on the coordinate planes through the point.

C.2.2 Momentum Balance Principles

Eulerian Description

The presence of the couple-stresses does not affect the linear momentum principle; hence the equations of motion of the nonpolar continuum, equa-

tion B.5.10, still applies

$$\rho \frac{\mathrm{d}v_i}{\mathrm{d}t} = \rho f_i + \sigma_{ij,j} \tag{C.2.11}$$

where $v_i\left(x_i, t\right) = \frac{\mathrm{d}x_i}{\mathrm{d}t}$. We must, however, reconsider the moment of momentum equation of the non-polar continuum, equation B.5.12

$$\int_S \varepsilon_{ijk} x_j \sigma_k \, \mathrm{d}S + \int_R \varepsilon_{ijk} x_j f_k \rho \, \mathrm{d}V = \frac{\mathrm{d}}{\mathrm{d}t} \int_R \rho \varepsilon_{ijk} x_j v_k \, \mathrm{d}V \tag{C.2.12}$$

Including the body couple, the surface couples and the spin angular momentum, this equation becomes (equation C.2.7)

$$\int_S \left(\varepsilon_{ijk} x_j \sigma_k + \mu_i\right) \, \mathrm{d}S + \int_R \rho \left(\varepsilon_{ijk} x_j f_k + c_i\right) \, \mathrm{d}V = \frac{\mathrm{d}}{\mathrm{d}t} \int_R \rho \left(\varepsilon_{ijk} x_j v_k + h_i^c\right) \, \mathrm{d}V \tag{C.2.13}$$

Substituting $\sigma_k = \sigma_{kr} n_r$ and $\mu_i = \mu_{ij} n_j$ yields

$$\int_S \left(\varepsilon_{ijk} x_j \sigma_{kr} n_r + \mu_{ij} n_j\right) \, \mathrm{d}S + \int_R \rho \left(\varepsilon_{ijk} x_j f_k + c_i\right) \, \mathrm{d}V = \frac{\mathrm{d}}{\mathrm{d}t} \int_R \rho \left(\varepsilon_{ijk} x_j v_k + h_i^c\right) \, \mathrm{d}V \tag{C.2.14}$$

The surface integral can be reduced to a volume integral by applying Gauss' theorem

$$\begin{aligned}
\int_S \left(\varepsilon_{ijk} x_j \sigma_{kr} n_r + \mu_{ij} n_j\right) \, \mathrm{d}S &= \int_S \left(\varepsilon_{ijk} x_j \sigma_{kr} n_r\right) \, \mathrm{d}S + \int_S \left(\mu_{ij} n_j\right) \, \mathrm{d}S \\
&= \int_R \left(\varepsilon_{ijk} x_j \sigma_{kr}\right)_{,r} \, \mathrm{d}V + \int_R \left(\mu_{ij}\right)_{,j} \, \mathrm{d}V \\
&= \int_R \varepsilon_{ijk} \left(x_{j,r} \sigma_{kr} + x_j \sigma_{kr,r}\right) \, \mathrm{d}V + \int_R \mu_{ij,j} \, \mathrm{d}V \\
&= \int_R \varepsilon_{ijk} \left(\delta_{jr} \sigma_{kr} + x_j \sigma_{kr,r}\right) \, \mathrm{d}V + \int_R \mu_{ij,j} \, \mathrm{d}V \\
&= \int_R \left[\varepsilon_{ijk} \left(\sigma_{kj} + x_j \sigma_{kr,r}\right) + \mu_{ij,j}\right] \, \mathrm{d}V
\end{aligned} \tag{C.2.15}$$

Hence equation C.2.14 becomes

$$\int_R \left[\varepsilon_{ijk}\left(\sigma_{kj} + x_j\sigma_{kr,r}\right) + \mu_{ij,j}\right]\,\mathrm{d}V + \int_R \rho\left(\varepsilon_{ijk}x_j f_k + c_i\right)\,\mathrm{d}V$$
$$= \frac{\mathrm{d}}{\mathrm{d}t}\int_R \rho\left(\varepsilon_{ijk}x_j v_k + h_i^c\right)\,\mathrm{d}V$$
$$= \int_R \rho\left[\varepsilon_{ijk}\left(v_j v_k + x_j\frac{\mathrm{d}v_k}{\mathrm{d}t}\right) + \frac{\mathrm{d}h_i^c}{\mathrm{d}t}\right]\,\mathrm{d}V$$

Thus,

$$\int_R \left[\varepsilon_{ijk}\left(\sigma_{kj} + x_j\sigma_{kr,r} + \rho x_j f_k - \rho v_j v_k - \rho x_j\frac{\mathrm{d}v_k}{\mathrm{d}t}\right) + \mu_{ij,j} + \rho c_i - \rho\frac{\mathrm{d}h_i^c}{\mathrm{d}t}\right]\,\mathrm{d}V = 0$$

Therefore

$$\int_R \left[\varepsilon_{ijk}\left(\sigma_{kj} + x_j\left(\sigma_{kr,r} + \rho f_k - \rho\frac{\mathrm{d}v_k}{\mathrm{d}t}\right) - \rho v_j v_k\right) + \mu_{ij,j} + \rho c_i - \rho\frac{\mathrm{d}h_i^c}{\mathrm{d}t}\right]\,\mathrm{d}V = 0 \tag{C.2.16}$$

Noting that $\varepsilon_{ijk}v_j v_k = 0$ and that

$$\sigma_{kr,r} + \rho f_k - \rho\frac{\mathrm{d}v_k}{\mathrm{d}t} = 0$$

is the equation of linear motion, equation C.2.11, then equation C.2.16 reduces to

$$\int_R \left[\varepsilon_{ijk}\sigma_{kj} + \mu_{ij,j} + \rho c_i - \rho\frac{\mathrm{d}h_i^c}{\mathrm{d}t}\right]\,\mathrm{d}V = 0 \tag{C.2.17}$$

Again this equation should hold true for any arbitrary region R of the continuum which results in

$$\varepsilon_{ijk}\sigma_{kj} + \mu_{ij,j} + \rho c_i = \rho\frac{\mathrm{d}h_i^c}{\mathrm{d}t} \tag{C.2.18}$$

With $\sigma_{kj} = \sigma_{kj}(x_i, t)$, $\mu_{ij} = \mu_{ij}(x_i, t)$, $\rho = \rho(x_i, t)$, $c_i = c_i(x_i, t)$, $h_i^c = h_i^c(x_i, t)$ and "$,i$" = $\frac{\partial}{\partial x_i}$. This is the Eulerian equation of angular momentum for a polar continuum. It forms a set of three partial differential equations expressing the rotational momentum principle in the presence of couple stresses μ_{ij}, body couples c_i per unit mass, and spin angular momentum h_i^c per unit mass. The Cauchy stress tensor σ_{ij} is nonsymmetric in general, though symmetry could be retained if c_i, μ_{ij} and h_i^c were to form an equilibrated system by themselves.

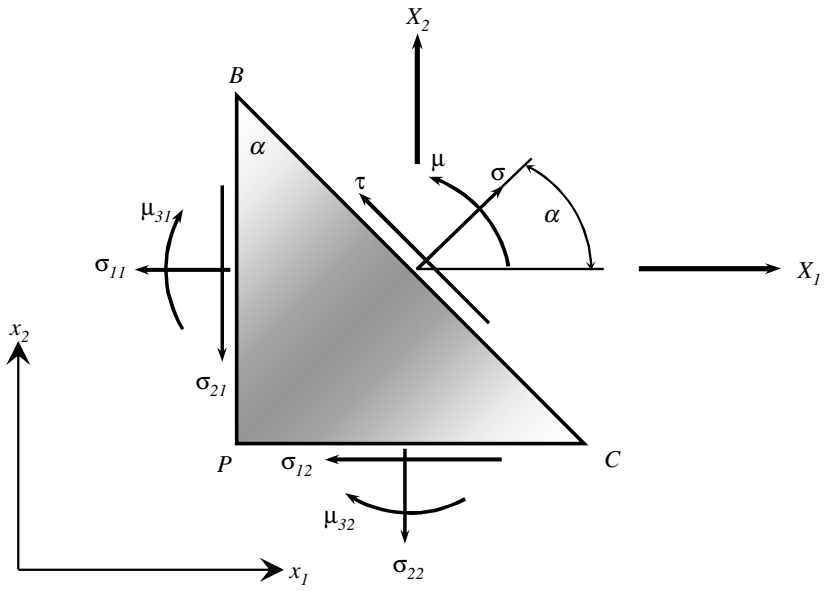

Figure C.4: Non-symmetric stress and couple stress state in a Cosserat continuum

Lagrangian Description

The Lagrangian linear momentum equation still holds, equation B.5.23.

$$\rho \frac{\partial^2 u_i}{\partial t^2} = \rho f_i + \sigma_{ij,j} \tag{C.2.19}$$

where $\rho = \rho\left(a_i, t\right)$, $f_i = f_i\left(a_i, t\right)$, $\sigma_{ij} = \sigma_{ij}\left(a_i, t\right)$ and the subscript "$,i$" means $\frac{\partial}{\partial a_i}$. The Eulerian angular momentum equation is given by equation C.2.18. Using the rules to convert from the Eulerian to the Lagrangian description (Appendix A), equation C.2.18 can be written as

$$\varepsilon_{ijk}\sigma_{kj} + \mu_{ij,j} + \rho c_i = \rho \frac{\partial h_i^c}{\partial t} \tag{C.2.20}$$

where all functions are expressed in terms of the Lagrangian coordinates a_i and time t.

C.2.3 Mohr's Circle of Non-Symmetric Stress Tensor

It is well known that the stress acting on any plane through a point at which the stress components are known, can be calculated from the equations of statics. This analysis leads to the Mohr circle representation. Consider a plane stress or plane strain problem in the x_1x_2 plane. Let point P be any point in the continuum with the known stress and couple-stress components σ_{12}, σ_{21}, σ_{22}, σ_{11}, μ_{31}, μ_{32} as depicted in figure C.4.

Take the plane BC parallel to the x_3 axis, at a small distance from P, so that this plane together with the two coordinate planes cuts out from the material a very small triangular prism PBC. Since the stresses vary continuously over the volume of the body, the stresses acting on the plane BC will approach the stresses on the parallel plane through P as the element is made smaller. In discussing the conditions of equilibrium of a small triangular prism, the body force and body moment can be neglected as a small quantity of a higher order.

Note that this is not the case when the equilibrium equation of a small volumetric cubic is considered for the derivation of the momentum balance principles (section C.2.2). This is because the body force and body moment have the same order of magnitude as the terms owing to the variations of the stress components that are under consideration. The triangular prism is also assumed very small and the variation of the stresses over the sides can be ignored and assumed to be uniformly distributed. If the area of side BC is A, the area of BP can be shown to be $A\cos\alpha$ and the area of side PC to be $A\sin\alpha$. If we denote by X_1 and X_2 the components of stress acting on the side BC, the equations of translational equilibrium of the prismatical element give

$$\begin{aligned} X_1 &= \sigma_{11}\cos\alpha + \sigma_{12}\sin\alpha \\ X_2 &= \sigma_{21}\cos\alpha + \sigma_{22}\sin\alpha \end{aligned} \tag{C.2.21}$$

The normal σ and shearing τ components of stress on plane BC can be written as

$$\begin{aligned} \sigma = X_1\cos\alpha + X_2\sin\alpha &= \sigma_{11}\cos^2\alpha + \sigma_{22}\sin^2\alpha + (\sigma_{12}+\sigma_{21})\sin\alpha\cos\alpha \\ \tau = X_2\cos\alpha - X_1\sin\alpha &= \sigma_{21}\cos^2\alpha - \sigma_{12}\sin^2\alpha + (\sigma_{22}-\sigma_{11})\sin\alpha\cos\alpha \end{aligned} \tag{C.2.22}$$

The rotational equilibrium equation is

$$\mu = \mu_{32}\sin\alpha + \mu_{31}\cos\alpha \tag{C.2.23}$$

After some algebraic manipulation (Iordache and Willam, 1998), equation C.2.22 can be written as

$$(\sigma - \sigma_c)^2 + (\tau - \tau_c)^2 = r^2 \tag{C.2.24}$$

where

$$\sigma_c = \frac{\sigma_{11}+\sigma_{22}}{2}, \quad \tau_c = \frac{\sigma_{21}-\sigma_{12}}{2}, \quad r^2 = \left(\frac{\sigma_{11}-\sigma_{22}}{2}\right)^2 + \left(\frac{\sigma_{12}+\sigma_{21}}{2}\right)^2$$

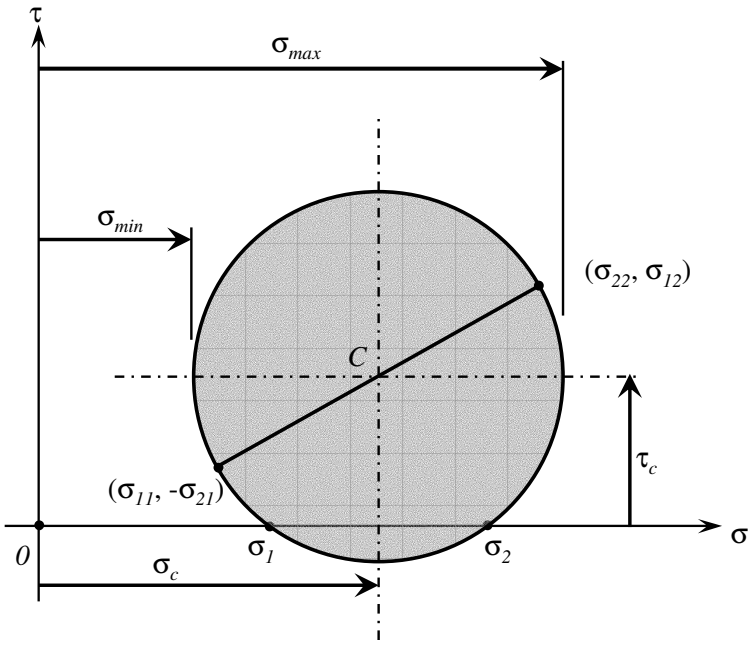

Figure C.5: Mohr's circle of a non-symmetric state of stress

Equation C.2.24 represents a circle called the generalised *Mohr's circle* as shown in figure C.5. Shear stress is taken positive in the upward direction (figure C.5) and consider shear stresses as positive when they give a couple in the clockwise direction (figure C.4). This representation of the non-symmetric state of stress in the Mohr plane, leads to a circle in two dimensions whose centre is no longer located on the σ-axis as is the case with a non-polar continuum. The shift of the centre of the Mohr's circle is a measure of the loss of symmetry. If the Mohr circle does not intersect the σ-axis, then there exist no real valued principal stresses. Setting $\tau = 0$, in equation C.2.24, yields the following quadratic equation in σ

$$\sigma^2 - 2\sigma_c\sigma + \left(\sigma_c^2 + \tau_c^2 - r^2\right) = 0 \tag{C.2.25}$$

Solving for the roots of σ

$$\begin{aligned} \sigma &= 2\sigma_c \pm \frac{\sqrt{4\sigma_c^2 - 4\left(\sigma_c^2 + \tau_c^2 - r^2\right)}}{2} \\ &= 2\sigma_c \pm \frac{\sqrt{\left(\sigma_{11} - \sigma_{22}\right)^2 + 4\sigma_{12}\sigma_{21}}}{2} \end{aligned} \tag{C.2.26}$$

The principal normal stresses σ_1 and σ_2 (figure C.5) are real-valued only as long as the discriminant is positive, i.e.

$$\Delta_\sigma > 0 \quad \text{where} \quad \Delta_\sigma = \left(\sigma_{11} - \sigma_{22}\right)^2 + 4\sigma_{12}\sigma_{21} \tag{C.2.27}$$

When $\Delta_\sigma < 0$, then the two eigenvalues turn complex, which corresponds to a Mohr circle that no longer intersects the σ-axis, and thus has no real-valued principal stresses. This can only happen if σ_{12} and σ_{21} have opposite signs. In this context it is important to recall the Bromwich bounds (Iordache and Willam, 1998) according to which the eigenvalues of the symmetrised state enclose the lowest and highest eigenvalues of the non-symmetric state of stress

$$\sigma_{\min} = \sigma_2^{\text{sym}} \leqslant \Re(\sigma_2) \leqslant \Re(\sigma_1) \leqslant \sigma_1^{\text{sym}} = \sigma_{\max} \tag{C.2.28}$$

For example, the non-symmetric state of stress

$$\sigma_{ij} = \begin{bmatrix} 1.5 & 0.3 \\ 0.7 & 0.5 \end{bmatrix} \tag{C.2.29}$$

has principal values $\sigma_1 = 1.678$ and $\sigma_2 = 0.322$, which are bound by the maximum and minimum values of the symmetrised stress state

$$\sigma_{ij} = \begin{bmatrix} 1.5 & 0.5 \\ 0.5 & 0.5 \end{bmatrix} \tag{C.2.30}$$

with principal values of $\sigma_1 = 1.707$ and $\sigma_2 = 0.293$. This elementary example illustrates that the real-valued maximum and minimum normal stresses bound the principal normal stresses of zero shear.

C.3 Kinematics of Cosserat Continua

The kinematics of micropolar continua are characterised by rotational degrees of freedom $w_i^c \to \mathbb{R}^3$, which are independent of the translatory motion described by the displacement field u_i. Thus the field of continuum macro-rotations does no longer coincide with that of micro-rotations at each material particle, i.e. the micro-rotation w_i^c differs from the classical macro-rotation w_i (equation B.6.34) since three rotational degrees-of-freedom are introduced in addition to the conventional three translational degrees-of-freedom. Assign a local rigid triad to every material point of the continuum body.

The symmetric linear strain tensor is given by equation B.6.16

$$e_{ij} = \frac{1}{2}\left(\frac{\partial u_i}{\partial x_j} + \frac{\partial u_j}{\partial x_i}\right) \tag{C.3.1}$$

and the skew-symmetric linear rotation tensor by equation B.6.29

$$w_{ij} = \frac{1}{2}\left(\frac{\partial u_i}{\partial x_j} - \frac{\partial u_j}{\partial x_i}\right) \tag{C.3.2}$$

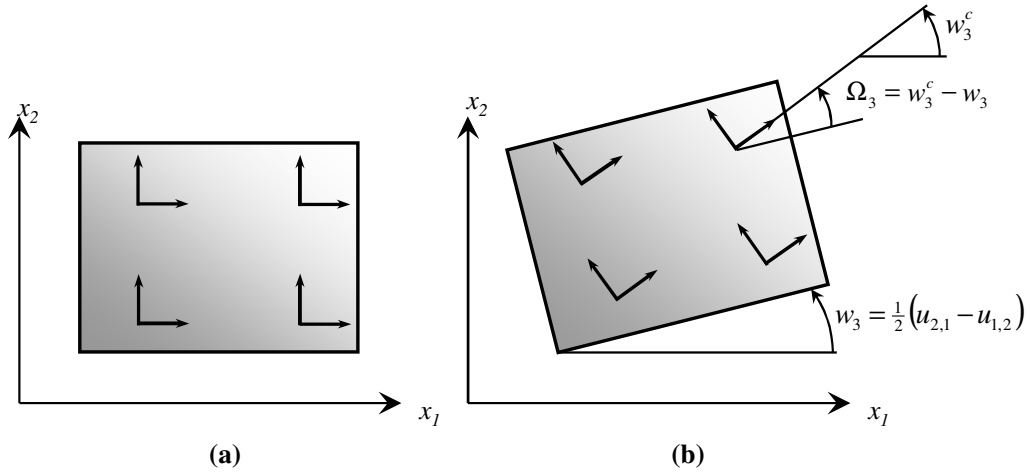

Figure C.6: (a) Unrotated and (b) rotated state in a Cosserat continuum

The rotation vector is given by equation B.6.34

$$w_i = \tfrac{1}{2}\varepsilon_{ijk} w_{kj} \tag{C.3.3}$$

For the formulation of constitutive relationships, we need deformation measures which are invariant with respect to rigid body motions. In the Cosserat theory, we have two other deformation measures, namely

$$\Omega_k = w_k - w_k^c \tag{C.3.4}$$

which represents the relative rotation between the material element and the Cosserat rotation at the material point, and

$$\kappa_{ij} = w_{i,j}^c \tag{C.3.5}$$

which is a measure for the relative Cosserat rotation between neighbouring material points. Figure C.6 shows the two-dimensional (planar deformation) formulation of the Cosserat continuum. Equation C.3.4 can also be written as follows (with the use of equation B.6.40)

$$\begin{aligned} \varepsilon_{ijk}\Omega_k = \varepsilon_{ijk} w_k - \varepsilon_{ijk} w_k^c \quad &\Rightarrow \quad \Omega_{ji} = w_{ji} - w_{ji}^c \\ &\Rightarrow \quad \Omega_{ij} = w_{ij} - w_{ij}^c \end{aligned} \tag{C.3.6}$$

Equations C.3.1 and C.3.6 can be combined into a single, tensorial deformation measure, namely

$$\lambda_{ij} = u_{i,j} + \varepsilon_{ijk} w_k^c \tag{C.3.7}$$

or

$$\lambda_{ij} = \begin{bmatrix} u_{1,1} & (u_{1,2} + w_3^c) & (u_{1,3} - w_2^c) \\ (u_{2,1} - w_3^c) & u_{2,2} & (u_{2,3} + w_1^c) \\ (u_{3,1} + w_2^c) & (u_{3,2} - w_1^c) & u_{3,3} \end{bmatrix} \tag{C.3.8}$$

This "relative deformation or strain" tensor can now be decomposed into symmetric and skew-symmetric components.

$$\begin{aligned} \lambda_{ij} &= \lambda_{ij}^{\text{sym}} + \lambda_{ij}^{\text{skew}} \\ &= \left[\tfrac{1}{2}\left(u_{i,j} + u_{j,i}\right)\right] + \left[\tfrac{1}{2}\left(u_{i,j} - u_{j,i}\right) + \varepsilon_{ijk} w_k^c\right] \\ &= e_{ij} + \left(w_{ij} + w_{ji}^c\right) \\ &= e_{ij} + \left(w_{ij} - w_{ij}^c\right) \\ &= e_{ij} + \Omega_{ij} = \tfrac{1}{2}\left(\lambda_{ij} + \lambda_{ji}\right) + \tfrac{1}{2}\left(\lambda_{ij} - \lambda_{ji}\right) \end{aligned} \tag{C.3.9}$$

The symmetric part reduces to the linear macro-strain tensor and the skew-symmetric part is the relative rotation. The shear deformation λ_{ij} can be interpreted as depicted in figure C.7, (Mindlin, 1964).

The relation between micro-curvature and couple-stresses is depicted in figure C.8 (Boresi and Chong, 2000) for the two-dimensional case. Mindlin (1964) calls the micro-curvature the macro-gradient of the micro-deformation. Where the application of shear stresses cause the material to deform as depicted in figure C.7, the couple stresses cause the material to deform as shown in figure C.8. The rigid triad at the lower left-hand corner (top figure) rotates by w_3^c while the triad at the lower right-hand corner rotates by $w_3^c + \frac{\partial w_3^c}{\partial x_1} \triangle x_1$. Thus, the relative rotation is, as shown, $\frac{\partial w_3^c}{\partial x_1} \triangle x_1$. Using the relation between arc length, radius and the angle, it can easily be shown that the radius R_{31} is the inverse of the curvature κ_{31}. The same reasoning can be applied to the bottom figure. The curvatures describe the kinematic field quantities that are energetically conjugate to the couple-stresses (Dietsche *et al.*, 1993).

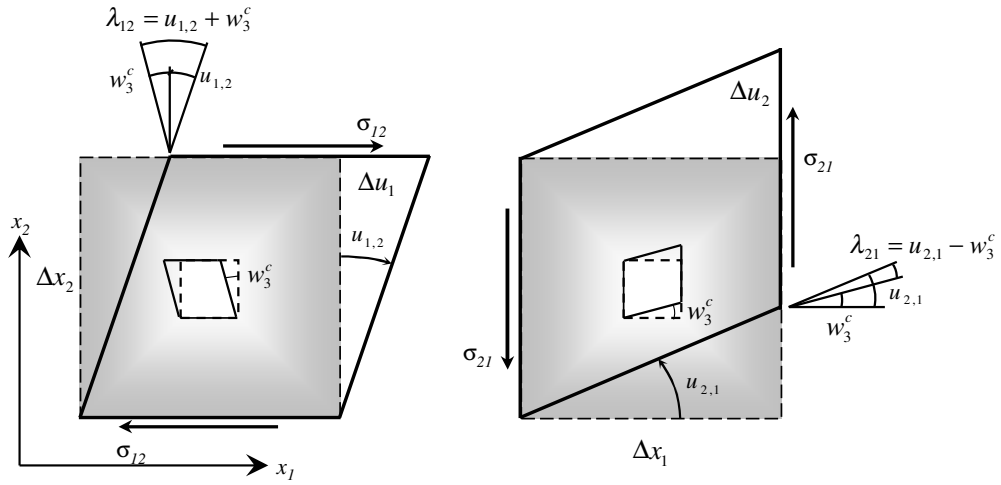

Figure C.7: Interpretation of the shear stress deformations in a Cosserat continuum

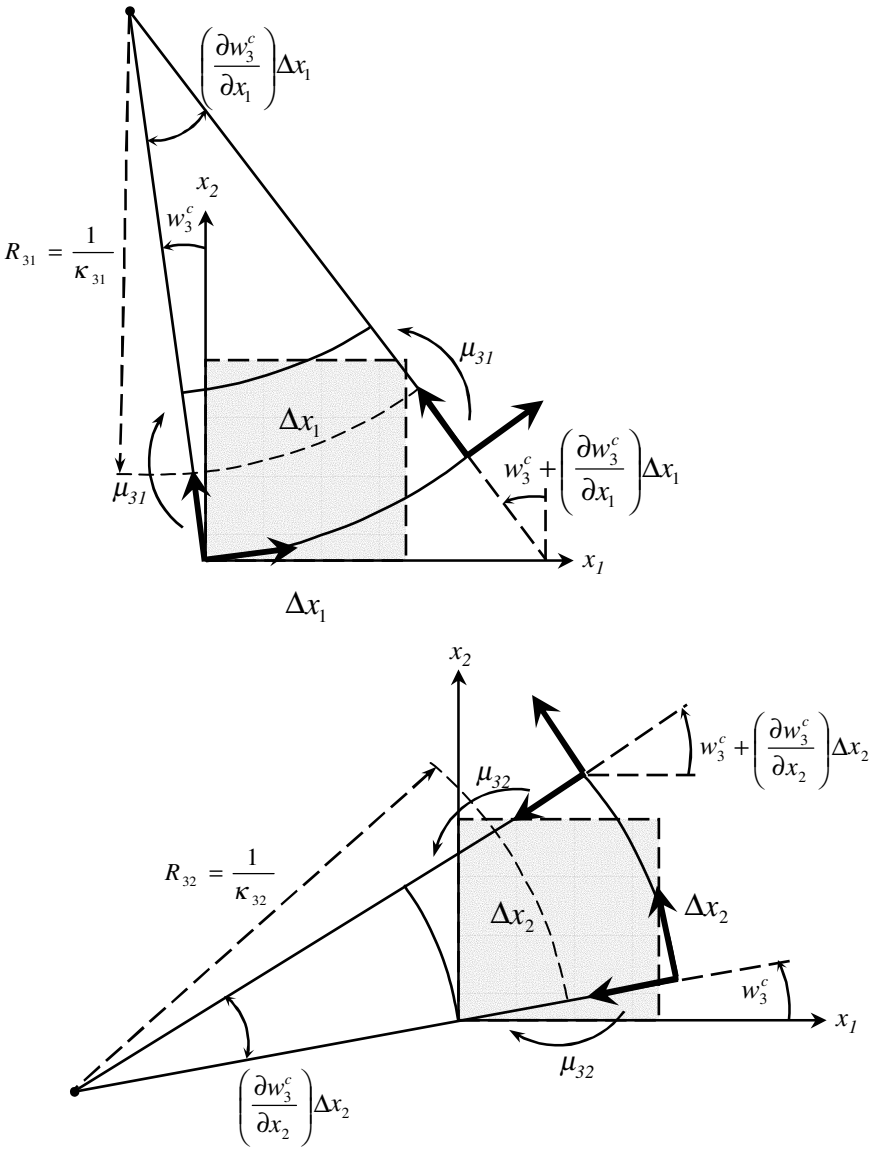

Figure C.8: Definition of curvatures in a Cosserat continuum

Appendix D

Rigid Body Motion

D.1 Introduction

In a Cosserat continuum, each material point has three translational degrees-of-freedom and three rotational degrees-of-freedom. The material points translate and rotate as rigid bodies. Although the kinematics of a two-dimensional (plane strain/stress) Cosserat continuum are relatively simple, the general three-dimensional formulation can be complicated. In this appendix, the general dynamics of a rigid body (particle) are described. If the body is rigid, the distance between any pair of points in the body is constant. This statement enables the description of the motion of a rigid body by using six coordinates, namely three translational and three rotational. Before the equations of motion of a body can be derived, we must define some kinematic relations. Tensor notation (Hassenpflug, 1993) is used.

D.2 Kinematic Relations

In order to describe the motion of a rigid body in a multi-body system, assign a coordinate system to each body. Figure D.1 shows two orthogonal reference systems, the inertial system s and the body system b. $\overrightarrow{x}$ is the position vector of the origin of the body system b of body j. The body has an angular velocity vector $\overrightarrow{\omega}$ as shown. Referring to figure D.1 the position of

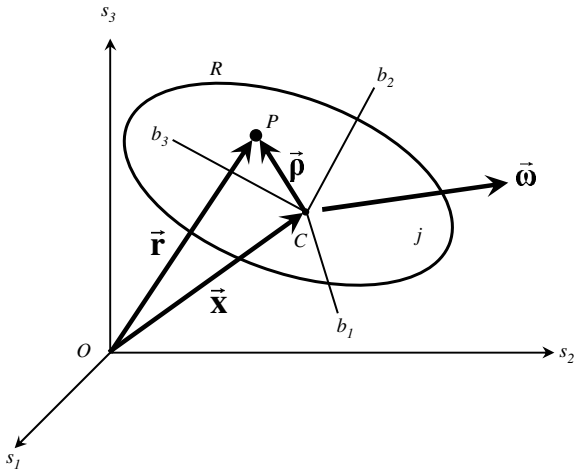

Figure D.1: Rigid body motion

any point c in the body j can be described in terms of the following vectors:

$$\overrightarrow{r} = \overrightarrow{x} + \overrightarrow{\rho} \tag{D.2.1}$$

This equation can be stated in orthogonal base notation with respect to base $\overrightarrow{\underline{E}}_s$ as

$$\overline{r}^s = \overline{x}^s + \overline{\rho}^s \tag{D.2.2}$$

Taking the first and second time derivative of this equation yields the velocity and acceleration relations:

$$\dot{\overline{r}}^s = \dot{\overline{x}}^s + \dot{\overline{\rho}}^s \tag{D.2.3}$$

$$\ddot{\overline{r}}^s = \ddot{\overline{x}}^s + \ddot{\overline{\rho}}^s \tag{D.2.4}$$

If the body is assumed rigid, the vector $\overrightarrow{\rho}$ is fixed in the body and will remain constant with respect to the body reference frame during any motion of the body. This implies that with respect to the body reference frame, b

$$\dot{\overline{\rho}}^b = \ddot{\overline{\rho}}^b = \overline{0} \tag{D.2.5}$$

Lets, for the moment, assume the body non-rigid. The following relation holds for the vector $\overrightarrow{\rho}$ in the two reference systems, s and b,

$$\overline{\rho}^s = \overline{\underline{E}}_b^s \overline{\rho}^b \tag{D.2.6}$$

with $\overline{\underline{E}}_b^s$ the transformation matrix between the two reference frames. By taking the time derivative of equation D.2.6, one obtains:

$$\begin{aligned} \dot{\overline{\rho}}^s &= \overline{\underline{E}}_b^s \dot{\overline{\rho}}^b + \dot{\overline{\underline{E}}}_b^s \overline{\rho}^b \\ &= \overline{\underline{E}}_b^s \left(\dot{\overline{\rho}}^b + \tilde{\overline{\omega}}_s^s \overline{\rho}^b \right) \end{aligned} \tag{D.2.7}$$

where $\tilde{\overline{\omega}}_s^s = \dot{\overline{\underline{E}}}_b^s \overline{\underline{E}}_s^b$ is the cross product tensor of the angular velocity vector of particle j with respect to reference frame s. The acceleration relation can be obtained by taking the time derivative of equation D.2.7.

$$\ddot{\overline{\rho}}^s = \overline{\underline{E}}_b^s \left(\ddot{\overline{\rho}}^b + 2\tilde{\overline{\omega}}_s^s \dot{\overline{\rho}}^b + \dot{\tilde{\overline{\omega}}}_s^s \overline{\rho}^b + \tilde{\overline{\omega}}_s^s \tilde{\overline{\omega}}_s^s \overline{\rho}^b \right) \tag{D.2.8}$$

The second term on the right-hand side of equation D.2.8 is called the *Coriolis acceleration*. The following relations can also be written:

$$\overline{\omega}^s = \overline{\underline{E}}_b^s \overline{\omega}^b \tag{D.2.9}$$

$$\tilde{\overline{\omega}}_s^s = \overline{\underline{E}}_b^s \tilde{\overline{\omega}}_b^b \overline{\underline{E}}_s^b \tag{D.2.10}$$

Using the relations for the vector $\overrightarrow{\rho}$ (equation D.2.7 and D.2.8), we can rewrite the velocity and acceleration relations of equation D.2.3 and D.2.4 as:

$$\begin{aligned}\dot{\overline{r}}^s &= \dot{\overline{x}}^s + \overline{\underline{E}}_b^s \left(\dot{\overline{\rho}}^b + \tilde{\underline{\omega}}_s^s \overline{\rho}^b\right) \\ &= \dot{\overline{x}}^s + \dot{\overline{\rho}}^s + \overline{\omega}^s \times \overline{\rho}^s\end{aligned} \tag{D.2.11}$$

$$\ddot{\overline{r}}^s = \ddot{\overline{x}}^s + \overline{\underline{E}}_b^s \left(\ddot{\overline{\rho}}^b + 2\tilde{\underline{\omega}}_s^s \dot{\overline{\rho}}^b + \dot{\tilde{\underline{\omega}}}_s^s \overline{\rho}^b + \tilde{\underline{\omega}}_s^s \tilde{\underline{\omega}}_s^s \overline{\rho}^b\right) \tag{D.2.12}$$

If the body is assumed rigid, equation D.2.5 holds and the velocity and acceleration vectors (equation D.2.11 and D.2.12) become

$$\dot{\overline{r}}^s = \dot{\overline{x}}^s + \overline{\omega}^s \times \overline{\rho}^s \tag{D.2.13}$$

$$\ddot{\overline{r}}^s = \ddot{\overline{x}}^s + \overline{\underline{E}}_b^s \left(\dot{\tilde{\underline{\omega}}}_s^s \overline{\rho}^b + \tilde{\underline{\omega}}_s^s \tilde{\underline{\omega}}_s^s \overline{\rho}^b\right) \tag{D.2.14}$$

In terms of physical vectors for the case of a non-rigid body

$$\dot{\overrightarrow{r}} = \dot{\overrightarrow{x}} + \dot{\overrightarrow{\rho}} + \overrightarrow{\omega} \times \overrightarrow{\rho} \tag{D.2.15}$$

$$\ddot{\overrightarrow{r}} = \ddot{\overrightarrow{x}} + \ddot{\overrightarrow{\rho}} + 2\overrightarrow{\omega} \times \dot{\overrightarrow{\rho}} + \dot{\overrightarrow{\omega}} \times \overrightarrow{\rho} + \overrightarrow{\omega} \times \left(\overrightarrow{\omega} \times \overrightarrow{\rho}\right) \tag{D.2.16}$$

and for a rigid body

$$\dot{\overrightarrow{r}} = \dot{\overrightarrow{x}} + \overrightarrow{\omega} \times \overrightarrow{\rho} \tag{D.2.17}$$

$$\ddot{\overrightarrow{r}} = \ddot{\overrightarrow{x}} + \dot{\overrightarrow{\omega}} \times \overrightarrow{\rho} + \overrightarrow{\omega} \times \left(\overrightarrow{\omega} \times \overrightarrow{\rho}\right) \tag{D.2.18}$$

The velocity and acceleration of any point in the body can be described in terms of the translation of the origin of a body reference system and the rotation of the reference system about the origin.

D.3 Linear and Angular Momentum of a Rigid Body

Consider again figure D.1. Assume that the body reference system origin C corresponds to the centre of mass of the body. The linear momentum $\overrightarrow{p}$ of the rigid body R can be shown to be

$$\overrightarrow{p} = m\overrightarrow{x} \tag{D.3.1}$$

where m is the total mass of the body. The angular momentum of moment of momentum of the body R about the origin O is defined as

$$\overrightarrow{h} = \int_R \overrightarrow{r} \times \dot{\overrightarrow{r}}\, \mathrm{d}m \tag{D.3.2}$$

or in orthogonal base notation

$$\overline{\boldsymbol{h}}^s = \int_R \overline{\boldsymbol{r}}^s \times \dot{\overline{\boldsymbol{r}}}^s \, \mathrm{d}m \tag{D.3.3}$$

Equation D.2.2 and D.2.3 can be substituted into equation D.3.3 to give

$$\begin{aligned} \overline{\boldsymbol{h}}^s &= \int_R (\overline{\boldsymbol{x}}^s + \overline{\boldsymbol{\rho}}^s) \times (\dot{\overline{\boldsymbol{x}}}^s + \dot{\overline{\boldsymbol{\rho}}}^s) \, \mathrm{d}m \\ &= \int_R (\overline{\boldsymbol{x}}^s \times \dot{\overline{\boldsymbol{x}}}^s) \, \mathrm{d}m + \overline{\boldsymbol{x}}^s \times \int_R \dot{\overline{\boldsymbol{\rho}}}^s \, \mathrm{d}m - \dot{\overline{\boldsymbol{x}}}^s \times \int_R \overline{\boldsymbol{\rho}}^s \, \mathrm{d}m + \int_R (\overline{\boldsymbol{\rho}}^s \times \dot{\overline{\boldsymbol{\rho}}}^s) \, \mathrm{d}m \end{aligned} \tag{D.3.4}$$

With C the centre of mass and $\overline{\boldsymbol{\rho}}$ from the centre of mass, the two middle terms on the right are zero since

$$\int_R \overline{\boldsymbol{\rho}}^s \, \mathrm{d}m = \int_R \dot{\overline{\boldsymbol{\rho}}}^s \, \mathrm{d}m = 0 \tag{D.3.5}$$

Equation D.3.4 can now be written as

$$\begin{aligned} \overline{\boldsymbol{h}}^s &= \int_R (\overline{\boldsymbol{x}}^s \times \dot{\overline{\boldsymbol{x}}}^s) \, \mathrm{d}m + \int_R (\overline{\boldsymbol{\rho}}^s \times \dot{\overline{\boldsymbol{\rho}}}^s) \, \mathrm{d}m \\ &= \int_R (\overline{\boldsymbol{x}}^s \times \dot{\overline{\boldsymbol{x}}}^s) \, \mathrm{d}m + \overline{\boldsymbol{h}}_c^s \end{aligned} \tag{D.3.6}$$

where

$$\overline{\boldsymbol{h}}_c^s = \int_R (\overline{\boldsymbol{\rho}}^s \times \dot{\overline{\boldsymbol{\rho}}}^s) \, \mathrm{d}m \tag{D.3.7}$$

Here we have the important result that the total angular momentum of a rigid body about a fixed point C is equal to the angular momentum of a body of mass m moving with the velocity of the centre of mass plus the angular momentum $\overline{\boldsymbol{h}}_c^s$ about the centre of mass. The first term in equation D.3.6 can be written as $(\overline{\boldsymbol{x}}^s \times \dot{\overline{\boldsymbol{x}}}^s)\, m$, where m is the total mass of the body.

Using equation D.2.7 with $\dot{\overline{\boldsymbol{\rho}}}^b = \overline{\boldsymbol{0}}$ (rigid body), equation D.3.7 becomes

$$\begin{aligned} \dot{\overline{\boldsymbol{\rho}}}^s &= \overline{\underline{\boldsymbol{E}}}_b^s \left(\tilde{\overline{\boldsymbol{\omega}}}_s^s \overline{\boldsymbol{\rho}}^b \right) = \overline{\boldsymbol{\omega}}^s \times \overline{\boldsymbol{\rho}}^s \\ \therefore \overline{\boldsymbol{h}}_c^s &= \int_R \left[\overline{\boldsymbol{\rho}}^s \times \left(\overline{\boldsymbol{\omega}}^s \times \overline{\boldsymbol{\rho}}^b \right) \right] \, \mathrm{d}m \end{aligned} \tag{D.3.8}$$

Applying the relation for a triple cross product, equation D.3.8 can be written as

$$\overline{\boldsymbol{h}}_c^s = \int_R \left[\overline{\boldsymbol{\omega}}^s \left(\overline{\boldsymbol{\rho}}^s \bullet \overline{\boldsymbol{\rho}}^s \right) - \overline{\boldsymbol{\rho}}^s \left(\overline{\boldsymbol{\omega}}^s \bullet \overline{\boldsymbol{\rho}}^s \right) \right] \, \mathrm{d}m \tag{D.3.9}$$

Let $\overline{\boldsymbol{\rho}}^s = [\rho_{s1}\ \rho_{s2}\ \rho_{s3}]^T$ and $\overline{\boldsymbol{\omega}}^s = [\omega_{s1}\ \omega_{s2}\ \omega_{s3}]^T$ then after algebraic manipulations of equation D.3.9 can be written in the form

$$\begin{aligned}\overline{\boldsymbol{h}}_c^s &= \begin{bmatrix} \int_R (\rho_{s2}^2 + \rho_{s3}^2)\ \mathrm{d}m & -\int_R (\rho_{s1}\rho s2)\ \mathrm{d}m & -\int_R (\rho_{s1}\rho s3)\ \mathrm{d}m \\ -\int_R (\rho_{s2}\rho s1)\ \mathrm{d}m & \int_R (\rho_{s1}^2 + \rho_{s3}^2)\ \mathrm{d}m & -\int_R (\rho_{s2}\rho s3)\ \mathrm{d}m \\ -\int_R (\rho_{s3}\rho s1)\ \mathrm{d}m & -\int_R (\rho_{s3}\rho s2)\ \mathrm{d}m & \int_R (\rho_{s1}^2 + \rho_{s2}^2)\ \mathrm{d}m \end{bmatrix} \begin{bmatrix} \omega_{s1} \\ \omega_{s2} \\ \omega_{s3} \end{bmatrix} \\ &= \begin{bmatrix} J_{11} & J_{12} & J_{13} \\ J_{21} & J_{22} & J_{23} \\ J_{31} & J_{32} & J_{33} \end{bmatrix} \begin{bmatrix} \omega_{s1} \\ \omega_{s2} \\ \omega_{s3} \end{bmatrix} \\ &= \underline{\overline{\boldsymbol{J}}}_s^s \overline{\boldsymbol{\omega}}^s \end{aligned} \tag{D.3.10}$$

The symmetric tensor $\underrightarrow{\underrightarrow{\boldsymbol{J}}}$ is a Cartesian second rank tensor called the *inertia tensor.* The diagonal elements are called the *moments of inertia* and the non-diagonal elements are called the *products of inertia*. The units are $\underrightarrow{\underrightarrow{\boldsymbol{J}}} = \mathrm{kg{\cdot}m^2}$ and $\overrightarrow{\boldsymbol{h}}_c = \mathrm{kg{\cdot}m^2{\cdot}s^{-1}}$

Appendix E

The Finite Element Method

E.1 Introduction

The Particle-in-Cell method is based on the standard finite element method (FEM). In this appendix, the general FEM formulation, using four node bilinear isoparametric elements, is given. To avoid confusion, x, y and z are used as indices for the three orthogonal coordinate directions. Similarly u and v are the displacements in the x and y directions respectively. Numerical subscripts (1,2,3,4) are used to indicate element node numbers unless stated otherwise.

E.2 Plane Bilinear Isoparametric Element

Isoparametric coordinates in a plane are shown in figure E.1a. For a four-node element, axes ξ and η pass through midpoints of opposite sides. Axes ξ and η do not have to be orthogonal, and neither need to be parallel to x- and y-axes. Sides of the element are at $\xi = \pm 1$ and $\eta = \pm 1$.

E.2.1 Stiffness Matrix Formulation

Coordinates x and y within the element are defined by

$$x = \underline{N}\bar{x} \quad y = \underline{N}\bar{y}$$

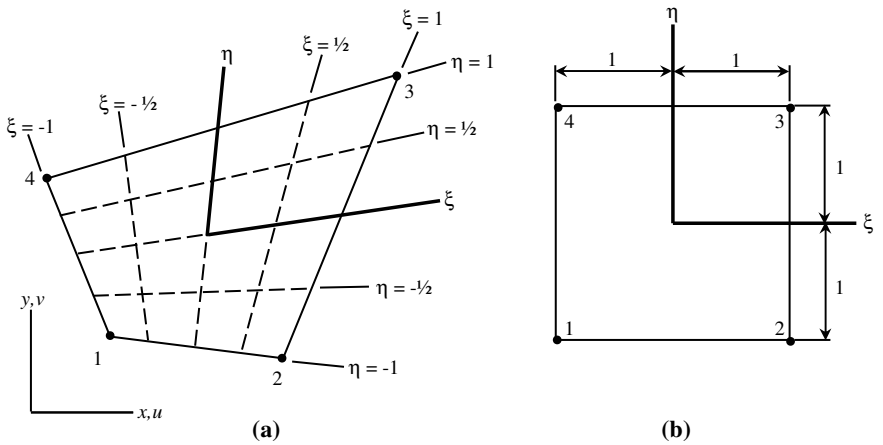

Figure E.1: (a) Four-node plane isoparametric element in xy-space, (b) plane isoparametric element in $\xi\eta$ space

or

$$x = \sum_{i=1}^{4} N_i x_i \quad y = \sum_{i=1}^{4} N_i y_i \tag{E.2.1}$$

where

$$\underline{\boldsymbol{N}} = \left[\tfrac{1}{4}(1-\xi)(1-\eta)\,;\tfrac{1}{4}(1+\xi)(1-\eta)\,;\tfrac{1}{4}(1+\xi)(1+\eta)\,;\tfrac{1}{4}(1-\xi)(1+\eta)\right] \tag{E.2.2}$$

is the shape function matrix and

$$\overline{\boldsymbol{x}} = \begin{bmatrix} x_1 \\ x_2 \\ x_3 \\ x_4 \end{bmatrix} \quad \text{and} \quad \overline{\boldsymbol{y}} = \begin{bmatrix} y_1 \\ y_2 \\ y_3 \\ y_4 \end{bmatrix} \tag{E.2.3}$$

are the x and y coordinates of the element nodes. For a given element geometry, the orientation of the $\xi\eta$ axes with respect to the xy-axes is dictated by equation E.2.2 and the node numbers assigned to the element at hand. For example, in figure E.1a, a cyclic change in node numbers (2 changed to 1, 3 changed to 2, etc.) would place the ξ axis where the η axis is now shown and would place the η axis in the present -ξ direction. Figure E.2b would not be changed because of equation E.2.2, node 1 is always at $\xi = \eta = -1$, node 2 always at $\xi = 1$ and $\eta = -1$, and so on. The point $\xi = \eta = 0$ can be regarded as the center of the element, but is not in general the centroid of the element area.

Let's, for the moment, consider a single scalar field element. Let the field quantity be $\phi = \phi(x, y)$ or $\phi = \phi(\xi, \eta)$. The simplest element has one d.o.f. per node. Within a four-node element ϕ is interpolated from the nodal values $\overline{\boldsymbol{\phi}}$

$$\phi = \underline{\boldsymbol{N}}\overline{\boldsymbol{\phi}} \quad \text{or} \quad \phi = \sum_{i=1}^{4} N_i \phi_i \quad \text{where} \quad \overline{\boldsymbol{\phi}} = \begin{bmatrix} \phi_1 \\ \phi_2 \\ \phi_3 \\ \phi_4 \end{bmatrix} \tag{E.2.4}$$

To make the element isoparametric, the N_i are taken from equation E.2.2. The derivatives of ϕ with respect to x and y can be written as

$$\frac{\partial \phi}{\partial x} = \phi_{,x} = \frac{\partial}{\partial x}\left(\underline{\boldsymbol{N}}\overline{\boldsymbol{\phi}}\right) = \frac{\partial \underline{\boldsymbol{N}}}{\partial x}\overline{\boldsymbol{\phi}} \quad \text{and} \quad \frac{\partial \phi}{\partial y} = \phi_{,y} = \frac{\partial}{\partial y}\left(\underline{\boldsymbol{N}}\overline{\boldsymbol{\phi}}\right) = \frac{\partial \underline{\boldsymbol{N}}}{\partial y}\overline{\boldsymbol{\phi}} \tag{E.2.5}$$

Equation E.2.5 can be combined and written in matrix notation as

$$\begin{bmatrix} \phi_{,x} \\ \phi_{,y} \end{bmatrix} = \begin{bmatrix} N_{1,x} & N_{2,x} & N_{3,x} & N_{4,x} \\ N_{1,y} & N_{2,y} & N_{3,y} & N_{4,y} \end{bmatrix} \overline{\boldsymbol{\phi}} \tag{E.2.6}$$

Similarly, the derivatives of ϕ with respect to ξ and η

$$\begin{bmatrix} \phi_{,\xi} \\ \phi_{,\eta} \end{bmatrix} = \begin{bmatrix} N_{1,\xi} & N_{2,\xi} & N_{3,\xi} & N_{4,\xi} \\ N_{1,\eta} & N_{2,\eta} & N_{3,\eta} & N_{4,\eta} \end{bmatrix} \overline{\boldsymbol{\phi}} \tag{E.2.7}$$

The relation between these two sets of derivatives can be written in the following form

$$\begin{bmatrix} \phi_{,x} \\ \phi_{,y} \end{bmatrix} = \underline{\overline{\Gamma}} \begin{bmatrix} \phi_{,\xi} \\ \phi_{,\eta} \end{bmatrix} \tag{E.2.8}$$

Now seek an expression for $\underline{\overline{\Gamma}}$ in equation E.2.8. By the chain rule

$$\frac{\partial \phi}{\partial x} = \frac{\partial \phi}{\partial \xi}\frac{\partial \xi}{\partial x} + \frac{\partial \phi}{\partial \eta}\frac{\partial \eta}{\partial x} \quad \text{and} \quad \frac{\partial \phi}{\partial y} = \frac{\partial \phi}{\partial \xi}\frac{\partial \xi}{\partial y} + \frac{\partial \phi}{\partial \eta}\frac{\partial \eta}{\partial y} \tag{E.2.9}$$

By comparing equation E.2.9 with equation E.2.8, the components of $\underline{\overline{\Gamma}}$ follows as $\Gamma_{11} = \xi_{,x}$, $\Gamma_{12} = \eta_{,x}$, $\Gamma_{21} = \xi_{,y}$ and $\Gamma_{22} = \eta_{,y}$. Unfortunately, the partial derivatives of ξ and η with respect to x and y are not available from the above equations. Therefore, we must write the inverse of equation E.2.9 first, which is easily done.

$$\frac{\partial \phi}{\partial \xi} = \frac{\partial \phi}{\partial x}\frac{\partial x}{\partial \xi} + \frac{\partial \phi}{\partial y}\frac{\partial y}{\partial \xi} \quad \text{and} \quad \frac{\partial \phi}{\partial \eta} = \frac{\partial \phi}{\partial x}\frac{\partial x}{\partial \eta} + \frac{\partial \phi}{\partial y}\frac{\partial y}{\partial \eta} \tag{E.2.10}$$

Writing equation E.2.10 in matrix notation

$$\begin{bmatrix} \phi_{,\xi} \\ \phi_{,\eta} \end{bmatrix} = \underline{\overline{J}} \begin{bmatrix} \phi_{,x} \\ \phi_{,y} \end{bmatrix} \tag{E.2.11}$$

where $\underline{\overline{J}}$ is called the *Jacobian matrix*,

$$\underline{\overline{J}} = \begin{bmatrix} x_{,\xi} & y_{,\xi} \\ x_{,\eta} & y_{,\eta} \end{bmatrix} \tag{E.2.12}$$

Using equation E.2.1, equation E.2.12 can be written in terms of the shape functions

$$\underline{\overline{J}} = \begin{bmatrix} x_{,\xi} & y_{,\xi} \\ x_{,\eta} & y_{,\eta} \end{bmatrix} = \begin{bmatrix} \sum_{i=1}^{4} N_{i,\xi} x_i & \sum_{i=1}^{4} N_{i,\xi} y_i \\ \sum_{i=1}^{4} N_{i,\eta} x_i & \sum_{i=1}^{4} N_{i,\eta} y_i \end{bmatrix} \tag{E.2.13}$$

Equation E.2.13 is valid for all isoparametric elements, where i would range over the number of nodes (and shape functions) used to define the element geometry. By comparing Equation E.2.8 with Equation E.2.11, it can be seen that $\underline{\overline{\Gamma}}$ is the inverse of $\underline{\overline{J}}$

$$\underline{\overline{\Gamma}} = \underline{\overline{J}}^{-1} = \frac{1}{J} \begin{bmatrix} J_{22} & -J_{12} \\ -J_{21} & J_{11} \end{bmatrix} \tag{E.2.14}$$

where J is the determinant of the Jacobian matrix

$$J = |\underline{\overline{J}}| = J_{11}J_{22} - J_{21}J_{12} \tag{E.2.15}$$

Writing equation E.2.14 in terms of the shape functions

$$\underline{\overline{\Gamma}} = \frac{\begin{bmatrix} \sum_{i=1}^{4} N_{i,\eta} y_i & -\sum_{i=1}^{4} N_{i,\xi} y_i \\ -\sum_{i=1}^{4} N_{i,\eta} x_i & \sum_{i=1}^{4} N_{i,\xi} x_i \end{bmatrix}}{\sum_{i=1}^{4} N_{i,\xi} x_i \sum_{i=1}^{4} N_{i,\eta} y_i - \sum_{i=1}^{4} N_{i,\eta} x_i \sum_{i=1}^{4} N_{i,\xi} y_i} \tag{E.2.16}$$

The Jacobian J can be regarded as a scale factor that yields area $\mathrm{d}x\mathrm{d}y$ from $\mathrm{d}\xi\mathrm{d}\eta$. Lets now focus on a plane stress element. There are now two fields, namely the displacements. The equivalent of equation E.2.4 can be written for the two fields

$$u = \sum_{i=1}^{4} N_i u_i \quad \text{and} \quad v = \sum_{i=1}^{4} N_i v_i \tag{E.2.17}$$

Displacements u and v are x-parallel and y-parallel; they are not ξ-parallel and η-parallel. The linear strain-displacement relation is

$$\overline{\varepsilon} = \underline{\overline{B}}\, \overline{d} \tag{E.2.18}$$

where $\overline{d} = [u_1\ v_1\ u_2\ v_2\ u_3\ v_3\ u_4\ v_4]^T$ is the nodal displacements and $\underline{\overline{B}}$ is the product of rectangular matrices in the following series of equations. First write the relation between strain and displacements as

$$\overline{\varepsilon} = \begin{bmatrix} \varepsilon_x \\ \varepsilon_y \\ \gamma_{xy} \end{bmatrix} = \begin{bmatrix} 1 & 0 & 0 & 0 \\ 0 & 0 & 0 & 1 \\ 0 & 1 & 1 & 0 \end{bmatrix} \begin{bmatrix} u_{,x} \\ u_{,y} \\ v_{,x} \\ v_{,y} \end{bmatrix} \quad \text{or} \quad \overline{\varepsilon} = \underline{\overline{H}} \begin{bmatrix} u_{,x} \\ u_{,y} \\ v_{,x} \\ v_{,y} \end{bmatrix} \tag{E.2.19}$$

Next, using an expanded form of equation E.2.8, write

$$\begin{bmatrix} u_{,x} \\ u_{,y} \\ v_{,x} \\ v_{,y} \end{bmatrix} = \begin{bmatrix} \Gamma_{11} & \Gamma_{12} & 0 & 0 \\ \Gamma_{21} & \Gamma_{22} & 0 & 1 \\ 0 & 0 & \Gamma_{11} & \Gamma_{12} \\ 0 & 0 & \Gamma_{21} & \Gamma_{22} \end{bmatrix} \begin{bmatrix} u_{,\xi} \\ u_{,\eta} \\ v_{,\xi} \\ v_{,\eta} \end{bmatrix} \quad \text{or} \quad \begin{bmatrix} u_{,x} \\ u_{,y} \\ v_{,x} \\ v_{,y} \end{bmatrix} = \underline{\overline{\overline{\Gamma}}} \begin{bmatrix} u_{,\xi} \\ u_{,\eta} \\ v_{,\xi} \\ v_{,\eta} \end{bmatrix} \tag{E.2.20}$$

The coefficients of $\underline{\overline{\overline{\Gamma}}}$ are given by equation E.2.16. Using the field definitions, equation E.2.17, the following relation can be written

$$\begin{bmatrix} u_{,\xi} \\ u_{,\eta} \\ v_{,\xi} \\ v_{,\eta} \end{bmatrix} = \begin{bmatrix} N_{1,\xi} & 0 & N_{2,\xi} & 0 & N_{3,\xi} & 0 & N_{4,\xi} & 0 \\ N_{1,\eta} & 0 & N_{2,\eta} & 0 & N_{3,\eta} & 0 & N_{4,\eta} & 0 \\ 0 & N_{1,\xi} & 0 & N_{2,\xi} & 0 & N_{3,\xi} & 0 & N_{4,\xi} \\ 0 & N_{1,\eta} & 0 & N_{2,\eta} & 0 & N_{3,\eta} & 0 & N_{4,\eta} \end{bmatrix} \begin{bmatrix} u_1 \\ v_1 \\ u_2 \\ v_2 \\ u_3 \\ v_3 \\ u_4 \\ v_4 \end{bmatrix}$$

or

$$\begin{bmatrix} u_{,\xi} \\ u_{,\eta} \\ v_{,\xi} \\ v_{,\eta} \end{bmatrix} = \overline{\underline{\widetilde{N}}}\,\overline{\boldsymbol{d}} \tag{E.2.21}$$

Substitution of equation E.2.21 and E.2.20 into equation E.2.19 yields

$$\overline{\boldsymbol{\varepsilon}} = \overline{\underline{\boldsymbol{H}}}\,\overline{\underline{\widetilde{\Gamma}}}\,\overline{\underline{\widetilde{N}}}\,\overline{\boldsymbol{d}} \tag{E.2.22}$$

Thus,

$$\overline{\underline{\boldsymbol{B}}} = \overline{\underline{\boldsymbol{H}}}\,\overline{\underline{\widetilde{\Gamma}}}\,\overline{\underline{\widetilde{N}}} \tag{E.2.23}$$

According to the Rayleigh-Ritz method (Cook *et al.*, 1989), the element stiffness matrix $\overline{\underline{\boldsymbol{k}}}$ for an elastic material is given by

$$\overline{\underline{\boldsymbol{k}}} = \iint \overline{\underline{\boldsymbol{B}}}^T \overline{\underline{\boldsymbol{E}}}\,\overline{\underline{\boldsymbol{B}}} t \,\mathrm{d}x\mathrm{d}y = \int_{-1}^{1}\int_{-1}^{1} \overline{\underline{\boldsymbol{B}}}^T \overline{\underline{\boldsymbol{E}}}\,\overline{\underline{\boldsymbol{B}}}\, tJ \,\mathrm{d}\xi\mathrm{d}\eta \tag{E.2.24}$$

where t is the element thickness and J is given by equation E.2.15.

E.2.2 Load Vector Formulation

The element load vector is given by the Rayleigh-Ritz methods (Cook *et al.*, 1989) as

$$\overline{\boldsymbol{r}}_e = \int_{V_e} \overline{\underline{\boldsymbol{B}}}^T \overline{\underline{\boldsymbol{E}}}\,\overline{\boldsymbol{\varepsilon}}_0 \,\mathrm{d}V - \int_{V_e} \overline{\underline{\boldsymbol{B}}}^T \overline{\sigma}_0 \,\mathrm{d}V + \int_{V_e} \overline{\underline{\boldsymbol{N}}}^T \overline{\boldsymbol{F}} \,\mathrm{d}V + \int_{S_e} \overline{\underline{\boldsymbol{N}}}^T \overline{\boldsymbol{\Phi}} \,\mathrm{d}S \tag{E.2.25}$$

For the plane stress element the following is defined

$$\begin{aligned}
\overline{\boldsymbol{\varepsilon}} &= \left[\varepsilon_x\ \varepsilon_y\ \gamma_{xy}\right]^T, \text{the strain field} \\
\overline{\boldsymbol{\varepsilon}}_0, \overline{\boldsymbol{\sigma}}_0 &= \text{initial strains and initial stresses} \\
\underline{\overline{\boldsymbol{E}}} &= \text{the material property matrix} \\
\overline{\boldsymbol{F}} &= \text{body forces} \\
\overline{\boldsymbol{\Phi}} &= \text{surface tractions} \\
\overline{\boldsymbol{D}} &= \text{nodal d.o.f. of the structure} \\
\overline{\boldsymbol{P}} &= \text{loads applied to d.o.f. by external agencies} \\
S_e, V_e &= \text{element surface and volume}
\end{aligned}$$

Ignoring for the moment the surface tractions $\overline{\boldsymbol{\Phi}}$, equation E.2.25 can be written as

$$\overline{\boldsymbol{r}}_e{}' = \int_{-1}^{1}\int_{-1}^{1}\left(\underline{\overline{\boldsymbol{B}}}^T\underline{\overline{\boldsymbol{E}}}\overline{\boldsymbol{\varepsilon}}_0 - \underline{\overline{\boldsymbol{B}}}^T\overline{\boldsymbol{\sigma}}_0 + \underline{\overline{\boldsymbol{N}}}^T\overline{\boldsymbol{F}}\right) tJ\ \mathrm{d}\xi\mathrm{d}\eta \tag{E.2.26}$$

For convenience in computer programming, the contributions to $\overline{\boldsymbol{r}}_e$ from the surface tractions $\overline{\boldsymbol{\Phi}}$ are evaluated separately. For this the manipulations associated with isoparametric coordinates may be unnecessary.

The contribution of the surface tractions to the element load vector can be written as

$$\overline{\boldsymbol{r}}_e{}'' = \int_{S_e}\underline{\overline{\boldsymbol{N}}}^T\overline{\boldsymbol{\Phi}}\ \mathrm{d}S \tag{E.2.27}$$

Let $\overline{\boldsymbol{\Phi}}$ be a distributed load of intensity q that acts normal to a linear edge of a plane element. The inclination of the edge with respect to global coordinates xy does not matter. As long as the edge-normal displacement varies linearly with edge-tangent coordinates s, loads can be allocated to nodes as follows. Since only the single edge of the element is considered, equation E.2.27 can be written as

$$\overline{\boldsymbol{r}}_e{}'' = \int_0^L \underline{\boldsymbol{N}}q\ \mathrm{d}s = \int_0^L \begin{bmatrix} \frac{L-s}{L} \\ \frac{s}{L} \end{bmatrix}\left[\left(\frac{L-s}{L}\right)q_1 + \left(\frac{s}{L}\right)q_2\right]\ \mathrm{d}s \tag{E.2.28}$$

where the shape functions of a one dimensional element are used and q is assumed to be linear as depicted in figure E.2a.

Evaluating equation E.2.28 yields the nodal forces as shown in figure E.2b.

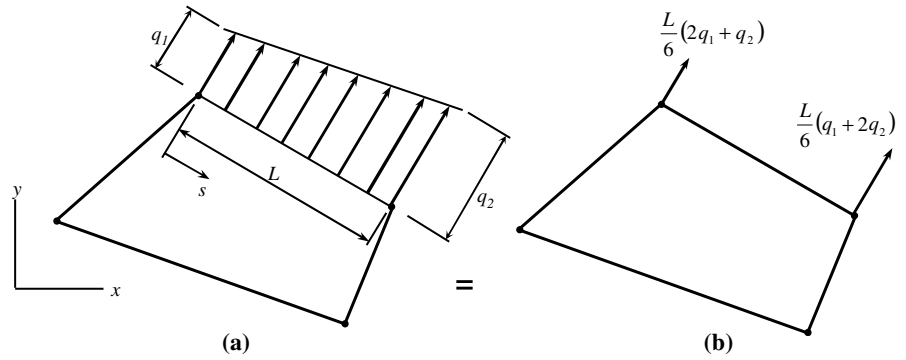

Figure E.2: (a) Linearly varying load on a linear edge and (b) the consistent nodal loads

E.3 Summary of Gauss Quadrature

"Quadrature" is the name applied to evaluating an integral numerically, rather than analytically as is done in tables of integrals, Cook *et al.* (1989). There are many quadrature rules. Only the Gauss rules are discussed here, as they are most appropriate for isoparametric elements as discussed in the above section.

E.3.1 One Dimension

An integral having arbitrary limits can be transformed so that its limits are from –1 to +1. With $f = f(x)$, and with the substitution $x = \frac{1}{2}(1-\xi)\,x_1 + \frac{1}{2}(1+\xi)\,x_2$,

$$I = \int_{x_1}^{x_2} f \,\mathrm{d}x \;\text{ becomes }\; I = \int_{-1}^{1} \phi \,\mathrm{d}\xi \tag{E.3.1}$$

Thus the integrand is changed from $f = f(x)$ to $\phi = \phi(\xi)$, where ϕ incorporates the Jacobian of the transformation, $J = \frac{\mathrm{d}x}{\mathrm{d}\xi} = \frac{1}{2}(x_2 - x_1)$. The latter form of equation E.3.1 makes it possible to write convenient quadrature formulas. The foregoing linear transformation suffices to make arbitrary limit changes. We can always consider a convenient reference interval such as –1 to +1. In practice the limit change is done automatically by the isoparametric transformation and J is usually more complicated than $\frac{1}{2}(x_2 - x_1)$.

To approximate the integral in the simplest way, one can sample (evaluate) ϕ at the midpoint $\xi = 0$ and multiply by the length of the interval (figure E.3a). Thus approximate the shaded area by a rectangular area of height ϕ_1 and length 2, so that $I \approx 2\phi_1$. This result is exact if $\phi = \phi(\xi)$ happens to describe a straight line of any finite slope. Generalisation of the foregoing procedure leads to the quadrature formula

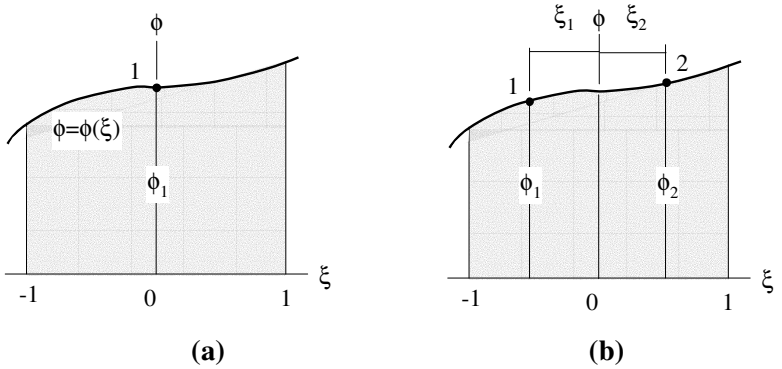

Figure E.3: Gauss quadrature to compute the shaded area under the curve $\phi = \phi(\xi)$, using (a) one and (b) two sampling points (Gauss points)

$$I = \int_{-1}^{1} \phi \, \mathrm{d}\xi \approx W_1\phi_1 + W_2\phi_2 + \cdots + W_n\phi_n \tag{E.3.2}$$

Thus, to approximate I, we must evaluate $\phi = \phi(\xi)$ at each of the several locations ξ_i to obtain ordinates ϕ_i, multiply each ϕ_i by an appropriate weight W_i, and add. In the one-point example, where $I \approx 2\phi_1$, we have $n = 1$ and $W_1 = 2$. Gauss was able to prescribe the locations ξ_i and weights W_i such that greatest accuracy is achieved for a given n. Sampling points are located symmetrically with respect to the center of the integration interval. Symmetrically paired points have the same weight W_i. Table E.1 gives sample point locations and weights for a few cases.

These values are sometimes called Gauss-Legendre coefficients because sampling point locations happen to be roots of Legendre polynomials. It can be shown that a polynomial of degree $(2n - 1)$ is integrated exactly by a n-point Gauss quadrature. Use of more than n points will still produce the exact result. If the function is not a polynomial, Gauss quadrature is inexact, but becomes more accurate as more points are used.

E.3.2 Two Dimensions

Multidimensional Gauss rules, called Gaussian product rules, are formed by successive application of one-dimensional Gauss rules. In two dimensions, consider the function $\phi = \phi(\xi, \eta)$. Elect to integrate first with respect

Table E.1: Sampling points and weights for Gauss quadrature over the interval $\xi = -1$ to $\xi = +1$

Order n	Location ξ_i of Sampling Point	Weight Factor W_i
1	0	2
2	$\pm 1 \frac{1}{\sqrt{3}}$	1
3	$\pm\sqrt{0.6}$	$\frac{5}{9}$
	0	$\frac{8}{9}$
4	$\pm\left[\frac{3+2\sqrt{1.2}}{7}\right]^{\frac{1}{2}}$	$\frac{1}{2} - \frac{1}{6\sqrt{1.2}}$
	$\pm\left[\frac{3-2\sqrt{1.2}}{7}\right]^{\frac{1}{2}}$	$\frac{1}{2} + \frac{1}{6\sqrt{1.2}}$

to ξ and then with respect to η.

$$\begin{aligned} I &= \int_{-1}^{1}\int_{-1}^{1} \phi(\xi,\eta)\, \mathrm{d}\xi \mathrm{d}\eta \approx \int_{-1}^{1} \left(\sum_{i=1}^{n} W_i \phi(\xi_i,\eta) \right) \mathrm{d}\eta \\ &\approx \sum_{j=1}^{m} W_j \left(\sum_{i=1}^{n} W_i \phi(\xi_i,\eta_j) \right) = \sum_{j=1}^{m}\sum_{i=1}^{n} W_i W_j \phi(\xi_i,\eta_j) \end{aligned} \tag{E.3.3}$$

Where m and n are the order of the Gauss rule in the ξ and η directions respectively. It is most common that the same rule is used in both directions, i.e. $n = m$. For the four-point rule depicted in figure E.4a, equation E.3.3 becomes

$$\begin{aligned} I &\approx W_1 W_1 \phi\left(\xi_1,\eta_1\right) + W_1 W_2 \phi\left(\xi_1,\eta_2\right) + W_2 W_1 \phi\left(\xi_2,\eta_1\right) + W_2 W_2 \phi\left(\xi_2,\eta_2\right) \\ &= \phi_1 + \phi_3 + \phi_2 + \phi_4 \end{aligned} \tag{E.3.4}$$

where ϕ_i is the numerical value of ϕ at the i^{th} Gauss point. For the nine-point rule in figure E.4b, equation E.3.3 yields

$$I \approx \tfrac{25}{81}\left(\phi_1 + \phi_3 + \phi_7 + \phi_9\right) + \tfrac{40}{81}\left(\phi_2 + \phi_4 + \phi_6 + \phi_8\right) + \tfrac{64}{81}\phi_5 \tag{E.3.5}$$

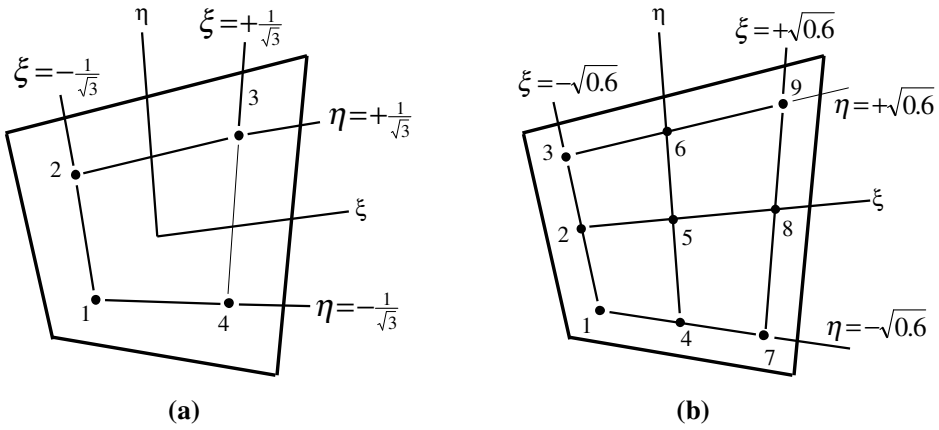

Figure E.4: Gauss point locations in a quadrilateral element using (a) four points (order 2 rule), and (b) nine points (order 3 rule)

Appendix F

The Particle-in-Cell Method Based on the Cosserat Continuum

F.1 Introduction

Problems in solid mechanics that involve history-dependent constitutive relations are expressed more naturally in a Lagrangian computational frame. Similarly, a Lagrangian description is useful when following material free surfaces or multiple materials. On the other hand, if large deformations are involved, a purely Lagrangian mesh can become tangled or require unreasonably small time steps to be successful (Sulsky *et al.*, 1995). For these reasons the particle methods seem to be increasing in popularity.

The Particle-In-Cell (PIC) method uses two discretisations of the material, one based on a computational mesh and the other based on a collection of material points or "particles". This approach combines the advantages of Eulerian and Largrangian descriptions of the material while avoiding the shortcomings of each. The equations of motion are solved in a Lagrangian frame on a computational grid, using standard finite element methods. Convection is modelled by moving the material points in the computed velocity field. Each material point carries its material properties without error while it is moved. Since all the properties of the continuum are assigned to the numerical material points, the information carried by these points is enough to characterise the flow and the grid carries no permanent information. Thus, the grid can be discarded and reconstructed for computational convenience each time step.

To avoid confusion, x, y and z are used as indices for the three orthogonal coordinate directions. Numerical subscripts (1,2,3,4) are used to indicate element node numbers unless stated otherwise.

F.2 PIC Mass Representation

In the Lagrangian description of continuum mechanics, the material is divided into infinitesimal mass elements. Each mass element contains a fixed amount of mass for all the time. In PIC, these infinitesimal mass elements are represented by a finite collection of N_p material points or "particles" with fixed mass m_p. Since m_p is fixed, mass conservation, equation F.3.3, is automatically satisfied.

Let the solid body under consideration initially occupy a region $V(0)$ in $\mathbb{R}^3$ and $V(t)$ for time $t > 0$. Let X_i be the initial position vector of a mate-

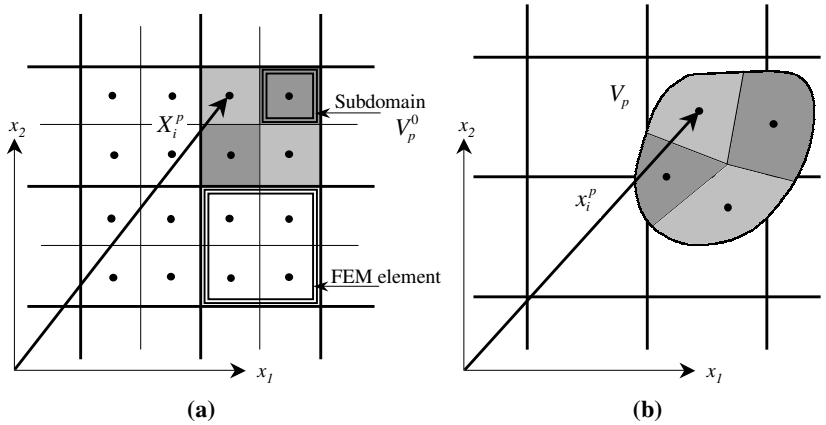

Figure F.1: Typical computational grid and material elements. (a) Initial configuration and (b) deformed configuration

rial point and x_i the current position. Divide the initial configuration $V(0)$ into N_p subdomains, V_p^0, with one material point ("particle") identified at the centroid of each V_p^0. The coordinates of the particles at the centroid of the subdomains is denoted by X_i^p and the particle initially located at the centroid of each subdomain will be tracked throughout the history of the material. Figure F.1 shows a typical rectangular FEM grid with 4-node elements. Each FEM element is divided into four subdomains with a material point at the centroid of each subdomain. The mass of a particle remains constant and is initially determined by

$$m_p = \int_{V_p^0} \rho_0 \left(X_i^p\right) \, \mathrm{d}V = \rho V_p^0 \tag{F.2.1}$$

where ρ_0 is the initial mass density of the material and assumed constant through the material. The density represented by this collection of discrete mass points will be approximated using a Dirac delta function

$$\tilde{\rho}_0 \left(X_i\right) = \sum_{p=1}^{N_p} m_p \delta \left(X_i - X_i^p\right) \tag{F.2.2}$$

where the Dirac delta function is defined as

$$\delta \left(x - a\right) = \begin{cases} 0 & x \neq a \\ \infty & x = a \end{cases} \quad \text{and} \quad \int_{-\infty}^{+\infty} \delta \left(x - a\right) \, \mathrm{d}x = 1 \tag{F.2.3}$$

Using this approximation, the total mass in the region is the same as the total mass given by the continuous density distribution $\rho_0 \left(X_i\right)$. Integration

over a subdomain gives

$$m_p = \int_{V_p^0} \rho_0 \left(X_i\right) \, \mathrm{d}V = \int_{V_p^0} \tilde{\rho}_0 \left(X_i\right) \, \mathrm{d}V \tag{F.2.4}$$

Now, consider a transformation to the current (deformed) configuration in which the same material points that were located at X_i^p at $t = 0$ are now located at x_i^p. Conservation of mass can be written as

$$\int_{V_p^0} \rho_0 \left(X_i\right) \, \mathrm{d}V = \int_{V_p} \rho \left(x_i, t\right) \, \mathrm{d}V \tag{F.2.5}$$

where $\rho \left(x_i, t\right)$ is the density and V_p is the current domain, figure F.1b. In deriving an approximation for the density in the current configuration, we require the approximation to satisfy conservation of mass which can also be written as

$$\int_{V_p^0} \rho_0 \left(X_i\right) \, \mathrm{d}V = \int_{V_p} \tilde{\rho} \left(x_i, t\right) \, \mathrm{d}V \tag{F.2.6}$$

where $\tilde{\rho} \left(x_i, t\right)$ is the discrete approximation of the density in the current configuration. Let J denote the Jacobian of the transformation from the initial to the current configuration. Using Equations F.2.2 and F.2.4, and noting that the Dirac delta function transforms as

$$\delta \left(X_i - X_i^p\right) = \frac{\delta \left(x_i - x_i^p\right)}{J} \tag{F.2.7}$$

we obtain

$$\begin{aligned} \int_{V_p^0} \rho_0 \left(X_i\right) \, \mathrm{d}V &= \int_{V_p^0} \tilde{\rho}_0 \left(X_i\right) \, \mathrm{d}V \\ &= \int_{V_p^0} \sum_{p=1}^{N_p} m_p \delta \left(X_i - X_i^p\right) \, \mathrm{d}V \\ &= \int_{V_p} \sum_{p=1}^{N_p} m_p \delta \left(X_i - X_i^p\right) \, J \, \mathrm{d}V \\ &= \int_{V_p} \sum_{p=1}^{N_p} m_p \delta \left(x_i - x_i^p\right) \, \mathrm{d}V \end{aligned} \tag{F.2.8}$$

Therefore, total mass is conserved if the density in the current configuration is given by the discrete approximation

$$\boxed{\tilde{\rho} \left(x_i, t\right) = \sum_{p=1}^{N_p} m_p \delta \left(x_i - x_i^p\right)} \tag{F.2.9}$$

F.3 The Cosserat Governing Equations

The linear momentum equation is given by equation C.2.11

$$\boxed{\rho \frac{\mathrm{d}v_i}{\mathrm{d}t} = \rho f_i + \sigma_{ij,j}} \tag{F.3.1}$$

and the angular momentum (moment of momentum) by equation C.2.18

$$\boxed{\varepsilon_{ijk}\sigma_{kj} + \mu_{ij,j} + \rho c_i = \rho \frac{\mathrm{d}h_i^c}{\mathrm{d}t}} \tag{F.3.2}$$

The conservation of mass (continuity equation) is given by

$$\boxed{\frac{\mathrm{d}\rho}{\mathrm{d}t} + \rho v_{i,i} = 0} \tag{F.3.3}$$

F.4 The Weak Form of the Governing Equations

For the PIC computations (as for the finite element method) we require the weak form of the linear momentum and angular momentum balance equations. The differential equations are said to state the problem in the *strong form*. An integral expression that implicitly contains the differential equations is called the *weak form*, Cook *et al.* (1989). The strong form states conditions that must be met at every material point, whereas the weak form states conditions that must be met only in an average sense. The weak form is obtained in the usual way by multiplying equations F.3.1 and F.3.2 with the test functions (vectors) w_i and ϕ_i respectively.

$$\sigma_{ij,j} w_i + \rho f_i w_i - \rho \frac{\mathrm{d}v_i}{\mathrm{d}t} w_i = 0 \tag{F.4.1}$$

$$\varepsilon_{ijk}\sigma_{kj}\phi_i + \mu_{ij,j}\phi_i + \rho c_i \phi_i - \rho \frac{\mathrm{d}h_i^c}{\mathrm{d}t}\phi_i = 0 \tag{F.4.2}$$

Combining these equations and integrating over the domain V gives, (Pilkey and Wunderlich, 1994; Cook *et al.*, 1989)

$$\begin{aligned}\int_V \sigma_{ij,j} w_i \,\mathrm{d}V + \int_V \rho f_i w_i \,\mathrm{d}V - \int_V \rho \frac{\mathrm{d}v_i}{\mathrm{d}t} w_i \,\mathrm{d}V + \int_V \varepsilon_{ijk}\sigma_{kj}\phi_i \,\mathrm{d}V + \\ \int_V \mu_{ij,j}\phi_i \,\mathrm{d}V + \int_V \rho c_i \phi_i \,\mathrm{d}V - \int_V \rho \frac{\mathrm{d}h_i^c}{\mathrm{d}t}\phi_i \,\mathrm{d}V = 0\end{aligned} \tag{F.4.3}$$

Define the specific stress and specific couple stress respectively as

$$\boxed{\sigma^s_{ij} = \frac{\sigma_{ij}}{\rho} \quad \rightarrow \quad \sigma_{ij} = \rho\sigma^s_{ij} \quad \text{and} \quad \mu^s_{ij} = \frac{\mu_{ij}}{\rho} \quad \rightarrow \quad \mu_{ij} = \rho\mu^s_{ij}} \tag{F.4.4}$$

where ρ is the material density. Assuming the material to be homogeneous, equation F.4.3 now becomes

$$\begin{aligned}\int_V \rho\sigma^s_{ij,j} w_i \,\mathrm{d}V + \int_V \rho f_i w_i \,\mathrm{d}V - \int_V \rho\frac{\mathrm{d}v_i}{\mathrm{d}t} w_i \,\mathrm{d}V + \int_V \rho\varepsilon_{ijk}\sigma^s_{kj}\phi_i \,\mathrm{d}V + \\ \int_V \rho\mu^s_{ij,j}\phi_i \,\mathrm{d}V + \int_V \rho c_i \phi_i \,\mathrm{d}V - \int_V \rho\frac{\mathrm{d}h^c_i}{\mathrm{d}t}\phi_i \,\mathrm{d}V = 0\end{aligned} \tag{F.4.5}$$

The first and fifth terms in equation F.4.5 can be expanded by using integration by parts (Washizu, 1975)

$$\begin{aligned}\int_V \rho\sigma^s_{ij,j} w_i \,\mathrm{d}V &= \int_S \rho\sigma^s_{ij} n_j w_i \,\mathrm{d}S - \int_V \rho w_{i,j}\sigma^s_{ij} \,\mathrm{d}V \\ &= \int_S \tau_i w_i \,\mathrm{d}S - \int_V \rho w_{i,j}\sigma^s_{ij} \,\mathrm{d}V\end{aligned} \tag{F.4.6}$$

$$\begin{aligned}\int_V \rho\mu^s_{ij,j}\phi_i \,\mathrm{d}V &= \int_S \rho\mu^s_{ij} n_j \phi_i \,\mathrm{d}S - \int_V \rho\phi_{i,j}\mu^s_{ij} \,\mathrm{d}V \\ &= \int_S m_i \phi_i \,\mathrm{d}S - \int_V \rho\phi_{i,j}\mu^s_{ij} \,\mathrm{d}V\end{aligned} \tag{F.4.7}$$

where

$$\begin{aligned}\tau_i &= \sigma_{ij} n_j = \rho\sigma^s_{ij} n_j \\ &= \text{ surface traction acting on surface with unit normal vector } n_j \\ m_i &= \mu_{ij} n_j = \rho\mu^s_{ij} n_j \\ &= \text{ surface couple moment acting on surface with unit normal vector } n_j\end{aligned}$$

This is an application of the divergence theorem of Gauss where S represents a surface and n_j the normal to the surface. Substitution of equation F.4.6 and F.4.7 into equation F.4.5, collecting of terms and noting that $\rho\varepsilon_{ijk}\sigma^s_{kj}\phi_i = \rho\varepsilon_{kji}\sigma^s_{ij}\phi_k = -\rho\varepsilon_{ijk}\sigma^s_{ij}\phi_k$, the governing equations can be written as

$$\begin{aligned}\int_V \left[\rho\sigma^s_{ij}\left(w_{i,j} + \varepsilon_{ijk}\phi_k\right) + \rho\phi_{i,j}\mu^s_{ij}\right] \,\mathrm{d}V = \\ \int_V \rho\left[\left(f_i - \frac{\mathrm{d}v_i}{\mathrm{d}t}\right) w_i + \left(c_i - \frac{\mathrm{d}h^c_i}{\mathrm{d}t}\right)\phi_i\right] \,\mathrm{d}V + \int_S \left(\tau_i w_i + m_i\phi_i\right) \,\mathrm{d}S\end{aligned} \tag{F.4.8}$$

Equation F.4.8 must hold for all kinematically admissible w_i and ϕ_i vanishing on those parts of the boundary where displacements and/or rotations are prescribed. Substitution of the discrete density representation, equation F.2.9 into equation F.4.8, yields a discrete expression where the integration is performed as a sum of particle properties.

$$\boxed{\begin{aligned}&\sum_{p=1}^{N_{ep}} m_p \left[\sigma_{ij}^{sp}\left(w_{i,j}^p + \varepsilon_{ijk}\phi_k^p\right) + \phi_{i,j}^p \mu_{ij}^{sp}\right] = \\ &\sum_{p=1}^{N_{ep}} m_p \left[\left(f_i^p - \frac{\mathrm{d}v_i^p}{\mathrm{d}t}\right) w_i^p + \left(c_i^p - \frac{\mathrm{d}h_i^{cp}}{\mathrm{d}t}\right)\phi_i^p\right] + \int_S \left(\tau_i w_i + m_i \phi_i\right) \mathrm{d}S\end{aligned}} \tag{F.4.9}$$

where the superscript p indicates that the value is evaluated at the particle position and N_{ep} is the number of particles in the finite element. Thus, equation F.4.9 is evaluated element-by-element.

F.5 The Finite Element Representation

Equation F.4.9 can be expanded into eight terms

$$\begin{aligned}&① \sum_{p=1}^{N_{ep}} m_p \dot{v}_i^p w_i^p + ② \sum_{p=1}^{N_{ep}} m_p \dot{h}_i^{cp} \phi_i^p = ③ \sum_{p=1}^{N_{ep}} m_p c_i^p \phi_i^p + ④ \sum_{p=1}^{N_{ep}} m_p f_i^p w_i^p - \\ &\qquad ⑤ \sum_{p=1}^{N_{ep}} m_p \sigma_{ij}^{sp} w_{i,j}^p - ⑥ \sum_{p=1}^{N_{ep}} m_p \sigma_{ij}^{sp} \varepsilon_{ijk} \phi_k^p - \\ &\qquad ⑦ \sum_{p=1}^{N_{ep}} m_p \phi_{i,j}^p \mu_{ij}^{sp} + ⑧ \int_S \left(\tau_i w_i + m_i \phi_i\right) \mathrm{d}S\end{aligned} \tag{F.5.1}$$

For the two-dimensional case, the terms are written in matrix notation:

$$① \sum_{p=1}^{N_{ep}} m_p \dot{v}_i^p w_i^p = \sum_{p=1}^{N_{ep}} m_p \begin{bmatrix} w_x^p & w_y^p & w_z^p \end{bmatrix} \begin{bmatrix} \dot{v}_x^p \\ \dot{v}_y^p \\ 0 \end{bmatrix} \tag{F.5.2}$$

where the velocity $\dot{v_z^p} = 0$.

$$② \sum_{p=1}^{N_{ep}} m_p \dot{h}_i^{cp} \phi_i^p = \sum_{p=1}^{N_{ep}} m_p \begin{bmatrix} \phi_x^p & \phi_y^p & \phi_z^p \end{bmatrix} \begin{bmatrix} 0 \\ 0 \\ \dot{h}_z^{cp} \end{bmatrix} \tag{F.5.3}$$

where the rate of angular momentum $\dot{h}_x^{cp} = \dot{h}_y^{cp} = 0$

$$③ \quad \sum_{p=1}^{N_{ep}} m_p c_i^p \phi_i^p = \sum_{p=}^{N_{ep}} m_p \begin{bmatrix} \phi_x^p & \phi_y^p & \phi_z^p \end{bmatrix} \begin{bmatrix} 0 \\ 0 \\ c_z^p \end{bmatrix} \tag{F.5.4}$$

where the body couples $c_x^p = c_y^p = 0$

$$④ \quad \sum_{p=1}^{N_{ep}} m_p f_i^p w_i^p = \sum_{p=}^{N_{ep}} m_p \begin{bmatrix} w_x^p & w_y^p & w_z^p \end{bmatrix} \begin{bmatrix} f_x^p \\ f_y^p \\ 0 \end{bmatrix} \tag{F.5.5}$$

where the body force $f_z^p = 0$

$$⑤ \quad \sum_{p=1}^{N_{ep}} m_p \sigma_{ij}^{sp} w_{i,j}^p = \sum_{p=1}^{N_{ep}} m_p \begin{bmatrix} w_{x,x}^p & w_{y,y}^p & w_{x,y}^p & w_{y,x}^p \end{bmatrix} \begin{bmatrix} \sigma_{xx}^{sp} \\ \sigma_{yy}^{sp} \\ \sigma_{xy}^{sp} \\ \sigma_{yx}^{sp} \end{bmatrix} \tag{F.5.6}$$

where only the stresses applicable to the two-dimensional case have been included.

$$⑥ \quad \sum_{p=1}^{N_{ep}} m_p \sigma_{ij}^{sp} \varepsilon_{ijk} \phi_k^p = \sum_{p=1}^{N_{ep}} m_p \begin{bmatrix} 0 & 0 & \phi_z^p & -\phi_z^p \end{bmatrix} \begin{bmatrix} \sigma_{xx}^{sp} \\ \sigma_{yy}^{sp} \\ \sigma_{xy}^{sp} \\ \sigma_{yx}^{sp} \end{bmatrix} \tag{F.5.7}$$

$$⑦ \quad \sum_{p=1}^{N_{ep}} m_p \phi_{i,j}^p \mu_{ij}^{sp} = \sum_{p=1}^{N_{ep}} m_p \begin{bmatrix} \phi_{z,x}^p \phi_{z,y}^p \end{bmatrix} \begin{bmatrix} \mu_{zx}^{sp} \\ \mu_{zy}^{sp} \end{bmatrix} \tag{F.5.8}$$

where the other couple stresses are zero.

$$⑧ \quad \begin{aligned} \int_S (\tau_i w_i + m_i \phi_i) \, \mathrm{d}S &= \int_S \left(\begin{bmatrix} w_x & w_y & w_z \end{bmatrix} \begin{bmatrix} \tau_x \\ \tau_y \\ 0 \end{bmatrix} + \begin{bmatrix} \phi_x & \phi_y & \phi_z \end{bmatrix} \begin{bmatrix} 0 \\ 0 \\ m_z \end{bmatrix} \right) \mathrm{d}S \\ &= \int_S \begin{bmatrix} w_x & w_y & \phi_z \end{bmatrix} \begin{bmatrix} \tau_x \\ \tau_y \\ m_z \end{bmatrix} \mathrm{d}S \end{aligned} \tag{F.5.9}$$

where the surface traction $\tau_z = 0$ and the surface couples $m_x = m_y = 0$. In the last equation the two sums have been added by simply discarding all zero products.

Using four node isoparametric finite elements, the test functions w_i and ϕ_i can be written in terms of the nodal values and shape functions, for example

$$w_x = [w_{x1}\ w_{x2}\ w_{x3}\ w_{x4}] \begin{bmatrix} N_1 \\ N_2 \\ N_3 \\ N_4 \end{bmatrix} \tag{F.5.10}$$

where w_{x1} is the scalar value of the test vector in the x-direction at node 1 of the element and the shape function is given by

$$\boxed{N_i = \left[\tfrac{1}{4}(1-\xi)(1-\eta)\,;\tfrac{1}{4}(1+\xi)(1-\eta)\,;\tfrac{1}{4}(1+\xi)(1+\eta)\,;\tfrac{1}{4}(1-\xi)(1+\eta)\right]} \tag{F.5.11}$$

The derivatives with respect to x and y can be written as

$$w_{x,x} = [w_{x1}\ w_{x2}\ w_{x3}\ w_{x4}] \begin{bmatrix} N_{1,x} \\ N_{2,x} \\ N_{3,x} \\ N_{4,x} \end{bmatrix} \tag{F.5.12}$$

which can be combined with the test function ϕ_i and the other derivatives into a matrix expression

$$\begin{bmatrix} w_{x,x} \\ w_{y,y} \\ w_{x,y} \\ w_{y,x} \\ \phi_{z,x} \\ \phi_{z,y} \end{bmatrix} =$$

$$\begin{bmatrix} N_{1,x} & 0 & 0 & N_{2,x} & 0 & 0 & N_{3,x} & 0 & 0 & N_{4,x} & 0 & 0 \\ 0 & N_{1,y} & 0 & 0 & N_{2,y} & 0 & 0 & N_{3,y} & 0 & 0 & N_{4,y} & 0 \\ N_{1,y} & 0 & 0 & N_{2,y} & 0 & 0 & N_{3,y} & 0 & 0 & N_{4,y} & 0 & 0 \\ 0 & N_{1,x} & 0 & 0 & N_{2,x} & 0 & 0 & N_{3,x} & 0 & 0 & N_{4,x} & 0 \\ 0 & 0 & N_{1,x} & 0 & 0 & N_{2,x} & 0 & 0 & N_{3,x} & 0 & 0 & N_{4,x} \\ 0 & 0 & N_{1,y} & 0 & 0 & N_{2,y} & 0 & 0 & N_{3,y} & 0 & 0 & N_{4,y} \end{bmatrix} \begin{bmatrix} w_{x1} \\ w_{y1} \\ \phi_{z1} \\ w_{x2} \\ w_{y2} \\ \phi_{z2} \\ w_{x3} \\ w_{y3} \\ \phi_{z3} \\ w_{x4} \\ w_{y4} \\ \phi_{z4} \end{bmatrix} \tag{F.5.13}$$

Similarly, the derivatives with respect to element coordinates can be written as

$$\begin{bmatrix} w_{x,\xi} \\ w_{y,\eta} \\ w_{x,\eta} \\ w_{y,\xi} \\ \phi_{z,\xi} \\ \phi_{z,\eta} \end{bmatrix} =$$

$$\begin{bmatrix} N_{1,\xi} & 0 & 0 & N_{2,\xi} & 0 & 0 & N_{3,\xi} & 0 & 0 & N_{4,\xi} & 0 & 0 \\ 0 & N_{1,\eta} & 0 & 0 & N_{2,\eta} & 0 & 0 & N_{3,\eta} & 0 & 0 & N_{4,\eta} & 0 \\ N_{1,\eta} & 0 & 0 & N_{2,\eta} & 0 & 0 & N_{3,\eta} & 0 & 0 & N_{4,\eta} & 0 & 0 \\ 0 & N_{1,\xi} & 0 & 0 & N_{2,\xi} & 0 & 0 & N_{3,\xi} & 0 & 0 & N_{4,\xi} & 0 \\ 0 & 0 & N_{1,\xi} & 0 & 0 & N_{2,\xi} & 0 & 0 & N_{3,\xi} & 0 & 0 & N_{4,\xi} \\ 0 & 0 & N_{1,\eta} & 0 & 0 & N_{2,\eta} & 0 & 0 & N_{3,\eta} & 0 & 0 & N_{4,\eta} \end{bmatrix} \begin{bmatrix} w_{x1} \\ w_{y1} \\ \phi_{z1} \\ w_{x2} \\ w_{y2} \\ \phi_{z2} \\ w_{x3} \\ w_{y3} \\ \phi_{z3} \\ w_{x4} \\ w_{y4} \\ \phi_{z4} \end{bmatrix} \tag{F.5.14}$$

In some of the terms in equation F.5.1, the vector $\begin{bmatrix} w_{x,x} & w_{y,y} & w_{x,y} & w_{y,x} & \phi_{z,x} & \phi_{z,y} \end{bmatrix}$ is needed, but cannot be obtained from expression F.5.13, since the partial derivatives of N_i with respect to x and y are not available. It is however possible to obtain the vector $\begin{bmatrix} w_{x,\xi} & w_{y,\eta} & w_{x,\eta} & w_{y,\xi} & \phi_{z,\xi} & \phi_{z,\eta} \end{bmatrix}$ from equation F.5.14 since the derivatives N_i with respect to ξ and η can easily be calculated using equation F.5.11.

Seek an expression for $\underline{\underline{\tilde{\Gamma}}}$ such that

$$\begin{bmatrix} w_{x,x} \\ w_{y,y} \\ w_{x,y} \\ w_{y,x} \\ \phi_{z,x} \\ \phi_{z,y} \end{bmatrix} = \underline{\underline{\tilde{\Gamma}}} \begin{bmatrix} w_{x,\xi} \\ w_{y,\eta} \\ w_{x,\eta} \\ w_{y,\xi} \\ \phi_{z,\xi} \\ \phi_{z,\eta} \end{bmatrix} \tag{F.5.15}$$

By the chain rule, for example

$$\begin{aligned} \frac{\partial w_x}{\partial x} &= \frac{\partial w_x}{\partial \xi}\frac{\partial \xi}{\partial x} + \frac{\partial w_x}{\partial \eta}\frac{\partial \eta}{\partial x} \\ \frac{\partial w_x}{\partial y} &= \frac{\partial w_x}{\partial \xi}\frac{\partial \xi}{\partial y} + \frac{\partial w_x}{\partial \eta}\frac{\partial \eta}{\partial y} \end{aligned} \tag{F.5.16}$$

Unfortunately, the partial derivatives of ξ and η with respect to x and y are not available from the above equations. Therefore, write the inverse first, which is easily done.

$$\begin{aligned}\frac{\partial w_x}{\partial \xi} &= \frac{\partial w_x}{\partial x}\frac{\partial x}{\partial \xi} + \frac{\partial w_x}{\partial y}\frac{\partial y}{\partial \xi} \\ \frac{\partial w_x}{\partial \eta} &= \frac{\partial w_x}{\partial x}\frac{\partial x}{\partial \eta} + \frac{\partial w_x}{\partial y}\frac{\partial y}{\partial \eta}\end{aligned} \tag{F.5.17}$$

Writing equation F.5.17 in matrix notation

$$\begin{bmatrix} w_{x,\xi} \\ w_{x,\eta} \end{bmatrix} = \underline{\overline{J}} \begin{bmatrix} w_{x,x} \\ w_{x,y} \end{bmatrix} = \begin{bmatrix} x_{,\xi} & y_{,\xi} \\ x_{,\eta} & y_{,\eta} \end{bmatrix} \begin{bmatrix} w_{x,x} \\ w_{x,y} \end{bmatrix} \tag{F.5.18}$$

where $\underline{\overline{J}}$ is called the *Jacobian matrix.* Using the definition of the coordinates (x, y) within an element with respect to the element nodal coordinates (x_i, y_i).

$$x = \sum_{i=1}^{4} N_i x_i \quad y = \sum_{i=1}^{4} N_i y_i \tag{F.5.19}$$

the Jacobian can be written as

$$\begin{aligned}\underline{\overline{J}} = \begin{bmatrix} x_{,\xi} & y_{,\xi} \\ x_{,\eta} & y_{,\eta} \end{bmatrix} &= \begin{bmatrix} \sum_{i=1}^{4} N_{i,\xi} x_i & \sum_{i=1}^{4} N_{i,\xi} y_i \\ \sum_{i=1}^{4} N_{i,\eta} x_i & \sum_{i=1}^{4} N_{i,\eta} y_i \end{bmatrix} \\ &= \begin{bmatrix} J_{11} & J_{12} \\ J_{21} & J_{22} \end{bmatrix}\end{aligned} \tag{F.5.20}$$

Applying a similar procedure to the other variables, it follows

$$\begin{aligned}\begin{bmatrix} w_{x,\xi} \\ w_{y,\eta} \\ w_{x,\eta} \\ w_{y,\xi} \\ \phi_{z,\xi} \\ \phi_{z,\eta} \end{bmatrix} = \underline{\overline{\overline{J}}} \begin{bmatrix} w_{x,x} \\ w_{y,y} \\ w_{x,y} \\ w_{y,x} \\ \phi_{z,x} \\ \phi_{z,y} \end{bmatrix} &= \begin{bmatrix} x_{,\xi} & 0 & y_{,\xi} & 0 & 0 & 0 \\ 0 & y_{,\eta} & 0 & x_{,\eta} & 0 & 0 \\ x_{,\eta} & 0 & y_{,\eta} & 0 & 0 & 0 \\ 0 & y_{,\xi} & 0 & x_{,\xi} & 0 & 0 \\ 0 & 0 & 0 & 0 & x_{,\xi} & y_{,\xi} \\ 0 & 0 & 0 & 0 & x_{,\eta} & y_{,\eta} \end{bmatrix} \begin{bmatrix} w_{x,x} \\ w_{y,y} \\ w_{x,y} \\ w_{y,x} \\ \phi_{z,x} \\ \phi_{z,y} \end{bmatrix} \\ &= \begin{bmatrix} J_{11} & 0 & J_{12} & 0 & 0 & 0 \\ 0 & J_{22} & 0 & J_{21} & 0 & 0 \\ J_{21} & 0 & J_{22} & 0 & 0 & 0 \\ 0 & J_{12} & 0 & J_{11} & 0 & 0 \\ 0 & 0 & 0 & 0 & J_{11} & J_{12} \\ 0 & 0 & 0 & 0 & J_{21} & J_{22} \end{bmatrix} \begin{bmatrix} w_{x,x} \\ w_{y,y} \\ w_{x,y} \\ w_{y,x} \\ \phi_{z,x} \\ \phi_{z,y} \end{bmatrix}\end{aligned} \tag{F.5.21}$$

By comparing equation F.5.15 with equation F.5.18, it can be seen that $\underline{\overline{\Gamma}}$ is the inverse of $\underline{\overline{J}}$

$$\underline{\overline{\Gamma}} = \underline{\overline{J}}^{-1} = \frac{1}{|J|}\begin{bmatrix} J_{22} & -J_{12} \\ -J_{21} & J_{11} \end{bmatrix} \tag{F.5.22}$$

where $|J|$ is the determinant of the Jacobian matrix. Applying this to equation F.5.21 yields

$$\begin{aligned} \begin{bmatrix} w_{x,x} \\ w_{y,y} \\ w_{x,y} \\ w_{y,x} \\ \phi_{z,x} \\ \phi_{z,y} \end{bmatrix} &= \underline{\underline{\overline{\Gamma}}} \begin{bmatrix} w_{x,\xi} \\ w_{y,\eta} \\ w_{x,\eta} \\ w_{y,\xi} \\ \phi_{z,\xi} \\ \phi_{z,\eta} \end{bmatrix} \\ &= \frac{1}{J}\begin{bmatrix} J_{22} & 0 & -J_{12} & 0 & 0 & 0 \\ 0 & J_{11} & 0 & -J_{21} & 0 & 0 \\ -J_{21} & 0 & J_{11} & 0 & 0 & 0 \\ 0 & -J_{12} & 0 & J_{22} & 0 & 0 \\ 0 & 0 & 0 & 0 & J_{22} & -J_{12} \\ 0 & 0 & 0 & 0 & -J_{21} & J_{11} \end{bmatrix} \begin{bmatrix} w_{x,\xi} \\ w_{y,\eta} \\ w_{x,\eta} \\ w_{y,\xi} \\ \phi_{z,\xi} \\ \phi_{z,\eta} \end{bmatrix} \end{aligned} \tag{F.5.23}$$

where $J = J_{11}J_{22} - J_{21}J_{12}$ is the determinant of $\underline{\underline{\overline{J}}}$. Taking the transpose

$$\begin{aligned} &\begin{bmatrix} w_{x,x} & w_{y,y} & w_{x,y} & w_{y,x} & \phi_{z,x} & \phi_{z,y} \end{bmatrix} = \\ &\frac{1}{J}\begin{bmatrix} w_{x,\xi} & w_{y,\eta} & w_{x,\eta} & w_{y,\xi} & \phi_{z,\xi} & \phi_{z,\eta} \end{bmatrix} \begin{bmatrix} J_{22} & 0 & -J_{21} & 0 & 0 & 0 \\ 0 & J_{11} & 0 & -J_{12} & 0 & 0 \\ -J_{12} & 0 & J_{11} & 0 & 0 & 0 \\ 0 & -J_{21} & 0 & J_{22} & 0 & 0 \\ 0 & 0 & 0 & 0 & J_{22} & -J_{21} \\ 0 & 0 & 0 & 0 & -J_{12} & J_{11} \end{bmatrix} \end{aligned} \tag{F.5.24}$$

and from equation F.5.14

$$\begin{bmatrix} w_{x,\xi} & w_{y,\eta} & w_{x,\eta} & w_{y,\xi} & \phi_{z,\xi} & \phi_{z,\eta} \end{bmatrix} =$$
$$\begin{bmatrix} w_{x1} & w_{y1} & \phi_{z1} & w_{x2} & w_{y2} & \phi_{z2} & w_{x3} & w_{y3} & \phi_{z3} & w_{x4} & w_{y4} & \phi_{z4} \end{bmatrix} \cdot$$
$$\begin{bmatrix} N_{1,\xi} & 0 & N_{1,\eta} & 0 & 0 & 0 \\ 0 & N_{1,\eta} & 0 & N_{1,\xi} & 0 & 0 \\ 0 & 0 & 0 & 0 & N_{1,\xi} & N_{1,\eta} \\ N_{2,\xi} & 0 & N_{2,\eta} & 0 & 0 & 0 \\ 0 & N_{2,\eta} & 0 & N_{2,\xi} & 0 & 0 \\ 0 & 0 & 0 & 0 & N_{2,\xi} & N_{2,\eta} \\ N_{3,\xi} & 0 & N_{3,\eta} & 0 & 0 & 0 \\ 0 & N_{3,\eta} & 0 & N_{3,\xi} & 0 & 0 \\ 0 & 0 & 0 & 0 & N_{3,\xi} & N_{3,\eta} \\ N_{4,\xi} & 0 & N_{4,\eta} & 0 & 0 & 0 \\ 0 & N_{4,\eta} & 0 & N_{4,\xi} & 0 & 0 \\ 0 & 0 & 0 & 0 & N_{4,\xi} & N_{4,\eta} \end{bmatrix} \quad \text{(F.5.25)}$$

Thus, equation F.5.24 becomes

$$\begin{bmatrix} w_{x,x} & w_{y,y} & w_{x,y} & w_{y,x} & \phi_{z,x} & \phi_{z,y} \end{bmatrix} =$$
$$\frac{1}{J} \begin{bmatrix} w_{x1} & w_{y1} & \phi_{z1} & w_{x2} & w_{y2} & \phi_{z2} & w_{x3} & w_{y3} & \phi_{z3} & w_{x4} & w_{y4} & \phi_{z4} \end{bmatrix} \cdot$$
$$\begin{bmatrix} N_{1,\xi} & 0 & N_{1,\eta} & 0 & 0 & 0 \\ 0 & N_{1,\eta} & 0 & N_{1,\xi} & 0 & 0 \\ 0 & 0 & 0 & 0 & N_{1,\xi} & N_{1,\eta} \\ N_{2,\xi} & 0 & N_{2,\eta} & 0 & 0 & 0 \\ 0 & N_{2,\eta} & 0 & N_{2,\xi} & 0 & 0 \\ 0 & 0 & 0 & 0 & N_{2,\xi} & N_{2,\eta} \\ N_{3,\xi} & 0 & N_{3,\eta} & 0 & 0 & 0 \\ 0 & N_{3,\eta} & 0 & N_{3,\xi} & 0 & 0 \\ 0 & 0 & 0 & 0 & N_{3,\xi} & N_{3,\eta} \\ N_{4,\xi} & 0 & N_{4,\eta} & 0 & 0 & 0 \\ 0 & N_{4,\eta} & 0 & N_{4,\xi} & 0 & 0 \\ 0 & 0 & 0 & 0 & N_{4,\xi} & N_{4,\eta} \end{bmatrix} \cdot$$
$$\begin{bmatrix} J_{22} & 0 & -J_{21} & 0 & 0 & 0 \\ 0 & J_{11} & 0 & -J_{12} & 0 & 0 \\ -J_{12} & 0 & J_{11} & 0 & 0 & 0 \\ 0 & -J_{21} & 0 & J_{22} & 0 & 0 \\ 0 & 0 & 0 & 0 & J_{22} & -J_{21} \\ 0 & 0 & 0 & 0 & -J_{12} & J_{11} \end{bmatrix} \quad \text{(F.5.26)}$$

Equation F.5.26 can now be substituted into terms 5 and 7 of equation F.5.1.

For the remainder of equation F.5.1, the combination of the two test functions can be written as

$$\begin{bmatrix} w_x & w_y & \phi_z \end{bmatrix} =$$

$$\begin{bmatrix} w_{x1} & w_{y1} & \phi_{z1} & w_{x2} & w_{y2} & \phi_{z2} & w_{x3} & w_{y3} & \phi_{z3} & w_{x4} & w_{y4} & \phi_{z4} \end{bmatrix} \begin{bmatrix} N_1 & 0 & 0 \\ 0 & N_1 & 0 \\ 0 & 0 & N_1 \\ N_2 & 0 & 0 \\ 0 & N_2 & 0 \\ 0 & 0 & N_2 \\ N_3 & 0 & 0 \\ 0 & N_3 & 0 \\ 0 & 0 & N_3 \\ N_4 & 0 & 0 \\ 0 & N_4 & 0 \\ 0 & 0 & N_4 \end{bmatrix} \tag{F.5.27}$$

The terms in equation F.5.1 can then be written and combined as follows.

① + ② :

$$\sum_{p=1}^{N_{ep}} m_p \left(\dot{v}_i^p w_i^p + \dot{h}_i^{cp} \phi_i^p\right) = \sum_{p=1}^{N_{ep}} m_p \begin{bmatrix} w_x^p & w_y^p & \phi_z^p \end{bmatrix} \begin{bmatrix} \dot{v}_x^p \\ \dot{v}_y^p \\ \dot{h}_z^{cp} \end{bmatrix}$$

$$= \sum_{p=1}^{N_{ep}} m_p \begin{bmatrix} w_{x1} & w_{y1} & \phi_{z1} & w_{x2} & w_{y2} & \phi_{z2} & w_{x3} & w_{y3} & \phi_{z3} & w_{x4} & w_{y4} & \phi_{z4} \end{bmatrix} \cdot$$

$$\begin{bmatrix} N_1 & 0 & 0 \\ 0 & N_1 & 0 \\ 0 & 0 & N_1 \\ N_2 & 0 & 0 \\ 0 & N_2 & 0 \\ 0 & 0 & N_2 \\ N_3 & 0 & 0 \\ 0 & N_3 & 0 \\ 0 & 0 & N_3 \\ N_4 & 0 & 0 \\ 0 & N_4 & 0 \\ 0 & 0 & N_4 \end{bmatrix}^p \cdot$$

$$\begin{bmatrix} N_1 & 0 & 0 & N_2 & 0 & 0 & N_3 & 0 & N_4 & 0 & 0 \\ 0 & N_1 & 0 & 0 & N_2 & 0 & 0 & N_3 & 0 & N_4 & 0 \\ 0 & 0 & N_1 & 0 & 0 & N_2 & 0 & 0 & N_3 & 0 & N_4 \end{bmatrix}^p \begin{bmatrix} \dot{v}_{x1} \\ \dot{v}_{y1} \\ \dot{h}_{z1}^c \\ \dot{v}_{x2} \\ \dot{v}_{y2} \\ \dot{h}_{z2}^c \\ \dot{v}_{x3} \\ \dot{v}_{y3} \\ \dot{h}_{z3}^c \\ \dot{v}_{x4} \\ \dot{v}_{y4} \\ \dot{h}_{z4}^c \end{bmatrix}$$

$$= \sum_{p=1}^{N_{ep}} m_p \begin{bmatrix} w_{x1} & w_{y1} & \phi_{z1} & w_{x2} & w_{y2} & \phi_{z2} & w_{x3} & w_{y3} & \phi_{z3} & w_{x4} & w_{y4} & \phi_{z4} \end{bmatrix} \cdot$$

$$\begin{bmatrix} N_1^2 & 0 & 0 & N_2N_1 & 0 & 0 & N_3N_1 & 0 & 0 & N_4N_1 & 0 & 0 \\ 0 & N_1^2 & 0 & 0 & N_2N_1 & 0 & 0 & N_3N_1 & 0 & 0 & N_4N_1 & 0 \\ 0 & 0 & N_1^2 & 0 & 0 & N_2N_1 & 0 & 0 & N_3N_1 & 0 & 0 & N_4N_1 \\ N_1N_2 & 0 & 0 & N_2^2 & 0 & 0 & N_3N_2 & 0 & 0 & N_4N_2 & 0 & 0 \\ 0 & N_1N_2 & 0 & 0 & N_2^2 & 0 & 0 & N_3N_2 & 0 & 0 & N_4N_2 & 0 \\ 0 & 0 & N_1N_2 & 0 & 0 & N_2^2 & 0 & 0 & N_3N_2 & 0 & 0 & N_4N_2 \\ N_1N_3 & 0 & 0 & N_2N_3 & 0 & 0 & N_3^2 & 0 & 0 & N_4N_3 & 0 & 0 \\ 0 & N_1N_3 & 0 & 0 & N_2N_3 & 0 & 0 & N_3^2 & 0 & 0 & N_4N_3 & 0 \\ 0 & 0 & N_1N_3 & 0 & 0 & N_2N_3 & 0 & 0 & N_3^2 & 0 & 0 & N_4N_3 \\ N_1N_4 & 0 & 0 & N_2N_4 & 0 & 0 & N_3N_4 & 0 & 0 & N_4^2 & 0 & 0 \\ 0 & N_1N_4 & 0 & 0 & N_2N_4 & 0 & 0 & N_3N_4 & 0 & 0 & N_4^2 & 0 \\ 0 & 0 & N_1N_4 & 0 & 0 & N_2N_4 & 0 & 0 & N_3N_4 & 0 & 0 & N_4^2 \end{bmatrix}^p \cdot$$

$$\begin{bmatrix} \dot{v}_{x1} \\ \dot{v}_{y1} \\ \dot{h}_{z1}^c \\ \dot{v}_{x2} \\ \dot{v}_{y2} \\ \dot{h}_{z2}^c \\ \dot{v}_{x3} \\ \dot{v}_{y3} \\ \dot{h}_{z3}^c \\ \dot{v}_{x4} \\ \dot{v}_{y4} \\ \dot{h}_{z4}^c \end{bmatrix} \tag{F.5.28}$$

③ + ④ :

$$\sum_{p=1}^{N_{ep}} m_p \begin{bmatrix} w_x^p & w_y^p & \phi_z^p \end{bmatrix} \begin{bmatrix} f_x^p \\ f_y^p \\ c_z^p \end{bmatrix} =$$

$$\sum_{p=1}^{N_{ep}} m_p \begin{bmatrix} w_{x1} & w_{y1} & \phi_{z1} & w_{x2} & w_{y2} & \phi_{z2} & w_{x3} & w_{y3} & \phi_{z3} & w_{x4} & w_{y4} & \phi_{z4} \end{bmatrix} \cdot$$

$$\begin{bmatrix} N_1 & 0 & 0 \\ 0 & N_1 & 0 \\ 0 & 0 & N_1 \\ N_2 & 0 & 0 \\ 0 & N_2 & 0 \\ 0 & 0 & N_2 \\ N_3 & 0 & 0 \\ 0 & N_3 & 0 \\ 0 & 0 & N_3 \\ N_4 & 0 & 0 \\ 0 & N_4 & 0 \\ 0 & 0 & N_4 \end{bmatrix}^p \begin{bmatrix} f_x^p \\ f_y^p \\ c_z^p \end{bmatrix} \quad \text{(F.5.29)}$$

⑤ + ⑦ :

$$\sum_{p=1}^{N_{ep}} m_p \left[w^p_{x,x}\ w^p_{y,y}\ w^p_{x,y}\ w^p_{y,x}\ \phi^p_{z,x}\ \phi^p_{z,y} \right] \begin{bmatrix} \sigma^{sp}_{xx} \\ \sigma^{sp}_{yy} \\ \sigma^{sp}_{xy} \\ \sigma^{sp}_{yx} \\ \mu^{sp}_{zx} \\ \mu^{sp}_{zy} \end{bmatrix} =$$

$$\sum_{p=1}^{N_{ep}} \frac{m_p}{J} \left[w_{x1} \quad w_{y1} \quad \phi_{z1} \quad w_{x2} \quad w_{y2} \quad \phi_{z2} \quad w_{x3} \quad w_{y3} \quad \phi_{z3} \quad w_{x4} \quad w_{y4} \quad \phi_{z4} \quad \right] \cdot$$

$$\begin{bmatrix} N_{1,\xi} & 0 & N_{1,\eta} & 0 & 0 & 0 \\ 0 & N_{1,\eta} & 0 & N_{1,\xi} & 0 & 0 \\ 0 & 0 & 0 & 0 & N_{1,\xi} & N_{1,\eta} \\ N_{2,\xi} & 0 & N_{2,\eta} & 0 & 0 & 0 \\ 0 & N_{2,\eta} & 0 & N_{2,\xi} & 0 & 0 \\ 0 & 0 & 0 & 0 & N_{2,\xi} & N_{2,\eta} \\ N_{3,\xi} & 0 & N_{3,\eta} & 0 & 0 & 0 \\ 0 & N_{3,\eta} & 0 & N_{3,\xi} & 0 & 0 \\ 0 & 0 & 0 & 0 & N_{3,\xi} & N_{3,\eta} \\ N_{4,\xi} & 0 & N_{4,\eta} & 0 & 0 & 0 \\ 0 & N_{4,\eta} & 0 & N_{4,\xi} & 0 & 0 \\ 0 & 0 & 0 & 0 & N_{4,\xi} & N_{4,\eta} \end{bmatrix}^p \cdot$$

$$\begin{bmatrix} J_{22} & 0 & -J_{21} & 0 & 0 & 0 \\ 0 & J_{11} & 0 & -J_{12} & 0 & 0 \\ -J_{12} & 0 & J_{11} & 0 & 0 & 0 \\ 0 & -J_{21} & 0 & J_{22} & 0 & 0 \\ 0 & 0 & 0 & 0 & J_{22} & -J_{21} \\ 0 & 0 & 0 & 0 & -J_{12} & J_{11} \end{bmatrix}^p \begin{bmatrix} \sigma^{sp}_{xx} \\ \sigma^{sp}_{yy} \\ \sigma^{sp}_{xy} \\ \sigma^{sp}_{yx} \\ \mu^{sp}_{zx} \\ \mu^{sp}_{zy} \end{bmatrix} \tag{F.5.30}$$

⑥ :

$$\sum_{p=1}^{N_{ep}} m_p \begin{bmatrix} 0 & 0 & \phi_z^p & -\phi_z^p & 0 & 0 \end{bmatrix} \begin{bmatrix} \sigma_{xx}^{sp} \\ \sigma_{yy}^{sp} \\ \sigma_{xy}^{sp} \\ \sigma_{yx}^{sp} \\ \mu_{zx}^{sp} \\ \mu_{zy}^{sp} \end{bmatrix} =$$

$$\sum_{p=1}^{N_{ep}} m_p \begin{bmatrix} w_{x1} & w_{y1} & \phi_{z1} & w_{x2} & w_{y2} & \phi_{z2} & w_{x3} & w_{y3} & \phi_{z3} & w_{x4} & w_{y4} & \phi_{z4} \end{bmatrix} \cdot$$

$$\begin{bmatrix} 0 & 0 & 0 & 0 & 0 & 0 \\ 0 & 0 & 0 & 0 & 0 & 0 \\ 0 & 0 & N_1 & -N_1 & 0 & 0 \\ 0 & 0 & 0 & 0 & 0 & 0 \\ 0 & 0 & 0 & 0 & 0 & 0 \\ 0 & 0 & N_2 & -N_2 & 0 & 0 \\ 0 & 0 & 0 & 0 & 0 & 0 \\ 0 & 0 & 0 & 0 & 0 & 0 \\ 0 & 0 & N_3 & -N_3 & 0 & 0 \\ 0 & 0 & 0 & 0 & 0 & 0 \\ 0 & 0 & 0 & 0 & 0 & 0 \\ 0 & 0 & N_4 & -N_4 & 0 & 0 \end{bmatrix}^p \begin{bmatrix} \sigma_{xx}^{sp} \\ \sigma_{yy}^{sp} \\ \sigma_{xy}^{sp} \\ \sigma_{yx}^{sp} \\ \mu_{zx}^{sp} \\ \mu_{zy}^{sp} \end{bmatrix} \tag{F.5.31}$$

where the stresses have been assembled in a matrix similar to that in equation F.5.30.

⑧ :

$$\int_S \begin{bmatrix} w_x & w_y & \phi_z \end{bmatrix} \begin{bmatrix} \tau_x \\ \tau_y \\ m_z \end{bmatrix} \, \mathrm{d}S =$$

$$\int_S \begin{bmatrix} w_{x1} & w_{y1} & \phi_{z1} & w_{x2} & w_{y2} & \phi_{z2} & w_{x3} & w_{y3} & \phi_{z3} & w_{x4} & w_{y4} & \phi_{z4} \end{bmatrix} \cdot$$

$$\begin{bmatrix} N_1 & 0 & 0 \\ 0 & N_1 & 0 \\ 0 & 0 & N_1 \\ N_2 & 0 & 0 \\ 0 & N_2 & 0 \\ 0 & 0 & N_2 \\ N_3 & 0 & 0 \\ 0 & N_3 & 0 \\ 0 & 0 & N_3 \\ N_4 & 0 & 0 \\ 0 & N_4 & 0 \\ 0 & 0 & N_4 \end{bmatrix}^p \begin{bmatrix} \tau_x \\ \tau_y \\ m_z \end{bmatrix} \, \mathrm{d}S \quad \text{(F.5.32)}$$

The vector $\begin{bmatrix} w_{x1} & w_{y1} & \phi_{z1} & w_{x2} & w_{y2} & \phi_{z2} & w_{x3} & w_{y3} & \phi_{z3} & w_{x4} & w_{y4} & \phi_{z4} \end{bmatrix}$ appears in all the above terms and since equation F.5.1 should hold for any test function w_i and ϕ_i, this vector can be dropped from each term. Adding the eight terms then yield the final form of the set of governing equations.

$$\sum_{p=1}^{N_{ep}} m_p \begin{bmatrix} N_1^2 & 0 & 0 & N_2N_1 & 0 & 0 & N_3N_1 & 0 & 0 & N_4N_1 & 0 & 0 \\ 0 & N_1^2 & 0 & 0 & N_2N_1 & 0 & 0 & N_3N_1 & 0 & 0 & N_4N_1 & 0 \\ 0 & 0 & N_1^2 & 0 & 0 & N_2N_1 & 0 & 0 & N_3N_1 & 0 & 0 & N_4N_1 \\ N_1N_2 & 0 & 0 & N_2^2 & 0 & 0 & N_3N_2 & 0 & 0 & N_4N_2 & 0 & 0 \\ 0 & N_1N_2 & 0 & 0 & N_2^2 & 0 & 0 & N_3N_2 & 0 & 0 & N_4N_2 & 0 \\ 0 & 0 & N_1N_2 & 0 & 0 & N_2^2 & 0 & 0 & N_3N_2 & 0 & 0 & N_4N_2 \\ N_1N_3 & 0 & 0 & N_2N_3 & 0 & 0 & N_3^2 & 0 & 0 & N_4N_3 & 0 & 0 \\ 0 & N_1N_3 & 0 & 0 & N_2N_3 & 0 & 0 & N_3^2 & 0 & 0 & N_4N_3 & 0 \\ 0 & 0 & N_1N_3 & 0 & 0 & N_2N_3 & 0 & 0 & N_3^2 & 0 & 0 & N_4N_3 \\ N_1N_4 & 0 & 0 & N_2N_4 & 0 & 0 & N_3N_4 & 0 & 0 & N_4^2 & 0 & 0 \\ 0 & N_1N_4 & 0 & 0 & N_2N_4 & 0 & 0 & N_3N_4 & 0 & 0 & N_4^2 & 0 \\ 0 & 0 & N_1N_4 & 0 & 0 & N_2N_4 & 0 & 0 & N_3N_4 & 0 & 0 & N_4^2 \end{bmatrix}^p .$$

$$\begin{bmatrix} \dot{v}_{x1} \\ \dot{v}_{y1} \\ \dot{h}^c_{z1} \\ \dot{v}_{x2} \\ \dot{v}_{y2} \\ \dot{h}^c_{z2} \\ \dot{v}_{x3} \\ \dot{v}_{y3} \\ \dot{h}^c_{z3} \\ \dot{v}_{x4} \\ \dot{v}_{y4} \\ \dot{h}^c_{z4} \end{bmatrix} = \sum_{p=1}^{N_{ep}} m_p \begin{bmatrix} N_1 & 0 & 0 \\ 0 & N_1 & 0 \\ 0 & 0 & N_1 \\ N_2 & 0 & 0 \\ 0 & N_2 & 0 \\ 0 & 0 & N_2 \\ N_3 & 0 & 0 \\ 0 & N_3 & 0 \\ 0 & 0 & N_3 \\ N_4 & 0 & 0 \\ 0 & N_4 & 0 \\ 0 & 0 & N_4 \end{bmatrix}^p \begin{bmatrix} f_x^p \\ f_y^p \\ c_z^p \end{bmatrix} -$$

$$\sum_{p=1}^{N_{ep}} \frac{m_p}{J} \begin{bmatrix} N_{1,\xi} & 0 & N_{1,\eta} & 0 & 0 & 0 \\ 0 & N_{1,\eta} & 0 & N_{1,\xi} & 0 & 0 \\ 0 & 0 & 0 & 0 & N_{1,\xi} & N_{1,\eta} \\ N_{2,\xi} & 0 & N_{2,\eta} & 0 & 0 & 0 \\ 0 & N_{2,\eta} & 0 & N_{2,\xi} & 0 & 0 \\ 0 & 0 & 0 & 0 & N_{2,\xi} & N_{2,\eta} \\ N_{3,\xi} & 0 & N_{3,\eta} & 0 & 0 & 0 \\ 0 & N_{3,\eta} & 0 & N_{3,\xi} & 0 & 0 \\ 0 & 0 & 0 & 0 & N_{3,\xi} & N_{3,\eta} \\ N_{4,\xi} & 0 & N_{4,\eta} & 0 & 0 & 0 \\ 0 & N_{4,\eta} & 0 & N_{4,\xi} & 0 & 0 \\ 0 & 0 & 0 & 0 & N_{4,\xi} & N_{4,\eta} \end{bmatrix}^p .$$

$$\begin{bmatrix} J_{22} & 0 & -J_{21} & 0 & 0 & 0 \\ 0 & J_{11} & 0 & -J_{12} & 0 & 0 \\ -J_{12} & 0 & J_{11} & 0 & 0 & 0 \\ 0 & -J_{21} & 0 & J_{22} & 0 & 0 \\ 0 & 0 & 0 & 0 & J_{22} & -J_{21} \\ 0 & 0 & 0 & 0 & -J_{12} & J_{11} \end{bmatrix}^p \begin{bmatrix} \sigma^{sp}_{xx} \\ \sigma^{sp}_{yy} \\ \sigma^{sp}_{xy} \\ \sigma^{sp}_{yx} \\ \mu^{sp}_{zx} \\ \mu^{sp}_{zy} \end{bmatrix} -$$

$$\sum_{p=1}^{N_{ep}} m_p \begin{bmatrix} 0 & 0 & 0 & 0 & 0 & 0 \\ 0 & 0 & 0 & 0 & 0 & 0 \\ 0 & 0 & N_1 & -N_1 & 0 & 0 \\ 0 & 0 & 0 & 0 & 0 & 0 \\ 0 & 0 & 0 & 0 & 0 & 0 \\ 0 & 0 & N_2 & -N_2 & 0 & 0 \\ 0 & 0 & 0 & 0 & 0 & 0 \\ 0 & 0 & 0 & 0 & 0 & 0 \\ 0 & 0 & N_3 & -N_3 & 0 & 0 \\ 0 & 0 & 0 & 0 & 0 & 0 \\ 0 & 0 & 0 & 0 & 0 & 0 \\ 0 & 0 & N_4 & -N_4 & 0 & 0 \end{bmatrix}^p \begin{bmatrix} \sigma^{sp}_{xx} \\ \sigma^{sp}_{yy} \\ \sigma^{sp}_{xy} \\ \sigma^{sp}_{yx} \\ \mu^{sp}_{zx} \\ \mu^{sp}_{zy} \end{bmatrix} + \int_S \begin{bmatrix} N_1 & 0 & 0 \\ 0 & N_1 & 0 \\ 0 & 0 & N_1 \\ N_2 & 0 & 0 \\ 0 & N_2 & 0 \\ 0 & 0 & N_2 \\ N_3 & 0 & 0 \\ 0 & N_3 & 0 \\ 0 & 0 & N_3 \\ N_4 & 0 & 0 \\ 0 & N_4 & 0 \\ 0 & 0 & N_4 \end{bmatrix}^p \begin{bmatrix} \tau_x \\ \tau_y \\ m_z \end{bmatrix} \mathrm{d}S \quad \text{(F.5.33)}$$

Equation F.5.33 is applicable to a single element since the sum runs over all

the particles in a single element N_{ep}. Equation F.5.33 can be written as

$$\boxed{M^e_{ij}\,\dot{v}^e_j = f_i^{e\,\text{int}} + f_i^{e\,\text{ext}} \quad \rightarrow \quad (12\times 1)\text{ matrix} \quad i,j = 1,2,\ldots,12} \tag{F.5.34}$$

where M^e_{ij} is called the element mass matrix, $f_i^{\text{e int}}$ is the internal element force vector (stresses) and $f_i^{\text{e ext}}$ is the external element force vector (body forces and surface tractions).

This derivation was based on the two-dimensional case, but following the same steps, the equations for the three-dimensional case can be derived. All stress components have to be included in the stress vector, equation F.5.6, F.5.7 and F.5.8 as well as the z-components of the acceleration, body and surface forces, and the x- and y-components of the rate of angular momentum and body and surface couples. Although σ_{zz} is included in the stress vector used in the plane strain constitutive model, it has not been included in the above derivation. The reason for this is that σ_{zz} does not directly play a role in the solution of the governing equations in the x- and y-directions. The stress σ_{zz} only enters the constitutive model. Adding σ_{zz} to equation F.5.33 can, however, easily be done as shown in equation F.5.35.

$$\sum_{p=1}^{N_{ep}} m_p \begin{bmatrix} N_1^2 & 0 & 0 & N_2N_1 & 0 & 0 & N_3N_1 & 0 & 0 & N_4N_1 & 0 & 0 \\ 0 & N_1^2 & 0 & 0 & N_2N_1 & 0 & 0 & N_3N_1 & 0 & 0 & N_4N_1 & 0 \\ 0 & 0 & N_1^2 & 0 & 0 & N_2N_1 & 0 & 0 & N_3N_1 & 0 & 0 & N_4N_1 \\ N_1N_2 & 0 & 0 & N_2^2 & 0 & 0 & N_3N_2 & 0 & 0 & N_4N_2 & 0 & 0 \\ 0 & N_1N_2 & 0 & 0 & N_2^2 & 0 & 0 & N_3N_2 & 0 & 0 & N_4N_2 & 0 \\ 0 & 0 & N_1N_2 & 0 & 0 & N_2^2 & 0 & 0 & N_3N_2 & 0 & 0 & N_4N_2 \\ N_1N_3 & 0 & 0 & N_2N_3 & 0 & 0 & N_3^2 & 0 & 0 & N_4N_3 & 0 & 0 \\ 0 & N_1N_3 & 0 & 0 & N_2N_3 & 0 & 0 & N_3^2 & 0 & 0 & N_4N_3 & 0 \\ 0 & 0 & N_1N_3 & 0 & 0 & N_2N_3 & 0 & 0 & N_3^2 & 0 & 0 & N_4N_3 \\ N_1N_4 & 0 & 0 & N_2N_4 & 0 & 0 & N_3N_4 & 0 & 0 & N_4^2 & 0 & 0 \\ 0 & N_1N_4 & 0 & 0 & N_2N_4 & 0 & 0 & N_3N_4 & 0 & 0 & N_4^2 & 0 \\ 0 & 0 & N_1N_4 & 0 & 0 & N_2N_4 & 0 & 0 & N_3N_4 & 0 & 0 & N_4^2 \end{bmatrix}^p .$$

$$\begin{bmatrix} \dot{v}_{x1} \\ \dot{v}_{y1} \\ \dot{h}^c_{z1} \\ \dot{v}_{x2} \\ \dot{v}_{y2} \\ \dot{h}^c_{z2} \\ \dot{v}_{x3} \\ \dot{v}_{y3} \\ \dot{h}^c_{z3} \\ \dot{v}_{x4} \\ \dot{v}_{y4} \\ \dot{h}^c_{z4} \end{bmatrix} = \sum_{p=1}^{N_{ep}} m_p \begin{bmatrix} N_1 & 0 & 0 \\ 0 & N_1 & 0 \\ 0 & 0 & N_1 \\ N_2 & 0 & 0 \\ 0 & N_2 & 0 \\ 0 & 0 & N_2 \\ N_3 & 0 & 0 \\ 0 & N_3 & 0 \\ 0 & 0 & N_3 \\ N_4 & 0 & 0 \\ 0 & N_4 & 0 \\ 0 & 0 & N_4 \end{bmatrix}^p \begin{bmatrix} f^p_x \\ f^p_y \\ c^p_z \end{bmatrix} -$$

$$\sum_{p=1}^{N_{ep}} \frac{m_p}{J} \begin{bmatrix} N_{1,\xi} & 0 & 0 & N_{1,\eta} & 0 & 0 & 0 \\ 0 & N_{1,\eta} & 0 & 0 & N_{1,\xi} & 0 & 0 \\ 0 & 0 & 0 & 0 & 0 & N_{1,\xi} & N_{1,\eta} \\ N_{2,\xi} & 0 & 0 & N_{2,\eta} & 0 & 0 & 0 \\ 0 & N_{2,\eta} & 0 & 0 & N_{2,\xi} & 0 & 0 \\ 0 & 0 & 0 & 0 & 0 & N_{2,\xi} & N_{2,\eta} \\ N_{3,\xi} & 0 & 0 & N_{3,\eta} & 0 & 0 & 0 \\ 0 & N_{3,\eta} & 0 & 0 & N_{3,\xi} & 0 & 0 \\ 0 & 0 & 0 & 0 & 0 & N_{3,\xi} & N_{3,\eta} \\ N_{4,\xi} & 0 & 0 & N_{4,\eta} & 0 & 0 & 0 \\ 0 & N_{4,\eta} & 0 & 0 & N_{4,\xi} & 0 & 0 \\ 0 & 0 & 0 & 0 & 0 & N_{4,\xi} & N_{4,\eta} \end{bmatrix}^p .$$

$$\begin{bmatrix} J_{22} & 0 & 0 & -J_{21} & 0 & 0 & 0 \\ 0 & J_{11} & 0 & 0 & -J_{12} & 0 & 0 \\ -J_{12} & 0 & 0 & J_{11} & 0 & 0 & 0 \\ 0 & -J_{21} & 0 & 0 & J_{22} & 0 & 0 \\ 0 & 0 & 0 & 0 & 0 & J_{22} & -J_{21} \\ 0 & 0 & 0 & 0 & 0 & -J_{12} & J_{11} \end{bmatrix}^p \begin{bmatrix} \sigma^{sp}_{xx} \\ \sigma^{sp}_{yy} \\ \sigma^{sp}_{zz} \\ \sigma^{sp}_{xy} \\ \sigma^{sp}_{yx} \\ \mu^{sp}_{zx} \\ \mu^{sp}_{zy} \end{bmatrix} -$$

$$\sum_{p=1}^{N_{ep}} m_p \begin{bmatrix} 0 & 0 & 0 & 0 & 0 & 0 & 0 \\ 0 & 0 & 0 & 0 & 0 & 0 & 0 \\ 0 & 0 & 0 & N_1 & -N_1 & 0 & 0 \\ 0 & 0 & 0 & 0 & 0 & 0 & 0 \\ 0 & 0 & 0 & 0 & 0 & 0 & 0 \\ 0 & 0 & 0 & N_2 & -N_2 & 0 & 0 \\ 0 & 0 & 0 & 0 & 0 & 0 & 0 \\ 0 & 0 & 0 & 0 & 0 & 0 & 0 \\ 0 & 0 & 0 & N_3 & -N_3 & 0 & 0 \\ 0 & 0 & 0 & 0 & 0 & 0 & 0 \\ 0 & 0 & 0 & 0 & 0 & 0 & 0 \\ 0 & 0 & 0 & N_4 & -N_4 & 0 & 0 \end{bmatrix}^p \begin{bmatrix} \sigma^{sp}_{xx} \\ \sigma^{sp}_{yy} \\ \sigma^{sp}_{zz} \\ \sigma^{sp}_{xy} \\ \sigma^{sp}_{yx} \\ \mu^{sp}_{zx} \\ \mu^{sp}_{zy} \end{bmatrix} + \int_S \begin{bmatrix} N_1 & 0 & 0 \\ 0 & N_1 & 0 \\ 0 & 0 & N_1 \\ N_2 & 0 & 0 \\ 0 & N_2 & 0 \\ 0 & 0 & N_2 \\ N_3 & 0 & 0 \\ 0 & N_3 & 0 \\ 0 & 0 & N_3 \\ N_4 & 0 & 0 \\ 0 & N_4 & 0 \\ 0 & 0 & N_4 \end{bmatrix}^p \begin{bmatrix} \tau_x \\ \tau_y \\ m_z \end{bmatrix} \mathrm{d}S \quad \text{(F.5.35)}$$

F.6 Numerical Algorithm

Equation F.5.35 is derived for a single finite element. The system is solved by sweeping through all the elements, calculating all the known terms (right hand side) in equation F.5.35 and assembling it into system arrays.

$$\sum_{e=1}^{N_e} M_{ij}^e \dot{v}_j^e = f_i^{\text{e int}} + f_i^{\text{e ext}} \qquad i,j = 1,2,\ldots,12 \tag{F.6.1}$$

where N_e is the number of elements. Summing over all the elements yields

$$\boxed{M_{ij}\dot{v}_j = f_i^{\text{int}} + f_i^{\text{ext}} \qquad i,j = 1,2,\ldots,N_{dof}} \tag{F.6.2}$$

where N_{dof} is the number of degrees-of-freedom. Equation F.6.2 has a form similar to that obtained by traditional finite element schemes, however, the mass matrix M_{ij} (assembled from element mass matrices, M_{ij}^e) varies with time and therefore must be computed each time step. Since the particles move through the mesh, the entries in the mass matrix can vary when particles move within the elements, but it can also change from size as particles move from one element to another. In other words, the total number of degrees-of-freedom in the system can vary. The following steps describe the numerical algorithm.

F.6.1 Initialisation Phase

In this phase, information is transferred from the particles to the grid. In order to solve the discrete governing equation, information must be gathered from the particles for the initialisation phase. The mass matrix must be formed, the internal forces accumulated at the nodes using the specific stresses at the particles and the gradient of the shape functions.

Begin by assuming that for each particle its position vector, velocity vector, accumulated strain components, accumulated stress components and history dependent variables are known. Linked lists are used to keep track of particles, elements and entities. An entity is defined as an *object* which may have specific properties and/or constitutive models.

Figure F.2 shows the relation between particles, elements and entities. The initial number (usually 4 or 9) and positions of particles within a single element are specified. To generate an entity, its boundary is specified and particles, with the properties of the specific entity, are generated at the specified element positions which are within the entity boundary. These particles will always belong to this entity, since they *define* the entity. Each element has a list containing particle addresses to all the particles within the element. Each entity has a list containing addresses to all the elements that contain one or more of its particles. For example, in figure F.2, entity A will have in its element list: element 1, 2, 3, 9, 10, 11, 17, 18, 19, 26 and

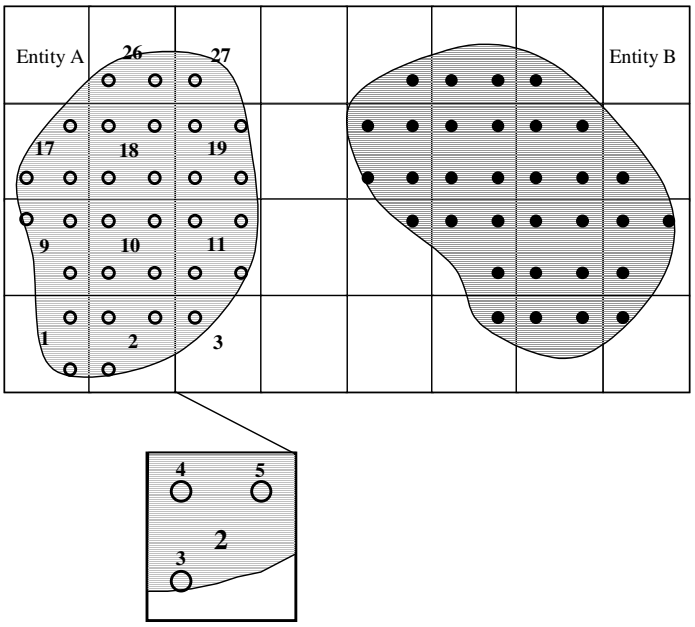

Figure F.2: Relation between particles, elements and entities

27. Element 2 will have in its particle list: particle 3, 4 and 5. In the initialisation phase, these lists are updated and used to calculate the mass matrix and force vectors.

Since there are generally more particles than grid points (nodes), a weighted least squares approach is used to determine nodal velocities from the velocities at the particles to initialise each time step. The weighting is the mass of the particle. The result is the following equation which must be solved for the nodal velocities v_j at time t, i.e. v_j^t.

$$\sum_{e=1}^{N_e} M_{ij}^{e,t} v_j^{e,t} = \sum_{e=1}^{N_e} \sum_{p=1}^{N_{ep}} m_p \begin{bmatrix} N_1 & 0 & 0 \\ 0 & N_1 & 0 \\ 0 & 0 & N_1 \\ N_2 & 0 & 0 \\ 0 & N_2 & 0 \\ 0 & 0 & N_2 \\ N_3 & 0 & 0 \\ 0 & N_3 & 0 \\ 0 & 0 & N_3 \\ N_4 & 0 & 0 \\ 0 & N_4 & 0 \\ 0 & 0 & N_4 \end{bmatrix}^{p,t} \begin{bmatrix} v_x^{p,t} \\ v_y^{p,t} \\ h_z^{cp,t} \end{bmatrix} \tag{F.6.3}$$

$$\sum_{e=1}^{N_e} M_{ij}^{e,t} v_j^{e,t} = v_i^{'e,t} \qquad i,j = 1,2,\ldots,12$$

where v_x^p and v_y^p are the particle x- and y-velocity components and h_z^{cp} is the particle angular momentum and all the variables are evaluated at time t as indicated by the superscript.

The vector v_j^e is given by $\left[v_{x1}\ v_{y1}\ h_{z1}^c\ v_{x2}\ v_{y2}\ h_{z2}^c\ v_{x3}\ v_{y3}\ h_{z3}^c\ v_{x4}\ v_{y4}\ h_{z4}^c\right]^T$. Summing over all the elements yields

$$\boxed{M_{ij}^t v_j^t = v_i^{'t} \qquad i,j = 1,2,\ldots,N_{dof}} \tag{F.6.4}$$

F.6.2 Lagrangian Phase

During the Lagrangian phase of the computation, the discrete governing equation, equation F.6.2, is solved for the nodal accelerations at time t. The solution in a Lagrangian frame means that the nonlinear convective terms that are troublesome in purely Eulerian calculations do not appear in the formulation (Sulsky *et al.*, 1995). With the nodal accelerations computed, the nodal velocities can be updated with the use of an explicit time integrator.

$$v_i^{t+1} = v_i^t + \Delta t \dot{v}_i^t \qquad i,j = 1,2,\ldots,12 \tag{F.6.5}$$

where Δt is the current time increment. During this phase of the computation, the nodes are assumed to move according to this computed velocity. The updates of particle velocity and position are consistent with the isoparametric approach

$$x_i^{p,t+1} = x_i^{p,t} + \Delta t \begin{bmatrix} N_1 & 0 & 0 & N_2 & 0 & 0 & N_3 & 0 & N_4 & 0 & 0 \\ 0 & N_1 & 0 & 0 & N_2 & 0 & 0 & N_3 & 0 & N_4 & 0 \\ 0 & 0 & N_1 & 0 & 0 & N_2 & 0 & 0 & N_3 & 0 & N_4 \end{bmatrix}^{p,t} \begin{bmatrix} v_{x1} \\ v_{y1} \\ h_{z1}^c \\ v_{x2} \\ v_{y2} \\ h_{z2}^c \\ v_{x3} \\ v_{y3} \\ h_{z3}^c \\ v_{x4} \\ v_{y4} \\ h_{z4}^c \end{bmatrix}^{t+1} \tag{F.6.6}$$

or in index notation

$$x_i^{p,t+1} = x_i^{p,t} + \Delta t\ N_{ij}^{p,t}\ v_j^{e,t+1} \tag{F.6.7}$$

The position vector is given by $x_i^p = \left[x^p \; y^p \; J_{zz}^p w_z^{cp}\right]$, where w_z^c is the Cosserat rotation, equation C.3.4, and should not be confused with the test function w_i. The vector $v_j^{e,t+1}$ is the nodal velocities of the element containing the particle. This vector is extracted from the system solution v_i^{t+1} in equation F.6.5. A similar equation can be written for the velocity update.

$$v_i^{p,t+1} = v_i^{p,t} + \Delta t \begin{bmatrix} N_1 & 0 & 0 & N_2 & 0 & 0 & N_3 & 0 & N_4 & 0 & 0 \\ 0 & N_1 & 0 & 0 & N_2 & 0 & 0 & N_3 & 0 & N_4 & 0 \\ 0 & 0 & N_1 & 0 & 0 & N_2 & 0 & 0 & N_3 & 0 & N_4 \end{bmatrix}^{p,t} \begin{bmatrix} \dot{v}_{x1} \\ \dot{v}_{y1} \\ \dot{h}_{z1}^c \\ \dot{v}_{x2} \\ \dot{v}_{y2} \\ \dot{h}_{z2}^c \\ \dot{v}_{x3} \\ \dot{v}_{y3} \\ \dot{h}_{z3}^c \\ \dot{v}_{x4} \\ \dot{v}_{y4} \\ \dot{h}_{z4}^c \end{bmatrix}^t \tag{F.6.8}$$

or in index notation

$$v_i^{p,t+1} = v_i^{p,t} + \Delta t \; N_{ij}^{p,t} \; \dot{v}_j^{e,t} \tag{F.6.9}$$

where $\dot{v}_j^{e,t}$ is the nodal acceleration of the element containing the particle. This vector is extracted from the system solution $\dot{v}_i^t$ obtained from solving equation F.6.2.

During the Lagrangian step, each element is assumed to deform in the flow of material so that points in the interior of the element move in proportion to the motion of the nodes, as given by the representation using the nodal shape (basis) functions. Since shape functions are used to map the nodal velocity continuously to the interior of the element, the positions of the particles are updated by moving them in a single-valued, continuous velocity field. Similarly, the velocity of a material is updated by mapping the nodal accelerations to the particle position. Because the velocity field is single-valued, interpenetration of material is precluded. This feature of the algorithm allows simulations of impact and penetration without the need for a special contact algorithm (Sulsky *et al.*, 1995).

For history dependent materials, it has been convenient to carry strain and stress, as well as history variables along with the material points. Applying constitutive equations at material points (particles) allows easy evaluation and tracking of history dependent variables. It also allows computations with multiple materials to be performed easily since each particle

retains its identity (material or entity properties) throughout the computation. Another difference between equation F.6.2 and traditional finite element formulations is that the particles, where constitutive equations are applied, move from one element to another rather than remain at the centre or Gauss points of an element.

To describe the stress computations in its simplest form, strain increments are obtained from gradients of the nodal velocities evaluated at the particle positions. Then, given a strain increment at the particle, along with current values of history variables and material parameters, standard routines are used to evaluate the stress increment and update history variables. The internal forces at the nodes are then calculated directly from the stress at the particles for the next time step.

The single, tensorial deformation measure is given by, equation C.3.7

$$\lambda_{ij} = u_{i,j} + \varepsilon_{ijk} w_k^c \tag{F.6.10}$$

or for planar deformation

$$\lambda_{ij} = \begin{bmatrix} \lambda_{xx} & \lambda_{xy} & \lambda_{xz} \\ \lambda_{yx} & \lambda_{yy} & \lambda_{yz} \\ \lambda_{zx} & \lambda_{zy} & \lambda_{zz} \end{bmatrix} = \begin{bmatrix} u_{x,x} & \left(u_{x,y} + w_z^c\right) & 0 \\ \left(u_{y,x} - w_z^c\right) & u_{y,y} & 0 \\ 0 & 0 & u_{z,z} \end{bmatrix}$$

The micro-curvature is given by

$$\kappa_{ij} = w_{i,j}^c \tag{F.6.11}$$

or for planar deformation

$$\kappa_{ij} = \begin{bmatrix} 0 & 0 & 0 \\ 0 & 0 & 0 \\ \kappa_{zx} & \kappa_{zy} & 0 \end{bmatrix}$$

In formulating elasto-plasticity, it is useful to rather use generalised curvatures $\kappa_{zx} l$ and $\kappa_{zy} l$, where l is a material parameter with the dimension of length. It is this parameter which effectively sets the internal length scale in the continuum, and therefore has the role of a "characteristic length".

The strain components can be assembled in a vector (for the two-dimensional case)

$$\varepsilon_i^c = \left[\lambda_{xx}\ \lambda_{yy}\ \lambda_{zz}\ \lambda_{xy}\ \lambda_{yx}\ \kappa_{zx} l\ \kappa_{zy} l\right] \tag{F.6.12}$$

Note that the normal strain in the z-direction, $\lambda_{zz} = u_{z,z}$, has also been included in the strain vector. This has been done because, although this strain component remains zero under plane strain conditions during the entire loading process, this is not necessarily the case for the elastic and plastic contributions of this strain component. Also note that by multiplying the

micro-curvatures by the length parameter l, all components of the strain vector ε_i^c have the same dimension. The strain rate vector can be written as

$$\dot{\varepsilon}_i^c = \left[v_{x,x}\ v_{y,y}\ v_{z,z}\ \left(v_{x,y} + \dot{w}_z^c\right)\ \left(v_{y,x} - \dot{w}_z^c\right)\ \dot{w}_{z,x}^c l\ \dot{w}_{z,y}^c l \right] \tag{F.6.13}$$

Making use of equation F.5.26, the terms in equation F.6.13 can be computed at the particle positions.

$$\begin{aligned}
&\left[v_{x,x}^p \quad v_{y,y}^p \quad v_{x,y}^p \quad v_{y,x}^p \quad \dot{w}_{z,x}^{cp} \quad \dot{w}_{z,y}^{cp} \right] = \\
&\frac{1}{J} \left[v_{x1} \quad v_{y1} \quad \dot{w}_{z1}^c \quad v_{x2} \quad v_{y2} \quad \dot{w}_{z2}^c \quad v_{x3} \quad v_{y3} \quad \dot{w}_{z3}^c \quad v_{x4} \quad v_{y4} \quad \dot{w}_{z4}^c \quad \right] \cdot \\
&\qquad \begin{bmatrix}
N_{1,\xi} & 0 & N_{1,\eta} & 0 & 0 & 0 \\
0 & N_{1,\eta} & 0 & N_{1,\xi} & 0 & 0 \\
0 & 0 & 0 & 0 & N_{1,\xi} & N_{1,\eta} \\
N_{2,\xi} & 0 & N_{2,\eta} & 0 & 0 & 0 \\
0 & N_{2,\eta} & 0 & N_{2,\xi} & 0 & 0 \\
0 & 0 & 0 & 0 & N_{2,\xi} & N_{2,\eta} \\
N_{3,\xi} & 0 & N_{3,\eta} & 0 & 0 & 0 \\
0 & N_{3,\eta} & 0 & N_{3,\xi} & 0 & 0 \\
0 & 0 & 0 & 0 & N_{3,\xi} & N_{3,\eta} \\
N_{4,\xi} & 0 & N_{4,\eta} & 0 & 0 & 0 \\
0 & N_{4,\eta} & 0 & N_{4,\xi} & 0 & 0 \\
0 & 0 & 0 & 0 & N_{4,\xi} & N_{4,\eta}
\end{bmatrix}^p \cdot \\
&\qquad\qquad \begin{bmatrix}
J_{22} & 0 & -J_{21} & 0 & 0 & 0 \\
0 & J_{11} & 0 & -J_{12} & 0 & 0 \\
-J_{12} & 0 & J_{11} & 0 & 0 & 0 \\
0 & -J_{21} & 0 & J_{22} & 0 & 0 \\
0 & 0 & 0 & 0 & J_{22} & -J_{21} \\
0 & 0 & 0 & 0 & -J_{12} & J_{11}
\end{bmatrix}^p
\end{aligned} \tag{F.6.14}$$

and $v_{z,z}^p = 0$. Further, $h_z^c \left[\mathrm{m}^2 \cdot \mathrm{s}^{-1}\right] = J_{zz} \left[\mathrm{m}^2\right] \dot{w}_z^c \left[\mathrm{s}^{-1}\right]$, equation D.3.10, i.e. $\dot{w}_z^c = \frac{h_z^c}{J_{zz}}$. Equation F.6.14 becomes

$$\begin{bmatrix} v^p_{x,x} & v^p_{y,y} & v^p_{x,y} & v^p_{y,x} & \dot{w}^{cp}_{z,x} & \dot{w}^{cp}_{z,y} \end{bmatrix} =$$
$$\frac{1}{J}\begin{bmatrix} v_{x1} & v_{y1} & \frac{h^c_{z1}}{J_{zz}} & v_{x2} & v_{y2} & \frac{h^c_{z2}}{J_{zz}} & v_{x3} & v_{y3} & \frac{h^c_{z3}}{J_{zz}} & v_{x4} & v_{y4} & \frac{h^c_{z4}}{J_{zz}} \end{bmatrix} \cdot$$
$$\begin{bmatrix} N_{1,\xi} & 0 & N_{1,\eta} & 0 & 0 & 0 \\ 0 & N_{1,\eta} & 0 & N_{1,\xi} & 0 & 0 \\ 0 & 0 & 0 & 0 & N_{1,\xi} & N_{1,\eta} \\ N_{2,\xi} & 0 & N_{2,\eta} & 0 & 0 & 0 \\ 0 & N_{2,\eta} & 0 & N_{2,\xi} & 0 & 0 \\ 0 & 0 & 0 & 0 & N_{2,\xi} & N_{2,\eta} \\ N_{3,\xi} & 0 & N_{3,\eta} & 0 & 0 & 0 \\ 0 & N_{3,\eta} & 0 & N_{3,\xi} & 0 & 0 \\ 0 & 0 & 0 & 0 & N_{3,\xi} & N_{3,\eta} \\ N_{4,\xi} & 0 & N_{4,\eta} & 0 & 0 & 0 \\ 0 & N_{4,\eta} & 0 & N_{4,\xi} & 0 & 0 \\ 0 & 0 & 0 & 0 & N_{4,\xi} & N_{4,\eta} \end{bmatrix}^p \cdot$$
$$\begin{bmatrix} J_{22} & 0 & -J_{21} & 0 & 0 & 0 \\ 0 & J_{11} & 0 & -J_{12} & 0 & 0 \\ -J_{12} & 0 & J_{11} & 0 & 0 & 0 \\ 0 & -J_{21} & 0 & J_{22} & 0 & 0 \\ 0 & 0 & 0 & 0 & J_{22} & -J_{21} \\ 0 & 0 & 0 & 0 & -J_{12} & J_{11} \end{bmatrix}^p \tag{F.6.15}$$

The strain increment at the particle position is

$$\Delta\varepsilon^{cp}_i = \Delta t \begin{bmatrix} v^p_{x,x} & v^p_{y,y} & v^p_{z,z} & \left(v^p_{x,y} + \dot{w}^{cp}_z\right) & \left(v^p_{y,x} - \dot{w}^{cp}_z\right) & \dot{w}^{cp}_{z,x} l & \dot{w}^{cp}_{z,y} l \end{bmatrix} \tag{F.6.16}$$

With the strain increment known, a constitutive model can be used to calculate the stress increment. The strain and stress are then updated according to

$$\varepsilon^{cp,t+1}_i = \varepsilon^{cp,t}_i + \Delta\varepsilon^{cp}_i \tag{F.6.17}$$

$$\sigma^{cp,t+1}_i = \sigma^{cp,t}_i + \Delta\sigma^{cp}_i \tag{F.6.18}$$

F.6.3 Convective Phase

At this point in the computational cycle, the particles are completely updated and carry the complete solution. During the convective phase, the particles are held fixed and the computational grid is redefined. The grid can be chosen in any convenient manner, for example adaptive grids can be

used to resolve sharp gradients and interfaces. A particular simple choice is the regular square mesh. Any motion of the grid relative to the particles models convection. Since the particles do not move during the convective phase, particle properties (position vector, velocity vector, strain and stress) have the same value at the end of the convective phase as they had at the end of the Lagrangian phase.

This completes the computational cycle. A new cycle is begun using the information carried by the particles to initialize nodal values on a new grid.

F.7 Numerical Implementation

With the algorithm described in the previous section, if a single particle crosses into an element and is close to the element boundary, the value of a shape function identified with a node at the opposite side of the element may be small. However, the internal force vector involves the gradient of the shape function, which does not approach zero for points close to the element boundary. The result is that computed accelerations at outer nodes can occasionally be unphysically and lead to particles separating from its entity. One approach to this problem is to detect small nodal masses and to set the corresponding internal force at the node to zero if the mass is below a certain cutoff value (Sulsky *et al.*, 1995). Although this approach is quite successful, it is difficult to justify the choice of the cutoff value. However, with a simple change in the algorithm, the need to apply a cutoff is eliminated.

The key to reordering operations is to work with momentum instead of velocity as much as possible. This avoids divisions by nodal masses. Define the system nodal momentum at time $t = 0$ as

$$p_i^t = M_{ij}^t v_j^t \tag{F.7.1}$$

and the particle momentum at time $t = 0$ as

$$p_i^{p,t} = m_p v_i^{p,t} \tag{F.7.2}$$

Equation F.6.3 can be rewritten

$$p_i^t = \sum_{e=1}^{N_e} \sum_{p=1}^{N_{ep}} \begin{bmatrix} N_1 & 0 & 0 \\ 0 & N_1 & 0 \\ 0 & 0 & N_1 \\ N_2 & 0 & 0 \\ 0 & N_2 & 0 \\ 0 & 0 & N_2 \\ N_3 & 0 & 0 \\ 0 & N_3 & 0 \\ 0 & 0 & N_3 \\ N_4 & 0 & 0 \\ 0 & N_4 & 0 \\ 0 & 0 & N_4 \end{bmatrix}^{p,t} \begin{bmatrix} m_p v_x^{p,t} \\ m_p v_y^{p,t} \\ m_p h_z^{cp,t} \end{bmatrix} \tag{F.7.3}$$

$$p_i^t = p_i^{'t}$$

Note that it is not necessary to divide by the nodal mass to solve the nodal momentum p_i^t, as it was necessary in equation F.6.4 to solve for the nodal velocity v_j^t. The momentum equation at time t, equation F.6.2, becomes

$$\dot{p}_i^t = f_i^{\text{int,t}} + f_i^{\text{ext,t}} \tag{F.7.4}$$

The solution of this equation provides the momentum update

$$\begin{aligned} p_i^{t+1} &= p_i^t + \Delta t \left(f_i^{\text{int,t}} + f_i^{\text{ext,t}} \right) \\ p_i^{t+1} &= p_i^t + \Delta t \; \dot{p}_i^t \end{aligned} \tag{F.7.5}$$

To update the particle position, the system nodal velocity is calculated

$$v_i^{t+1} = \left(M_{ij}^t \right)^{-1} p_j^{t+1} \tag{F.7.6}$$

where $\left(M_{ij}^t \right)^{-1}$ is the inverse of the mass matrix and the position update becomes (similar to equation F.6.7)

$$x_i^{p,t+1} = x_i^{p,t} + \Delta t \; N_{ij}^{p,t} \; v_j^{e,t+1} \tag{F.7.7}$$

where $v_j^{e,t+1}$ is the nodal velocities of the element containing the particle. This vector is extracted from the system solution v_i^{t+1} in equation F.7.6. To update the particle velocity, the system nodal acceleration is calculated

$$\dot{v}_i{}^t = \left(M_{ij}^t \right)^{-1} \dot{p}_j^t \tag{F.7.8}$$

and the velocity update becomes (similar to equation F.6.9)

$$v_i^{p,t+1} = v_i^{p,t} + \Delta t \; N_{ij}^{p,t} \; \dot{v}_j^{e,t} \tag{F.7.9}$$

where $\dot{v}_j^{e,t}$ is the nodal acceleration of the element containing the particle. This vector is extracted from the system solution $\dot{v}_i^t$ obtained from solving equation F.7.8.

Velocity gradients are needed for the strain increment. The Lagrangian grid velocity can be obtained from the updated particle velocity by solving the equation

$$\sum_{e=1}^{N_e} M_{ij}^{e,t} v_j^{e,t+1} = \sum_{e=1}^{N_e} \sum_{p=1}^{N_{ep}} m_p \begin{bmatrix} N_1 & 0 & 0 \\ 0 & N_1 & 0 \\ 0 & 0 & N_1 \\ N_2 & 0 & 0 \\ 0 & N_2 & 0 \\ 0 & 0 & N_2 \\ N_3 & 0 & 0 \\ 0 & N_3 & 0 \\ 0 & 0 & N_3 \\ N_4 & 0 & 0 \\ 0 & N_4 & 0 \\ 0 & 0 & N_4 \end{bmatrix}^{p,t} \begin{bmatrix} v_x^{p,t+1} \\ v_y^{p,t+1} \\ h_z^{cp,t+1} \end{bmatrix} \tag{F.7.10}$$

$$\sum_{e=1}^{N_e} M_{ij}^{e,t} v_j^{e,t+1} = v_i^{'e,t+1}$$

Summing over all the elements yield (similar to equation F.6.4)

$$\boxed{M_{ij}^t v_j^{t+1} = v_i^{'t+1} \qquad i,j = 1,2,\ldots,N_{dof}} \tag{F.7.11}$$

Mathematically, there is no difference between the algorithm in this section and the last, if the consistent mass matrix M_{ij} is invertible. However, the numerical properties are improved. In equation F.7.6 and F.7.7, the multiplication of the momentum with the shape functions and division by the mass matrix has the effect of balancing the numerator and denominator in the case of small nodal masses. The same applies to equation F.7.8 and F.7.9.

In practice, to simplify computations, a lumped mass matrix is used instead of the consistent mass matrix given in equation F.5.33. The lumped mass matrix is a diagonal matrix with each entry being the corresponding row sum of the consistent mass matrix. Matrix inversions become trivial if a lumped matrix is used, at the cost of introducing a small amount of numerical dissipation. Burgess *et al.* (1992) have shown that the mapping of particle velocities to the nodes (equation F.6.4, F.7.3 and F.7.11) implies that the kinetic energy, linear momentum and angular momentum are conserved. Kinetic energy is, however, only conserved provided the consistent mass matrix is used. The result of using a lumped mass matrix is some dissipation of kinetic energy that has been quantified by Burgess *et al.* (1992);

Brackbill *et al.* (1988); Brackbill & Ruppel (1988). The mass matrix can also be singular for certain arrangements of the particles. A simple example is a single particle with unit mass in the center of a computational element. In one dimension, using linear interpolation, the particle contributed equally to two vertices. If the element has unit length, the mass matrix is (Burgess *et al.*, 1992)

$$M_{ij}^{e} = \begin{bmatrix} \frac{1}{4} & \frac{1}{4} \\ \frac{1}{4} & \frac{1}{4} \end{bmatrix} \tag{F.7.12}$$

There appears to be only a few arrangements of particles that yield a singular mass matrix, but nearby arrangements might result in an ill-conditioned matrix. On the other hand, the lumped matrix is diagonal and well conditioned. It is possible to partially lump the mass matrix in order to improve the numerical computations, at a cost of adding a small amount of dissipation. The partially lumped mass matrix $M_{ij}^{\text{part lumped}}$ is defined as

$$M_{ij}^{\text{part lumped}} = (1-\epsilon)\, M_{ij} + \epsilon M_{ij}^{\text{lumped}} \tag{F.7.13}$$

When $\epsilon = 1$, $M_{ij}^{\text{part lumped}}$ reduces to the lumped mass matrix M_{ij}^{lumped}, and when $\epsilon = 0$, it is the full mass matrix M_{ij}. Lumping of the mass matrix has no effect on the conservation of linear and angular momentum, but does influence the conservation of kinetic energy. Burgess *et al.* (1992) showed that for positive ϵ there is a loss in kinetic energy during grid mapping in the Lagrangian phase. The dissipation introduced by lumping the mass matrix is $O\left(\Delta t^2\right)$, and this accounts for relatively low energy dissipation even if $\epsilon = 1$. Further, Cook *et al.* (1989, §13.10) showed that explicit time integration is usually more accurate with lumped mass matrices than with consistent mass matrices.

F.8 Numerical Algorithm

This section summarises the numerical algorithm. Assume that at time = t, the position vector, $x_i^{p,t}$, velocity vector, $v_i^{p,t}$, accumulated strain, $\varepsilon_i^{cp,t}$, accumulated stress, $\sigma_i^{cp,t}$ and history variables of each particle are known. The coordinates of the nodes (grid points) are also known. The lists of elements in entities and particles in elements are known for time = $t-1$.

The different vectors are structured as follows.

$$\begin{aligned} x_i^p &= \left[x^p \; y^p \; J_{zz}^p w_z^{cp}\right]^T \\ v_i^p &= \left[v_x^p \; v_y^p \; h_z^{cp}\right]^T = \left[v_x^p \; v_y^p \; \left(J_{zz}^p \dot{w}_z^{cp}\right)\right]^T \\ \varepsilon_i^{cp} &= \left[\lambda_{xx}^p \; \lambda_{yy}^p \; \lambda_{zz}^p \; \lambda_{xy}^p \; \lambda_{yx}^p \; \kappa_{zx}^p l \; \kappa_{zy}^p l\right] \\ \sigma_i^{cp} &= \left[\sigma_{xx}^p \; \sigma_{yy}^p \; \sigma_{zz}^p \; \sigma_{xy}^p \; \sigma_{yx}^p \; \frac{\mu_{zx}^p}{l} \; \frac{\mu_{zy}^p}{l}\right] \end{aligned} \tag{F.8.1}$$

Step 1:

Cycle through all the particles and update the particles-in-element and element-in-entity lists for time = t. Only the nodes of elements containing particles will be active nodes during this time step. Set up an array to identify the active nodes on the grid. The total number of degrees-of-freedom N_{dof} will be three times the number of active nodes (two translational and one rotational degree-of-freedom per node). With the position vector of a particle and its element known, the particle coordinates in the element coordinate system $\xi\eta$ can be calculated. Zhao *et al.* (1999) developed an algorithm to calculate the element coordinates for four-node bilinear quadrilateral elements. The $\xi\eta$-coordinate of each particle is stored since it is used more than once during one time step.

Step 2:

Map the particles momentum to the active nodes to obtain the system nodal momentum $p_i^t \;\; \left(N_{dof} \times 1\right)$ at time = t.

$$\begin{aligned} p_i^t &= \sum_{e=1}^{N_e} \sum_{p=1}^{N_{ep}} \begin{bmatrix} N_1 & 0 & 0 \\ 0 & N_1 & 0 \\ 0 & 0 & N_1 \\ N_2 & 0 & 0 \\ 0 & N_2 & 0 \\ 0 & 0 & N_2 \\ N_3 & 0 & 0 \\ 0 & N_3 & 0 \\ 0 & 0 & N_3 \\ N_4 & 0 & 0 \\ 0 & N_4 & 0 \\ 0 & 0 & N_4 \end{bmatrix}^{p,t} \begin{bmatrix} m_p v_x^{p,t} \\ m_p v_y^{p,t} \\ m_p h_z^{cp,t} \end{bmatrix} \\ p_i^t &= p_i^{'t} \end{aligned} \tag{F.8.2}$$

Step 3:

Calculate the system force vectors. The internal force vector $f_i^{\text{e int,t}}\ \left(N_{dof} \times 1\right)$ is calculated using the particle stresses at time t and the external force vector $f_i^{\text{e ext,t}}\ \left(N_{dof} \times 1\right)$ is calculated using the body forces and surface tractions. The system consistent mass matrix $M_{ij}^t\ \left(N_{dof} \times N_{dof}\right)$ is constructed from the current particle positions, equation F.5.35. With the force vectors known, the rate of change in momentum at time t is simply

$$\dot{p}_i^t = f_i^{\text{int,t}} + f_i^{\text{ext,t}} \tag{F.8.3}$$

Step 4:

With the nodal momentum and the rate of nodal momentum known at time t, the momentum at time $t+1$, $p_i^{t+1}\ \left(N_{dof} \times 1\right)$, can be calculated using a explicit integration scheme.

$$p_i^{t+1} = p_i^t + \Delta t\ \dot{p}_i^t \tag{F.8.4}$$

Step 5:

The consistent mass matrix can be used, but for simplicity and better numerical properties, the lumped or partially lumped mass matrix can be used

$$M_{ij}^{\text{part lumped}} = (1-\epsilon)\, M_{ij} + \epsilon M_{ij}^{\text{lumped}} \tag{F.8.5}$$

Solving a system of equations is trivial when the lumped matrix is used, but when the consistent or partially-lumped mass matrix is used, special algorithms are needed.

Step 6:

To update the particle positions, the updated system nodal velocity, $v_i^{t+1}\ \left(N_{dof} \times 1\right)$, is calculated

$$v_i^{t+1} = \left(M_{ij}^t\right)^{-1} p_j^{t+1} \tag{F.8.6}$$

The particle positions are now updated according to

$$x_i^{p,t+1} = x_i^{p,t} + \Delta t\ N_{ij}^{p,t}\ v_j^{e,t+1} \tag{F.8.7}$$

where $v_j^{e,t+1}$ (12×1) are the nodal velocities of the element containing the particle. This vector is extracted from the system solution v_i^{t+1} $\left(N_{dof} \times 1\right)$ in equation F.8.6. To update the particle velocity, the updated system nodal acceleration, $\dot{v}_i^t$ $\left(N_{dof} \times 1\right)$, is calculated

$$\dot{v}_i{}^t = \left(M_{ij}^t\right)^{-1} \dot{p}_j^t \tag{F.8.8}$$

and the velocity update becomes

$$v_i^{p,t+1} = v_i^{p,t} + \Delta t \; N_{ij}^{p,t} \; \dot{v}_j^{e,t} \tag{F.8.9}$$

where $\dot{v}_j^{e,t}$ is the nodal acceleration of the element containing the particle. This vector is extracted from the system solution $\dot{v}_i^t$ obtained from solving equation F.8.8.

Step 7:

The grid velocity, v_j^{t+1}, is obtained from the updated particle velocity by solving

$$\sum_{e=1}^{N_e} M_{ij}^{e,t} v_j^{e,t+1} = \sum_{e=1}^{N_e} \sum_{p=1}^{N_{ep}} m_p \begin{bmatrix} N_1 & 0 & 0 \\ 0 & N_1 & 0 \\ 0 & 0 & N_1 \\ N_2 & 0 & 0 \\ 0 & N_2 & 0 \\ 0 & 0 & N_2 \\ N_3 & 0 & 0 \\ 0 & N_3 & 0 \\ 0 & 0 & N_3 \\ N_4 & 0 & 0 \\ 0 & N_4 & 0 \\ 0 & 0 & N_4 \end{bmatrix}^{p,t} \begin{bmatrix} v_x^{p,t+1} \\ v_y^{p,t+1} \\ h_z^{cp,t+1} \end{bmatrix} \tag{F.8.10}$$

$$\sum_{e=1}^{N_e} M_{ij}^{e,t} v_j^{e,t+1} = v_i^{'e,t+1}$$

$$M_{ij}^t v_j^{t+1} = v_i^{'t+1}$$

Step 8:

The strain increment $\Delta\varepsilon_i^{cp}$ is calculated at particle positions, using the solution of equation F.8.10

$$\Delta\varepsilon_i^{cp} = \Delta t \left[v_{x,x}^p \; v_{y,y}^p \; v_{z,z}^p \; \left(v_{x,y}^p + \dot{w}_z^{cp}\right) \; \left(v_{y,x}^p - \dot{w}_z^{cp}\right) \; \dot{w}_{z,x}^{cp} l \; \dot{w}_{z,y}^{cp} l \right] \tag{F.8.11}$$

where the velocity derivatives are given by equation F.6.15. With the strain increment known, a constitutive model can be used to calculate the stress increment. The strain and stress are then updated according to

$$\varepsilon_i^{cp,t+1} = \varepsilon_i^{cp,t} + \Delta\varepsilon_i^{cp} \tag{F.8.12}$$

$$\sigma_i^{cp,t+1} = \sigma_i^{cp,t} + \Delta\sigma_i^{cp} \tag{F.8.13}$$

Particle history variables are updated and step 1 repeated to initiate a new time step.

F.9 Numerical Integration: Convergence and Stability

In the previous sections, a simple forward-difference explicit time integrator was used of which the time step should satisfy the stability condition, i.e., the critical time step should be the smallest ratio of the element size to the wave speed. For small displacements, the spatial discretisation in PIC is equivalent to that of FEM using Guass points at the same locations as those of the material points in each cell. Therefore, the convergence behaviour of the integrator used is similar to that employed to integrate the corresponding equation in FEM. However, no consistent theoretical results have been obtained for the convergence behaviour of time integrators when large deformations occur and a reasonable time step is usually found through numerical experiments (Chen *et al.*, 2002).

Wieckowski *et al.* (1999) pointed out that the PIC method in general may require a shorter time increment than the standard FEM method. The following stability analysis follows from Wieckowski *et al.* (1999). In standard FEM, for the one-dimensional element with linear shape functions, the condition of stability has the form

$$\Delta t \leq \Delta t_{crit}^{FEM} = \begin{cases} \frac{2h}{\sqrt{3}C} & \text{for a consistent mass matrix} \\ \frac{2h}{\sqrt{2}C} & \text{for a lumped mass matrix} \end{cases} \tag{F.9.1}$$

where h is the element size and C denotes the speed of elastic wave propagation. In the PIC method the critical time step, however, depends on the mutual position of the material points and the computational mesh. The critical time step can be derived from the stability condition

$$\Delta t^2 \leq \frac{4m}{k} \tag{F.9.2}$$

where m and k are coefficients in the single homogeneous equation

$$m\ddot{u} + c\dot{u} + ku = 0 \tag{F.9.3}$$

obtained as a result of modal decomposition of the dynamic system of equations. In the one-dimensional case, for linear elements with one degree of freedom, the following expression were obtained for the diagonal term of the mass matrix

$$m_{ii} = \begin{cases} \sum_{p=1}^{N_p} M_p(\xi_p)^2 & \text{for a consistent mass matrix} \\ \sum_{p=1}^{N_p} M_p\xi_p & \text{for a lumped mass matrix} \end{cases} \tag{F.9.4}$$

where $(1-\xi_p)h$ is the distance between the p^{th} material point and the i^{th} node of the element, h denotes the length of the element, and N_p the number of material points in the element. Wieckowski *et al.* (1999) showed that the diagonal term of the element stiffness matrix is

$$k_{ii} = \sum_{p=1}^{N_p} M_p \left(\frac{C}{h}\right)^2 \tag{F.9.5}$$

where the relation $C^2 = \frac{E}{\rho}$ is used, with E Young's modulus and ρ the material density. Applying equations F.9.2 to F.9.5, they obtained the following stability criterion.

$$\Delta t \leq \Delta t_{crit}^{PIC} = \begin{cases} \frac{2h}{C}\sqrt{\frac{\sum_{p=1}^{N_p} M_p(\xi_p)^2}{\sum_{p=1}^{N_p} M_p}} & \text{for a consistent mass matrix} \\ \frac{2h}{C}\sqrt{\frac{\sum_{p=1}^{N_p} M_p\xi_p}{\sum_{p=1}^{N_p} M_p}} & \text{for a lumped mass matrix} \end{cases} \tag{F.9.6}$$

Comparing equation F.9.6 to equation F.9.1 shows that the value Δt_{crit} may be significantly lower for PIC than for FEM. This is especially true when the material points are located near one of the ends (or corners in the two-dimensional case) of the element.

F.10 Damping

In order to obtain static or quasi-static solutions, the equations of motion must be damped. The objective is to achieve the steady state in a numerically stable way with minimal computational effort. Steady state may be either equilibrium or steady-flow.

Viscous (velocity-proportional) damping can be added to the equation of motion, equation F.6.2, by lagging the velocity by one-half time step, (Cook *et al.*, 1989).

$$M_{ij}\dot{v}_j + C_{ij}v_j = f_i^{\text{int}} + f_i^{\text{ext}} \tag{F.10.1}$$

where C_{ij} is the damping matrix. The velocity is approximated by

$$v_i^{t-\frac{1}{2}} = \frac{1}{\Delta t}\left(x_i^t - x_i^{t-1}\right) \tag{F.10.2}$$

and the acceleration by

$$\begin{aligned}\dot{v}_j^t &= \frac{1}{\Delta t}\left(v_i^{t+\frac{1}{2}} - v_i^{t-1}\right) \\ &= \frac{1}{\Delta t^2}\left(x_i^{t+1} - 2x_i^t + x_i^{t-1}\right)\end{aligned} \tag{F.10.3}$$

Combination of equations F.10.1 to F.10.3 yields

$$\frac{1}{\Delta t^2}M_{ij}^t x_j^{t+1} = f_i^{\text{int},t} + f_i^{\text{ext},t} + \frac{1}{\Delta t^2}M_{ij}^t\left(x_j^t + \Delta t\, v_j^{t-\frac{1}{2}}\right) - C_{ij}v_j^{t-\frac{1}{2}} \tag{F.10.4}$$

If M_{ij} is lumped, then the computation of x_j^{t+1} does not require the solution of simultaneous equations. There are no restrictions to the form of C_{ij}. The method can be started by using the initial displacement x_j^0 and the approximation that $v_j^{t-\frac{1}{2}} \simeq v_j^0$. Although the central difference formulas, equations F.10.1 and F.10.3, are second-order accurate, only first order accuracy can be guaranteed when $C_{ij} \neq 0$ because the viscous forces lag by half a time step.

Solving for x_j^{t+1} in equations F.10.4 yields,

$$x_j^{t+1} = \Delta t^2(M_{ij}^t)^{-1}\left(f_i^{\text{int},t} + f_i^{\text{ext},t}\right) + x_j^t + \Delta t\, v_j^{t-\frac{1}{2}} - \Delta t^2(M_{ij}^t)^{-1}C_{ij}v_j^{t-\frac{1}{2}} \tag{F.10.5}$$

Using this equation together with equation F.10.2 in the form,

$$x_j^{t+1} = x_j^t + \Delta t\, v_j^{t+\frac{1}{2}} \tag{F.10.6}$$

the velocity at time $t + \frac{1}{2}$ can be written as

$$v_j^{t+\frac{1}{2}} = \Delta t\,(M_{ij}^t)^{-1}\left(f_i^{\text{int},t} + f_i^{\text{ext},t}\right) + v_j^{t-\frac{1}{2}} - \Delta t\, Dv_j^{t-\frac{1}{2}} \tag{F.10.7}$$

where $D = C_{ij}^t (M_{ij}^t)^{-1}$. In order to implement these equations into the algorithm given in section F.8, it must be written in terms of nodal momentum. Multiplying equation F.10.7 by the mass matrix yields

$$\begin{aligned} p_i^{t+\frac{1}{2}} &= \Delta t\ \dot{p}_i^t + p_i^{t-\frac{1}{2}} - \Delta t D p_i^{t-\frac{1}{2}} \\ &= p_i^{t-\frac{1}{2}} + \Delta t\ \left(\dot{p}_i^t - D p_i^{t-\frac{1}{2}} \right) \end{aligned} \tag{F.10.8}$$

which replaces equation F.8.4. Equation F.8.6 becomes

$$v_i^{t+\frac{1}{2}} = \left(M_{ij}^t \right)^{-1} p_j^{t+\frac{1}{2}} \tag{F.10.9}$$

And the particle positional update, equation F.8.7, becomes

$$x_i^{p,t+1} = x_i^{p,t} + \Delta t\ N_{ij}^{p,t}\ v_j^{e,t+\frac{1}{2}} \tag{F.10.10}$$

Using equation F.8.8, the velocity update, equation F.8.9, becomes

$$v_i^{p,t+\frac{1}{2}} = v_i^{p,t-\frac{1}{2}} + \Delta t\ N_{ij}^{p,t} \left(\dot{v}_j^{e,t} - D v_j^{t-\frac{1}{2}} \right) \tag{F.10.11}$$

The use of velocity-proportional damping, however, involves three main difficulties (FLAC, 1998):

1. The damping introduces body forces, which are erroneous in flowing regions and may influence the mode of failure in some cases.

2. The optimum damping constant depends on the eigenvalues of the system. To calculate the eigenvalues a complete modal analysis must be done. In a linear problem, this analysis needs almost as must computer effort as the dynamic calculation itself. In nonlinear problems, eigenvalues may be undefined.

3. In its standard form, viscous damping is applied equally to all nodes, i.e., a single damping constant is used throughout the whole system. In many cases, a variety of behaviour may be observed in different parts of the system. For example, one part may be failing while another is stable and for these problems, different amounts of damping are appropriate for different regions.

In order to overcome all three difficulties, a form of damping, called *local non-viscous damping* is proposed by FLAC (1998). The damping force on a node is proportional to the magnitude of the unbalanced force at the node.

The direction of the damping force is such that energy is always dissipated. The damping force is added to the equation of motion, equation F.7.4

$$\dot{p}_i^t = f_i^{\text{int,t}} + f_i^{\text{ext,t}} + f_i^{\text{damp}} \tag{F.10.12}$$

where

$$f_i^{\text{damp}} = -\alpha \left| f_i^{\text{int,t}} + f_i^{\text{ext,t}} \right| \text{ sign} \left(p_i^{t-\frac{1}{2}} \right) \tag{F.10.13}$$

f_i^{damp} is the damping force and α is the damping constant. The difficulties reported above are addressed: body forces vanish for steady-state conditions, the magnitude of the damping constant is dimensionless and is independent of properties or boundary conditions, and the amount of damping varies from node to node (FLAC, 1998).

Appendix G

Particle-in-Cell Contact Model

G.1 Introduction

Bardenhagen *et al.* (2000) developed a PIC model for granular materials that describes both the internal deformation of each granule and the interactions between grains. Interaction between grains is calculated with a contact algorithm that forbids interpenetration, but allows separation and sliding and rolling with friction. Although this model was developed for an assembly of granules, it can be applied to any system of different bodies (entities).

In the basic PIC algorithm, as described in Appendix F, no slip contact between different bodies is contained without additional cost. This is the result of the entities moving in a single-valued velocity field $\overline{v}$. Since this velocity field is determined using mass weighting, Bardenhagen *et al.* (2000) calls it the centre-of-mass velocity field. Here it will be called the system velocity field since all the particles in the system are used to calculate it. The solution procedure described in Appendix F can also be followed, but where the loops range over only the particles making up one entity. This would solve the equations of motion for each entity, ignoring the presence of all the others. In that case, the result is a single-valued entity velocity field $\overline{v}^{\,ent}$.

Obviously, the entity motion cannot be determined solely from consideration of each individual entity in isolation. The novelty here is (Bardenhagen *et al.*, 2000) that contacts between entities are handled by comparing the velocity fields $\overline{v}^{\,ent}$ to the single, system velocity field $\overline{v}$. The resulting algorithm is linear in the number of entities and requires no iteration.

Matrix tensor notation (Hassenpflug, 1993) is used for clarity and subscripts should not be confused with the indices of index notation.

G.2 Contact Model

Normal and tangential kinematic constraints on the velocity are handled separately. Suppose that the boundary of each entity has been identified and the unit outward normal $\overline{n}_b^{\,ent}$ is known at nodes along the boundary (the subscript b indicates that it is a value/property at boundary node b). If one entity is isolated from the rest, i.e. not in contact with others, then the two velocity fields $\overline{v}^{\,ent}$ and $\overline{v}$ will be identical in the neighbourhood of that entity. It is only as the entity approaches other entities that the two fields will differ. Contact is then defined when these two velocity fields differ. Constraints are only necessary when entities are approaching each other

and not when they are moving apart from one another. The following condition is used to check whether an entity is in contact with another entity and whether they are approaching each other.

$$\left(\overline{v}_b^{\,ent} - \overline{v}_b\right) \bullet \overline{n}_b^{\,ent} > 0 \tag{G.2.1}$$

This condition is satisfied when the entity velocity, at a boundary node, is overtaking the system velocity along the normal to the surface. Once this condition is satisfied, the entity velocity is adjusted to a new value $\tilde{\overline{v}}_b^{\,ent}$ so that

$$\tilde{\overline{v}}_b^{\,ent} \bullet \overline{n}_b^{\,ent} = \overline{v}_b \bullet \overline{n}_b^{\,ent} \tag{G.2.2}$$

holds. Equation G.2.2 states that the normal of the entity velocity is set equal to the normal component of the system velocity. Equation G.2.2 can also be written as

$$\tilde{\overline{v}}_b^{\,ent} = \overline{v}_b^{\,ent} - \left[\left(\overline{v}_b^{\,ent} - \overline{v}_b\right) \bullet \overline{n}_b^{\,ent}\right] \overline{n}_b^{\,ent} \tag{G.2.3}$$

To prove equation G.2.3, take the scalar product on each side of the equal sign with respect to the unit normal $\overline{n}_b^{\,ent}$.

$$\begin{aligned} \tilde{\overline{v}}_b^{\,ent} \bullet \overline{n}_b^{\,ent} &= \left[\overline{v}_b^{\,ent} - \left[\left(\overline{v}_b^{\,ent} - \overline{v}_b\right) \bullet \overline{n}_b^{\,ent}\right] \overline{n}_b^{\,ent}\right] \bullet \overline{n}_b^{\,ent} \\ &= \overline{v}_b^{\,ent} \bullet \overline{n}_b^{\,ent} - \left(\overline{v}_b^{\,ent} - \overline{v}_b\right) \bullet \overline{n}_b^{\,ent} \\ &= \overline{v}_b^{\,ent} \bullet \overline{n}_b^{\,ent} - \overline{v}_b^{\,ent} \bullet \overline{n}_b^{\,ent} + \overline{v}_b \bullet \overline{n}_b^{\,ent} \\ &= \overline{v}_b \bullet \overline{n}_b^{\,ent} \end{aligned} \tag{G.2.4}$$

The system velocity does not allow interpenetration of entities, so this choice of a contact constraint in the normal direction is natural. Note that the inequality in equation G.2.1 allows entities to separate freely without any constraints. The constraint in equation G.2.2 is equivalent to applying a normal force $\overline{f}_b^{\,ent,normal}$ to the entity boundary node

$$\begin{aligned} \overline{f}_b^{\,ent,normal} &= -\frac{M_b^{ent}}{\Delta t} \left[\left(\overline{v}_b^{\,ent} - \overline{v}_b\right) \bullet \overline{n}_b^{\,ent}\right] \overline{n}_b^{\,ent} \\ &= \frac{M_b^{ent}}{\Delta t} \left[\left(\tilde{\overline{v}}_b^{\,ent} - \overline{v}_b^{\,ent}\right) \bullet \overline{n}_b^{\,ent}\right] \overline{n}_b^{\,ent} \end{aligned} \tag{G.2.5}$$

where M_b^{ent} is the entity mass at boundary node b. This mass is the value of the entity lumped mass matrix at this node. The entity mass matrix is calculated summing only over the entity's particles.

If there is no contact friction between the entities, then the above adjustment of the normal component of the entity velocity, equation G.2.3, is all that is required. The tangential component of the entity velocity will be unconstrained. This can be proven by writing down the expression for

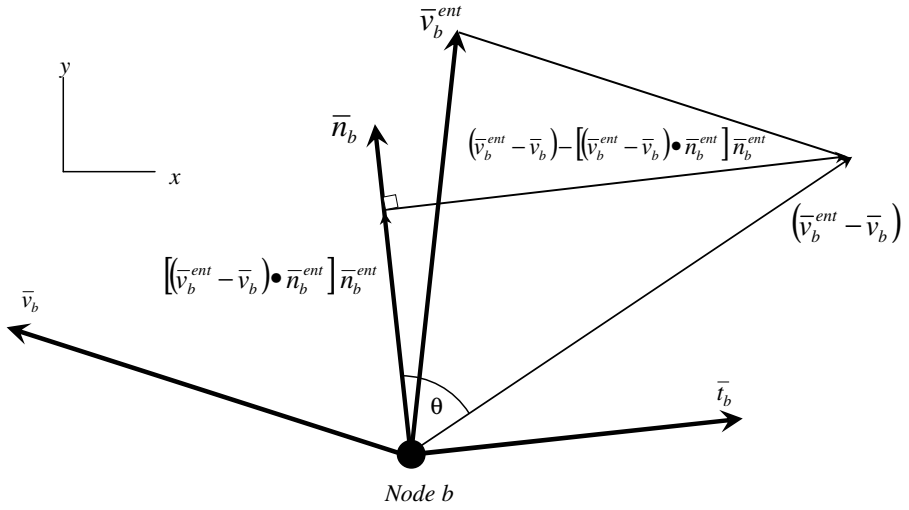

Figure G.1: System, entity and relative velocities

the corrected tangential entity velocity. Using equation G.2.2 and equation G.2.3,

$$\tilde{\overline{\boldsymbol{v}}}_b^{ent} - \left(\tilde{\overline{\boldsymbol{v}}}_b^{ent} \bullet \overline{\boldsymbol{n}}_b^{ent}\right) \overline{\boldsymbol{n}}_b^{ent} = \overline{\boldsymbol{v}}_b^{ent} - \left(\overline{\boldsymbol{v}}_b^{ent} \bullet \overline{\boldsymbol{n}}_b^{ent}\right) \overline{\boldsymbol{n}}_b^{ent} \tag{G.2.6}$$

it is shown that the tangential component of the corrected entity velocity is the same as the tangential component before the correction was applied.

Where equation G.2.1 is based on the relative normal velocity, the tangential contact constraint is based on the relative tangential velocity given by (Figure G.1)

$$\left(\overline{\boldsymbol{v}}_b^{ent} - \overline{\boldsymbol{v}}_b\right) - \left[\left(\overline{\boldsymbol{v}}_b^{ent} - \overline{\boldsymbol{v}}_b\right) \bullet \overline{\boldsymbol{n}}_b^{ent}\right] \overline{\boldsymbol{n}}_b^{ent} \tag{G.2.7}$$

This tangential velocity vector can also be written making use of cross products.

$$\overline{\boldsymbol{n}}_b^{ent} \times \left[\left(\overline{\boldsymbol{v}}_b^{ent} - \overline{\boldsymbol{v}}_b\right) \times \overline{\boldsymbol{n}}_b^{ent}\right] \tag{G.2.8}$$

To prove this equation, first look at the second cross product, using the definition thereof (AppendixA.2.6)

$$\left[\left(\overline{\boldsymbol{v}}_b^{ent} - \overline{\boldsymbol{v}}_b\right) \times \overline{\boldsymbol{n}}_b^{ent}\right] = \left|\left(\overline{\boldsymbol{v}}_b^{ent} - \overline{\boldsymbol{v}}_b\right)\right| sin\theta\, \overline{\boldsymbol{e}}_z \tag{G.2.9}$$

where θ is the angle between the two vectors, figure G.1, and $\overline{\boldsymbol{e}}_z$ is the unit vector in the z-direction, i.e., the out-of-plane direction. Looking at the first cross product, the vector can be written as

$$\begin{aligned} \overline{\boldsymbol{n}}_b^{ent} \times \left[\left(\overline{\boldsymbol{v}}_b^{ent} - \overline{\boldsymbol{v}}_b\right) \times \overline{\boldsymbol{n}}_b^{ent}\right] &= \left|\left(\overline{\boldsymbol{v}}_b^{ent} - \overline{\boldsymbol{v}}_b\right)\ sin\theta\right| sin\tfrac{\pi}{2}\ \overline{\boldsymbol{t}}_b \\ &= \left|\left(\overline{\boldsymbol{v}}_b^{ent} - \overline{\boldsymbol{v}}_b\right)\ sin\theta\right| \overline{\boldsymbol{t}}_b \end{aligned} \tag{G.2.10}$$

since the angle between $\overline{\boldsymbol{n}}_b$ and $\overline{\boldsymbol{e}}_z$ is 90° and $\overline{\boldsymbol{t}}_b$ is the tangential unit vector at the contacting node. Making use of figure G.1, $sin\theta$ can be written as

$$sin\theta = \frac{\left(\overline{\boldsymbol{v}}_b^{ent} - \overline{\boldsymbol{v}}_b\right) - \left[\left(\overline{\boldsymbol{v}}_b^{ent} - \overline{\boldsymbol{v}}_b\right) \bullet \overline{\boldsymbol{n}}_b^{ent}\right] \overline{\boldsymbol{n}}_b^{ent}}{\left(\overline{\boldsymbol{v}}_b^{ent} - \overline{\boldsymbol{v}}_b\right)} \tag{G.2.11}$$

Substitution of this definition into equation G.2.10 leads to

$$\begin{aligned} \overline{\boldsymbol{n}}_b^{ent} \times \left[\left(\overline{\boldsymbol{v}}_b^{ent} - \overline{\boldsymbol{v}}_b\right) \times \overline{\boldsymbol{n}}_b^{ent}\right] &= \left| \left(\overline{\boldsymbol{v}}_b^{ent} - \overline{\boldsymbol{v}}_b\right) - \left[\left(\overline{\boldsymbol{v}}_b^{ent} - \overline{\boldsymbol{v}}_b\right) \bullet \overline{\boldsymbol{n}}_b^{ent}\right] \overline{\boldsymbol{n}}_b^{ent} \right| \overline{\boldsymbol{t}}_b \\ &= \left(\overline{\boldsymbol{v}}_b^{ent} - \overline{\boldsymbol{v}}_b\right) - \left[\left(\overline{\boldsymbol{v}}_b^{ent} - \overline{\boldsymbol{v}}_b\right) \bullet \overline{\boldsymbol{n}}_b^{ent}\right] \overline{\boldsymbol{n}}_b^{ent} \end{aligned} \tag{G.2.12}$$

which concludes the proof.

To apply Coulomb friction, first calculate the force required for no slip. Again the comparison of the entity velocity to the system velocity provides the correct constraint for no slip contact, in the form of the relative tangential velocity, equation G.2.7. The constraining tangential force, $\overline{\boldsymbol{f}}_b^{ent,stick}$, to cause the entities to stick, is

$$\overline{\boldsymbol{f}}_b^{ent,stick} = -\frac{M_b^{ent}}{\Delta t} \overline{\boldsymbol{n}}_b^{ent} \times \left[\left(\overline{\boldsymbol{v}}_b^{ent} - \overline{\boldsymbol{v}}_b\right) \times \overline{\boldsymbol{n}}_b^{ent}\right] \tag{G.2.13}$$

The friction force equals the sticking force if the magnitude of the sticking force is small. That is, friction just balances the tangential force and prevents relative tangential motion, when the magnitude of the tangential force is small. For larger tangential forces, the magnitude of the friction force is proportional to the magnitude of the normal force and independent of the contact area. The proportionality constant (friction coefficient) is μ. Limiting the frictional force to have magnitude less than the sticking force allows tangential slip between contacting entities since the applied frictional force is not sufficient to prevent relative tangential motion, figure G.2. The direction of the frictional force is chosen as in equation G.2.13 to oppose relative motion. Putting all these requirements together yields

$$\overline{\boldsymbol{f}}_b^{ent,fric} = \frac{\overline{\boldsymbol{f}}_b^{ent,stick}}{\left|\overline{\boldsymbol{f}}_b^{ent,stick}\right|} \min\left(\mu \left|\overline{\boldsymbol{f}}_b^{ent,normal}\right|, \left|\overline{\boldsymbol{f}}_b^{ent,stick}\right|\right) \tag{G.2.14}$$

Using equation G.2.13 it can be shown that

$$\begin{aligned} \frac{\overline{\boldsymbol{f}}_b^{ent,stick}}{\left|\overline{\boldsymbol{f}}_b^{ent,stick}\right|} &= \frac{-\frac{M_b^{ent}}{\Delta t} \overline{\boldsymbol{n}}_b^{ent} \times \left[\left(\overline{\boldsymbol{v}}_b^{ent} - \overline{\boldsymbol{v}}_b\right) \times \overline{\boldsymbol{n}}_b^{ent}\right]}{\left|\frac{M_b^{ent}}{\Delta t} \overline{\boldsymbol{n}}_b^{ent} \times \left[\left(\overline{\boldsymbol{v}}_b^{ent} - \overline{\boldsymbol{v}}_b\right) \times \overline{\boldsymbol{n}}_b^{ent}\right]\right|} \\ &= -\frac{\overline{\boldsymbol{n}}_b^{ent} \times \left[\left(\overline{\boldsymbol{v}}_b^{ent} - \overline{\boldsymbol{v}}_b\right) \times \overline{\boldsymbol{n}}_b^{ent}\right]}{\left|\left(\overline{\boldsymbol{v}}_b^{ent} - \overline{\boldsymbol{v}}_b\right) \times \overline{\boldsymbol{n}}_b^{ent}\right|} \end{aligned} \tag{G.2.15}$$

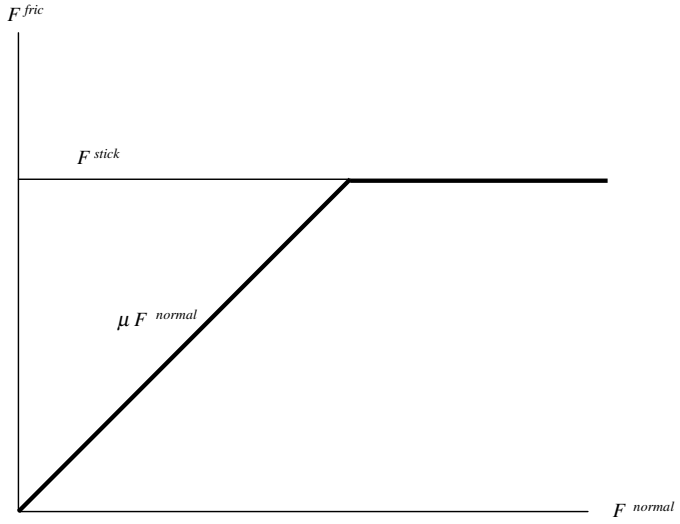

Figure G.2: Coulomb friction contact model

and using equation G.2.5 and G.2.13 it can be shown

$$\begin{aligned}
&\left[\mu \left|\overline{f}_b^{\,ent,normal}\right|, \left|\overline{f}_b^{\,ent,stick}\right|\right] \\
&= \frac{M_b^{ent}}{\Delta t}\left[\left|\mu\left[\left(\overline{v}_b^{\,ent} - \overline{v}_b\right) \bullet \overline{n}_b^{\,ent}\right]\overline{n}_b^{\,ent}\right|, \left|\overline{n}_b^{\,ent} \times \left[\left(\overline{v}_b^{\,ent} - \overline{v}_b\right) \times \overline{n}_b^{\,ent}\right]\right|\right] \\
&= \frac{M_b^{ent}}{\Delta t}\left[\mu\left|\left[\left(\overline{v}_b^{\,ent} - \overline{v}_b\right) \bullet \overline{n}_b^{\,ent}\right]\right|, \left|\left[\left(\overline{v}_b^{\,ent} - \overline{v}_b\right) \times \overline{n}_b^{\,ent}\right]\right|\right] \\
&= \frac{M_b^{ent}}{\Delta t}\left[\mu, \frac{\left|\left[\left(\overline{v}_b^{\,ent} - \overline{v}_b\right) \times \overline{n}_b^{\,ent}\right]\right|}{\left[\left(\overline{v}_b^{\,ent} - \overline{v}_b\right) \bullet \overline{n}_b^{\,ent}\right]}\right]\left[\left(\overline{v}_b^{\,ent} - \overline{v}_b\right) \bullet \overline{n}_b^{\,ent}\right]
\end{aligned} \tag{G.2.16}$$

where $\left(\overline{v}_b^{\,ent} - \overline{v}_b\right) \bullet \overline{n}_b^{\,ent} = \left|\left(\overline{v}_b^{\,ent} - \overline{v}_b\right) \bullet \overline{n}_b^{\,ent}\right|$ since $\left(\overline{v}_b^{\,ent} - \overline{v}_b\right) \bullet \overline{n}_b^{\,ent} > 0$ for contact to occur. Equation G.2.14 now becomes

$$\begin{aligned}
\overline{f}_b^{\,ent,fric} &= -\frac{M_b^{ent}}{\Delta t}\,\frac{\overline{n}_b^{\,ent} \times \left[\left(\overline{v}_b^{\,ent} - \overline{v}_b\right) \times \overline{n}_b^{\,ent}\right]}{\left|\left(\overline{v}_b^{\,ent} - \overline{v}_b\right) \times \overline{n}_b^{\,ent}\right|}\,\mu'\,\left[\left(\overline{v}_b^{\,ent} - \overline{v}_b\right) \bullet \overline{n}_b^{\,ent}\right] \\
&= -\frac{M_b^{ent}}{\Delta t}\,\mu'\,\left[\left(\overline{v}_b^{\,ent} - \overline{v}_b\right) \bullet \overline{n}_b^{\,ent}\right]\,\left(\overline{n}_b^{\,ent} \times \hat{\overline{\omega}}\right)
\end{aligned} \tag{G.2.17}$$

where

$$\mu' = \min\left[\mu, \frac{\left|\left[\left(\overline{v}_b^{\,ent} - \overline{v}_b\right) \times \overline{n}_b^{\,ent}\right]\right|}{\left[\left(\overline{v}_b^{\,ent} - \overline{v}_b\right) \bullet \overline{n}_b^{\,ent}\right]}\right] \tag{G.2.18}$$

and the unit vector $\hat{\overline{\omega}}$ is

$$\hat{\overline{\omega}} = \frac{\left[\left(\overline{v}_b^{\,ent} - \overline{v}_b\right) \times \overline{n}_b^{\,ent}\right]}{\left|\left(\overline{v}_b^{\,ent} - \overline{v}_b\right) \times \overline{n}_b^{\,ent}\right|} \tag{G.2.19}$$

Similarly to where equation G.2.3 is the only correction needed for normal correction, the result from equation G.2.17 can be used to write a corrected velocity taking only the tangential correction into account.

$$\tilde{\overline{v}}_b^{\,ent} = \mu' \ \left[\left(\overline{v}_b^{\,ent} - \overline{v}_b\right) \bullet \overline{n}_b^{\,ent}\right] \ \left(\overline{n}_b^{\,ent} \times \hat{\overline{\omega}}\right) \tag{G.2.20}$$

Finally, imposing both the frictional constraint force and the normal constraint force, the altered entity velocity is

$$\boxed{\tilde{\overline{v}}_b^{\,ent} = \overline{v}_b^{\,ent} - \left[\left(\overline{v}_b^{\,ent} - \overline{v}_b\right) \bullet \overline{n}_b^{\,ent}\right] \left(\overline{n}_b^{\,ent} + \mu' \, \overline{n}_b^{\,ent} \times \hat{\overline{\omega}}\right)} \tag{G.2.21}$$

This equation is simply a vector sum of equation G.2.3 and equation G.2.20. To obtain a no-slip contact, using equation G.2.21, the friction coefficient μ should be given a high value.

In order to implement these equations efficiently, the following definitions are made (the subscript b being omitted for clarity): The difference in velocity is defined by $\overline{v}_{diff}$

$$\overline{v}^{\,diff} \equiv \begin{bmatrix} v_x^{\,diff} \\ v_y^{\,diff} \end{bmatrix} = \overline{v}^{\,ent} - \overline{v} = \begin{bmatrix} v_x^{\,ent} - v_x \\ v_y^{\,ent} - v_y \end{bmatrix} \tag{G.2.22}$$

The scalar (dot) product of the velocity difference with the unit normal vector is as follows

$$D = v_x^{\,diff} \ n_x^{\,ent} + v_y^{\,diff} \ n_y^{\,ent} \tag{G.2.23}$$

The vector (cross) product of the two same vectors can be shown to be

$$\overline{C} = \begin{bmatrix} 0 \\ 0 \\ v_x^{\,diff} \ n_y^{\,ent} - v_y^{\,diff} \ n_x^{\,ent} \end{bmatrix} \tag{G.2.24}$$

Note that this results in only an out-of-plane (z-direction) component, the absolute value of this vector being $\left|\overline{C}\right| = \left|v_x^{\,diff} \ n_y^{\,ent} - v_y^{\,diff} \ n_x^{\,ent}\right|$. The unit vector $\hat{\overline{\omega}}$ can be shown to have the form

$$\hat{\overline{\omega}} = \frac{\overline{C}}{\left|\overline{C}\right|} = \begin{bmatrix} 0 \\ 0 \\ \dfrac{v_x^{\,diff} \ n_y^{\,ent} - v_y^{\,diff} \ n_x^{\,ent}}{\left|v_x^{\,diff} \ n_y^{\,ent} - v_y^{\,diff} \ n_x^{\,ent}\right|} \end{bmatrix} \tag{G.2.25}$$

Equation G.2.18 will simply be

$$\mu' = \min \left[\mu, \frac{|\overline{C}|}{D} \right] \tag{G.2.26}$$

which is, of course, a scalar quantity. Equation G.2.21 can now be written as

$$\begin{bmatrix} \tilde{v}_x^{ent} \\ \tilde{v}_y^{ent} \end{bmatrix} = \begin{bmatrix} v_x^{ent} \\ v_y^{ent} \end{bmatrix} - D \left(\begin{bmatrix} n_x^{ent} \\ n_y^{ent} \end{bmatrix} + \mu' \begin{bmatrix} \frac{n_y^{ent} \left(v_x^{diff} \; n_y^{ent} - v_y^{diff} \; n_x^{ent} \right)}{|\overline{C}|} \\ \frac{-n_x^{ent} \left(v_x^{diff} \; n_y^{ent} - v_y^{diff} \; n_x^{ent} \right)}{|\overline{C}|} \end{bmatrix} \right) \tag{G.2.27}$$

where only the first two components are shown since the out-of-plane component is zero, as expected. Thus, after calculation of the components of $\overline{v}_{diff}$, D, $|\overline{C}|$ and μ', equation G.2.27 can be used to calculate each of the new nodal velocity components individually.

Using a polar continuum, each node has two translational velocities and one rotational velocity. The translational velocities are corrected in the same way as above, while the rotation is either set to be zero at the contacting nodes or free, i.e. not constraint or changed.

G.3 Boundary Unit Normal Vector Calculation

Sulsky & Brackbill (1991) proposed a method for calculating the divergence of a vector quantity and the gradient of a scalar quantity at grid points. The derivations are done for the two-dimensional case, but in general, the same procedure can be followed for the three-dimensional case. For each entity, the particle mass is interpolated to the finite element centres, $\overline{x}_c$ and divided by the element volume V_e, to obtain a density.

$$\rho_c = \frac{1}{V_e} \sum_{p=1}^{N_{ep}} m_p S^{(1)} (\overline{x}_c - \overline{x}_p) \tag{G.3.1}$$

The shape function $S^{(1)}$ is constructed from bilinear b-splines (Dierckx, 1996; Piegl and Tiller, 1997). The gradient of ρ_c evaluated at the nodes of the computational mesh provides the normal direction at the surface of each entity. The interaction between entities is therefore not along a common normal, which results in small errors in momentum conservation (Bardenhagen *et al.*, 2000).

Let $\overline{x}_{i,j}, \overline{x}_{i+1,j}, \overline{x}_{i+1,j+1}, \overline{x}_{i,j+1}$ denote the vertices of the computational element (i, j), figure G.3. With natural (element) coordinates (ξ, η) which as-

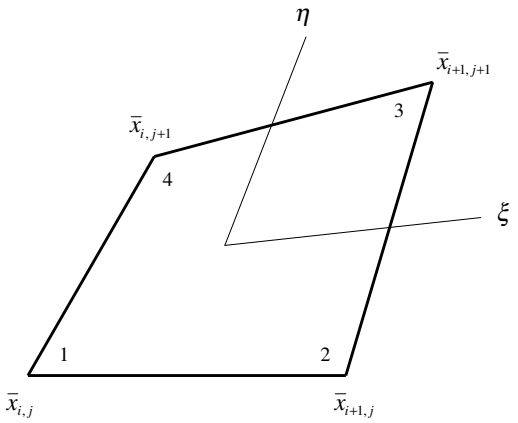

Figure G.3: Computational element with numbered vertices

sume integer values at the vertices and using bilinear interpolation, any point $\overline{\boldsymbol{x}}$ in the element is given by

$$\overline{\boldsymbol{x}} = \xi' \left[\left(1-\eta'\right) \overline{\boldsymbol{x}}_{i+1,j} + \eta' \overline{\boldsymbol{x}}_{i+1,j+1} \right] + \left(1-\xi'\right) \left[\left(1-\eta'\right) \overline{\boldsymbol{x}}_{i,j} + \eta' \overline{\boldsymbol{x}}_{i,j+1} \right] \tag{G.3.2}$$

with $\xi_1' = \xi_1 - i$ and $\eta' = \eta - j$. This mapping can also be written as (Sulsky and Brackbill, 1991)

$$\overline{\boldsymbol{x}} = \sum_{n=1}^{N_{en}} \overline{\boldsymbol{x}}_n s^{(1)} \left(\xi - i, \eta - j\right) \tag{G.3.3}$$

where N_{en} is the number of nodes (vertices) per element, $\overline{\boldsymbol{x}}_n$ is the node coordinates and

$$s^{(1)} \left(\xi - i, \eta - j\right) = s^{(1)} \left(\xi', \eta'\right) = \left(1 - |\xi|\right) \left(1 - |\eta|\right) \tag{G.3.4}$$

A corresponding interpolation function in physical coordinates can be written for a rectangular element

$$S^{(1)} \left(\overline{\boldsymbol{x}}\right) = S^{(1)} \left(x, y\right) = \left(1 - \frac{|x|}{\Delta x}\right) \left(1 - \frac{|y|}{\Delta y}\right) \tag{G.3.5}$$

where Δx and Δy are the element size in the x and y directions respectively. Make use of a vector $\overline{\boldsymbol{u}} = \left[u_x \; u_y\right]^T$ (known at the nodes), which can be a velocity vector, acceleration vector or any other vector field, to derive the necessary equations. A derivative of a nodal variable results in an element-centred quantity and is calculated as an average over the element. The

average of the derivative of the x-component of $\overline{\boldsymbol{u}}$ with respect to the x-coordinate is

$$\langle \frac{\partial u_x}{\partial x} \rangle_c \equiv \frac{1}{V_e} \int_{V_e} \frac{\partial u_x}{\partial x} \, \mathrm{d}V \tag{G.3.6}$$

where the subscript c indicates that the average derivative is an element-centred value. To evaluate equation G.3.6, make use of equation G.3.3 and G.3.5. Define $\overline{\boldsymbol{u}}$ throughout the cell from its values at the nodes

$$\overline{\boldsymbol{u}}(\overline{\boldsymbol{x}}, t) = \sum_{n=1}^{N_{en}} \overline{\boldsymbol{u}}_n S^{(1)} \left(\overline{\boldsymbol{x}} - \overline{\boldsymbol{x}}_n \right) \tag{G.3.7}$$

To evaluate equation G.3.6, we need the element-centred quantity which can be written as

$$\overline{\boldsymbol{u}}(\overline{\boldsymbol{x}}_c, t) = \sum_{n=1}^{N_{en}} \overline{\boldsymbol{u}}_n S^{(1)} \left(\overline{\boldsymbol{x}}_c - \overline{\boldsymbol{x}}_n \right) \tag{G.3.8}$$

Now equation G.3.6 becomes

$$\begin{aligned} \langle \frac{\partial u_x}{\partial x} \rangle_c &= \frac{1}{V_e} \int_{V_e} \sum_{n=1}^{N_{en}} u_{xn} \frac{\partial}{\partial x} S^{(1)} \left(\overline{\boldsymbol{x}}_c - \overline{\boldsymbol{x}}_n \right) \, \mathrm{d}V \\ &= \frac{1}{V_e} \sum_{n=1}^{N_{en}} u_{xn} c_x^{cv} \end{aligned} \tag{G.3.9}$$

where

$$c_x^{cv} = \int_{V_e} \frac{\partial}{\partial x} S^{(1)} \left(\overline{\boldsymbol{x}}_c - \overline{\boldsymbol{x}}_n \right) \, \mathrm{d}V \tag{G.3.10}$$

Since equation G.3.9 is summed over all the nodes of the element, there will be N_{en} c_x^{cv} values, one for each node.

An equation similar to equation G.3.9 can be written for the derivative with respect to the y-coordinate. This will result in N_{en} c_y^{cv} coefficients. It is useful to form a vector $\overline{\boldsymbol{c}}^{cv} = [c_x^{cv} \; c_y^{cv}]^T$ of the geometric coefficients. One can now combine derivatives to form a discrete divergence operator, acting on nodal quantities and defined at the cell centre.

$$D_c(\overline{\boldsymbol{u}}_n) = \frac{1}{V_e} \int_{V_e} \overline{\boldsymbol{\nabla}} \bullet \overline{\boldsymbol{u}} \, \mathrm{d}V = \frac{1}{V_e} \sum_{n=1}^{N_{en}} \overline{\boldsymbol{c}}^{cv} \bullet \overline{\boldsymbol{u}}_n \tag{G.3.11}$$

In the same way, derivatives are combined to form a discrete gradient operator defined at an element centre

$$\overline{\boldsymbol{G}}_c(\rho_n) = \frac{1}{V_e} \int_{V_e} \overline{\boldsymbol{\nabla}} \rho \, \mathrm{d}V = \frac{1}{V_e} \sum_{n=1}^{N_{en}} \overline{\boldsymbol{c}}^{cv} \rho_n \tag{G.3.12}$$

where ρ is a scalar quantity and not a vector like $\overline{\boldsymbol{u}}$. We now have formulas for the divergence and gradient, acting on element nodal data defined at the element centre. The "inverse" will now be constructed, i.e. formulas for divergence and gradient operators, acting on element-centred data and located at the nodes. These formulas are constructed to satisfy a discrete form of the divergence theorem (Sulsky and Brackbill, 1991)

$$\begin{aligned}\int_S \rho\overline{\boldsymbol{u}} \bullet \overline{\boldsymbol{n}}\, \mathrm{d}S &= \int_V \overline{\boldsymbol{\nabla}} \bullet (\rho\overline{\boldsymbol{u}})\, \mathrm{d}V \\ &= \int_V \overline{\boldsymbol{u}} \bullet \overline{\boldsymbol{\nabla}}\rho\, \mathrm{d}V + \int_V \rho\overline{\boldsymbol{\nabla}} \bullet \overline{\boldsymbol{u}}\, \mathrm{d}V\end{aligned} \tag{G.3.13}$$

where we assume that $\overline{\boldsymbol{u}}$ is defined at nodes and ρ defined at element centres. An approximation for the last term in equation G.3.13 is already defined in equation G.3.11

$$\sum_{e\in V} \rho_c D_c(\overline{\boldsymbol{u}}_n) V_e = \sum_{e\in V} \rho_c \sum_{n=1}^{N_{en}} \overline{\boldsymbol{c}}^{cv} \bullet \overline{\boldsymbol{u}}_n \tag{G.3.14}$$

where the sum $\sum_{e\in V}$ is over all the elements in V. At this point, postulate a form for the gradient at a vertex (Sulsky and Brackbill, 1991) analogous to equation G.3.12.

$$V_n \overline{\boldsymbol{G}}_n(\rho_c) = \sum_e \tilde{\overline{\boldsymbol{c}}}^{cv} \rho_c \tag{G.3.15}$$

where the components of the geometric coefficients $\tilde{\overline{\boldsymbol{c}}}^{cv}$are still unknown. The control volume V_n centred at a node $\overline{\boldsymbol{x}}_n$ is given by

$$V_n = \tfrac{1}{4} \sum_e V_e \tag{G.3.16}$$

The sum in equation G.3.15 and equation G.3.16 is over all the elements e that have $\overline{\boldsymbol{x}}_n$ as a node. Combining equations G.3.13, G.3.14 and G.3.15 yields

$$\begin{aligned}\int_S \rho\overline{\boldsymbol{u}} \bullet \overline{\boldsymbol{n}}\, \mathrm{d}S &= \sum_{n\in V} \overline{\boldsymbol{u}}_n \bullet \sum_e \tilde{\overline{\boldsymbol{c}}}^{cv} \rho_c + \sum_{e\in V} \rho_c \sum_{n=1}^{N_{en}} \overline{\boldsymbol{c}}^{cv} \bullet \overline{\boldsymbol{u}}_n \\ &= \sum_{n\in V} \overline{\boldsymbol{u}}_n \bullet \sum_e \left(\tilde{\overline{\boldsymbol{c}}}^{cv} + \overline{\boldsymbol{c}}^{cv}\right) \rho_c\end{aligned} \tag{G.3.17}$$

where $\sum_{n\in V}$ is the sum over all the nodes in the control volume V. The left hand side of equation G.3.17 is a surface integral, so the right-hand side should only involve nodes on the boundary of V. Since $\overline{\boldsymbol{u}}$ and ρ are arbitrary, for any interior element e we need the integral in equation G.3.17 to

vanish, i.e. $\tilde{\overline{\boldsymbol{c}}}^{cv} = -\,\overline{\boldsymbol{c}}^{cv}$. The required formula for a gradient operator acting on a centred quantity, defined at the nodes follows from equation G.3.15

$$\boxed{V_n \overline{\boldsymbol{G}}_n(\rho_c) = -\sum_e \overline{\boldsymbol{c}}^{cv} \rho_c} \tag{G.3.18}$$

To obtain the formula for the divergence at a node, the process is similar. Start with equation G.3.13, but now let $\overline{\boldsymbol{u}}$ be defined at element centres, let ρ be a nodal quantity and let V be a union of node-centred control volumes. Use equation G.3.12 to define an approximation to the first term on the right-hand side of equation G.3.13, and proceed as above to obtain

$$\boxed{V_n D_n(\overline{\boldsymbol{u}}_c) = -\sum_e \overline{\boldsymbol{c}}^{cv} \bullet \overline{\boldsymbol{u}}_c} \tag{G.3.19}$$

Applying the gradient operator, equation G.3.18, to the element-centred density defined in equation G.3.1, the result is a vector approximately normal to the entity surface at node n.

All that remains is to calculate the components of the geometric coefficient vector $\overline{\boldsymbol{c}}^{cv}$. The coefficients are defined by equation G.3.10.

$$\begin{aligned} c_x^{cv} &= \int_{V_e} \frac{\partial}{\partial x} S^{(1)}\left(\overline{\boldsymbol{x}}_c - \overline{\boldsymbol{x}}_n\right) \,\mathrm{d}V \\ c_y^{cv} &= \int_{V_e} \frac{\partial}{\partial y} S^{(1)}\left(\overline{\boldsymbol{x}}_c - \overline{\boldsymbol{x}}_n\right) \,\mathrm{d}V \end{aligned} \tag{G.3.20}$$

The derivatives of $S^{(1)}$, equation G.3.5, for a rectangular element (figure G.4) with respect to the x- and y-coordinates are

$$\begin{aligned} \frac{\partial S^{(1)}(x,y)}{\partial x} &= \frac{-\mathrm{sign}(x)}{\Delta x}\left(1 - \frac{|y|}{\Delta y}\right) \\ \frac{\partial S^{(1)}(x,y)}{\partial y} &= \frac{-\mathrm{sign}(y)}{\Delta y}\left(1 - \frac{|x|}{\Delta x}\right) \end{aligned} \tag{G.3.21}$$

The value of c_x^{cv} for node 1 follows as

$$\begin{aligned} c_{x1}^{cv} &= \int_{V_e} \frac{\partial}{\partial x} S^{(1)}\left(\overline{\boldsymbol{x}}_c - \overline{\boldsymbol{x}}_1\right) \,\mathrm{d}V \\ &= \int_{V_e} \frac{-\mathrm{sign}(x_c - x_1)}{\Delta x}\left(1 - \frac{|y_c - y_1|}{\Delta y}\right) \,\mathrm{d}V \\ &= \int_{V_e} \frac{-1}{\Delta x}\left(1 - \frac{\Delta y}{2\Delta y}\right) \,\mathrm{d}V \\ &= \frac{-1}{2\Delta x}\,\Delta x \Delta y \\ &= \frac{-\Delta y}{2} \end{aligned} \tag{G.3.22}$$

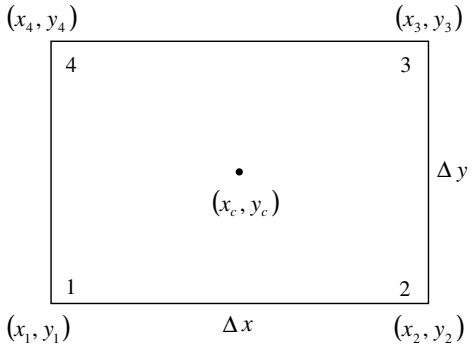

Figure G.4: Rectangular computational element

Table G.1: Geometric coefficients for a rectangular element

Node n	c_x^{cv}	c_y^{cv}
1	$-\frac{\Delta y}{2}$	$-\frac{\Delta x}{2}$
2	$\frac{\Delta y}{2}$	$-\frac{\Delta x}{2}$
3	$\frac{\Delta y}{2}$	$\frac{\Delta x}{2}$
4	$-\frac{\Delta y}{2}$	$\frac{\Delta x}{2}$

where $\Delta x \Delta y$ is the volume of the element (unit thickness is assumed). Table G.1 summarises the results by following the same procedure for the other nodes and the y-derivatives.

As an example, consider figure G.5 where node n has been identified as a boundary node. Elements $1, 2$ and 3 are boundary elements and contain node n as one of their vertices. Assume that the element centre densities, equation G.3.1, have been calculated. Applying equation G.3.18 to node n then gives

$$\begin{aligned} V_n \overline{\mathbf{G}}_n(\rho_c) &= -\sum_e \overline{\mathbf{c}}^{cv} \rho_c \\ &= -\left(\overline{\mathbf{c}}_3^{cv} \rho_{c1} + \overline{\mathbf{c}}_4^{cv} \rho_{c2} + \overline{\mathbf{c}}_2^{cv} \rho_{c3}\right) \\ &= -\left(\begin{bmatrix} c_{x3}^{cv} \\ c_{y3}^{cv} \end{bmatrix} \rho_{c1} + \begin{bmatrix} c_{x4}^{cv} \\ c_{y4}^{cv} \end{bmatrix} \rho_{c2} + \begin{bmatrix} c_{x2}^{cv} \\ c_{y2}^{cv} \end{bmatrix} \rho_{c3} \right) \end{aligned} \tag{G.3.23}$$

Since V_n is only a scalar quantity and the gradient vector needs to be normalised to obtain the unit normal vector, it can be discarded and the unit

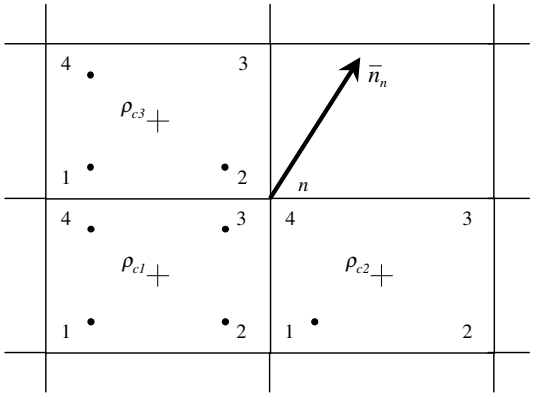

Figure G.5: Example of boundary unit normal calculation

normal vector follows as

$$\overline{\boldsymbol{n}}_n = \begin{bmatrix} n_{nx} \\ n_{ny} \end{bmatrix} = \frac{-\left(\begin{bmatrix} c_{x3}^{cv} \\ c_{y3}^{cv} \end{bmatrix} \rho_{c1} + \begin{bmatrix} c_{x4}^{cv} \\ c_{y4}^{cv} \end{bmatrix} \rho_{c2} + \begin{bmatrix} c_{x2}^{cv} \\ c_{y2}^{cv} \end{bmatrix} \rho_{c3} \right)}{\left| \left(\begin{bmatrix} c_{x3}^{cv} \\ c_{y3}^{cv} \end{bmatrix} \rho_{c1} + \begin{bmatrix} c_{x4}^{cv} \\ c_{y4}^{cv} \end{bmatrix} \rho_{c2} + \begin{bmatrix} c_{x2}^{cv} \\ c_{y2}^{cv} \end{bmatrix} \rho_{c3} \right) \right|} \tag{G.3.24}$$

G.4 Implementation

In section F.8 the numerical algorithm is summarised. Equation F.8.6 gives the system nodal velocity v_i^{t+1} at time $t+1$. The same procedure is then followed for each entity to obtain an entity nodal velocity $v_i^{ent,t+1}$. In this analysis the summation is performed only over particles belonging to the entity in question. Each active node will now have at least two velocity vectors. One system velocity vector and at least one entity velocity vector. If there are particles of more than one entity in the same element, the nodes of this element will have a velocity vector for each entity as well as the system velocity.

At this stage in the calculation the boundary nodes of each entity are identified. The entity velocity field is then compared to the system velocity field at the boundary nodes. Contact is defined by equation G.2.1 and a correction, equation G.2.21, is made to the entity nodal velocity if necessary. The corrected entity velocity is used to update the entity's particles according to equation F.8.7. To update the particle velocity, the new acceleration first needs to be calculated.

$$\dot{\tilde{v}}_i^{ent,t+1} = \frac{\tilde{v}_i^{ent,t+1} - v_i^{ent,t}}{\Delta t} \tag{G.4.1}$$

The entity's particle velocity is then updated according to equation F.8.9.

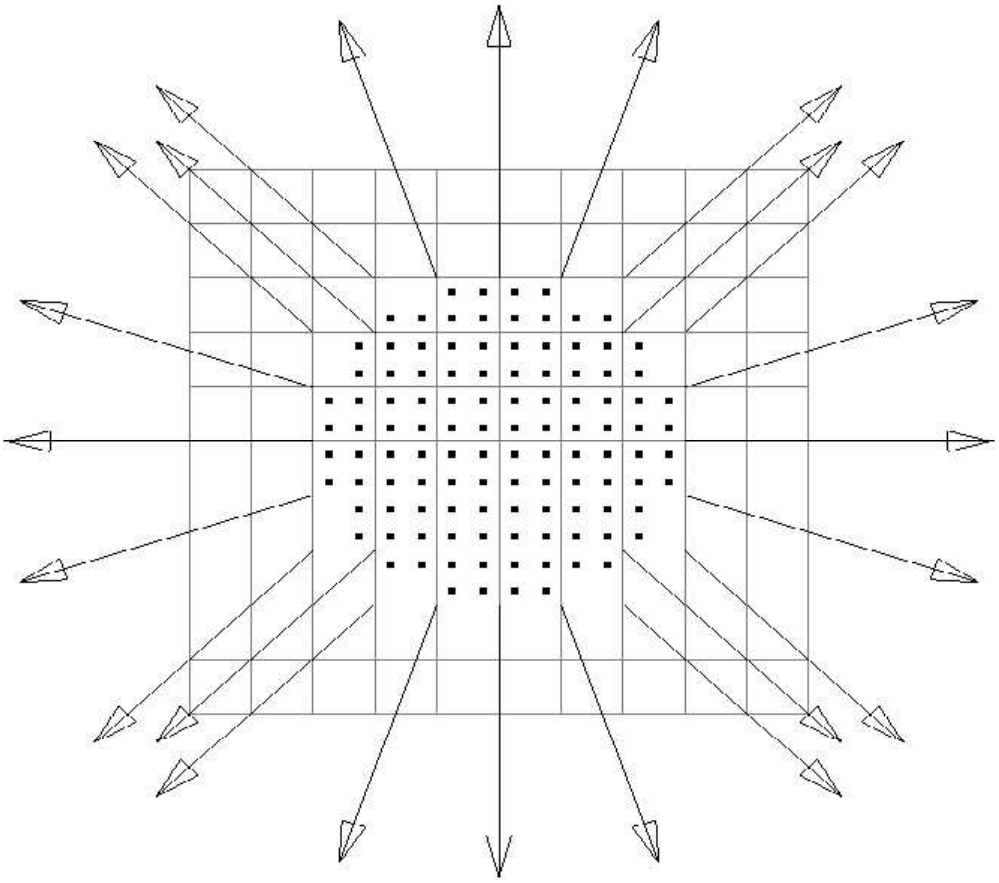

Figure G.6: Example of boundary unit normal vectors

Figure G.6 is an example of unit normal vectors calculated with the above algorithm.

Appendix H

Nonpolar Constitutive Models and Implementation

H.1 Introduction

In this appendix, the different nonpolar constitutive models employed are described. These include

1. Elastic, Isotropic Model
2. Drucker-Prager Model
3. von Mises Model
4. Mohr-Coulomb Model

The formulation given in this appendix closely follows that of FLAC (1998).

H.2 Elastic, Isotropic Model

These stress-strain laws are linear and path independent. The incremental relation between stress and strain is expressed by Hook's law for the cases of plane strain and plane stress.

H.2.1 Plane Strain

$$\begin{aligned} \Delta\sigma_{11} &= \alpha_1 \Delta\varepsilon_{11} + \alpha_2 \Delta\varepsilon_{22} \\ \Delta\sigma_{22} &= \alpha_2 \Delta\varepsilon_{11} + \alpha_1 \Delta\varepsilon_{22} \\ \Delta\sigma_{12} &= \Delta\sigma_{21} = 2G\Delta\varepsilon_{12} = 2G\Delta\varepsilon_{21} \\ \Delta\sigma_{33} &= \alpha_2 \left(\Delta\varepsilon_{11} + \Delta\varepsilon_{22}\right) \end{aligned} \tag{H.2.1}$$

where

$$\begin{aligned} \alpha_1 &= K + \tfrac{4}{3}G \\ \alpha_2 &= K - \tfrac{2}{3}G \\ K &= \frac{E}{3\left(1-2\nu\right)} \quad = \text{bulk modulus} \\ G &= \frac{E}{2\left(1+\nu\right)} \quad = \text{shear modulus} \end{aligned} \tag{H.2.2}$$

with E Young's modulus and ν Poisson's ratio.

H.2.2 Plane Stress

$$\begin{aligned}\Delta\sigma_{11} &= \beta_1\Delta\varepsilon_{11} + \beta_2\Delta\varepsilon_{22}\\ \Delta\sigma_{22} &= \beta_2\Delta\varepsilon_{11} + \beta_1\Delta\varepsilon_{22}\\ \Delta\sigma_{12} &= \Delta\sigma_{21} = 2G\Delta\varepsilon_{12} = 2G\Delta\varepsilon_{21}\\ \Delta\sigma_{33} &= 0\end{aligned} \tag{H.2.3}$$

where

$$\begin{aligned}\beta_1 &= \alpha_1 - \left(\frac{\alpha_2^2}{\alpha_1}\right)\\ \beta_2 &= \alpha_2 - \left(\frac{\alpha_2^2}{\alpha_1}\right)\end{aligned} \tag{H.2.4}$$

H.3 Drucker-Prager Model

The different plastic models are characterised by their yield function, hardening/softening functions and the flow (potential function) rule. The yield function defines the stress combination for which plastic flow takes place. These functions or criteria are represented by one or more limiting surfaces in a generalised stress space with points below or on the surface being characterised by an incremental elastic or plastic behaviour, respectively. The plastic flow formulation rests on the basic assumptions from plasticity theory that the total strain increment may be decomposed into elastic and plastic parts, with only the elastic part contributing to the stress increment by means of an elastic law. The flow rule specifies the direction of the plastic strain increment vector as the normal to the potential surface. It is called associated if the potential and yield functions coincide and non-associated otherwise. See Vermeer & De Borst (1984), Mendelson (1968) and Blazynski (1983) for more detail on the theory of plasticity and associated and non-associated flow rules.

The Drucker-Prager model consists of a Drucker-Prager yield criterion with tension cutoff. The shear flow rule is non-associated and the tensile flow rule is associated.

H.3.1 Incremental Elastic Law

The model is expressed in terms of two generalised stress components: the tangential stress q and mean normal stress p defined as

$$\begin{aligned}q &= \sqrt{J_2}\\ p &= \tfrac{1}{3}\left(\sigma_{11} + \sigma_{22} + \sigma_{33}\right)\end{aligned} \tag{H.3.1}$$

where J_2 is the second invariant of the stress deviator tensor, expressed as (Mendelson, 1968)

$$J_2 = \frac{1}{6}\left[(\sigma_{11}-\sigma_{22})^2 + (\sigma_{22}-\sigma_{33})^2 + (\sigma_{11}-\sigma_{33})^2 + 6\left(\sigma_{12}^2+\sigma_{23}^2+\sigma_{31}^2\right)\right] \tag{H.3.2}$$

for a nonpolar continuum. Under the assumption of plane strain J_2 becomes

$$J_2 = \frac{1}{6}\left[(\sigma_{11}-\sigma_{22})^2 + (\sigma_{22}-\sigma_{33})^2 + (\sigma_{11}-\sigma_{33})^2\right] + \sigma_{12}^2 \tag{H.3.3}$$

The shear strain increment $\Delta\varepsilon_q$ and volumetric strain increment $\Delta\varepsilon_p$ associated with q and p respectively, have the form

$$\begin{aligned} \Delta\varepsilon_q &= 2\sqrt{\Delta J_2'} \\ \Delta\varepsilon_p &= \Delta\varepsilon_{11} + \Delta\varepsilon_{22} + \Delta\varepsilon_{33} \end{aligned} \tag{H.3.4}$$

where $\Delta J_2'$ is the second invariant of the incremental strain deviator tensor, given by

$$\Delta J_2' = \frac{1}{6}\left[(\Delta\varepsilon_{11}-\Delta\varepsilon_{22})^2 + (\Delta\varepsilon_{22}-\Delta\varepsilon_{33})^2 + (\Delta\varepsilon_{11}-\Delta\varepsilon_{33})^2\right] + \Delta\varepsilon_{12}^2 \tag{H.3.5}$$

The strain components are decomposed in elastic and plastic parts.

$$\begin{aligned} \Delta\varepsilon_q &= \Delta\varepsilon_q^e + \Delta\varepsilon_q^p \\ \Delta\varepsilon_p &= \Delta\varepsilon_p^e + \Delta\varepsilon_p^p \end{aligned} \tag{H.3.6}$$

where the superscript e and p refer to elastic and plastic parts respectively. The incremental expression of Hook's law in terms of generalised stresses and strains is (Kachanov, 1971; Johnson and Mellor, 1983)

$$\begin{aligned} \Delta q &= G\Delta\varepsilon_q^e \\ \Delta p &= K\Delta\varepsilon_p^e \end{aligned} \tag{H.3.7}$$

with G and K the shear and bulk modulus respectively.

H.3.2 Yield and Potential Functions

The failure (yield) criteria are described in the pq-plane, figure H.1. From point A to B the criterion is defined by the Drucker-Prager shear yield function

$$f^s = q + q_\phi p - k_\phi \tag{H.3.8}$$

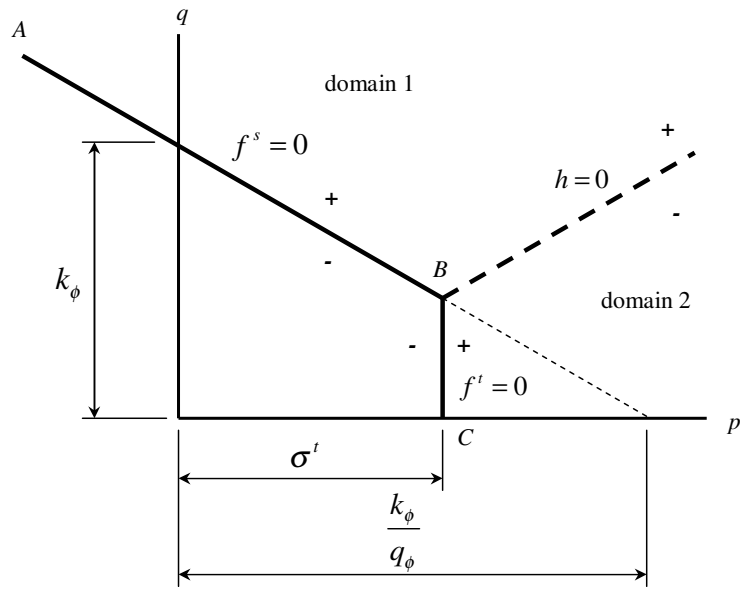

Figure H.1: Drucker-Prager failure criterion

and from B to C by the tension yield function (tension cutoff)

$$f^t = p - \sigma^t \tag{H.3.9}$$

where q_ϕ and k_ϕ are constant material properties and σ^t is the tensile strength for the Drucker-Prager model. This value is defined as the maximum of the mean normal stress for the material. For a material whose q_ϕ is not equal to zero, the tensile strength cannot exceed the maximum value σ^t_{max} given by (figure H.1)

$$\sigma^t_{max} = \frac{k_\phi}{q_\phi} \tag{H.3.10}$$

The default value of the tensile strength σ^t is zero if the material property q_ϕ is zero. The shear potential function g^s corresponds in general to a non-associated flow rule and has the form

$$g^s = q + q_\psi p \tag{H.3.11}$$

where q_ψ is a material constant, equal to q_ϕ if the flow rule is associated. The flow rule for tensile failure is associated. It is given by

$$g^t = p \tag{H.3.12}$$

The flow rules are given a unique definition (FLAC, 1998) in the vicinity of an edge of the composite yield function, point B in figure H.1. A function $h(p,q) = 0$ is defined which is represented by the diagonal between the

representation of $f^s = 0$ and $f^t = 0$ in the pq-plane. This function is given by

$$h = q - \tau^p - \alpha^p(p - \sigma^t) \tag{H.3.13}$$

where τ^p and α^p are two constants defined as

$$\begin{aligned} \tau^p &= k_\phi - q_\phi \sigma^t \\ \alpha^p &= \sqrt{1 + q_\phi^2} - q_\phi \end{aligned} \tag{H.3.14}$$

An elastic guess violating the failure criterion is represented by a point in the pq- plane located either in domain 1 or 2, corresponding to positive or negative values of h, respectively. If in domain 1, shear failure is declared, and the stress point is brought back to the curve $f^s = 0$ using a flow rule derived using the potential function g^s. If in domain 2, tensile failure takes place and the stress point is brought back to $f^t = 0$ using a flow rule derived using g^t.

H.3.3 Plastic Corrections

First consider shear failure. The flow rule has the form

$$\begin{aligned} \Delta\varepsilon_q^p &= \lambda^s \frac{\partial g^s}{\partial q} \\ \Delta\varepsilon_p^p &= \lambda^s \frac{\partial g^s}{\partial p} \end{aligned} \tag{H.3.15}$$

where the magnitude of the parameter λ^s remains to be defined. Using equation H.3.11 for g^s, these expressions give, after partial differentiation

$$\begin{aligned} \Delta\varepsilon_q^p &= \lambda^s \\ \Delta\varepsilon_p^p &= q_\psi \lambda^s \end{aligned} \tag{H.3.16}$$

Using equation H.3.6, the elastic strain increments may be expressed as the total strain increment minus the plastic increment.

$$\begin{aligned} \Delta\varepsilon_q^e &= \Delta\varepsilon_q - \Delta\varepsilon_q^p \\ &= \Delta\varepsilon_q - \lambda^s \\ \Delta\varepsilon_p^e &= \Delta\varepsilon_p - \Delta\varepsilon_p^p \\ &= \Delta\varepsilon_p - q_\psi \lambda^s \end{aligned} \tag{H.3.17}$$

The increment in generalised stress can now be written, using Hook's law, equation H.3.7

$$\begin{aligned} \Delta q &= G\Delta\varepsilon_q - G\lambda^s \\ \Delta p &= K\Delta\varepsilon_p - Kq_\psi \lambda^s \end{aligned} \tag{H.3.18}$$

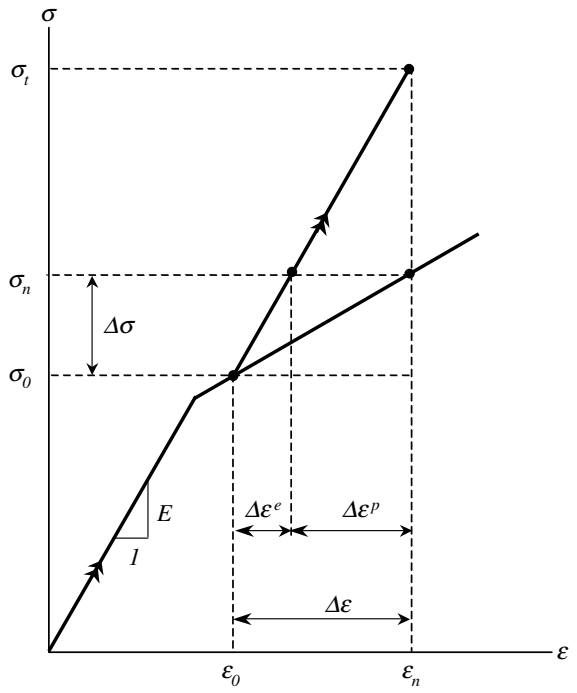

Figure H.2: One-dimensional representation of elasto-plastic relation

The new stress state is given by

$$\begin{aligned} q^N &= q^O + \Delta q \\ p^N &= p^O + \Delta p \end{aligned} \tag{H.3.19}$$

where the superscripts N and O refer to the new and old stress states respectively. Substitution of equation H.3.18 into equation H.3.19 leads to

$$\begin{aligned} q^N &= \left(q^O + G\Delta\varepsilon_q\right) - G\lambda^s \\ &= q^I - G\lambda^s \\ p^N &= \left(p^O + K\Delta\varepsilon_p\right) - Kq_\psi\lambda^s \\ &= p^I - Kq_\psi\lambda^s \end{aligned} \tag{H.3.20}$$

where the superscript I is used to represent the elastic guess obtained by adding to the old stress, elastic increments computed using the total strain increment, figure H.2.

The new stress point should be located on the shear yield surface. Using this, the parameter λ^s can be calculated by substitution of q^N and p^N for q and p in $f^s = 0$. Using equation H.3.8 and equation H.3.20, and after some

manipulation, λ^s is given by

$$\lambda^s = \frac{f^s\left(p^I, q^I\right)}{G + Kq_\phi q_\psi} \tag{H.3.21}$$

With the new generalised stresses known, the new stress tensor needs to be calculated. Noting that the new deviatoric stresses may be obtained by multiplying the corresponding deviatoric elastic guess with the ratio $\frac{q^N}{q^I}$, the new stresses may be written as (FLAC, 1998)

$$\sigma_{ij}^N = \left(\sigma_{ij}^I - p^I\delta_{ij}\right)\frac{q^N}{q^I} + p^N\delta_{ij} \tag{H.3.22}$$

where δ_{ij} is the Kronecker delta symbol

For tensile failure, the same procedure is followed. The flow rule has the form

$$\begin{aligned} \Delta\varepsilon_q^p &= \lambda^t\frac{\partial g^t}{\partial q} \\ \Delta\varepsilon_p^p &= \lambda^t\frac{\partial g^t}{\partial p} \end{aligned} \tag{H.3.23}$$

Using equation H.3.12 for g^t, these plastic strain increments become

$$\begin{aligned} \Delta\varepsilon_q^p &= 0 \\ \Delta\varepsilon_p^p &= \lambda^t \end{aligned} \tag{H.3.24}$$

The increments in elastic strains become

$$\begin{aligned} \Delta\varepsilon_q^e &= \Delta\varepsilon_q - \Delta\varepsilon_q^p \\ &= \Delta\varepsilon_q \\ \Delta\varepsilon_p^e &= \Delta\varepsilon_p - \Delta\varepsilon_p^p \\ &= \Delta\varepsilon_p - \lambda^t \end{aligned} \tag{H.3.25}$$

Using Hook's law, the increments in stress become

$$\begin{aligned} \Delta q &= G\Delta\varepsilon_q \\ \Delta p &= K\Delta\varepsilon_p - K\lambda^t \end{aligned} \tag{H.3.26}$$

The new stress states are given by equation H.3.19. Using this equation and

equation H.3.26, the new stress states are given by

$$\begin{aligned} q^N &= \left(q^O + G\Delta\varepsilon_q\right) \\ &= q^I \\ p^N &= \left(p^O + K\Delta\varepsilon_p\right) - K\lambda^t \\ &= p^I - K\lambda^t \end{aligned} \tag{H.3.27}$$

The parameter λ^t is calculated, using $f^t = 0$

$$\lambda^t = \frac{p^I - \sigma^t}{K} \tag{H.3.28}$$

Substitution of this equation in equation H.3.27 yields

$$\begin{aligned} q^N &= q^I \\ p^N &= \sigma^t \end{aligned} \tag{H.3.29}$$

In the tensile mode of failure the new deviatoric stresses correspond to the elastic guess $\left(\frac{q^N}{q^I} = 1\right)$ and the new stress tensor follows as

$$\sigma_{ij}^N = \sigma_{ij}^I + \left(\sigma^t - p^I\right)\delta_{ij} \tag{H.3.30}$$

H.3.4 Implementation Procedure

In this section describes the implementation of the Drucker-Prager model in the numeric code.

Step1:

Calculate an elastic guess σ_{ij}^I. This is done by assuming that the total strain increment is elastic. For the case of plane strain, equation H.2.1 is used.

Step2:

Calculate the generalised stress components $\left(p^I, q^I\right)$ using the elastic guess σ_{ij}^I and equation H.3.1 and H.3.3. If these stresses violate the composite yield criterion (equation H.3.8 and H.3.9), a correction must be applied to the generalised stress components to give the new stress state. The yield criteria is violated if $f^s >= 0$ or $f^t >= 0$. The function h (equation H.3.13) is used to determine if shear failure or tensile failure has occurred, i.e. $h(p^I, q^I) > 0$ or $h(p^I, q^I) \leq 0$ respectively.

Step3a:

If shear failure is declared, new generalised stresses are calculated from equation H.3.20 using equation H.3.21 for λ^s.

Step3b:

If tensile failure is declared, new generalised stresses are calculated from equation H.3.27 using equation H.3.28 for λ^t.

Step4a:

In the case of shear failure the stress tensor components in the system of reference axes are calculated from the corrected generalised stresses using equation H.3.22.

Step4b:

In the case of tensile failure the stress tensor components in the system of reference axes are calculated from the corrected generalised stresses using equation H.3.30.

H.4 The von Mises Model

The von Mises yield criterion is also known as the *distortion energy theory*. It assumes that yielding begins when the distortion energy equals the distortion energy at yield in simple tension (Mendelson, 1968). The yield condition is given by

$$\frac{1}{2}\left[(\sigma_{11}-\sigma_{22})^2+(\sigma_{22}-\sigma_{33})^2+(\sigma_{11}-\sigma_{33})^2+6\left(\sigma_{12}^2+\sigma_{23}^2+\sigma_{31}^2\right)\right]=\sigma_y^2 \tag{H.4.1}$$

And under the assumption of plane strain this becomes

$$\frac{1}{2}\left[(\sigma_{11}-\sigma_{22})^2+(\sigma_{22}-\sigma_{33})^2+(\sigma_{11}-\sigma_{33})^2+6\sigma_{12}^2\right]=\sigma_y^2 \tag{H.4.2}$$

where σ_y is the yield stress in simple tension. Using the second invariant of the stress deviator tensor, J_2, equation H.3.3, this becomes

$$\begin{aligned} 3J_2 &= \sigma_y^2 \\ \therefore \sqrt{J_2} &= \frac{\sigma_y}{\sqrt{3}} \end{aligned} \tag{H.4.3}$$

The yield function follows as

$$f = \sqrt{J_2} - \frac{\sigma_y}{\sqrt{3}} \tag{H.4.4}$$

Using the definition of the tangential stress, equation H.3.1, this becomes

$$f = q - \frac{\sigma_y}{\sqrt{3}} \tag{H.4.5}$$

Using an associated flow rule, the flow potential function becomes

$$g = q \tag{H.4.6}$$

H.4.1 Plastic Corrections

Following the same general procedure as in the previous section, the increments in plastic strain can be written as

$$\begin{aligned} \Delta\varepsilon_q^p &= \lambda \frac{\partial g}{\partial q} \\ &= \lambda \\ \Delta\varepsilon_p^p &= \lambda \frac{\partial g}{\partial p} \\ &= 0 \end{aligned} \tag{H.4.7}$$

Using equation H.3.6, the elastic strain increments may be expressed as the total strain increment minus the plastic increment.

$$\begin{aligned} \Delta\varepsilon_q^e &= \Delta\varepsilon_q - \Delta\varepsilon_q^p \\ &= \Delta\varepsilon_q - \lambda \\ \Delta\varepsilon_p^e &= \Delta\varepsilon_p - \Delta\varepsilon_p^p \\ &= \Delta\varepsilon_p \end{aligned} \tag{H.4.8}$$

The increment in generalised stress, can now be written, using Hook's law, equation H.3.7

$$\begin{aligned} \Delta q &= G\Delta\varepsilon_q - G\lambda \\ \Delta p &= K\Delta\varepsilon_p \end{aligned} \tag{H.4.9}$$

The new stress state is given by

$$\begin{aligned} q^N &= q^O + \Delta q \\ p^N &= p^O + \Delta p \end{aligned} \tag{H.4.10}$$

where the superscripts N and O refer to the new and old stress states respectively. Substitution of equation H.4.9 into equation H.4.10 leads to

$$\begin{aligned} q^N &= \left(q^O + G\Delta\varepsilon_q\right) - G\lambda \\ &= q^I - G\lambda \\ p^N &= \left(p^O + K\Delta\varepsilon_p\right) \\ &= p^I \end{aligned} \tag{H.4.11}$$

where the superscript I is used to represent the elastic guess obtained by adding to the old stress, elastic increments computed using the total strain increment, figure H.2.

The new stress point should be located on the yield surface. Using this, the parameter λ can be calculated by substitution of q^N and p^N for q and p in $f = 0$. Using equation H.4.5 and equation H.4.11, and after some manipulation, λ is given by

$$\lambda = \frac{q^I - \frac{\sigma_y}{\sqrt{3}}}{G} \tag{H.4.12}$$

With the new generalised stresses known, the new stress tensor needs to be calculated. Noting that the new deviatoric stresses may be obtained by multiplying the corresponding deviatoric elastic guess with the ratio $\frac{q^N}{q^I}$, the new stress tensor may be written as (FLAC, 1998)

$$\sigma_{ij}^N = \left(\sigma_{ij}^I - p^I\delta_{ij}\right)\frac{q^N}{q^I} + p^N\delta_{ij} \tag{H.4.13}$$

where δ_{ij} is the Kronecker delta symbol

H.4.2 Implementation Procedure

This section describes the implementation of the von Mises model in the numeric code.

Step1:

Calculate an elastic guess σ_{ij}^I. This is done by assuming that the total strain increment is elastic. For the case of plane strain, equation H.2.1 is used.

Step2:

Calculate the generalised stress components $\left(p^I, q^I\right)$ using the elastic guess σ_{ij}^I and equation H.3.1 and H.3.3. If these stresses violate the yield criterion (equation H.4.5), a correction must be applied to the generalised stress

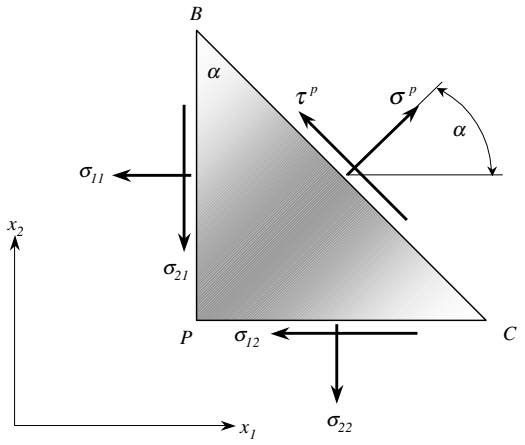

Figure H.3: Plane stress at a point in a continuum

components to give the new stress state. The yield criterion is violated if $f >= 0$.

Step3:

New generalised stresses are calculated from equation H.4.11 using equation H.4.12 for λ.

Step4:

The stress tensor components in the system of reference axes are calculated from the corrected generalised stresses using equation H.4.13.

H.5 The Mohr-Coulomb Model

The failure envelope for this model corresponds to a Mohr-Coulomb criterion with tension cutoff. The shear flow rule is non-associated and the tensile flow rule associated.

Referring to figure H.3, consider a point in a granular material with a plane passing through it. A stress vector with normal component σ^p and shear component τ^p to the plane acts at the point. Based on experimental evidence (Sokolovski, 1954), the Mohr-Coulomb strength criterion, in analogy with the law of dry friction between sliding surfaces, states that

$$|\tau^p| \leq c - \sigma^p tan\phi \tag{H.5.1}$$

with ϕ the angle of internal friction and c the coefficient of cohesion.

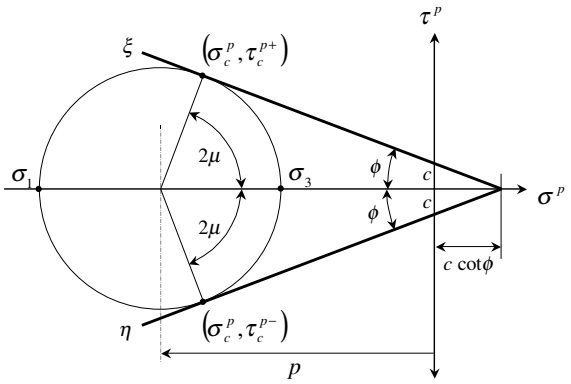

Figure H.4: Yield state according to Mohr-Coulomb criterion

This yield condition is depicted in figure H.4 on the Mohr circle with the two conditions of equation H.5.1 shown as lines ξ and η. With the Mohr circle not touching the ξ and η lines, no yielding takes place, but with the Mohr circle touching these lines, yielding is defined. This is the condition shown in figure H.4, and the corresponding principal stresses are $\sigma_3 \geq \sigma_1$. From the diagram it can be shown that

$$sin\phi = \frac{\frac{1}{2}(\sigma_3 - \sigma_1)}{c\ cot\phi - \frac{1}{2}(\sigma_3 + \sigma_1)} \tag{H.5.2}$$

After some manipulation, this equation can also be written as

$$\begin{aligned} \sigma_1 &= \sigma_3 N_\phi - 2c\sqrt{N_\phi} \\ \therefore f^s &= \sigma_1 - \sigma_3 N_\phi + 2c\sqrt{N_\phi} \end{aligned} \tag{H.5.3}$$

where f^s is the failure envelope (yield function) and N_ϕ is given by

$$N_\phi = \frac{1 + sin\phi}{1 - sin\phi} \tag{H.5.4}$$

FLAC (1998) introduces a tension yield function of the form

$$f^t = \sigma^t - \sigma_3 \tag{H.5.5}$$

where σ^t is the material tensile strength. With the ordering convention,

$$\sigma_1 \leq \sigma_2 \leq \sigma_3 \tag{H.5.6}$$

the failure criterion may be represented in the (σ_1, σ_3) plane as depicted in figure H.5. The shear yield function is defined from point A to B and the tensile yield function from B to C.

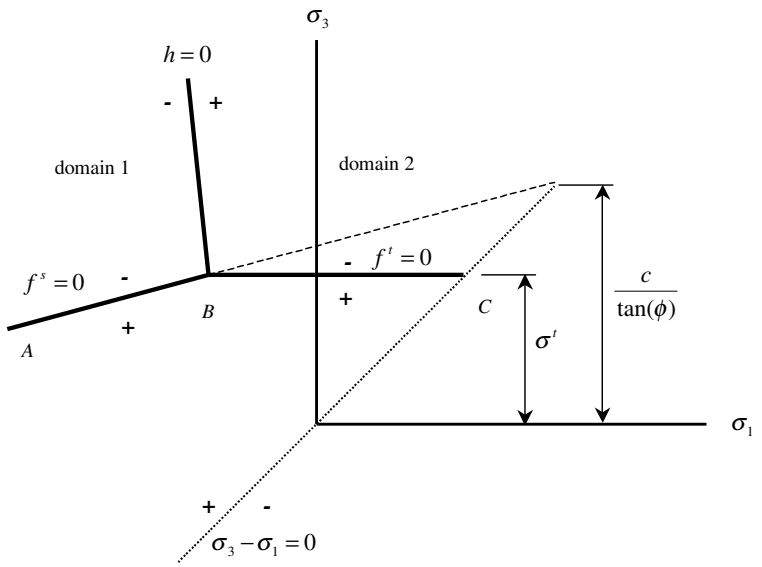

Figure H.5: Mohr-Coulomb failure criterion

Note that the intermediate principal stress σ_2 has no effect on the yield criterion. For a material with friction $\phi = 0$, the tensile strength cannot exceed the value σ^t_{max} given by (figure H.5)

$$\sigma^t_{max} = \frac{c}{tan\phi} \tag{H.5.7}$$

The shear potential function g^s corresponds to a non-associated flow rule

$$g^s = \sigma_1 - \sigma_3 N_\psi \tag{H.5.8}$$

where ψ is the dilatancy angle and

$$N_\psi = \frac{1+sin\psi}{1-sin\psi} \tag{H.5.9}$$

The associated flow rule for the tensile failure is derived from the potential function f^t

$$g^t = -\sigma_3 \tag{H.5.10}$$

The composite yield criterion is handled by defining a function $h(\sigma_1, \sigma_3) = 0$ which is represented by the diagonal between the representation of $f^s = 0$ and $f^t = 0$ in the (σ_1, σ_3) plane, figure H.5.

$$h(\sigma_1, \sigma_3) = \sigma_3 - \sigma^t + \alpha^p \left(\sigma_1 - \sigma^p\right) \tag{H.5.11}$$

where α^p and σ^p are constants defined as

$$\begin{aligned} \alpha^p &= \sqrt{1+N_\phi^2}+N_\phi \\ \sigma^p &= \sigma^t N_\phi - 2c\sqrt{N_\phi} \end{aligned} \tag{H.5.12}$$

An elastic guess violating the composite yield criterion is represented by a point in the (σ_1, σ_3) plane. This point will be either in domain 1 or domain 2 for negative and positive values of $h(\sigma_1, \sigma_3)$ respectively. Note that yielding occurs when the yield functions, f^s and f^t, turn negative, and not positive as in the case of the Drucker-Prager and von Mises models. If in domain 1, shear failure is declared and the stress point is brought back to the function $f^s = 0$ using the flow rule derived from g^s. If in domain 2, tensile failure is defined and the stress point is brought back to $f^t = 0$ using the flow rule derived from g^t.

H.5.1 Plastic Corrections

Lets first consider shear failure ($f^s \leq 0$). The flow rule has the following form in terms of principal stresses

$$\Delta\varepsilon_i^p = \lambda^s \frac{\partial g^s}{\partial \sigma_i} \qquad i = 1,2,3 \tag{H.5.13}$$

where the plastic multiplier λ^s is still unknown in magnitude. Using equation H.5.8, the increments in principal plastic strain become

$$\begin{aligned} \Delta\varepsilon_1^p &= \lambda^s \\ \Delta\varepsilon_2^p &= 0 \\ \Delta\varepsilon_3^p &= -\lambda^s N_\psi \end{aligned} \tag{H.5.14}$$

Writing the elastic increment in strain as the total increment in strain minus the plastic increment in strain, and using equation H.5.14

$$\begin{aligned} \Delta\varepsilon_1^e &= \Delta\varepsilon_1 - \lambda^s \\ \Delta\varepsilon_2^e &= \Delta\varepsilon_2 \\ \Delta\varepsilon_3^e &= \Delta\varepsilon_3 + \lambda^s N_\psi \end{aligned} \tag{H.5.15}$$

The incremental expression of Hook's law in terms of principal stress and strain has the form (FLAC, 1998)

$$\begin{aligned} \Delta\sigma_1 &= \alpha_1 \Delta\varepsilon_1^e + \alpha_2 \left(\Delta\varepsilon_2^e + \Delta\varepsilon_3^e\right) \\ \Delta\sigma_2 &= \alpha_1 \Delta\varepsilon_2^e + \alpha_2 \left(\Delta\varepsilon_1^e + \Delta\varepsilon_3^e\right) \\ \Delta\sigma_3 &= \alpha_1 \Delta\varepsilon_3^e + \alpha_2 \left(\Delta\varepsilon_1^e + \Delta\varepsilon_2^e\right) \end{aligned} \tag{H.5.16}$$

Using the increments in elastic strain from equation H.5.15 and Hook's law, the increments in principal stresses can be written as

$$\begin{aligned}
\Delta\sigma_1 &= \alpha_1\Delta\varepsilon_1 + \alpha_2\left(\Delta\varepsilon_2 + \Delta\varepsilon_3\right) - \lambda^s\left(\alpha_1 - \alpha_2 N_\psi\right)\\
\Delta\sigma_2 &= \alpha_1\Delta\varepsilon_2 + \alpha_2\left(\Delta\varepsilon_1 + \Delta\varepsilon_3\right) - \lambda^s\alpha_2\left(1 - N_\psi\right)\\
\Delta\sigma_3 &= \alpha_1\Delta\varepsilon_3 + \alpha_2\left(\Delta\varepsilon_1 + \Delta\varepsilon_2\right) - \lambda^s\left(-\alpha_1 N_\psi + \alpha_2\right)
\end{aligned} \tag{H.5.17}$$

Using the superscripts N and O to refer to the new and old stress states respectively, the new principal stress state follows as

$$\sigma_i^N = \sigma_i^O + \Delta\sigma_i \tag{H.5.18}$$

Substitution of equation H.5.17 in these equations yields

$$\begin{aligned}
\sigma_1^N &= \sigma_1^I - \lambda^s\left(\alpha_1 - \alpha_2 N_\psi\right)\\
\sigma_2^N &= \sigma_2^I - \lambda^s\alpha_2\left(1 - N_\psi\right)\\
\sigma_3^N &= \sigma_3^I - \lambda^s\left(-\alpha_1 N_\psi + \alpha_2\right)
\end{aligned} \tag{H.5.19}$$

where the superscript I indicates the elastic guess obtained by adding to the old stress state elastic components computed using the total strain increment.

$$\begin{aligned}
\sigma_1^I &= \sigma_1^O + \alpha_1\Delta\varepsilon_1 + \alpha_2\left(\Delta\varepsilon_2 + \Delta\varepsilon_3\right)\\
\sigma_2^I &= \sigma_2^O + \alpha_1\Delta\varepsilon_2 + \alpha_2\left(\Delta\varepsilon_1 + \Delta\varepsilon_3\right)\\
\sigma_3^I &= \sigma_3^O + \alpha_1\Delta\varepsilon_3 + \alpha_2\left(\Delta\varepsilon_1 + \Delta\varepsilon_2\right)
\end{aligned} \tag{H.5.20}$$

The new stress point should be located on the shear yield surface. Substitution of σ_1^N and σ_3^N for σ_1 and σ_3 in $f^s = 0$ gives, after some manipulation the magnitude of the plastic multiplier

$$\lambda^s = \frac{f^s(\sigma_1^I, \sigma_3^I)}{(\alpha_1 - \alpha_2 N_\psi) - (\alpha_2 - \alpha_1 N_\psi)N_\phi} \tag{H.5.21}$$

In the case of tensile failure, the flow rule has the form

$$\Delta\varepsilon_i^p = \lambda^t\frac{\partial g^t}{\partial\sigma_i} \qquad i = 1, 2, 3 \tag{H.5.22}$$

Using equation H.5.10 for g^t, and after partial differentiation, this expression gives

$$\begin{aligned}
\Delta\varepsilon_1^p &= 0\\
\Delta\varepsilon_2^p &= 0\\
\Delta\varepsilon_3^p &= -\lambda^t
\end{aligned} \tag{H.5.23}$$

The new stress state follows as

$$\begin{aligned}\sigma_1^N &= \sigma_1^I + \lambda^t \alpha_2 \\ \sigma_2^N &= \sigma_2^I + \lambda^t \alpha_2 \\ \sigma_3^N &= \sigma_3^I + \lambda^t \alpha_1\end{aligned} \tag{H.5.24}$$

The magnitude of λ^t is calculated by requiring that the new stress state should be on the tensile yield surface, $f^t = 0$

$$\lambda^t = \frac{f^t(\sigma_3^I)}{\alpha_1} \tag{H.5.25}$$

H.5.2 Implementation Procedure

This section describes the implementation of the Mohr-Coulomb model in the numeric code.

Step1:

First, an elastic guess σ_{ij}^I is computed by adding to the old stress components, increments calculated by application of Hook's law to the total strain increment for the step, equation H.5.16.

Step2:

The stress tensor σ_{ij}^I is used to calculate the principal stresses σ_1^I, σ_2^I and σ_3^I. In the case of plane strain the stress tensor always has the form

$$\begin{bmatrix} \sigma_{11}^I & \sigma_{12}^I & 0 \\ \sigma_{21}^I & \sigma_{22}^I & 0 \\ 0 & 0 & \sigma_{33}^I \end{bmatrix} \tag{H.5.26}$$

with $\sigma_{12}^I = \sigma_{21}^I$. With the stress tensor in this form, σ_{33}^I is always one of the principal stresses. To calculate the other two principal stresses, the eigenvalues of the following tensor can be solved

$$\begin{bmatrix} \sigma_{11}^I & \sigma_{12}^I \\ \sigma_{21}^I & \sigma_{22}^I \end{bmatrix} \tag{H.5.27}$$

The two roots of the quadratic characteristic equation can easily be solved

$$\beta = \frac{(\sigma_{11}^I + \sigma_{33}^I) \pm \sqrt{(\sigma_{11}^I + \sigma_{33}^I)^2 - 4(\sigma_{11}^I \sigma_{33}^I - (\sigma_{12}^I)^2)}}{2} \tag{H.5.28}$$

In the code, only the larger of the two eigenvalues β is calculated. The corresponding normalised eigenvector follows as

$$\begin{bmatrix} \frac{1}{\Omega} & \frac{\beta-\sigma_{11}^I}{\sigma_{12}^I\Omega} \end{bmatrix} \tag{H.5.29}$$

where Ω is the size of the eigenvector

$$\Omega = \sqrt{1 + \frac{(\beta - \sigma_{11}^I)^2}{(\sigma_{12}^I)^2}} \tag{H.5.30}$$

Only the first component of the eigenvector is calculated in the code, since it corresponds to a rotation angle θ

$$cos\theta = \pm\frac{1}{\Omega} \tag{H.5.31}$$

Rotation of the stress tensor σ_{ij}^I through the angle θ yields a tensor with the two principal stresses (eigenvalues) on the diagonal and zeros elsewhere.

$$\begin{bmatrix} \beta_{11} & \beta_{12} \\ \beta_{21} & \beta_{22} \end{bmatrix} = \begin{bmatrix} \beta_{11} & 0 \\ 0 & \beta_{22} \end{bmatrix} \tag{H.5.32}$$

where $\beta_{12} = \beta_{21} = 0$. This can be written in matrix notation as (Benham *et al.*, 1996)

$$\begin{bmatrix} \beta_{11} \\ \beta_{22} \\ \beta_{12} \end{bmatrix} = \begin{bmatrix} \beta_{11} \\ \beta_{22} \\ 0 \end{bmatrix} = \begin{bmatrix} c^2 & s^2 & 2sc \\ s^2 & c^2 & -2sc \\ -sc & sc & (c^2 - s^2) \end{bmatrix} \begin{bmatrix} \sigma_{11}^I \\ \sigma_{22}^I \\ \sigma_{12}^I \end{bmatrix} \tag{H.5.33}$$

Where $c = cos\theta$ and $s = sin\theta$. With the three principal stresses known in value ($\beta_{11}, \beta_{22}, \sigma_{33}^I$) they are ordered according to equation H.5.6.

Step3:

If these principal stresses violate the composite yield criterion, a correction must be applied to the elastic guess to give the new stress state. In this situation we have either $h(\sigma_1^I, \sigma_3^I) \leq 0$ or $h(\sigma_1^I, \sigma_3^I) > 0$, equation H.5.11. In the first case shear failure is declared and in the second case tensile failure.

Step4a:

If shear failure is declared, new principal stresses are calculated using equation H.5.19 and equation H.5.21 for λ^s.

Step4b:

If tensile failure is declared, new principal stresses are calculated using equation H.5.24 and equation H.5.25 for λ^t.

Step5:

The stress components in the system of reference axes are then calculated from the corrected principal values by assuming that the principal directions have not been effected by the occurrence of a plastic correction (FLAC, 1998). In the code this is done by rotating the tensor in equation H.5.32 (with the corrected principal values) through an angle $-\theta$.

$$\begin{bmatrix} \sigma_{11}^N \\ \sigma_{22}^N \\ \sigma_{12}^N \end{bmatrix} = \begin{bmatrix} c^2 & s^2 & 2sc \\ s^2 & c^2 & -2sc \\ -sc & sc & (c^2 - s^2) \end{bmatrix} \begin{bmatrix} \beta_{11} \\ \beta_{22} \\ 0 \end{bmatrix} \tag{H.5.34}$$

Where $c = cos(-\theta)$ and $s = sin(-\theta)$. The new stress tensor follows as

$$\begin{bmatrix} \sigma_{11}^N & \sigma_{12}^N & 0 \\ \sigma_{21}^N & \sigma_{22}^N & 0 \\ 0 & 0 & \sigma_{33}^N \end{bmatrix} \tag{H.5.35}$$

where σ_{33}^N is the corrected (new) principal stress corresponding to σ_{33}^I, i.e in the 33-direction.

H.5.3 Strain-Hardening and -Softening

In this model, the cohesion, friction, dilation and tensile strength may harden or soften in the plastic range. The user define the cohesion, friction, dilation and tensile strength a piecewise-linear functions of a hardening parameter. The hardening parameter for shear and tensile failure differs. The shear hardening parameter is used for cohesion, dilation and friction hardening while the tensile hardening parameter is used for tensile strength hardening.

Plastic shear strain is measured by the shear hardening parameter ε^{ps}. The incremental form is defined as (Vermeer and De Borst, 1984)

$$\Delta\varepsilon^{ps} = \left[\tfrac{1}{2} \left(\Delta\varepsilon_1^{ps} - \Delta\varepsilon_m^{ps} \right)^2 + \tfrac{1}{2} \left(\Delta\varepsilon_m^{ps} \right)^2 + \tfrac{1}{2} \left(\Delta\varepsilon_3^{ps} - \Delta\varepsilon_m^{ps} \right)^2 \right]^{\frac{1}{2}} \tag{H.5.36}$$

where

$$\Delta\varepsilon_m^{ps} = \tfrac{1}{3} \left(\Delta\varepsilon_1^{ps} + \Delta\varepsilon_3^{ps} \right) \tag{H.5.37}$$

and $\Delta\varepsilon_i^{ps}$, $i = 1, 3$ are principal plastic strain increments. These strain increments are given by equation H.5.14, the superscript s is just to indicate that it is related to shear failure and shear hardening/softening.

The tensile hardening parameter ε^{pt} measures the accumulated tensile plastic strain and is defined in incremental form as

$$\Delta\varepsilon^{pt} = \Delta\varepsilon_3^{pt} \tag{H.5.38}$$

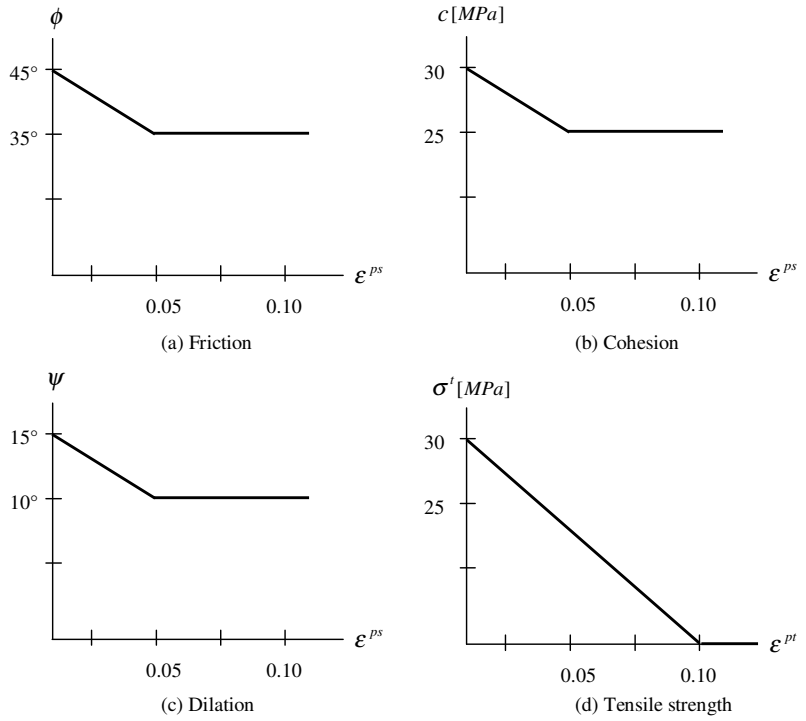

Figure H.6: Piecewise-linear functions for (a) friction, (b) cohesion, (c) dilation and (e) tensile strength

where $\Delta\varepsilon_3^{pt}$ is the increment of tensile plastic strain in the direction of the major principal stress and is given by equation H.5.23. Again, the superscript t denotes that the plastic strain is related to the tensile yield surface and not the shear yield surface.

The user defines the cohesion, friction and dilation as a function of the shear hardening parameter and the tensile strength as a function of the tensile hardening parameter. Figure H.6 shows examples of these piecewise-linear functions. The functions are defined by the user in the form of tables. It is assumed that the properties vary linearly between the entries in the table, i.e. linear interpolation is used.

Hardening increments are calculated at each particle and the hardening parameters updated. These new hardening parameters are used and new model (material) properties are evaluated by linear interpolation of the values given in the tables. The hardening/softening lags one step behind the corresponding plastic deformation. The time steps in this explicit code are, however, small and the lagging hardening/softening produces only a small error. The maximum value of the tensile strength, equation H.5.7, is still enforced.

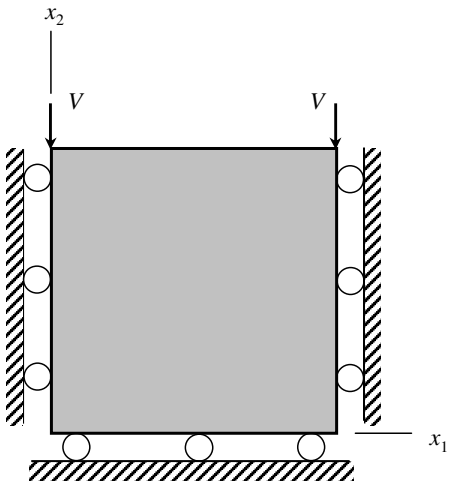

Figure H.7: Boundary conditions for oedometer test (FLAC, 1998)

H.5.4 Oedometer Test

This example (FLAC, 1998) is used to evaluate the ability of the code to determine stresses in a Mohr-Coulomb material subjected to an oedometer test. In the principal stress space the Mohr-Coulomb shear criterion is represented by an irregular hexagonal pyramid. In an oedometer experiment, two of the principal stress components are equal, and during plastic flow, the stress point evolves along an edge of the pyramid. The purpose of this simulation is to indicate that the Mohr-Coulomb model implemented, can handle such a situation. Results are compared to analytical solutions.

The boundary conditions for the plane strain oedometer test are shown in figure H.7. This corresponds to the uniform strain rates

$$\begin{aligned} \Delta\varepsilon_{11} &= 0 \\ \Delta\varepsilon_{22} &= \frac{V\Delta t}{L} \\ \Delta\varepsilon_{33} &= 0 \\ \Delta\varepsilon_{12} &= \Delta\varepsilon_{21} = 0 \end{aligned} \tag{H.5.39}$$

Since the shear stresses are all zero, the normal stresses are principal stresses. The constant velocity V is applied to the sample ($V < 0$) with a height L and a time step Δt.

Assuming zero initial stresses, the principal directions of the stresses and strains are those of the coordinate axes. For simplicity a sample of unit height $L = 1$ is used. Application of Hook's law gives (in the elastic range),

using $\varepsilon_{22} = Vt$ at time t

$$\begin{aligned} \sigma_{11} &= \alpha_2 Vt \\ \sigma_{22} &= \alpha_1 Vt \\ \sigma_{33} &= \alpha_2 Vt = \sigma_{11} \end{aligned} \tag{H.5.40}$$

The Mohr-Coulomb yield functions are given by equation H.5.3

$$\begin{aligned} f^1 &= \sigma_{22} - \sigma_{11} N_\phi + 2c\sqrt{N_\phi} \\ f^2 &= \sigma_{22} - \sigma_{33} N_\phi + 2c\sqrt{N_\phi} \end{aligned} \tag{H.5.41}$$

At the onset of yield $f^1 = f^2 = 0$. Using equation H.5.40 and equation H.5.41, we find

$$t = \frac{2c\sqrt{N_\phi}}{-V(\alpha_1 - \alpha_2 N_\phi)} \tag{H.5.42}$$

Yielding only takes place provided that $\alpha_1 - \alpha_2 N_\phi > 0$. During plastic flow, the strain increments are composed of elastic and plastic parts

$$\begin{aligned} \Delta\varepsilon_{11} &= \Delta\varepsilon_{11}^e + \Delta\varepsilon_{11}^p \\ \Delta\varepsilon_{22} &= \Delta\varepsilon_{22}^e + \Delta\varepsilon_{22}^p \\ \Delta\varepsilon_{33} &= \Delta\varepsilon_{33}^e + \Delta\varepsilon_{33}^p \end{aligned} \tag{H.5.43}$$

Using the boundary conditions in equation H.5.39 it follows that

$$\begin{aligned} \Delta\varepsilon_{11}^e &= -\Delta\varepsilon_{11}^p \\ \Delta\varepsilon_{22}^e &= V\Delta t - \Delta\varepsilon_{22}^p \\ \Delta\varepsilon_{33}^e &= -\Delta\varepsilon_{33}^p \end{aligned} \tag{H.5.44}$$

The flow rule for plastic flow along the edge of the Mohr-Coulomb criterion corresponding to $\sigma_{11} = \sigma_{33}$ has the form (FLAC, 1998)

$$\begin{aligned} \Delta\varepsilon_{11}^p &= \lambda_1 \frac{\partial g^1}{\partial \sigma_{11}} + \lambda_2 \frac{\partial g^2}{\partial \sigma_{11}} \\ \Delta\varepsilon_{22}^p &= \lambda_1 \frac{\partial g^1}{\partial \sigma_{22}} + \lambda_2 \frac{\partial g^2}{\partial \sigma_{22}} \\ \Delta\varepsilon_{33}^p &= \lambda_1 \frac{\partial g^1}{\partial \sigma_{33}} + \lambda_2 \frac{\partial g^2}{\partial \sigma_{33}} \end{aligned} \tag{H.5.45}$$

where g^1 and g^2 are the potential functions corresponding to f^1 and f^2, equation H.5.8

$$\begin{aligned} g^1 &= \sigma_{22} - \sigma_{11} N_\psi \\ g^2 &= \sigma_{22} - \sigma_{33} N_\psi \end{aligned} \tag{H.5.46}$$

After partial differentiation and substitution into equation H.5.45, we find

$$\begin{aligned} \Delta\varepsilon^p_{11} &= -\lambda_1 N_\psi \\ \Delta\varepsilon^p_{22} &= \lambda_1 + \lambda_2 \\ \Delta\varepsilon^p_{33} &= -\lambda_2 N_\psi \end{aligned} \tag{H.5.47}$$

In further considering that, by symmetry, $\lambda_1 = \lambda_2$, we obtain

$$\begin{aligned} \Delta\varepsilon^p_{11} &= -\lambda_1 N_\psi \\ \Delta\varepsilon^p_{22} &= 2\lambda_1 \\ \Delta\varepsilon^p_{33} &= -\lambda_2 N_\psi \end{aligned} \tag{H.5.48}$$

The stress increments (Hook's law) are given by

$$\begin{aligned} \Delta\sigma_{11} &= \alpha_1 \Delta\varepsilon^e_{11} + \alpha_2(\Delta\varepsilon^e_{22} + \Delta\varepsilon^e_{11}) \\ \Delta\sigma_{22} &= \alpha_1 \Delta\varepsilon^e_{22} + 2\alpha_2 \Delta\varepsilon^e_{11} \\ \Delta\sigma_{33} &= \Delta\sigma_{11} \end{aligned} \tag{H.5.49}$$

where $\Delta\varepsilon^e_{11} = \Delta\varepsilon^e_{33}$. Substitution of equation H.5.44 in equation H.5.49 and using equation H.5.48 yields

$$\begin{aligned} \Delta\sigma_{11} &= \alpha_1\lambda_1 N_\psi + \alpha_2(V\Delta t - 2\lambda_1 + \lambda_1 N_\psi) \\ \Delta\sigma_{22} &= \alpha_1(V\Delta t - 2\lambda_1) + 2\alpha_2\lambda_1 N_\psi \\ \Delta\sigma_{33} &= \Delta\sigma_{11} \end{aligned} \tag{H.5.50}$$

The plastic multiplier λ_1 may now be determined by expressing the condition that, during plastic flow, $\Delta f^1 = 0$. Using equation H.5.41, this condition takes the form

$$\Delta\sigma_{22} - \Delta\sigma_{11} N_\phi = 0 \tag{H.5.51}$$

Substitution of equation H.5.50 in equation H.5.51 yields, after some manipulations

$$\lambda_1 = V\lambda\Delta t \tag{H.5.52}$$

where

$$\lambda = \frac{\alpha_1 - \alpha_2 N_\phi}{(\alpha_1 + \alpha_2)N_\phi N_\psi - 2\alpha_2(N_\phi + N_\psi) + 2\alpha_1} \tag{H.5.53}$$

This analytical (exact) solution is compared to a numeric experiment using one element with 9 particles (3x3) in Chapter 4.

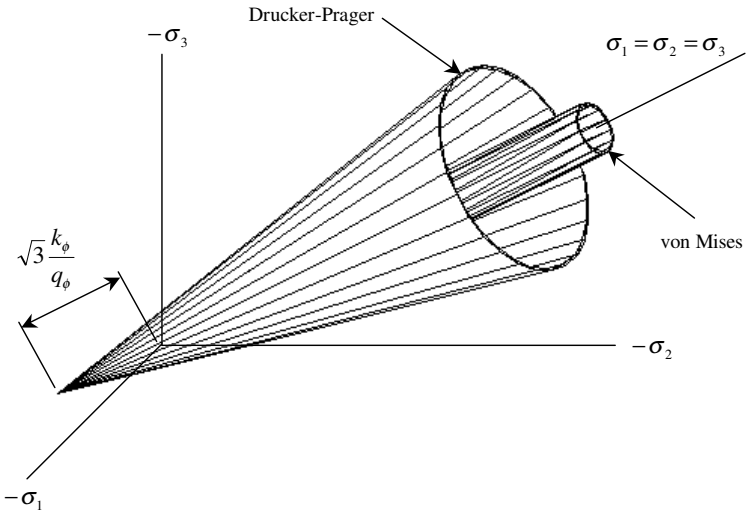

Figure H.8: Drucker-Prager and von Mises shear yield surfaces in the principal stress space

H.6 The Relation Between the Different Constitutive Models

The Drucker-Prager shear criterion $f^s = 0$ is represented in the principal stress space $(\sigma_1, \sigma_2, \sigma_3)$ by a cone with the axis along $\sigma_1 = \sigma_2 = \sigma_3$ and the apex at $(\sigma_1, \sigma_2, \sigma_3) = (\frac{k_\phi}{q_\phi}, \frac{k_\phi}{q_\phi}, \frac{k_\phi}{q_\phi})$. This is depicted in figure H.8. The Mohr-Coulomb shear criterion, characterised by the two parameters cohesion c and friction angle ϕ, is represented by an irregular hexagonal pyramid, figure H.9. The parameters q_ϕ and k_ϕ can be adjusted so that the Drucker-Prager cone will either pass through the outer or the inner edges of the Mohr-Coulomb pyramid (FLAC, 1998). For outer adjustment

$$\begin{aligned} q_\phi &= \frac{6}{\sqrt{3}\,(3 - sin\phi)}\, sin\phi \\ k_\phi &= \frac{6}{\sqrt{3}\,(3 - sin\phi)}\, c\, cos\phi \end{aligned} \tag{H.6.1}$$

and for inner adjustment

$$\begin{aligned} q_\phi &= \frac{6}{\sqrt{3}\,(3 + sin\phi)}\, sin\phi \\ k_\phi &= \frac{6}{\sqrt{3}\,(3 + sin\phi)}\, c\, cos\phi \end{aligned} \tag{H.6.2}$$

In the special case of $q_\phi = 0$, the Drucker-Prager shear criterion, degenerates into a von Mises criterion which corresponds to a cylinder in the principal stress space. Note that this von Mises criterion is not necessarily the same as described in section H.4. The Drucker-Prager shear flow rule is

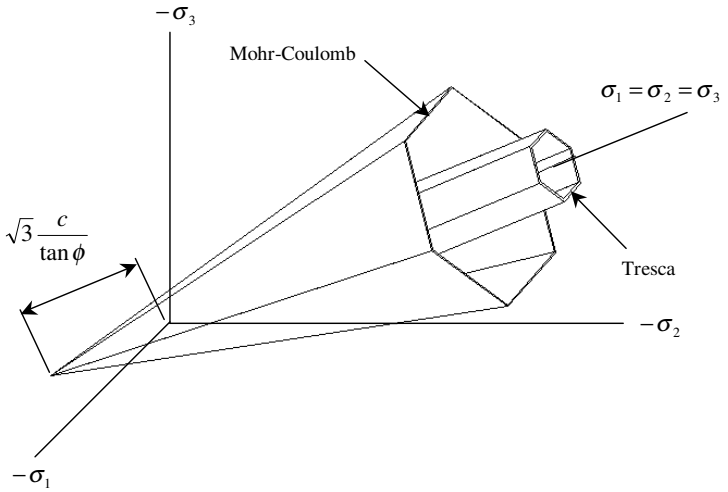

Figure H.9: Mohr-Coulomb and Tresca shear yield surfaces in the principal stress space

non-associated, while the von Mises flow rule employed here has an associated flow rule. The Drucker-Prager model, however, reduces to the von Mises model described in section H.4 if the following parameter values are used.

$$\begin{aligned} q_\phi &= 0 \\ k_\phi &= \frac{\sigma_y}{\sqrt{3}} \\ \sigma_t &= \frac{k_\phi}{q_\phi} = \infty \\ q_\psi &= 0 \end{aligned} \tag{H.6.3}$$

where σ_y is the yield stress in simple tension and with $q_\psi = 0$, the shear flow rule is associated. With $\sigma_t = \infty$, the tensile yield mode is not employed.

The Tresca criterion is a special case of the Mohr-Coulomb criterion for which $\phi = 0$. It is represented by a regular hexagonal prism. The von Mises cylinder circumscribes the Tresca prism for

$$\begin{aligned} q_\phi &= 0 \\ k_\phi &= \frac{2}{\sqrt{3}}\, c \end{aligned} \tag{H.6.4}$$

Appendix I

Cosserat Continuum Constitutive Models and Implementation

I.1 Introduction

Constitutive models for a Cosserat continuum are presented. This includes elasticity and elasto-plastic models.

I.2 Cosserat Plane Strain Elasticity

This section closely follows the work of de Borst (1991) and de Borst (1993). In this model, two-dimensional, planar motion is considered. In this case, each material point has two translational degrees-of-freedom, namely u_1 and u_2 and a rotational degree-of-freedom w_3^c, the rotation axis of which is orthogonal to the x_1x_2-plane.

The single, tensorial deformation measure is given by (Appendix C), equation C.3.7

$$\lambda_{ij} = u_{i,j} + \varepsilon_{ijk} w_k^c \tag{I.2.1}$$

or for planar deformation

$$\underline{\overline{\lambda}} = \begin{bmatrix} \lambda_{11} & \lambda_{12} & \lambda_{13} \\ \lambda_{21} & \lambda_{22} & \lambda_{23} \\ \lambda_{31} & \lambda_{32} & \lambda_{33} \end{bmatrix} = \begin{bmatrix} u_{1,1} & (u_{1,2} + w_3^c) & 0 \\ (u_{2,1} - w_3^c) & u_{2,2} & 0 \\ 0 & 0 & u_{3,3} \end{bmatrix}$$

The micro-curvature is given by

$$\kappa_{ij} = w_{i,j}^c \tag{I.2.2}$$

or for planar deformation

$$\underline{\overline{\boldsymbol{\kappa}}} = \begin{bmatrix} 0 & 0 & 0 \\ 0 & 0 & 0 \\ \kappa_{31} & \kappa_{32} & 0 \end{bmatrix}$$

In formulating elasto-plasticity, it is useful to rather use generalised curvatures $\kappa_{31}l$ and $\kappa_{32}l$, where l is a material parameter with the dimension of length. It is this parameter which effectively sets the internal length scale in the continuum, and therefore has the role of a "characteristic length".

The strain components can be assembled in a vector (for the two-dimensional case)

$$\overline{\boldsymbol{\varepsilon}}^c = [\lambda_{11}\ \lambda_{22}\ \lambda_{33}\ \lambda_{12}\ \lambda_{21}\ \kappa_{31}l\ \kappa_{32}l]^{\mathrm{T}} \tag{I.2.3}$$

Note that the normal strain in the x_3-direction, $\lambda_{33} = u_{3,3}$, has also been included in the strain vector. This has been done because, although this strain component remains zero under plane strain conditions during the entire loading process, this is not necessarily the case for the elastic and plastic contributions of this strain component. Also note that by multiplying the micro-curvatures by the length parameter l, all components of the strain vector $\overline{\boldsymbol{\varepsilon}}^c$ have the same dimension.

While the strain vector $\underline{\boldsymbol{\varepsilon}}^c$ is comprised of seven components for planar deformations, so is the stress vector $\overline{\boldsymbol{\sigma}}^c$. The couple-stresses μ_{ij} are conjugate to the micro-curvatures κ_{ij}. Dividing the couple-stresses by the length parameter l, we obtain a stress vector $\underline{\boldsymbol{\sigma}}^c$ in which all the entries have the same dimension.

$$\overline{\boldsymbol{\sigma}}^c = \left[\sigma_{11}\ \sigma_{22}\ \sigma_{33}\ \sigma_{12}\ \sigma_{21}\ \frac{\mu_{31}}{l}\ \frac{\mu_{32}}{l}\right]^{\mathrm{T}} \tag{I.2.4}$$

Assuming that the elastic strain vector is linearly related to the stress vector, the following equation can be written

$$\overline{\boldsymbol{\sigma}}^c = \underline{\overline{\boldsymbol{D}}}^e \overline{\boldsymbol{\varepsilon}}^{ce} \tag{I.2.5}$$

where $\underline{\overline{\boldsymbol{D}}}^e$ is the stiffness matrix containing the elastic moduli

$$\underline{\overline{\boldsymbol{D}}}^e = \begin{bmatrix} 2Gc_1 & 2Gc_2 & 2Gc_2 & 0 & 0 & 0 & 0 \\ 2Gc_2 & 2Gc_1 & 2Gc_2 & 0 & 0 & 0 & 0 \\ 2Gc_2 & 2Gc_2 & 2Gc_1 & 0 & 0 & 0 & 0 \\ 0 & 0 & 0 & (G+G^c) & (G-G^c) & 0 & 0 \\ 0 & 0 & 0 & (G-G^c) & (G+G^c) & 0 & 0 \\ 0 & 0 & 0 & 0 & 0 & 2G & 0 \\ 0 & 0 & 0 & 0 & 0 & 0 & 2G \end{bmatrix} \tag{I.2.6}$$

with $c_1 = \frac{1-\nu}{1-2\nu}$ and $c_2 = \frac{\nu}{1-2\nu}$, G is the shear modulus and v Poisson's ratio. G^c is an additional material constant, completing the four material constants that are needed to describe the elastic behaviour of an isotropic Cosserat continuum under planar deformations. The coefficient 2 has been introduced in terms D^e_{66} and D^e_{77} in order to arrive at a convenient form of the elasto-plastic constitutive equations. The total (bending) stiffness that sets the relation between the micro-curvatures and the couple stresses is basically determined by the value of the internal length scale l.

Expanding equation I.2.5, the terms become

$$\begin{aligned}\sigma_{11}^c &= 2G\left(\frac{1-v}{1-2v}\right)\lambda_{11} + 2G\left(\frac{v}{1-2v}\right)\lambda_{22} + 2G\left(\frac{v}{1-2v}\right)\lambda_{33} \\ &= 2G\left(\frac{1-v}{1-2v}\right)\varepsilon_{11} + 2G\left(\frac{v}{1-2v}\right)\varepsilon_{22} + 2G\left(\frac{v}{1-2v}\right)\varepsilon_{33}\end{aligned} \tag{I.2.7}$$

$$\begin{aligned}\sigma_{22}^c &= 2G\left(\frac{v}{1-2v}\right)\lambda_{11} + 2G\left(\frac{1-v}{1-2v}\right)\lambda_{22} + 2G\left(\frac{v}{1-2v}\right)\lambda_{33} \\ &= 2G\left(\frac{v}{1-2v}\right)\varepsilon_{11} + 2G\left(\frac{1-v}{1-2v}\right)\varepsilon_{22} + 2G\left(\frac{v}{1-2v}\right)\varepsilon_{33}\end{aligned} \tag{I.2.8}$$

$$\begin{aligned}\sigma_{33}^c &= 2G\left(\frac{v}{1-2v}\right)\lambda_{11} + 2G\left(\frac{v}{1-2v}\right)\lambda_{22} + 2G\left(\frac{1-v}{1-2v}\right)\lambda_{33} \\ &= 2G\left(\frac{v}{1-2v}\right)\varepsilon_{11} + 2G\left(\frac{v}{1-2v}\right)\varepsilon_{22} + 2G\left(\frac{1-v}{1-2v}\right)\varepsilon_{33}\end{aligned} \tag{I.2.9}$$

It can be seen that the expressions for normal stress are the same as in the case of the classical non-polar continuum. The expressions for the shear stresses, however, are different.

$$\begin{aligned}\sigma_{12}^c &= (G+G^c)\,\lambda_{12} + (G-G^c)\,\lambda_{21} \\ &= (G+G^c)\left(\frac{\partial u_1}{\partial x_2} + w_3^c\right) + (G-G^c)\left(\frac{\partial u_2}{\partial x_1} - w_3^c\right) \\ &= G\left(\frac{\partial u_1}{\partial x_2} + \frac{\partial u_2}{\partial x_1}\right) + 2G^c\left[\frac{1}{2}\left(\frac{\partial u_1}{\partial x_2} - \frac{\partial u_2}{\partial x_1}\right) + w_z^c\right] \\ &= G\varepsilon_{12} + 2G^c\left[\frac{1}{2}\left(\frac{\partial u_1}{\partial x_2} - \frac{\partial u_2}{\partial x_1}\right) + w_3^c\right] \\ &= \text{nonpolar} + \text{ polar}\end{aligned} \tag{I.2.10}$$

$$\begin{aligned}\sigma_{21}^c &= (G-G^c)\,\lambda_{12} + (G+G^c)\,\lambda_{21} \\ &= G\left(\frac{\partial u_1}{\partial x_2} + \frac{\partial u_2}{\partial x_1}\right) + 2G^c\left[\frac{1}{2}\left(\frac{\partial u_2}{\partial x_1} - \frac{\partial u_1}{\partial x_2}\right) - w_3^c\right] \\ &= G\varepsilon_{21} + 2G^c\left[\frac{1}{2}\left(\frac{\partial u_2}{\partial x_1} - \frac{\partial u_1}{\partial x_2}\right) - w_3^c\right] \\ &= \text{nonpolar} + \text{polar}\end{aligned} \tag{I.2.11}$$

The curvature equations are

$$\frac{\mu_{31}}{l} = 2G\kappa_{31}l \;\rightarrow\; \mu_{31} = 2G\kappa_{31}l^2 \tag{I.2.12}$$

$$\frac{\mu_{32}}{l} = 2G\kappa_{32}l \;\rightarrow\; \mu_{32} = 2G\kappa_{32}l^2 \tag{I.2.13}$$

Thus, for Cosserat elasticity, the following material constants must be known:

1. Shear modulus, G
2. Poisson's ration, v
3. Characteristic length, l
4. Cosserat shear modulus, G^c

I.3 Cosserat von Mises Elasto-Plasticity

This section closely follows the work of de Borst (1991). In this treatment a restriction of J_2-flow theory is used. The yield function f can be written as

$$f = (3J_2)^{\frac{1}{2}} - \tilde{\sigma}(\gamma) \tag{I.3.1}$$

with $\tilde{\sigma}$ the yield stress which is a function of the hardening parameter γ. J_2 is the second invariant of the deviatoric stresses, and for a polar-continuum it can be generalised as (Muhlhaus and Vardoulakis, 1987).

$$J_2 = a_1 s_{ij}s_{ij} + a_2 s_{ij}s_{ji} + \frac{a_3\mu_{ij}\mu_{ij}}{l^2} \tag{I.3.2}$$

s_{ij} is the deviatoric stress tensor, $\mu_{ij}$is the couple-stress tensor and a_1, a_2 and a_3 are material parameters. In the absence of couple stresses, $\mu_{ij} = 0$, $s_{ij} = s_{ji}$ and equation I.3.2 reduces to

$$J_2 = (a_1 + a_2)\, s_{ij}s_{ij} \tag{I.3.3}$$

which implies that the constraint

$$a_1 + a_2 = \tfrac{1}{2} \tag{I.3.4}$$

must be enforced so as to achieve that the classical expression for J_2 be retrieved properly. For the case of planar deformations, J_2 can be written in the following form

$$J_2 = \tfrac{1}{2}\left[s_{11}^2 + s_{22}^2 + s_{33}^2\right] + a_1\sigma_{12}^2 + 2a_2\sigma_{12}\sigma_{21} + a_1\sigma_{21}^2 + a_3\left[\left(\frac{\mu_{31}}{l}\right)^2 + \left(\frac{\mu_{32}}{l}\right)^2\right] \tag{I.3.5}$$

Muhlhaus & Vardoulakis (1987) proposed values of $a_1 = \frac{3}{4}$, $a_2 = -\frac{1}{4}$ and $a_3 = \frac{1}{8}$. de Borst (1991) used $a_1 = \frac{1}{4}$, $a_2 = \frac{1}{4}$ and $a_3 = \frac{1}{2}$, since these

values give rise to a particularly simple numerical algorithm. Using matrix notation, equation I.3.5 can be written as

$$J_2 = \tfrac{1}{2}\underline{\boldsymbol{\sigma}}^c \underline{\overline{\boldsymbol{P}}}\, \overline{\boldsymbol{\sigma}}^c \tag{I.3.6}$$

where $\underline{\overline{\boldsymbol{P}}}$ (for planar deformation) is given by

$$\underline{\overline{\boldsymbol{P}}} = \begin{bmatrix} \frac{2}{3} & -\frac{1}{3} & -\frac{1}{3} & 0 & 0 & 0 & 0 \\ -\frac{1}{3} & \frac{2}{3} & -\frac{1}{3} & 0 & 0 & 0 & 0 \\ -\frac{1}{3} & -\frac{1}{3} & \frac{2}{3} & 0 & 0 & 0 & 0 \\ 0 & 0 & 0 & 2a_1 & 2a_2 & 0 & 0 \\ 0 & 0 & 0 & 2a_2 & 2a_1 & 0 & 0 \\ 0 & 0 & 0 & 0 & 0 & 2a_3 & 0 \\ 0 & 0 & 0 & 0 & 0 & 0 & 2a_3 \end{bmatrix} \tag{I.3.7}$$

Substituting equation I.3.6 into equation I.3.1 leads to

$$f = \left(\tfrac{3}{2}\underline{\boldsymbol{\sigma}}^c \underline{\overline{\boldsymbol{P}}}\, \overline{\boldsymbol{\sigma}}^c\right)^{\frac{1}{2}} - \tilde{\sigma}\left(\gamma\right) \tag{I.3.8}$$

An associated flow rule is now obtained in a fashion identical to that in a classical non-polar continuum.

$$\dot{\bar{\boldsymbol{\varepsilon}}}^{cp} = \dot{\lambda}\frac{\partial f}{\partial \overline{\boldsymbol{\sigma}}^c} \tag{I.3.9}$$

Using equation I.3.8 and the fact that $f = 0$ during plastic flow, this becomes

$$\dot{\bar{\boldsymbol{\varepsilon}}}^{cp} = \dot{\lambda}\frac{3\underline{\overline{\boldsymbol{P}}}\, \overline{\boldsymbol{\sigma}}^c}{2\left(\tfrac{3}{2}\underline{\boldsymbol{\sigma}}^c \underline{\overline{\boldsymbol{P}}}\, \overline{\boldsymbol{\sigma}}^c\right)^{\frac{1}{2}}} = \frac{3\dot{\lambda}}{2\tilde{\sigma}\left(\gamma\right)}\underline{\overline{\boldsymbol{P}}}\, \overline{\boldsymbol{\sigma}}^c \tag{I.3.10}$$

$\dot{\lambda}$ is the plastic multiplier which, in analogy with classical plasticity, is determined from the consistency condition $\dot{f} = 0$.

The hardening parameter γ for Cosserat J_2-flow theory remains to be identified. The conventional strain-hardening hypothesis

$$\dot{\gamma} = \left[\tfrac{2}{3}\dot{e}^p_{ij}\dot{e}^p_{ij}\right]^{\frac{1}{2}} \tag{I.3.11}$$

with $\dot{e}^p_{ij}$ the plastic deviatoric strain-rate tensor. For uniaxial stress conditions $\dot{\gamma}$ reduces to the uniaxial plastic strain rate, $\dot{\gamma} = \dot{\varepsilon}^p_{11}$. Since there are no couple-stress effects in pure uniaxial loading, we require that any modification to equation I.3.11 for Cosserat media does not affect the result for pure uniaxial loading. A possible generalisation is to postulate that (equation I.3.2)

$$\dot{\gamma} = \left[b_1\dot{e}^p_{ij}\dot{e}^p_{ij} + b_2\dot{e}^p_{ij}\dot{e}^p_{ji} + b_3\dot{\kappa}^p_{ij}\dot{\kappa}^p_{ij}l^2\right]^{\frac{1}{2}} \tag{I.3.12}$$

with

$$b_1 + b_2 = \tfrac{2}{3} \tag{I.3.13}$$

for the case of planar deformations, $\dot{\gamma}$ can be elaborated as

$$\dot{\gamma} = \left[\tfrac{2}{3}\left[\left(\dot{e}^p_{11}\right)^2 + \left(\dot{e}^p_{22}\right)^2 + \left(\dot{e}^p_{33}\right)^2\right] + b_1\left(\dot{\varepsilon}^p_{12}\right)^2 + 2b_2\dot{\varepsilon}^p_{12}\dot{\varepsilon}^p_{21} + b_1\left(\dot{\varepsilon}^p_{21}\right)^2 + b_3\left[\left(\dot{\kappa}^p_{31}l\right)^2 + \left(\dot{\kappa}^p_{32}l\right)^2\right]\right]^{\frac{1}{2}} \tag{I.3.14}$$

Introduction of the matrix

$$Q = \begin{bmatrix} \frac{2}{3} & -\frac{1}{3} & -\frac{1}{3} & 0 & 0 & 0 & 0 \\ -\frac{1}{3} & \frac{2}{3} & -\frac{1}{3} & 0 & 0 & 0 & 0 \\ -\frac{1}{3} & -\frac{1}{3} & \frac{2}{3} & 0 & 0 & 0 & 0 \\ 0 & 0 & 0 & \frac{3}{2}b_1 & \frac{3}{2}b_2 & 0 & 0 \\ 0 & 0 & 0 & \frac{3}{2}b_2 & \frac{3}{2}b_1 & 0 & 0 \\ 0 & 0 & 0 & 0 & 0 & \frac{3}{2}b_3 & 0 \\ 0 & 0 & 0 & 0 & 0 & 0 & \frac{3}{2}b_3 \end{bmatrix} \tag{I.3.15}$$

allows the rate of the hardening parameter to be written in a similar format as the yield function

$$\dot{\gamma} = \left[\tfrac{2}{3}\dot{\underline{\boldsymbol{\varepsilon}}}^{cp}\overline{\underline{\boldsymbol{Q}}}\,\dot{\overline{\boldsymbol{\varepsilon}}}^{cp}\right]^{\frac{1}{2}} \tag{I.3.16}$$

Substituting equation I.3.10 into equation I.3.16 leads to

$$\dot{\gamma} = \left[\frac{2}{3}\frac{3\dot{\lambda}}{2\tilde{\sigma}(\gamma)}\underline{\boldsymbol{\sigma}}^c\,\overline{\underline{\boldsymbol{P}}}^T\,\overline{\underline{\boldsymbol{Q}}}\frac{3\dot{\lambda}}{2\tilde{\sigma}(\gamma)}\overline{\underline{\boldsymbol{P}}}\,\overline{\boldsymbol{\sigma}}^c\right]^{\frac{1}{2}} \tag{I.3.17}$$

With $b_1 = \frac{1}{3}$, $b_2 = \frac{1}{3}$ and $b_3 = \frac{2}{3}$ we have that $\overline{\underline{\boldsymbol{Q}}} = \overline{\underline{\boldsymbol{P}}}$ and equation I.3.17 reduces to

$$\dot{\gamma} = \frac{\dot{\lambda}}{\tilde{\sigma}(\lambda)}\left[\tfrac{3}{2}\underline{\boldsymbol{\sigma}}^c\overline{\underline{\boldsymbol{P}}}^T\,\overline{\underline{\boldsymbol{P}}}\,\overline{\underline{\boldsymbol{P}}}\,\overline{\boldsymbol{\sigma}}^c\right]^{\frac{1}{2}} \tag{I.3.18}$$

With the current choice of parameters a_1, a_2, a_3, b_1, b_2 and b_3 it follows that

$$\overline{\underline{\boldsymbol{P}}}^T\,\overline{\underline{\boldsymbol{P}}}\,\overline{\underline{\boldsymbol{P}}} = \overline{\underline{\boldsymbol{P}}} \tag{I.3.19}$$

so that equation I.3.18 reduces to

$$\dot{\gamma} = \frac{\dot{\lambda}}{\tilde{\sigma}(\gamma)}\left(\tfrac{3}{2}\underline{\boldsymbol{\sigma}}^c\overline{\underline{\boldsymbol{P}}}\,\overline{\boldsymbol{\sigma}}^c\right)^{\frac{1}{2}} \tag{I.3.20}$$

In the plastic state $f = 0$ and from equation I.3.8 it follows that

$$f = \left(\tfrac{3}{2}\underline{\boldsymbol{\sigma}}^c \underline{\overline{\boldsymbol{P}}}\, \overline{\boldsymbol{\sigma}}^c\right)^{\frac{1}{2}} - \tilde{\sigma}(\gamma) = 0 \;\; \rightarrow \;\; \left(\tfrac{3}{2}\underline{\boldsymbol{\sigma}}^c \underline{\overline{\boldsymbol{P}}}\, \overline{\boldsymbol{\sigma}}^c\right)^{\frac{1}{2}} = \tilde{\sigma}(\gamma) \tag{I.3.21}$$

Substituting this into equation I.3.20 leads to

$$\dot{\gamma} = \dot{\lambda} \tag{I.3.22}$$

which is the same format as obtained in classical J_2-flow theory.

I.3.1 Algorithm

In this section an algorithm that determines the stress increment in a finite loading step is given. A one-step return-mapping algorithm in which the gradient is evaluated at the trail stress state is used. As in classical plasticity the algorithm starts by computing a trail stress state

$$\overline{\boldsymbol{\sigma}}_t^c = \overline{\boldsymbol{\sigma}}_0^c + \underline{\overline{\boldsymbol{D}}}^e \Delta\overline{\boldsymbol{\varepsilon}}^c \tag{I.3.23}$$

The trail stress state is checked whether plasticity will indeed occur for this integration point within this loading step. $\overline{\boldsymbol{\sigma}}_0^c$ is the stress at the beginning of the loading step. If plasticity indeed occurs, i.e. if $f\left(\overline{\boldsymbol{\sigma}}_t^c, \gamma_0\right) > 0$, a correction for plastic flow is applied.

The yield function $f\left(\overline{\boldsymbol{\sigma}}^c, \gamma\right) = 0$, is written as a truncated Taylor series (Gerald and Wheatley, 1999) around $\left(\overline{\boldsymbol{\sigma}}_t^c, \gamma_0\right)$.

$$\begin{aligned} f\left(\overline{\boldsymbol{\sigma}}^c, \gamma\right) = f\left(\overline{\boldsymbol{\sigma}}_t^c, \gamma_0\right) + \left(\frac{\partial f}{\partial \overline{\boldsymbol{\sigma}}^c}\right)^T \left(\overline{\boldsymbol{\sigma}}^c - \overline{\boldsymbol{\sigma}}_t^c\right) + \frac{\partial f}{\partial \gamma}\left(\gamma - \gamma_0\right) + \\ \left(\frac{\partial^2 f}{\partial \overline{\boldsymbol{\sigma}}^{c2}}\right)^T \frac{\left(\overline{\boldsymbol{\sigma}}^c - \overline{\boldsymbol{\sigma}}_t^c\right)^2}{2!} + \frac{\partial^2 f}{\partial \gamma^2}\, \frac{\left(\gamma - \gamma_0\right)^2}{2!} + \cdots = 0 \end{aligned} \tag{I.3.24}$$

Evaluating this series at $\left(\overline{\boldsymbol{\sigma}}_n^c, \gamma_n\right)$ where n denotes the value of a quantity after correction for plastic flow and noting that (figure I.1),

$$\left(\overline{\boldsymbol{\sigma}}_n^c - \overline{\boldsymbol{\sigma}}_t^c\right) = \underline{\overline{\boldsymbol{D}}}^e\, \Delta\overline{\boldsymbol{\varepsilon}}^{cp} \;\; = -\underline{\overline{\boldsymbol{D}}}^e\, \Delta\lambda\, \frac{\partial f}{\partial \overline{\boldsymbol{\sigma}}^c} \tag{I.3.25}$$

equation I.3.24 can be written as

$$\begin{aligned} f\left(\overline{\boldsymbol{\sigma}}_t^c, \gamma_0\right) - \Delta\lambda \left(\frac{\partial f}{\partial \overline{\boldsymbol{\sigma}}^c}\right)^T \underline{\overline{\boldsymbol{D}}}^e \frac{\partial f}{\partial \overline{\boldsymbol{\sigma}}^c} + \Delta\gamma \frac{\partial f}{\partial \gamma} + \\ \frac{1}{2}\Delta\lambda^2 \left(\frac{\partial f}{\partial \overline{\boldsymbol{\sigma}}^c}\right)^T \underline{\overline{\boldsymbol{D}}}^e \frac{\partial^2 f}{\partial \overline{\boldsymbol{\sigma}}^{c2}} \underline{\overline{\boldsymbol{D}}}^e \frac{\partial f}{\partial \overline{\boldsymbol{\sigma}}^c} + \frac{1}{2}\Delta\gamma^2 \frac{\partial^2 f}{\partial \gamma^2} + \cdots = 0 \end{aligned} \tag{I.3.26}$$

Introduction of the hardening modulus in a fashion identical to classical plasticity

$$h(\gamma) = \frac{\partial \tilde{\sigma}}{\partial \gamma} \tag{I.3.27}$$

and use of the finite counterpart of equation I.3.22 permit equation I.3.26 to be written as

$$f(\overline{\sigma}_t^c, \gamma_0) - \Delta\lambda \left(h + \left(\frac{\partial f}{\partial \overline{\sigma}^c} \right)^T \underline{\overline{D}}^e \frac{\partial f}{\partial \overline{\sigma}^c} \right) + \frac{1}{2}\Delta\lambda^2 \left(\frac{\partial^2 f}{\partial \gamma^2} + \left(\frac{\partial f}{\partial \overline{\sigma}^c} \right)^T \underline{\overline{D}}^e \frac{\partial^2 f}{\partial \overline{\sigma}^{c2}} \underline{\overline{D}}^e \frac{\partial f}{\partial \overline{\sigma}^c} \right) + \cdots = 0 \tag{I.3.28}$$

where

$$\frac{\partial f}{\partial \gamma} = \frac{\partial f}{\partial \tilde{\sigma}} \frac{\partial \tilde{\sigma}}{\partial \gamma} = \frac{\partial \tilde{\sigma}}{\partial \gamma} \tag{I.3.29}$$

For the present choice of a_1, a_2, a_3, b_1, b_2 and b_3 and restricting the treatment to linear hardening or softening, $h(\gamma) = h$, second and higher-order contributions in $\Delta\lambda$ vanish (de Borst, 1991), so that we obtain an explicit expression for the plastic multiplier $\Delta\lambda$

$$\Delta\lambda = \frac{f(\overline{\sigma}_t^c, \gamma_0)}{h + \frac{\partial f^T}{\partial \overline{\sigma}^c} \underline{\overline{D}}^e \frac{\partial f}{\partial \overline{\sigma}^c}} \tag{I.3.30}$$

Note that in this explicit formulation the gradient of the yield function $\frac{\partial f}{\partial \overline{\sigma}^c}$ is evaluated for $\overline{\sigma}^c = \overline{\sigma}_t^c$.

With equation I.3.30 for the magnitude of the plastic strain increment the algorithm for elasto-plasticity in a Cosserat continuum can be formulated in complete analogy to a conventional plasticity model. The strain increment is decomposed in an elastic part $\overline{\varepsilon}^{ce}$ and a plastic part $\overline{\varepsilon}^{cp}$.

$$\Delta\overline{\varepsilon}^c = \Delta\overline{\varepsilon}^{ce} + \Delta\overline{\varepsilon}^{cp} \tag{I.3.31}$$

Similar to classical plasticity, a bijective relationship is assumed between the elastic strain increment and the stress increment, figure I.1.

$$\Delta\overline{\sigma}^c = \underline{\overline{D}}^e \Delta\overline{\varepsilon}^{ce} \tag{I.3.32}$$

The new stress state, i.e. the stress at the end of the increment, is the sum of the stress at the beginning of the step and the stress increment.

$$\overline{\sigma}_n^c = \overline{\sigma}_0^c + \Delta\overline{\sigma}^c \tag{I.3.33}$$

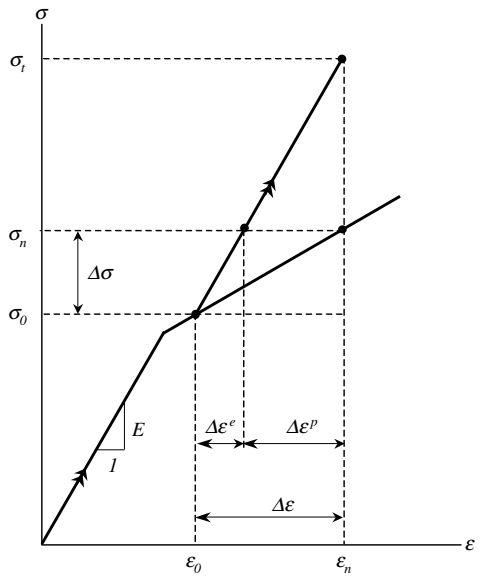

Figure I.1: One-dimensional representation of elasto-plastic relation

Substituting equation I.3.32 into equation I.3.33 leads to

$$\overline{\sigma}_n^c = \overline{\sigma}_0^c + \underline{\overline{D}}^e \Delta\overline{\varepsilon}^{ce} \tag{I.3.34}$$

where $\overline{\sigma}_0^c$ is known, but $\Delta\overline{\varepsilon}^{ce}$ still unknown. Using equation I.3.31, equation I.3.34 can be written as

$$\begin{aligned} \overline{\sigma}_n^c &= \overline{\sigma}_0^c + \underline{\overline{D}}^e \left(\Delta\overline{\varepsilon}^c - \Delta\overline{\varepsilon}^{cp}\right) \\ &= \overline{\sigma}_0^c + \underline{\overline{D}}^e \Delta\overline{\varepsilon}^c - \underline{\overline{D}}^e \Delta\overline{\varepsilon}^{cp} \\ &= \overline{\sigma}_t^c - \underline{\overline{D}}^e \Delta\overline{\varepsilon}^{cp} \end{aligned} \tag{I.3.35}$$

where $\overline{\sigma}_t^c$ is the trial stress by assuming the total strain increment to be elastic. Using equation I.3.10 for the plastic strain increment, the new stress state can be written as

$$\overline{\sigma}_n^c = \overline{\sigma}_t^c - \frac{3\lambda}{2\tilde{\sigma}(\gamma)} \underline{\overline{D}}^e \underline{\overline{P}}\, \overline{\sigma}_t^c \tag{I.3.36}$$

where the plastic increment is given by equation I.3.30. Note that by virtue of the vanishing of the second and higher-order contributions in $\Delta\lambda$ in equation I.3.28 the algorithm as laid down in equation I.3.36 provides a rigorous return to the yield surface.

I.4 Generalisation of J_2-flow Theory

A pressure dependent J_2-flow theory is proposed by de Borst (1993) for use within the framework of the Cosserat continuum.

Pressure dependent J_2-flow theory (Drucker-Prager) is employed with the yield function f as follows

$$f = (3J_2)^{\frac{1}{2}} + \alpha p - \tilde{\sigma}(\gamma) \tag{I.4.1}$$

with $\tilde{\sigma}$ the yield stress and a function of the hardening parameter γ. α is a constant friction coefficient and

$$p = \tfrac{1}{3}(\sigma_{11} + \sigma_{22} + \sigma_{33}) \tag{I.4.2}$$

J_2 is the second invariant of the deviatoric stresses, defined for a Cosserat continuum (Muhlhaus and Vardoulakis, 1987) as

$$J_2 = a_1 s_{ij} s_{ij} + a_2 s_{ij} s_{ji} + \frac{a_3 \mu_{ij} \mu_{ij}}{l^2} \tag{I.4.3}$$

s_{ij} is the deviatoric stress tensor, $\mu_{ij}$is the couple-stress tensor and a_1, a_2 and a_3 are material parameters. In the absence of couple stresses, $\mu_{ij} = 0$, $s_{ij} = s_{ji}$ and equation I.4.3 reduces to

$$J_2 = (a_1 + a_2)\, s_{ij} s_{ij} \tag{I.4.4}$$

which implies that the constraint

$$a_1 + a_2 = \tfrac{1}{2} \tag{I.4.5}$$

must be enforced so as to achieve that the classical expression for J_2 be retrieved properly. For the case of planar deformations, J_2 can be written in the following form

$$J_2 = \tfrac{1}{2}\left[s_{11}^2 + s_{22}^2 + s_{33}^2\right] + a_1\sigma_{12}^2 + 2a_2\sigma_{12}\sigma_{21} + a_1\sigma_{21}^2 + a_3\left[\left(\frac{\mu_{31}}{l}\right)^2 + \left(\frac{\mu_{32}}{l}\right)^2\right] \tag{I.4.6}$$

combining equation I.4.1 and equation I.4.6, and introducing the matrix

$$\overline{\underline{\boldsymbol{P}}} = \begin{bmatrix} \frac{2}{3} & -\frac{1}{3} & -\frac{1}{3} & 0 & 0 & 0 & 0 \\ -\frac{1}{3} & \frac{2}{3} & -\frac{1}{3} & 0 & 0 & 0 & 0 \\ -\frac{1}{3} & -\frac{1}{3} & \frac{2}{3} & 0 & 0 & 0 & 0 \\ 0 & 0 & 0 & 2a_1 & 2a_2 & 0 & 0 \\ 0 & 0 & 0 & 2a_2 & 2a_1 & 0 & 0 \\ 0 & 0 & 0 & 0 & 0 & 2a_3 & 0 \\ 0 & 0 & 0 & 0 & 0 & 0 & 2a_3 \end{bmatrix} \tag{I.4.7}$$

leads to a compact form of the yield function

$$f = \left(\tfrac{3}{2}\underline{\boldsymbol{\sigma}}^c \overline{\underline{\boldsymbol{P}}}\, \overline{\boldsymbol{\sigma}}^c\right)^{\frac{1}{2}} + \alpha \underline{\boldsymbol{\sigma}}\, \overline{\boldsymbol{\pi}} - \tilde{\sigma}(\gamma) \tag{I.4.8}$$

with $\underline{\boldsymbol{\pi}} = \left[\frac{1}{3}\ \frac{1}{3}\ \frac{1}{3}\ 0\ 0\ 0\right]$ A non-associated flow rule is obtained in an identical fashion to that in a nonpolar continuum.

$$\dot{\overline{\boldsymbol{\varepsilon}}}^{cp} = \dot{\lambda}\frac{\partial g}{\partial \overline{\boldsymbol{\sigma}}^{c}} \tag{I.4.9}$$

where

$$g = \left(\tfrac{3}{2}\underline{\boldsymbol{\sigma}}^{c}\overline{\underline{\boldsymbol{P}}}\,\overline{\boldsymbol{\sigma}}^{c}\right)^{\frac{1}{2}} + \beta\,\underline{\boldsymbol{\sigma}}\,\overline{\boldsymbol{\pi}} - \tilde{\sigma}\left(\gamma\right) \tag{I.4.10}$$

is the plastic potential function and β is a dilatancy factor. Equation I.4.9 becomes

$$\dot{\overline{\boldsymbol{\varepsilon}}}^{cp} = \dot{\lambda}\frac{3\overline{\underline{\boldsymbol{P}}}\,\overline{\boldsymbol{\sigma}}^{c}}{2\left(\frac{3}{2}\underline{\boldsymbol{\sigma}}^{c}\overline{\underline{\boldsymbol{P}}}\,\overline{\boldsymbol{\sigma}}^{c}\right)^{\frac{1}{2}}} + \beta\,\overline{\boldsymbol{\pi}} \tag{I.4.11}$$

$\dot{\lambda}$ is the plastic multiplier which, in analogy with classical plasticity, is determined from the consistency condition $\dot{f} = 0$.

It now remains to identify the plastic strain measure γ (hardening parameter) for a J_2-flow theory in a Cosserat continuum. For this purpose, recall the conventional strain-hardening hypothesis

$$\dot{\gamma} = \left[\tfrac{2}{3}\dot{e}^{p}_{ij}\dot{e}^{p}_{ij}\right]^{\frac{1}{2}} \tag{I.4.12}$$

with $\dot{e}^{p}_{ij}$ the plastic deviatoric strain-rate tensor. For uniaxial stress conditions $\dot{\gamma}$ reduces to the uniaxial plastic strain rate, $\dot{\gamma} = \dot{\varepsilon}^{p}_{11}$. Since there are no couple-stress effects in pure uniaxial loading, we require that any modification to equation I.4.12 for Cosserat media does not affect the result for pure uniaxial loading. A possible generalisation is to postulate that, analogous to equation I.4.3

$$\dot{\gamma} = \left[b_1\dot{e}^{p}_{ij}\dot{e}^{p}_{ij} + b_2\dot{e}^{p}_{ij}\dot{e}^{p}_{ji} + b_3\dot{\kappa}^{p}_{ij}\dot{\kappa}^{p}_{ij}l^2\right]^{\frac{1}{2}} \tag{I.4.13}$$

with

$$b_1 + b_2 = \tfrac{2}{3} \tag{I.4.14}$$

for the case of planar deformations, $\dot{\gamma}$ can be elaborated as

$$\dot{\gamma} = \left[\tfrac{2}{3}\left[\left(\dot{e}^{p}_{11}\right)^2 + \left(\dot{e}^{p}_{22}\right)^2 + \left(\dot{e}^{p}_{33}\right)^2\right] + b_1\left(\dot{\varepsilon}^{p}_{12}\right)^2 + 2b_2\dot{\varepsilon}^{p}_{12}\dot{\varepsilon}^{p}_{21} + b_1\left(\dot{\varepsilon}^{p}_{21}\right)^2 + b_3\left[\left(\dot{\kappa}^{p}_{31}l\right)^2 + \left(\dot{\kappa}^{p}_{32}l\right)^2\right]\right]^{\frac{1}{2}} \tag{I.4.15}$$

Introduction of the matrix

$$Q = \begin{bmatrix} \frac{2}{3} & -\frac{1}{3} & -\frac{1}{3} & 0 & 0 & 0 & 0 \\ -\frac{1}{3} & \frac{2}{3} & -\frac{1}{3} & 0 & 0 & 0 & 0 \\ -\frac{1}{3} & -\frac{1}{3} & \frac{2}{3} & 0 & 0 & 0 & 0 \\ 0 & 0 & 0 & \frac{3}{2}b_1 & \frac{3}{2}b_2 & 0 & 0 \\ 0 & 0 & 0 & \frac{3}{2}b_2 & \frac{3}{2}b_1 & 0 & 0 \\ 0 & 0 & 0 & 0 & 0 & \frac{3}{2}b_3 & 0 \\ 0 & 0 & 0 & 0 & 0 & 0 & \frac{3}{2}b_3 \end{bmatrix} \tag{I.4.16}$$

allows the rate of the hardening parameter to be written in a similar format as the yield function

$$\dot{\gamma} = \left[\tfrac{2}{3} \dot{\underline{\boldsymbol{\varepsilon}}}^{cp} \overline{\underline{\boldsymbol{Q}}} \, \dot{\overline{\boldsymbol{\varepsilon}}}^{cp} \right]^{\frac{1}{2}} \tag{I.4.17}$$

Substitution of equation I.4.11 into equation I.4.17 and noting that $\overline{\underline{\boldsymbol{Q}}} \, \overline{\boldsymbol{\pi}} = \overline{\mathbf{0}}$, it follows

$$\dot{\gamma} = \dot{\lambda} \left[\frac{\underline{\boldsymbol{\sigma}} \, \overline{\underline{\boldsymbol{P}}} \, \overline{\underline{\boldsymbol{Q}}} \, \overline{\underline{\boldsymbol{P}}} \, \overline{\boldsymbol{\sigma}}}{\underline{\boldsymbol{\sigma}} \, \overline{\underline{\boldsymbol{P}}} \, \overline{\boldsymbol{\sigma}}} \right]^{\frac{1}{2}} \tag{I.4.18}$$

if the parameters a_1, a_2, a_3, b_1, b_2 and b_3 are chosen such that

$$\overline{\underline{\boldsymbol{P}}} \, \overline{\underline{\boldsymbol{Q}}} \, \overline{\underline{\boldsymbol{P}}} = \overline{\underline{\boldsymbol{P}}} \tag{I.4.19}$$

equation I.4.18 reduces to exactly the same format as obtained in standard J_2-flow theory:

$$\dot{\gamma} = \dot{\lambda} \tag{I.4.20}$$

I.4.1 A Return-mapping Algorithm

The trial stress state $\overline{\boldsymbol{\sigma}}_t^c$ is defined as

$$\overline{\boldsymbol{\sigma}}_t^c = \overline{\boldsymbol{\sigma}}_0^c + \overline{\underline{\boldsymbol{D}}}^e \Delta \overline{\boldsymbol{\varepsilon}}^c \tag{I.4.21}$$

where $\overline{\boldsymbol{\sigma}}_0^c$ is the stress at the beginning of the loading step. It has been shown by (de Borst, 1991) (section I.3) that for certain classes of material parameters, there exists a set of values a_1, a_2, a_3, b_1, b_2 and b_3, which ensures a return to the yield surface in a single iteration. These advantageous properties are obtained for $a_1 = a_2 = \frac{1}{4}$, $a_3 = \frac{1}{2}$, $b_1 = b_2 = \frac{1}{3}$ and $b_3 = \frac{2}{3}$. This set of constants is referred to as the "standard" set.

When these conditions are not satisfied, an Euler backward algorithm can be employed. In this algorithm, the total strain increment in a finite loa-

ding step $\Delta\overline{\boldsymbol{\varepsilon}}^c$ is decomposed into an elastic contribution $\Delta\overline{\boldsymbol{\varepsilon}}^{ce}$ and a plastic contribution $\Delta\overline{\boldsymbol{\varepsilon}}^{cp}$.

$$\Delta\overline{\boldsymbol{\varepsilon}}^c = \Delta\overline{\boldsymbol{\varepsilon}}^{ce} + \Delta\overline{\boldsymbol{\varepsilon}}^{cp} \tag{I.4.22}$$

Between the stress increment $\Delta\overline{\boldsymbol{\sigma}}^c$ and the elastic strain increment $\Delta\overline{\boldsymbol{\varepsilon}}^c$, we have the bijective relationship (figure I.1)

$$\Delta\overline{\boldsymbol{\sigma}}^c = \underline{\overline{\boldsymbol{D}}}^e \Delta\overline{\boldsymbol{\varepsilon}}^{ce} \tag{I.4.23}$$

The new stress state, i.e. the stress at the end of the increment, is the sum of the stress at the beginning of the step and the stress increment.

$$\overline{\boldsymbol{\sigma}}_n^c = \overline{\boldsymbol{\sigma}}_0^c + \Delta\overline{\boldsymbol{\sigma}}^c \tag{I.4.24}$$

Substituting equation I.4.23 into equation I.4.24 leads to

$$\overline{\boldsymbol{\sigma}}_n^c = \overline{\boldsymbol{\sigma}}_0^c + \underline{\overline{\boldsymbol{D}}}^e \Delta\overline{\boldsymbol{\varepsilon}}^{ce} \tag{I.4.25}$$

where $\overline{\boldsymbol{\sigma}}_0^c$ is known, but $\Delta\overline{\boldsymbol{\varepsilon}}^{ce}$ still unknown. Using equation I.4.22, equation I.4.25 can be written as

$$\begin{aligned} \overline{\boldsymbol{\sigma}}_n^c &= \overline{\boldsymbol{\sigma}}_0^c + \underline{\overline{\boldsymbol{D}}}^e \left(\Delta\overline{\boldsymbol{\varepsilon}}^c - \Delta\overline{\boldsymbol{\varepsilon}}^{cp}\right) \\ &= \overline{\boldsymbol{\sigma}}_0^c + \underline{\overline{\boldsymbol{D}}}^e \Delta\overline{\boldsymbol{\varepsilon}}^c - \underline{\overline{\boldsymbol{D}}}^e \Delta\overline{\boldsymbol{\varepsilon}}^{cp} \\ &= \overline{\boldsymbol{\sigma}}_t^c - \underline{\overline{\boldsymbol{D}}}^e \Delta\overline{\boldsymbol{\varepsilon}}^{cp} \end{aligned} \tag{I.4.26}$$

where $\overline{\boldsymbol{\sigma}}_t^c$ is the trial stress by assuming the total strain increment to be elastic. Furthermore,, the expression for the plastic strain rate, equation I.4.11, is integrated using a single-point Euler backward rule (Gerald and Wheatley, 1999).

$$\Delta\overline{\boldsymbol{\varepsilon}}^{cp} = \Delta\lambda \left[\frac{3\underline{\overline{\boldsymbol{P}}}\, \overline{\boldsymbol{\sigma}}_n^c}{2\left(\frac{3}{2}\underline{\boldsymbol{\sigma}}_n^c \underline{\overline{\boldsymbol{P}}}\, \overline{\boldsymbol{\sigma}}_n^c\right)^{\frac{1}{2}}} + \beta\, \overline{\boldsymbol{\pi}} \right] \tag{I.4.27}$$

where the subscript n refers to the value at the end of the loading step. Substitution of equation I.4.27 into equation I.4.26 leads to

$$\overline{\boldsymbol{\sigma}}_n^c = \overline{\boldsymbol{\sigma}}_t^c - \Delta\lambda \left[\frac{3\, \underline{\overline{\boldsymbol{D}}}^e\, \underline{\overline{\boldsymbol{P}}}\, \overline{\boldsymbol{\sigma}}_n^c}{2\left(\frac{3}{2}\underline{\boldsymbol{\sigma}}_n^c \underline{\overline{\boldsymbol{P}}}\, \overline{\boldsymbol{\sigma}}_n^c\right)^{\frac{1}{2}}} + \beta\, \underline{\overline{\boldsymbol{D}}}^e\, \overline{\boldsymbol{\pi}} \right] \tag{I.4.28}$$

The condition that at the end of the loading step the yield condition must be satisfied, $f\left(\overline{\boldsymbol{\sigma}}_n^c, \gamma_n\right)$, is used. Equation I.4.28 transforms into

$$\overline{\boldsymbol{\sigma}}_n^c = \overline{\boldsymbol{\sigma}}_t^c - \Delta\lambda \left[\frac{3\, \underline{\overline{\boldsymbol{D}}}^e\, \underline{\overline{\boldsymbol{P}}}\, \overline{\boldsymbol{\sigma}}_n^c}{2\left[\tilde{\sigma}(\gamma_n) - \alpha\ \underline{\boldsymbol{\pi}}\, \overline{\boldsymbol{\sigma}}_n^c\right]} + \beta\, \underline{\overline{\boldsymbol{D}}}^e\, \overline{\boldsymbol{\pi}} \right] \tag{I.4.29}$$

A complication now arises, since we wish to express $\overline{\sigma}_n^c$ as a function of $\overline{\sigma}_t^c$ and $\Delta\lambda$, while in equation I.4.29 $\overline{\sigma}_n^c$ also occurs in the denominator of the second term on the right-hand side. To overcome this problem, we express $\underline{\boldsymbol{\pi}}\ \overline{\sigma}_n^c$ as a function of $\underline{\boldsymbol{\pi}}\ \overline{\sigma}_t^c$ and $\Delta\lambda$ by pre-multiplying equation I.4.29 by the projection vector $\underline{\boldsymbol{\pi}}$. Since $\underline{\boldsymbol{\pi}}\ \underline{\overline{\boldsymbol{D}}}^e \underline{\overline{\boldsymbol{P}}} = \underline{\mathbf{0}}$, this gives

$$\begin{aligned} \underline{\boldsymbol{\pi}}\ \overline{\sigma}_n^c &= \underline{\boldsymbol{\pi}}\ \overline{\sigma}_t^c - \Delta\lambda\beta\ \underline{\boldsymbol{\pi}}\ \underline{\overline{\boldsymbol{D}}}^e\ \overline{\boldsymbol{\pi}} \\ &= \underline{\boldsymbol{\pi}}\ \overline{\sigma}_t^c - \Delta\lambda\beta\ K \end{aligned} \tag{I.4.30}$$

Substitution of this identity into equation I.4.29 results in the desired formulation.

$$\begin{aligned} \overline{\sigma}_n^c &= \overline{\sigma}_t^c - \Delta\lambda \left[\frac{3\ \underline{\overline{\boldsymbol{D}}}^e\ \underline{\overline{\boldsymbol{P}}}\ \overline{\sigma}_n^c}{2\left[\tilde{\sigma}(\gamma_n) - \alpha\ (\underline{\boldsymbol{\pi}}\ \overline{\sigma}_t^c - \Delta\lambda\beta\ K)\right]} + \beta\ \underline{\overline{\boldsymbol{D}}}^e\ \overline{\boldsymbol{\pi}} \right] \\ &= \underline{\overline{\boldsymbol{A}}}^{-1} \left(\overline{\sigma}_t^c - \Delta\lambda\beta\ \underline{\overline{\boldsymbol{D}}}^e\ \overline{\boldsymbol{\pi}} \right) \end{aligned} \tag{I.4.31}$$

where

$$\underline{\overline{\boldsymbol{A}}} = \underline{\overline{\boldsymbol{I}}} + \frac{3\ \Delta\lambda\ \underline{\overline{\boldsymbol{D}}}^e\ \underline{\overline{\boldsymbol{P}}}}{2\left[\tilde{\sigma}(\gamma_n) + \Delta\lambda\ \alpha\ \beta\ K - \alpha\ \underline{\boldsymbol{\pi}}\ \overline{\sigma}_t^c\right)} \tag{I.4.32}$$

and $\underline{\overline{\boldsymbol{I}}}$ is a 7×7 matrix with ones on the diagonal and zeros everywhere else. Substitution of equation I.4.31 into the yield condition $f\left(\overline{\sigma}_n^c, \gamma_n\right) = 0$ results in a non-linear equation in $\Delta\gamma$

$$\begin{aligned} f(\Delta\lambda) = \left[\tfrac{3}{2} \left(\overline{\sigma}_t^c - \Delta\lambda\beta\ \underline{\overline{\boldsymbol{D}}}^e\ \overline{\boldsymbol{\pi}} \right)^T \left(\underline{\overline{\boldsymbol{A}}}^{-1} \right)^T\ \underline{\overline{\boldsymbol{P}}} \left(\underline{\overline{\boldsymbol{A}}}^{-1} \right) \left(\overline{\sigma}_t^c - \Delta\lambda\beta\ \underline{\overline{\boldsymbol{D}}}^e\ \overline{\boldsymbol{\pi}} \right) \right]^{\frac{1}{2}} \\ + \alpha\ \underline{\boldsymbol{\pi}}\ \left(\underline{\overline{\boldsymbol{A}}}^{-1} \right) \left(\overline{\sigma}_t^c - \Delta\lambda\beta\ \underline{\overline{\boldsymbol{D}}}^e\ \overline{\boldsymbol{\pi}} \right) - \tilde{\sigma}(\gamma_n) = 0 \end{aligned} \tag{I.4.33}$$

This equation can be solved using the Regula-Falsi method (Phillips *et al.*, 1998). Convergence is achieved within 4-5 iterations (de Borst, 1993).

I.5 Cosserat Drucker-Prager Elasto-Plasticity

This model is similar to the model described in the previous section, but with some small changes in implementation. The model was proposed by Muhlhaus (1987). The description given here closely follows that of Tejchman (1997).

The yield function f is given by

$$f = q + \alpha(\gamma^p)p - c \tag{I.5.1}$$

and the potential function g by

$$g = q + \beta(\gamma^p)p \tag{I.5.2}$$

where

$$q = \sqrt{J_2} \tag{I.5.3}$$

and

$$p = \frac{1}{2}\left(\sigma_{11} + \sigma_{22} + \sigma_{33}\right) \tag{I.5.4}$$

The second invariant of the deviatoric stress tensor J_2 is given by equation I.3.2.

$$J_2 = a_1 s_{ij} s_{ij} + a_2 s_{ij} s_{ji} + \frac{a_3 \mu_{ij} \mu_{ij}}{l^2} \tag{I.5.5}$$

s_{ij} is the deviatoric stress tensor, α is a friction factor, β a dilatancy factor, c is cohesion and a_1, a_2 and a_3 are material parameters as described in the previous two sections with the constraint that $a_1 + a_2 = \frac{1}{2}$. The plastic shear strain rate $\dot{\gamma}^p$, is again given by equation I.3.12

$$\dot{\gamma}^p = \left[b_1 \dot{e}^p_{ij} \dot{e}^p_{ij} + b_2 \dot{e}^p_{ij} \dot{e}^p_{ji} + b_3 \dot{\kappa}^p_{ij} \dot{\kappa}^p_{ij} l^2\right]^{\frac{1}{2}} \tag{I.5.6}$$

Muhlhaus (1987) derived, on macroscopic level, and expression for $\dot{\gamma}$ by taking into account slip and rotation in a random assembly of circular rods with a fixed diameter,

$$\dot{\gamma}^p = \left[3\dot{e}^p_{ij} \dot{e}^p_{ij} - \dot{e}^p_{ij} \dot{e}^p_{ji} + \dot{\kappa}^p_{ij} \dot{\kappa}^p_{ij} l^2\right]^{\frac{1}{2}} \tag{I.5.7}$$

i.e. $b_1 = 3$, $b_2 = -1$ and $b_3 = 1$. Further, by assuming that q and $\dot{\gamma}^p$ are work-conjugate (Muhlhaus, 1987)

$$q\dot{\gamma}^p = s_{ij}\dot{e}_{ij} + \mu_i \dot{\kappa}_i \tag{I.5.8}$$

it can be shown that $a_1 = \frac{3}{8}$, $a_2 = \frac{1}{8}$ and $a_3 = 1$. This complies to the constraint that $a_1 + a_2 = \frac{1}{2}$. From micromechanical considerations it can also be shown that (Muhlhaus and Vardoulakis, 1987)

$$G^c = \frac{G}{2\left(a_1 - a_2\right)} \tag{I.5.9}$$

The stresses and strains are assembled in vectors as shown by equation I.2.3 and I.2.4

$$\begin{aligned} \underline{\boldsymbol{\varepsilon}}^c &= \left[\lambda_{11}\ \lambda_{22}\ \lambda_{33}\ \lambda_{12}\ \lambda_{21}\ \kappa_{31} l\ \kappa_{32} l\right] \\ \underline{\boldsymbol{\sigma}}^c &= \left[\sigma_{11}\ \sigma_{22}\ \sigma_{33}\ \sigma_{12}\ \sigma_{21}\ \frac{\mu_{31}}{l}\ \frac{\mu_{32}}{l}\right] \end{aligned} \tag{I.5.10}$$

A trial stress method (linearised expansion of the yield condition about the trial stress point) using an elastic predictor and a plastic corrector with radial return mapping is used (Tejchman, 1997). According to this algorithm, the plastic multiplier $\Delta\lambda$ is given by

$$\Delta\lambda = \frac{f\left(\overline{\sigma}_t^c, \gamma_0\right)}{h + \frac{\partial f^T}{\partial \overline{\sigma}^c} \underline{\overline{\boldsymbol{D}}}^e \frac{\partial g}{\partial \overline{\sigma}^c}} \tag{I.5.11}$$

where $\overline{\sigma}_t^c$ is the trial stress state, calculated by assuming the total strain increment to be elastic, equation I.3.23, and h is the hardening modulus. Note that this expression is similar to what is given by equation I.3.30. The gradients $\frac{\partial f}{\partial \overline{\sigma}^c}$ and $\frac{\partial g}{\partial \overline{\sigma}^c}$ are evaluated at the trial stress point. Similar to equation I.3.36, the new stress state can be calculated using

$$\overline{\sigma}_n^c = \overline{\sigma}_t^c - \Delta\lambda \underline{\overline{\boldsymbol{D}}}^e \frac{\partial g}{\partial \overline{\sigma}^c} \tag{I.5.12}$$

This new stress state $\overline{\sigma}_n^c$ would not necessarily be on the yield function $f = 0$. Therefor, the calculations are continued until the stress state lies on the yield surface. Iterations are used where the newest stress state is substituted for $\overline{\sigma}_t^c$ in equation I.5.12 and f, $\frac{\partial f}{\partial \overline{\sigma}^c}$, $\frac{\partial g}{\partial \overline{\sigma}^c}$, α, β and h are computed in each iteration using the newest stress state. No more than two or three iterations were needed to satisfy the condition $\frac{f}{q} \leq 10^{-6}$.

The gradients are calculated as follows (Tejchman, 1997)

$$\frac{\partial f}{\partial \overline{\sigma}^c} = \frac{1}{q} \begin{bmatrix} \frac{s_{11}}{2} \\ \frac{s_{22}}{2} \\ \frac{s_{33}}{2} \\ \frac{3s_{12}}{8} + \frac{s_{21}}{8} \\ \frac{3s_{21}}{8} + \frac{s_{12}}{8} \\ \frac{\mu_{31}}{l^2} \\ \frac{\mu_{32}}{l^2} \end{bmatrix} + \frac{1}{2} \begin{bmatrix} \alpha \\ \alpha \\ 0 \\ 0 \\ 0 \\ 0 \\ 0 \end{bmatrix} \tag{I.5.13}$$

$$\frac{\partial g}{\partial \overline{\sigma}^c} = \frac{1}{q} \begin{bmatrix} \frac{s_{11}}{2} \\ \frac{s_{22}}{2} \\ \frac{s_{33}}{2} \\ \frac{3s_{12}}{8} + \frac{s_{21}}{8} \\ \frac{3s_{21}}{8} + \frac{s_{12}}{8} \\ \frac{\mu_{31}}{l^2} \\ \frac{\mu_{32}}{l^2} \end{bmatrix} + \frac{1}{2} \begin{bmatrix} \beta \\ \beta \\ 0 \\ 0 \\ 0 \\ 0 \\ 0 \end{bmatrix} \tag{I.5.14}$$

and also

$$\frac{\partial f^T}{\partial \overline{\sigma}^c} \underline{\overline{\boldsymbol{D}}}^e \frac{\partial g}{\partial \overline{\sigma}^c} = G + \alpha\beta B \tag{I.5.15}$$

where $B = \frac{G}{1-2\nu}$ and it has been assumed that $a_1 = \frac{3}{8}$, $a_2 = \frac{1}{8}$ and $a_3 = 1$

References

Adhikary, D., Muhlhaus, H.-B. and Dyskin, A. (1999). Modelling the large deformations in stratified media - the cosserat continuum approach. *Mechanics of Cohesive-Frictional Materials*, vol. 4, pp. 195–213. (Cited on pages 7 and 9.)

Albert, R., Pfeifer, M., Shiffer, P. and Barabasi, A. (1998). Drag force in a granular medium. Www.nd.edu. (Cited on page 95.)

Bagster, D. and Bridgwater, J. (1967). The measurement of the force needed to move blades through a bed of cohesionless granules. *Powder Technology*. (Cited on page 95.)

Bardenhagen, S.G., Brackbill, J.U. and Sulsky, D.L. (2000). The material-point method for granular materials. *Computational Methods in Applied Mechanics and Engineering*, vol. 187, pp. 529–541. (Cited on pages 11, 28, 39, 270, and 276.)

Belytschko, T., Krongauz, Y., Organ, D., Flemming, M. and Krysl, P. (1996). Meshless methods: An overview and recent developments. Tech. Rep., , Northmestern University. (Cited on pages 8 and 9.)

Belytschko, T., Lu, Y.Y. and Gu, L. (1994). Element free galerkin methods. *Int. Journal. Numer. Methods. Eng.*, vol. 37, pp. 229–256. (Cited on page 10.)

Benham, P., Crawford, R. and Armstrong, C. (1996). *Mechanics of Eninee-ring Materials*. 2nd edn. Addison Wesley Longman Limited. (Cited on page 301.)

Benson, D. (1992). Computational methods in lagrangian and eulerian hydrocodes. *Computer Methods in Applied Mechanics and Engineering*, vol. 99, pp. 235–394. (Cited on page 10.)

Beverloo, W., Leniger, H. and Van de Velde, J. (1961). The flow of granular solids through orifices. *Chemical Engineering Science*, vol. 15, pp. 260–269. (Cited on page 58.)

Blazynski, T. (1983). *Applied Elasto-Plasticity of Solids*. MacMillan Press, London, England. (Cited on page 285.)

Bohatier, C. and Nouguier, C. (1999). *Numerical Modelling of Large Deformations in Soils: Continuum or Granular Medium*. Energy Sources Technology Conference & Exhibition, ETCE99-6713, ASME. (Cited on pages 3, 9, and 14.)

Bohatier, C. and Nouguier, C. (2000). Dynamic soil-tool interaction forces and flow state. In: *International Conference on Applied Mechanics*, pp. 294–299. Durban, South Africa. (Cited on pages 3 and 95.)

Boresi, A. and Chong, K. (2000). *Elasticity in Engineering Mechanics*. 2nd edn. John Wiley & Sons, Inc., New York. (Cited on pages 4 and 212.)

Brackbill, J.U., Kothe, D.B. and Ruppel, H.M. (1988). Flip: A low-dissipation, particle-in-cell method for fluid flow. *Comput. Phys. Commun*, vol. 48, pp. 25–38. (Cited on pages 20 and 261.)

Brackbill, J.U. and Ruppel, H.M. (1988). Flip: A method for adaptively zoned, particle-in-cell calculations in two dimensions. *J. Comput. Phys.*, vol. 65, pp. 314–343. (Cited on pages 10 and 261.)

Brown, C., Lahlouh, E. and Rotter, J. (2000). Experiments on a square planform steel silo. *Chemical Engineering Science*, vol. 55, pp. 4399–4413. (Cited on pages 131 and 133.)

Burgess, D., Sulsky, D. and Brackbill, J.U. (1992). Mass matrix formulation of the FLIP particle-in-cell method. *J. Comput. Phys.*, vol. 103, pp. 1–15. (Cited on pages 11, 19, 260, and 261.)

Cerrolaza, M., Sulem, J. and Elbied, A. (1999). A cosserat non-linear finite element analysis software for blocky structures. *Advances in Engineering Software*, vol. 30, pp. 69–83. (Cited on page 7.)

Chen, Z., Hu, W., Shen, L., Xin, X. and Brannon, R. (2002). An evaluation of the MPM for simulating dynamic failure with damage diffusion. *Engineering Fracture Mechanics*, vol. 69, pp. 1873–1890. (Cited on pages 22 and 265.)

Chi, L. and Kushwaha, R.L. (1991). Three-dimensional, finite element interaction between soil and simple tillage tool. *Transactions of the ASAE*, vol. 32, no. 2, pp. 361–366. (Cited on page 9.)

Cleary, P.W., Metcalfe, G. and Liffman, K. (1998). How well do discrete element granular flow models capture the essentials of mixing processes? *Applied Mathematical Modelling*, vol. 22, pp. 995–1008. (Cited on page 2.)

Cleary, P.W. and Sawley, M.L. (1999 6–8 December). Three-dimensional modelling of industrial granular flows. In: *Second International Conference on CFD in the Minerals and Process Industries*. CSIRO, Melbourne, Australia. (Cited on page 3.)

Cleary, P.W. (1997 September). Modelling industrial granular flows for draglines and centrifugal mills. *Australian Journal of Mining*. (Cited on page 3.)

Cleary, P.W. (1998 Jun*a*). Draglines, ball mills, commodity sampling and other industrial applications: Modelling using object oriented discrete element methods. In: *World Congress on Particle Technology 3*. (Cited on page 3.)

Cleary, P.W. (1998*b*). The filling of dragline buckets. *Mathematical Engineering in Industry*, vol. 7, no. 1, pp. 1–24. (Cited on pages 14 and 126.)

Cleary, P.W. (2000). Dem simulations of industrial particle flows: case studies of dragline excavators, mixing in tumblers and centrifugal mills. *Powder Technology*, vol. 109, pp. 83–104. (Cited on page 3.)

Coetzee, C.J. (2000). *Forced Granular Flow*. Msc Thesis Mechanical Engineering, University of Stellenbosch, Stellenbosch, South Africa. (Cited on pages xii, xvi, 3, 4, 14, 90, 91, 92, 93, 94, 95, 105, 108, 117, 124, and 132.)

Cook, R.D., Malkus, D.S. and Plesha, M.E. (1989). *Concepts and Applications of Finite Element Analysis*. 3rd edn. John Wiley & Sons. (Cited on pages 224, 226, 233, 261, and 267.)

Cramer, H., Findeiss, R., Steinl, G. and Wunderlich, W. (1999). An approach to the adaptive finite element analysis in associated and non-associated plasticity considering localization phenomina. *Comput. Methods Appl. Mech. Engrg*, vol. 176, pp. 187–202. (Cited on pages 7 and 9.)

Cundall, P.A. and Strack, O.D.L. (1979). A discrete numerical method for granular assemblies. *Geotechnique*, vol. 29, no. 1, pp. 47–65. (Cited on pages 2 and 3.)

Dai, C., Muhlhaus, H.-B., Meek, J. and Duncan Fama, M. (1996). Modelling of blocky rock masses using the cosserat method. *Int. J. Rock Mech. Min. Sci. & Geomech. Abstr*, vol. 33, pp. 425–432. (Cited on page 6.)

de Borst, R. (1991). Simulation of strain localization: A reappraisal of the cosserat continuum. *Engrg. Comput.*, vol. 8, pp. 317–332. (Cited on pages 5, 9, 26, 309, 312, 316, and 320.)

de Borst, R. (1993). A generalisation of j2-flow theory for polar continua. *Comp. Methods Appl. Mech. Engrg.*, vol. 103, pp. 347–362. (Cited on pages 5, 7, 26, 309, 317, and 322.)

Dierckx, P. (1996). *Curve and Surface Fitting with Splines*. Oxford University Press Inc., New York. (Cited on page 276.)

Dietsche, A., Steinmann, P. and William, K. (1993). Micropolar elastoplastcity and its role in localization. *International Journal of Plasticity*, vol. 9, pp. 813–831. (Cited on page 212.)

Eringen, C. (1999). *Microcontinuum Field Theories, I: Foundations and Solids*. Springer, New York. (Cited on pages 4 and 5.)

Esterhuyse, S. (1997). *The influence of Geometry on Dragline Bucket Filling Performance*. Master's thesis, University of Stellenbosch. (Cited on page 13.)

Fatemi, J. and van Keulen, F. (2002 July, 7-12). Finite element analysis of bone structures based on micropolar continuum theory. In: Mang *et al.* (2002). Online at http://wccm.tuwien.ac.at. (Cited on page 7.)

Favier, J.F., Abbaspour-Fard, M.H., Kremmer, M. and Raji, A.O. (1999). Shape representation of axi-symmetrical, non-spherical particles in discrete element simulation using multi-element model particles. *Engineering Computations*, vol. 16, no. 4, pp. 467–480. (Cited on page 2.)

Finnie, I. (1960). Erosion of surfaces by solid particles. *Wear*, vol. 3, pp. 87–103. (Cited on page 126.)

Finnie, I. (1972). Some observations on the erosion of ductile metals. *Wear*, vol. 19, pp. 81–90. (Cited on page 126.)

FLAC (1998). *Fast Lagrangian Analysis of Continua: Theory and Background*. Available at: `www.itascacg.com` (Cited on pages xi, xv, 24, 25, 30, 31, 50, 51, 268, 269, 284, 287, 290, 294, 296, 298, 302, 304, 305, and 307.)

Frederick, D. and Chang, T.S. (1972). *Continuum Mechanics*. Scientific Publishers, Inc., Cambridge. (Cited on pages 4, 145, and 165.)

Gerald, C. and Wheatley, P. (1999). *Applid Numerical Analysis*. six edn. Addison-Wesley Longman, New York, USA. (Cited on pages 315 and 321.)

Goh, A.T.C. (1993). Behaviour of cantilever retaining walls. *Journal of Geotechnical Engineering*, vol. 119, no. 11, pp. 1751–1771. (Cited on page 9.)

Grisso, R., Yasin, M. and Kocher, M. (1996). Tillage implement forces operating in silty clay loam. *Transactions of the ASAE*, vol. 39, pp. 1977–1982. (Cited on page 95.)

Hansen, J. (1961). *Earth pressure calculation*. The Danish Technical Press, Copenhagen. (Cited on page 59.)

Harlow, F.H. (1964). The particle-in-cell computing method for fluid dynamics. *Methods for Computational Physics*, vol. 3, pp. 319–343. (Cited on page 11.)

Hassenpflug, W.C. (1993). Matrix tensor notation Part I. Rectilinear orthogonal coordinates. *Comput. Math. Appl.*, vol. 26, no. 3, pp. 55–93. (Cited on pages 16, 145, 215, and 270.)

Herrmann, H. (1999). Institute for computer applications: Physics on supercomputers. Tech. Rep., University of Stuttgart, ICA1 Annual Report. (Cited on page 4.)

Iordache, M.M. and Willam, K., . (1998). Localized failure analysis in elastoplastic cosserat continua. *Comput. Methods Appl. Mech. Engrg.*, vol. 151, pp. 559–586. (Cited on pages 7, 9, 208, and 210.)

Itasca (1999). *PFC2D: User Manual, Theory and Background, Version 2.0*. (Cited on page 94.)

Jaky, J. (1944 October). The coefficient of earth pressure at rest. *Journal for Society of Hungarian Architects and Engineers*, pp. 355–358. (Cited on pages 30 and 79.)

Johnson, G.R. and Beissel, S.R. (1996). Normalized smoothing functions for sph. *International Journal for Numerical Methods in Engineering*. (Cited on page 10.)

Johnson, W. and Mellor, P.B. (1983). *Engineering Plasticity*. Ellis Horwood Ltd., Southampton, Great Britain. (Cited on page 286.)

Kachanov, L.M. (1971). *Foundations of the theory of plasticity*. North-Holland Publishing Company, Amsterdam, London. (Cited on page 286.)

Karlsson, T., Klisinski, M. and Runesson, K. (1998). Finite element simulation of granular material flow in plane silos with complicated geometry. *Powder Technology*, vol. 99, pp. 29–39. (Cited on page 131.)

Kulhawy, F. and Mayne, P. (1990). *Manual on Estimating Soil Properties for Foundation Design*, final report edn. (Cited on page 89.)

Kunar, R.R., Beresford, P. and Cundall, P. (1977). A tested soil-structure model for surface. Roorkee University, Meerut, India. (Cited on page 28.)

Liu, W.K., Jun, S. and Zhang, Y.F. (1995). Reproducing kernel particle methods. *International Journal for Numerical Methods in Engineering*, vol. 20, pp. 1081–1106. (Cited on page 10.)

Lucy, L.B. (1977). A nummerical approach to the testing of the fission hypothesis. *The Astronomical Journal*, vol. 82, no. 12, pp. 1013–1024. (Cited on page 10.)

Luth, H. and Wismer, R. (1971). Performance of plane soil cutting blades in sand. *Transactions of the ASAE*, p. 255. (Cited on page 95.)

Lysmer, J. and Kuhlemeyer, R. (1969). Finite dynamic model for infinite media. *Journal of Engineering Mechanics*, vol. 95, pp. 859–877. (Cited on page 28.)

Malvern, L.E. (1969). *Introduction to the Mechanics of a Continuum Medium*. Prentice-Hall, Inc., Englewood Cliffs, New Jersey. (Cited on page 4.)

Mang, H., Rammerstorfer, F. and Eberhardsteiner, J. (eds.) (2002 July, 7-12). *Fifth World Congress on Computational Mechanics, WCCM V*. TU Vienna, Vienna, Austria. Online at http://wccm.tuwien.ac.at. (Cited on pages 328 and 334.)

Martinez, M., Alfaro, I. and Doblare, M. (2002). Simulation of axisymmetric discharging in metallic silos. analysis of the induced pressure distribution and comparison with different standards. *Engineering Structures*, vol. 24, pp. 1561–1574. (Cited on page 131.)

Masson, S. and Martinez, J. (2000). Effect of particle mechanical properties on silo flow and stress from distinct element simulations. *Powder Technology*, vol. 109, pp. 164–178. (Cited on page 131.)

Mendelson, A. (1968). *Plasticity: Theory and Application*. Macmillan, New York. (Cited on pages 285, 286, and 292.)

Mindlin, R.D. and Deresiewicz, H. (1953). Elastic spheres in contact under varying oblique forces. *Trans. ASME, Series E, Journal of Applied Mechanics*, vol. 20, p. 327. (Cited on page 3.)

Mindlin, R.D. (1949). Compliance of elastic bodies in contact. *Trans. ASME, Series E, Journal of Applied Mechanics*, vol. 16, p. 259. (Cited on page 3.)

Mindlin, R.D. (1964). Micro-structure in linear elasticity. *Arch. Rational Mech. Anal.*, vol. 16, pp. 51–78. (Cited on pages 5 and 212.)

Monaghan, J.J. (1982). Why particle methods work. *SIAM Journal of Scientific and Statistical Computing*, vol. 3, no. 3, pp. 422–. (Cited on page 10.)

Monaghan, J.J. (1988). An introduction to sph. *Computer physics Communications*, vol. 48, pp. 89–96. (Cited on page 10.)

Muhlhaus, H.B., Sakaguchi, H., Moresi, L. and Fahey, M. (2000 Berlin). Discrete and continuum modelling of granular materials. In: ZZ: (2000). (Cited on pages 11 and 14.)

Muhlhaus, H.B. and Vardoulakis, I. (1987). The thickness of shear bands in granular materials. *Geotechnique*, vol. 37, pp. 271–283. (Cited on pages 6, 7, 27, 109, 312, 318, and 323.)

Muhlhaus, H. (1987). Berucksichtigung von inhomogenitaten im gebirge im rahmen einer kontinuumstheorie. Tech. Rep. 106, Intitutes fur Boden- und Felsmechanik, Universitat Karlsruhe. (Cited on pages 26, 27, 322, and 323.)

Muhlhuas, H.B. and Hornby, P. (1997). On the reality of antisymmetric stresses in fast granular flows. In: *IUTAM Symposium on Mechanics of Granular and Porous Materials*, pp. 299–311. Kluwer Academic Publishers, Netherlands. (Cited on page 7.)

Murray, E. and Geddes, J. (1989). Resistance of passive inclined anchors in cohesionless medium. *Geotechnique*, vol. 39, no. 3, pp. 417–431. (Cited on pages 75 and 76.)

Nayroles, B., Touzet, G. and Villon, P. (1992). Generalizing the finite element method: diffuse approximation and diffuse elements. *Computational Mechanics*, vol. 10, pp. 307–318. (Cited on page 10.)

Nouguier, C., Bohatier, C., Moreau, J.J. and Radjai, F. (2000). Force fluctuations in pushed granular material. *Granular Matter*, vol. 2, pp. 171–178. (Cited on page 3.)

Oda, M. (1993). Micro-fabric and couple stress in shear bands of granular materials. In: Behringer, R.P. and Jenkins, J.T. (eds.), *Powders & Grains 97*, pp. 161–167. Balkema, Rotterdam. (Cited on page 6.)

Perumpral, J., Chance, L., Woeste, F. and Desai, C. (1980). A matrix method for force and moment analysis on a tillage tool. *Transactions of the ASAE*, p. 1072. (Cited on page 59.)

Perumpral, J., Grisso, R. and Desai, C. (1983). A soil-tool model based on limit equilibrium analysis. *Transactions of the ASAE*, p. 991. (Cited on page 59.)

Phillips, J., Price, G., Fry, S., Arcziscewski, T. and DeMonsabert, S. (1998). An object-oriented approach to numerical methods: the regula falsi method for solving equations with tight tolerances for environmental applications. *Journal of Hazardous Materials*, vol. B:63, pp. 145–162. (Cited on page 322.)

Piegl, L. and Tiller, W. (1997). *The Nurbs Book*. 2nd edn. Springer-Verlag. (Cited on page 276.)

Pilkey, W.D. and Wunderlich, W. (1994). *Mechanics of Structures: Variational and Computational Methods*. CRC Press, Inc., Boca Raton, Florida, USA. (Cited on page 233.)

PLAXIS (2 June 2003). Finite element code for soil and rock analyses, balkema, rotterdam. http://www.plaxis.com. (Cited on page 81.)

Poulos, H. and Davis, E. (1974). *Elastic Solutions for Soil and Rock Mechanics*. Wiley and Sons, Inc., New York. (Cited on page 69.)

Reimbert, M. and Reimbert, A. (1976). Silos, theory and practice. *Transactions Tech. Publications, Clausthal, Germany*. (Cited on page 95.)

Rhodes, M. (1998). *Introduction to Particle Technology*. John Wiley and Sons Ltd, Chichester, England. (Cited on page 1.)

Rilling, B. (1994). *Untersuchungen zur Grenztragfahigkeit bindiger Scuttstoffe am Beispiel von Losslehm*. Ph.D. thesis, Institute for Geotechnical Engineering, University of Stuttgart. (Cited on pages xii, 81, and 82.)

Rowe, R. and Davis, E. (1982*a*). The behaviour of anchor plates in sand. *Geotechnique*, vol. 32, no. 1, pp. 25–41. (Cited on pages 71, 74, 76, and 79.)

Rowe, R. and Davis, E. (1982*b*). The behaviour of anchor plates in sand. *Geotechnique*, vol. 32, no. 1, pp. 9–23. (Cited on pages 71, 76, and 79.)

Rowlands, J.C. (1991). *Dragline Bucket Filling*. Ph.D. thesis, University of Queensland, Queensland, Australia. (Cited on pages xiii, 92, 124, and 125.)

Schreyer, H.L., Sulsky, D.L. and Zhouc, S.J. (2002). Modeling delamination as a strong discontinuity. *Comput. Methods Appl. Mech. Engrg.*, vol. 191, pp. 2483–2507. (Cited on page 12.)

Shen, Y.-L., Li, W., D.L., S. and Schreyer, H. (2000). Localization of plastic deformation along grain boundaries in a hardening material. *International Journal of Mechanical Sciences*, vol. 42, pp. 2167–2189. (Cited on page 12.)

Siemens, J., Weber, J. and Thornburn, T. (1965). Mechanics of soil as influenced by model tillage tools. *Transactions of the ASAE*, p. 1. (Cited on page 95.)

Silling, S. (1992). An algorithm for eulerian simulation of penetration. *New Methods in Transient Analysis, ASME*, vol. PVP-Vol 246/AMD-Vol 143, pp. 123–125. (Cited on page 34.)

Sokolovski, V. (1954). *Statics of soil media*. Butterworth Scientific Publishers, London. (Cited on pages 59, 103, and 295.)

Steinmann, P. (2000 Berlin). A view on the variational setting of micropolar continua. In: ZZ: (2000). (Cited on pages 5 and 6.)

Sulsky, D. and Brackbill, J.U. (1991). A numerical method for suspension flow. *Journal of Computational Physics*, vol. 96, pp. 339–368. (Cited on pages 276, 277, and 279.)

Sulsky, D., Chen, Z. and Schreyer, H.L. (1994). A particle method for history-dependent materials. *Comput. Methods Appl. Mech. Engrg.*, vol. 118, pp. 179–196. (Cited on pages 11 and 44.)

Sulsky, D. and Schreyer, H. (1993). A particle method with large rotations applied to the penetration of history-dependent materials. *Advances in Numerical Simulation Techniques for Penetration and Perforation of Solids, ASME, AMD*, vol. AMD-Vol 171, pp. 95–102. (Cited on pages x, 11, 12, 32, 33, and 34.)

Sulsky, D. and Shreyer, H. (1996). Axisymmetric form of the material point method with application to upsetting and taylor impact problems. *Computer Methods in Applied Mechanics and Engineering*, vol. 139, pp. 409–429. (Cited on page 11.)

Sulsky, D., Zhou, S.J. and Schreyer, H.L. (1995). Application of a particle-in-cell method to solid mechanics. *Computer Physics Communications*, vol. 87, pp. 236–252. (Cited on pages 9, 10, 12, 34, 230, 253, 254, and 258.)

Swegle, J.W., Hicks, D.L. and Attaway, S.W. (1995). Smooth particle hydrodynamics stability analysis. *Journal of Computational Physics*, vol. 116, pp. 123–134. (Cited on pages 10 and 12.)

Tejchman, J. and Bauer, E. (1996). Numerical simulation of shear band formation with a polar hypoplastic constitutive mode. *Computers and Geotechnics*, vol. 19, no. 3, pp. 221–244. (Cited on pages 7 and 9.)

Tejchman, J. and Gudehus, G. (1993). Silo-music and silo-quake experiments and a numerical cosserat approach. *Powder Technology*, vol. 76, pp. 201–212. (Cited on page 7.)

Tejchman, J. and Wu, W. (1996). Numerical simulation of shear band formation in a hypoplastic constitutive model. *Computers and Geotechnics*, vol. 18, no. 1, pp. 71–84. (Cited on page 6.)

Tejchman, J. (1996). Numerical simulation of filling in silos with a polar hypoplastic constitutive model. *Powder Technology*, vol. 96, pp. 227–239. (Cited on pages 7, 9, and 14.)

Tejchman, J. (1997). *Modelling of shear localisation and autogeneous dynamic effects in granular bodies*. Ph.D. thesis, des Institutes fur Bodenmechanik und Felsmechanik der Universitat Fridericiana in Karlsruhe. (Cited on pages 27, 29, 96, 100, 103, 105, 107, 108, 109, 113, 133, 322, and 324.)

Timoshenko, S.P. and Goodier, J.N. (1970). *Theory of Elasticity, Third Edition*. McGraw-Hill Book Co. (Cited on pages 4 and 40.)

Ting, C., Sills, G. and Wijeyesekera, D. (1994). Development of ko in soft soils. *Geotechnique*, vol. 44, no. 1, pp. 101–109. (Cited on page 30.)

Toupin, R. (1962). Elastic materials with couple-stresses. *Arch. Rational Mech. Anal.*, vol. 11, pp. 385–414. (Cited on page 5.)

Trucano, T. and Grady, D. (1985). Study of intermediate velocity penetration of steel spheres into deep aliminium targets. Technical report sand82-2338, Sandia National Laboratories. (Cited on page 34.)

Vermeer, P.A. and De Borst, R. (1984). Non-associated plasticity for soils, concrete and rock. *Heron*, vol. 29, no. 3. (Cited on pages 103, 134, 285, and 302.)

Walton, O.R. and Braun, R.L. (1986). Viscosity, granular-temperature, and stress calculations for shearing assemblies of inelastic, frictions discs. *Journal of Reology*, vol. 30, no. 5, pp. 949–980. (Cited on page 3.)

Walton, O.R. (1982). Explicit particle dynamics model for granular materials. (Cited on page 2.)

Washizu, K. (1975). *Variational methods in elasticity and plasticity*. Pergamon Press. (Cited on page 234.)

Wieckowski, Z., Youn, S.-K. and Yeon, J.-H. (1999). A particle-in-cell solution to the silo discharging problem. *International Journal for Numerical Methods in Engineering*, vol. 45, pp. 1203–1225. (Cited on pages 11, 20, 265, and 266.)

Wieckowski, Z. (1998). A particle-in-cell method in analysis of motion of a granular material in a silo. *Computational Mechanics: New trends and Applications*. (Cited on pages xi, 11, 54, 56, 57, and 58.)

Wieckowski, Z. (2000). Numerical modeling of silo discharge. Electronic copy obtained from author. (Cited on page 11.)

Wieckowski, Z. (2001 June, 26-29). Analysis of granular flow by the material point method. In: *European Conference on Computational Mechanics*. Cracow, Poland. (Cited on page 11.)

Wieckowski, Z. (2002 July, 7-12). The dynamic analysis of large strain problems by the material point method. In: Mang *et al.* (2002). Online at http://wccm.tuwien.ac.at. (Cited on pages 9 and 11.)

Williams, J.R. and O'Connor, R. (1995 Jul). Discrete element simulation and the contact problem. *Archives of Computational Methods in Engineering*. (Cited on page 2.)

Wood, D.M. (2000). *Constitutive Modelling of Granular Materials, Kolymbas, D. (Editor)*, chap. The role of models in civil engineering, pp. 37–55. Springer-Verlag. (Cited on page 1.)

Wroth, C. (1984). Interpretation of in-situ soil tests. *Geotechnique*, vol. 34, no. 4, pp. 449–489. (Cited on page 89.)

Yang, A.-C. and Hsiau, S.-S. (2001). The simulation and experimental study of granular materials discharged from a silo with the placement of inserts. *Powder Technology*, vol. 120, pp. 244–255. (Cited on page 131.)

Zhao, C., Hobbs, B.E., Muhlhaus, H.B. and Ord, A. (1999). A consistent point-search algorithm for solution interpolation in unstructured meshes consisting of 4-node bilinear quadrilateral elements. *International Journal for Numerical Methods in Engineering*, vol. 45, pp. 1509–1526. (Cited on page 262.)

(2000 Berlin). *Continuous and Discontinuous Modelling of Cohesive Frictional Materials, Lecture Notes in Physics: Vol. 568*, Continuous and Discontinuous Modelling of Cohesive Frictional Materials, Lecture Notes in Physics: Vol. 568. Springer. (Cited on pages 330 and 332.)